

# **Oxygen Reduction and Evolution Reactions in Alkaline and Non-aqueous Electrolytes for Li-Air Batteries: RRDE and DEMS Investigations**

**Dissertation**

zur

Erlangung des Doktorgrades (Dr. rer. nat.)

der

Mathematisch-Naturwissenschaftlichen Fakultät

der

Rheinischen Friedrich-Wilhelms-Universität Bonn

vorgelegt von

**Hatem M. A. Amin**

aus

Beheira, Ägypten

Bonn, 2016



Angefertigt mit Genehmigung der Mathematisch-Naturwissenschaftlichen Fakultät der  
Rheinischen Friedrich-Wilhelms-Universität Bonn

Erster Gutachter: Prof. Dr. Helmut Baltruschat

Zweiter Gutachter: Prof. Dr. Thomas Bredow

Fachnaher Gutachter: Prof. Dr. Werner Mader

Fachfremder Gutachter: Prof. Dr. Andreas Hense

Tag der mündlichen Prüfung: 07.11.2016

Erscheinungsjahr: 2016



*To my motherland, my parents, my  
brothers and my family  
In remembrance of my grandfather*



*"Was wir wissen, ist ein Tropfen; was wir nicht wissen, ein Ozean"*  
*Isaac Newton*

*"If we knew what it was we were doing, it would not be called research, would it?"*

*Albert Einstein*



## **Acknowledgement**

*The work presented in this thesis and realized at Bonn University could not have seen the light without collaboration and support of many people. First of all, I would like to express my deep sense of gratitude to my research supervisor Prof. Dr. Helmut Baltruschat for giving me the opportunity to share his scientific knowledge. I am extremely indebted to his rich critical insights, selflessness and continuous support at all stages of the work. No time was too bad to ask him for help. His encouragement from the beginning to discuss in German has an important role in my language improvement. Thanks for the scientific and networking experience he has given to me.*

*Thanks to all the members of the Ph.D. Jury: Prof. Dr. Thomas Bredow, Prof. Dr. Werner Mader and Prof. Dr. Andreas Hense for their interest and availability to evaluate my thesis.*

*I am grateful to all partners of the LuLi project for the successful collaboration and fruitful information during the project period.*

*I am thankful to the Ministry of Higher Education of Egypt and DAAD for the Ph.D. scholarship (GERLS) I received to make this project possible, and I would like to express my thanks to the employee of DAAD in Cairo and in Bonn for their timely administrative support.*

*I would like to deeply thank everyone in my research group at Bonn University, who supported my research, and I had unforgettable time with them; Ali, Christoph B., Christoph M., Ehab, Claudia, Zan, Mehdi, Shahid, Philip. R., Philipp H., Sevda, Soltani, Dilek, Martina, Jan, Akos, Ana, Nikolay, Markus, Pawol, Sergi, prof. Magdi, Ahmed, Annchristin, Da and special thanks to Dr. Ernst for his suggestions in RRDE evaluations, Elke for her kind help in the lab and providing me with new German expressions, Carole for her kind help in administration, and Knut for his IT support. I will always remember the moments we shared together.*

*My gratitude extends to the members of the fine mechanics, electronic and glass blowing workshops for their technical support. Especially, I would like to express my deepest appreciation to Mr. Königshoven for his friendly and professional support in the build-up of the new DEMS cell, without his valuable suggestions, this would not have been possible, and the support from Mr. Paulig, Mr. Böhmer, Mr. Koll is also grateful.*

*I am thankful to my former professors, who introduced me the fascinating field of electrochemistry during my M.Sc. and their encouragement during my application for a Ph.D. stipend; Prof. Ahmed, Prof. Nada, Prof. Wahid, and all Chemistry Dept. staff of Cairo Univ.*

*Special thanks to my friends and housemates in Bonn for all fun we had together, and for your friendship; Rihan, Ahmed, Ibrahim, Marie, Mr. Stocker, Samer, Amar, Ali, Pietro, Mihau, Ana, my DAAD colleagues and football friends. I am gratitude to DAAD-Freundskreis and the international office of Bonn Uni. for the nice events, they organized.*

*Words are insufficient to express my gratitude to my parents and my brothers for their continuous encouragement, affection and motivation. I am indebted to my parents for all endless love, prayers and sacrifices they have made since my birth. They, although far away, are always with me, and to them, I dedicate this thesis. My deep thanks are as well extending to all my relatives, friends and well wishers.*

*Above all, praises and thanks to Almighty Allah.*



## Abstract

Due to the worldwide growing energy demand and depletion of fossil fuel resources, sustainable renewable energy conversion and storage systems have to be developed. One of the promising possibilities is the rechargeable battery. Li-air batteries could be a key technology for automotive applications because they could theoretically provide high energy density that cannot be reached with the state-of-the-art Li-ion batteries (3-5 times higher). However, this technology is still facing some challenges such as the poor round-trip efficiency, high overpotential and electrolyte instability. Despite the intensive work in the last decade, the initial hope of a rapid realization of such high energy battery is not fulfilled so far. This is related to the use of an organic electrolyte in Li-air battery, and the fundamental investigations of the electrochemical reactions such as oxygen reduction (ORR) and evolution (OER) in such electrolytes were rarely carried out, and are not well understood. Therefore, comprehensive understanding of these reactions in an aprotic electrolyte is a pre-requisite for achieving the targeted goal of a reversible Li-air battery in order to improve their performance. In this work, two main issues are studied: *i*) development of an efficient carbon-free bifunctional catalyst for the air electrode in alkaline media, where the concept of aqueous or mixed nonaqueous-aqueous battery could be possible with a protective membrane for the Li-anode. *ii*) mechanistic, kinetic and quantitative investigations of ORR/OER in an aprotic electrolyte for the concept of non-aqueous battery.

This thesis consists of an *introduction* about Li-air batteries and electrocatalysis, then a *theoretical brief* of the fundamentals, followed by a description of the *experimental* methods. Subsequently, the *results and discussion* section consists of 6 chapters, including my peer-reviewed scientific publication together with other chapters of the rest of the work. The thesis is then closed with the *summary and future perspectives*.

The introduction includes the basics and configurations of the battery and how it works. A literature survey follows on the early studies in aprotic Li-O<sub>2</sub> battery using carbonate-based electrolyte, recent developments in other organic electrolytes and the suggested mechanism. The second part of the introduction reviews the kinetics and mechanisms of ORR/OER in aqueous electrolytes with a survey on the catalysts, which have been recently reported. The results and discussion section starts with chapter 4 (as a publication) on the investigation of an efficient bifunctional catalyst based on Ag+Co<sub>3</sub>O<sub>4</sub> for ORR/OER in alkaline media. Results revealed that Co<sub>3</sub>O<sub>4</sub> is a promising candidate for OER, although it has lower activity for ORR. On the other hand, silver (Ag) is a good substitute to carbon since carbon faces corrosion problems. Thus, a combination of both in one mixture showed better activity than its single

components along with good stability. The optimization of the composition of the mixed catalyst is described. Ag+Co<sub>3</sub>O<sub>4</sub> mixed catalyst containing 10-20 wt% of Co<sub>3</sub>O<sub>4</sub> showed the optimum activity. The kinetics is studied using rotating ring-disc electrode (RRDE) technique. Oxygen evolution is monitored using differential electrochemical mass spectrometry (DEMS). In chapter 5, surface and XPS analyses are presented to understand the origin of such synergistic effect between Ag and Co<sub>3</sub>O<sub>4</sub>. Further investigations on the activity of Ag+perovskite catalyst and the role of the support (Ni vs. Ag) are shown in chapter 6. Additional results are presented in appendix A.

In chapter 7, to better understand the mechanism of OER on Co<sub>3</sub>O<sub>4</sub> and mixed catalyst, DEMS measurements together with isotope labeling are conducted, and the oxygen exchange process in the lattice oxygen is inferred. In this part, a new DEMS cell is developed, for the first time, for application of small-volume electrolytes and massive electrodes.

The last two chapters are devoted to measurements in aprotic electrolytes for Li-O<sub>2</sub> system. RRDE and DEMS are used to characterize the reactions in Tetraglyme G4, DMSO and their mixture. The significant role of the solvent properties (e.g. donor number) on the lifetime of LiO<sub>2</sub> intermediate and the mechanism is assessed (chapter 8). DEMS enabled us not only to detect the main products and by-products but also the number of electrons transferred per oxygen molecule consumed/evolved upon reduction/oxidation. Moreover, the Au-sputtered membrane electrode is successful as a gas diffusion electrode and the results showed the formation and decomposing of Li<sub>2</sub>O<sub>2</sub> as the main discharge product. The catalytic activity of Co<sub>3</sub>O<sub>4</sub> catalyst in DMSO is reported. In chapter 9, a novel electrolyte based on 1,3-dimethylimidazolidinone solvent is investigated for the first time for Li-O<sub>2</sub> battery. The kinetics and possible mechanism are reported. The formation of Li<sub>2</sub>O<sub>2</sub> is detected despite the side reactions. Although further research has to be done, this better understanding of the processes could help in the development of strategies for the realization of such Li-air batteries.

## Zusammenfassung

Aufgrund des weltweit wachsenden Energiebedarfs und der Erschöpfung fossiler Brennstoffe müssen nachhaltige, erneuerbare Energiewandlungs- und Speichersysteme entwickelt werden. Hierfür stellen wiederaufladbare Batterien vielversprechende Möglichkeiten dar. Insbesondere Li-Luft-Batterien könnten eine Schlüsseltechnologie für Automobilanwendungen sein, weil sie höhere (3-5 mal) theoretische Kapazitäten im Vergleich zu herkömmlichen Li-Ionen-Batterien haben. Diese Technologie steht jedoch vor einigen kritischen Herausforderungen wie schlechte Wiederaufladbarkeit, hohe Überspannung und Elektrolytinstabilität. Die aktuelle Forschung konzentriert sich auf zwei Arten von Li-Luft-Batterien, nämlich aprotische und wässrige Elektrolyt-Batterien. Trotz der intensiven Arbeit im letzten Jahrzehnt sind die grundlegenden elektrochemischen Reaktionen wie Sauerstoffreduktion (ORR) und -entwicklung (OER) in aprotischen Elektrolyten nicht gut verstanden. Da bei aprotischen Elektrolyten die Entladungsprodukte der ORR die Elektrode blockieren und dadurch die Kapazität der Batterie begrenzen, stellen Li-Luft-Batterien mit wässrigem Elektrolyt eine Alternative dar. Die vorliegende Arbeit befasst sich mit zwei Hauptthemen: i) Entwicklung eines effizienten, kohlenstofffreien bifunktionellen Katalysators für die Luftpole in alkalischen Medien. ii) Mechanistische, kinetische und quantitative Untersuchungen von ORR/OER in aprotischen Elektrolyten.

Diese Arbeit besteht aus einer Einführung in die Grundlagen und den Aufbau der Batterie, die neuesten Entwicklungen in aprotischen Elektrolyten und die vorgeschlagenen Mechanismen sowie Elektrokatalyse der ORR/OER in wässrigen Elektrolyten mit einer Übersicht über neue Katalysatoren. Dann wird eine theoretische Kurzfassung der Grundlagen, gefolgt von einer Beschreibung der experimentellen Methoden, dargestellt. Anschließend werden die Ergebnisse und die Diskussion in 6 Kapiteln dargestellt. Die Arbeit wird dann mit der Zusammenfassung und einem Ausblick geschlossen.

Die Ergebnisse und Diskussion beginnen mit Kapitel 4 (schon veröffentlicht, *Electrochimica Acta* 2015, 151, 332) zur Untersuchung eines effizienten bifunktionellen Katalysators auf der Basis von Ag + Co<sub>3</sub>O<sub>4</sub> für ORR/OER in alkalischen Elektrolyten. Interessanterweise zeigte eine Kombination von beiden Komponenten eine höhere Aktivität als die einzelnen Komponenten und darüber hinaus eine gute Stabilität. Ag + Co<sub>3</sub>O<sub>4</sub>-Mischkatalysator, der 10-20 Gew.% Co<sub>3</sub>O<sub>4</sub> enthielt, zeigte die optimale Aktivität. Die rotierende Ringscheibenelektrode (RRDE) zeigte eine vernachlässigbare Bildung des Peroxid-Intermediates. Die Sauerstoffentwicklung wurde mittels differentieller elektrochemischer Massenspektrometrie (DEMS) nachgewiesen. In Kapitel 5 werden Oberflächen- und XPS-Analysen gezeigt, um den

Ursprung eines solchen synergistischen Effekts zwischen Ag und  $\text{Co}_3\text{O}_4$  zu verstehen. Weitere Untersuchungen über die Aktivität des Ag+Perowskit-Katalysators und die Rolle des Trägers (Ni und Ag) sind in Kapitel 6 dargestellt.

Zum besseren Verständnis des Mechanismus der OER auf  $\text{Co}_3\text{O}_4$  und Mischkatalysatoren wurden DEMS-Messungen zusammen mit Isotopenmarkierung durchgeführt und der Austausch des Gittersauerstoffs nachgewiesen. Hierfür wurde eine DEMS-Zelle mit kleinem Elektrolytvolumen für die Verwendung von massiven Elektroden entwickelt.

Die letzten beiden Kapitel widmen sich Messungen in aprotischen Elektrolyten für das Li-O<sub>2</sub>-System. RRDE und DEMS wurden verwendet, um die Reaktionen in Tetraglyme G4, DMSO und deren Gemische zu charakterisieren. Die signifikante Rolle der Lösungsmiteigenschaften (z.B. Donorzahl) auf den Mechanismus wird in Kapitel 8 evaluiert. DEMS ermöglichte es uns, nicht nur die Hauptprodukte und Nebenprodukte zu detektieren, sondern auch die Anzahl der übertragenen Elektronen pro Sauerstoffmolekül während der Entladung und Ladung. Die reversible Bildung von  $\text{Li}_2\text{O}_2$  als Hauptentladungsprodukt wurde trotz der Nebenreaktionen nachgewiesen. Die katalytische Aktivität des  $\text{Co}_3\text{O}_4$  Katalysators in DMSO wird gleichfalls beschrieben. In Kapitel 9 wird ein neuartiger Elektrolyt auf Basis von 1,3-Dimethylimidazolidinon-Lösungsmittel erstmals für Li-O<sub>2</sub>-Batterien untersucht. Obgleich weitere Forschungen durchgeführt werden müssen, könnte das bessere Verständnis der Prozesse bei der Entwicklung von Strategien für die Realisierung solcher Li-Luft-Batterien helfen.

# TABLE OF CONTENTS

<b>Acknowledgment</b> .....	I
<b>Abstract</b> .....	III
<b>Zusammenfassung</b> .....	V
<b>Table of contents</b> .....	VII
<b>List of abbreviations</b> .....	XI
<b>List of notations</b> .....	XII
<b>Motivation and aim of the work</b> .....	XIII

## 1. Introduction

1.1. Lithium-ion batteries.....	1
1.2. Lithium-air batteries.....	3
1.2.1. How does Li-O <sub>2</sub> battery work? .....	5
1.2.1.1. Components of Li-air battery.....	5
1.2.1.2. Designs of Li-air battery.....	5
1.2.1.3. Reactions in Li-air battery.....	7
1.2.2. Rechargeability parameters and the role of electrocatalyst.....	9
1.2.3. Aprotic electrolyte is a key challenge.....	10
1.2.4. The search for a stable electrolyte: Influence of solvent and salt.....	11
1.2.5. Growth mechanism of Li <sub>2</sub> O <sub>2</sub> .....	12
1.3. ORR and OER in alkaline media: Electrocatalysis.....	13
1.3.1. Electrochemical oxygen reactions-Acids vs. Alkaline medium: Thermodynamic and kinetic advantages.....	14
1.3.2. Mechanisms of ORR in alkaline media.....	15
1.3.3. Mechanisms of OER in alkaline media .....	17
1.3.4. Mechanistic insights from Tafel slope in aqueous media.....	20
1.3.5. Survey of electrocatalysts for ORR and OER in alkaline media.....	20
1.3.6. Support effect in the catalyst.....	23
1.4. References.....	24

## 2. Theoretical background

2.1. Electrode kinetics.....	31
2.1.1. Interface structure.....	31
2.1.2. Activation control.....	32
2.2. Mass transport in electrochemistry.....	35
2.3. Mechanistic aspects of ORR in aprotic solution from Tafel slope.....	41
2.4. Voltammetric methods.....	44
2.4.1. Cyclic voltammetry (CV) .....	44
2.4.2. Chronoamperometry.....	47
2.4.3. Adsorption in CV.....	47
2.5. Under-potential deposition (UPD).....	47
2.6. Electrochemical impedance spectroscopy (EIS).....	48
2.7. References.....	50

### 3. Experimental

3.1. Chemicals and materials.....	51
3.2. Procedure for undertaking an electrochemical experiment .....	52
3.2.1. The cleaning procedure.....	52
3.2.2. Catalyst-modified electrode preparation.....	52
3.2.3. Electrolyte preparation.....	53
3.3. The potentiostat.....	53
3.4. Rotating Ring-Disc electrode (RRDE).....	54
3.5. Differential electrochemical mass spectrometry (DEMS) .....	58
3.5.1. DEMS setup.....	59
3.5.2. The cells used.....	60
3.5.3. Evaluation of the DEMS data.....	65
3.5.4. Calibration leak experiment.....	65
3.6. Surface characterization .....	67
3.6.1. SEM and EDX.....	67
3.6.2. EC-XPS.....	67
3.6.3. XRD.....	68
3.7. Electrochemical impedance spectroscopy.....	68
3.8. References.....	69

### 4. A Highly efficient bifunctional catalyst for alkaline air-electrodes

#### based on a Ag and Co<sub>3</sub>O<sub>4</sub> hybrid: RRDE & DEMS (publication)

4.1. Introduction.....	72
4.2. Experimental.....	72
4.3. Results and discussion.....	74
4.3.1. Electrochemical properties and performance.....	74
4.3.2. DEMS measurements.....	75
4.3.3. Surface characterization.....	76
4.4. Conclusion.....	78
4.5. References.....	78

### 5. Further characterization of carbon-free Ag+Co<sub>3</sub>O<sub>4</sub> mixed catalyst

#### for ORR/OER: Pb-UPD & XPS

5.1. Introduction.....	81
5.2. Experimental.....	83
5.3. Results .....	84
5.3.1. Electrochemical performance of the catalyst.....	84
5.3.2. XPS analysis.....	88
5.3.3. Electrochemically active surface area estimation: Pb-UPD.....	97
5.3.4. Influence of catalyst loading and electrolyte concentration.....	98
5.4. Discussion.....	101
5.5. Conclusion.....	104
5.6. References.....	104

### 6. Further investigation of various non-precious bifunctional catalysts

#### in alkaline media: Explorative study

6.1. Introduction.....	111
------------------------	-----

6.2.	Investigation of Ag catalysts in alkaline media.....	111
6.3.	Effect of catalyst loading on activity.....	117
6.4.	Effect of concentration and nature of cationic species on activity.....	118
6.5.	Activity on bimetallic Ag/CoO (50/50 w%) catalyst.....	121
6.6.	Kinetic analysis on Ag+Co <sub>3</sub> O <sub>4</sub> mixed catalyst.....	122
6.7.	Stability of the catalysts.....	125
6.8.	Additional surface analysis.....	126
6.9.	Synergistic effect in Ag+perovskite catalyst.....	128
6.10.	Synergistic effect in Ni+Co <sub>3</sub> O <sub>4</sub> catalyst.....	132
6.11.	EIS on Ag, Co <sub>3</sub> O <sub>4</sub> and mixed Ag+Co <sub>3</sub> O <sub>4</sub> catalysts.....	134
6.12.	Conclusion.....	138
6.13.	References.....	139

## **7. Do oxygen atoms in Co<sub>3</sub>O<sub>4</sub> spinel take part in oxygen evolution reaction? Isotope labeling together with a new DEMS cell approach**

7.1.	Introduction.....	141
7.2.	Experimental.....	143
7.3.	Results .....	145
7.3.1.	Co <sub>3</sub> O <sub>4</sub> (40 μm) catalyst with 100 μg cm <sup>-2</sup> loading in 0.1M LiOH .....	146
7.3.2.	Co <sub>3</sub> O <sub>4</sub> (50 nm) catalyst with 200 μg cm <sup>-2</sup> loading in 0.1M LiOH.....	152
7.3.3.	New small-volume DEMS cell: Co <sub>3</sub> O <sub>4</sub> (50 nm) in 20% marked H <sub>2</sub> <sup>18</sup> O solution.....	154
7.3.4.	Co <sub>3</sub> O <sub>4</sub> (50 nm) in 50% marked H <sub>2</sub> <sup>18</sup> O solution using the new small volume DEMS cell.....	156
7.3.5.	Co <sub>3</sub> O <sub>4</sub> (10 μm) in 20% marked H <sub>2</sub> <sup>18</sup> O solution using the new small volume DEMS cell.....	158
7.3.6.	Ag+Co <sub>3</sub> O <sub>4</sub> (10w%) mixed catalyst in 50% marked H <sub>2</sub> <sup>18</sup> O solution using new small volume DEMS cell.....	158
7.4.	Discussion.....	161
7.5.	Conclusion.....	162
7.6.	References.....	165

## **8. Quantitative & mechanistic insights into ORR/OER in DMSO, Tetraglyme and their mixed solvent for Li-O<sub>2</sub> batteries**

8.1.	Introduction.....	175
8.2.	Experimental.....	177
8.3.	Results & discussion.....	178
8.3.1.	Elucidation of reaction mechanism of ORR/OER in DMSO-based electrolyte.....	179
8.3.2.	Determination of diffusion coefficient of superoxide radical using RRDE potential step.....	187
8.3.3.	ORR in TBA <sup>+</sup> /Tetraglyme(G4).....	190
8.3.4.	ORR and OER in a blended G4-DMSO based electrolyte.....	190
8.3.5.	The role of catalyst in DMSO-based electrolyte: Co <sub>3</sub> O <sub>4</sub> catalyst.....	195
8.3.6.	Quantitative investigation of ORR/OER in G4 and G4-DMSO electrolytes: DEMS.....	199
8.3.6.1.	ORR/OER in TBA <sup>+</sup> - and K <sup>+</sup> -containing electrolyte: Calibration of DEMS for O <sub>2</sub> .....	199
8.3.6.2.	ORR and OER in LiClO <sub>4</sub> /G4: Deactivation and reactivation.....	200
8.3.6.3.	ORR and OER in LiClO <sub>4</sub> / G4-DMSO mixed electrolyte.....	204
8.3.6.4.	Gas diffusion electrode experiments.....	206

8.4. Conclusion.....	209
8.5. References.....	210
<b>9. A novel electrolyte based on DMI for ORR/OER in Li-O<sub>2</sub> batteries: RRDE and DEMS insights</b>	
9.1. Introduction.....	225
9.2. Experimental.....	227
9.3. Results & discussion.....	230
9.3.1. Oxygen electrochemistry in TBAClO <sub>4</sub> in DMI: RRDE investigations.....	230
9.3.2. Oxygen electrochemistry in LiClO <sub>4</sub> in DMI: RRDE investigations.....	237
9.3.3. Tafel slope and RRDE chronoamperometry.....	243
9.3.4. Quantitative investigations of ORR/OER in DMI-based electrolyte: DEMS insight.....	246
9.4. Conclusion.....	250
9.5. References.....	251
<b>10. Summary and future directions</b>	259
Appendix A: .....	267
Appendix B: .....	285
List of publications.....	293

## List of abbreviations

ORR	Oxygen reduction reaction
OER	Oxygen evolution reaction
LIB	Lithium-ion battery
CV	Cyclic voltammogram
DEMS	Differential electrochemical mass spectrometry
MSCV	Mass spectrometric cyclic voltammogram
RRDE	Rotating ring-disc electrode
EIS	Electrochemical impedance spectroscopy
FTIR	Fourier transform infrared spectroscopy
GC	Glassy carbon
SEM	Scanning electron microscopy
EDX	Energy dispersive X-ray spectroscopy
XRD	X-ray diffraction
RHE	Reversible hydrogen electrode
UPD	Underpotential deposition
IHP	Inner Helmholtz plane
OHP	Outer Helmholtz plane
rpm	Round per minute
DN	Donor number
GDE	Gas diffusion electrode
XPS	X-ray photoelectron spectroscopy
UHV	Ultrahigh vacuum
PTFE	Poly tetrafluoroethylene
TBA	Tetrabutylammonium
OTf	Triflate
DMI	1,3-dimethylimidazolidinone
G4	Tetraglyme
PC	Propylene carbonate
DMSO	Dimethylsulfoxide
Ag (pc)	Polycrystalline silver
LSF	Lanthanum strontium ferrite
CE	Counter electrode
RE	Reference electrode
WE	Working electrode

## List of Notations

$c$	Concentration
$C$	Coulomb
$D$	Diffusion coefficient
$E$	Potential
$E_{ad}$	Adsorption potential
$t_{ad}$	Adsorption time
$I$	Current
$J$	Current density
$J_L$	Limiting current density
$A$	Ampere or electrode area
$F$	Faraday constant (96485 C/mol)
$N_A$	Avogadro's number ( $6.022 \times 10^{23} \text{ mol}^{-1}$ )
$I_F$	Faradaic current
$I_i$	Ionic current
$K^0, K^*$	Calibration constants
$m/z$	Mass to charge ratio
$n_F$	Total amount of species produced electrochemically
$n_i$	Amount of mass-spectrometrically detected species
$N$	Transfer efficiency
$Q_F$	Faradaic charge (integrated charge)
$Q_i$	Ionic charge (integrated ion current of corresponding mass)
$z$	Number of electrons transferred
$t$	Time
$\tau$	Time constant
$\alpha$	Transfer coefficient
$\delta$	Diffusion layer thickness
$\epsilon$	Dielectric constant
$\omega$	Angular frequency ( $\omega=2\pi f$ ), $f$ is rotation speed in rpm
$\eta$	Overpotential
$\nu$	Kinematic viscosity
$v$	Scan rate
$V$	Volt

## Motivation and aim of the work

The worldwide growing energy demand has become one of the major concerns of the 21<sup>st</sup> century. The international energy agency (IEA) estimated that the world's total primary energy supply in 2013 was 13.5 Mtoe, and oil represented 31% of this amount, and the world's total energy consumption was 9.3 Mtoe, from which 39.9% are oil.[1] Thereby, oil provides the largest part of energy. Unfortunately, the reservoirs of fossil fuels are being depleted. Moreover, from the environmental point of view, the combustion of fossil fuels leads to CO<sub>2</sub> emissions, the major cause of global warming.[2] Nowadays, oil accounts for 34% of the total CO<sub>2</sub> emissions and 37% of the emissions arise from OECD countries. It should be highlighted that an important percentage of CO<sub>2</sub>-emissions arises from the transportation sector. In fact, CO<sub>2</sub> emissions increased dramatically from 23 Mt in 2000 to 32 Mt in 2013,[1] despite the Kyoto protocol. Therefore, the development of renewable and sustainable energy sources is necessary and an urgent need for our society.

For instance, in line with the climate change and the international energy policy, the transportation has to be switched to regenerative energy sources. Therefore, innovative high energy storage and conversion systems have to be developed for future energy supply. One of the central possibilities is the storage of electrical energy in rechargeable batteries. Despite the wide utilization of secondary batteries in today's portable devices, the use of electric automobiles is still limited due to its short range of travel pro "full tank", which is due to the low energy density of the conventional lithium-ion batteries used there. The energy density of the existing batteries, including Li-ion batteries, is not high enough for the car to achieve today's normal travel distance of at least 500 km. Thus, intensive research has been conducted in the last decade on the 4<sup>th</sup> generation of batteries, in particular, Li-air batteries. Li-air batteries have a promising potential as an alternative energy source. The idea is to use air (namely oxygen) as a reagent rather than inserting the required chemicals inside a battery, leading to a lighter battery. They are expected to use cost-effective materials and help environmental balance. Therefore, the major advantage of Li-air batteries is their high theoretical energy density, which is a measure of the amount of energy stored in the battery per unit mass. Also, consumer products require long run times with moderate load (specific power), which can be achieved by Li-air batteries. This will be a breakthrough to higher capacity battery, which could pave the way of new generation of electric vehicles, portable devices and mobile phones. The theoretical energy density of Li-air battery is 11500 Wh kg<sup>-1</sup> (in the charged state) or 3500 Wh kg<sup>-1</sup> (in the uncharged state for Li<sub>2</sub>O<sub>2</sub>, where the mass of oxygen is considered), while the theoretical value for the classical Li-ion batteries is 450 Wh kg<sup>-1</sup> and only half or one-third of this value is practically realizable.[3]

From the theoretical and fundamental point of view, there are no scientific obstacles to build up batteries with ten times the energy content of the currently available Li-ion batteries. However, many challenges are facing their realization.

Despite the intensive efforts done so far, the realization of this principle in the Li-air batteries industry has not been achieved yet. This arises from the necessary use of an organic electrolyte (which is in contact with the lithium metal) instead of an aqueous electrolyte, but the basics and the electrochemical reactions like oxygen reduction reaction (ORR) and oxygen evolution reaction (OER) in this type of electrolytes were hardly studied in the past.

The O<sub>2</sub>-electrode and also the Li-anode represent one of the challenges in terms of performance and stability. ORR and OER on the cathode in these electrolytes suffer from sluggish kinetics, thus the performance of the air electrode has to be improved. The mechanism of these reactions, the influence of electrode design, the role of the catalyst and the choice of the electrolyte are not well understood so far. On the other hand, ORR has been thoroughly investigated in aqueous media. So, lessons from the electrochemistry in these media have to be learnt and applied to organic media. The use of an air electrode in an aqueous electrolyte for Li-air battery should be possible if the Li anode is protected by a Li<sup>+</sup>-conducting membrane.[4] Thus, the development of an efficient bifunctional catalyst to reduce the overpotential and increase the kinetics in alkaline media is necessary. Platinum based catalysts are widely used for fuel cells, but cost analysis of the fuel cells showed that Pt represents one of the most expensive components in the cell.[5] Non-noble metal catalysts and especially cobalt-containing catalysts are good candidates in this aspect. Ag is also a conductive and cheaper alternative to Pt. Therefore, we investigated a combination of Ag, which is good for ORR, and Co<sub>3</sub>O<sub>4</sub>, which is good for OER, in one mixture which gives a superior catalytic activity for both OER and ORR with good stability in alkaline media. Importantly, this mixed catalyst is carbon-free (i.e. avoids corrosion problems). Better understanding of the origin of such synergistic effect (electrochemically and electronically) is also beneficial for universalization of this idea in other catalytic materials. The role of catalyst in Li-O<sub>2</sub> batteries is still not well understood. Despite the presence of some promising approaches towards the realization of the Li-air technology, a series of problems and challenges are still not solved and have to be addressed. These include:

- Sluggish kinetics of OER and OER: thus, the aim is to reduce the overpotential by searching for an optimum catalyst for alkaline oxygen electrodes. This is possible by screening different catalyst materials to find the optimum components and the best bifunctional catalyst, which make these reactions more reversible. The influence of oxygen electrocatalysis in organic electrolytes is also a key point.
- Microscopic and macroscopic investigation of the electrode processes at the metal-electrolyte interface: this helps understanding which mechanism of reactions occurs at the catalyst surface.
- Better understanding of the structure of the surface: the performance of bimetallic catalysts in the processes on the atomic scale is mainly a question of structure. Also in organic electrolytes, the structure is important due to the formation of insoluble Li-oxide particles on the surface.
- The lower true coulombic efficiency and reversibility, which are due to the higher overpotential between charge and discharge processes.
- Poor round trip efficiency and cyclability of charge and discharge, since there is a loss in capacity during cycling.
- Instability of the electrolyte: possible side and parasitic reactions of the organic electrolytes, which arise, for example, from the formed intermediate superoxide.
- corrosion of the lithium electrode due to crossover of oxygen from the air electrode to the lithium anode.
- Blocking of the active sites of electrode surface or clogging of the pores of the air electrode with the formed lithium peroxide or other films.

In this work, new strategies for the development of air electrodes for alkaline media are followed. The use of carbon-free mixed catalysts is one possibility. For organic Li-O<sub>2</sub> battery, the idea of combining the desired properties of two single solvents in one mixed electrolyte is examined in our work. Investigation of new electrolytes is ongoing to find a stable electrolyte with desired properties. The exact influence of some factors (e.g. donor number of solvent, catalyst role) on the electrochemical reactions is so far insufficiently known in organic electrolytes. Therefore, the behavior of each component has to be known in order to improve their performance. An alternative scenario for Li-air system is the use of hybrid aqueous-nonaqueous electrolyte battery (as mentioned above), in which an aqueous alkaline electrolyte is used for the air electrode and a nonaqueous electrolyte for the lithium anode, and they are separated by a Lithium ion-conducting membrane. Thus, higher current densities can be achieved in alkaline electrolytes than in organic ones. Therefore, both concepts (organic or alkaline aqueous electrolyte systems) should be studied since the knowledge so far does not prefer one over the other. In this work, we investigated bifunctional catalysis in alkaline media with detailed mechanistic and kinetic insights, in addition to ORR/OER investigations in aprotic single and mixed electrolytes. Application of gas diffusion electrode (GDE) as an air electrode is critical to realize the idea of using a membrane to separate electrolyte and air. Finally, the results obtained from the air electrode in alkaline electrolyte can be used for other metal-air systems.



## 1. Introduction

In the early twentieth century, the automobile evolved from an expensive toy for the rich to a popular means of transportation among the public. It gives many people an incredible freedom of movement whenever and wherever they want. The development of automobiles has had an effect on people's way of life. However, fossil fuels (e.g. gasoline or diesel) are the main power source for internal combustion engines in cars. And due to their contribution to climate change and global warming,[5] and their expected shortage in the future,[6] electrification of the traffic is an eco-alternative solution to keep environmental balance and to reduce the reliance on fossil fuels. In this context, the *electric vehicle* (EV) could be powered by fuel cells or batteries.

The main difference between fuel cells and rechargeable batteries is that a fuel cell is an *energy conversion* device while a battery is an *energy conversion and storage* device. In fuel cells, the fuel is externally supplied, and thus the electrodes are not consumed, but act only as *chemical to electrical energy converters*, thus the amount of energy is determined by the amount of fuel provided. In contrast, in batteries, the electrical energy can be stored and converted into chemical energy. The electric energy provided by a battery is determined by the amount of chemicals in the battery (i.e. the weight and size of the whole system).

Basically, in batteries, the reaction of an element with oxygen releases a large amount of energy that can be exploited. For example, the energy generated from the reaction of only 2.3g of lithium with oxygen to form  $\text{Li}_2\text{O}_2$  is sufficient to accelerate a 1000 kg car from zero to 50 km/h (neglecting all energy losses).[3, 7] Whilst, ca. 2.1 g of gasoline would be required. Despite the slight difference, the combustion of fossil fuels is an irreversible process on the large scale since a great percentage of energy is in the form of heat. And about 78% of the global energy consumption in 2013 was obtained from fossil fuels.[8] Therefore, it is highly desirable to have devices that reversibly convert the energy produced from oxidation reactions into electric energy. This is one of the great challenges in the future energy technology. *Rechargeable secondary batteries* are one of the technical solutions in which the reversible electrochemical reactions can be used to store and release energy.

### 1.1. Lithium-ion batteries (LIBs)

Many types of secondary batteries are commercially available. Fig. 1 shows the *Ragone plot* comparing the specific energy and specific power of the most common technologies ( e.g. Lead-acid, Nickel-metal hydride, LIB).[9] Despite the inverse relation between specific energy and specific power, LIBs have a clear edge over other electrochemical approaches when optimized. It is still significantly far from gasoline performance (12.3 kWh/kg).[9] LIBs are nowadays common in most portable electronic devices. LIBs possess the highest energy storage capability commercially available.[10] Due to their high energy density (210 Wh  $\text{kg}^{-1}$ ; 650 Wh  $\text{l}^{-1}$ ),[11] small memory effect and long life cycle, LIBs have captured the portable electronic market, previously an exclusive of nickel-metal hydride technologies. However, the application of LIB technology in EV is facing major challenges. The limited specific energy and high cost of the state-of-the-art LIBs represent a hurdle for wide-scale commercialization of EVs. In particular, the battery pack is heavy and its use in a smaller and inexpensive car is a big challenge. Therefore, reduction of the battery weight and cost are crucial issues.

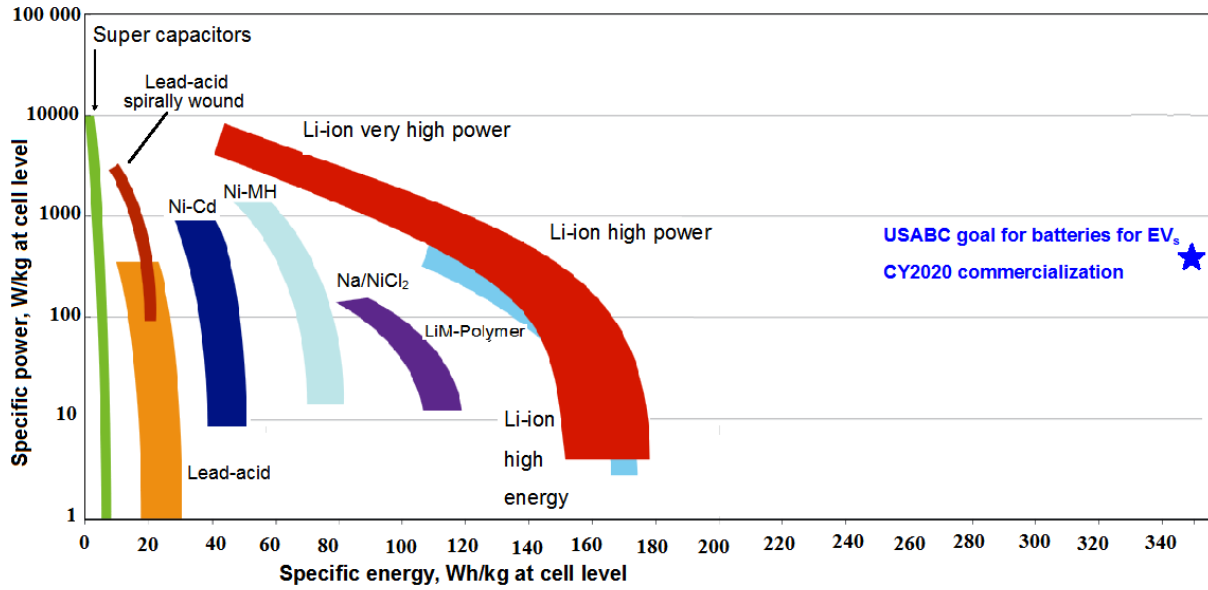
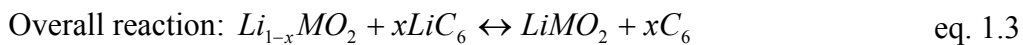
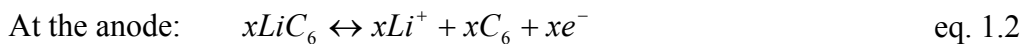
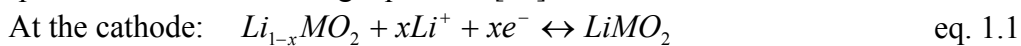


Fig. 1. Ragone plot for specific energy and specific power of different battery types. Adapted according to [9] and [12]. USABC data considered C/3 discharge rate and 30 s pulse.

An LIB consists of cathode, anode, electrolyte and separator. In contrast to the disposable lithium batteries which contain metallic lithium as the anode, an LIB consists of graphite or amorphous silicon as anode and an intercalated lithium compound (Li metal oxide in the uncharged state) as the cathode. The electrolyte used is a mixture of lithium salt (e.g.  $\text{LiPF}_6$ ,  $\text{LiClO}_4$ ) and organic solvent (e.g. ethylene carbonate, propylene carbonate). In order to allow current flow, Copper and Aluminum are used as electric connectors. During discharge, the positive lithium ion moves from the negative electrode and enters the positive electrode (lithium containing compound). When the cell is charging, the reverse occurs. Both anode and cathode allow lithium ion to move in and out of the electrode during intercalation and deintercalation (see Fig. 2).[13] The electrochemical reactions taking place in the cell are represented in the following equations:[13]



where,  $\text{LiC}_6$  represents the lithium-graphite intercalation, and  $\text{LiMO}_2$  is the lithium metal oxide cathode. Li-ion cells come in button, cylindrical, or prismatic forms.[10] A schematic showing the two shapes and the components of LIB is displayed in Fig. 2.

The major contribution to the weight of the LIB originates from the pack components and electronics, which upon its mass reduction would reduce the safety of the battery. The second main weight contribution is the positive electrode. Commercial cathode materials can be classified into three families:[14, 15] layered compounds (e.g.  $\text{LiCoO}_2$ ,  $\text{LiMnO}_2$ , lithium nickel manganese cobalt oxide LNMC); the olivine compounds (e.g.  $\text{LiFePO}_4$ ,  $\text{LiMnPO}_4$ ) and the spinel compounds ( $\text{LiMn}_2\text{O}_4$ ). LNMC is promising and has  $200 \text{ mAh g}^{-1}$  and 4V cell potential.[15] Unfortunately, these materials suffer from different problems such as safety issue, antisite defects and lower energy density. The commercial anodes are made of graphite with high energy density. However, the graphite anode limits not only the rate of charge, but also the discharge power density. Therefore, efforts have been made to replace graphite with

$\text{Li}_4\text{Ti}_5\text{O}_{12}$  (LTO). LTO has a stable operating voltage of 1.5V vs.  $\text{Li}/\text{Li}^+$  which is higher than the one of graphite, but gives outstanding results (power density and stability) when combined with the  $\text{LiFePO}_4$  positive electrode. The only drawback of the substitution of graphite with LTO is a loss of energy density.[14]

Intensive work has been done to improve the performance by reducing the size of particles, surface modification and cheaper synthesis methods. To increase the specific energy, the cell voltage or the specific capacity has to be increased. Since the positive electrode is the heaviest in the cell, any increase of its specific energy (i.e. reduction in weight) would result in a substantial enhancement of the overall battery energy density. Improvements have been done to the current LIB technology: however, the cathode materials have a limited practical capacity (less than  $200 \text{ mAh g}^{-1}$ ) and a working potential in the range of 3-4.5V vs.  $\text{Li}/\text{Li}^+$ .[15, 16]

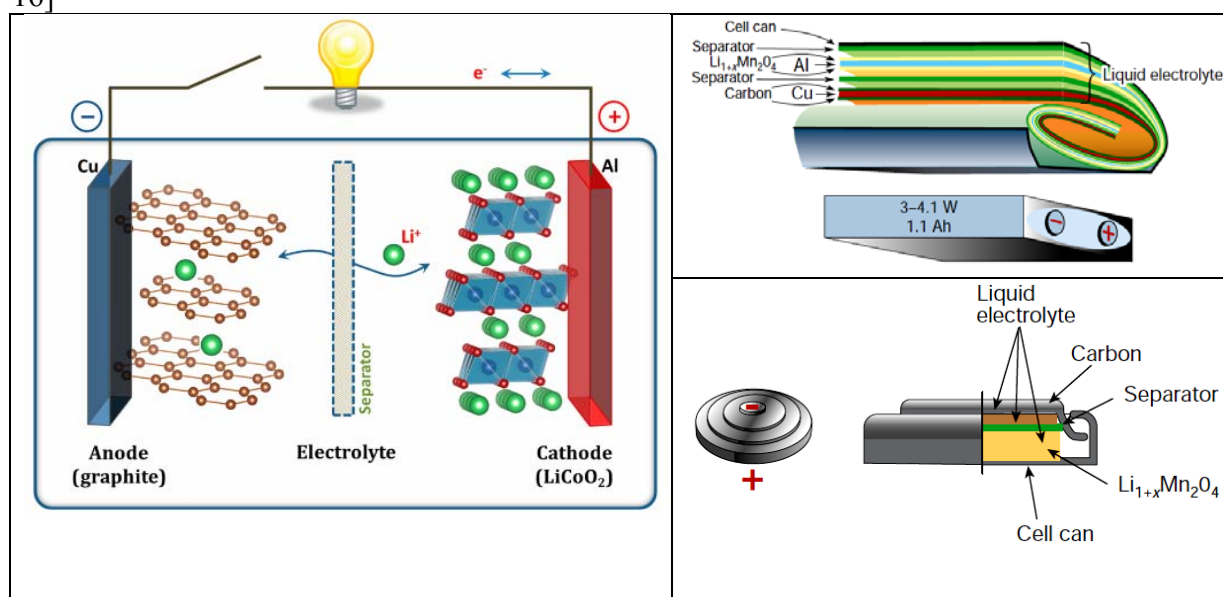


Fig. 2. Schematic showing the charging and discharging reactions in LIB (left panel).(adapted from [13]) Right panel: a drawing shows the components of LIB in the prismatic and coin forms.(images adapted from [10])

## 1.2. Lithium-air batteries

To overcome the constraints of lithium intercalation and lower energy density in LIB, alternative chemistries and mechanisms are required to exceed LIB and compete with the combustion engines technology. Rechargeable Li-air batteries have the highest proposed specific energy density among metal-air battery technologies. Therefore, they are the most promising for EV applications. The first non-aqueous Li-air battery was presented in 1996 by Abraham and co-workers, in which Li anode, carbon cathode and polymer membrane were used.[17] Oxygen reduction at the cathode (air electrode) is a determining factor of the cell performance. The basic difference from LIB is the replacement of the heavy metal oxides used for intercalation with atmospheric oxygen, which consequently saves much weight and in turn increases the energy density significantly. Fig. 3 shows a comparison of Li-air with other metal-air cells or even the commercial technologies currently available.[18] The superior specific energy expected from this type of batteries over other rechargeable batteries is shown. Li-air battery attracted a strong focus after the Bruce group in 2006 has

demonstrated its rechargeability.[19] This progressive step stimulated a scientific race towards better development of the battery. IBM was one of the leading enterprises through the Battery 500 project to develop Li-air battery for EV with a driving range of 500 miles.

Lithium-air batteries, also known as Li-O<sub>2</sub>, have a great potential, providing up to five to ten times more energy than the current LIB, which currently power our cell phones and tablets. It may even be possible to have a rechargeable battery of up to 1000 wh/Kg, and all it will need is oxygen.[3] The theoretical specific energy density for Li-O<sub>2</sub> battery was calculated at a nominal potential of 3V and found to be 5 kWh kg<sup>-1</sup> for the reaction forming LiOH (Li+1/4O<sub>2</sub>+1/2H<sub>2</sub>O<sub>2</sub> ↔ LiOH) and 11.5 kWh/kg (neglecting the mass of oxygen, since it is free) or 3.5 kWh/kg (taking into account the mass of Li<sub>2</sub>O<sub>2</sub>) for the reaction forming Li<sub>2</sub>O<sub>2</sub> (2 Li + O<sub>2</sub> ↔ Li<sub>2</sub>O<sub>2</sub>), which is comparable to the 13 kWh kg<sup>-1</sup> of gasoline and far exceeding the theoretical value of the conventional Li-ion battery (400 Wh/kg).[18] This value for Li-air battery is more than five times higher than LIB. Gasoline has a practical value of 1.7 kWh/kg of energy provided to the wheels after losses, and this value could also be assumed for Li-air battery after several losses. This would match, if successful, the USABC goals for advanced batteries for EVs (350 Wh/kg and 700 W/kg at the cell level) shown in Fig. 1. Assuming now the same factor of 5 for specific energy loss found in the commercial LIB, a Li-air battery would provide a maximum of ~700 Wh/kg<sub>pack</sub> which is 3 times higher than the current LIB.[20] Since there is no expectation for the current Li-ion battery to reach this target, Li-air cells are required to achieve this target. This would be sufficient to power cars with a reasonable travel range, but engineering a Li-air battery has been a challenge.

The term "Li-air" batteries which is commonly used is actually improper since oxygen instead of air is used in testing the cells, therefore, it can be used when talking about the technology in general or when using air as the oxygen source. Otherwise, the term "Li-O<sub>2</sub>" batteries is more appropriate when using oxygen.

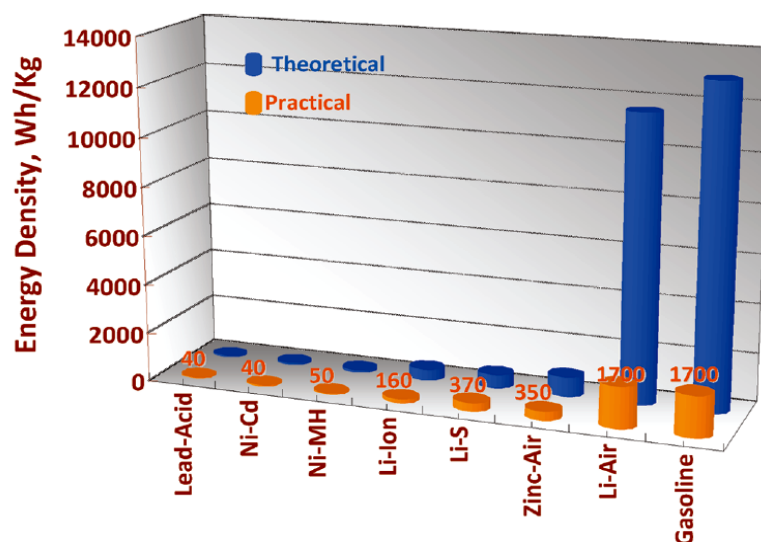


Fig. 3. Comparison between the theoretical and practical energy densities of various types of rechargeable battery. The practical value of Li-air is an optimistic value.(graph from [18])

### 1.2.1. How does Li-O<sub>2</sub> battery work?

#### 1.2.1.1. Components of Li-air battery

Although there are four approaches to Li-air battery designs, the basic components of the four types are similar. These include:

- *The cathode:* porous carbon is a widely used cathode material because of its structural variability and low cost. Most of the limitations come from the air-electrode: for example, blocking of the pores by deposited Li<sub>2</sub>O<sub>2</sub> is the most serious issue; high overpotentials, and water contaminants could affect the cathode too. The specific capacity of Li-air battery depends strongly on the pore size, volume and structure of the cathode.[21] Advanced materials as carbon nanotubes[22] or graphene[23] have been investigated as cathode materials and showed an enhanced response. Nevertheless, non-carbon materials such as TiO<sub>2</sub> have been also used.[24] The influence of the catalyst in the cathode is discussed later.
- *The anode:* metallic lithium is the typical anode material considered. Li has high specific capacity (3840 mAh g<sup>-1</sup>) compared to Zn (815 mAh g<sup>-1</sup>), Mg (~2200 mAh g<sup>-1</sup>) or Al (2965 mAh g<sup>-1</sup>).[21] The so-called solid electrolyte interface (SEI) is formed upon charge/discharge where layers of the lithium salt precipitate onto the anode, and possibly form dendrites. To overcome this problem, Li-ion conducting glass membranes (e.g. LiSICON, NASICON) are used as a protective layer.[4] Reaction of Li anode with electrolyte has to be avoided.
- *The electrolyte:* the electrolyte nature defines the design of the battery. Aprotic electrolytes[25] used to date include: organic carbonates (EC, PC, DMC), ethers (DMSO, Diglyme, Triglyme, Tetraglyme, THF), amides (N-methyl acetamide), lactams (NMP), sulfones and nitriles (acetonitrile). They showed different performances and stabilities. Several salts have been tested (LiClO<sub>4</sub>, LiPF<sub>6</sub>, LiBF<sub>4</sub>, LiTFSI, Li-triflate, LiNO<sub>3</sub>). The salts also showed to have an effect on the battery: LiClO<sub>4</sub> was less reactive than F-containing salts.[26] Laoire et al. showed that the anion of the salt has a very little effect on the mechanism of reduction in MeCN.[27] Therefore, we used LiClO<sub>4</sub> in our experiments. Additives have been found to improve the process: for example, tris(pentafluorophenyl)borane showed to dissolve the Li<sub>2</sub>O<sub>2</sub>, but has also negative effects on viscosity;[28] redox mediators were first introduced in Li-O<sub>2</sub> system by the Owen group,[29] where they used Ethylviologenditriplate. The function of a redox mediator is to reduce the oxidation overpotential and enhance the rechargeability. Later, the Bruce group reported that incorporation of a Redox mediator, tetrathiafulvalene (TTF), enables recharging at rates that are impossible for the cell in the absence of the mediator, and achieve 100 charge/discharge cycles and improved reversibility.[30, 31] LiI has also been recently studied as a redox mediator with promising results.[32]

#### 1.2.1.2. Designs of Li-air batteries

The Li-air batteries are classified into four configurations according to the nature of electrolyte, as shown in Fig. 4. All versions use Li metal as the anode and porous carbon or catalyst-modified carbon as the cathode, but electrolyte compositions are different. Three

versions involve a liquid electrolyte while the fourth version includes an all solid-state electrolyte.[18, 33] These four configurations are:

- i. aqueous electrolyte
- ii. nonaqueous aprotic electrolyte
- iii. mixed nonaqueous-aqueous electrolyte, and
- iv. all solid-state electrolyte

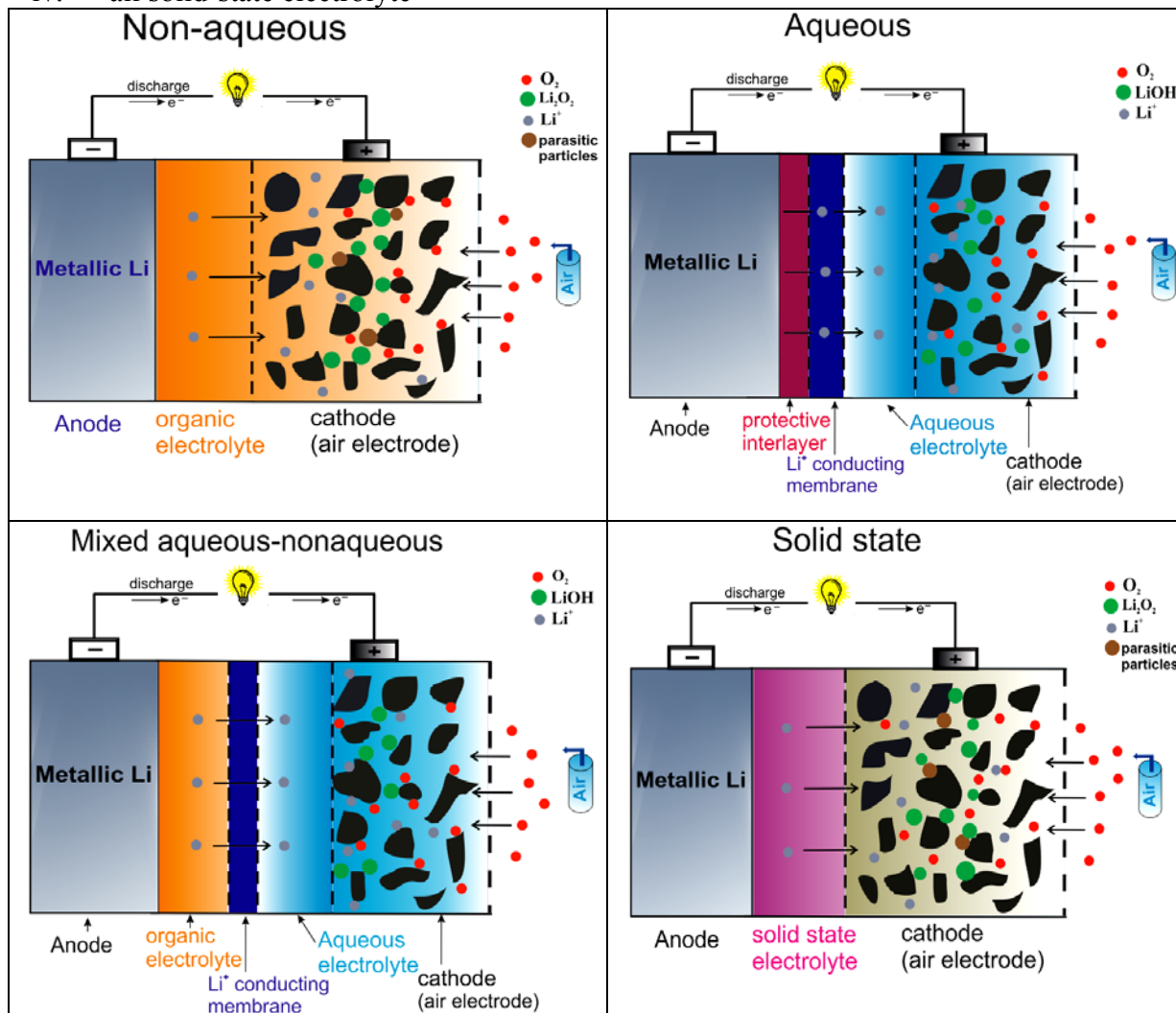


Fig. 4. Schematic of the cell configuration of the four designs for Li-air batteries.

We focus on aprotic and aqueous electrolytes since the solid-state electrochemistry is not well understood. Each system has its advantages, hence the question of which is the best configuration is still open. In non-aqueous design, Li-anode is the source of Li ions and is in direct contact with the aprotic electrolyte so that a solid electrolyte interface (SEI) is formed. The cathode is used as  $Li_2O_2$  reservoir, which is formed upon ORR. The formed  $Li_2O_2$  causes clogging of the cathode and deterioration of the battery. This version was first introduced by Abraham,[17] Read[34] and Bruce[19] groups. This version will be discussed in details later. The solid-state system is similar in function to the non-aqueous system.

In aqueous and mixed systems, the cathode chemistry is the same, where the reaction product ( $LiOH$ ) is soluble in water, which is preferred for higher conductivity and avoids surface blocking. In both systems, a Li-ion conducting glass membrane has to be used to prevent a

vigorous reaction of Li anode with the aqueous electrolyte.[4] The aqueous system and the Li<sup>+</sup> conductive membrane has been introduced in 2010 by Polyplus company.[35] The mixed system was introduced by Polyplus and later by the Zhou group.[36] Most recently, researchers were able to build up a battery which produces LiOH instead of Li<sub>2</sub>O<sub>2</sub>. [37] This reduces the voltage gap to 0.2V, a number closer to what is seen in a Li-ion battery. This novel battery was rechargeable for more than 2000 times, However the lithium metal anode in their battery can sometimes form dendrites that hinder its performance.

Nevertheless, a big challenge for all four designs is the development of an air-breathing system which selectively passes only oxygen and keeps other contaminants out. Here, we will focus only on the aprotic electrolyte-based battery.

### 1.2.1.3. Reactions in Li-air batteries

The possible reactions occurring at the O<sub>2</sub>-cathode in non-aqueous and aqueous electrolytes[33, 38] are presented in Table 1. The standard cell potentials (E<sup>0</sup>) are also given based on the standard Gibbs free energy (ΔG<sup>0</sup>) according to the equation: ΔG<sup>0</sup> = -nFE<sup>0</sup>, where n is the number of electrons and F is Faraday constant.

#	Redox reaction	E <sup>0</sup> / V vs. Li/Li <sup>+</sup>
1	$Li \leftrightarrow Li^+ + e^-$	0.0
2	$O_2 + Li^+ + e^- \leftrightarrow LiO_2(aq)$	3.0
3	$2LiO_2 \leftrightarrow Li_2O_2(s) + O_2$	Chemical reaction
4	$LiO_2 + Li^+ + e^- \leftrightarrow Li_2O_2(s)$	2.96
5	$Li_2O_2 + 2Li^+ + 2e^- \leftrightarrow 2Li_2O(s)$	2.91
6	$O_2 + 2Li^+ + 2e^- \leftrightarrow Li_2O_2(s)$	2.96
7	$2O_2 + 4Li^+ + 4e^- \leftrightarrow 2Li_2O(s)$	2.91
8	$O_2 + 4Li^+ + 2H_2O \leftrightarrow 4LiOH(aq)$	3.2

Table 1. Possible ORR reactions involved in non-aqueous electrolyte together with the standard cell potential.

ORR (discharge) in non-aqueous electrolytes is proposed to proceed via series of reduction steps. During the discharge process, the lithium anode is oxidized with electron donation to the external circuit (reaction 1). Whereas, at the cathode, oxygen is adsorbed, and then it is reduced to either superoxide, peroxide or oxide[38] depending on the electrode and electrolyte. The first reduction step is possibly a one-electron process to superoxide (LiO<sub>2</sub>)(reaction 2). Nevertheless, the formed LiO<sub>2</sub> could be a short-lived intermediate, further reacting either chemically or electrochemically forming insoluble peroxide (Li<sub>2</sub>O<sub>2</sub>) according to reactions (3) and (4).[39] In fact, electrochemical reduction has been observed from the 2e<sup>-</sup>/O<sub>2</sub> using DEMS.[40] Noteworthy, LiO<sub>2</sub> is stable, for instance, at lower overpotentials at Au in DMSO.[41] where only disproportionation reaction could take place. Although, the formation of Li<sub>2</sub>O is thermodynamically possible (reaction 5), it is kinetically unfavorable.[38] Direct 2e-reduction to Li<sub>2</sub>O<sub>2</sub> or direct 4e-reduction to Li<sub>2</sub>O can also be proposed as shown in reactions 6 and 7.[38] Formation of LiOH (reaction 8) has been recently observed in water-containing organic electrolytes and with LiI as an additive.[37]

Nevertheless,  $\text{Li}_2\text{O}_2$  is known to be the discharge product commonly observed in practice. Upon charging, the reverse process occurs where the formed  $\text{Li}_2\text{O}_2$  is oxidized. The ideal reaction in aprotic electrolytes is the two-electron process:



Formation of  $\text{LiOH}$  (reaction 8) is recently observed in water-containing organic electrolytes and with  $\text{LiI}$  as an additive.[37] For aqueous system, the reactions are different from the aprotic one, where the soluble  $\text{LiOH}$  is produced during ORR in alkaline media according to reaction 8 in table 1, thus a three-phase (solid-liquid-gas) interface is formed at the cathode as shown in Fig. 5.

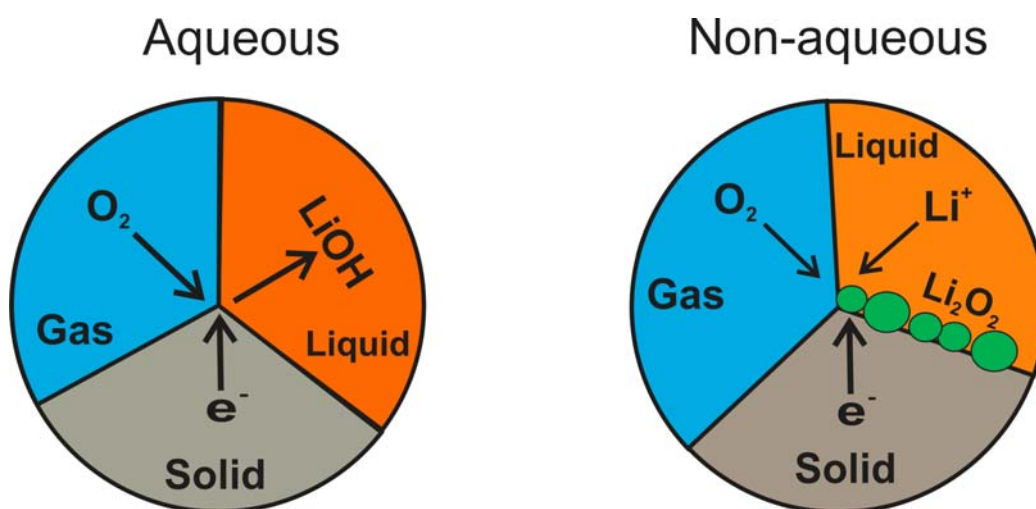


Fig. 5. Schematic illustration of the interfaces at the air-electrode.

On the other hand, in nonaqueous electrolyte, oxygen diffuses to the cathode, where it reacts with the  $\text{Li}^+$  moved from the anode through the electrolyte and forms insoluble  $\text{Li}_2\text{O}_2$  solid deposits during discharge, see Fig. 4 and 5. Therefore, a four-phase (catalyst- $\text{Li}_2\text{O}_2$  solid-gas-liquid electrolyte) interface is formed (see Fig. 5).

The solvent has shown to have a significant role in the type of the discharge products and the mechanism. Laoire et al. reported that high donor number (DN) solvents (e.g. DMSO) tend to form stable Li-solvated ion pair with superoxide according to the hard soft acid base theory (HSAB), so that the  $\text{O}_2/\text{O}_2^-$  couple can be detected in solution.[42] In contrast, in low DN solvents (acetonitrile),  $\text{Li}_2\text{O}_2$  is formed since the superoxide tends to decompose or undergo reduction to  $\text{O}_2^{2-}$ . Moreover, superoxide can react with aprotic electrolytes forming undesired products as in the case of propylene carbonate.[43] Most recently, Bruce group proposed a generalized mechanism for all solvents.[44] They reported that the solvent affects the  $\text{LiO}_2$  stability and in turn either a surface mechanism or a solution mechanism occurs. In low DN solvents, the surface pathway causes  $\text{Li}_2\text{O}_2$  film growth on surface, electrode blocking and cell death. Whereas, in high DN solvents,  $\text{Li}_2\text{O}_2$  particles are formed in solution at high potentials. More details on the mechanism and how the solvent and catalysts influence the process will be addressed in the results of chapters 8 and 9.

In the chapters dealing with non-aqueous electrolyte, we will focus on the factors that have the greatest contribution to ORR and OER in aprotic electrolyte: solvent effect on stability of  $\text{LiO}_2$  intermediate, electrolyte stability, catalyst effect and kinetic and mechanistic studies.

### 1.2.2. Rechargeability parameters and the role of electrocatalyst

Despite many advantages of Li-air batteries, still the low rechargeability and high overpotentials of ORR/OER are limiting and crucial factors. In LIB any degradation due to parasitic reactions appears as capacity loss, which is not significant.[45] Therefore, the *coulombic efficiency*, ratio of faradaic charge of oxidation (charge) to reduction (discharge), was used as a criterion for rechargeability. On the other hand, in Li-air batteries, electrochemical decomposition is severe. Therefore, the coulombic efficiency is not any more a proper characteristic. Instead, the term "*true coulombic efficiency*", which is the ratio of oxygen consumed during ORR to oxygen released during OER, gives a proper description of rechargeability. For ideal systems, the true coulombic efficiency should be equal to 100%, which is not yet achieved in practice. Another important term is the number of electrons transferred ( $z$ ) during charge/discharge.  $Z$ -value can be determined from the faradaic current and the ionic current of mass 32 in mass spectrometry. The absence of side reactions is indicative of good cyclability. Stability of the electrolyte against Li,  $\text{LiO}_2$  or  $\text{Li}_2\text{O}_2$  is an important issue in rechargeability. Therefore, the seek for a stable electrolyte is still going on. Galvanostatic charge-discharge hysteresis is commonly applied in battery research as a characteristic of cyclability and functionality of the cell.[7] Since we conducted potentiodynamic and potentiostatic experiments, explanation of the galvanostatic experiment is important to have a wider picture of both in mind for comparison. In a typical discharge/charge cycle, a constant current density (negative) is applied so that cathodic polarization (discharge) occurs at the positive electrode. The discharge is limited by a certain capacity or potential. Upon charge, the cell is polarized in the opposite direction, and a positive current is applied, see Fig. 6. The two steps are repeated for several cycles.  $j$ - $E$  curve and discharge/charge curves are shown in Fig. 6.[7] The plotted potential is usually of the positive electrode against the reference electrode.  $J$ - $E$  curves at different states of discharge are also plotted in Fig. 6A. The solid line is the intermediate case where discharge and charge are possible. At equilibrium,  $j=0$  and  $E=E^0$ . At  $E < E^0$  (i.e. discharge), the current decays exponentially reaching a diffusion limitation or saturation, while at  $E > E^0$  (i.e. charge) the current decreases until limitation. The difference  $E-E^0$  is the *overpotential*. The overpotential has many origins such as sluggish kinetics or limited transport.[7] In an ideal charge/discharge loop, see Fig. 6b, applying constant current leads to a constant potential (i.e. plateau as a function of time) until rapid potential drop occurs due to the end of discharge  $q=q_{\text{max}}$  (i.e. no more  $\text{Li}_2\text{O}_2$  is formed), see dotted dark grey line. In the reverse process, rapid potential increase is observed as  $\text{Li}_2\text{O}_2$  starts to decompose and plateau for charge occurs until  $q=0$  at the end of process, dashed light grey line. However, this ideal behavior is not easy to achieve in practice since  $\text{Li}_2\text{O}_2$  passivates the surface and blocks some of the effective surface area, which in turn leads to an increase of the true current density and overpotential.

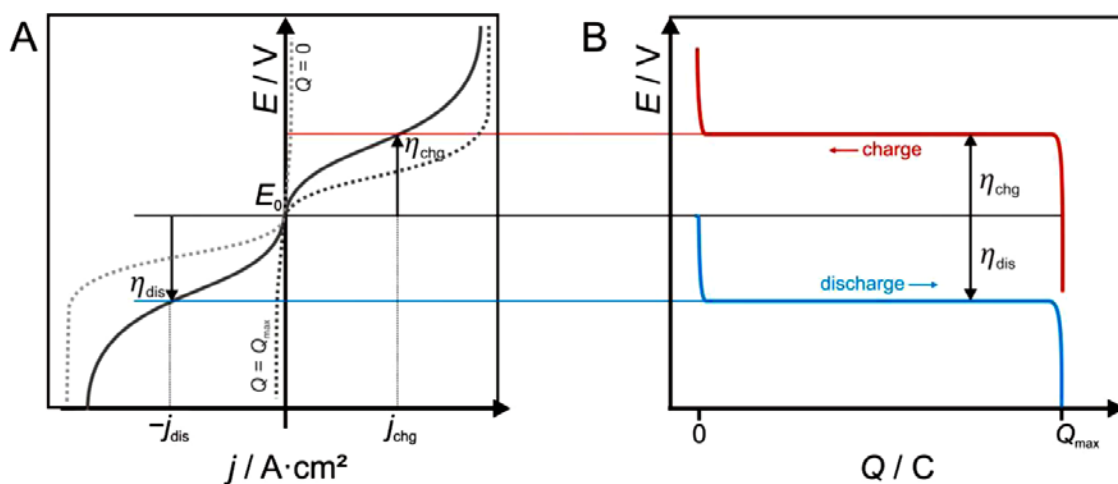


Fig. 6. A) J-E curves of a positive electrode in Li-O<sub>2</sub> cell at different states of discharge. B) ideal galvanostatic discharge/charge curve of the cell.[7]

The sluggish OER and ORR kinetics in organic electrolytes is one of the key issues that have to be addressed. Several reports focused on the use of catalyst to reduce the overpotential, including noble metals (Pt, Au, Ru, Pd)[41, 46] or oxides.[47] Au is more effective than Vulcan carbon upon discharge, while Pt showed the lowest charge voltage of  $3.8V_{\text{Li}}$ .[48, 49] MnO<sub>2</sub> nanotubes modified graphene showed excellent ORR activity in aprotic electrolyte.[50] Other Mn and Co-based catalysts performed superiorly in Li-O<sub>2</sub> batteries.[51, 52] One interesting article showed the bifunctional effect of a mixed Pt-Au catalyst for Li-air cells, where Pt was responsible for OER and Au for ORR.[53] However, the role of catalyst in organic electrolytes on the performance of the battery is still contradictory. Two issues are discussed:

*i)* Some research groups find different results: for example, McCloskey group demonstrated no catalytic effect on charging, when a pre-discharge electrode was used,[54] however the Shao-horn group found a catalytic effect (2 times higher current) of Pt and Ru on charge of a chemically produced Li<sub>2</sub>O<sub>2</sub>[55], although one could argue that the difference in the two results could be due to the difference in Li<sub>2</sub>O<sub>2</sub> morphology.

*ii)* Another controversial case is the role of Au: Shao-horn et al. showed that Au (50 nm)/C was inactive towards oxidation of Li<sub>2</sub>O<sub>2</sub>[55], whereas Marinaro et al. revealed the enhanced OER kinetics and reduced overpotential at Au (50 nm)/C.[49] However, the role of the different particle size of Au is not yet clear.

In this work, we investigated the role of Co<sub>3</sub>O<sub>4</sub> catalysts on the OER/ORR kinetics in organic electrolytes. This catalyst was shown to have an outstanding OER activity in alkaline media.[56]

### 1.2.3. Aprotic electrolyte is a key challenge

The nature of the electrolyte (salt+solvent) affects strongly the mechanism of ORR/OER, the discharge products and cycle life. Therefore, the seek for a better electrolyte is one of the currently attractive issues in Li-O<sub>2</sub> battery research since to date there is not a stable and optimum electrolyte for real application.

### Requirements of a desired electrolyte

- stability in a wide potential range of operation, in particular, at higher potentials
- high donor number to favor the formation of the desired  $\text{Li}_2\text{O}_2$  product
- high conductivity
- high oxygen solubility and diffusivity
- stability against oxygen and the reduction products (i.e.  $\text{Li}_2\text{O}_2$  and  $\text{LiO}_2$ )
- stabilize the Li-anode by forming a protective layer
- low vapor pressure
- safety and higher boiling and flash points

#### 1.2.4. The search for a stable electrolyte: Influence of solvent and salt

Intensive research has been done to identify a proper electrolyte; however, this problem is only partly solved. Organic carbonate-based electrolytes were chosen in the early stage of Li-air research as first candidates due to their wide use in Li-ion batteries and their efficient stabilization of the Li-anode. Unfortunately, they showed to decompose irreversibly through reaction with reduction products ( $\text{O}_2^{\bullet-}$ ). Moreover, Li(alkyl)carbonate and  $\text{Li}_2\text{CO}_3$  were produced as the main discharge products (evolution of  $\text{CO}_2$  was predominant) instead of  $\text{Li}_2\text{O}_2$ . [57, 58] Since  $\text{LiO}_2$  is the intermediate formed during ORR,  $\text{O}_2^{\bullet-}$  reacts with propylene carbonate, decomposing it as shown in the mechanism (Fig. 7). [59] Therefore, the data obtained from these electrolytes should be carefully judged.

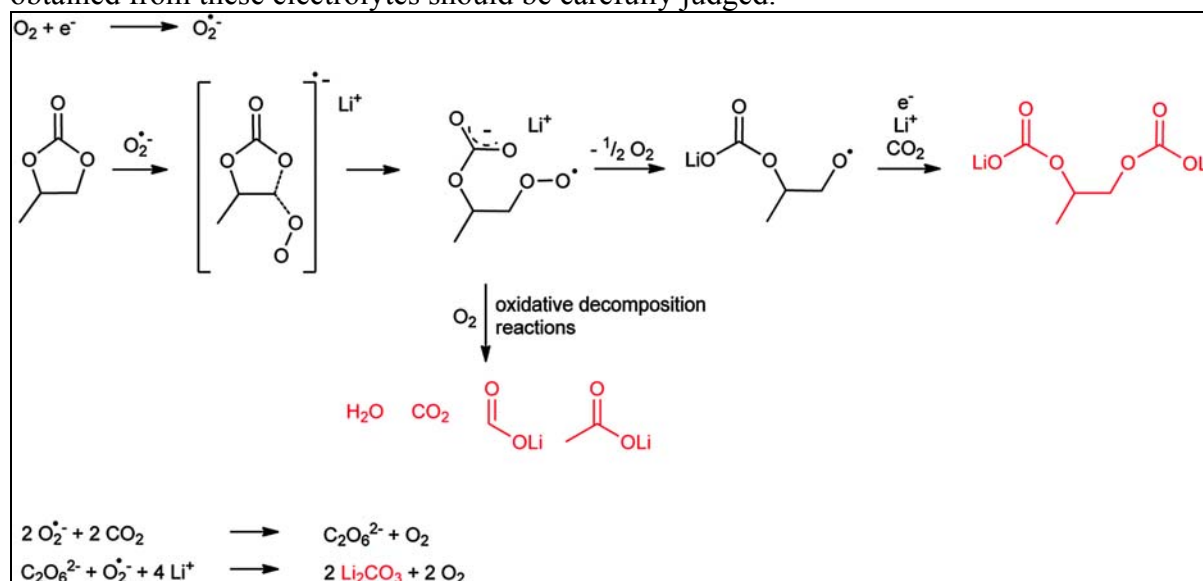


Fig. 7. Proposed mechanism for degradation of propylene carbonate-based electrolyte upon discharge via attack of  $\text{O}_2^{\bullet-}$  on the ring. [59]

Despite the failure of carbonate-based electrolyte cells, the search for a suitable electrolyte did not stop. In 2006, Read suggested ether-based electrolytes for use in the Li- $\text{O}_2$  cell due to both, good stability and excellent rate capability. [60] Bryantsev et al. reported, by DFT calculations, the reaction of  $\text{O}_2^{\bullet-}$  with several classes of solvents. [25] They showed the dependence of solvent reactivity with superoxide on the basicity of the solvent. In recent years, Tetraglyme (G4) was extensively studied by many research groups and its suitability is questionable: Laoire et al. reported the formation of  $\text{Li}_2\text{O}_2$  as the discharge product in  $\text{LiPF}_6/\text{G4}$ , but with capacity decay during continued cycling due to the poor cycling

efficiency of the Li anode and the high resistance arising from  $\text{Li}_2\text{O}_2$  deposit on the cathode.[61] This decomposition was also confirmed using spectroscopic methods by Bruce et al.[62] In contrast, Scrosati group showed that G4 is a suitable solvent, and their cell delivered a capacity of  $1000 \text{ mAh g}^{-1}$  for at least 100 cycles.[63] As an alternative, DMSO was suggested as a convenient solvent.[40, 42, 64] DMSO-based electrolyte showed 95% capacity retention after 100 cycles with a limited capacity regime and reversible  $\text{Li}_2\text{O}_2$  formation on a porous gold electrode.[40] Our group showed previously the reversible formation of  $\text{Li}_2\text{O}_2$  in DMSO-based electrolyte.[41] However, an XPS study recently showed the decomposition of DMSO to carbonate or other species when it is in contact with  $\text{Li}_2\text{O}_2$  for long time.[65] The formed species might on the other hand act as a protective film against further attack. Furthermore,  $\text{LiOH}$  is formed by a chemical reaction of the superoxide with DMSO.[66] Although DMSO has lower  $\text{O}_2$ -solubility and higher volatility, it is more prone to be stable and kinetically favorable for ORR and OER than G4 due to its higher ionic conductivity and  $\text{O}_2$ -diffusivity.[42, 67] We conclude, using these solvents (e.g. DMSO or G4), fairly reversible  $\text{Li}_2\text{O}_2$  formation was obtained as the main discharge product.

Also, Nitriles have been investigated as electrolytes for the Li- $\text{O}_2$  battery: acetonitrile (MeCN) is found to form  $\text{Li}_2\text{O}_2$  with no detection of  $\text{LiO}_2$  intermediate,[68] However, it is stable against reaction with  $\text{Li}_2\text{O}_2$ .[65]

Sulfone-based electrolytes were firstly used in 2012 by Dan et al. who found a good performance and observed  $\text{Li}_2\text{O}_2$  formation.[69] Later, the Bruce group studied sulfones and showed their stability for five cycles, but afterwards decomposition to  $\text{Li}_2\text{CO}_3$  leads to capacity fading.[70]

Ionic liquids (ILs) were proposed as candidates due to their high conductivity and lower volatility. Imidazolium based IL, in particular, EMITFSI showed multiple cycles without electrode passivation and with high reversibility.[39] Although Pyrrolidinium based ILs have 3-times higher stability against superoxide, They showed poor discharge capacity.[71]

The idea of using mixed electrolytes has been reported to improve the cycle life of the cell, but they mainly contain an ionic liquid which has high viscosity and lower diffusion coefficient.[72, 73] A mixed electrolyte of PC and MeCN was reported to be suitable for Li- $\text{O}_2$  battery.[74] This is because the diffusion coefficient of  $\text{O}_2$  is significantly higher in the mixed electrolyte than in the pure PC electrolyte. Addition of DMSO to MeCN stabilizes soluble  $\text{LiO}_2$ .[75] Moreover, G4-DMSO blended electrolyte has been proposed as a promising electrolyte. This electrolyte showed improved cyclability, although 80 wt% DMSO was used in this mixture, which already possesses high performance. Unfortunately, no kinetic or mechanistic studies were reported.[76] In our work, we present detailed kinetic and mechanistic studies together with DEMS measurements in single and mixed electrolytes to better understand the reactions in these electrolytes.

### 1.2.5. Growth mechanism of $\text{Li}_2\text{O}_2$

The growth of  $\text{Li}_2\text{O}_2$  particles is not as simple as expected. During discharge, different morphologies and structures of  $\text{Li}_2\text{O}_2$  can be formed. The exact effect of this structure on cycling performance is not well understood yet. A toroid-like structure of  $\text{Li}_2\text{O}_2$  of ca. 350 nm was observed on carbon fiber.[77] Two pathways for oxide particles growth were presented, where in both cases solid nuclei are formed at the electrode which then grow to crystals[7]:

a) Build up on the electrode surface:  $\text{LiO}_2$  is firstly electrochemically formed at the electrode and then diffuses onto the surface or through the electrolyte. Subsequently,  $\text{Li}_2\text{O}_2$  is formed, and a saturation state is reached, and a precipitate is formed on the electrode's active sites. The precipitation follows a nucleation and growth mechanism depending on the rate of  $\text{LiO}_2$  formation.

b) Build up on  $\text{Li}_2\text{O}_2$ :  $\text{Li}_2\text{O}_2$  can be formed on previously formed  $\text{Li}_2\text{O}_2$  particles. These particles are themselves electrochemically active. In that case, the growth mechanism of  $\text{Li}_2\text{O}_2$  is favored and takes place at low current densities. In contrast, at high current densities small  $\text{Li}_2\text{O}_2$  crystals or thin film rather than large crystals are formed if the electrode surface is more active than the oxide film.[7]

Nucleation/precipitation mechanism was also proposed for the formation of  $\text{Li}_2\text{O}_2$  by the Nazar group.[78] The growth was found to depend on the current rate of  $\text{LiO}_2$  formation. Nanocrystallite  $\text{Li}_2\text{O}_2$  toroids with size of  $\sim 18$  nm were formed at low current densities. In this mechanism,  $\text{LiO}_2$  is formed in solution as an intermediate, which then disproportionates to  $\text{Li}_2\text{O}_2$ , that nucleates and precipitates on the surface. At higher current densities, few nanometers quasi-amorphous thin film of  $\text{Li}_2\text{O}_2$  was formed and leads to lower charge overpotential due to their close contact with the electrode surface and electric transport properties. Viswanathan et al. found that an average film thickness of 5 to 10 nm is the critical film thickness above which there is no more charge transfer and cell death is attained.[79] The thickness was calculated from the charge of  $\text{Li}_2\text{O}_2$  formation and its bulk density and was comparable to the theoretical calculations.

Thus, the structure of  $\text{Li}_2\text{O}_2$  affect the performance. Sluggish charge transport within  $\text{Li}_2\text{O}_2$  might lead to higher overpotential. Amorphous  $\text{Li}_2\text{O}_2$  was found to have 12-times higher ionic conductivity and 4-times higher electronic conductivity than the crystalline phase.[80] Therefore, the amorphous phase could enhance the charging process. Gebirg et al. showed experimentally that defects in  $\text{Li}_2\text{O}_2$  could induce charge transport. They proposed that  $\text{Li}_2\text{O}_2$  is a mixed conductor with lithium vacancies (origin of ionic conductivity) and mobile electron holes (origin of electronic conductivity).[81] The electric conductivity of  $\text{Li}_2\text{O}_2$  layer influences the growth mechanism. Nørskov and co-workers addressed that there are some metallic states, which are present in/on the surface of  $\text{Li}_2\text{O}_2$  during cell operation.[82] One cannot exclude that  $\text{Li}_2\text{O}_2$  is insulating although it can be cycled with lower overpotential as in the case of sulfur in Li-S batteries. Finally, the nature of  $\text{Li}_2\text{O}_2$  and its electric properties is still a topic for further exploration.

### **1.3. Oxygen reduction (ORR) and evolution (OER) reactions in alkaline media: Electrocatalysis**

ORR and OER are at the heart of the processes taking place in the most promising energy sources as fuel cell, electrolyzers and metal-air batteries. These two reactions play a critical role in the large-scale application of such technologies. Due to the sluggish kinetics of ORR/OER and the higher overpotential in aqueous media[83], the development of a corrosion-resistant highly effective catalyst for both OER and ORR (*Bifunctional catalyst*) is of strong interest for researchers and industry members. Currently, Pt-based materials are the most practical ORR catalysts in alkaline and acidic solutions.[84, 85] However, the main drawbacks of Pt-containing catalysts are their high cost and low abundance, which

consequently, stimulate extensive research over the past decades to develop alternative catalysts, including non-noble metals, which will be discussed in details later. We first give an overview on the electrochemical reactions in acidic and alkaline media, mechanisms of ORR and OER in alkaline media, simple kinetics and electrocatalysis.

### 1.3.1. Electrochemical oxygen reactions-Acid vs. Alkaline medium: Thermodynamic and kinetic advantages

The pH of the electrolyte (i.e. the nature of  $H^+$  and  $OH^-$ ) plays a major role in the electrochemical reactions of oxygen.[86] It also affects the thermodynamics drawn from the Pourbaix diagram. The change from acidic to alkaline media leads to two effects:

a) Nernstian potential shift; where a potential shift of -59 mV occurs for each increase of 1 pH unit. The working potential range shifts by -0.83V vs. SHE when changing from strong acid to a strong base occurs, as shown in the standard redox potential scheme of Fig. 8B. This shift can change the double layer structure at the electrode/electrolyte interface, which leads to different adsorption energies.[87]

b) Change of the adsorption potential of species due to the potential shift. The so-called kinetic facility, which is referred to the stability of peroxide intermediate during ORR, is also attributed to an outer-sphere electron transfer mechanism in alkaline media.[85]

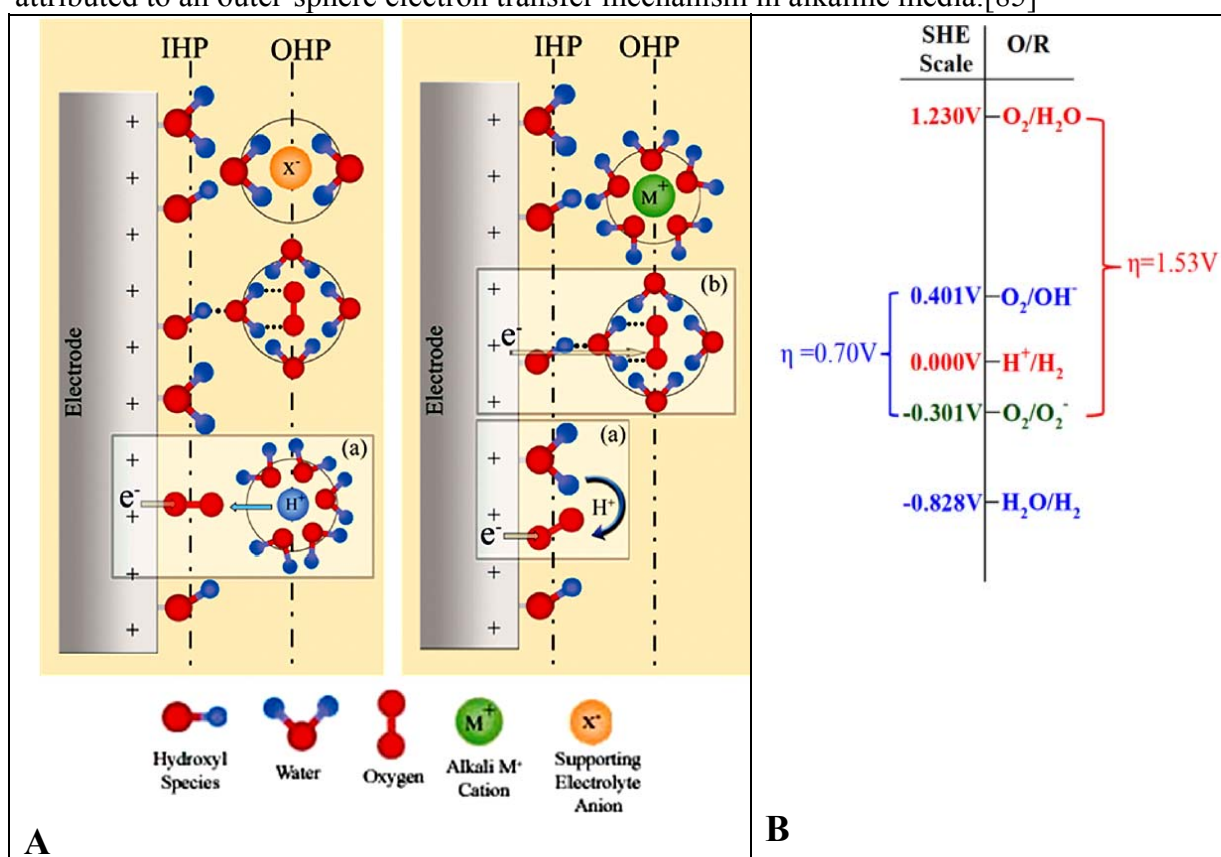


Fig. 8. A: Scheme of the double layer structure during ORR in acidic (left drawing) and alkaline (right drawing) solutions. Insets (a) and (b) represent the inner and outer sphere electron transfer processes. Reprinted from [85]. B: standard electrode potentials of  $O_2$  reduction vs. SHE in alkaline and acidic media.

The kinetic facility was investigated in terms of the double layer structure and adsorption strength.[85] The structures of the double layer in acidic and alkaline media at Pt electrode are shown in Fig. 8A. In alkaline media, inner-sphere and outer-sphere electron transfer processes compete, while in acidic media, the inner-sphere transfer is dominant. Specifically adsorbed  $\text{OH}^-$  is proposed to promote an outer-sphere electron transfer mechanism of ORR in alkaline media,(see Fig. 8A) as inferred from the RRDE results and the observation of a sharp peak at the ring corresponding to Pt-OH formation at Pt-disc at  $\sim 0.9\text{V}$  in the cathodic scan. This process is surface independent, and leads to a 2e-peroxide intermediate as the final product.[85] In acidic media, the inner-Helmholtz plane (IHP) consists of hydroxyl anions, oxygen molecules and water dipoles, while the outer-Helmholtz plane (OHP) contains solvated oxygen, protons and anion molecules (Fig. 8A). Since ORR occurs typically at potentials more positive to the potential of zero charge, OHP has net positive charge in acidic media. Proton transfer from OHP to IHP occurs only after the first electron transfer to  $\text{O}_{2,\text{ads}}$  and formation of superoxide. This superoxide remains adsorbed until  $4\text{e}^-$  and  $4\text{H}^+$  are transferred followed by desorption of  $\text{H}_2\text{O}$  as the product. In contrast, in alkaline media water acts as a solvent and a proton source. In the inner-sphere process, proton transfer to  $\text{O}_2^-$  occurs from adsorbed water molecules or from the partial solvation shell of adsorbed  $\text{O}_2/\text{O}_2^-$ . The superoxide formation ( $\text{O}_2 + \text{e}^- \rightarrow \text{O}_2^-$ ) is the outer-sphere process. As the pH increases, the rate of proton transfer from water is higher so that it stabilizes the superoxide. This process has lower overpotential in alkaline media (0.7V) than in acidic media (1.53V) as shown in Fig. 8B. Therefore, strong chemisorption of  $\text{O}_2$  is not necessary in alkaline media since other forces (e.g. dipole-dipole interactions) could be sufficient to overcome this overpotential.[85] The nonspecific outersphere mechanism which is due to formation of oxide on the metal surface, and its interaction with solvated oxygen molecules could be the reason for the activity of many non-noble metals and their oxides as catalysts for ORR in alkaline media.[85]

From the kinetic point of view, the higher the Tafel slope is the faster the overpotential increase with current density. Therefore, the best catalyst should have a low Tafel slope to get higher currents at low overpotentials. It is usual that two Tafel slopes are obtained for ORR, namely 60 and 120  $\text{mV dec}^{-1}$  at lower and higher overpotentials, respectively, at most catalysts. More details will be given below.

### 1.3.2. Mechanisms of ORR in alkaline media

In alkaline media, we aimed at investigation of electrocatalysis. Typical ORR processes and their corresponding thermodynamic standard electrode potentials are shown in Fig. 9. ORR is a quite complicated reaction and includes several intermediates (e.g.  $\text{O}_2^-$ ,  $\text{HO}_2^-$ ,  $\text{OH}^-$ ) depending on the electrode material and electrolyte.[88] Therefore, several mechanisms have been proposed for ORR. The most general scheme for ORR pathways in acidic and alkaline media is shown in Fig. 9, adapted from [89, 90].

In General, there are two electrochemical pathways of ORR in aqueous electrolytes (see Fig. 9): *direct pathway* in which four electrons are consumed to reduce  $\text{O}_2$  to water (or  $\text{OH}^-$  in alkaline) with the rate constant  $k_1$ ; *series pathway* in which  $\text{H}_2\text{O}_2$  (or  $\text{HO}_2^-$ ) may be produced as intermediate with a rate constant  $k_2$  along the sequential pathway. Subsequently, hydrogen peroxide can be electrochemically reduced to water (or  $\text{OH}^-$ ) with the rate constant  $k_3$ ,

catalytically decomposed on the electrode surface ( $k_4$ ), or desorbed ( $k_5$ ). In this pathway, each step needs 2 electrons. If  $k_1 > k_2$ , the direct reduction of oxygen to water is more dominant than to peroxide, whereas if  $k_1/k_2$  is less than 1 and  $k_3$  is large, reduction to peroxide and further to water dominates. The 4e-reduction of  $O_2$  can also proceed via stepwise of two 2e-reduction steps. Whether ORR proceeds via direct 4-es or two 2-es pathway is not easy to distinguish and depends on the electrode nature. For most electrocatalysts, ORR takes place via the series pathway to water due to the high stability of O-O bond of oxygen, which has a dissociation energy of  $492 \text{ kJ mol}^{-1}$ . Also, the formation of superoxide anion  $O_2^-$  at Pt during ORR in alkaline media was confirmed by surface-enhanced infrared spectroscopy technique, implying the occurrence of the series pathway.[91]

In alkaline media, the lower working potential of the electrode would facilitate desorption of  $HO_2$  as  $HO_2^-$ , while the higher working potential in acidic media would prevent  $HO_2$  desorption, thus further protonation to  $H_2O_2$  occurs before its desorption. Therefore, the term *series pathway* is more proper for alkaline media. Each ORR pathway has its own importance: for fuel cells and metal-air batteries, the 4e-pathway is highly preferred, while the 2e-pathway is used for industrial production of  $H_2O_2$ . Generation of  $H_2O_2$  is impractical for fuel cells since  $H_2O_2$  blocks the active sites of metal complexes and causes loss of activity.[92]

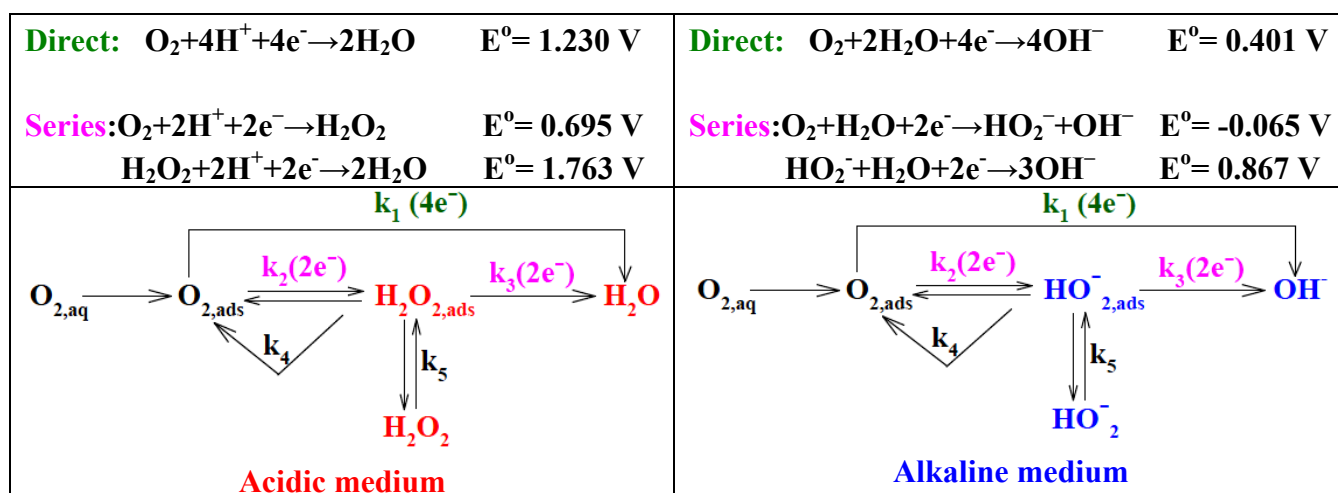


Fig. 9. General scheme of ORR pathways in alkaline (right panels) and acidic media (left panels). The direct and series pathways are included.  $k_i$  is the overall rate constant of the  $i^{\text{th}}$  step. Adapted from [89, 90, 93].

Here, details on the different ORR mechanisms are presented. Damjanovic et al. listed in 1966 a summary of the 14 different stepwise pathways.[94] Later, Pillai and Bockris extended the list to include two more mechanisms.[95] we show the most common ORR mechanisms from Bockris list, as displayed in Table 2 along with the predicted Tafel slope in each of the steps being the rate determining step (rds) and the reaction order with respect to  $O_2$  partial pressure.[95] The theoretical mechanistic parameters are quoted for Langmuir type ( $\Theta \rightarrow 0$  and  $\Theta \rightarrow 1$ ). The different mechanisms match the general scheme shown in Fig. 9 with little difference in how  $OH_{\text{ads}}$  is formed. Generally, ORR starts with diffusion of oxygen from the bulk electrolyte to the electrode interface where adsorption of O-species takes place, followed

by protonation to either  $\text{OH}_{\text{ads}}$  or to peroxide  $\text{H}_2\text{O}_{2,\text{ads}}$  depending on the electrode nature. The final step in all mechanisms is the reduction (desorption) of  $\text{OH}_{\text{ads}}$  to  $\text{OH}^-$  in alkaline media.

Mechanism	Stepwise reactions	Tafel slope		$\left(\frac{\partial \ln i}{\partial \ln p_{\text{O}_2}}\right)_{E,\text{pH}}$
		$\Theta \rightarrow 0$	$\Theta \rightarrow 1$	$\Theta \rightarrow 0$
<b>Bockris's Oxide Path</b>	$\text{O}_2 \leftrightarrow 2\text{O}_{\text{ads}}$	$\infty$	--	1
	$\text{O}_{\text{ads}} + \text{H}_2\text{O} \leftrightarrow 2\text{OH}_{\text{ads}}$	$\infty$	$\infty$	0.5
	$\text{OH}_{\text{ads}} + e^- \leftrightarrow \text{OH}^-$	2RT/F	2RT/F	0.25
<b>Bockris's electrochemical oxide path</b>	$\text{O}_2 \leftrightarrow 2\text{O}_{\text{ads}}$	$\infty$	--	1
	$\text{O}_{\text{ads}} + \text{H}_2\text{O} + e^- \leftrightarrow \text{OH}_{\text{ads}} + \text{OH}^-$	2RT/F	2RT/F	0.5
	$\text{OH}_{\text{ads}} + e^- \leftrightarrow \text{OH}^-$	2RT/3F	2RT/F	0.5
<b>Hydrogen Peroxide path</b>	$\text{O}_2 + \text{H}_2\text{O} \leftrightarrow \text{O}_2\text{H}_{\text{ads}} + \text{OH}_{\text{ads}}$	$\infty$	--	1
	$\text{O}_2\text{H}_{\text{ads}} + \text{H}_2\text{O} \leftrightarrow \text{O}_2\text{H}_{2\text{ads}} + \text{OH}_{\text{ads}}$	RT/F	$\infty$	1
	$\text{O}_2\text{H}_{2\text{ads}} \leftrightarrow 2\text{OH}_{\text{ads}}$	RT/2F	$\infty$	1
	$\text{OH}_{\text{ads}} + e^- \leftrightarrow \text{OH}^-$	2RT/F	2RT/F	0.25
<b>Krasil'shchikov's path</b>	$\text{O}_2 \leftrightarrow 2\text{O}_{\text{ads}}$	$\infty$	--	1
	$\text{O}_{\text{ads}} + e^- \leftrightarrow \text{O}_{\text{ads}}^-$	2RT/F	2RT/F	0.5
	$\text{O}_{\text{ads}}^- + \text{H}_2\text{O} \leftrightarrow \text{OH}_{\text{ads}} + \text{OH}^-$	RT/F	$\infty$	0.5
	$\text{OH}_{\text{ads}} + e^- \leftrightarrow \text{OH}^-$	2RT/3F	2RT/F	0.5
<b>O'Grady's path</b>	$\text{O}_2 + 2\text{H}_2\text{O} \leftrightarrow 2\text{OH}_{\text{ads}}^+ + 2\text{OH}^-$	$\infty$	--	1
	$\text{OH}_{\text{ads}}^+ + e^- \leftrightarrow \text{OH}_{\text{ads}}$	2RT/F	2RT/F	0.5
	$\text{OH}_{\text{ads}} + e^- \leftrightarrow \text{OH}^-$	2RT/3F	2RT/F	0.5

Table 2. The most common ORR mechanisms and the predicted kinetic parameters.[95] Tafel slopes are calculated on the basis of Langmuir adsorption conditions.

### 1.3.3. Mechanisms of OER in alkaline media

Due to the large number of possible intermediates in OER, in 1965 Bockris reported a kinetic mechanistic analysis of the possible OER pathways, reaction order and the expected Tafel slopes for each step under Langmuir conditions.[96] Later, Damjanovic listed the 14 possible OER pathways at both low and high adsorbate coverages.[94] In Table 3 a summary of the five most commonly considered OER pathways is presented. This is reproduced from the original work of Bockris and Otagawa.[97]

Bockris-Otagawa[97] mechanism for OER on perovskites proposed a two-step reaction pathway (Fig. 10). In the first reaction step (a) the accumulation of a water molecule due to dipole interactions on the transition metal cation of perovskite takes place. Then, proton transfer from the adsorbed water molecule to the molecules of water solvated in the electrolyte results in the formation of a hydroxide ion, which is adsorbed on the transition metal cation. Afterwards, electron transfer occurs in the rds, forming an M-OH bond. In the second reaction step (b), M-OH reacts further with hydroxide ion from the electrolyte so that  $\text{H}_2\text{O}_2$  is generated on the metal surface through another proton and electron transfer. These

two steps correspond to the first and second steps in Bockris's oxide mechanism shown in Table 3.

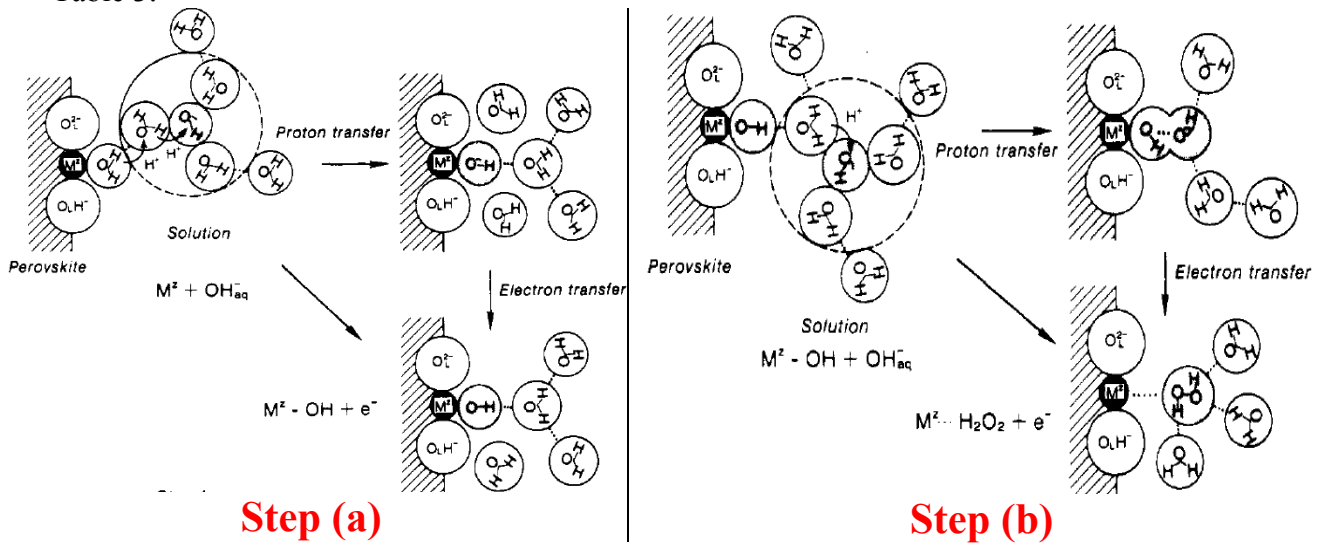


Fig. 10. Schematic illustration of OER at perovskite electrode according to Bockris and Otagawa.[97]

Bockris and Otagawa also found that the OER activity is inversely proportional to the surface bond energy of OH, and thus the rds is the desorption of OH or oxygenated species.[97] DFT calculations by Rossmeisl et al. were performed on rutile oxides of  $\text{RuO}_2$ ,  $\text{IrO}_2$  and  $\text{TiO}_2$  and found that the oxides has lower OER overpotentials than their metals, due to the stronger OH binding to the surface.[98] Suntivic et al. reported that the degree of occupancy of the  $e_g$ -level in transition metals is a suitable descriptor of the OER activity of perovskites, whereas Subbaraman et al. found a correlation between the M-OH bond strength in M-OOH clusters and their OER activity.[99]

In all of these mechanisms, the first step involves the discharge of hydroxide ions at the surface to form adsorbed intermediate as OH radicals. The subsequent steps involve the formation of a range of surface adsorbed intermediates such as MO, MOOH or physisorbed peroxide species.[100] These intermediates can react with each other, with other intermediates or with the electrolyte and release oxygen. If the stability of a certain adsorbate increases, the rate control can shift to a later step.[100] Hence, low Tafel slopes are attributed to the interaction of strongly adsorbed intermediates.

O'Grady mechanism showed the participation of metal oxide in OER, where OER is facilitated by a redox transition and the formation of an oxide intermediate containing higher oxidation state of the metal than its initial state.[100, 101] This mechanism explains the low Tafel slope without the need to consider strong surface adsorption. The electrocatalytic activity of the various oxide films can be ascribed to the presence of complex anionic surface groups, consisting of octahedrally coordinated metal complexes – the surfaquo group.[100]

Cominellis and co-workers proposed a generalized scheme for OER at metal oxides in acidic media. Their model involves the transition of the metal oxide to higher valent state, which then contributes to OER.[102, 103] This is so-called "Oxygen exchange mechanism" during OER and it is later proved on  $\text{IrO}_2$  and  $\text{RuO}_2$  using isotope labeling and DEMS by Wohlfahrt-Mehren, Baltruschat and Krttil groups.[103, 104] The authors revealed that lattice oxygen is taking part in OER and only the outermost layers of the oxide are active. We proposed a

similar model for  $\text{Co}_3\text{O}_4$  in alkaline media, and the catalytic cycle of  $\text{Co}_3\text{O}_4$  will be discussed in details in chapter 7.

Mechanism	Stepwise reactions	Tafel slope		$(\frac{\partial \ln i}{\partial \ln C_{\text{OH}^-}})_{E,\zeta}$	$\nu$
		$\Theta \rightarrow 0$	$\Theta \rightarrow 1$		
Bockris's oxide	$M + \text{OH}^- \rightarrow \text{MOH} + e^-$	2RT/F	--	1	4
	$\text{MOH} \rightarrow \text{MOH} + M + \text{H}_2\text{O}$	RT/2F	$\infty$	2	2
	$2\text{MO} \rightarrow 2M + \text{O}_2$	RT/4F	$\infty$	4	1
Bockris's electrochemical	$M + \text{OH}^- \leftrightarrow \text{MOH} + e^-$	2RT/F	--	1	2
	$\text{MOH} + \text{OH}^- \leftrightarrow \text{MO} + \text{H}_2\text{O} + e^-$	2RT/3F	$\infty$	2	2
	$2\text{MO} \rightarrow 2M + \text{O}_2$	RT/4F	2RT/F	4	1
Krasil'shchikov	$M + \text{OH}^- \rightarrow \text{MOH} + e^-$	2RT/F	--	1	2
	$\text{MOH} + \text{OH}^- \rightarrow \text{MO}^- + \text{H}_2\text{O}$	RT/F	$\infty$	2	2
	$\text{MO}^- \rightarrow \text{MO} + e^-$	2RT/3F	2RT/F	2	2
	$2\text{MO} \rightarrow 2M + \text{O}_2$	RT/4F	$\infty$	4	1
O'Grady	$M^z + \text{OH}^- \rightarrow M^z\text{OH} + e^-$	2RT/F	--	1	2
	$M^z\text{OH} + \text{OH}^- \rightarrow M^{z+1}\text{OH} + e^-$	2RT/3F	2RT/F	1	2
	$2M^{z+1}\text{OH} + 2\text{OH}^- \rightarrow M^z + \text{H}_2\text{O} + \text{O}_2$	RT/4F	$\infty$	4	1
Kobussens	$M + \text{OH}^- \rightarrow \text{MOH} + e^-$	2RT/F	--	1	1
	$\text{MOH} + \text{OH}^- \rightarrow \text{MO} + \text{H}_2\text{O} + e^-$	2RT/3F	2RT/3	2	1
	$\text{MO} + \text{OH}^- \rightarrow \text{MO}_2\text{H}^-$	RT/2F	F $\infty$	3	1
	$\text{MO}_2\text{H}^- + \text{OH}^- \rightarrow \text{MO}_2^- + \text{H}_2\text{O} + e^-$	2RT/5F	2RT/F	4	1
	$\text{MO}_2^- \rightarrow M + \text{O}_2 + e^-$	2RT/7F	$\infty$	4	1

Table 3. The most common OER mechanisms and the predicted kinetic parameters.[97] Tafel slopes are calculated on the basis of Langmuir adsorption conditions.  $\nu$  is the stoichiometric number (the number of times the step occurs per cycle of the overall reaction) and  $\zeta$  is the potential difference between the OHP and the bulk of the solution.

Recently, Suntivich et al.[105] proposed design principles for OER activity on perovskites and mentioned that the activity is dependent of  $e_g$  orbital filling of the transition metal cation. They proposed reaction mechanisms for ORR and OER at perovskite, where redox transition of the metal cation is involved in the catalytic cycle, as shown in Fig. 11. Both ORR (scheme B) and OER (scheme A) proceed via 4e-pathway. For ORR, for  $e_g$  filling greater than 1, the rds is the surface hydroxide displacement due to insufficient energy gain in  $\text{O}_2^{2-}/\text{OH}^-$  (step 1), while for  $e_g$  filling less than 1, the rds is the surface  $\text{OH}^-$  regeneration (step 4). Similarly, For OER, for  $e_g$  filling more than 1 the rds is the formation of O-O bond in  $\text{OOH}$  adsorbate (step 2), while for  $e_g$  filling less than 1, the deprotonation of oxy-hydroxide group to form peroxide

ion may be the rds (step 3). Therefore, the diversity of the mechanisms for OER or ORR makes it complicated to assign a single reaction to oxygen electrocatalysis on oxide surfaces.

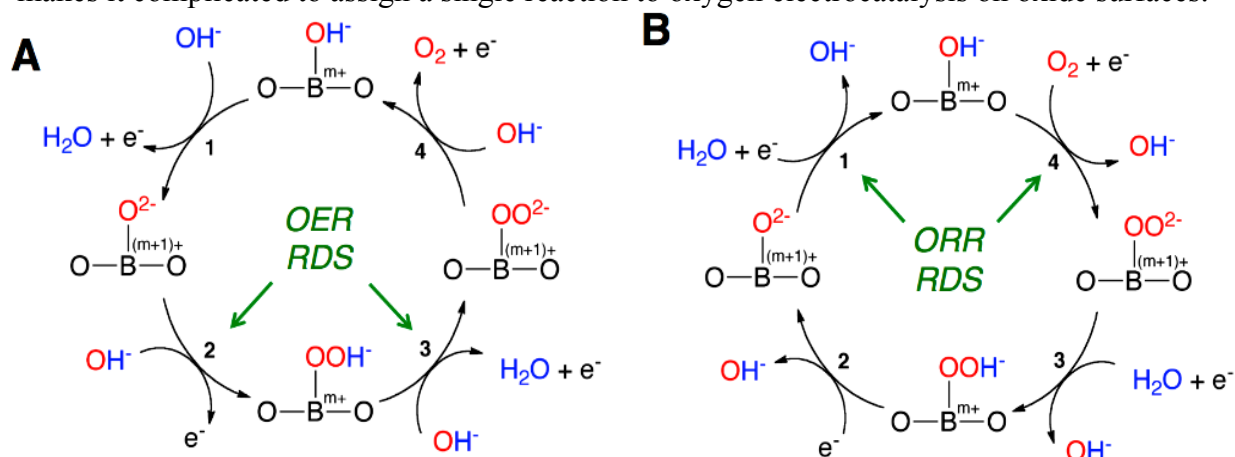


Fig. 11. Proposed mechanisms of OER (A) and ORR (B) for perovskite transition metal catalysts. Reprinted from [105].

### 1.3.4. Mechanistic insights from Tafel slope in aqueous media

Tafel slopes are indicative of the mechanism and the rds. For ORR, Tafel plots at Pt as well as at Ag in acidic and alkaline media showed two Tafel slopes, namely 60 mV/dec at low overpotential and  $\geq 120$  mV/dec at high overpotential.[106, 107] Change of Tafel slope could be due to change of the rds in the same pathway. The 60 mV/dec slope is attributed to a chemical step following the first electron transfer (most probable) according to eq. 1.9 or to a second electron transfer as the rds[107]:



In contrast, at higher overpotential, the rds is the first electron transfer to adsorbed oxygen or the dissociative adsorption of oxygen as follows[91, 106]:



These results have been supported by DFT, IR and other methods.[106] In Acidic media, the difference in Tafel slope indicates that the mechanism on Pt/PtO surface is different from that on a pure Pt surface. On Pt/PtO, the rds is a pseudo 2-electron procedure, which gives Tafel slope of 60 mV/dec, while on pure Pt surface, the first electron transfer is the rds, resulting in 120 mV/dec.[108]

For OER, in addition to what discussed above in the mechanism, a Tafel slope of 60 mV/dec means that the rds is the deprotonation of  $\text{H}_2\text{O}$  ( $\text{OH} \rightarrow \text{O} + \text{H}^+ + e^-$ ), while 120 mV/dec implies the dissociation of water as the rds ( $\text{H}_2\text{O} \rightarrow \text{OH} + \text{H}^+ + e^-$ ).

Most of the catalysts (e.g.  $\text{Co}_3\text{O}_4$ [101], Pd/C, CoPC/C[109], Ag/ $\text{Mn}_3\text{O}_4$ /C[110], LCCO-Ag/C[111]) showed a similar trend of two Tafel regions for ORR (one close to 60 mV/dec and the other is  $\geq 120$  mV/dec), and a slope  $\geq 60$  mV/dec for OER.[101, 112]

### 1.3.5. Survey of electrocatalysts for ORR and OER in alkaline media

The function of an electrocatalyst is to reduce the overpotential and enhance the kinetics. The optimum catalyst is the one which can improve the activity of both ORR and OER. This catalyst is then called "Bifunctional catalyst".

*The requirements for a good bifunctional catalyst are:*

- i. good electronic conductivity
- ii. low overpotential for ORR and OER
- iii. enhanced kinetics (lower Tafel slope) and fast electron transfer
- iv. chemical and structural stability
- v. direct 4-electron reduction of oxygen or ability to decompose the H<sub>2</sub>O<sub>2</sub> intermediate
- vi. thermal stability and corrosion resistance
- vii. tolerance to contaminants (halides, methanol, NO<sub>x</sub>, CO<sub>x</sub>)
- viii. low cost and wide abundance

### ***Pt-metal group***

It has been admitted that the most active catalysts in alkaline and acidic media are the Pt-group metals and their oxides: Pt is the best catalyst for ORR while IrO<sub>2</sub> or RuO<sub>2</sub> are best for OER.[84, 113] However, Pt has some drawbacks: sensitivity to contaminants like benzene, halides, NO<sub>2</sub>, CO and SO<sub>2</sub>:[114] non-tolerance to alcohols; dissolution under acidic conditions which reduces the Pt activity.[115] It is found that Ru and RuO<sub>2</sub> are unstable[116] and Pt/IrO<sub>2</sub> can easily agglomerate, leading to loss of activity.[117] Nevertheless, the main hurdle, which is facing the wide application of Pt-group metals is their high cost.

To reduce the cost, reduction of the Pt loading is one possibility. For that, several approaches have been investigated: i) Dispersing Pt on an appropriate support: carbon is one of the most used supports due to its high surface area, good electronic conductivity, mechanical stability and low cost.[118] ii) Reducing the Pt particle size.[119] iii) Using bimetallic catalysts in different architectures (e.g. core-shell or alloy) to minimize the Pt amount. Higher kinetic current (10-20 times) for ORR in acidic media has been observed on Pt alloys with Ni, Co, and Fe compared to that of pure Pt.[120] Markovic et al. demonstrated the outperformance of Pd modified-Pt film in alkaline solution for ORR compared to single metals or other bimetallics.[121] Metal complexes of macrocycles such as phthalocyanine, porphyrin, and metal organic frameworks have also been shown to compete with Pt catalysts: however, they are not good catalysts for OER.[85, 109]

Chalcogenites are also active only for ORR(e.g. RuSe or metal sulfides)[122], as well as nitrides (e.g. FeN<sub>4</sub>).[123]

In the aim of replacing noble-metal catalysts, a series of non-noble materials (e.g. transition metals) and also non-metal catalysts (e.g. graphene, CNT) have been examined as bifunctional catalysts. Silver is also shown to have good ORR activity. In the last years, intensive research has been conducted to explore new materials or compositions as bifunctional catalysts. Here, we focus on the following categories which were investigated in the last few years and are related to our work. These include:

### ***Ag catalyst***

Silver is a promising catalyst to replace Pt due to its relatively low cost, wide abundance, well known kinetics and high ORR activity.[90, 124] DFT calculations showed that on the surface of Pt and Ag, adsorption of oxygen on the surface decreases the binding energy, which in turn increases their activity, making them proper for ORR in alkaline media.[125] Although Ag is unstable in acidic media due to its dissolution, it is more stable in alkaline media. Different forms of Ag have been investigated for ORR, and showed good activity and methanol tolerance.[126] Kinetics of ORR on single crystalline Ag is structure-sensitive,[90] although

all the structures followed the 4e-reduction pathway. The loading effect of Ag nanoparticles has been studied and similar activities, but different diffusion limited currents have been observed.[124] Also, comparable activities of Ag nanoparticles and Ag polycrystalline towards ORR have been reported.[124] They also estimated the real surface area of Ag using Pb-UPD. However, Ag nanopowder showed negligible OER activity. This indicates that Ag is not suitable for OER.[127]

#### ***Transition metal oxides and perovskites:***

The three structures of the metal oxide (spinel, perovskite and pyrochlore) are promising candidates for oxygen catalysis in alkaline media. Cobalt oxide-based catalysts are among the best non-precious materials with bifunctional activity:  $\text{Co}_3\text{O}_4$ -carbon porous nanowires,[128] delithiated  $\text{Li}_{0.5}\text{CoO}_2/\text{C}$ ,[129] and recently,  $\text{Co}_3\text{O}_4/\text{N}$ -doped graphene hybrid exhibited a combination of higher OER and ORR activity.[112] The later has higher ORR activity than individual  $\text{Co}_3\text{O}_4$  or GO. It also exhibited a similar ORR activity as Pt and with superior stability in alkaline solutions. However, another cobalt oxide-based catalyst showed lower activity for ORR.[130] Perovskites showed good activity and stability to OER/ORR in alkaline media (e.g.  $\text{LaCoO}_3$ ,  $\text{NiCo}_2\text{O}_4$ ).[131-134] The later has low overpotential (0.84V) and is also tested in a Zn-air battery and revealed good performance and cyclability.  $\text{LaNiO}_3$  supported on nitrogen doped carbon revealed 3-fold activity of the 6 nm  $\text{IrO}_2$  and showed no hysteresis during OER. It also exhibited a lower total overpotential (1.02V) than that of Pt (1.16V) or Ir (0.92V).[135]

Moreover, the structure plays an effective role in their activity. Mesoporous  $\text{Co}_3\text{O}_4$  spinel showed better activity than  $\text{Co}_3\text{O}_4$  nanoparticles. It has an overpotential of 1.034V which is comparable to noble metal catalysts.[136] Structure-property relationship was investigated also for  $\text{MnO}_2$  too. The bifunctional activity follows the following order (from lower to higher overpotential):  $\alpha\text{-MnO}_2 > \text{amorphous-MnO}_2 > \beta\text{-MnO}_2 > \delta\text{-MnO}_2$ . [137]

All the previously mentioned catalysts are typically loaded on carbon support to increase their conductivity.

#### ***Mixed bifunctional catalysts***

One interesting approach is the combination of the best characteristics of two components in one catalyst (*mixed catalyst*). This could include bimetallic or trimetallic catalyst or a physical mixture of two components. However, these mixed catalysts were mostly investigated for only ORR. Markovic et al. have found 10 times higher ORR activity on  $\text{Pt}_3\text{Ni}(111)$  than on  $\text{Pt}(111)$  and also higher than the commercial Pt/C in acidic media,[138] Similar improvement was observed for Metal-Co catalysts in acidic[139] or alkaline media.[140]

Since Co and Mn-based catalysts are inexpensive, researchers examined the synergistic effect resulting from coupling these materials with other components. Combination of Ag and metaloxides is reported. Lima et al. studied ORR kinetics on Ag-Co/C bimetallic catalyst in alkaline media, and showed that ORR was shifted to lower overpotentials on the mixed catalyst.[140] This was attributed to a sort of electronic interaction between Ag and Co in the mixture. Later, Ag/ $\text{Co}_3\text{O}_4$ -C was also studied and showed high activity and methanol tolerance.[141] A three-times mass activity enhancement for ORR was observed for Ag- $\text{MnO}_x/\text{C}$  ( $125\text{mA}/\text{mg}_{\text{Ag}+\text{MnO}_x}$ ) over the linear combination of pure component activities using RDE, and is comparable to commercial Pt/C ( $136\text{ mA}/\text{mg}_{\text{Pt}}$ ). The synergy was attributed to electronic effect and ensemble effect in which Ag facilitates  $\text{HO}_2^-$  formation, while  $\text{MnO}_x$

helps disproportionation.[142] These Ag-containing catalysts were only ORR active, and OER was not studied since Ag alone is known to be inactive for OER, thus they are not considered as bifunctional catalysts. Mn and Co co-substituted  $\text{Fe}_3\text{O}_4$  on graphene oxide catalyst has been effectively combined the OER activity of Co-oxide with the ORR activity of Mn-oxide in one hybrid.[131] Enhanced bifunctional activity of  $\text{Mn}_x\text{Cu}_{1-x}\text{Co}_2\text{O}_4/\text{C}$  was reported, and the higher OER activity was attributed to the transition from  $\text{Co}^{3+}$  to  $\text{Co}^{4+}$  at active sites.[143]  $\text{Ba}_{0.9}\text{Co}_{0.5}\text{Fe}_{0.4}\text{Nb}_{0.1}\text{O}_{3-\delta}/\text{C}$  perovskite was reported as a good bifunctional catalyst, but less ORR activity was observed.[144]

Most recently, the synergistic bifunctional effect observed on Pt-BSCF/C (or even only ORR improvement on Ag- $\text{LaMnO}_3/\text{C}$  or Ag-Co alloy) was attributed to several reasons: spillover effect; ligand effect and electronic effect.[145-147]

Nevertheless, most of the studied bifunctional catalysts are supported on carbon, although carbon is known to have corrosion problems at higher potentials. Therefore, we aimed in this work at a carbon-free bifunctional catalyst. Carbon-free bifunctional catalyst reports are very few in literature. For example, a matrix catalyst containing  $\text{MnO}_2$  and Cr showed good bifunctional activity, but with a non-facile synthesis method.[148] Very small loading of Co-Ni/ $\text{TeO}_2$  showed to have high bifunctional catalytic activity.[149] Therefore, a combination of Co and Ni seems highly promising, and thus it is examined in our work.

Physical mixing of Pt with BSCF in one mixture was reported, although it is not a cost-effective material.[145] One report presented the enhanced activity of Ag- $\text{MnO}_2$  hybrid and its stability for 270 cycles.[150] However, it has a higher OER overpotential (onset  $> 1.65V_{\text{RHE}}$ ). Carbon-free Mn-oxide nanostructures showed to be very active for both ORR and OER and showed excellent activity with the lower overpotentials. However no mechanistic or kinetic details are provided, and the stability of the catalyst is not reported.[151]  $\text{Mn}_{0.9}\text{Co}_{2.1}\text{O}_4$  showed also good bifunctionality, but with  $\sim 3.7$  electrons transferred.[152]

Thus, the idea followed and achieved in our work was to combine the benefits of a cost-effective and highly conductive Ag catalyst with a spinel  $\text{Co}_3\text{O}_4$  in one mixture. We reported the enhanced bifunctional activity of Ag+ $\text{Co}_3\text{O}_4$  with detailed mechanistic and kinetic studies in our publication.[56] The long-term stability and EIS experiments were also reported.[153] Further structural investigations on the same composite has been recently reported by our project partners.[154] They reported that electronic changes in the catalyst are the reason for the enhanced OER activity. They also confirmed the formation of  $\text{Ag}^I\text{Ag}^{III}\text{O}_2$  at high potentials, and showed its instability under dry conditions. In parallel to my work, our project partners screened various catalysts, including noble metals and perovskites, for the purpose of finding a suitable bifunctional catalyst.[155] The activity of a carbon-free Ni/ $\text{Co}_3\text{O}_4$  catalyst is here investigated using RRDE and the mechanism is elucidated. On the other hand, the long-term stability measurements on this catalyst were carried out on a GDE and the results showed good stability for ORR and OER.[156]

### 1.3.6. Support effect in the catalytic activity

The use of conductive support was found to influence the performance of the catalyst loaded on it. Carbon is the most commonly used catalyst support.  $\text{TiO}_2$  was used as a conductive support for bifunctional catalysts as  $\text{CuCo}_2\text{O}_4$ , and showed higher current densities compared to Vulcan carbon.[157] Furthermore, support effect was studied on  $\text{SnO}_x$  substrate and it was

found that Au-SnO<sub>x</sub> is active for ORR whereas Au/C is inactive, suggesting that SnO<sub>x</sub> imparts the ORR activity of Au in acid, and during ORR OH<sup>-</sup> adsorption was enhanced through a ligand effect.[158] This implies a synergistic interaction between SnO<sub>x</sub> and Au. Also, ORR was enhanced on Ag/CeO<sub>2</sub> compared to bare Ag. This is due to the lower energy barrier for O<sub>2</sub> dissociation on the triple phase boundaries in Ag/CeO<sub>2</sub> than on the double phase boundaries in bare Ag.[159] Thus, the investigation of the synergistic effect between catalyst and support would be promising for development of high activity for ORR and OER. In this work, in order to find out the influence of the metal properties on the overall activity, two materials (Ag or Ni) which act as the support of Co<sub>3</sub>O<sub>4</sub> were investigated. Ag showed better activity than Ni when it is combined with Co<sub>3</sub>O<sub>4</sub> in a mixed catalyst.

#### 1.4. References

- [1] Key world energy statistics, International Energy Agency, <http://www.iea.org/publications/>, Paris, France, 2015.
- [2] D.A. Lashof, D.R. Ahuja, *Nature* 344 (1990) 529-531.
- [3] G. Girishkumar, B. McCloskey, A.C. Luntz, S. Swanson, W. Wilcke, *The Journal of Physical Chemistry Letters* 1 (2010) 2193-2203.
- [4] D. Safanama, D. Damiano, R.P. Rao, S. Adams, *Solid State Ionics* 262 (2014) 211-215.
- [5] U.S.D.o.E. Office of Energy Efficiency and Renewable Energy, <http://energy.gov/eere/fuelcells/fuel-cells>, 2015.
- [6] D. Meadows, D. Meadows, J. Randers, *The Limits to Growth*, Universe Books, 1972.
- [7] P. Hartmann, A rechargeable room-temperature sodium superoxide (NaO<sub>2</sub>) battery, Doctoral thesis, Universität Gießen, Giessen, Germany, 2013.
- [8] REN21, *Renewables 2015 Global Status Report*, Renewable Energy Policy Network for the 21st Century, Paris, 2015.
- [9] I.E. Agency, *Technology roadmap: Electric and plug-in hybrid electric vehicles*, [http://www.iea.org/publications/freepublications/publication/EV\\_PHEV\\_Roadmap.pdf](http://www.iea.org/publications/freepublications/publication/EV_PHEV_Roadmap.pdf), OECD/IEA, Paris, 2011.
- [10] J.M. Tarascon, M. Armand, *Nature* 414 (2001) 359-367.
- [11] J.M. Tarascon, *Philosophical Transactions of the Royal Society of London A: Mathematical, Physical and Engineering Sciences* 368 (2010) 3227-3241.
- [12] U.s.c.f.a. research, *EV battery goals-CY2020 commercialization*, <http://www.uscar.org/guest/publications.php>, USCAR, Southfield, USA, 2014.
- [13] J.B. Goodenough, K.-S. Park, *Journal of the American Chemical Society* 135 (2013) 1167-1176.
- [14] K. Zaghbi, A. Mauger, H. Groult, J.B. Goodenough, C.M. Julien, *Materials* 6 (2013) 1028-1049.
- [15] C.M. Julien, A. Mauger, K. Zaghbi, H. Groult, *Inorganics* 2 (2014) 132-154.
- [16] J.B. Goodenough, Y. Kim, *Chemistry of Materials* 22 (2010) 587-603.
- [17] K.M. Abraham, Z. Jiang, *Journal of the Electrochemical Society* 143 (1996) 1-5.
- [18] G. Girishkumar, B. McCloskey, A.C. Luntz, S. Swanson, W. Wilcke, *J. Phys. Chem. Lett.* 1 (2010) 2193-2203.
- [19] T. Ogasawara, A. Débart, M. Holzapfel, P. Novák, P.G. Bruce, *Journal of the American Chemical Society* 128 (2006) 1390-1393.
- [20] J. Christensen, P. Albertus, R.S. Sanchez-Carrera, T. Lohmann, B. Kozinsky, R. Liedtke, J. Ahmed, A. Kojic, *Journal of The Electrochemical Society* 159 (2012) R1-R30.
- [21] A. Kraytsberg, Y. Ein-Eli, *Journal of Power Sources* 196 (2011) 886-893.
- [22] T. Zhang, H. Zhou, *Angewandte Chemie International Edition* 51 (2012) 11062-11067.

- [23] J. Xiao, D. Mei, X. Li, W. Xu, D. Wang, G.L. Graff, W.D. Bennett, Z. Nie, L.V. Saraf, I.A. Aksay, J. Liu, J.-G. Zhang, *Nano Letters* 11 (2011) 5071-5078.
- [24] G. Zhao, R. Mo, B. Wang, L. Zhang, K. Sun, *Chem. Mat.* 26 (2014) 2551-2556.
- [25] V.S. Bryantsev, V. Giordani, W. Walker, M. Blanco, S. Zecevic, K. Sasaki, J. Uddin, D. Addison, G.V. Chase, *The Journal of Physical Chemistry A* 115 (2011) 12399-12409.
- [26] G.M. Veith, J. Nanda, L.H. Delmau, N.J. Dudney, *The Journal of Physical Chemistry Letters* 3 (2012) 1242-1247.
- [27] C.O. Laoire, S. Mukerjee, K.M. Abraham, E.J. Plichta, M.A. Hendrickson, *Journal of Physical Chemistry C* 113 (2009) 20127-20134.
- [28] W. Xu, J. Xiao, D.Y. Wang, J. Zhang, J.G. Zhang, *Journal of the Electrochemical Society* 157 (2010) A219-A224.
- [29] M.J. Lacey, J.T. Frith, J.R. Owen, *Electrochem. Commun.* 26 (2013) 74-76.
- [30] Y. Chen, S.A. Freunberger, Z. Peng, O. Fontaine, P.G. Bruce, *Nat Chem* 5 (2013) 489-494.
- [31] S. Schaltin, G. Vanhoutte, M. Wu, F. Barde, J. Fransaer, *Physical chemistry chemical physics : PCCP* 17 (2015) 12575-12586.
- [32] H.-D. Lim, H. Song, J. Kim, H. Gwon, Y. Bae, K.-Y. Park, J. Hong, H. Kim, T. Kim, Y.H. Kim, X. Lepro, R. Ovalle-Robles, R.H. Baughman, K. Kang, *Angewandte Chemie-International Edition* 53 (2014) 3926-3931.
- [33] J.-S. Lee, S. Tai Kim, R. Cao, N.-S. Choi, M. Liu, K.T. Lee, J. Cho, *Advanced Energy Materials* 1 (2011) 34-50.
- [34] J. Read, *Journal of The Electrochemical Society* 149 (2002) A1190-A1195.
- [35] S.J. Visco, Y.S. Nimon, B.D. Katz, *Ionically Conductive Composites For Protection Of Active Metal Anodes*, PolyPlus Battery Company, US, 2007.
- [36] Y.G. Wang, H.S. Zhou, *Journal of Power Sources* 195 (2010) 358-361.
- [37] T. Liu, M. Leskes, W. Yu, A.J. Moore, L. Zhou, P.M. Bayley, G. Kim, C.P. Grey, *Science* 350 (2015) 530-533.
- [38] R. Black, B. Adams, L.F. Nazar, *Advanced Energy Materials* 2 (2012) 801-815.
- [39] C.J. Allen, S. Mukerjee, E.J. Plichta, M.A. Hendrickson, K.M. Abraham, *J. Phys. Chem. Lett.* 2 (2011) 2420-2424.
- [40] Z. Peng, S.A. Freunberger, Y. Chen, P.G. Bruce, *Science* 337 (2012) 563-566.
- [41] C. Bondue, P. Reinsberg, A.-E.-A.A. Abd-El-Latif, H. Baltruschat, *Phys. Chem. Chem. Phys.* 17 (2015) 25593-25606.
- [42] C.O. Laoire, S. Mukerjee, K.M. Abraham, E.J. Plichta, M.A. Hendrickson, *Journal of Physical Chemistry C* 114 (2010) 9178-9186.
- [43] D. Aurbach, M. Daroux, P. Faguy, E. Yeager, *Journal of Electroanalytical Chemistry and Interfacial Electrochemistry* 297 (1991) 225-244.
- [44] L. Johnson, C. Li, Z. Liu, Y. Chen, S.A. Freunberger, P.C. Ashok, B.B. Praveen, K. Dholakia, J.-M. Tarascon, P.G. Bruce, *Nat Chem* 6 (2014) 1091-1099.
- [45] A.C. Luntz, B.D. McCloskey, *Chemical Reviews* 114 (2014) 11721-11750.
- [46] Y.-C. Lu, H.A. Gasteiger, Y. Shao-Horn, *Journal of the American Chemical Society* 133 (2011) 19048-19051.
- [47] A. Debart, J. Bao, G. Armstrong, P.G. Bruce, *Journal of Power Sources* 174 (2007) 1177-1182.
- [48] Y.-C. Lu, H.A. Gasteiger, M.C. Parent, V. Chiloyan, Y. Shao-Horn, *Electrochem. Solid-State Lett.* 13 (2010) A69-A72.
- [49] M. Marinaro, U. Riek, S.K. Eswara Moorthy, J. Bernhard, U. Kaiser, M. Wohlfahrt-Mehrens, L. Jörissen, *Electrochem. Commun.* 37 (2013) 53-56.
- [50] H.W. Park, D.U. Lee, L.F. Nazar, Z. Chen, *Journal of the Electrochemical Society* 160 (2013) A344-A350.

- [51] L. Wang, X. Zhao, Y. Lu, M. Xu, D. Zhang, R.S. Ruoff, K.J. Stevenson, J.B. Goodenough, *Journal of The Electrochemical Society* 158 (2011) A1379-A1382.
- [52] J. Zeng, C. Francia, J. Amici, S. Bodoardo, N. Penazzi, *Journal of Power Sources* 272 (2014) 1003-1009.
- [53] Y.-C. Lu, Z. Xu, H.A. Gasteiger, S. Chen, K. Hamad-Schifferli, Y. Shao-Horn, *Journal of the American Chemical Society* 132 (2010) 12170–12171.
- [54] B.D. McCloskey, R. Scheffler, A. Speidel, D.S. Bethune, R.M. Shelby, A.C. Luntz, *Journal of the American Chemical Society* 133 (2011) 18038-18041.
- [55] J.R. Harding, Y.-C. Lu, Y. Tsukada, Y. Shao-Horn, *Phys. Chem. Chem. Phys.* 14 (2012 ) 10540-10546.
- [56] H.M.A. Amin, H. Baltruschat, D. Wittmaier, K.A. Friedrich, *Electrochimica Acta* 151 (2015) 332-339.
- [57] B.D. McCloskey, D.S. Bethune, R.M. Shelby, G. Girishkumar, A.C. Luntz, *J. Phys. Chem. Lett.* 2 (2011) 1161-1166.
- [58] M. Holzapfel, A. Wursig, W. Scheifele, J. Vetter, P. Novak, *Journal of Power Sources* 174 (2007) 1156-1160.
- [59] S.A. Freunberger, Y. Chen, Z. Peng, J.M. Griffin, L.J. Hardwick, F. Bardé , P. Novák, P.G. Bruce, *Journal of the American Chemical Society* 133 (2011) 8040-8047.
- [60] J. Read, *Journal of the Electrochemical Society* 153 (2006) A96-A100.
- [61] C.O. Laoire, S. Mukerjee, E.J. Plichta, M.A. Hendrickson, K.M. Abraham, *Journal of the Electrochemical Society* 158 (2011) A302-A308.
- [62] S.A. Freunberger, Y. Chen, N.E. Drewett, L.J. Hardwick, F. Barde, P.G. Bruce, *Angewandte Chemie-International Edition* 50 (2011) 8609-8613.
- [63] H.-G. Jung, J. Hassoun, J.-B. Park, Y.-K. Sun, B. Scrosati, *Nature Chemistry* 4 (2012) 579-585.
- [64] D. Xu, Z.-l. Wang, J.-j. Xu, L.-l. Zhang, X.-b. Zhang, *Chem. Commun.* 48 (2012) 6948-6950.
- [65] R. Younesi, P. Norby, T. Vegge, *ECS Electrochemistry Letters* 3 (2014) A15-A18.
- [66] M.J. Trahan, S. Mukerjee, E.J. Plichta, M.A. Hendrickson, K.M. Abraham, *Journal of the Electrochemical Society* 160 (2013) A259-A267.
- [67] F.S. Gittleson, R.C. Sekol, G. Doubek, M. Linardi, A.D. Taylor, *Phys. Chem. Chem. Phys.* 16 (2014) 3230-3237.
- [68] M.J. Trahan, I. Gunasekara, S. Mukerjee, E.J. Plichta, M.A. Hendrickson, K.M. Abraham, *Journal of the Electrochemical Society* 161 (2014) A1706-A1715.
- [69] D. Xu, Z.-l. Wang, J.-j. Xu, L.-l. Zhang, L.-m. Wang, X.-b. Zhang, *Chem. Commun.* 48 (2012) 11674-11676.
- [70] F. Barde, Y. Chen, L. Johnson, S. Schaltin, J. Fransaer, P.G. Bruce, *Journal of Physical Chemistry C* 118 (2014) 18892-18898.
- [71] J. Herranz, A. Garsuch, H.A. Gasteiger, *Journal of Physical Chemistry C* 116 (2012) 19084-19094.
- [72] L. Cecchetto, M. Salomon, B. Scrosati, F. Croce, *Journal of Power Sources* 213 (2012) 233-238.
- [73] A. Khan, C. Zhao, *Electrochem. Commun.* 49 (2014) 1-4.
- [74] D. Zheng, X.Q. Yang, D.Y. Qu, *Chem.-Asian J.* 6 (2011) 3306-3311.
- [75] E.J. Calvo, N. Mozzhukhina, *Electrochem. Commun.* 31 (2013) 56-58.
- [76] J. Zeng, C. Francia, S. Bodoardo, N. penazzi, *Rsc Advances* 5 (2013) 83056-83064.
- [77] Y.C. Lu, D.G. Kwabi, K.P.C. Yao, J.R. Harding, J.G. Zhou, L. Zuin, Y. Shao-Horn, *Energy Environ. Sci.* 4 (2011) 2999-3007.
- [78] B.D. Adams, C. Radtke, R. Black, M.L. Trudeau, K. Zaghbi, L.F. Nazar, *Energy Environ. Sci.* 6 (2013) 1772-1778.

- [79] V. Viswanathan, K.S. Thygesen, J.S. Hummelshøj, J.K. Nørskov, G. Girishkumar, B.D. McCloskey, A.C. Luntz, *Journal of Chemical Physics* 135 (2011) 10.
- [80] F. Tian, M.D. Radin, D.J. Siegel, *Chem. Mat.* 26 (2014) 2952-2959.
- [81] O. Gerbig, R. Merkle, J. Maier, *Advanced Materials* 25 (2013) 3129-3133.
- [82] J.S. Hummelshøj, J. Blomqvist, S. Datta, T. Vegge, J. Rossmeisl, K.S. Thygesen, A.C. Luntz, K.W. Jacobsen, J.K. Nørskov, *Journal of Chemical Physics* 132 (2010) 071101.
- [83] V. Nikolova, P. Iliev, K. Petrov, T. Vitanov, E. Zhecheva, R. Stoyanova, I. Valov, D. Stoychev, *Journal of Power Sources* 185 (2008) 727-733.
- [84] K.A. Striebel, F.R. McLarnon, E.J. Cairns, *Journal of The Electrochemical Society* 137 (1990) 3351-3359.
- [85] N. Ramaswamy, S. Mukerjee, *The Journal of Physical Chemistry C* 115 (2011) 18015-18026.
- [86] J.S. Spendelow, A. Wieckowski, *Physical Chemistry Chemical Physics* 9 (2007) 2654-2675.
- [87] S.A. Wasileski, M.T.M. Koper, M.J. Weaver, *Journal of Physical Chemistry B* 105 (2001) 3518-3530.
- [88] J.L. Valdes, H.Y. Cheh, *Journal of The Electrochemical Society* 132 (1985) 2635-2640.
- [89] N.M. Markovic, P.N. Ross, *Surface Science Reports* 45 (2002) 117-229.
- [90] B.B. Blizanac, P.N. Ross, N.M. Markovic, *Journal of Physical Chemistry B* 110 (2006) 4735-4741.
- [91] M.-h. Shao, P. Liu, R.R. Adzic, *Journal of the American Chemical Society* 128 (2006) 7408-7409.
- [92] C.W.B. Bezerra, L. Zhang, K.C. Lee, H.S. Liu, A.L.B. Marques, E.P. Marques, H.J. Wang, J.J. Zhang, *Electrochimica Acta* 53 (2008) 4937-4951.
- [93] H.S. Wroblowa, P. Yen Chi, G. Razumney, *J. Electroanal. Chem.* 69 (1976) 195-201.
- [94] A. Damjanovic, A. Dey, J.O.M. Bockris, *Electrochimica Acta* 11 (1966) 791-814.
- [95] K.C. Pillai, J.O.M. Bockris, *Journal of The Electrochemical Society* 131 (1984) 568-579.
- [96] J.O.M. Bockris, *J. Chem. Phys.* 24 (1965) 817-827.
- [97] J.O. Bockris, T. Otagawa, *J. Phys. Chem.* 87 (1983) 2960-2971.
- [98] J. Rossmeisl, Z.W. Qu, H. Zhu, G.J. Kroes, J.K. Nørskov, *Journal of Electroanalytical Chemistry* 607 (2007) 83-89.
- [99] R. Subbaraman, D. Tripkovic, K.-C. Chang, D. Strmcnik, A.P. Paulikas, P. Hirunsit, M. Chan, J. Greeley, V. Stamenkovic, N.M. Markovic, *Nat Mater* 11 (2012) 550-557.
- [100] R.L. Doyle, I.J. Godwin, M.P. Brandon, M.E.G. Lyons, *Physical Chemistry Chemical Physics* 15 (2013) 13737-13783.
- [101] E. Rios, J. Gautier, G. Poillerat, P. Chartier, *Electrochimica Acta* 44 (1998) 1491-1497.
- [102] G. Foti, D. Gandini, C. Comninellis, *Current Topics in Electrochemistry* 5 (1997) 71-91.
- [103] S. Fierro, T. Nagel, H. Baltruschat, C. Comninellis, *Electrochemistry Communications* 9 (2007) 1969-1974.
- [104] K. Macounova, M. Makarova, P. Krtil, *Electrochemistry Communications* 11 (2009) 1865-1868.
- [105] J. Suntivich, K.J. May, H.A. Gasteiger, J.B. Goodenough, Y. Shao-Horn, *Science* 334 (2011) 1383-1385.
- [106] J.K. Nørskov, J. Rossmeisl, A. Logadottir, L. Lindqvist, J.R. Kitchin, T. Bligaard, H. Jonsson, *Journal of Physical Chemistry B* 108 (2004) 17886-17892.
- [107] D. Šepa, M. Vojnović, A. Damjanovic, *Electrochimica Acta* 15 (1970) 1355-1366.

- [108] N. Wakabayashi, M. Takeichi, M. Itagaki, H. Uchida, M. Watanabe, *Journal of Electroanalytical Chemistry* 574 (2005) 339-346.
- [109] J. Guo, H. Li, H. He, D. Chu, R. Chen, *Journal of Physical Chemistry C* 115 (2011) 8494-8502.
- [110] Q. Tang, L. Jiang, J. Qi, Q. Jiang, S. Wang, G. Sun, *Applied Catalysis B: Environmental* 104 (2011) 337-345.
- [111] S. Zhuang, K. Huang, C. Huang, H. Huang, S. Liu, M. Fan, *Journal of Power Sources* 196 (2011) 4019-4025.
- [112] Y. Liang, Y. Li, H. Wang, J. Zhou, J. Wang, T. Regier, H. Dai, *Nature Materials* 10 (2011) 780-786.
- [113] Y. Lee, J. Suntivich, K.J. May, E.E. Perry, Y. Shao-Horn, *The Journal of Physical Chemistry Letters* 3 (2012) 399-404.
- [114] T.J. Schmidt, U.A. Paulus, H.A. Gasteiger, R.J. Behm, *Journal of Electroanalytical Chemistry* 508 (2001) 41-47.
- [115] L. Colmenares, Z. Jusys, R.J. Behm, *Journal of Physical Chemistry C* 111 (2007) 1273-1283.
- [116] Y. Takasu, N. Yoshinaga, W. Sugimoto, *Electrochemistry Communications* 10 (2008) 668-672.
- [117] F.-D. Kong, S. Zhang, G.-P. Yin, N. Zhang, Z.-B. Wang, C.-Y. Du, *Electrochemistry Communications* 14 (2012) 63-66.
- [118] W.Z. Li, C.H. Liang, W.J. Zhou, J.S. Qiu, Z.H. Zhou, G.Q. Sun, Q. Xin, *Journal of Physical Chemistry B* 107 (2003) 6292-6299.
- [119] L.R. Merte, F. Beharfarid, D.J. Miller, D. Friebel, S. Cho, F. Mbuga, D. Sokaras, R. Alonso-Mori, T.-C. Weng, D. Nordlund, A. Nilsson, B. Roldan Cuenya, *ACS Catalysis* 2 (2012) 2371-2376.
- [120] T. Toda, H. Igarashi, H. Uchida, M. Watanabe, *Journal of the Electrochemical Society* 146 (1999) 3750-3756.
- [121] N.M. Markovic, T.J. Schmidt, V. Stamenkovic, P.N. Ross, *Fuel Cells - From Fundamentals to Systems* 1 (2001) 105-116.
- [122] N.A. Alonso-Vante, W. Jaegermann, H. Tributsch, W. Honle, K. Yvon, *Journal of the American Chemical Society* 109 (1987) 3251-3257.
- [123] U.I. Kramm, J. Herranz, N. Larouche, T.M. Arruda, M. Lefevre, F. Jaouen, P. Bogdanoff, S. Fiechter, I. Abs-Wurmbach, S. Mukerjee, J.-P. Dodelet, *Physical Chemistry Chemical Physics* 14 (2012) 11673 - 11688.
- [124] G.K.H. Wiberg, K.J.J. Mayrhofer, M. Arenz, *Fuel Cells* 10 (2010) 575-581.
- [125] H.A. Hansen, J. Rossmeisl, J.K. Nørskov, *Physical Chemistry Chemical Physics* 10 (2008) 3722-3730.
- [126] C.-L. Lee, C.-M. Syu, C.-H. Huang, H.-P. Chiou, Y.-J. Chao, C.-C. Yang, *Applied Catalysis B: Environmental* 132-133 (2013) 229-236.
- [127] N. Sasikala, K. Ramya, K.S. Dhathathreyan, *Energy Conversion and Management* 77 (2014) 545-549.
- [128] T.Y. Ma, S. Dai, M. Jaroniec, S.Z. Qiao, *Journal of the American Chemical Society* 136 (2014) 13925-13931.
- [129] T. Maiyalagan, K.A. Jarvis, S. Therese, P.J. Ferreira, A. Manthiram, *Nat Commun* 5 (2014).
- [130] Y. Zhao, L. Xu, L. Mai, C. Han, Q. An, X. Xu, X. Liu, Q. Zhang, *Proc. Nat. Acad. Sci. USA* 109 (2012) 19569-19574.
- [131] Y. Zhan, C. Xu, M. Lu, Z. Liu, J.Y. Lee, *Journal of Materials Chemistry A* 2 (2014) 16217-16223.
- [132] W. Yang, J. Salim, S. Li, C. Sun, L. Chen, J.B. Goodenough, Y. Kim, *Journal of Materials Chemistry* 22 (2012) 18902-18907.

- [133] T. Poux, A. Bonnefont, G. Kéranguéven, G.A. Tsirlina, E.R. Savinova, *ChemPhysChem* 15 (2014) 2108-2120.
- [134] M. Prabu, K. Ketpang, S. Shanmugam, *Nanoscale* 6 (2014) 3173-3181.
- [135] W.G. Hardin, D.A. Slanac, X. Wang, S. Dai, K.P. Johnston, K.J. Stevenson, *The Journal of Physical Chemistry Letters* 4 (2013) 1254-1259.
- [136] Y.J. Sa, K. Kwon, J.Y. Cheon, F. Kleitz, S.H. Joo, *Journal of Materials Chemistry A* 1 (2013) 9992-10001.
- [137] Y. Meng, W. Song, H. Huang, Z. Ren, S.-Y. Chen, S.L. Suib, *Journal of the American Chemical Society* 136 (2014) 11452-11464.
- [138] V.R. Stamenkovic, B. Fowler, B.S. Mun, G. Wang, P.N. Ross, C.A. Lucas, N.M. Markovic, *Science* 315 (2007) 493-497.
- [139] J.L. Fernandez, D.A. Walsh, A.J. Bard, *Journal of the American Chemical Society* 127 (2005) 357-365.
- [140] F.H.B. Lima, J.F.R. de Castro, E.A. Ticianelli, *Journal of Power Sources* 161 (2006) 806-812.
- [141] Y. Wang, X. Lu, Y. Liu, Y. Deng, *Electrochemistry Communications* 31 (2013) 108-111.
- [142] D.A. Slanac, A. Lie, J.A. Paulson, K.J. Stevenson, K.P. Johnston, *The Journal of Physical Chemistry C* 116 (2012) 11032-11039.
- [143] M. De Koninck, B. Marsan, *Electrochimica Acta* 53 (2008) 7012-7021.
- [144] C. Jin, Z. Yang, X. Cao, F. Lu, R. Yang, *International Journal of Hydrogen Energy* 39 (2014) 2526-2530.
- [145] Y. Zhu, C. Su, X. Xu, W. Zhou, R. Ran, Z. Shao, *Chemistry – A European Journal* 20 (2014) 15533-15542.
- [146] S.-A. Park, E.-K. Lee, H. Song, Y.-T. Kim, *Scientific Reports* 5 (2015) 13552.
- [147] A. Holewinski, J.-C. Idrobo, S. Linc, *Nat. Chem.* 6 (2014) 828-834.
- [148] F. Yin, G. Li, H. Wang, *Catalysis Communications* 54 (2014) 17-21.
- [149] V. Rashkova, S. Kitova, I. Konstantinov, T. Vitanov, *Electrochimica Acta* 47 (2002) 1555-1560.
- [150] F.W.T. Goh, Z. Liu, X. Ge, Y. Zong, G. Du, T.S.A. Hor, *Electrochimica Acta* 114 (2013) 598-604.
- [151] Y. Gorlin, T.F. Jaramillo, *Journal of the American Chemical Society* 132 (2010) 13612-13614.
- [152] X. Wu, K. Scott, *Journal of Power Sources* 206 (2012) 14-19.
- [153] D. Wittmaier, N. Wagner, K.A. Friedrich, H.M.A. Amin, H. Baltruschat, *Journal of Power Sources* 265 (2014) 299-308.
- [154] D. Wittmaier, N.A. Cañas, I. Biswas, K.A. Friedrich, *Advanced Energy Materials* 5 (2015) 1500763-1500771.
- [155] D. Wittmaier, T. Danner, N. Wagner, K.A. Friedrich, *Journal of Applied Electrochemistry* 44 (2014) 73-85.
- [156] D. Wittmaier, S. Aisenbrey, N. Wagner, K.A. Friedrich, *Electrochimica Acta* 149 (2014) 355-363.
- [157] M.D. Koninck, P. Manseau, B. Marsan, *Journal of Electroanalytical Chemistry* 611 (2007) 67-79.
- [158] D.S. Gatewood, D.E. Ramaker, K. Sasaki, K.E. Swider-Lyons, *Journal of The Electrochemical Society* 155 (2008) B834-B842.
- [159] J.-H. Wang, M. Liu, M.C. Lin, *Solid State Ionics* 177 (2006) 939-947.



## 2. Theoretical background

### 2.1. Electrode kinetics

#### 2.1.1. Interface structure

The electrochemical reactions at interface and in solution involve electron transfer and charged species transport, and thus called *interfacial processes*. Considering the following generic reaction:



where, O and R are the oxidized and reduced forms of a redox couple.  $k_c$  and  $k_a$  are the rate constants of cathodic and anodic reactions, respectively. Across the electrified interface, a net charge separation must develop at equilibrium, which creates a potential difference given by  $\Delta\phi$ . This potential difference differs from the applied potential (E) by a constant, which depends on the reference electrode. The *Nernst equation* is then given by eq. 2.2:

$$E = E^\circ + \left(\frac{RT}{nF}\right) \ln\left(\frac{[\text{O}]}{[\text{R}]}\right) \quad \text{eq. 2.2}$$

where,  $E^\circ$  is the equilibrium potential and [O] and [R] are the concentrations of species O and R in eq. 2.1. A simple electrode reaction involves diffusion of reactant from bulk solution to the electrode interface. Then, a potential is applied to the electrode such that the potential difference at the interface induces the exchange of electrons between the electrode and the species in solution, and in turn electrolysis occurs. The magnitude of the current produced by electron motion is related to the flux of the species in solution ( $dn/dt$ ) according to eq. 2.3.[1]

$$I = nFA \frac{dn}{dt} \quad \text{eq. 2.3}$$

where,  $n$  is the number of electrons transferred per molecule and  $A$  is the electrode area. A schematic representation of the electrode-electrolyte interface is shown in Fig. 1. The closest layer to the surface is the *compact layer* in which the potential varies linearly with the distance from the surface while in the *diffuse layer* the potential changes exponentially. The compact layer consists of the inner Helmholtz plane (IHP) where anions are adsorbed and outer Helmholtz plane (OHP) where solvated cations exist. The double layer region is where the truncation of the metal's electronic structure is compensated for in the solution. It is ca. 1-10 nm thick, and about 1V is dropped across this region, which corresponds to fields in the order of  $10^7$ - $10^8$  V/m.[1] The effects of this field at the interface are numerous and is the essence of electrochemistry. Since the potential changes in the dynamic experiments, the orientation of the surface changes and perturbation of the concentration of species takes place where the diffusion layer is related to the diffusion coefficient of these species.

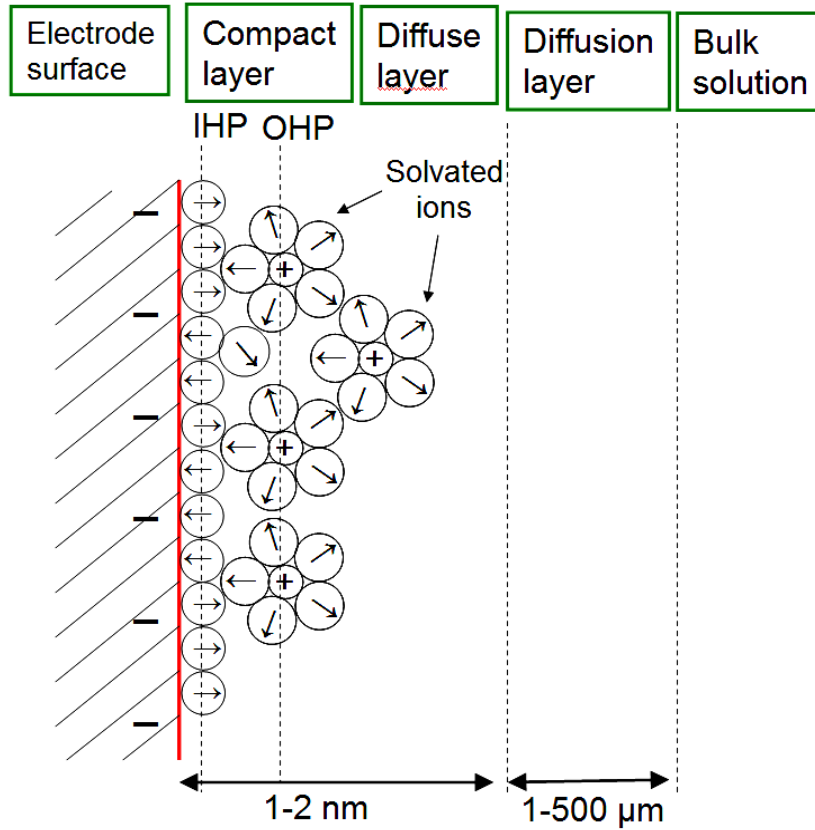


Fig. 1. Schematic illustration of the composition of electrode|electrolyte interface.

### 2.1.2. Activation control

For the reaction given in eq. 2.1, the relationship between the current density ( $j$ ) and the applied potential ( $E$ ) is given in eq. 2.4:[2]

$$\begin{aligned} j_c &= nFk_c [O] \exp(-\alpha_c nFE / RT) \\ j_a &= nFk_a [R] \exp(\alpha_a nFE / RT) \end{aligned} \quad \text{eq. 2.4}$$

This relation is valid as long as there are no diffusion or depletion layer effects at the electrode. The transfer coefficient ( $\alpha$ ) can be obtained from the Tafel plot of  $\ln|j_c|$  versus  $E$ . The derivative  $dE/d\ln|j_c|$  gives the cathodic Tafel slope. At equilibrium potential  $E^o$ , the net current density is the sum of both the cathodic and anodic current densities according to eq. 2.5.

$$\begin{aligned} j &= j_a + j_c \\ j &= nFk_a [R] \exp(\alpha_a nFE / RT) - nFk_c [O] \exp(-\alpha_c nFE / RT) \end{aligned} \quad \text{eq. 2.5}$$

where,  $[R]$  and  $[O]$  are the volume concentrations on the electrode surface. The parameters  $n$ ,  $F$ ,  $E$ ,  $R$ ,  $\alpha$  and  $T$  have their usual significance previously described. At equilibrium, the oxidation and reduction currents balance each other exactly, thus no net current flows and  $j=0$ , and we obtain:[2]

$$\begin{aligned} j^o &= j_a = j_c \\ j^o &= nFk_a [R] \exp(\alpha_a nFE^o / RT) = nFk_c [O] \exp(-\alpha_c nFE^o / RT) \end{aligned} \quad \text{eq. 2.6}$$

$$\frac{[O]}{[R]} = \left( \frac{k_a}{k_c} \right) \exp[(\alpha_a + \alpha_c) nFE^o / RT] \quad \text{eq. 2.7}$$

where,  $E^o$  is the formal equilibrium potential and  $j^o$  is the *exchange current density*, which is the absolute value of anodic and cathodic current densities when they are equal at  $E^o$ . Since

Nernst equation is applied to equilibrium, we obtain from eq. 2.7 that  $(\alpha_a + \alpha_b)=1$  and  $k_a/k_c=\exp(-nFE^0/RT)$ . Combining eq. 2.5 with eq. 2.6 gives the so-called *Butler-Volmer equation* (eq. 2.8):

$$j = j^o [\exp(1 - \alpha_c)nF\eta / RT - \exp(-\alpha_c)nF\eta / RT] \quad \text{eq. 2.8}$$

where,  $\eta=E-E^0$  is called the *overpotential*. The polarization curve which shows the measurable net current density, and the value of  $j^o$  is presented in Fig. 2 (left panel). As can be seen from the graphical plot, the measurable current densities approach the respective contribution of the anodic or the cathodic current densities at large positive or negative overpotentials so that the reverse reaction can be ignored. Consequently, for large cathodic overpotentials *Butler-Volmer equation* is simplified to eq. 2.9.

$$j = j_c = -j^o [\exp(-\alpha_c)nF\eta / RT] \quad \text{eq. 2.9}$$

By taking the normal logarithm of  $|j|$ , it follows to the following *Tafel equation* (eq. 2.10) in the cathodic overpotential region:

$$\ln j = \ln j^o - \frac{\alpha_c nF}{RT} \eta \quad \text{or} \quad \lg j = \lg j^o - \frac{\alpha_c nF}{2.303RT} \eta \quad \text{eq. 2.10}$$

The normal logarithmic plot of the overpotential against the current density is also shown in Fig. 2 (right panel). This plot is called *Tafel plot*.

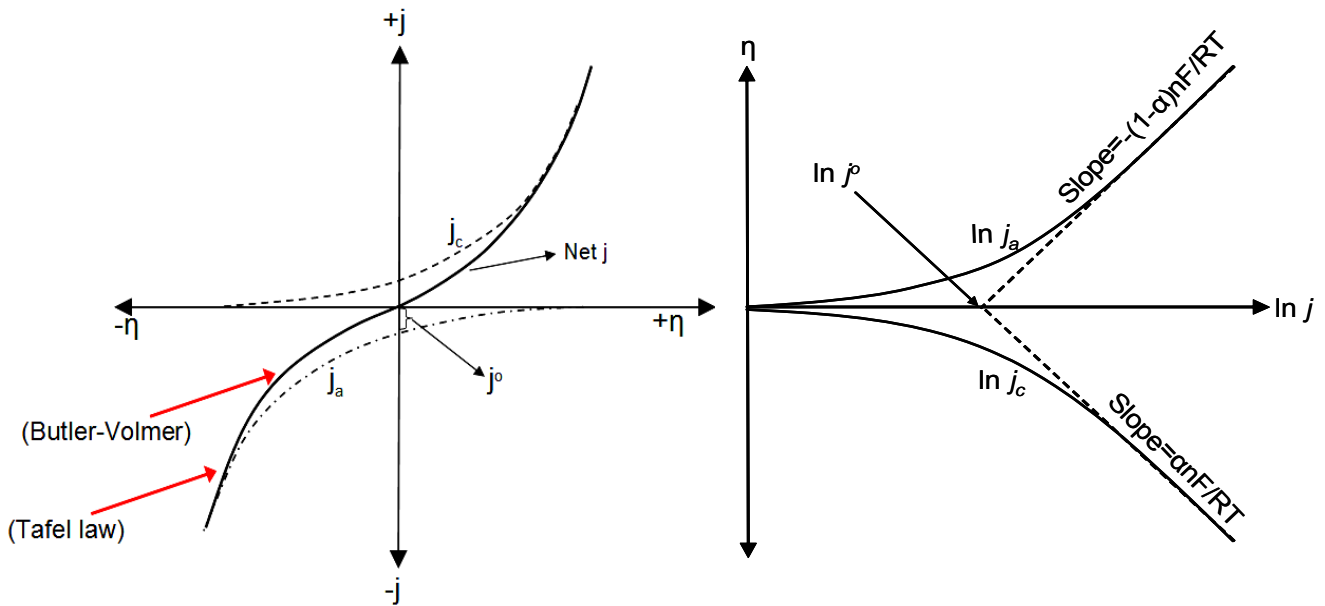


Fig. 2. Left panel: Plots of the cathodic current density  $j_a$  (upper dashed line), anodic current density  $j_c$  (lower dash dotted line) and the net current density  $j$  (solid line) versus the overpotential. Right panel: Plot of the overpotential versus the logarithm of the expected anodic and cathodic current densities, while the dashed lines represent the Tafel slopes. Curves are according to Butler-Volmer equation with  $\alpha=0.5$ .

A linear relationship between the current density and the applied potential is obtained only at large enough overpotentials (i.e. when  $\eta \gg RT/nF$ ). At other potentials, the curve obeys Butler-Volmer equation. The slope of the tangent of the linear part is the *Tafel slope*. The intercept of the linear part with the x-axis (at  $\eta=0$ ) gives the normal logarithm of the exchange current density ( $\ln j^o$ ). The  $j^o$  is generally small when more than one electron needs to be transferred or multiple or strong bonds are broken. Tafel slope (b) is important to determine

the rate determining step in electrochemical reactions. Tafel slope is defined according to eq. 2.11 for cathodic reactions.

$$b = -\frac{2.303RT}{\alpha_c nF} = -\frac{59mV}{\alpha_c n} \quad \text{eq. 2.11}$$

For a reaction which involves a one-electron transfer in the rate determining step (rds), a Tafel slope of 118 mV per decade of current is expected to obtain, while for a reaction which involves two-electron in the rds a Tafel slope of 59 mV/dec is typical. The above equations are also valid for the practically measured current instead of the current density.

Another important factor is the *transfer coefficient*  $\alpha$  which is a measure of the symmetry of the free energy curve. It signifies how the transition state is influenced by the application of voltage. Fig. 3 (upper panels) depicts the energy profiles for a heterogeneous electron transfer process at different  $\alpha$ . The graphs show how the free energy changes with potential at different  $\alpha$ . The dashed line represents the energy barrier when no potential is applied, where the process is thermodynamically uphill. When a potential is applied (solid curve), the free energy of reactants is raised since  $\Delta G^{\circ} = -nF(E-E^{\circ})$ . Thus, the energy barrier is reduced and the process is downhill and thermodynamically favorable. The  $\alpha$  has typically a value of 0.5, which means that the transition state behaves mid-way between the reactants and products response to the potential. Thereby, the polarization curve is symmetrical so that the anodic and cathodic portions are equivalent as shown in Fig. 3 (lower panel, red curve). The blue and green curves are the result of the same system, but with  $\alpha=0.6$  and  $0.7$ , respectively. It also gives an indication on the reversibility of the reaction, where reversible reaction has  $\alpha=0.5$ , while for irreversible reactions a value inferior or superior to 0.5 is expected.

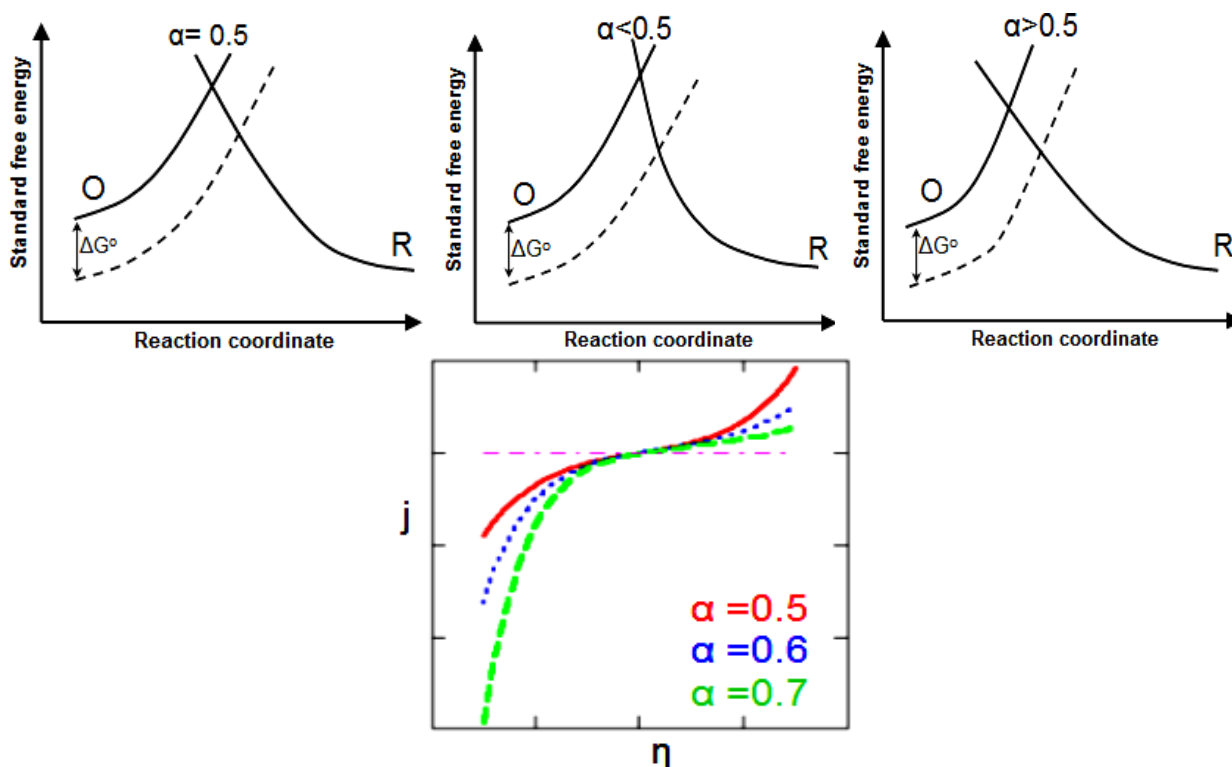


Fig. 3. Upper panels: Schematic of the energy profiles along the reaction coordinate with different transfer coefficients. The dashed line is the case when no potential is applied. Lower panel: Polarization curves at different  $\alpha$ .

## 2.2. Mass transport in electrochemistry

The rate of redox reactions is influenced by the cell potential difference. However, the rate of transport of reactants to the surface can also affect the overall reaction rate. A general scheme of an electrode reaction is shown in Fig. 4, which involves the diffusion of reactant from bulk to surface, then electron transfer between electrode and reactants, and then diffusion of products into solution. The observed electrode current depends on the mass transport, which usually takes place beside other reactions as adsorption, chemical reactions or electron transfer reaction. Typically, the working electrode is immersed in a solution containing the supporting electrolyte to improve the conductivity and reduce the  $iR$ -drop. There are three forms of mass transport, which can influence an electrolysis reaction:

- **Diffusion**
- **Migration**
- **Convection**

Mass transport of a reactant is governed by the *Nernst-Planck equation* (eq. 2.12):[1]

$$J_i = -D_i \frac{\partial C_i(x)}{\partial x} - \frac{n_i F}{RT} D_i C_i \frac{\partial \phi(x)}{\partial x} + C_i v(x) \quad \text{eq. 2.12}$$

where,  $j_i(x)$  is the flux of the electroactive species  $i$  at distance  $x$  from the electrode,  $D_i$  is the diffusion coefficient,  $\partial C_i(x)/\partial x$  is the concentration gradient,  $\partial \phi(x)/\partial x$  is the potential gradient,  $n_i$  and  $C_i$  are the charge and concentration of species  $i$ , respectively and  $v(x)$  is the velocity with which a volume element moves along the  $x$ -axis in solution. The three key terms of eq. 2.12 represent the contribution of diffusion, migration and convection, respectively, to the flux of species.

Each of these mass transport modes has a different effect on the reaction. The influence of each type of mass transport on the current-voltage curves is discussed below in details:

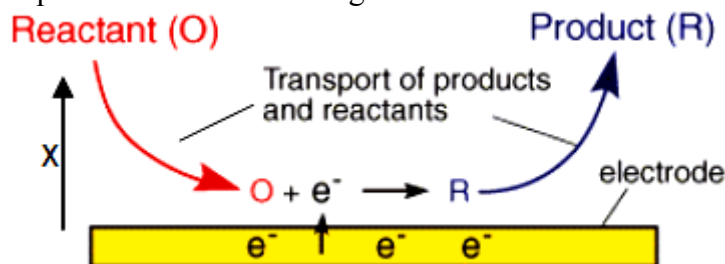


Fig. 4. Schematic illustration of a simple electrode reaction.

### i) Diffusion-limited mass transport

In essence, any electrode reaction is a heterogeneous redox reaction. The Butler-Volmer equation in the form of eq. 2.8 is only valid for simple reactions, where their rate is only limited by the charge transfer. For large overpotentials, in particular, where the transfer reaction is fast, the rate of mass transport of products can significantly influence the overall reaction rate and in turn the measured current in the experiment. If the rate depends exclusively on the rate of mass transfer, then we have a mass-transfer controlled electrode reaction. If the only mechanism of mass transfer is diffusion (i.e. the spontaneous transfer of the electroactive species from regions of higher concentrations to regions of lower concentrations), then we have a diffusion-controlled electrode reaction.

Diffusion occurs in all solutions and arises from the local uneven concentrations of reagents. Entropic forces act to smooth out this uneven distribution of concentrations, and are therefore the main driving force for this process. For a large enough sample, statistics can be used to predict how far a material will move in a certain time, and this is often referred to as a random walk model, where the mean square displacement in terms of the time elapsed and the diffusivity equals:  $x^2 = 2Dt$

For an electrochemical reaction, which occurs in a stagnant solution such that migration and convection terms can be neglected from eq. 2.12, so that the only mode of mass transport to the electrode surface is diffusion, the rate of movement of species by diffusion is quantified by Fick's first and second laws.[2] The Fick's first law is given in eq. 2.13.

$$J_i(x) = -D_i \frac{\partial C_i(x)}{\partial x} \quad \text{eq. 2.13}$$

This relates the diffusional flux to the concentration gradient and the diffusion coefficient. In order to obtain the concentration of the electroactive species at a location  $x$  and time  $t$ , the partial differential equation should be solved, which is possible if the initial (values at  $t = 0$ ) and boundary conditions (values at certain location  $x$ ) are known. The negative sign indicates that the material moves down a concentration gradient (i.e. from a higher concentration to a lower concentration region). However, in some measurements we need to know how the concentration of a material changes with time, and this can be predicted from Fick's second law given in eq. 2.14:

$$\frac{\partial C_i}{\partial t} = -D_i \frac{\partial^2 C_i(x)}{\partial x^2} \quad \text{eq. 2.14}$$

Fick's second law is an important relationship since it permits the prediction of the variation of concentration of different species as a function of time within the electrochemical cell. In order to solve these expressions, analytical or computational models are usually applied.

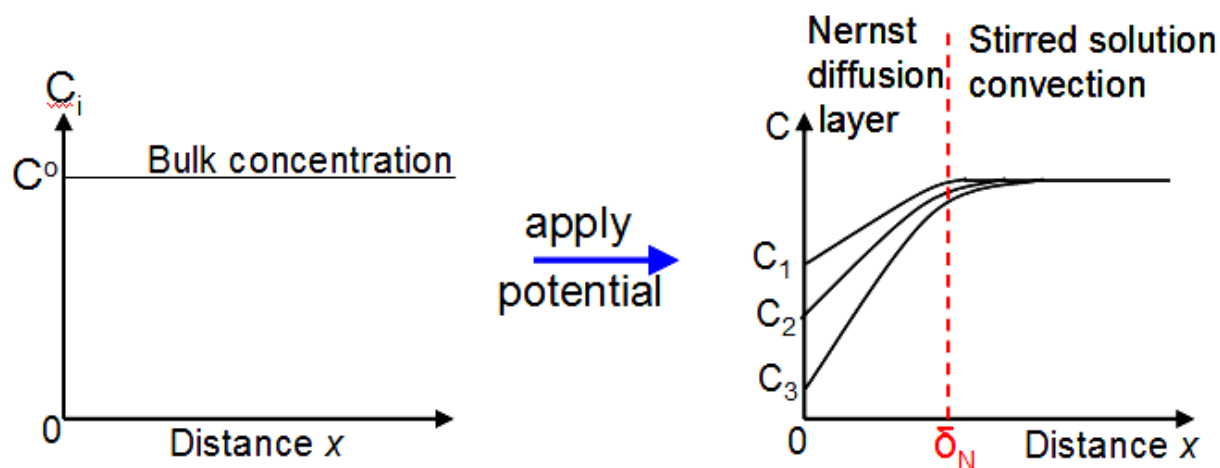


Fig. 5. Concentration profile before and after applying potential. The diffusion layer is also limited with the red dashed line.

The products of electrochemical reaction in solutions, in which strong convection prevails, must traverse a quasi quiescent solvent layer directly in front of the electrode surface. This layer is the *diffusion layer* and has a thickness ( $\delta_N$ ). As shown in Fig. 5, as a potential is applied, a diffusion layer is formed, and the concentration gradient in the Nernst diffusion

layer appears since the concentration deviates from bulk concentration ( $C^o$ ), while beyond the diffusion layer, the concentration is constant. The different behaviors at  $C_1$ ,  $C_2$  and  $C_3$  are due to different potentials.

The thickness of diffusion layer ranges between 10-500  $\mu\text{m}$ , depending on the condition of the hydrodynamic flow. The Nernst diffusion layer is different from the electric double layer, which has a thickness of 1-2 nm. The concentration gradient could be defined as follows:

$$\left(\frac{\partial C}{\partial x}\right)_{x=0} = \frac{C^o - C}{\delta_N} \quad \text{eq. 2.15}$$

where,  $C$  is the concentration at the electrode surface. Thus, the flux of ions towards the electrode surface is given from the definition of the diffusion layer as follows:

$$J = D \frac{C^o - C}{\delta_N} \quad \text{eq. 2.16}$$

Since each ion possesses an electric charge, thus the current density is given by eq. 2.17.

$$j = nFJ = nFD \frac{C^o - C}{\delta_N} \quad \text{eq. 2.17}$$

where,  $F$  is the Faraday constant,  $n$  is the charge transferred by each ion. The maximum flux of ions can be achieved when  $C=0$  at large overpotentials, where each molecule is reduced as soon as it reaches the electrode surface. Consequently, the *diffusion limited current density*  $j_L$  is given by eq. 2.18.

$$j_L = nFD \frac{C^o}{\delta_N} \quad \text{eq. 2.18}$$

The concentration difference leads to another overpotential which is called the *concentration overpotential*. As current flows in the cell, the consumption of electroactive species near to the electrode surface leads to a concentration gradient, and thus the diffusion of species from bulk solution to the electrode is the rate limiting process. Therefore, a large overpotential is needed to produce a given current. This overpotential is called *concentration overpotential*  $\eta_c$  and is given as follow:

$$\eta_c = \frac{RT}{nF} \ln \frac{C}{C^o} \quad \text{eq. 2.19}$$

## ii) Convection-limited mass transport

Convection results from the action of a force on the solution. This can be pumping, stirring, rotation, flow of gas or even gravity. There are two forms of convection; the first is termed *natural convection* and is present in any solution. This natural convection is generated by small thermal or density differences and acts to mix the solution in a random and therefore, unpredictable manner. However, this effect is small. Nevertheless, it is possible to draw out the natural convection effects from an electrochemical experiment by externally introducing convection into the cell. This form of convection is termed *forced convection*. It is typically several orders of magnitude greater than any natural convection effects, and therefore, it effectively removes the random convection from the experimental measurements. This, of course, is only true if the convection is introduced in a well-defined and quantitative manner.

One possibility to have a defined hydrodynamics and forced convection in the solution is the use of Rotating Ring-Disc Electrode (RRDE) setup. Despite the strong convection during rotation, there is still a static layer in front of the electrode, in which the transport is controlled

by diffusion and thus an experiment under well-defined flow conditions can be performed. The thickness of the static diffusion layer ( $\delta_N$ ) depends on the rotation rate (precisely the angular velocity  $\omega$ ), the diffusion coefficient of electroactive species (D) and the kinematic viscosity ( $\nu$ ) of the solution according to the following equation:[3]

$$\delta_N = 1.61\omega^{-1/2}\nu^{1/6}D^{1/3} \quad \text{eq. 2.20}$$

where,  $\omega=2\pi f$ , and  $f$  is the rotation speed in rpm. This equation is valid for the range of  $10\text{Hz} < \omega < 1000\text{ Hz}$ . Under these boundaries, the flow is stable without mixing in the lateral direction, and called laminar flow. For very slow rotation speeds, the diffusion layer is thick with respect to the radius of the electrode. The diffusion layer depends also on the radius of the electrode. For very high rotation speeds, the flow becomes turbulent. The mass transport for convection in case of laminar flow is given by the following equation:

$$\frac{\partial C^o}{\partial t} = -v_x \left( \frac{\partial C^o}{\partial x} \right) \quad \text{eq. 2.21}$$

where,  $v_x$  is the velocity of solution in x-direction. Due to the convective diffusion, the mass transfer takes place uniformly over the entire electrode surface, so that the current density is independent of the position of the species on the electrode.[4]

Combining eq. 2.18 and 2.20 is then used to calculate the diffusion limited current ( $I_L$ ). The resulting equation is the so-called *Levich equation* (eq. 2.22).

$$I_L = 0.62nFAC^o\nu^{-1/6}D^{2/3}\omega^{1/2} \quad \text{eq. 2.22}$$

Levich equation shows the dependence of the current density on the rotation speed in the diffusion limited region. Plotting  $I_L$  versus  $\omega^{1/2}$  should reveal a straight line for the pure diffusion limitation region. In the previous aspects, the kinetic currents of the electrochemical reaction at the electrode surface are not considered. It is important to note that the transport of electrochemically active species in the electrolyte is limited by a diffusion barrier layer on the electrode surface, while the measured current is the total current. The total measured current (I) consists of the kinetic current ( $I_k$ ) and the diffusion current ( $I_L$ ) according to *Koutecký-Levich equation* shown below (eq. 2.23).

$$\frac{1}{I} = \frac{1}{I_k} + \frac{1}{I_L} = \frac{1}{nFAkC^o} + \frac{1}{0.62nFAC^o\nu^{-1/6}D^{2/3}\omega^{1/2}} \quad \text{eq. 2.23}$$

where,  $k$  is the reaction rate constant. The other parameters have their typical significance. For determination of the kinetic current, the diffusion limited current must be first calculated. According to eq. 2.23, Plot of  $I^{-1}$  versus  $\omega^{-1/2}$  is called *Koutecký-Levich* (K-L) plot and gives a straight line passing through the origin at potentials, where only diffusion limitation takes place (e.g. higher overpotentials). In some cases, the current is limited by other additional effects, such as diffusion through a porous blocking film or a preceding chemical reaction, then the K-L plot intersects the y-axis at certain current corresponding to such limitation ( $I_A$ ), and the observed diffusion limited current is not the real diffusion limited current but apparent. This additional limitation is then taken into account in K-L equation according to eq. 2.24.[1]

$$\frac{1}{I} = \frac{1}{I_k} + \frac{1}{I_L} + \frac{1}{I_A} \quad \text{eq. 2.24}$$

To get the true kinetic current, a correction has to be made, where the intercept of K-L plot at potentials of diffusion limitation is determined, and this value is then taken as an offset according to eq. 2.24 to calculate the intercepts at other potentials. This is valid assuming the current  $I_A$  is independent of the potential and rotation speed. A disadvantage of the later process is that the additional limitation may be time-dependent, and thus the extrapolated value of  $I_A^{-1}$  is not any more a suitable correction for the measured points taken at earlier times. However, this is not the case because of the steady-state character of the currents, and since the blocking film is oxidized and removed at higher potentials.

Another method to calculate the kinetic current is the mass transport correction of the measured current according to eq. 2.25.

$$I_k = \frac{I_L * I}{I_L - I} \quad \text{eq. 2.25}$$

In RRDE technique, one advantage is the creation of a laminar flow of electrolyte, which delivers the dissolved reactants to the surface of the electrode, as shown in Fig. 6(left panel). The rotation rate of the electrode can be correlated to the rate of convection of the reactants, as discussed above. As the solution is swept away to the peripheries of the electrode, it crosses the ring and goes back into the bulk solution in a well-defined manner. Thus, a diffusion layer near to the electrode surface is constructed, and the mass-transport in the bulk is under control, as shown in the schematic. In this work, for investigation of ORR mechanism in alkaline media, the potential of the disc was scanned with a scan rate of 5 or 10 mV/s and a rotation rate of 540-2940 rpm, while the ring was held at a constant potential of 1.2V<sub>RHE</sub>. At this potential, the peroxide anion intermediate is oxidized to O<sub>2</sub> and generates ring current ( $I_R$ ), which is simultaneously recorded with the disc current ( $I_D$ ). ORR proceeds via a direct 4e-pathway to OH<sup>-</sup> or a 2e-pathway with production of HO<sub>2</sub><sup>-</sup> intermediate. The generated HO<sub>2</sub><sup>-</sup> at the disc is then transferred to the ring and is oxidized, as displayed in Fig. 6 (right panel).

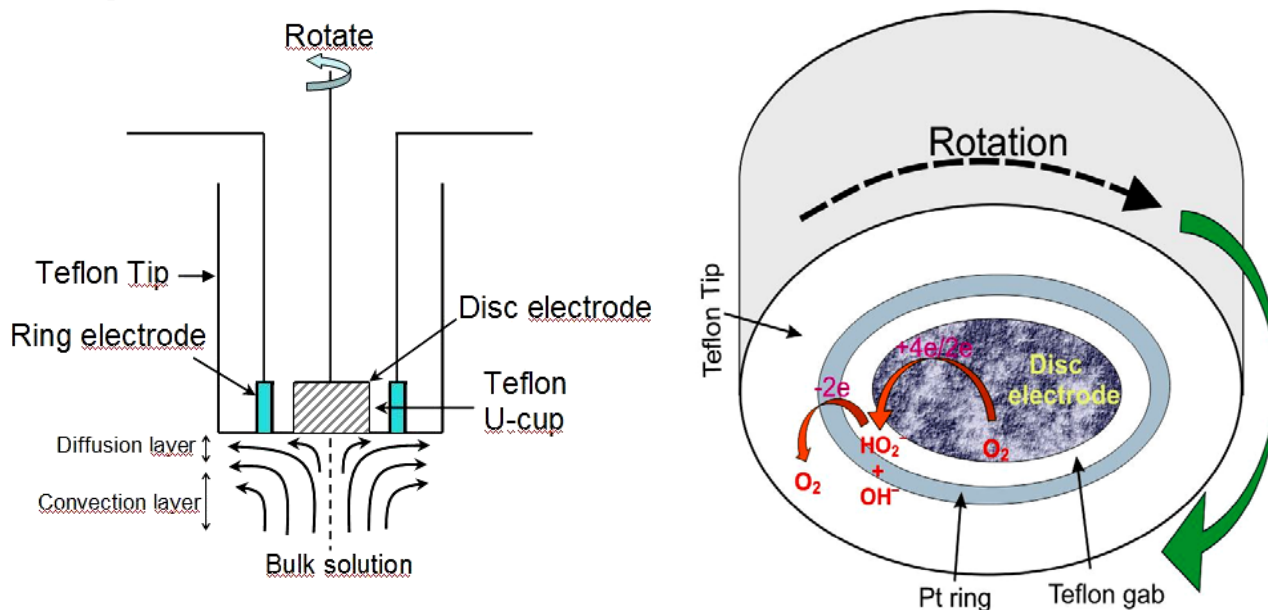


Fig. 6. Left panel: schematic of the RRDE tip. Right panel: a top view of the tip with the reactions taking place on the disc and ring during ORR in alkaline media.

Typical polarization curves of ORR, for example, of Ag311 catalyst ( $1 \text{ mg/cm}^2$  loading), are shown in Fig. 7. Three regions can be distinguished on the polarization curve: a) the *kinetic-limited current region*, which appears at the early stages of the reaction, where the kinetics of the reaction limits the rate of the reaction. For a good catalyst, this kinetic-controlled region should be minimum. b) the *mixed diffusion-kinetic limited-current region*, in which both the kinetic and the mass-transport limitations control the rate of reaction. For an active catalyst, this region should have a steep slope. Analysis of the current in this region (e.g. Koutecky-Levich plot) is important for investigation of the kinetics of the reaction. c) *the diffusion-limited current region*, which represents the pure mass-transport (diffusion) limitation. In this region, the applied potential is high such that the rate of oxygen consumption is higher than the rate of oxygen transport. Thus, as the rotation rate increases, the rate of oxygen transport increases, and consequently, the mass-transport (diffusion) limited current increases.

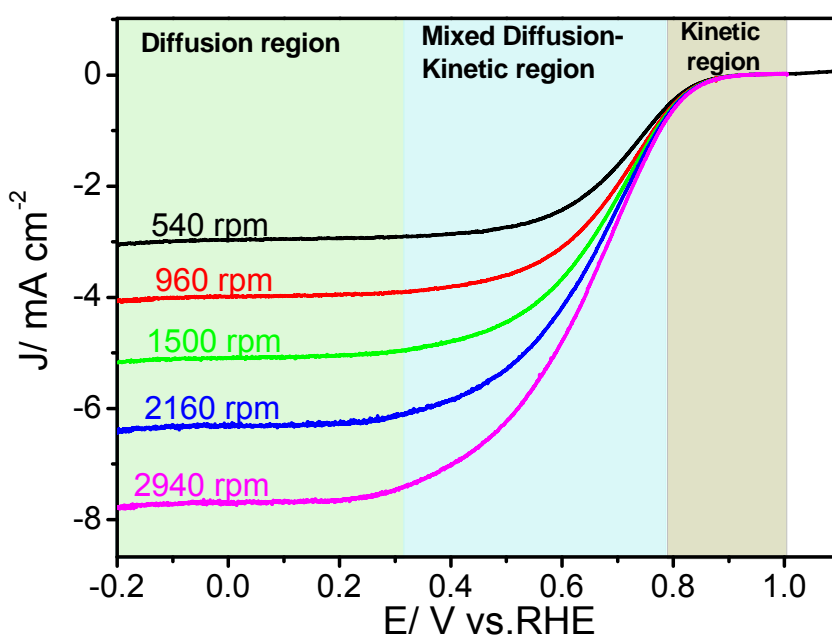


Fig. 7. ORR polarization curves (anodic scan) of Ag311 ( $1 \text{ mg/cm}^2$ )/GC catalyst in  $\text{O}_2$ -saturated  $0.1\text{M LiOH}$  solution with  $10 \text{ mV/s}$  at different rotation rates.

One important parameter for RRDE setup is the *collection efficiency* ( $N$ ). Since not every molecule of peroxide generated at the disc can reach the ring, the collection efficiency has to be considered in evaluations. This ( $N$ ) represents the percentage of the molecules generated at the disc and is detected at the ring. It can be determined practically by the shielding experiment. However, the theoretical  $N^o$  is dependent only on the electrode's geometry (disc OD, ring ID, ring OD). Thus, for a given RRDE tip dimensions, the collection efficiency can be theoretically calculated from fluid dynamics first principles. For our setup and used tip,  $N^o = 0.256$  and is used for all calculations in this work. The peroxide yield ( $\text{HO}_2^-$ ) and the number of electrons transferred ( $n$ ) during ORR are calculated from the ring ( $I_R$ ) and disc ( $I_D$ ) currents according to the following equations:

$$\text{HO}_2^- \% = \frac{2I_R}{N^o I_D + I_R} \times 100 \quad \text{eq. 2.26}$$

$$n = 4 \times \frac{I_D}{I_D + I_R/N^0} \quad \text{eq. 2.27}$$

The ring current is sometimes corrected, where a base line is considered at a potential of 1.2V for alkaline electrolyte and -0.5 V for organic electrolytes since no reactions take place at the disc at this potential.

To get more information on the mechanism of ORR, the ring current is used to detect the amount of the soluble intermediates reaching the ring. For alkaline media, the percentage of the peroxide anion is calculated as above. In case of organic electrolytes, the intermediate  $\text{LiO}_2$ , which is generated by a one-electron reduction step is soluble, and can be oxidized at the ring. On the other hand, if only  $\text{Li}_2\text{O}_2$  is produced at the disc, no ring currents can be detected since  $\text{Li}_2\text{O}_2$  is insoluble. The ratio of the ring to disc currents ( $N=I_R/I_D$ ) is calculated. The normalized ratio of the detected superoxide ( $N/N^0$ ) is used to estimate the produced superoxide in the reaction, where  $N^0=0.25$  is the theoretical collection efficiency.

### iii) Migration-limited mass transport

The final form of mass transport we need to address is the migration. This is essentially an electrostatic effect, which arises from the application of a voltage on the electrodes. This creates effectively a charged interface (at the electrodes). Any charged species near that interface will either be attracted or repelled from it by electrostatic forces. If there is no excess of the supporting electrolyte, the charged ions migrate along the potential gradient  $\phi$ , and they can participate in the electron transfer process, and thus the current density due to migration ( $j_m$ ) should be separated from the total current in eq. 2.12 and is given according to eq. 2.28:

$$j_m = \frac{nF}{RT} DC^0 \frac{\partial \phi}{\partial x} \quad \text{eq. 2.28}$$

Since oxygen molecules in ORR are uncharged and an excess of supporting electrolyte is used, the contribution of migration can be neglected.

In some cases, the transfer of charge carriers through a formed film can play a role in the overall process. The potential dependence of diffusion of ions through a film can be described by the high field model.[5] If the transfer is neither through the pores of the film nor through electron conduction, but by diffusion of ions through the ionic lattice, then the relation between the measured current and the applied potential becomes complex. This high field model was developed for valve metals, which easily form oxide layer and the current flows in one direction. When a potential is applied, a thicker oxide film is formed and the current drops fast. This oxide film is mostly irreversible. Hence, the current flow in the anodic direction is again observed only if a potential that exceeds the previously applied potential by at least 50% is applied.[5] By applying lower potentials, no additional oxide is formed, and the current stays very small. In our work, in some cases a deactivating passive film is formed during oxygen reduction in organic electrolytes such that this film is irreversible (unless in some cases a reactivation occurs by scanning to higher potentials), and in turn the current decreases with cycling.

## 2.3. Mechanistic aspects of ORR from Tafel slope

ORR mechanism is different in aqueous from nonaqueous media. In aprotic electrolytes, the reduction products are either superoxide and/or peroxide through the transfer of one or two electrons, respectively. On the other hand, in aqueous electrolytes, there is either a two-

electron reduction to peroxide intermediate or four-electron reduction to water/OH<sup>-</sup>. This depends on the electrode material and the electrolyte. For example, ORR in alkaline and also acidic media on Pt catalysts is a direct 4-electron process,[6] while on carbon, it is a direct 2-electron reduction process with peroxide formation. On Au, it can be a 2-es or a 4-es transfer, depending on the electrolyte.[7]

In organic aprotic electrolytes, the mechanism is not widely studied. The criteria on which either superoxide or/and peroxide is formed, is still unclear or questionable. The fact is that superoxide is formed when TBA<sup>+</sup> salt is used.[8] In Li-salts, both superoxide and peroxide can be formed. For instance, at Au electrode, at lower overpotentials superoxide is formed in DMSO solution, while peroxide is formed at higher overpotentials. In contrast, at Pt, only peroxide formation can be observed.[9, 10] In K<sup>+</sup> salts, superoxide is also dominating.[9] In case of Na-salts, the potential dependence on the formation of either superoxide or peroxide is reported.[8, 11] There are several mechanisms of ORR in organic electrolytes. However, it is common in all of them that the adsorption of oxygen from solution onto the electrode surface is the first step prior the reduction. The adsorbed oxygen is then reduced to superoxide intermediate, which has been experimentally identified even if peroxide is the final product.[8, 12] Then, superoxide has two pathways: i) *Direct pathway*, in which a second electron transfer to superoxide and formation of peroxide take place. ii) *Indirect pathway*, in which superoxide disproportionates chemically to peroxide. Also, the desorption of superoxide is possible. The most probable mechanism of direct ORR pathway is shown in Fig. 8.



Fig. 8. The direct pathway of ORR in Li<sup>+</sup> containing electrolyte.

Here,  $k_1$ ,  $k_2$ ,  $k_3$ ,  $k_4$  and  $k_5$  are the forward rate constants,  $E_2^0$ ,  $E_4^0$  are formal potentials for the one-electron transfer steps and  $K_3$ ,  $K_5$  are equilibrium constants.

In the frequent case, in which a multistep electrode reaction consists of a sequence of elementary one-electron transfer steps and chemical steps, the quasi-equilibrium method can be applied, which assumes that all the steps are in equilibrium, with only the exception of the rds.[2] In general, this assumption requires that the rate constant of the rds is at least 100 times smaller than those of all steps that precede the rds. Under these conditions, the Nernst equation is applied to the one-electron transfer steps in quasi-equilibrium, while the law of mass action is applied to the chemical steps in quasi-equilibrium.[2] Although it is advocated in literature that the direct pathway is the most probable, it is unclear, which is the rate determining step (rds), and which step is at equilibrium. Therefore, by analysis of Tafel slope and the reaction order, the different mechanisms can be distinguished. Here, we discuss the possibility that each step could be the rds and explain the expected Tafel slope in each case:

**i) assume step b is the rds**

The transport of oxygen to the surface (step a) does not influence the mechanistics of the electrochemical reactions. If the first electron transfer step is the rds, then the reduction current  $I_c$  (in the cathodic overpotential region, where anodic current is neglected) according to Butler-Volmer equation is given by:

$$I_c = -2FAk_2[O_2] \exp\left[\frac{-\alpha F(E - E_2^o)}{RT}\right] \quad \text{eq. 2.29}$$

where,  $A$  is the electrode area,  $E$  is the applied potential and  $[O_2]$  is the concentration of oxygen at the electrode. The overpotential  $\eta$  can be expressed as  $\eta = E - E^o$ . Thus, the logarithm of the current varies with potential according to eq. 2.30:

$$\frac{\partial \lg(I_c)}{\partial \eta} = \frac{-\alpha F}{2.303RT} \quad \text{eq. 2.30}$$

Assuming a transfer coefficient  $\alpha = 0.5$ , a Tafel slope of 118 mV/dec is expected for this case.

**ii) assume step c is the rds**

If the formation of superoxide ion pair is the rds and its further reduction is a fast step, the current is then given by:

$$I_c = -2FAk_3[Li^+][O_2^-] \quad \text{eq. 2.31}$$

where,  $[O_2^-]$  and  $[Li^+]$  are the concentrations of superoxide and Li cations, respectively. By applying to step (b) the quasi-equilibrium conditions, namely, the Nernst equation, we obtain:

$$\frac{[O_2]}{[O_2^-]} = \exp\left[\frac{F(E - E_2^o)}{RT}\right] \quad \text{eq. 2.32}$$

By replacing  $[O_2^-]$  from eq. 2.32 into eq. 2.31, we get:

$$I_c = -2FAk_3[Li^+][O_2] \exp\left[\frac{-F\eta}{RT}\right] \quad \text{eq. 2.33}$$

As a result, the variation of current with potential is given by:

$$\frac{\partial \lg(I_c)}{\partial \eta} = \frac{-F}{2.303RT} \quad \text{eq. 2.34}$$

In this case, the plot of  $\lg(I_c)$  versus  $E$  at constant oxygen concentration  $[O_2]$  provides a transfer coefficient equals unity, and a Tafel slope equals 59 mV/dec.

**iii) assume step d is the rds**

Considering the second electron transfer is the rds, and then the cathodic current is given by:

$$I_c = -2FAk_4[LiO_2] \exp\left[\frac{-\alpha F(E - E_4^o)}{RT}\right] = -2FAk_4K'_{1 \rightarrow 3}[LiO_2] \exp\left[\frac{-\alpha F(E - E_2^o)}{RT}\right] \quad \text{eq. 2.35}$$

where,

$$K'_{1 \rightarrow 3} \equiv \exp\left[\frac{-\alpha F(E_2^o - E_4^o)}{RT}\right] \quad \text{eq. 2.36}$$

By applying to step (c) the quasi-equilibrium conditions, we obtain:

$$\frac{[LiO_2]}{[O_2^-][Li^+]} = K_3 \quad \text{eq. 2.37}$$

Upon replacing  $[LiO_2]$  from eq. 2.37 into eq. 2.35 and  $[O_2^-]$  from eq. 2.32 into the resulting equation, we get:

$$I_c = -2FAk_4K'_{1\rightarrow3}K_2[Li^+][O_2]\exp\left[\frac{-(1+\alpha)F(E-E_2^o)}{RT}\right] \quad \text{eq. 2.38}$$

In this case, the plot of  $\lg(I_c)$  versus  $E$  at constant oxygen concentration  $[O_2]$  provides a transfer coefficient equals  $(1+\alpha)$ , and the Tafel slope equals 39 mV/dec assuming  $\alpha=0.5$  according to following equation:

$$\frac{\partial \lg(I_c)}{\partial \eta} = \frac{-(1+\alpha)F}{2.303RT} \quad \text{eq. 2.39}$$

*iv) assume step e is the rds*

Finally, considering the formation of peroxide is the rds, the cathodic current is given by:

$$I_c = -2FAk_5[LiO_2^-][Li^+] \quad \text{eq. 2.40}$$

Upon applying the quasi-equilibrium conditions to the electron transfer step (d), we have:

$$\frac{[LiO_2^-]}{[LiO_2]} = \exp\left[\frac{-F(E-E_4^o)}{RT}\right] = K'_{2\rightarrow4} \exp\left[\frac{-F(E-E_2^o)}{RT}\right] \quad \text{eq. 2.41}$$

where,

$$K'_{2\rightarrow4} \equiv \exp\left[\frac{-F(E_2^o - E_4^o)}{RT}\right] \quad \text{eq. 2.42}$$

Upon replacing  $[LiO_2^-]$  from eq. 2.41 into eq. 2.40, and then  $[LiO_2]$  from eq. 2.37 and  $[Li^+]$  from eq. 2.32 into the resulting equation we obtain:

$$I_c = -2FAk_5K'_{2\rightarrow4}K_3[Li^+]^2[O_2]\exp\left[\frac{-2F(E-E_2^o)}{RT}\right] \quad \text{eq. 2.43}$$

The plot of  $\lg(I_c)$  versus  $E$  at constant oxygen  $[O_2]$  gives  $\alpha=2$  according to the following equation:

$$\frac{\partial \lg(I_c)}{\partial \eta} = \frac{-2F}{2.303RT} \quad \text{eq. 2.44}$$

In this case, a Tafel slope equals 30 mV/dec is expected.

We conclude that the Tafel slope can vary according to the nature of the rds and the concentration of oxygen and Li cation at the electrode. Therefore, when we obtain a Tafel slope close to 118 mV/dec this implies that the first electron reduction is the rds, and if we assume that the reaction order is zero with respect to oxygen and  $Li^+$  concentrations, then the rds is either the first electron transfer step and the surface coverage of oxygen is high, or the second electron transfer step and the pre-formed superoxide ion pair is reversible or irreversible but recovered with new ion pairs.

## 2.4. Voltammetric methods

### 2.4.1. Cyclic voltammetry

*Cyclic voltammetry* (CV) is one of the most popular and extensively used techniques for investigation of electrochemical reactions. It provides appreciable information on the redox potentials of electroactive species under investigation, thermodynamics of redox processes, kinetics of heterogeneous electron transfer reactions and analysis of adsorption processes. The potential of the working electrode is scanned linearly with time, and this is the simplest way of voltammetry and called *linear sweep voltammetry* (LSV). LSV is a half of one CV. The

rate of change of potential with time is referred to as the scan rate ( $v$ ). In CV, the potential is reversed at the end of the first scan, thus the potential wave form is usually triangular as shown in Fig. 9. Therefore, the product of electron transfer reaction that occurred in the forward scan can be probed again in the reverse scan as long as the reaction is reversible. The CV can consist of one cycle or many cycles.

Considering a simple redox reaction of  $O + ne^- \rightarrow R$ , starting the scan from a potential where no faradaic reactions take place, thus no faradaic current is observed. As the potential approaches the  $E^\circ$  for the redox (or potential of ORR in our work), a cathodic current starts to increase until a peak is formed. The resulting current peak reflects the continuous change of the concentration gradient with the time. Thus, the increase to the peak current corresponds to the achievement of diffusion control, then current decreases due to depletion effects. After reaching the end of the peak, the scan direction is reversed and products of reduction, which are accumulated near the surface, are reoxidized and an anodic peak is observed, see Fig. 9.

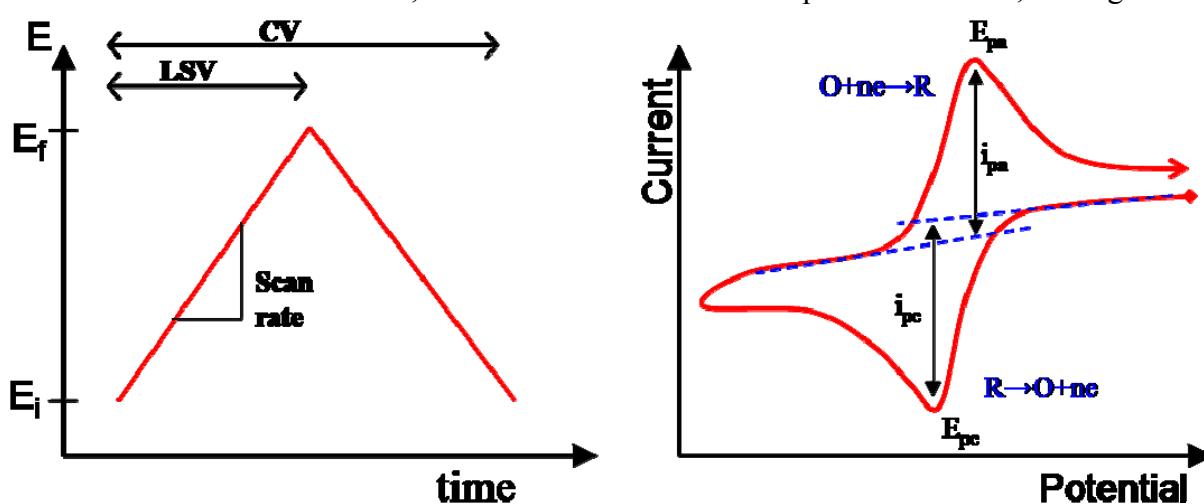


Fig. 9. Left panel: Potential–time profile used to perform linear sweep and cyclic voltammetry showing the triangular signal and the initial and final potentials. Right panel: The resulting CV showing the calculation of peak currents and potentials.

The peak currents and positions are the basis for the diagnostic of CV. The characteristics of a CV are different from reversible to irreversible systems. Fig. 10 (left panel) depicts the CVs for redox reactions with different reversibilities.

#### For reversible reactions:

The peak current for a reversible reaction at 25°C is given by *Randles-Sevcik equation* (eq. 2.45):

$$I_p = (2.69 \times 10^5) n^{3/2} A C D^{1/2} v^{1/2} \quad \text{eq. 2.45}$$

where,  $n$  is the number of electrons,  $A$  is the electrode area (in  $\text{cm}^2$ ),  $C$  is the concentration (in  $\text{mol}/\text{cm}^3$ ),  $D$  is the diffusion coefficient (in  $\text{cm}^2/\text{s}$ ), and  $v$  is the scan rate (in  $\text{V}/\text{s}$ ). Accordingly, the current is directly proportional to the concentration and the square root of the scan rate. A simple reversible system has the following characteristics:

- The ratio of the anodic to cathodic peak currents is unity. i.e.  $I_{pa}/I_{pc}=1$ . This ratio can be affected by chemical reactions accompanying the redox process.
- Peak positions are related to the formal potential of redox process;  $E^\circ = (E_{pa} + E_{pc})/2$

- The separation between the peak potentials (for a reversible couple) is given by:  $\Delta E_p = 59 \text{ mV}/n$ , where  $n$  is the number of electrons transferred. This can be used as a criterion for Nernstian behavior (e.g. for a fast one-electron process,  $\Delta E_p$  is about 59 mV). The Peak potentials should be independent of scan rate.
- The half-peak potential ( $E_{p/2}$ ) is related to the half-wave potential ( $E_{1/2}$ ) according to the equation:  $E_{p/2} = E_{1/2} \pm 28 \text{ mV}/n$ . The positive sign for reduction reaction.
- The peak width is  $E_p - E_{p/2} = 2.3RT/nF$ .

Indeed, the situation is different if the pure ORR is slow or coupled with a chemical reaction.

#### For irreversible reactions:

Here, the reactions are slow and the kinetics are sluggish, and thus the equilibria are not established rapidly. The peaks are widely separated. The peak current is given by *Nicholson-Shain equation* (eq. 2.46):

$$I_p = (2.99 \times 10^5) n (\alpha n^*)^{1/2} A C D^{1/2} \nu^{1/2} \quad \text{eq. 2.46}$$

where, these parameters have their typical significance as previous. The  $\alpha$  is the transfer coefficient,  $n^*$  is the number of electrons in the rds, while  $n$  is the overall number of electrons.

Some of the characteristics for this system are:

- The shape of voltammogram depends on  $\alpha$  and on a dimensionless parameter  $\lambda = k^0 [RT/\pi DF \nu]^{1/2}$ , where  $k^0$  is a standard heterogeneous rate constant. As  $\lambda$  increases, the process approaches the reversible case (for  $\lambda > 7$ , system is reversible). For small values of  $\lambda$ , the system exhibits an irreversible behavior.
- The peak current  $I_p$  is proportional to  $C$ , but it is less dependent on  $\alpha$ . Assuming  $\alpha = 0.5$ , the ratio of the reversible to irreversible peak currents is 1.27 (i.e. about 20% lower currents for irreversible system). When  $\alpha$  deviates from 0.5, the CV is asymmetric and cathodic peak becomes sharper.
- The peak position shifts with the scan rate.
- The ratio  $I_{pa}/I_{pc} \neq 1$ .
- The peak width is given by  $E_p - E_{p/2} = 1.86RT/\alpha n = 47.7 \text{ mV}/n$ .

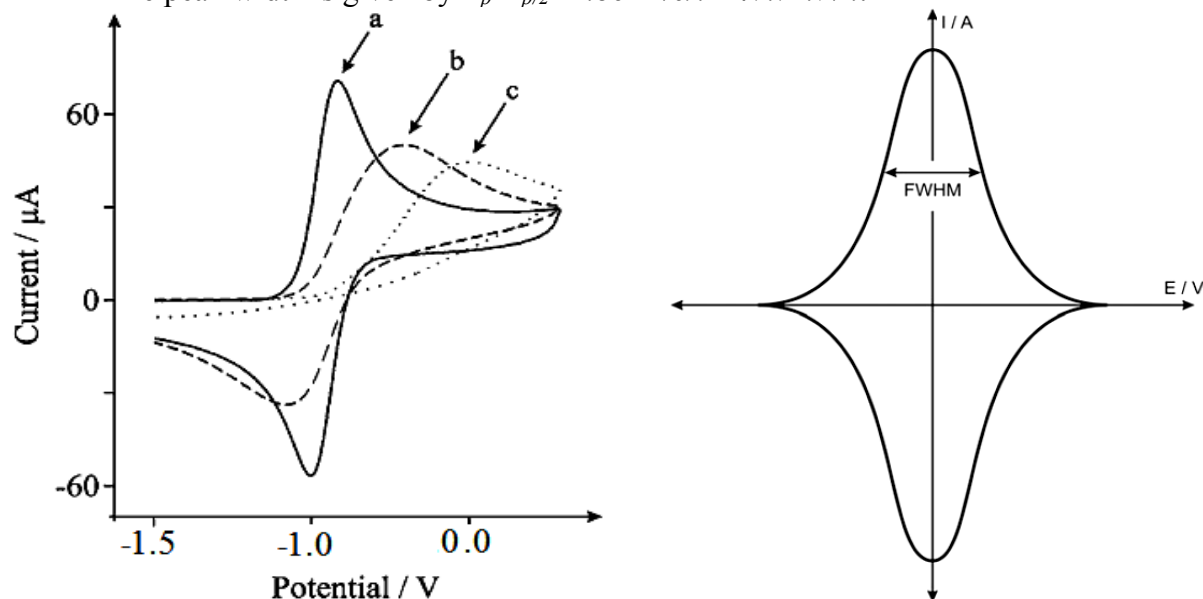


Fig. 10. Left panel: CVs for reversible (a), quasi-reversible (b) and irreversible (c) electron transfer. Right panel: ideal CV of reduction and oxidation of an adsorbed species.

**For quasi-reversible systems:**

- The current is controlled by both the charge transfer and mass transport rates.
- The CV is drawn out and exhibits a larger separation compared to the reversible one.
- The shape depends on  $k^0$  and scan rate.
- The CV exhibits an irreversible behavior at very fast scan rate.

**2.4.2. Chronoamperometry**

This technique is also noteworthy to study the growth of  $\text{Li}_2\text{O}_2$  and deactivation of the surface in organic electrolytes. In this technique, the potential of the working electrode is stepped from a potential at which no faradaic reaction takes place to a potential at which faradaic surface reaction happens (e.g. ORR), and the corresponding current-time is recorded. This involves a continuous growth of the diffusion layer and consequently, a decrease in concentration gradient with time. This method together with rotation can be used to determine the diffusion coefficient of species in solution. Additionally, it can be used to record the steady-state currents during OER.

**2.4.3. Adsorption in CV**

In some instances, the species of interest or even side products adsorb on the surface of the electrode and alters the voltammetry. Fig. 10 (right panel) shows a typical CV of adsorbed species. Since the adsorbed species do not have to diffuse to electrode surface, the CV is symmetrical. It is notable that the peak separation is smaller than in the redox couple, and equals zero for ideal system. Peak current is directly proportional to the surface coverage ( $\Gamma$ ) and scan rate for reversible process as follows:

$$I_p = \frac{n^2 F^2 \Gamma A \nu}{4RT} \quad \text{eq. 2.47}$$

The area occupied by a molecule can be determined from the charge of the peak, which can give orientational information, where  $Q=nFA\Gamma$ . The full width of the peak maximum height (FWHM) equals  $90.6/n$  mV at  $25^\circ\text{C}$ .

The variation of the peak current with the scan rate should give a straight line in case of an adsorption process. Symmetric CV with nearly the same reduction and oxidation peak heights reveals a thin layer behavior. The shape of the voltammogram differs depending on whether the reactants or products are strongly or weakly adsorbed. In some cases, for instance, the formation of side products from organic electrolyte decomposition or formation of a deactivating layer on the surface, the adsorbed layer is porous until certain thickness and then completely blocks the surface. Oxygen diffuses through this porous film to the electrode surface, where it is reduced. This leads to a different diffusion regime into the porous thin film.

For detailed and comprehensive description of the above methods and equations, valuable information is given in the book from Bard and Faulkner.[1]

**2.5. Under-Potential Deposition (UPD)**

UPD is the deposition of metal adatoms at a foreign metal substrate in potential ranges, which are hundred millivolts more positive to the reversible Nernst potential.[13] UPD is limited to the formation of (sub)monolayer (up to two layers in case of Tl on Ag) of species on a different metal. On the other hand, bulk deposition of multilayers is called *over-potential*

*deposition*. UPD can be inferred from CV, wherein peaks corresponding to (sub)monolayer adsorption are observed. Thus, the charge involved in the adsorption and deposition processes can be conveniently analyzed by integrating the observed current response (which is a measure of the rate). Because the origin of this phenomenon lies in the enhanced interaction of the depositing metal with the foreign substrate, the work function differences play a predominant role in specifying the *underpotential shift*. [14] This potential shift can be understood as representing the difference in the bond energies between the metal adatom on a foreign substrate and on the metal itself (i.e. the potential difference between bulk and monolayer stripping peaks).

The formation of monolayer using UPD involves the following processes: *i*) desorption of solvent dipoles from the electrode surface, and then diffusion of solvated ions from bulk to the substrate, losing their solvation sheath. *ii*) bond formation with the metal substrate after ion transfer. [15]

UPD can be influenced by crystal structure of substrate, supporting electrolyte, deposition time and potential, operating potential window, adsorption of ions and interaction between adatoms. UPD is a useful technique to determine the real surface area of some catalysts. However, there is no straightforward method for all metals. Each metal has its own procedure. For instance, for Ag metals, Pb-UPD can be effectively used as will be discussed in the results. A good description of several UPD systems can be found elsewhere. [13]

## 2.6. Electrochemical Impedance Spectroscopy (EIS)

EIS is a complementary technique that distinguishes between electric and dielectric properties of individual contributions of the components under investigation. EIS is a non-destructive tool that can give time-dependent information on the processes taking place such as progress of discharge products in Li-O<sub>2</sub> cell or analysis of the properties (e.g. conductivities) of the formed oxide film upon Ag oxidation. It provides useful information on the electrochemical behavior at the electrode/electrolyte interface. It is useful for determination of the solution resistance, double layer capacitance and charge transfer resistance. Modeling of the electrochemical data is achieved by constructing a proper equivalent circuit, which consists of components such as a resistor and a capacitor. Like the resistance, the impedance is a measure of the ability of a circuit to resist the flow of electric current. However, in a resistor, its value is independent of the frequency. In this technique, AC potential is applied to the working electrode of the cell, and the resulting AC current is measured. Most of the information displayed in this section on EIS are based on the Gamry Instruments website and [1, 16].

Electrochemical Impedance is normally measured using a small excitation signal. This is done so that the cell's response is pseudo-linear. In a linear (or pseudo-linear) system, the current response to a sinusoidal potential is a sinusoid at the same frequency, but with a phase shift. The impedance ( $Z$ ) at any frequency ( $\omega$ ) is a complex number because AC current contains phase information as well as magnitude, as follows:

$$Z = Z_{Re} - jZ_{Im} = R - j\left(\frac{i}{\omega C}\right) \quad \text{eq. 2.48}$$

where,  $j$  is the imaginary number and equals  $\sqrt{-1}$ . The real part ( $Z_{Re}$ ) of the impedance is represented by a resistance, while the imaginary part ( $Z_{Im}$ ) by a capacitive reactance, which is

a function of the excitation frequency  $\omega$ . The AC current may have a phase lag ( $\phi$ ) with respect to the excitation voltage as follows:

$$\phi = \arctan\left(\frac{Z_{Im}}{Z_{Re}}\right) \quad \text{eq. 2.49}$$

Thus, the impedance can be represented as a complex number as follows:

$$Z = E/I = Z_o \exp(i\phi) = Z_o (\cos \phi + i \sin \phi) \quad \text{eq. 2.50}$$

If the real part is plotted versus the imaginary part, the so-called *Nyquist plot* is obtained (Fig. 11a). On this plot, the impedance can be represented as a vector of length  $|Z|$ . The angle between this vector and x-axis is the phase angle ( $\phi$ ). Low frequency data are on the right of the semicircle, while higher frequencies are on the left side. The equivalent circuit for a simple parallel RC circuit is displayed also in Fig. 11a. This semicircle is a characteristic of a single *time constant*. The diameter corresponds to the resistance R. In many cases, there are more than one time constant and only parts of the semicircle are often observed.

Another presentation of the data is the *Bode plot*, in which  $\log|Z|$  or  $\phi$  are plotted as a function of  $\lg(f)$ , see Fig. 11b. This plot has the advantage of showing the frequency information, which is invisible in the Nyquist plot.

Notably, the capacitors in EIS experiments often do not behave ideally. Instead, they act like a constant phase element (CPE), in which  $Z=A(i\omega)^{-\alpha}$ . For a capacitor, the constant A is the inverse of the capacitance ( $A=1/C$ ), and the exponent  $\alpha = 1$ . For a CPE, the exponent  $\alpha$  is less than one, and it can be treated as an empirical constant.

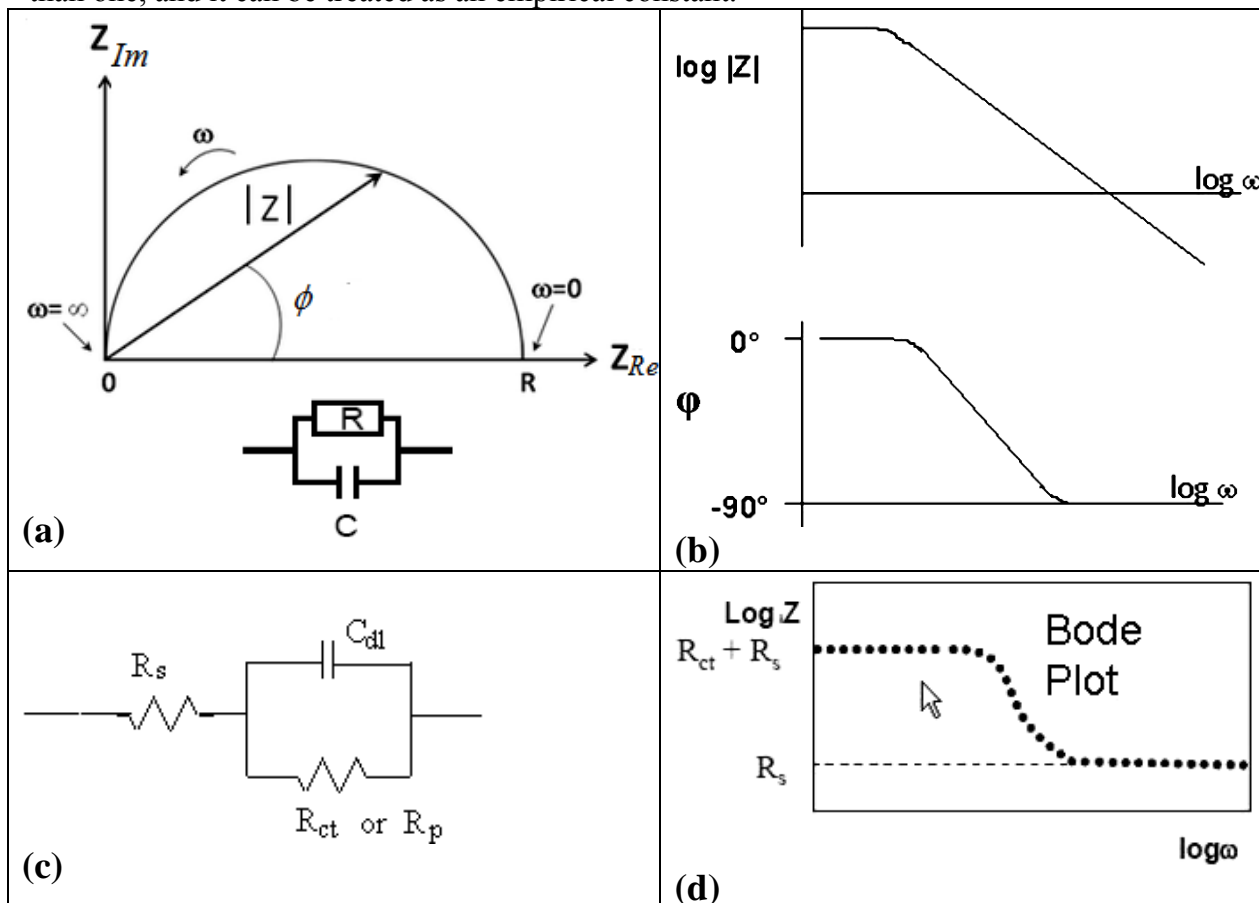


Fig. 11. Schematic of a typical Nyquist (a) and Bode (b) plots for a simple RC circuit shown in the inset of (a). (c) Randles equivalent circuit and (d) its Bode plot.

The impedance curves have to be fitted with a proper equivalent circuit to get information on the magnitude of its components, which mimic the electrochemical system. Each component in the circuit should have a physical meaning, and is representative of a process in the system. As long as the circuit is simple, it is more proper. The *Randles cell* is one of the simplest and most common models, see Fig. 11c. It includes a solution resistance ( $R_s$ ) in series with a parallel double layer capacitor ( $C_{dl}$ ) and a charge transfer ( $R_{ct}$ ) or polarization resistance ( $R_p$ ). In addition to being a useful model in its own right, the Randles cell model is often the starting point for other more complex models. The solution resistance can be clearly observed, and easily determined from the Bode plot, as shown, Fig. 11d.

## 2.7. References

- [1] A.J. Bard, L.R. Faulkner, *Electrochemical Methods: Fundamentals and Applications*, 2nd ed., John Wiley & Sons Inc., New York, Weinheim, 2001.
- [2] R. Guidelli, R.G. Compton, J.M. Feliu, E. Gileadi, J. Lipkowski, W. Schmickler, S. Trasatti, *Pure and Applied Chemistry* 36 (2014) 259-262.
- [3] B.G. Levich, *Physicochemical Hydrodynamics*, Prentice-Hall, Inc., Englewood Cliffs, N.J., USA, 1962.
- [4] C.H. Hamann, W. Vielstich, *Elektrochemie*, Zweite Auflage ed., VCh, Weinheim, 1985.
- [5] M.M. Lohrengel, *Materials Science and Engineering: R: Reports* 11 (1993) 243-294.
- [6] S. Strbac, *Electrochimica Acta* 56 (2011) 1597-1604.
- [7] J.H. Shim, J. Kim, C. Lee, Y. Lee, *The Journal of Physical Chemistry C* 115 (2011) 305-309.
- [8] C.O. Laoire, S. Mukerjee, K.M. Abraham, E.J. Plichta, M.A. Hendrickson, *Journal of Physical Chemistry C* 113 (2009) 20127-20134.
- [9] C.J. Bondue, A.A. Abd-El-Latif, P. Hegemann, H. Baltruschat, *Journal of the Electrochemical Society* 162 (2015) A479-A487.
- [10] C. Bondue, P. Reinsberg, A.-E.-A.A. Abd-El-Latif, H. Baltruschat, *Phys. Chem. Chem. Phys.* 17 (2015) 25593–25606.
- [11] P. Hartmann, C.L. Bender, J. Sann, A.K. Durr, M. Jansen, J. Janek, P. Adelhelm, *Phys. Chem. Chem. Phys.* 15 (2014) 11661-11672.
- [12] R. Cao, E.D. Walter, W. Xu, E.N. Nasybulin, P. Bhattacharya, M.E. Bowden, M.H. Engelhard, J.-G. Zhang, *ChemSusChem* 7 (2014) 2436-2440.
- [13] E. Budevski, G. Staikov, W.J. Lorenz, *Electrochemical Phase Formation and Growth*, VCH, Weinheim, 1996.
- [14] D. Kolb, *Advances in Electrochemistry and Electrochemical Engineering*, John Wiley Interscience, New York, 1978.
- [15] J.O.M. Bockris, A.K.N. Reddy, *Modern Electrochemistry*, 2nd. ed., Kluwer Academic / Plenum Publishers, 2000.
- [16] P.T. Kissinger, W.R. Heineman, *Laboratory Techniques in Electroanalytical Chemistry*, 2nd. ed., Marcel Dekker, Inc., 1996.

### 3. Experimental

#### 3.1. Chemicals and materials

Table 1 (below) summarizes the chemicals and materials used in this work and their properties. Unless stated otherwise, they were used as received.

Chemical	Formula	Purity	Manufacturer
<i>Non-aqueous solutions</i>			
Lithium perchlorate	LiClO <sub>4</sub>	battery grade	Sigma-Aldrich
Tetrabutylammonium perchlorate	TBAClO <sub>4</sub>	99 %	Fluka
Potassium perchlorate	KClO <sub>4</sub>	99%	Sigma-Aldrich
Tetrabutylammoniumtriflate	TBAOTf	≥99%	Sigma-Aldrich
Dimethylsulfoxide (DMSO)	C <sub>2</sub> H <sub>6</sub> SO	99.7% over molecular sieves	Acros Organics
Tetraglyme (G4)	C <sub>10</sub> H <sub>22</sub> O <sub>5</sub>	≥99%	Sigma-Aldrich
Propylene carbonate (PC)	C <sub>4</sub> H <sub>6</sub> O <sub>3</sub>	Anhydrous, 99.7%	Sigma-Aldrich
1,2-Dimethyl-2-imidazolidinone (DMI)	C <sub>5</sub> H <sub>10</sub> N <sub>2</sub> O	Absolute over molecular sieves (≤0.04%H <sub>2</sub> O), ≥99.5%	Sigma-Aldrich
Silver nitrate	AgNO <sub>3</sub>	99.8 % p. a. grade	AppliChem.
<i>Aqueous solutions</i>			
Water- <sup>18</sup> O	H <sub>2</sub> <sup>18</sup> O	98 atom% <sup>18</sup> O	Sigma-Aldrich
Lithium hydroxide monohydrate	LiOH.H <sub>2</sub> O	99%	Sigma-Aldrich
Potassium hydroxide	KOH	99.98%	Acros Organics
Ethylene glycol	C <sub>2</sub> H <sub>6</sub> O <sub>2</sub>	99.5%	Sigma-Aldrich
Nafion <sup>®</sup> 117 solution	C <sub>7</sub> HF <sub>13</sub> O <sub>5</sub> S·C <sub>2</sub> F <sub>4</sub>	~5% in a mixture of lower aliphatic alcohols and water	Sigma-Aldrich
Lead (II) nitrate	Pb(NO <sub>3</sub> ) <sub>2</sub>	EMSURE <sup>®</sup> ACS, Reag. Ph Eur	Merck
Alumina 0.05 μm	Al <sub>2</sub> O <sub>3</sub>	Gamma alumina Micropolish II	Buehler
Polishing cloth	fibers	MicroCloth PSA 2-7/8"	Buehler
Chrom(VI)oxide	CrO <sub>3</sub>	99 %	Merck
Sulfuric acid	H <sub>2</sub> SO <sub>4</sub>	95-97 % p. a.	Merck
PTFE-Paste	(C <sub>2</sub> F <sub>4</sub> ) <sub>n</sub>	PTFE + PFPE	Roth
Phosphorus pentoxide	P <sub>4</sub> O <sub>10</sub>	99 %	Roth
Acetone	C <sub>3</sub> H <sub>6</sub> O	≥99.5%, Puriss. p.a.	Sigma-Aldrich
<i>Catalysts</i>			
Silver particles	Ag311	1-2μm, >99.5%	Ferro GmbH
Ag flakes	Ag	~40μm	Ferro GmbH
Cobalt oxide	Co <sub>3</sub> O <sub>4</sub>	Spinel, ≤50nm, 99.5%	Sigma-Aldrich
Cobalt oxide	Co <sub>3</sub> O <sub>4</sub>	Spinel, ≤10μm, 99.5%	Sigma-Aldrich

Cobalt oxide	Co <sub>3</sub> O <sub>4</sub>	Spinel, <40µm	Cerac
Ag/CoO mixture powder	Ag/CoO	50/50 wt%	Ferro GmbH
20% Pt on Vulcan XC-72	Pt/C	20%Pt on carbon	ETEK
Lanthanum strontium ferrite (LSF)	La <sub>0.6</sub> Sr <sub>0.4</sub> FeO <sub>3</sub>	0.1-0.5µm	Sigma-Aldrich
<i>Gases</i>			
Oxygen ALPHAGAZ™ 2	O <sub>2</sub>	99.9995 %	Air Liquide
Argon N50	Ar	99.999 %	Air Liquide

All aqueous solutions and cleaning baths were prepared using deionized Milli-Q water. The water purification system was provided from Merck Millipore company, Germany, and the purification process involves multi-stage ion exchange system, followed by filtration with active carbon, so that the resultant water contains a negligible amount of impurities ( specific resistance of 18.2 MΩ cm, TOC of 5 ppm, CO<sub>2</sub> of 1 ppb).

All organic electrolytes and their chemicals are prepared and stored in a glove box (LABmaster<sup>Pro</sup> dp, MBraun) under Ar atmosphere.

Coulometric Karl-Fischer Titrator (C20, Metler Toledo) with a diaphragm electrode is used to determine the water content in the electrolyte. Samples were taken from the fresh electrolyte in the glove box and also from the RRDE-cell or the classical DEMS cell after installation.

### 3.2. Procedure for undertaking an electrochemical experiment

#### 3.2.1. The cleaning procedure

The most important issue in electrochemistry experiments is the cleanliness since any contaminants either organic or inorganic could result in uninterpretable results. Thus, handling of the cells is always with Latex gloves. All the used glass wares, Teflon cells and tubes and even the steel holder were cleaned before every experiment in KOH bath, where they were soaked in a 3M KOH bath overnight to remove any organic contaminants. For cleaning of glass wares (in particular, the DEMS glass parts, cells after Pb-UPD, electrolyte reservoirs) from metal-containing electrolytes, the glass wares were first rinsed thoroughly with Milli-Q water, then they were placed for few hours in a chromic-sulfuric acid bath to remove any traces of metals. This cleaning bath consisting of 640 ml sulfuric acid, 360 ml Milli-Q water and 21.4 g of chromium (VI) oxide. After that, they were cleaned in KOH path. Finally, they were rinsed with Milli-Q water and dried in an oven. The chromic acid cleaning process is not necessary for glassware that has not been contaminated with metal ions.

#### 3.2.2. Catalyst-modified electrode preparation

Prior to loading the catalysts on the glassy carbon (GC) electrodes (0.196 cm<sup>2</sup>), the GC electrodes were polished to a mirror finish with the help of 0.05µm alumina slurry on a polishing cloth (Microcloth PSA 2, Buehler). The GC electrodes were then cleaned from the suspension residues and adhering impurities with acetone and Milli-Q water. Finally, the electrodes were cleaned in an ultrasonic bath (VWR®, Germany) with Milli-Q water for 5 minutes, and then dried with KIMTECH wipes, and coated with the respective catalyst suspension. The procedure for preparing the modified GC electrode (catalyst loaded GC) is as follows: an appropriate amount of the catalyst powder were dispersed in a certain volume of ethylene glycol (EG) in a glass vial by ultrasonication for 40 minutes to prepare the catalyst ink. For mixed catalysts, the appropriate weight ratios of both powder components were

mixed together in EG. Then 20  $\mu\text{l}$  of the catalyst ink was drop-cast onto the surface of the GC electrode by Eppendorf-Pipette, yielding a catalyst loading of  $200 \text{ mg cm}^{-2}_{\text{disc}}$ , and then dried for 10 minutes at  $190 \text{ }^\circ\text{C}$  in an oven. For preparation of  $1 \text{ mg cm}^{-2}$  loading, addition of 20  $\mu\text{l}$  ink was done 5 times and in between drying in an oven (or just the proper amount of catalyst powder was used in the ink preparation). For fixing and confining the catalyst on the GC electrode surface, 20  $\mu\text{l}$  of Nafion solution (1.44 mg Nafion® in 1 ml Millipore-Water) was pipetted onto the surface of the coated glassy carbon and dried again at  $190 \text{ }^\circ\text{C}$  for 30 minutes. Nafion layer thickness was made sufficiently thin (less than  $0.2 \text{ }\mu\text{m}$  as calculated from a covered electrode area of  $0.196 \text{ cm}^2$  and apparent film density of  $2.0 \text{ g cm}^{-3}$ ) so that the film diffusion resistance becomes negligible,[1] and thereby, avoiding further mathematical calculations and interference from Nafion resistance. The catalyst suspensions were protected from light by aluminum foil. After cooling the electrode, the distribution of the particles on the surface of GC was examined by an optical microscope and finally installed in the measuring set up.

### 3.2.3. Electrolyte preparation

All organic electrolytes were prepared in a glove box (MBraun), in which the  $\text{H}_2\text{O}$  and  $\text{O}_2$  contents do not exceed 0.5 ppm. The prepared electrolytes were kept in 10 ml closed glass vials inside the glove box and used within a week or prepared freshly in a round flask on the same day in case of RRDE experiments. The appropriate amount of the salt was added in portions to the solvent under stirring in a round flask with a side stopcock to avoid strong heating. Then 1 ml was pulled into a syringe, and the needle was protected from air by insertion into a rubber stopper, and then transferred out of the glove box directly to the cell (which is already under Ar flow). For RRDE cell, about 50 ml was transferred in larger syringes. DMSO solvent was used as received since it is provided over molecular sieves.  $\text{LiClO}_4$  was battery grade and used without further drying. Also, TBAOTf was used as received. Tetraglyme was further dried over molecular sieves for a week.  $\text{KClO}_4$  was dried at  $180 \text{ }^\circ\text{C}$  under reduced pressure (ca. 0.01 mbar) for two days. The water contents of the as-prepared electrolytes were  $\sim 20$  ppm for G4, mixed G4+DMSO (5 v%) and G4+DMSO (50 v%) electrolytes,  $\sim 20$  ppm for  $\text{KClO}_4/\text{G4}$ ,  $\sim 30$  for TBAOTf/G4 and  $\sim 100$  ppm for  $\text{LiClO}_4/\text{DMSO}$ . The major source of water is the salt since pure solvents have lower water content. The electrolyte picks up some water (up to double the amount from initial value) during transfer from the glove box to the cell.

For alkaline solutions, the appropriate amount of LiOH or KOH was weighed and dissolved in milli-Q water in a 1 litre measuring flask.

### 3.3. The potentiostat

In cyclic voltammetry, the electrode potential is scanned between two potential limits with a constant scan rate. Typically, the start point of sweeping is at potential, where only double layer can contribute to the current and no other electrode processes takes place. Scanning in the negative-going direction is called *cathodic scan*, whereas scanning in the positive-going direction is called *anodic scan*. Plotting the measured current against the potentials gives the so-called *Cyclic Voltammogram (CV)*. The technical basis of this method is the so-called three-electrode arrangement, which is connected to the *potentiostat*, as sketched in Fig. 1. If the potential was kept constant in the experiment, one can record the current versus time, and

the so-called *chronoamperogramm* is obtained. Here, the CV has been carried out on the same setup of RRDE, where the disc acts as the working electrode.

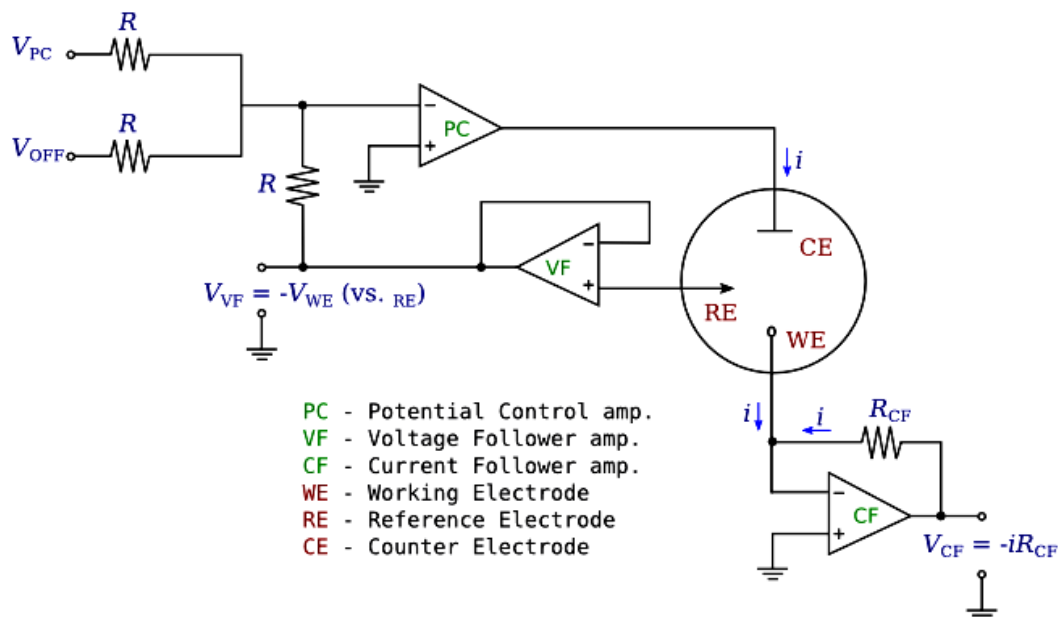


Fig. 1. Schematic of a potentiostat.[2]

The potentiostat consists of an electric circuit, which is usually described in terms of simple operational amplifiers. The potential, which is specified by the function generator, is applied through the potentiostat to the WE, and is kept at a constant level with respect to the reference electrode by adjusting the current at an auxiliary electrode. For this, a circuit with three operational amplifiers (PC, VF, CF) is necessary, as shown in Fig. 1. The potential control amplifier (PC) maintains the voltage between the RE and the WE as closely as possible to the input voltage ( $V_{pc}$ ). Its counterpart is realized via a voltage follower (VF) so that the RE remains unloaded. The actual potential of the RE is provided from the output of the VF to the A/D converter for data acquisition. It should be noted that  $V_{VF} = -V_{WE}$  because the potential is inverted at PC. The third operational amplifier is the current follower (CF), which inverts the current of the cell at the working electrode into voltage. This is done without altering the potential, therefore, the inverse of the cell current flows through the  $R_{CF}$ .

In case of RRDE, a bipotentiostat is needed to control the two working electrodes (disc and ring). Basically, it has the same components of the potentiostat, but with simply an additional copy of the WE part and some more interconnections.

### 3.4. Rotating Ring-Disc Electrode (RRDE)

Electrochemical characterization of the catalytic activity of the catalysts with better understanding of the kinetics and mechanisms are provided by RRDE technique. RRDE is double working electrode setup, which is used in hydrodynamic voltammetry. The half-cell electrochemical measurements are useful for fast evaluation and screening of electrocatalysts. For CV and RRDE measurements, a setup consisting of the Pine potentiostat (AFCBP 1, Pine Research Instrumentation, Pennsylvania, USA), motor (Model: AFMSRCE, Pine) and the three-electrode glass cell was used. An actual photo and a schematic illustration of the three-electrode cell containing RRDE shaft, which is used in this work are shown in Fig. 2. The

working electrode consists of a GC, Au or catalyst-modified GC disc (5 mm diameter), which is radially surrounded by a platinum ring (99.99% Pt, 6.5 mm ID, 7.5mm OD). The ring and disc are separated by a thin layer Teflon U-cup and are mounted into a Teflon tip. This tip is then fixed into a PEEK rotating shaft, which is controlled by a rotator, see Fig. 2.

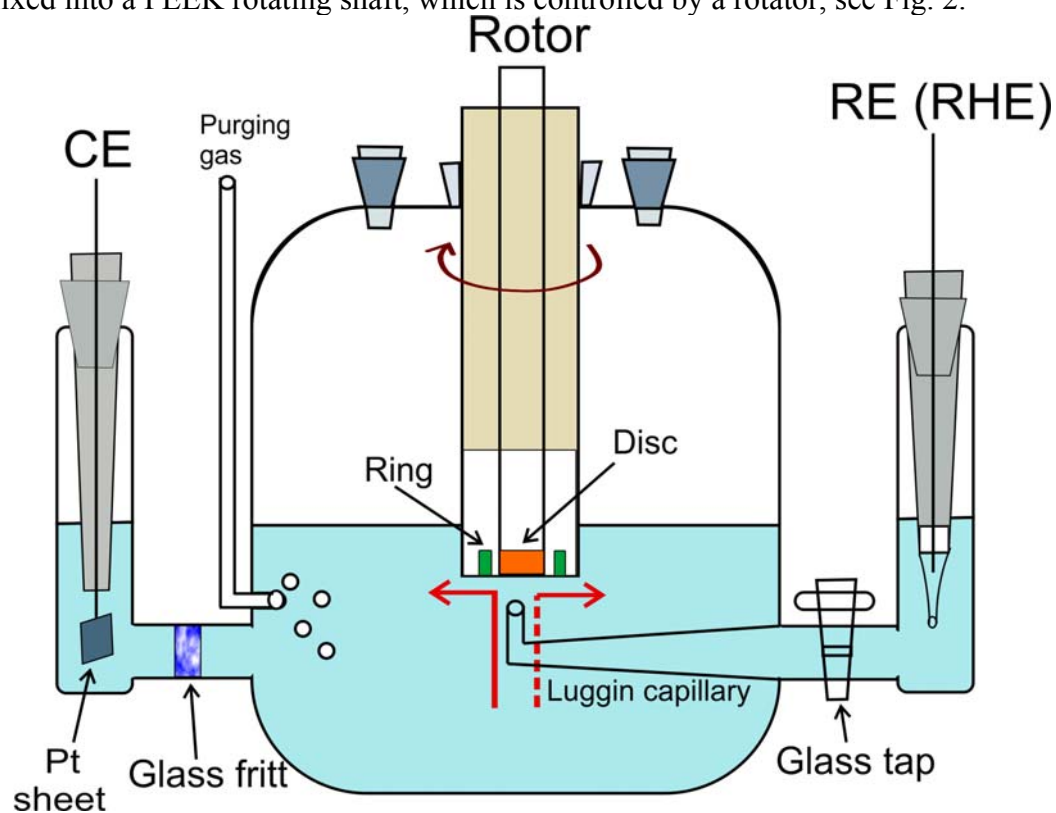


Fig. 2. Schematic and an actual photo of the experimental setup of RRDE with the glass cell containing the three-electrode arrangement.

The counter electrode was a (1cm x1cm) Pt sheet immersed in a glass tube and connected to the cell via a glass frit to avoid contamination of the cell with Pt. Normally, the level of solution in the counter electrode compartment should be lower than that in the WE partition. For the work with organic electrolyte, a normal glass H-cell is used.

#### *The reference electrode:*

Two types of the reference electrode were used in this work:

i) Reversible hydrogen electrode (RHE) for aqueous electrolytes; where it is freshly prepared on the day of the experiment. As shown in Fig. 2, it consists of a Pt wire which is sealed in a glass cylinder having a bulb. Using a water pump and external glass cylinder, the bulb is filled with the electrolyte due to the low pressure and suction at the open arm of the glass cylinder. One should make sure that there are no bubbles inside the bulb. By electrolysis of the solution (e.g. 0.1M LiOH), where about 1.5 V DC constant voltage is applied between the enclosed Pt wire and an additional Pt wire (as positive electrode) using a DC power supply (10-20V), hydrogen is evolved at the negative electrode in the bulb, and displaces the solution inside the bulb creating a gas/liquid interface in contact with the Pt. This continues till the solution level decreases to the half or more of the Pt wire length in the cavity. The potential of RHE is pH dependent where:  $E_{RHE} = E_{NHE} - 0.059pH$ .

ii) Ag/0.1M AgNO<sub>3</sub>/solvent was used as the reference electrode for organic electrolytes. It is prepared by immersing a Ag wire in a 0.1M AgNO<sub>3</sub> dissolved in the solvent used in the experiment. Exception was the case of Tetraglyme, where AgNO<sub>3</sub> does not dissolve in Tetraglyme and instead DMSO was used. For RRDE experiments, the wire and the solution were placed directly in the RE partition. The working electrode was separated from the reference electrode by means of a wetted glass stopcock, which is kept closed to avoid contamination with Ag. This stopcock is made of glass, and thus hydrophilic. The thin layer of electrolyte wetting the walls of its glass has sufficient conductivity to keep a potential control even if the stopcock is closed. The WE was placed very close to the RE (~ 3 mm distance) via a Luggin capillary, as shown in Fig. 2.

While in DEMS setup, RE was prepared in a separate glass cylinder and connected to the DEMS cell via a Teflon tube ending with a glass bead, see more details elsewhere.[3]

#### *Cell and Tip preparation:*

Prior to each experiment, the Pt ring electrode was cleaned mechanically by polishing with 0.05 μm alumina slurry onto a Buehler bad, then washed with Milli-Q water under sonication for 2 minutes. Cycling the ring in 0.5M H<sub>2</sub>SO<sub>4</sub> solution for several cycles might be needed for electrochemical cleaning.

The solutions in the RRDE cell were continually purged with Ar gas for about 30 minutes before starting the experiment, and then with O<sub>2</sub> for additional 30 minutes for ORR experiments. During the experiment, oxygen gas was purged over the solution to keep gaseous contaminants out of the cell. Under Ar-saturated solution, CV is recorded and is a measure of the capacitive current since no other electroactive species are present, and can be taken as a background current.

For non-aqueous electrolyte, RRDE glass cell was well-dried in an oven before the experiment and purged empty with Ar. In order to keep the humidity in the cell and water content as low as possible, all openings in the cell were closed with glass caps except shaft

inlet. Then, the electrolyte which is already filled in a syringe in the glove box is injected in the bottom of the cell under flow of Ar. Later, the solution was purged with O<sub>2</sub>.

*iR-correction:*

For *iR*-correction of the RRDE data which is necessary, in particular, for Tafel plots, the following equation has been used:

$$E_{iR\text{corr}} = E_{\text{measured}} - iR \quad \text{eq. 3.1}$$

where, *i* and *E* are the measured current and potential, respectively, and *R* is the ohmic solution resistance. The solution resistance is typically determined by EIS, where a simple RC circuit is used. The solution resistance depends on the distance between the Luggin capillary and the working electrode surface, see Fig. 2. In this work for alkaline media, a distance of ca. 6 mm was always kept, and the resistance was calculated to be 48, 12 and 6 Ω for LiOH with concentration 0.1, 1.0 and 2.5M, respectively. For 1.0 MKOH, it was about 10 Ω. If the distance was 3 mm, a solution resistance of ~40 Ω was found in 0.1M LiOH, and for 1 cm it was ~52 Ω. For organic electrolytes, the EIS was not stable; therefore, we used the galvanostatic pulse method to determine the solution resistance, as will be discussed below.

*Determination of electrolyte resistance by galvanostatic pulse method*

The galvanostatic pulse experiment was conducted prior or after the voltammetry experiments for organic electrolytes in the same cell and with the same electrodes. The three electrodes were disconnected from the potentiostat. A purpose built, battery powered, constant current source (external pocket galvanostat) was connected between the disc electrode and the counter electrode. A current pulse of 100 μA was applied for about 2 ms and at the same time the voltage difference between the reference and the working electrodes was recorded. The resultant voltage transient was monitored using a Labview data acquisition program, which was modified to record hundred thousands of data points per second. As, an example, the voltage transient in TBA<sup>+</sup>-DMI-containing electrolyte is shown in Fig. 3a. Just before the current pulse starts, the voltage was constant and then dropped suddenly as the pulse was given. The unexpected jump appeared before the pulse could be due to internal perturbation in the galvanostat since it still appears when only external resistance is used.

The appropriate equivalent circuit describing this polarization process is the simple Randles circuit as shown in the inset of Fig.3b. This polarization is simply a charging process of a capacitor. As the current pulse is given, the voltage drops immediately across *R<sub>s</sub>*, where *R<sub>s</sub>* is quite high, and the charge transfer resistance *R* and double layer capacitance *C* do not contribute to the resistance since *C* is quite high at this time, and accordingly an increasing polarization and a positive potential shift is observed. This voltage jump corresponds to the ohmic resistance (*R<sub>s</sub>*), as shown in the magnified graph in Fig. 3b. At longer times, the resistance increases across *R* slowly since the capacitor *C* charges. The solution resistance (*R<sub>s</sub>*) was in range of 50-110 Ω for DMI depending on the electrolyte and on the distance between the Luggin capillary and the working electrode. In the shown case, it is ~110 Ω. For DMSO/Li<sup>+</sup> and 3 mm distance, 80-110 Ω was obtained. IR-correction was not considered in every evaluation since the ohmic loss is not large at the measured currents. This method was shown to give reasonable results to that obtained by impedance spectroscopy method.

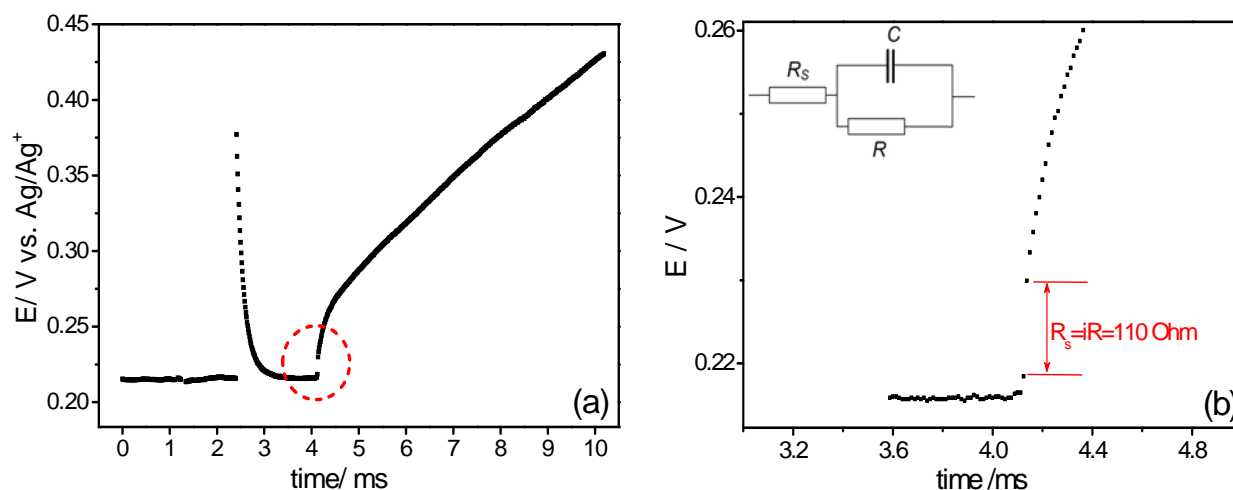


Fig. 3. (a) Voltage transients recorded with a current pulse of  $100 \mu\text{A}$  and 3mm distance between WE and Luggin capillary. (b) an expansion of the marked red circle of (a). Inset is the equivalent circuit corresponding to this experiment.

### 3.5. Differential electrochemical mass spectrometry (DEMS)

DEMS is an essential technique that monitors the volatile gaseous products immediately after their release from an electrochemical reaction. Thus, it combines the voltammetry with the mass spectrometry techniques in one setup. This tool has been intensively used in our group for the last three decades, in particular, for aqueous systems.[4, 5] One of the applications of DEMS in this work is to monitor OER in alkaline media at different catalysts, and to use isotope labeling together with DEMS to elucidate the OER mechanism through monitoring the different isotopes of  $\text{O}_2$  generated.[6] DEMS is also an informative tool for characterization of the ORR (discharge) and OER (charge) of Li- $\text{O}_2$  batteries and metal- $\text{O}_2$  batteries in general, as it enables determination of:

- i) number of electrons consumed per oxygen molecule ( $e^-/\text{O}_2$ ) and in turn the type of the reaction products ( $\text{Li}_2\text{O}_2$  or  $\text{LiO}_2$ ).
- ii) reversibility of the OER/ORR.
- iii) side reactions and decomposition reaction products.

These are key criteria in defining rechargeability. The high sensitivity of the mass spectrometer enables quantitative measurements of the  $\text{O}_2$  consumption and evolution as well as  $\text{CO}_2$  evolution from decomposition reactions.[7]

The idea of detecting gaseous products of an electrochemical reaction spectrometrically was originally proposed by Bruckenstein et al. in 1971.[8] They collected gaseous electrochemical reaction products in a vacuum system through a Teflon membrane, and detected the gases by mass spectrometry. Later, Wolter and Heitbaum[9] improved the vacuum system by using differential pumping (i.e. two pumping stages) to allow online detection with short time constant. In a typical DEMS measurement, the ionic current of a certain mass is simultaneously recorded with the faradaic current, yielding the so-called *mass spectrometric voltammogram* (MSCV) in parallel to the CV. In the last two or three decades, the technique has been improved much further. Different types of cells have been developed to accommodate the electrode geometry and the purpose of the experiment. Some of them will be discussed later.

For battery research, DEMS has been employed to investigate the decomposition of organic electrolytes as propylene carbonate[10] and ionic liquids.[11] The application of DEMS for Li-O<sub>2</sub> battery has been reported by the Bruce group in 2006, where they monitored oxygen evolution during charge using a similar setup to Bruckenstein.[12] This setup has been improved by McCloskey group in 2011 for analysis of gas consumption as well as evolution and the degradation process in Li-O<sub>2</sub> batteries.[13] We have used the benefits of our high sensitive DEMS setup and the well designed cells to online detect the amounts of gas consumed and released. One more advantage of our setup is the ability to use the classical cell as a gas diffusion electrode with very short delay time.

### 3.5.1. DEMS setup

The experimental setup of DEMS is shown in Fig. 4. It consists of an electrochemical cell attached to the inlet of a mass spectrometer (MS) via the main valve. The gaseous products flow in the first vacuum chamber (A) and to the ionization chamber (B), where the recipient is evacuated differentially by two turbo molecular pumps TPU of Balzer (2) in the two chambers. The cell is connected to the first chamber via a flange of the inlet valve at position 3, while another valve at position 4 can be connected to the calibration leak volume (discussed in results chapters). This valve at 4 is also connected to a pre-rotary pump, which is opened before opening the main valve to reduce the pressure underneath the cell to about 0.01 mbar. Then, it is closed and the main valve is opened. The second TPU is placed between the ionization chamber and the quadrupole rods, where a much lower pressure below  $10^{-5}$  mbar is achieved. The pressure in the first and the second vacuum chambers are about  $10^{-5}$  and  $10^{-6}$  mbar when the cell is connected and about  $10^{-8}$  and  $10^{-9}$  mbar without cell (using blind flange), respectively. A shutter between the ionization chamber and the analyzer allows the difference in pressure. The secondary electron multiplier (7) is placed perpendicular to the main axis, which has the advantage, that light from the filament does not reach the multiplier.

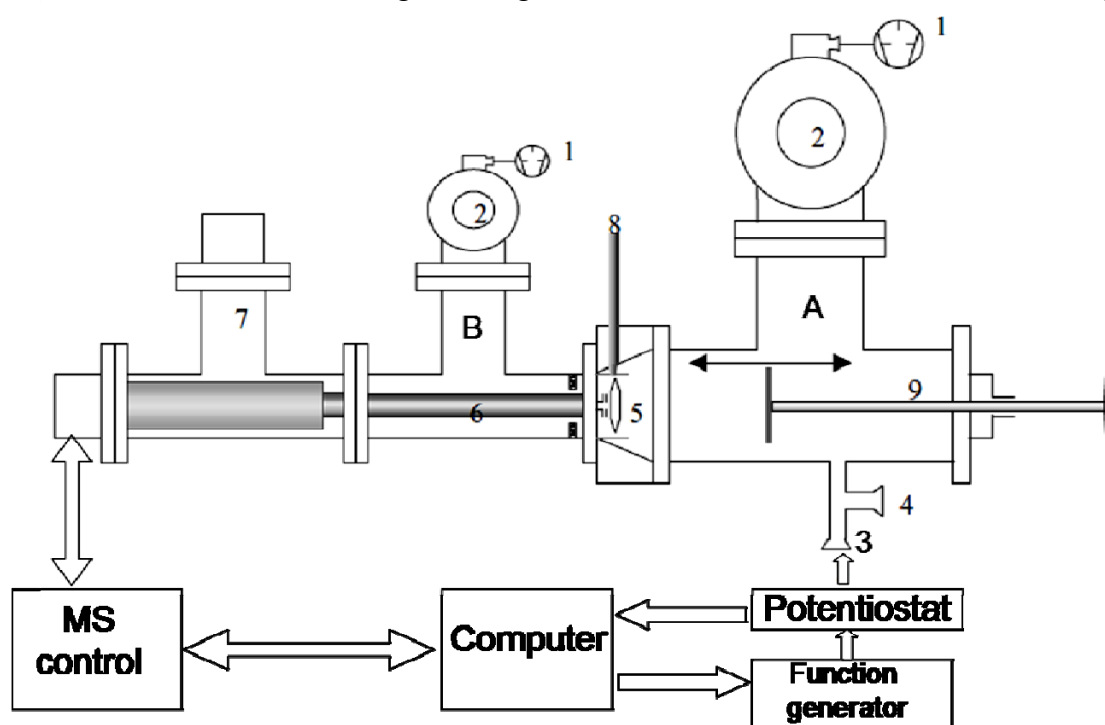


Fig. 4. Sketch of the vacuum system and setup of DEMS. 1 rotary pump; 2 Turbomolecular pumps; 3 Connection to the electrochemical cell; 4 Connection to calibration leak; 5 ion

source; 6 Quadrupole rods; 7 Secondary electron multiplier; 8 Direct inlet; 9 linear drive; *A* first vacuum chamber; *B* second (ionization) chamber. Modified according to [5].

In this method, the volatile products of a reaction and the solvent vapor, which reach the ionization chamber, are ionized by electron bombardment. The ions produced are then accelerated towards the mass filter (quadrupole rods), and only the ions of the selected masses ( $m/z$ ) reach the detector. The masses can be selected with the help of a control unit (Balzer QMG 422). Multiple ion detection is set using a personal computer with a commercial GUAD STAT software. The electrochemical measurements were performed in a three-electrode cell connected to a potentiostat driven by a function generator, and the output was read by Lab View software.

The potentiostat, function generation and MS control unit are controlled by a computer. The potentiostat used for DEMS experiments has been manufactured in the electronic workshop of Uni. Bonn. The common feature in all cells (with different materials and designs) is the use of a Teflon membrane. Thanks to the hydrophobic nature of the Teflon, aqueous electrolytes and some organic electrolytes can be separated from the vacuum phase. This membrane acts as an interface between electrolyte and MS, where liquids cannot penetrate while volatile species readily evaporate in the pores to vacuum. A typical PTFE membrane (Gore-Tex) has pore diameter of 20 nm with a porosity of 50% and 50  $\mu\text{m}$  thick. The working electrode has to be very close to the membrane. One possibility to achieve this is to use metal-sputtered Teflon membrane. The typical thickness of the catalyst layer (e.g. Au, Pt) is  $\sim 50$  nm. Other cell types are discussed below. Some of this DEMS information and more details can be found elsewhere.[4, 5, 14]

### 3.5.2. Cells configurations used

Interfacing an electrochemical cell to a mass spectrometer via a porous Teflon membrane can be achieved using a variety of cells as reported by Baltruschat.[5] The cells used in this study are:

#### i) Classical cell

This cell was the conventional cell, firstly, used in DEMS. It allows the use of small volume ( $\sim 1$  ml) electrolyte, see Fig. 5. So, it is beneficial for expensive compounds like isotope labeled experiments. It is proper of catalytic studies of metals that can be sputtered. The Au-sputtered membrane is the working electrode, a schematic of the electrode is reported elsewhere.[5] The membrane is mechanically supported on a steel frit. The response time of this cell is about 0.1s. Unfortunately, this cell cannot be used for massive disc electrodes. A continuous forced convection can be achieved by bubbling with Ar or O<sub>2</sub> via a Teflon tube inside the solution. This cell is used in this study for ORR/OER in organic electrolytes and as a gas diffusion electrode.

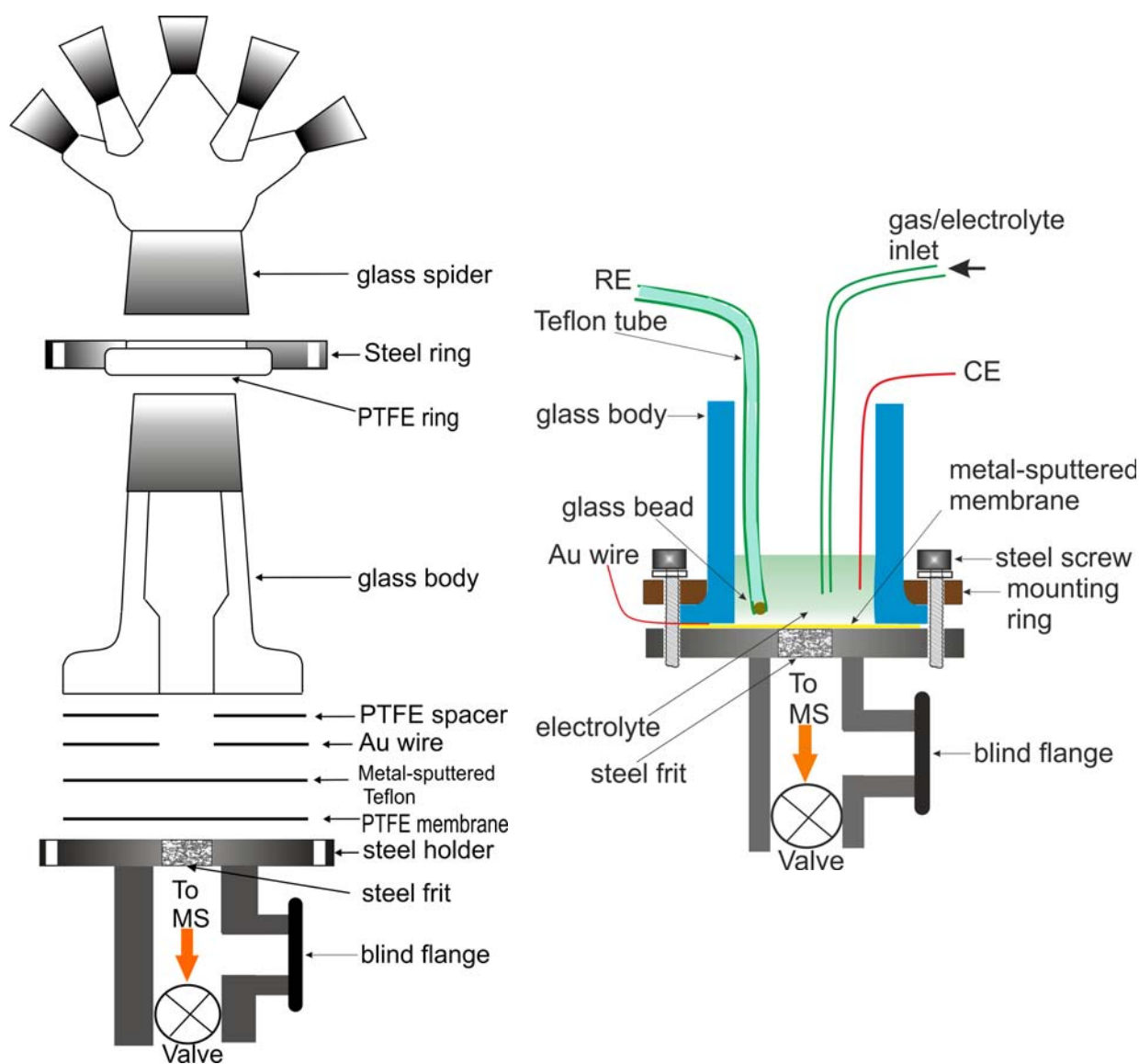


Fig. 5. Schematic of the classical DEMS cell setup (left panel) and with details of the electrodes used (right panel). The GDE setup is also shown in the steel holder.

## ii) Dual thin layer flow cell

To be able to use massive electrodes (e.g. single crystals) or catalyst-modified discs, and under continuous flow of electrolyte, the dual thin layer flow cell has been developed.[15] The cell, as shown in Fig. 6, consists of two separate compartments: the electrochemical compartment, where the electrolyte first enters underneath the electrode and then flows to the lower detection compartment through six capillaries, where the volatile products reach the Teflon membrane and pass through to the MS. The pure disc or catalyst-loaded disc with a diameter of 1 cm was used. The exposed area and electrolyte volume underneath the electrode is defined by a Teflon spacer (4 layers) with 6 mm inner diameter and 12 mm outer diameter. The volume in the lower compartment was created by using four layers of Teflon spacer each of 50  $\mu\text{m}$  above the Teflon membrane. The membrane is supported onto a steel frit. Two capillaries positioned at opposite sides serve as the electrolyte inlet and outlet and also as a connection to the reference and counter electrodes. Because of the larger ohmic drop in this cell, a higher concentration of salt has to be used ( $\sim 0.5\text{M}$ ) and two counter electrodes both at

the outlet and inlet of electrolyte are used. These counter electrodes are connected to the potentiostat via different resistors: a 100 k $\Omega$  resistance at the inlet, while 100-1000  $\Omega$  resistance at the outlet. Therefore, the total current is divided into two parts so that the current through the capillary to the reference electrode is much less than 50% of the total current. For this cell, a significant part of the products is transported out of the cell with electrolyte flow since it is formed near the outlet and has little chance to reach the Teflon membrane, and thus it is lost. Experimentally, transfer efficiency of about 0.2 for a flow rate of 1  $\mu\text{l/s}$  was found.[4]

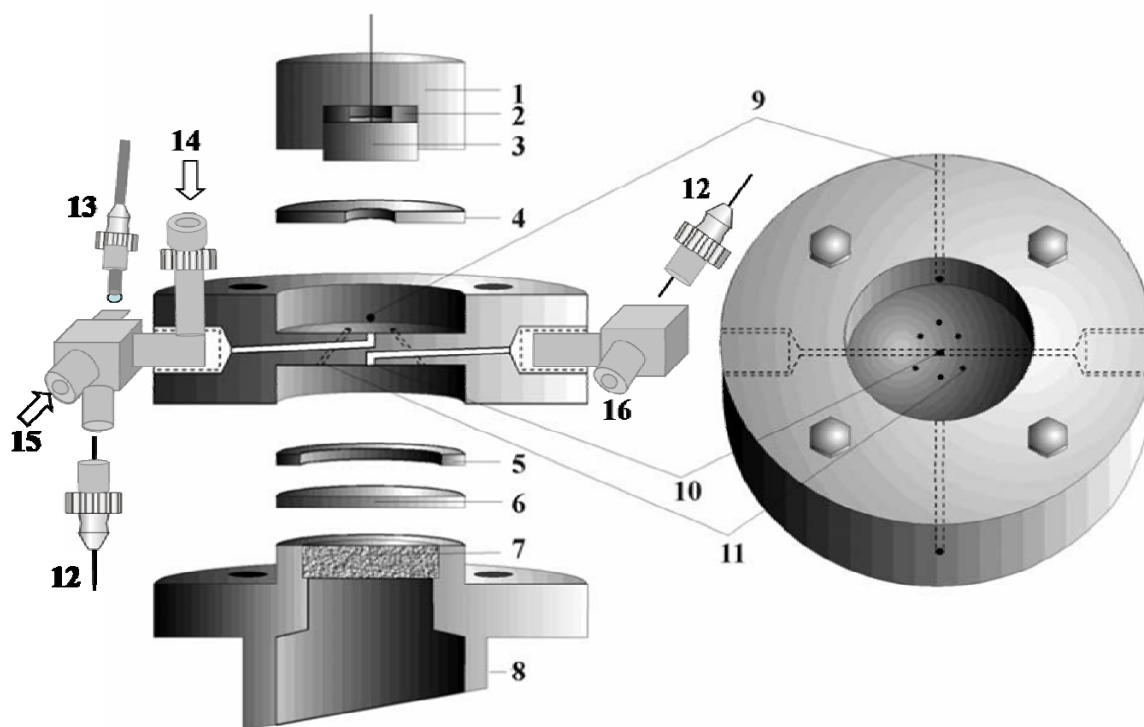


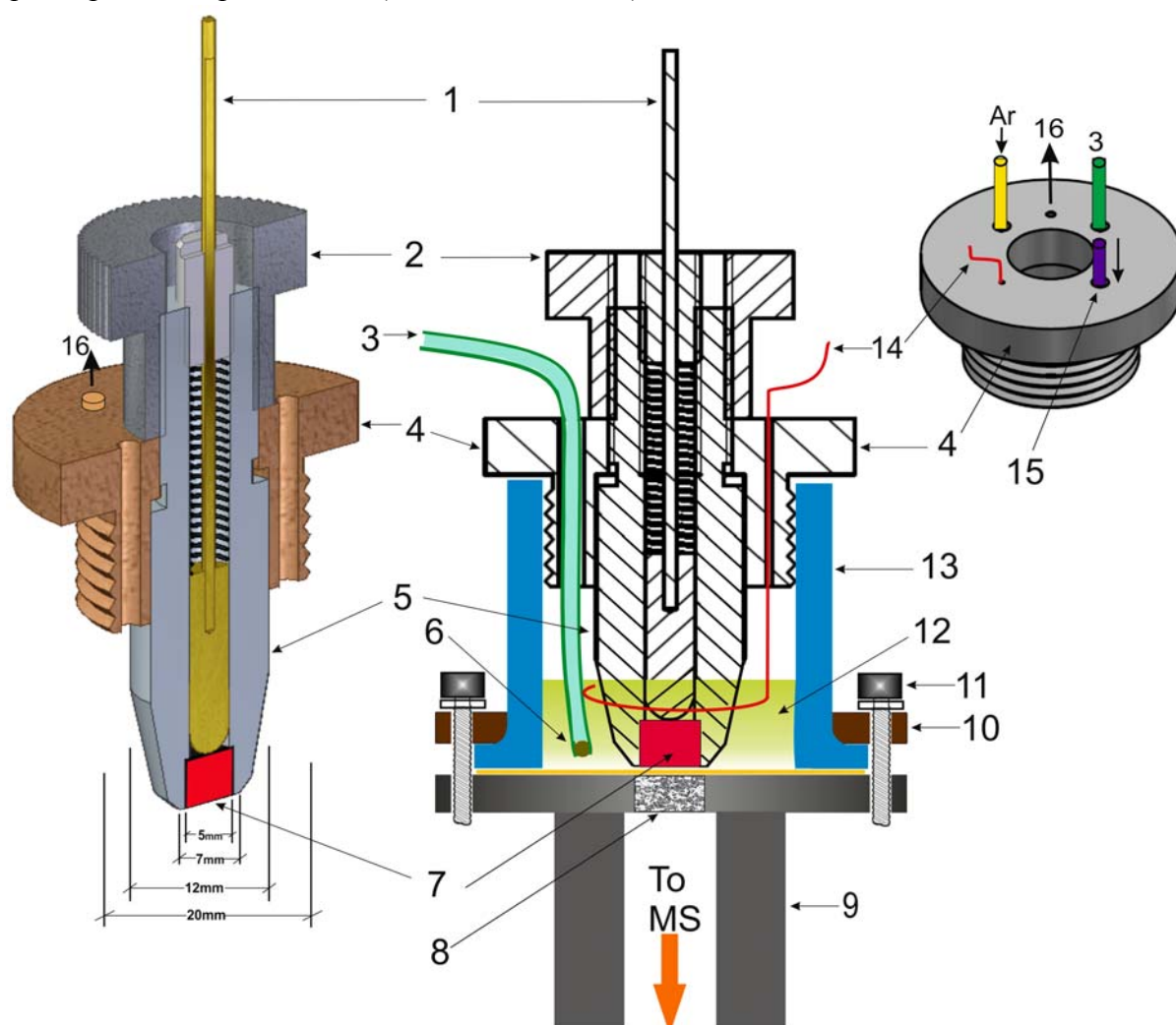
Fig. 6. Schematic of the dual thin layer flow cell made of Kel-F : 1 Kel-F support; 2 Kalrez; 3 disc electrode; 4, 5 Teflon spacer; 6 porous Teflon membrane; 7 stainless steel frit; 8 stainless steel connection to MS; 9 capillaries for flushing with Ar; 10 inlet-outlet capillaries; 11 connecting capillaries; 12 counter electrode; 13 reference electrode connection; 14 electrolyte inlet; 15 injection inlet; 16 electrolyte out to pump. Left: Side view; Right: top view of the cell. Modified after [5].

### iii) Novel small-volume cell

To be able to use massive small discs, to examine catalysts loaded on disc electrodes, and because of the practical difficulty to control catalyst casting on the porous membrane electrode, the need of a new cell for small-volume electrolytes was an important goal. Therefore, we developed a novel cell, which is appropriate for massive disc electrodes and suitable for studying the electrochemistry on nanoparticles-modified electrode. These functions were not possible in the classical cell, which employs a metal-sputtered membrane as the working electrode,[5] and not in the dual thin layer flow cell, which requires a large amount of solution. This cell is called the *small-volume DEMS cell*. A schematic drawing and photos of the small-volume cell is shown in Fig. 7. The main advantage of this cell is the need of only  $\leq 0.5$  ml of the electrolyte, which is important issue for expensive chemicals. Constant

convection in the cell is achieved by continuous constant bubbling of Ar inside the electrolyte using Teflon tube. This cell is used here for isotope exchange experiments.

For the novel cell, the catalyst ink can be easily loaded on a disc massive electrode, which is then carefully installed and pressed into a Kel-F shaft so that both disc and shaft forefronts lie on the same planar level. The disc working electrode has a diameter of 5 mm ( $0.196 \text{ cm}^2$ ). The shaft is an analogue to RDE tip. It has a conical shape at the apex, as shown in the drawing, which gives good electrochemical performance. This is found to be important, after some trials with a pure cylindrical shape tip, because it allows a shorter distance between the working disc and reference electrode (ca. 3mm). The tip containing the working electrode is inserted into a PTFE lid, and screwed into an upper Teflon mounting nut. The nut acts as a manipulator since it controls the distance of the working electrode from the Teflon membrane. The Teflon lid fits tightly into the glass housing, which is suitable for a small-volume electrolyte. The glass cell is mounted on a stainless steel holder, which contains 5 mm diameter steel frit in the centre, which is directly connected to a differentially pumped quadrupole mass spectrometer (QMG-422, Pfeiffer).



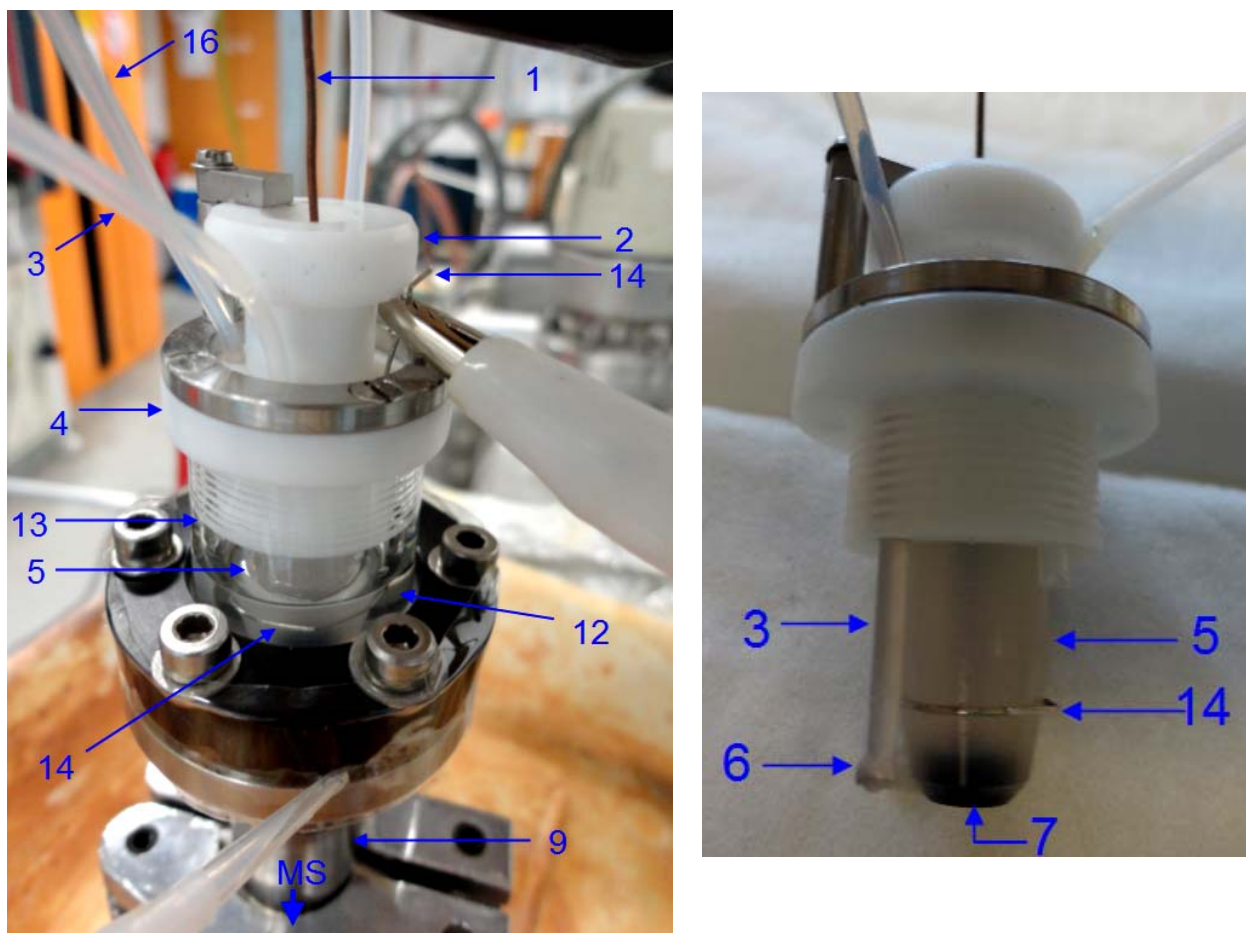


Fig. 7. Sketch and cross section of the new small-volume DEMS cell with its components, where 1 copper contact pin, 2 Teflon mounting nut, 3 reference electrode connection, 4 Teflon lid, 5 Kel-F shaft, 6 glass bead, 7 disc working electrode, 8 steel frit, 9 stainless steel connection to MS, 10 mounting ring, 11 steel screw, 12 electrolyte, 13 glass housing, 14 counter electrode, 15 electrolyte inlet and outlet, 16 gas outlet. Photos are also shown.

A porous Teflon membrane of 20 nm pore size and 50 $\mu$ m thick (Gore Tex®, Germany) was mechanically supported on the steel frit, and acts as an interface between the liquid phase and the high vacuum of the mass spectrometer. The membrane was clamped between the glass body and the steel holder using a mounting ring and steel screws. Due to the hydrophobic nature of the membrane and the high surface tension of the used solution, the solution does not penetrate into the capillaries of the membrane, but volatile products generated at the electrode surface diffuse through the membrane to the mass spectrometer to be online detected. The working electrode was exactly facing the steel frit to allow efficient transfer of volatile products to the mass spectrometer. The working electrode was connected from the back side via a copper wire and a contact pin to get electrical contact with the potentiostat. The distance between the working electrode and the Teflon membrane is variable.

Noteworthy, the shaft containing the working electrode can be manipulated away or near to the membrane by screwing the upper manipulating nut: the front of the tip was firstly made at the same plane with the glass housing, and then the mounting nut was screwed so that a gab between the tip and the zero line was created. Knowing the distance which arises from one complete rotation of the nut (from the marked starting point), the used gab was thus

determined. We found it is important control this distance, and it is critical for the delay time and the ionic current signal. An optimization of the distance was done, and we found that few tens of micrometers ( $\sim 50 \mu\text{m}$ ) are optimal, allowing very short delay time in our setup. A Pt wire was inserted through the PTFE lid to the electrolyte as a counter electrode. Ar-purging was achieved by a Teflon tube which was also immersed into the solution in the glass housing at certain distance from the membrane.

The reference electrode was a reversible hydrogen electrode (RHE) in the same alkaline electrolyte. The reference electrode was electrically connected to the working solution through a salt bridge made of a Teflon tube filled with the same solution and ended with a glass bead. This tube was inserted inside the glass housing. The electrolyte was saturated with Ar for about 10 minutes prior to the experiment.

### 3.5.3. Evaluation of the DEMS data

Base line correction of the raw data was necessary since in some cases the ionic current was exponentially decaying with time due to rest gas in the vacuum system or some gases leaks into the system even when no potential is applied. For evaluations, the faradaic current is also corrected with respect to the base line of the double layer current. After base line correction of the ionic current, both the faradaic and ionic currents are plotted against a common time-axis so that the starting measured point is at  $t=0$ . Then, the MSCV is moved on the time axis (if necessary) such that the respective characteristics (e.g. cathodic limit potential or peak position) lay on the same time. This is necessary since the recordings of CV and MSCV do not start synchronously, and the recording programs show the relative time with different intervals. This allocation is important for calculation of the number of electrons. In the curves, the measured faradaic current density is abbreviated as  $J_F$ , and the ionic current density of mass 32 as  $J_{32}$ .

### 3.5.4. Calibration leak experiment

In a calibration leak experiment, a T-shaped connection piece with a volume of 54 mL was connected via a dosing valve to the vacuum system and underneath the cell. The calibration volume was, firstly, cleaned by evacuation to ca. 0.02 mbar with a dual-stage rotary vane pump (DUO 2.5, Pfeiffer Vacuum), then filled with oxygen. A pressure of about 6 mbar was adjusted and is stable after 20 min. A defined flow rate of oxygen into the vacuum system was then adjusted via the dosing valve. In the same time, we recorded both the pressure drop in calibration volume by an attached pressure gauge and the ionic current of mass 32 ( $I_{32}$ ) by MS.

A baseline correction of  $I_{32}$  is performed. The ion current continued to decline over time, as the flux of oxygen decreases in the system because of the falling pressure in the calibration volume. From the respective pressure, the amount of substance is calculated using the ideal gas law, assuming a temperature of  $25^\circ \text{C}$ . Then, from the temporal change of the amount of substance ( $dn/dt$ ) the calibration constant  $K^o$  is determined according to eq. 3.2. The slope of the linear regression is  $K^o$ . One example for the  $K^o$  determination ( $K^o=0.7$ ) is shown in Fig. 8.

$$I_i = K^o \left( \frac{dn}{dt} \right) \quad \text{eq. 3.2}$$

It is also reasonable to assume an error of up to  $\pm 20\%$  in DEMS results, which could arise from change in collection efficiency or calibration constant. Due to possible uncertainty in

pressure measurements (main reason of uncertainty in  $K^o$ ), a multiple determination of  $K^o$  is fair. An average calibration constant of  $1.0 \pm 0.2 \text{ C mol}^{-1}$  is obtained for the time of experiments on the used DEMS instrument depending on how often the filament is in use. Calibration leak experiment was performed under the same conditions of the experiment, and the corresponding  $K^o$  value is used for evaluations.

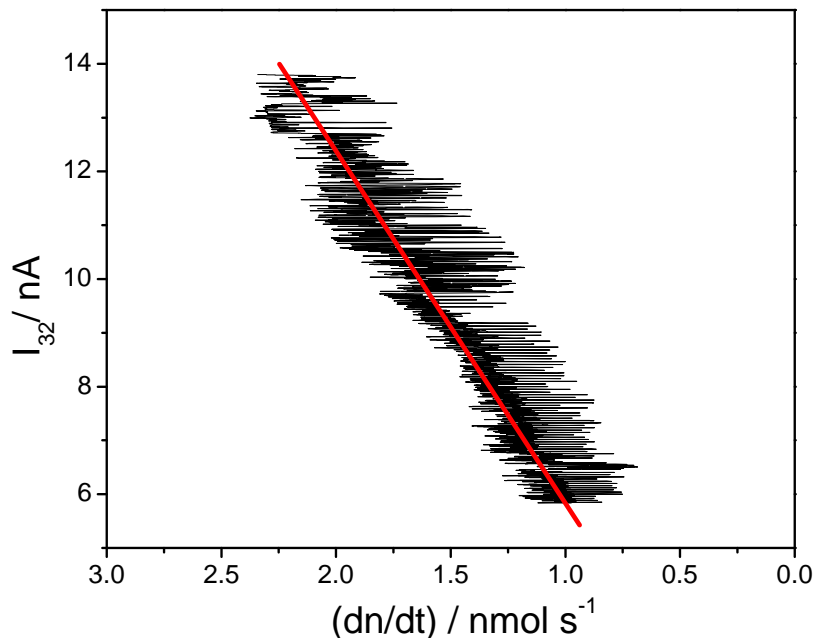


Fig. 8. Plot of ionic current of  $O_2$  ( $I_{32}$ ) vs. the rate of  $O_2$  entering the mass spectrometer from the calibration volume.

In DEMS experiments, the electrolyte is continually purged with  $O_2$ , thus  $O_2$  concentration in the electrolyte is constant. The constant flow of oxygen provides a constant convection in the electrolyte. Over the membrane originates a concentration gradient since oxygen permanently diffuses into the vacuum. As the structure of the Nernstian diffusion layer and the concentration gradient are constant, the total flow ( $\dot{n}_t = dn/dt$ ) to the membrane and vacuum is constant, and is calculated according to the 1<sup>st</sup> Fick's law (eq. 3.3):

$$\dot{n}_t = -D \frac{\partial C}{\partial x} = -D \frac{C}{\delta} \quad \text{eq. 3.3}$$

where,  $D$  is the diffusion constant and  $\delta$  is the thickness of the diffusion layer.  $\dot{n}_t$  is the sum of the flow into the mass spectrometer  $\dot{n}_{MS}$  and the amount of  $O_2$  consumed by electrochemical reduction of oxygen  $\dot{n}_F$ . From this, eq. 3.4 can be derived.

$$\dot{n}_t = \dot{n}_{MS} + \dot{n}_F \quad \text{eq. 3.4}$$

$\dot{n}_{MS}$  is proportional to  $I_i$  where,  $\dot{n}_{MS} = I_i/K^o$  and  $\dot{n}_F$  is proportional to  $I_F$  where,  $\dot{n}_{MS} = I_F/nF$ , thus eq. 3.5 is valid:

$$\frac{I_i}{K^o} = \text{const.} - \frac{I_F}{nF} \quad \text{eq. 3.5}$$

### 3.6. Surface characterization

Fundamental investigation of the structure, morphology and composition of the catalyst is required to understand the origin of the activity, and thus for further development of the catalyst. BET data were obtained based on N<sub>2</sub>-adsorption method. The physical characterization techniques used here are:

#### 3.6.1. SEM and EDX

SEM is based on emitting several types of radiation by interaction of the incident electron beam with the sample. The secondary electrons and back-scattered electrons are used to construct SEM images. This characterization technique is fast and simple to study the microstructure. With addition of an X-ray detector, the surface elemental composition of the catalyst can also be provided from the energy dispersive X-ray spectroscopy (EDX). Here, SEM is used to monitor the morphology of the Ag+Co<sub>3</sub>O<sub>4</sub> mixed catalyst, and to examine the distribution of Co<sub>3</sub>O<sub>4</sub> particles onto Ag particles. SEM and EDX analyses were performed on the catalysts loaded on a 5mm GC electrode, and this has been done prior as well as after several ORR/OER cycles. The samples are prepared in our lab and sent to our project partner (University of Ulm, central facility of electron microscopy) for SEM analysis. The instrument used is Zeiss dual-beam NVISION 40 with an operating voltage of 5-30kV. The EDX was obtained using AMETEK EDAX, type Genesis APEX2.

#### 3.6.2. EC-XPS

XPS is an outstanding surface characterization technique, which is used to study the electronic state of the sample elements. It is more sensitive (to about 1-10 nm of the sample surface) than EDX or XRD. The combination of an electrochemical cell with an UHV system was originally developed by Hubbard et al. in 1976.[16] Later, Itaya et al. employed the sample transfer system in EC-XPS.[17] XPS is based on the interaction of X-ray photon with the electrons of the sample under UHV atmosphere.[18] As the X-ray photons interact with the sample, energy is transferred from photons to the electrons occupying different energy states according to the equation:  $E_{photon} = E_{binding} + E_{kinetic} + \Phi$ , where  $E_{binding}$  is the binding energy of the electron at different energy state,  $E_{kinetic}$  is the kinetic energy of the ejected electron, and  $\Phi$  is the work function of the spectrometer. By detecting the number of electrons emitted at different binding energies, an energy spectrum specific to different elements can be obtained. In this study, XPS (done by C. Bondue) is used to investigate the redox switching process of Co in Co<sub>3</sub>O<sub>4</sub> in the mixed Ag+Co<sub>3</sub>O<sub>4</sub> catalyst, and to know whether this transition is potential dependent. This is achieved by recording the XP spectra of Co, Ag and O atoms. XPS were collected in the main chamber of a UHV system with an attached Omicron EA125 hemispheric electron energy analyzer and a X-ray tube with magnesium. In this technique, electrochemical experiments were firstly performed, then the XPS measurement was done in the main chamber under UHV conditions. Schematic of the EC-XPS showing its components and the three-electrode electrochemical cell is displayed in Chapter. 5. Prior to transfer to main chamber, the surface was rinsed with a more dilute solution (0.1 mM LiOH) several times under potential control to minimize the contribution of excess salts present in the liquid film upon removal from solution.[19] The positioning of the working electrode in the Ante-

chamber and transfer to the main chamber in a specific location is achieved by the manipulator.

### 3.6.3. XRD

X-ray diffraction (XRD) is a common technique, which is used to identify the crystal structure of materials. It is based on the interaction of X-ray with the electron density of sample atoms. In this study, XRD is used to study the structure and phases of Ag in the pure Ag and mixed Ag+Co<sub>3</sub>O<sub>4</sub> catalysts. This was done at different potentials to monitor the change in the structure and identify the different oxidation states at different potentials. XRD pattern is obtained by plotting the diffraction pattern intensity versus the Bragg angle, which is a characteristic to a specific material. XRD analysis was conducted at a gas diffusion electrode at DLR, Institute of technical thermodynamics using Bruker D8 Discover GADDS with monochromatized Cu K<sub>α</sub> radiation. Each diffraction pattern was measured in four frames with a step size of 23°, starting with 12° (Bragg-Brentano condition), and the exposure time for each frame was 180 s.

### 3.7. Electrochemical impedance spectroscopy (EIS)

EIS is used in the aqueous media to determine the solution resistance and to investigate the behavior of the catalyst at different potentials (i.e. upon oxidation and reduction), and in different electrolytes. Some information on the charge transfer process in the electrochemical reaction and catalyst conductivity can be determined by EIS.

All EIS measurements were carried out with an impedance instrument model 1260 (Solartron) in combination with a potentiostat EG& G (model 273, Princeton Applied Research, Oak Ridge). Automatic recording of the impedance spectra was achieved using the software ZPlot Version 2.0 (Scribner Associated). A GPIB card is used as an interface between the potentiostat and the impedance instrument. The impedance spectra were recorded in a frequency range of 0.1 Hz to 100 kHz with an excitation amplitude of 3 mV. In this setup, the impedance instrument serves not only as an analyzer for the measured impedance, but also as a frequency generator for the applied AC voltage, which is forwarded to the external input of the potentiostat. The AC current of the total current is analyzed to phase shift and amplitude change. Thereby, the resistance, capacitance and/or inductance can be calculated by constructing the proper equivalent circuit, and fitting the data using the software Zview 2.0 (Scribner Associated).

### 3.8. References

- [1] T.J. Schmidt, H.A. Gasteiger, G.D. Stab, P.M. Urban, D.M. Kolb, R.J. Behm, *Journal of the Electrochemical Society* 145 (1998) 2354-2358.
- [2] Potentiostat, Public lab, <https://publiclab.org/wiki/potentiostat>, accessed on 15.02.2016.
- [3] C.J. Bondue, A.A. Abd-El-Latif, P. Hegemann, H. Baltruschat, *Journal of the Electrochemical Society* 162 (2015) A479-A487.
- [4] H. Baltruschat, in: A. Wieckowski (Ed.), *Interfacial Electrochemistry*, Marcel Dekker, Inc., New York, Basel, 1999, pp. 577 - 597.
- [5] H. Baltruschat, *Journal of the American Society for Mass Spectrometry* 15 (2004) 1693-1706.
- [6] S. Fierro, T. Nagel, H. Baltruschat, C. Comninellis, *Electrochemistry Communications* 9 (2007) 1969-1974.
- [7] C. Bondue, P. Reinsberg, A.-E.-A.A. Abd-El-Latif, H. Baltruschat, *Phys. Chem. Chem. Phys.* 17 (2015) 25593–25606.
- [8] R.R. Bruckenstein, J. Gadde, *Journal of the American Chemical Society* 93 (1971) 793.
- [9] O. Wolter, J. Heitbaum, *Ber. Bunsenges. Phys. Chem.* 88 (1984) 2-6.
- [10] G. Eggert, J. Heitbaum, *Electrochimica Acta* 31 (1986) 1443-1448.
- [11] C.-P. Maschmeier, H. Baltruschat, *Electrochimica Acta* 37 (1992) 759.
- [12] T. Ogasawara, A. Débart, M. Holzapfel, P. Novák, P.G. Bruce, *Journal of the American Chemical Society* 128 (2006) 1390–1393.
- [13] B.D. McCloskey, D.S. Bethune, R.M. Shelby, G. Girishkumar, A.C. Luntz, *The Journal of Physical Chemistry Letters* 2 (2011) 1161-1166.
- [14] B. Bittins-Cattaneo, E. Cattaneo, P. Königshoven, W. Vielstich (Eds.), *New developments in Electrochemical Mass Spectroscopy*, 1991.
- [15] T. Hartung, H. Baltruschat, *Langmuir* 6 (1990) 953-957.
- [16] R.M. Ishikawa, A.T. Hubbard, *Journal of Electroanalytical Chemistry* 69 (1976) 317-338.
- [17] T. Yamada, N. Batina, K. Itaya, *Surface Science* 335 (1995) 204-209.
- [18] H. Hoster, H. Gasteiger, in: G. HA, V. W, L. A (Eds.), *Handbook of Fuel Cells - Fundamentals, Technology and Applications*, John Wiley & Sons, Ltd. Chichester, 2003, pp. 236 - 265.
- [19] F. Lu, G.N. Salaita, H. Baltruschat, A.T. Hubbard, *Journal of Electroanalytical Chemistry* 222 (1987) 305-320.



#### 4. A Highly efficient bifunctional catalyst for ORR/OER based on a Ag and $\text{Co}_3\text{O}_4$ hybrid: RRDE & DEMS

The Ph.D. work began with the search for an efficient bifunctional catalyst for both ORR and OER in alkaline media. A bifunctional catalyst is necessary to reduce to the overpotential of oxygen reactions in fuel cells and metal-air battery applications. The idea behind that was the possibility of using an  $\text{O}_2$ -electrode in an aqueous Li-air battery. Pt catalysts are known to be efficient for ORR; however, they are not cost-effective. Moreover, most of the non-noble catalysts reported in literature are loaded on a carbon support, which suffers from corrosion problems at higher potentials. Therefore, catalysts based on Ag and Co-oxides are here investigated. Noteworthy, they are relatively inexpensive and carbon-free. The results demonstrate that a mixed catalyst based on Ag+ $\text{Co}_3\text{O}_4$  with a certain ratio has a good bifunctional activity and good stability. Furthermore, the ratio of the two components in the mixture is varied to get the optimum composition. 10-20 w% of  $\text{Co}_3\text{O}_4$  in the mixture shows the best bifunctional activity.

RRDE technique was used to study the kinetics and mechanism. DEMS allowed us to monitor  $\text{O}_2$ -evolution. XRD analysis was done to examine the oxidation state of Ag at different potentials. The morphology was characterized by SEM and EDX. A detailed introduction on this topic, theoretical background and a wider literature survey are presented in chapter 1 of this thesis. A summary of the main results of this chapter together with other chapters is presented at the end of the thesis (chapter 10). In cooperation with project partners from DLR, the major findings were filed as a patent application (DE 10 2014 102 301.8), and two articles were published: one in the *Journal of Power Sources*, 265 (2014) 299-308, and the second paper in the journal of *Electrochimica Acta* (as first author, see following publication).

This paper was written in major by me, and edited by all co-authors. The experiments were designed and carried out by me. Samples for SEM and EDX were prepared by me, and the analyses were kindly carried out by S. Eswara and U. Kaiser from Ulm University. XRD measurements were carried out by D. Wittmaier under supervision of K. Friedrich from DLR.

The article is reprinted with permission from Elsevier Ltd. Copyright 2014.

[doi:10.1016/j.electacta.2014.11.017](https://doi.org/10.1016/j.electacta.2014.11.017) .



Contents lists available at ScienceDirect

Electrochimica Acta

journal homepage: [www.elsevier.com/locate/electacta](http://www.elsevier.com/locate/electacta)

## A Highly Efficient Bifunctional Catalyst for Alkaline Air-Electrodes Based on a Ag and Co<sub>3</sub>O<sub>4</sub> Hybrid: RRDE and Online DEMS Insights



Hatem M.A. Amin<sup>a,b</sup>, Helmut Baltruschat<sup>a,\*</sup>, Dennis Wittmaier<sup>c</sup>, K.Andreas Friedrich<sup>c,1</sup>

<sup>a</sup> Institute of Physical and Theoretical Chemistry, University of Bonn, 53117 Bonn, Germany

<sup>b</sup> Dept. of Chemistry, Faculty of Science, Cairo University, 12613 Giza, Egypt

<sup>c</sup> Deutsches Zentrum für Luft- und Raumfahrt (DLR), Institut für Technische Thermodynamik, 70569 Stuttgart, Germany

### ARTICLE INFO

#### Article history:

Received 29 September 2014

Accepted 4 November 2014

Available online 6 November 2014

#### Keywords:

bimetallic catalyst  
cobalt oxide  
metal-air battery  
oxygen  
silver

### ABSTRACT

Enhanced catalytic activity towards oxygen reduction (ORR) and evolution (OER) reactions has been achieved by combination of spinel Co<sub>3</sub>O<sub>4</sub> nanoparticles with Ag particles. Quasi-stationary polarization curves showed that the mixed catalyst, Ag + Co<sub>3</sub>O<sub>4</sub> (10 wt%), outperformed its components. Rotating ring-disc electrode (RRDE) measurements revealed a negligible peroxide species formation and a 4-electron pathway for ORR. A tafel slope of ca. 75 mV dec<sup>-1</sup> has been observed. The overpotential for ORR at 10% Co<sub>3</sub>O<sub>4</sub> catalyst is ca. 70 mV lower than that of Ag and only ca. 80 mV higher than that of the commercial Pt catalyst. DEMS technique provided a direct evidence for oxygen evolution at these bimetallic catalysts. This hybrid is therefore one of the (or even the) most active, carbon-free, durable, non-precious ORR and OER electrocatalysts reported to date.

© 2014 Published by Elsevier Ltd.

### 1. Introduction

The world-wide growing energy demand has boosted the deep research on alternative energy conversion and storage systems which are environmentally friendly, highly efficient and cost-effective. Lithium-air battery is one of the promising approaches which could lead to at least a four-fold higher specific energy compared to conventional Li rechargeable batteries [1,2]. In one possible approach, an oxygen gas diffusion electrode using an alkaline aqueous electrolyte is combined with a Li anode which is protected with a Li<sup>+</sup> permeable membrane [3]. For this and also other metal-air batteries [3], it is important to develop efficient bifunctional catalysts for both ORR during discharge and OER during charge.

For ORR in alkaline electrolytes, Ag is known to be very active. ORR follows the 4-e<sup>-</sup> pathway at Ag [4] and carbon supported Ag [5]. Its activity can be increased by modification with other metals as Co/Fe and Co<sub>3</sub>O<sub>4</sub> [6–8]. But for OER, Ag is not active. Besides iridium and ruthenium oxides, also some non-noble metal oxides (first row spinel and perovskites) have a high activity for OER in alkaline media [9]. However, they are usually much less active for ORR. Some reports showed high catalytic activity, but the catalysts

were loaded on a carbon support, which suffers from corrosion [10,11].

It is highly challenging to develop an efficient carbon-free bifunctional catalyst for both ORR and OER in air-electrode. The strategy followed here was to prepare a non-precious metal hybrid by mixing a catalyst which has superior activity for ORR (Ag) with one which is highly active and stable for OER. As components we used a standard silver catalyst (Ag311 microparticles, 1–2 μm) and Co<sub>3</sub>O<sub>4</sub> spinel nanoparticles (≤50 nm). Only in few previous reports, a similar strategy was followed. However, they either lack steady state data or stability tests [12–14] or have a larger potential gap between ORR and OER compared to ours [15,16]. Tuning the activity of the catalyst was achieved by varying the ratio of Ag to Co<sub>3</sub>O<sub>4</sub> in the mixture. Monitoring oxygen evolution at these catalysts by online mass spectrometry provides a direct evidence for their OER activity. The morphology and composition of the mixed catalyst were examined using scanning electron microscopy and X-ray diffraction techniques. The optimized hybrid exhibited an outstanding performance and stability for OER/ORR, thus leading to a promising bifunctional catalyst alkaline air-electrodes.

### 2. Experimental

#### 2.1. Chemicals and materials

The Ag311 standard silver catalyst (1–2 μm particle size) was obtained from Ferro GmbH, Germany. Spinel Co<sub>3</sub>O<sub>4</sub> nanoparticles (≤50 nm size), Nafion<sup>®</sup> 117 solution (~5% in a mixture of lower

\* Corresponding author. Tel.: +49 228 73 4162; fax: +49 228 73 4540.

E-mail addresses: [baltruschat@uni-bonn.de](mailto:baltruschat@uni-bonn.de), [hatem@pc.uni-bonn.de](mailto:hatem@pc.uni-bonn.de) (H. Baltruschat).

<sup>1</sup> ISE member

aliphatic alcohols and water), Lithium hydroxide monohydrate (99%) were purchased from Sigma-Aldrich, Germany. The commercial 20 wt.% Pt supported on Vulcan XC-72 catalyst was purchased from E-TEK. Ultra-high pure argon (99.999%, Air Liquide) and oxygen (99.9995%, Air Liquide) were used. All aqueous solutions were prepared with Milli-Q water (18.2 M $\Omega$  cm, TOC of 5 ppm, MILLIPORE, Schwalbach, Germany) and were bubbled with Ar or O<sub>2</sub> for at least 40 minutes before use.

## 2.2. Catalyst preparation

Prior to loading the catalysts on the glassy carbon (GC) electrodes (0.196 cm<sup>2</sup>), the GC electrodes were polished to a mirror finish with the help of 0.05  $\mu$ m alumina slurry on a polishing cloth (Microcloth PSA 2, Buehler). The GC electrodes were then cleaned from the suspension residues and adhering impurities with acetone (99.5%, Sigma-Aldrich) and Milli-Q water. Finally, the electrodes were cleaned with Milli-Q water in an ultrasonic bath (VWR<sup>®</sup>, Germany) for 5 minutes and then dried with a KIMTECH wipes and coated with the respective catalyst suspension. The procedure for preparing the modified GC electrode (catalyst loaded GC) is as follows: An appropriate amount of the catalyst was dispersed ethylene glycol (99.5%, KMF GmbH, Germany) by ultrasonication for 40 minutes. The catalyst suspensions were protected from light by aluminium foil. The appropriate volume of the catalyst suspension was drop-cast onto the surface of the GC electrode by Eppendorf-Pipette yielding a catalyst loading of 1 mg cm<sup>-2</sup><sub>disc</sub> and then dried for 10 minutes at 190 °C in an oven. For fixing and confining the catalyst on the GC electrode surface, 20  $\mu$ l of Nafion solution (1.44 mg Nafion<sup>®</sup> in 1 ml Millipore-Water) was pipetted onto the cooled surface of the coated glassy carbon and dried again at 190 °C for 30 minutes. Nafion layer thickness was made sufficiently thin (less than 0.2  $\mu$ m as calculated from a covered electrode area of 0.196 cm<sup>2</sup> and apparent film density of 2.0 g cm<sup>-3</sup>) so that the film diffusion resistance becomes negligible [17] and thereby, avoiding further mathematical calculations and interference from Nafion resistance. After cooling the electrode, the distribution of the particles on the surface of GC was examined by an optical microscope and finally installed in the measuring set up.

## 2.3. Physical and electrochemical characterization

RRDE and CV measurements were performed in a three-electrode glass cell and using a rotator (Pine Research Instrumentation, Pennsylvania, USA) to which the working electrode was attached. The working electrode (WE) consisted of the modified GC disc of 5 mm diameter which was insulated by a layer of Teflon surrounded radially by a platinum ring electrode of 6.5 mm internal diameter and 7.5 mm outer diameter (Pine Research Instrumentation, Pennsylvania, USA). Prior to use, the ring electrode was polished with 0.05  $\mu$ m alumina slurry and then washed by Milli-Q water under sonication, the disc was inserted in, and then the ring-disc electrode was screwed into a PEEK shaft which was fed through a Teflon stopper to the cell. The counter electrode was a Pt sheet immersed in a glass tube filled with electrolyte and terminated with a glass frit in the cell. The reference electrode was a reversible hydrogen electrode in the base electrolyte (RHE) and was placed very close to the WE via a Luggin capillary. A bipotentiostat model AFCBP 1 (Pine Research Instrumentation, Pennsylvania, USA), which has a built-in function generator, and a LabVIEW software (National Instruments GmbH, Munich, Germany) were used. The electrolytes were continuously O<sub>2</sub>-saturated by purging with O<sub>2</sub> before the experiment start into the electrolyte for about 40 minutes and over the electrolyte during

the experimental run. All experiments were conducted at room temperature, 25  $\pm$  1 °.

The morphology of the catalyst was examined by SEM at the University of Ulm (Zeiss dual-beam NVISION 40 with an operating voltage of 5–30 kV). The composition and distribution of the mixed catalyst over the GC substrate were tested by EDX from the company AMETEK EDAX, type Genesis APEX2. The XRD measurements were carried out with a Bruker D8 Discover GADDS with monochromatized Cu K $\alpha$  radiation. Each diffraction pattern was measured in four frames with a step size of 23°, starting with  $\theta_1 = \theta_2 = 12^\circ$  (Bragg–Brentano condition). The exposure time for each frame was 180 s.

Differential electrochemical mass spectrometry (DEMS) was used to record the evolved O<sub>2</sub> simultaneously to the current in cyclic voltammetry [18]. A dual thin layer cell was used in which the electrolyte is under continuous flow of 15  $\mu$ l s<sup>-1</sup>. This type of cells achieves well-defined diffusion and convection of reactants. O<sub>2</sub> evolved at the electrode in the electrochemical compartment is transported to a second compartment where it diffuses through a porous Teflon<sup>®</sup> membrane (Gore Tex<sup>®</sup>, Germany) into the vacuum of a mass spectrometer (Balzer QMG-422) to be simultaneously and online detected. A GC electrode with 1 cm diameter and 1 mg cm<sup>-2</sup> catalyst loading were used here. The design of the cell is described in detail elsewhere [18,19]. It should be noted that the electrolyte resistance in this cell is much larger than that of the RRDE setup.

For the iR-correction of the RRDE data in the Tafel plots (Fig. 2 and 3), the solution resistance (R<sub>s</sub>) between the Luggin capillary and the working electrode surface was determined using electrochemical impedance spectroscopy. In our setup, R<sub>s</sub> of 49  $\Omega$  was determined in 0.1M LiOH solution.

For RRDE measurements, the potential at the disc was scanned with a scan rate of 5 or 10 mV s<sup>-1</sup> with a varying rotation speed of 540 – 2940 rpm, while the ring potential was kept constant at 1.2 V vs. RHE, where the transported peroxide species from the disc is oxidized to oxygen [20] with the ring current (I<sub>r</sub>) which is simultaneously recorded with the disc current (I<sub>d</sub>). The theoretical collection efficiency is N = 0.256. The peroxide species yield (H<sub>2</sub>O<sub>2</sub>) and the overall electron transfer number (n) were determined according to the following equations [21]:

$$\text{yield (H}_2\text{O}_2) = \frac{2I_r}{NI_d + I_r}$$

$$n = 4 \times \frac{I_d}{I_d + I_r/N}$$

where I<sub>r</sub> is the ring current, I<sub>d</sub> is the disc current and N is the collection efficiency of the ring. (The amount of H<sub>2</sub>O<sub>2</sub> may depend on the rotation speed, but since this amount is very small in our case, we did not analyse this dependence.) Koutecky-Levich plots (J<sup>-1</sup> vs.  $\omega^{-1/2}$ ) were constructed for further analysis of the catalyst activity on the basis of the Koutecky-Levich equation [22]:

$$\frac{1}{J} = \frac{1}{J_L} + \frac{1}{J_K} = \frac{1}{0.62nFC_0D_0^{2/3}\nu^{-1/6}\omega^{1/2}} + \frac{1}{nFkC_0}$$

where J is the measured current density, J<sub>L</sub> and J<sub>K</sub> are the diffusion- and kinetic limited current densities, respectively, F is Faraday constant, C<sub>0</sub> and D<sub>0</sub> are the saturated concentration and diffusion coefficient of oxygen, respectively,  $\nu$  is the kinematic viscosity of the solution,  $\omega$  is the rotation rate and k is the rate constant for ORR. Our electrode behaves as a thin film and flat electrode. The diffusion layer thickness was calculated in our solution and found to be  $\sim$ 17  $\mu$ m (at 960 rpm), which is larger than the 1  $\mu$ m Ag particles. In addition, Nafion film was made thin so that its effect on the kinetic parameters

was negligible. Tafel plots were constructed in which the kinetic current densities were calculated by mass-transport correction of the corresponding polarization curves as follows:

$$j_k = \frac{j_L \times j}{j_L - j}$$

where  $j_L$  is the diffusion limited current density and  $j$  is the measured current density.

### 3. Results and Discussion

#### 3.1. Electrochemical properties and performance

To probe the intrinsic catalytic activity of the catalysts and to decouple it from mass-transport, the RRDE was used. A thin layer of catalyst particles ( $1 \text{ mg cm}^{-2}$ ) was attached to a glassy carbon substrate by Nafion binder (see Experimental Section). Quasi-stationary current-voltage curves of the mixed Ag+Co<sub>3</sub>O<sub>4</sub> catalyst in alkaline electrolyte are shown in Fig. 1 together with those for the components Ag and Co<sub>3</sub>O<sub>4</sub>. For ORR, the positive-going scan corresponds to the true activity, whereas in negative-going scan oxides and adsorbed hydroxide blocking the surface are still being reduced. At high potentials, in the positive-going scan the current for the formation of silver oxides ( $\text{Ag}^I/\text{Ag}^{III}\text{O}_2$ , see Fig. 6 and [23]) and also further oxidation of the Co-Oxide is superimposed on the oxygen evolution current, and therefore the current in negative-going direction corresponds to the activity for O<sub>2</sub>-evolution. The Ag311 + Co<sub>3</sub>O<sub>4</sub> (10 wt%) bimetallic catalyst shows superior activity to ORR compared to its components: The onset of oxygen reduction is shifted by 70 mV in positive scan with respect to pure Ag, whereas the Co-spinel hardly reaches the diffusion limited current value.

This latter catalyst is superior to the Ag catalyst for oxygen evolution, but again the mixed catalysts (particularly that containing 20%, but also the one with 10% Co<sub>3</sub>O<sub>4</sub>) give an even larger oxygen evolution current density.

In order to determine the steady state activity, the potential was held at various values during positive and negative-going scans for at least 3 min. (see SI, Fig. S1). Steady state current values are included in Fig. 1, demonstrating that for the mixed catalyst the currents of the negative-going scan really reflect the oxygen reduction. For the pure Ag catalyst, however, steady state oxygen evolution currents are much lower than those in the negative-going sweep. Obviously, the latter currents are dominated by continuing Ag-oxide formation and activity to OER is negligible. On

the other hand, 20% mixed catalyst shows 60% increase in current at 1.8 V compared to pure Co<sub>3</sub>O<sub>4</sub>. Higher Co<sub>3</sub>O<sub>4</sub> content in the mixture revealed lower currents for OER. OER activity was also examined in Ar-saturated solution to clear that the enhancement in OER activity is not from the dissolved oxygen.

In order to find the optimum composition, the mass ratio of Ag311 to Co<sub>3</sub>O<sub>4</sub> in the mixture was varied (Fig. 2a). Ag311+Co<sub>3</sub>O<sub>4</sub> (10 wt%) outperformed other compositions in terms of onset potential defined by  $200 \mu\text{A cm}^{-2}$  ( $E_{200} \sim 0.91 \text{ V}$ ), half wave potential ( $E_{1/2} \sim 0.79 \text{ V}$ ). Whereas the spinel Co<sub>3</sub>O<sub>4</sub> showed very poor ORR activity ( $E_{200} \sim 0.62 \text{ V}$  and  $E_{1/2} \sim 0.42 \text{ V}$ ), Ag311 exhibited a good activity but its  $E_{200}$  ( $\sim 0.85 \text{ V}$ ) and  $E_{1/2}$  ( $\sim 0.72 \text{ V}$ ) still located more negative to the 10 wt% mixed catalyst. The Ag311 + Co<sub>3</sub>O<sub>4</sub> (5 wt%) has comparable activity to that of pure Ag311. By increasing the content of Co<sub>3</sub>O<sub>4</sub> nanoparticles in the mixed catalyst (> 20 wt%), the catalytic performance of the catalyst decreases but is still better than Co<sub>3</sub>O<sub>4</sub> alone (Fig. 2a). Thus, the 10 wt% Co<sub>3</sub>O<sub>4</sub> in the hybrid showed to be optimum for ORR, where the overpotential is ca. 70 mV lower than that in Ag311 and only about 80 mV higher than that of the commercial Pt/C catalyst. Because a thin film of catalyst had to be used for the RRDE experiments, resulting in an incomplete coverage of the inert GC substrate, the diffusion limited current for some studied catalysts is lower than the theoretical value ( $3.6 \text{ mA cm}^{-2}$  at 960 rpm for the 4-electron process). It also depends on the Co<sub>3</sub>O<sub>4</sub> content. The Pt/C catalyst has a higher diffusion limited current due to a surface roughness and C-particle thickness approaching the dimensions of the diffusion layer. For OER, the onset potential ( $E_{200}$ ) was ca. 1.55 V for Co<sub>3</sub>O<sub>4</sub>, ca. 1.54 V for 10 wt% catalyst and ca. 1.52 V for the 20 wt% catalyst.

Fig. 2b shows that the yield of peroxide species (% H<sub>2</sub>O<sub>2</sub>, as determined from the ring currents) for the 10 wt% Co<sub>3</sub>O<sub>4</sub> mixed catalyst is less than 1% over the measured potential range, which is comparable to that of 20% Pt/C. Catalysts of higher Co<sub>3</sub>O<sub>4</sub> content produced less than 8% H<sub>2</sub>O<sub>2</sub>. Therefore, ORR on the mixed catalyst obeys the 4-electron pathway. For the Ag311 catalyst, the large amount of H<sub>2</sub>O<sub>2</sub> is a result of the large particle size and non uniform distribution, leading to a considerable contribution of the GC substrate with the 2-electron pathway. K-L plots, shown in Fig. 2c, verify the behavior of this electrode as a thin-film. K-L plots showed parallel and linear lines at various potentials, indicating a first order reaction with respect to the dissolved oxygen concentration. Knowing the kinematic viscosity ( $0.01 \text{ cm}^2 \text{ s}^{-1}$ ),  $C_0$  ( $0.9 \text{ mol cm}^{-3}$ ),  $D_0$  ( $2.0 \times 10^{-5} \text{ cm}^2 \text{ s}^{-1}$ ) in 0.1 M LiOH solution [24] and the number of electrons  $n$  calculated from the ring current, the K-L slope for Ag311+Co<sub>3</sub>O<sub>4</sub> (10 wt%) catalyst is calculated and found to be  $2.9 \times 10^3 \text{ cm}^2 \text{ A}^{-1} \text{ s}^{1/2}$ , which is similar to that obtained from the measured K-L plots (average K-L slope is  $2.6 \times 10^3 \text{ cm}^2 \text{ A}^{-1} \text{ s}^{1/2}$ ).

The catalytic activity of the different catalysts towards ORR is more clearly compared in terms of mass-transport corrected Tafel plots ( $\log j_k$  vs  $E$ , Fig. 2d). These should also reveal differences in the mechanism between the catalysts. The kinetic current density ( $j_k$ ) is expressed as  $(j_L \times j / (j_L - j))$ , as described in the experimental section. Using the polarization curves of Fig. 2a, two Tafel slopes were observed for ORR on these mixed catalysts. The Tafel slope at lower overpotentials was about  $167 \text{ mV dec}^{-1}$  for pure Co<sub>3</sub>O<sub>4</sub>. For the mixed Ag311+Co<sub>3</sub>O<sub>4</sub> catalyst and pure Ag, the Tafel slope is  $\sim 75 \text{ mV dec}^{-1}$ , which is comparable to that of 20% Pt catalyst. At higher overpotentials (<0.8 V), Tafel slopes for Ag311 and mixed catalysts reached higher values ( $96\text{--}166 \text{ mV dec}^{-1}$ ), which is most probably due to the potential dependence of the adsorption isotherm of adsorbed oxygen species [25]. At low overpotential, the rate determining step (rds) could be a chemical step following the first electron transfer ( $\text{M-O}_2^- + \text{H}_2\text{O} \rightarrow \text{products}$ ) [26]. Similar Tafel slopes for ORR at low overpotential were reported in the literature for various catalysts [7,27,28].

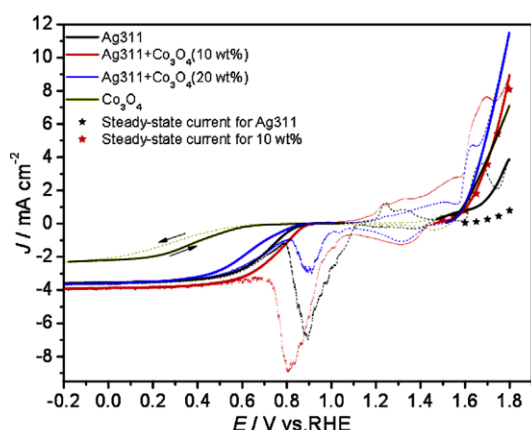
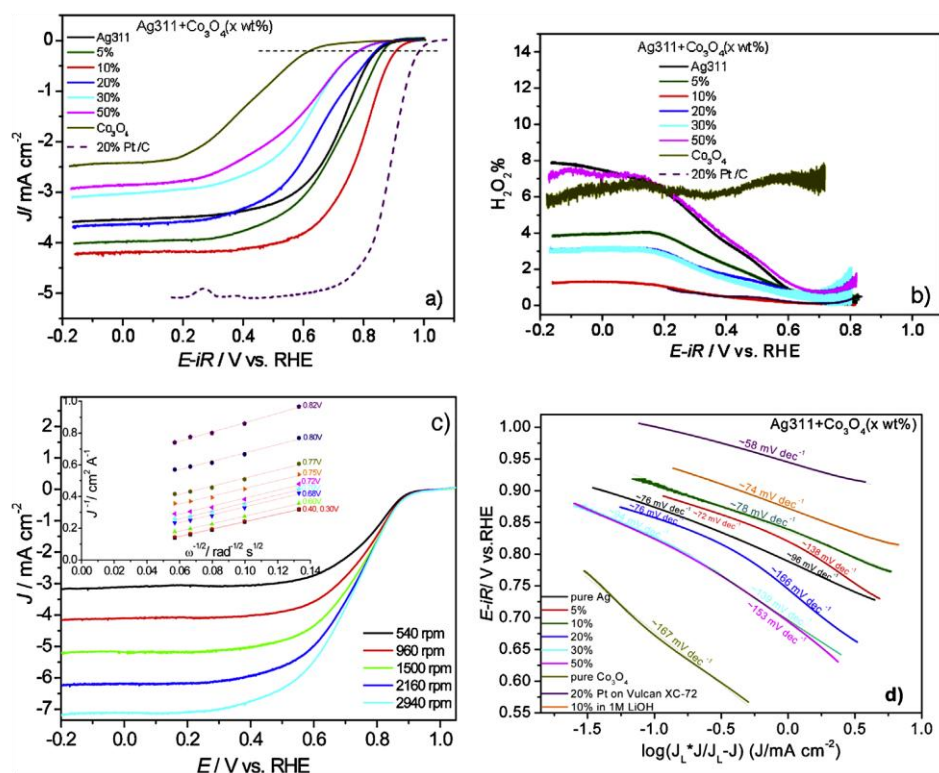
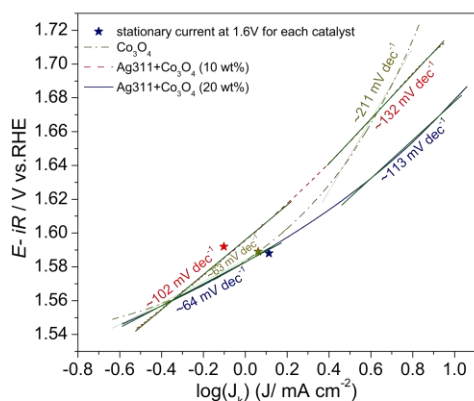


Fig. 1. Polarization curves of various catalysts ( $1 \text{ mg cm}^{-2}$ ) in O<sub>2</sub>-saturated 0.1M LiOH solution. The disc was scanned at  $5 \text{ mV s}^{-1}$  and a rotation speed of 960 rpm. The stationary values are recorded at 2160 rpm.



**Fig. 2.** a) iR-corrected RRDE voltammograms (positive-going scan) of ORR in  $O_2$ -saturated 0.1M LiOH solution at a scan rate of  $5 \text{ mV s}^{-1}$  and a rotation rate of 960 rpm. b)  $H_2O_2\%$  derived from the corresponding RRDE data in a). c) polarization curves of the mixed  $Ag_{311}+Co_3O_4$  (10 wt%) catalyst in  $O_2$ -saturated 0.1M LiOH solution with scan rate of  $10 \text{ mV s}^{-1}$  at different rotation rates in the positive-going direction. The inset of c) is the corresponding Koutecky-Levich (K-L) plots at different potentials. d) iR-corrected Tafel plots of ORR obtained by mass-transport correction of the corresponding data in a).

Tafel plots for OER are shown in Fig. 3. At low overpotentials ( $< 1.61 \text{ V}$ ), Tafel slopes were  $\sim 64 \text{ mV dec}^{-1}$  for  $Co_3O_4$  and the 20% mixed catalysts and  $\sim 102 \text{ mV dec}^{-1}$  for 10 wt%. The slope increased to more than  $110 \text{ mV dec}^{-1}$  at high overpotentials ( $> 1.62 \text{ V}$ ) for all. Similar results were reported at low overpotential for  $Co_3O_4$  and  $Co_3O_4/N$ -rmGO hybrid [11] and  $Ag-MnO_2$  [16]. This change of the Tafel slope most likely is caused by an increase of the coverage with adsorbed OH as the intermediate [29]. The rds could be the proton extraction of the hydroxide group [30]. The similarity



**Fig. 3.** iR-corrected Tafel plot for OER at the mixed and pure  $Co_3O_4$  catalysts obtained from the corresponding CV in Fig. 1. The stars in Fig. are the steady state current values at 2160 rpm and about 1.6V.

of the Tafel slopes between  $Co_3O_4$  and the mixed (20 wt%) catalysts signifies that there is no change in the mechanism due to the presence of Ag. Comparative study to the literature was made. Previous reports either lack the steady state data and stability tests [12], which are important specially for Ag-containing catalysts, or have a larger difference in onset potential between OER and ORR compared our catalyst. In detail, Mn oxide showed lower ORR activity ( $E_{200} \sim 0.82 \text{ V}$  and  $E_{1/2} \sim 0.72 \text{ V}$ ) and comparable OER activity but a time-consuming synthesis procedure was used [13]. A perovskite showed also bifunctionality with stability, although it reveals less ORR activity compared to our catalyst ( $> 100 \text{ mV}$  higher overpotential) [15]. A similar hybrid of Ag and  $MnO_2$  showed good activity but with larger potential gap between OER and ORR ( $E_{onset, OER} > 1.72 \text{ V}$ ) [16]. In addition, Pt/C catalyst is well known to be unstable for OER and has less durability.

### 3.2. DEMS measurements

Further insight into the catalytic activity of these catalysts for OER was obtained by online differential electrochemical mass spectrometry (DEMS) using a dual-thin layer flow-through cell [18]: DEMS allows for a separation of the rate of oxygen evolution from pseudo capacitive processes such as the oxidation of the catalyst. Typical cyclic voltammograms (CV) and mass spectrometric cyclic voltammograms (MSCV) of OER on various catalysts are shown in Fig. 4. Simultaneously to the faradaic current, the mass spectrometric signal for oxygen ( $m/z \ 32$ ) was recorded. The GC substrate has a negligible activity to OER. For the  $Co_3O_4$  catalyst, the ion current closely follows the current; the small hysteresis is due to the time constant of the flow-through cell of about 2 s. For

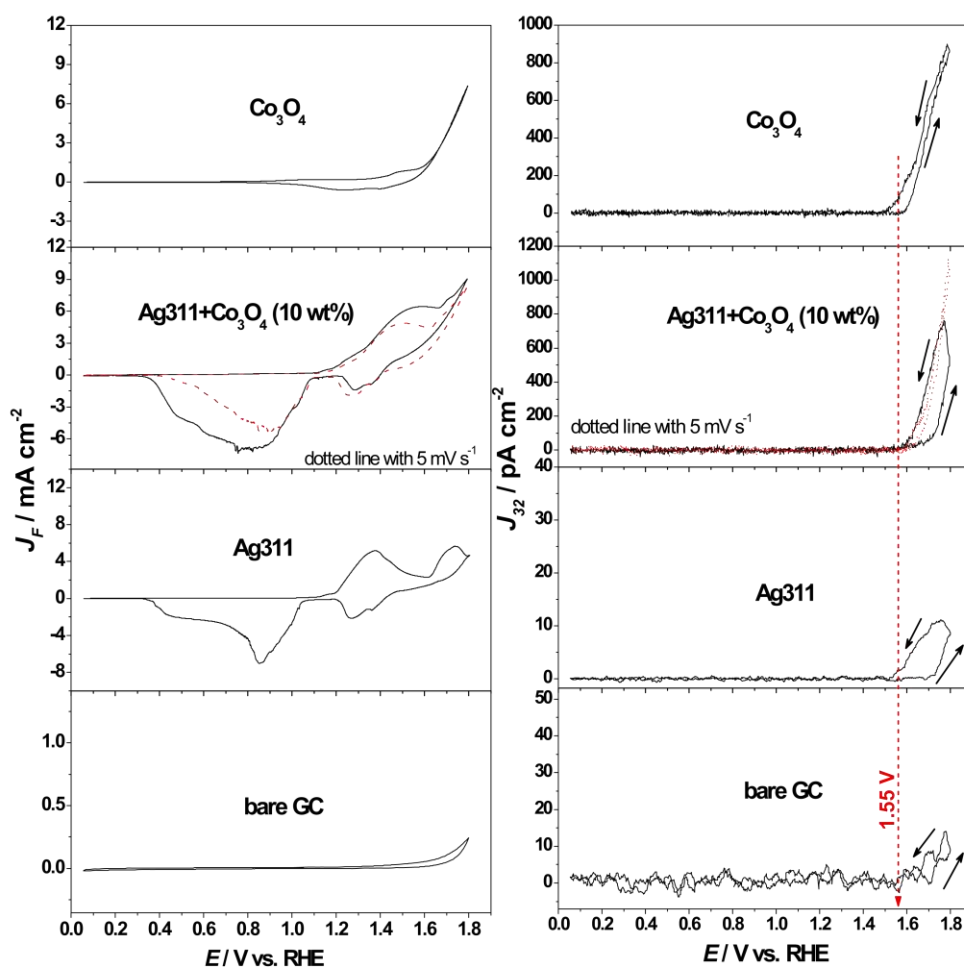


**Fig. 4.** Simultaneously recorded CVs (left panel) with MSCVs (right panel) for O<sub>2</sub> in Ar-saturated 1M LiOH solution in the dual-thin layer flow-through cell at mixed catalysts and Co<sub>3</sub>O<sub>4</sub> with 15  $\mu\text{L}\cdot\text{s}^{-1}$  flow rate and at Ag311 and GC with 5  $\mu\text{L}\cdot\text{s}^{-1}$  and 10  $\text{mV}\cdot\text{s}^{-1}$  scan rate for all.

pure Ag, oxygen evolution sets in only around 1.73 V, and continues during the negative-going scan but remains much lower than for the other catalysts, although the faradaic current is similar. The hysteresis in the ion current for the mixed catalyst is mainly caused by the oxide formation during the positive-going scan; at 5  $\text{mV}\cdot\text{s}^{-1}$  it is largely decreased. Therefore, as anticipated in the discussion of Fig. 1, the current observed corresponds to oxygen evolution in the negative sweep

### 3.3. Surface characterization

The morphology and distribution of the catalyst was examined by scanning electron microscope (SEM). Only an image without Nafion is shown (Fig. 5), because the presence of Nafion leads to somewhat blurred images. Co<sub>3</sub>O<sub>4</sub> with  $\sim 50$  nm particle size partially covers the 2  $\mu\text{m}$  large Ag particles and also part of the GC surface. Energy dispersive X-ray (EDX) spectra revealed that areas covered by the small particles are rich in Co indeed and areas of the large particles not covered by small particles are rich in Ag (Fig. 7). Obviously, a large part of the surface of the Ag particles is blocked by the Co<sub>3</sub>O<sub>4</sub> particles, further experiments, in which we determined the free Ag surface area by Pb-UPD; confirm that Ag surface area decreased by 88% with addition of 10% Co<sub>3</sub>O<sub>4</sub> [31].

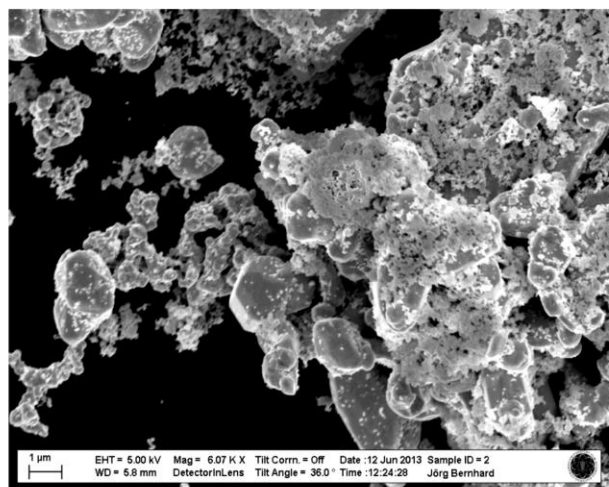


**Fig. 5.** SEM images of Ag311+Co<sub>3</sub>O<sub>4</sub> (10 wt %) hybrid on GC substrate without addition of Nafion binder.

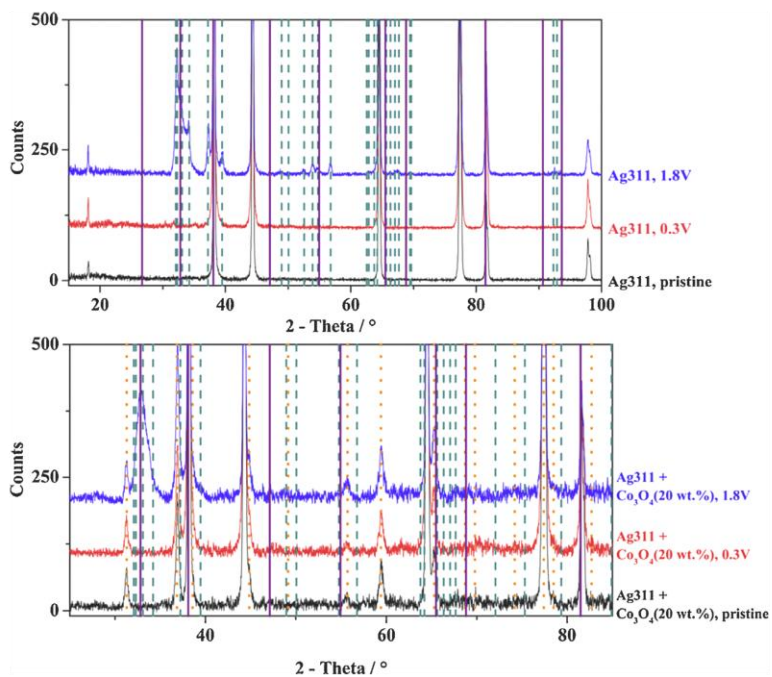


Fig. 6. XRD-measurements on pure Ag311 and Ag311 mixed with 20 wt.% Co<sub>3</sub>O<sub>4</sub> after reaching the potentials of 0.3 and 1.8V vs. RHE at gas diffusion electrodes in the CV's.

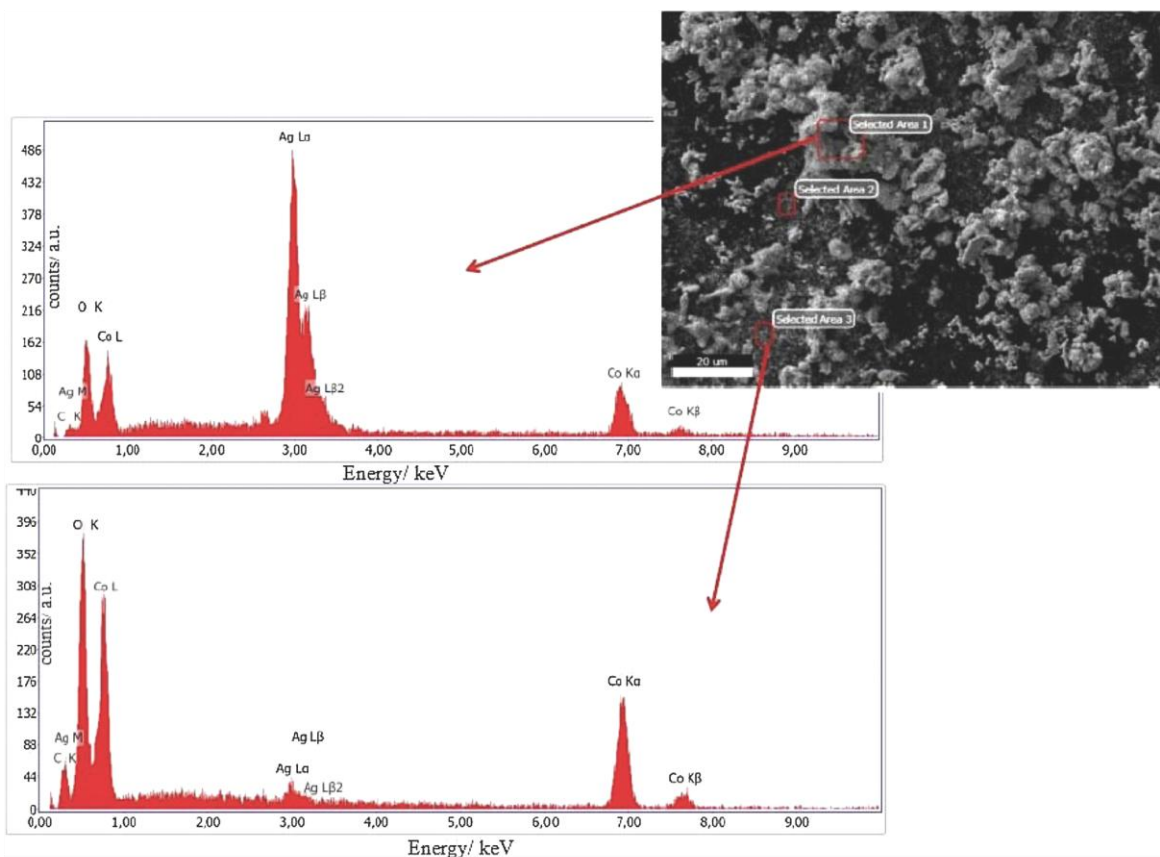


Fig. 7. EDX spectra of Ag311+Co3O4 (10 wt%) hybrid catalyst.gr7

Therefore, the increased activity of the mixed catalyst goes always with a decreased surface area of Ag.

To confirm the presence of Ag<sup>I</sup>Ag<sup>III</sup>O<sub>2</sub>, XRD-measurements at pure Ag311 and Ag311 + Co<sub>3</sub>O<sub>4</sub> (20 wt%) gas diffusion electrodes were carried out. The XRD spectra (Fig. 6) show the presence of an Ag<sup>I</sup>Ag<sup>III</sup>O<sub>2</sub> and Ag<sup>I</sup>O species at potential of 1.8 V vs. RHE. In pristine state and at 0.3 V only pure metallic silver was observed. The presence of mixed species Ag<sup>I</sup>Ag<sup>III</sup>O<sub>2</sub> and Ag<sup>I</sup>O at 1.8 V is due to the short dwell time at this potential. With a longer dwell time at 1.8 V Ag<sup>I</sup>O would be transformed to Ag<sup>I</sup>Ag<sup>III</sup>O<sub>2</sub> completely. Rietveld refinement was used (Topas 4.2 software, Bruker) to calculate the ratio Ag/Ag-oxides and the ratio of Ag<sup>I</sup>Ag<sup>III</sup>O<sub>2</sub>/Ag<sup>I</sup>O for each electrode at 1.8 V. The integrated area of Ag reflexes was calculated for both: the pristine electrode and the electrode at 1.8 V. For the Ag311 + Co<sub>3</sub>O<sub>4</sub> electrode, this area reduces in 21 % after testing at 1.8 V and for the pure Ag311 electrode, 15.5%. This diminution is due to the formation of the Ag oxides. Moreover, the ratio Ag<sup>I</sup>Ag<sup>III</sup>O<sub>2</sub>/Ag<sup>I</sup>O for the electrodes Ag311 + Co<sub>3</sub>O<sub>4</sub> and Ag311 was 3.5 and 5.4, respectively.

Further surface characterization was done using EDX. Two areas were selected at the surface and showed the elemental composition of the catalytic surface. In the upper EDX spectrum (Fig. 7), Ag particles were covered with Co<sub>3</sub>O<sub>4</sub> nanoparticles which lead to strong Ag and Co signals. But in the lower EDX spectrum, an area between the large Ag particles was selected and showed the dispersion of almost Co<sub>3</sub>O<sub>4</sub> in this region with minimal Ag particles.

We conclude that both OER and ORR are subject to a synergistic catalytic effect: Co<sub>3</sub>O<sub>4</sub> cocatalyses oxygen reduction at Ag, Ag cocatalyses water oxidation at Co<sub>3</sub>O<sub>4</sub>. More important for practical purposes is the fact that the formation of H<sub>2</sub>O<sub>2</sub> is negligible and that the catalyst is stable. In a parallel publication the use of these catalysts in gas diffusion electrodes is demonstrated [32].

What is the origin of the synergistic effect? The discussion is complicated by the fact that at potentials of OER, Ag is present as its oxide (Ag<sub>2</sub>O or Ag<sup>I</sup>Ag<sup>III</sup>O<sub>2</sub>), Fig. 6. This also excludes a simple explanation of the increased oxidation rate at Co<sub>3</sub>O<sub>4</sub> as being caused by an increase of conductivity due to the Ag content. In short, possible origins are the following (also cf. the discussion in [8] for ORR):

- 1) An agglomeration of the Ag particles might be prevented when they are covered by Co<sub>3</sub>O<sub>4</sub>.
- 2) The electronic structure of Ag might be changed in the neighbourhood of the Co<sub>3</sub>O<sub>4</sub> particles. Particularly for Co<sub>3</sub>O<sub>4</sub>, a possible effect of band bending has to be considered.
- 3) The two components may be active for two different reaction steps of the overall reaction. E.g., an intermediately formed oxygen species in the ORR reaction could diffuse to the Co<sub>3</sub>O<sub>4</sub> (as suggested by DFT calculations for Ag on CeO<sub>2</sub> [33]), where it is released as water. For OER, the reverse process involves oxidation of water at Co<sub>3</sub>O<sub>4</sub> and diffusion of an oxygen species to the Ag-oxide. Co<sub>3</sub>O<sub>4</sub> also catalyses the formation of silver oxides: its reduction peak is largest for the 10% Co<sub>3</sub>O<sub>4</sub> catalyst. This is confirmed by the XRD measurements (Fig. 6) which show that the amount of Ag oxides is increased for the mixed catalyst.
- 4) The O<sub>2</sub> molecule reacts (or is formed) directly at the interphase boundary line between Ag and Co<sub>3</sub>O<sub>4</sub> with a simultaneous binding to both surfaces.

#### 4. Conclusions

We believe that several of these factors contribute to the overall catalytic activity. In particular the different size of the Ag and Co<sub>3</sub>O<sub>4</sub> particles may be important for good distribution and an intimate contact between the components. Moreover, repetitive cycling revealed that the mixed catalysts are stable for at least 30 measured cycles. In conclusion, we described a non-precious bifunctional hybrid catalyst with a potential difference between ORR and OER of

0.8 V (at a current density of 1 mA cm<sup>-2</sup>). In comparison to the Ag-MnO<sub>2</sub> catalyst described in literature [16], which seems to be the best catalyst reported to our knowledge, this is less by ~0.1 V, which however may in part be due to the 10-fold lower loading used there. In addition, the Ag-MnO<sub>2</sub> reported in [16] catalyst shows electron transfer numbers in the range of 3.7 which still indicates significant H<sub>2</sub>O<sub>2</sub> formation. A detailed comparison is difficult because of different loadings (ours is 10 times higher) and different particle sizes and thus active surface areas (ours is much smaller due to the 1 μm Ag particles as compared to 10 nm Ag particles used in [16]). However, this also shows that further improvements by optimizing the particle size should be possible.

#### Acknowledgements

This work was supported by the BMBF (LuLi, Fkz: 03X4624A). We thank S.K. Eswara and U. Kaiser for performing the SEM measurements. H.M.A.Amin acknowledges the support by MoHESR (Egypt) and DAAD (GERLS scholarship).

#### Appendix A. Supplementary data

Supplementary data associated with this article can be found, in the online version, at <http://dx.doi.org/10.1016/j.electacta.2014.11.017>.

#### References

- [1] Y.-C. Lu, H.A. Gasteiger, E. Crumlin, R. McGuire Jr., Y. Shao-Horn, Electrocatalytic Activity Studies of Select Metal Surfaces and Implications in Li-Air Batteries, *J. Electrochem. Soc.* 157 (2010) A1016.
- [2] K.M. Abraham, Z. Jiang, A Polymer Electrolyte-Based Rechargeable Lithium/Oxygen Battery, *J. Electrochem. Soc.* 143 (1996) 1.
- [3] J.-S. Lee, S. Tai Kim, R. Cao, N.-S. Choi, M. Liu, K.T. Lee, J. Cho, Metal-Air Batteries with High Energy Density: Li-Air versus Zn-Air, *Advanced Energy Materials* 1 (2011) 34.
- [4] B.B. Bliznac, P.N. Ross, N.M. Markovic, Oxygen reduction on silver low-index single-crystal surfaces in alkaline solution: Rotating ring Disk(Ag(hkl)) studies, *J. Phys. Chem. B* 110 (2006) 4735.
- [5] J.-J. Han, N. Li, T.-Y. Zhang, Ag/C nanoparticles as a cathode catalyst for a zinc-air battery with a flowing alkaline electrolyte, *J. Power Sources* 193 (2009) 885.
- [6] M. Innocenti, G. Zangari, C. Zaffaroni, I. Bencistà, L. Becucci, A. Lavacchi, F. Di Benedetto, S. Bellandi, F. Vizza, M.L. Foresti, Selective electrodesorption based atomic layer deposition (SEBALD) modifications of silver surfaces for enhancing oxygen reduction reaction activity, *J. Power Sources* 241 (2013) 80.
- [7] F.H.B. Lima, J.F.R. de Castro, E.A. Ticianelli, Silver-cobalt bimetallic particles for oxygen reduction in alkaline media, *J. Power Sources* 161 (2006) 806.
- [8] Y. Wang, X. Lu, Y. Liu, Y. Deng, Silver supported on Co<sub>3</sub>O<sub>4</sub> modified carbon as electrocatalyst for oxygen reduction reaction in alkaline media, *Electrochem. Commun.* 31 (2013) 108.
- [9] S. Trasatti, *Electrodes of conductive metallic oxides*, Elsevier Scientific Pub. Co., Amsterdam, 1980.
- [10] Y. Zhan, C. Xu, M. Lu, Z. Liu, J.Y. Lee, Mn and Co co-substituted Fe<sub>3</sub>O<sub>4</sub> nanoparticles on nitrogen-doped reduced graphene oxide for oxygen electrocatalysis in alkaline solution, *Journal of Materials Chemistry A* 2 (2014) 16217.
- [11] Y. Liang, Y. Li, H. Wang, J. Zhou, J. Wang, T. Regier, H. Dai, Co<sub>3</sub>O<sub>4</sub> nanocrystals on graphene as a synergistic catalyst for oxygen reduction reaction, *Nature Mater.* 10 (2011) 780.
- [12] X. Wu, K. Scott, A non-precious metal bifunctional oxygen electrode for alkaline anion exchange membrane cells, *J. Power Sources* 206 (0) (2012) 14–19.
- [13] Y. Gorlin, T.F. Jaramillo, A Bifunctional Nonprecious Metal Catalyst for Oxygen Reduction and Water Oxidation, *J. Am. Chem. Soc.* 132 (2010) 13612.
- [14] W. Yang, J. Salim, S. Li, C. Sun, L. Chen, J.B. Goodenough, Y. Kim, Perovskite Sr<sub>0.95</sub>Ce<sub>0.05</sub>CoO<sub>3-δ</sub> loaded with copper nanoparticles as a bifunctional catalyst for lithium-air batteries, *J. Mater. Chem.* 22 (2012) 18902.
- [15] C. Jin, Z. Yang, X. Cao, F. Lu, R. Yang, A novel bifunctional catalyst of Ba<sub>0.9</sub>Co<sub>0.5</sub>Fe<sub>0.4</sub>Nb<sub>0.1</sub>O<sub>3-δ</sub> perovskite for lithium-air battery, *Int. J. Hydrogen Energy* 39 (2014) 2526.
- [16] F.W.T. Goh, Z. Liu, X. Ge, Y. Zong, G. Du, T.S.A. Hor, Ag nanoparticle-modified MnO<sub>2</sub> nanorods catalyst for use as an air electrode in zinc@air battery, *Electrochim. Acta* 114 (0) (2013) 598–604.
- [17] T.J. Schmidt, H.A. Gasteiger, G.D. Stab, P.M. Urban, D.M. Kolb, R.J. Behm, Characterization of high-surface area electrocatalysts using a rotating disk electrode configuration, *J. Electrochem. Soc.* 145 (1998) 2354.

- [18] H. Baltruschat, Differential Electrochemical Mass Spectrometry, *J. Am. Soc. Mass. Spectrom.* 15 (2004) 1693.
- [19] Z. Jusys, H. Massong, H. Baltruschat, A New Approach for Simultaneous DEMS and EQCM: Electro-oxidation of Adsorbed CO on Pt and Pt-Ru, *J. Electrochem. Soc.* 146 (1999) 1093.
- [20] M.R. Miah, T. Ohsaka, Cathodic Detection of H<sub>2</sub>O<sub>2</sub> Using Iodide-Modified Gold Electrode in Alkaline Media, *Anal. Chem.* 78 (2006) 1200.
- [21] U.A. Paulus, T.J. Schmidt, H.A. Gasteiger, R.J. Behm, Oxygen reduction on a high-surface area Pt/Vulcan carbon catalyst: a thin-film rotating ring-disk electrode study, *J. Electroanal. Chem.* 495 (2001) 134.
- [22] A.J. Bard, L.R. Faulkner, *Electrochemical Methods: Fundamentals and Applications*, John Wiley & Sons Inc.-New York, Weinheim, 2001.
- [23] D. Tudela, Silver(II) Oxide or Silver(I,III) Oxide? *J. Chem. Educ.* 85 (2008) 863.
- [24] M. Khodayari, H. Baltruschat, Determination of solubility and diffusion coefficient of alkaline and aprotic electrolytes using mass spectrometry, To be published.
- [25] N. Markovic, H. Gasteiger, Kinetics of oxygen reduction on Pt(hkl) electrodes: Implications for the crystallite size effect with supported Pt electrocatalysts, *J. Electrochem. Soc.* 144 (1997) 1591.
- [26] D. Šepa, M. Vojnovic, A. Damjanovic, Oxygen reduction at silver electrodes in alkaline solutions, *Electrochim. Acta* 15 (1970) 1355.
- [27] E. Rios, J. Gautier, G. Poillerat, P. Chartier, Mixed valency spinel oxides of transition metals and electrocatalysis: case of the Mn<sub>x</sub>Co<sub>3-x</sub>O<sub>4</sub> system, *Electrochimica Acta* 44 (1998) 1491.
- [28] S. Zhuang, K. Huang, C. Huang, H. Huang, S. Liu, M. Fan, Preparation of silver-modified La<sub>0.6</sub>Ca<sub>0.4</sub>CoO<sub>3</sub> binary electrocatalyst for bi-functional air electrodes in alkaline medium, *J. Power Sources* 196 (2011) 4019.
- [29] K.L. Hsueh, D.T. Chin, S. Srinivasan, Electrode-Kinetics of Oxygen Reduction – a Theoretical and Experimental-Analysis of the Rotating Ring-Disc Electrode Method, *J. Electroanal. Chem.* 153 (1983) 79.
- [30] J. Suntivich, K.J. May, H.A. Gasteiger, J.B. Goodenough, Y. Shao-Horn, A Perovskite Oxide Optimized for Oxygen Evolution Catalysis from Molecular Orbital Principles, *Science* 334 (2011) 1383.
- [31] H.M.A. Amin, H. Baltruschat, Real surface area determination for metal oxide catalysts using isotope labelling and Pb-UPD, in preparation.
- [32] D. Wittmaier, N. Wagner, K.A. Friedrich, H.M.A. Amin, H. Baltruschat, Modified carbon-free silver electrodes for the use as cathodes in lithium-air batteries with an aqueous alkaline electrolyte, *J. Power Sources* 265 (2014) 299.
- [33] J.-H. Wang, M. Liu, M.C. Lin, Oxygen reduction reactions in the SOFC cathode of Ag/CeO<sub>2</sub>, *Solid State Ionics* 177 (2006) 939.

## Supporting Information

A Highly Efficient Bifunctional Catalyst for Alkaline Air-Electrodes Based on a Ag and Co<sub>3</sub>O<sub>4</sub> Hybrid: RRDE and Online DEMS InsightsHatem M.A. Amin<sup>a,b</sup>, Helmut Baltruschata,<sup>\*,1</sup> Dennis Wittmaier<sup>c</sup>, K. Andreas Friedrich<sup>c,1</sup>

## Chronoamperometric response

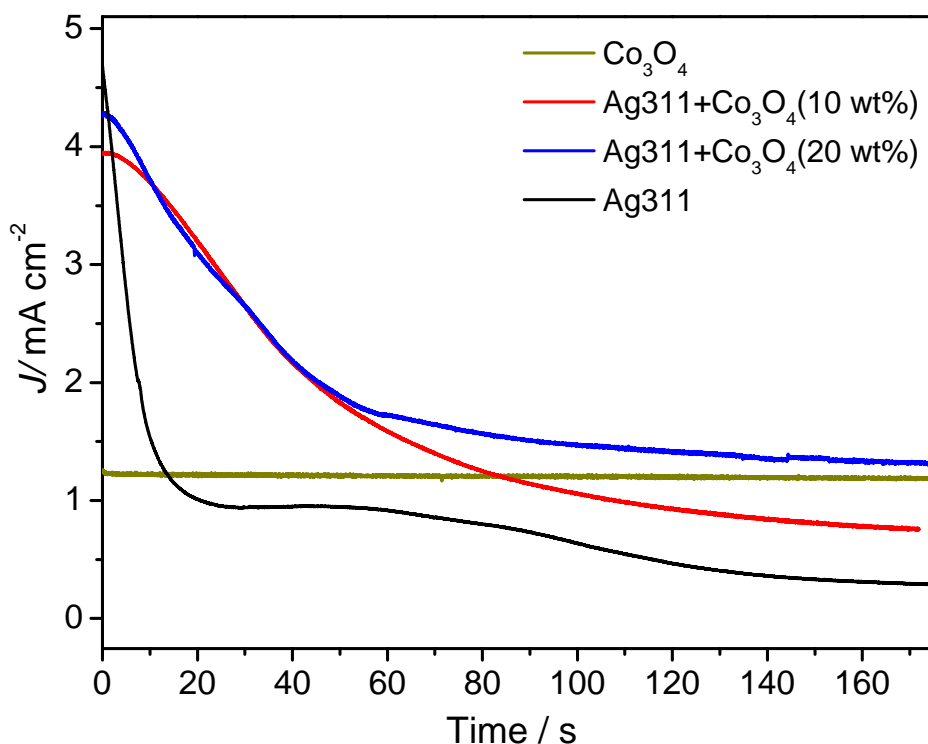


**Fig. S1.** Chronoamperometric response of the different catalyst electrodes kept at 1.6V (in the positive-going scan) in O<sub>2</sub>-saturated 0.1M LiOH solution with a rotation rate of 2160 rpm. Ag catalyst was kept at 1.7V.

The short-term stability of the pure and mixed bimetallic catalysts was tested at constant potential of ca. 1.6 V in O<sub>2</sub>-saturated 0.1M LiOH solution, as shown in Fig. S1. For pure Co<sub>3</sub>O<sub>4</sub>, there is no change in current over the measured time. Ag-containing catalysts showed higher currents in the first minute which is due to continuing Ag-oxide formation, then the OER current starts after nearly one minute. For the 10% and 20% mixed catalysts, the current did not attenuate much after 1 minute ( $<0.2 \mu\text{A s}^{-1}$ ). In contrast, Ag311 catalysts showed large decay in the steady state current values in the first few minutes. 20% Pt showed exponential current loss of about 70% in the first 2 minutes, not shown here. Moreover, all these catalysts exhibited good stability for ORR for at least the measured 3 minutes, not shown here. This suggests that our mixed catalyst has comparable activity and superior stability to the commercial Pt catalyst. These observations suggest that the mixed Ag311+Co<sub>3</sub>O<sub>4</sub> (10 and 20 wt%) catalyst serves as a good candidate for rechargeable metal-air batteries. Though Pt catalyst showed high catalytic activity to ORR, our bimetallic hybrid with low cost and facile preparation procedure will be a valuable catalyst for O<sub>2</sub>-cathodes in alkaline media.

## 5. A synergistic bifunctional catalyst for oxygen reduction/evolution based on a carbon-free Ag and Co<sub>3</sub>O<sub>4</sub> hybrid: Catalyst characterization

### Abstract

A key challenge for electrochemical energy devices is the development of a bifunctional cost-effective catalyst for both oxygen evolution (OER) and reduction (ORR) reactions. Here, the carbon-free hybrid based on a combination of Ag and Co<sub>3</sub>O<sub>4</sub> spinel is further characterized. This optimized composite exhibited a good bifunctional activity in alkaline media. Rotating ring-disc electrode (RRDE) measurements revealed better activity for the mixed catalyst, and a negligible peroxide species formation and thus a 4-electron pathway of ORR. This makes it not far from the most active Pt/C. For OER, the activity of the bimetallic catalyst is 1.5-fold and at least 4-fold compared to Co<sub>3</sub>O<sub>4</sub> and Ag, respectively. This catalyst showed higher activity than Pt/C for OER. The potential difference between OER and ORR (i.e. the sum of the overpotentials at 1 mA cm<sup>-2</sup>) is ca. 0.85 V, which is comparable to noble metal based catalysts. To better understand the origin of this synergism, surface analyses were performed. XPS analysis showed that only after oxidation of the mixed catalyst, Co<sub>3</sub>O<sub>4</sub> is reduced to Co(OH)<sub>2</sub> at potentials of the ORR, probably due to the presence of Ag<sup>+</sup>. This redox switching, which is not observed for pure Co<sub>3</sub>O<sub>4</sub>, is a probable explanation for the increased catalytic activity. The morphology and the electrochemically active surface area (ECA) of Ag on the surface are examined by electron microscopy and lead-underpotential deposition, respectively. The combination of low-cost and high performance endows this catalyst as a promising candidate for fuel cells and Li-O<sub>2</sub> batteries, and this synergistic effect can be extended to other non-noble metals.

### 5.1. Introduction

Today's energy demand has stimulated scientists to focus on research for developing feasible energy conversion/storage systems. Among the numerous electrochemical devices, regenerative fuel cells and rechargeable Li-batteries are considered the most promising systems for future applications, particularly for automobile industry. Rechargeable Li-O<sub>2</sub> batteries would have less weight, less cost and higher theoretical energy density than the state-of-the art Li-ion batteries.[1] The use of an oxygen electrode in an aqueous electrolyte should be possible if the Li electrode is protected by a Li<sup>+</sup>-ion conducting membrane.[2, 3] One of the main obstacles that face the commercialization of such rechargeable batteries and limit the applications of regenerative fuel cells is the sluggish kinetics of OER and ORR, which leads to higher charge-discharge overpotential and lower efficiency.[4] Therefore, an efficient bifunctional catalyst is indispensable to improve the activity, reversibility and durability of the O<sub>2</sub>-electrode and reduce the overpotential and total cost.

Pt-based materials are the most conventional catalysts for ORR in alkaline and acidic media.[5-8] Also, other noble metals such as Ru-based catalysts were investigated and found to be ORR efficient and methanol tolerant catalysts (e.g. RuSe).[9, 10] However, the high cost, sensitivity to contaminants and deficiency in resources of Pt limit its large-scale application. Numerous intensive efforts have been reported to develop cost-effective catalysts. One approach, mostly done in acidic media, is reducing the Pt loading by alloying with

transition metals like Co[11] or Ni,[12] or by control of the size of Pt,[13] or by using the core-shell architecture as in the case of Ni@Pt.[14] An effective approach was to combine noble metals with transition metal oxides: a synergistic bifunctional activity has recently been reported for a mixture of Pt/C and perovskite/C with outstanding electrocatalytic activity.[15] However, this composite is still not cost-effective for large scale applications. Another strategy is the use of noble metal-free materials based on transition metal oxides or perovskites.[16-19] Some studies showed the bifunctionality of metal oxides and perovskites and their combination with non precious metals (e.g. Ag).[20-23] Cobaltoxide-based electrodes were reported as bifunctional catalysts and showed good activity.[24-26] However, they are typically loaded on a carbon support,[25, 26] which suffers from corrosion. Most recently, it was shown that the state-of-the-art Pt/C exhibited severe degradation in alkaline media (3 times worse than in acidic)[27] and the cycle life of carbon-based electrodes was limited by the corrosion/oxidation of carbon rather than the catalyst under anodic conditions.[28] Thus, one of the milestones in air electrodes is to develop an efficient carbon-free bifunctional catalyst for both ORR and OER with high stability. Cobalt oxide has high activity and stability towards OER but is less active for ORR.[29] On the other hand, silver is a promising catalyst to replace Pt due to its relatively low cost, high crustal abundance, well-known kinetics and high ORR activity.[30-32] However, it is less active and not stable for OER.

The idea followed here is to combine the benefits of a cost-effective highly conductive silver catalyst (active for ORR) with those of Co<sub>3</sub>O<sub>4</sub> (highly active for OER) in a mixed catalyst. Ag is also used to substitute the commonly used carbon particles support. Few previous reports used a similar procedure with carbon-free catalysts, but they either showed higher overpotential for OER/ORR or absence of steady-state data and durability tests.[33-35] One report demonstrated the design of a Ag-Co surface alloy but only showed its ORR application.[36] We recently reported that a good bifunctional catalyst is obtained by an appropriate mixing of Co<sub>3</sub>O<sub>4</sub> and Ag particles. Although this is not a surface alloy, the resulting catalyst even shows a synergistic effect of the two components: for both OER and ORR, it is better than its constituents, i.e. Co<sub>3</sub>O<sub>4</sub> or Ag.[37] An optimization of the ratio of the two components was also performed in our previous reports.[37, 38] The optimized composite was tested in different alkaline media and as well was used in a gas diffusion electrode and analyzed by XRD.[38, 39] It is the aim of this paper to further characterize this bifunctional catalyst and to obtain a better understanding of the origin of the synergistic effect.

One of the fundamental issues in catalyst characterization and comparison of activities is the determination of electrochemical active surface area (ECA) of the catalyst, since there is no straightforward and standard method for all non-platinum catalysts. Pb-under potential deposition (Pb-UPD) has been applied for Ag-based catalysts.[40-42] Therefore, we will use this method here for ECA estimation for Ag in the mixed catalyst in LiOH media. Moreover, the morphology is also examined with electron microscopy. Different catalyst loadings have also been tested, and their activities towards ORR/OER are compared. To monitor the intrinsic catalytic activity of the catalysts, and decouple it from the mass-transport loss, RRDE technique is used. By RRDE technique, stationary measurements under a controlled mass-transport of the electrochemically active species (oxygen) in the electrolyte were

conducted. In addition, the effect of catalyst loading is investigated. In order to understand changes in surface chemistry under different reaction conditions, the electrochemical features of the catalyst are identified using CV, and simultaneously the surface oxidation states of the catalyst are probed using XPS. Thereby, an elucidation of the (possible routes of the) synergistic interaction between Ag and  $\text{Co}_3\text{O}_4$  is achieved by XPS analysis. The catalytic activity of this bimetallic mixture, and its stability suggest one of the most non-precious and highly efficient carbon-free catalysts in alkaline media to date.

## 5.2. Experimental Section

### 5.2.1. Electrode preparation

Ag311 microparticles (Ferro GmbH) and spinel  $\text{Co}_3\text{O}_4$  nanoparticles (Aldrich) were used as components of our mixed catalyst. Ag311 and  $\text{Co}_3\text{O}_4$  powders were used for preparation as provided. Chemicals used are listed in the supporting information with the manufacturer data. The bimetallic catalyst was loaded on a glassy carbon substrate. GC electrodes ( $0.196 \text{ cm}^2$ ) were polished to a mirror finish, with the help of  $0.05 \mu\text{m}$  alumina slurry on a polishing cloth (Microcloth PSA 2, Buehler). Afterwards, the GC electrodes were cleaned from the suspension residues and adhering impurities with acetone (99.5%, Sigma-Aldrich) and Milli-Q water. Finally, the electrodes were cleaned with Milli-Q water in an ultrasonic bath (VWR<sup>®</sup>, Germany) for 5 minutes and then dried with KIMTECH wipes and coated with the respective catalyst suspension. The procedure for preparing the modified GC electrode was mentioned in our previous paper.[37] Briefly, the catalyst suspension was prepared by dispersing an appropriate amount of the catalyst powder ( $\text{Co}_3\text{O}_4$  or Ag311 used as provided) in ethylene glycol (EG) using ultrasonic path for 40 minutes to get the required loading ( $10 \text{ mg powder in } 5 \text{ ml EG} = 200 \mu\text{g cm}^{-2}$ ). For the mixed catalyst, both powder components were mixed together in ethylene glycol where 10 wt%  $\text{Co}_3\text{O}_4$  is added. Then  $20 \mu\text{l}$  of the catalyst suspension was drop-cast onto the surface of the GC electrode by Eppendorf-Pipette yielding the required loading ( $200 \mu\text{g cm}^{-2}$ ), and then dried for 10 minutes at  $190 \text{ }^\circ\text{C}$  in an oven. This addition was repeated five times to get the  $1 \text{ mg cm}^{-2}$  loading. It can also be done in one step by using  $10 \text{ mg catalyst in } 1 \text{ ml EG}$ , but we used this to get well mixing and to be able to apply also lower loadings.

The loading with the catalyst was chosen such that the thickness of the catalyst does not exceed one layer of the Ag-particles. Using ball model,  $1 \text{ mg cm}^{-2}$  of  $\text{Co}_3\text{O}_4$  (50 nm) would correspond to about 50 monolayers of  $\text{Co}_3\text{O}_4$  particles, and considering a thickness of  $\sim 0.2 \text{ nm}$  for monolayer, one could get  $\sim 10 \text{ nm}$  thickness. In addition, we have examined different loadings by an optical microscope, and found that with lower loadings the surface of GC is not good covered. Thus, we chose to work with  $1 \text{ mg cm}^{-2}$  loading. The loading effect is explained in the results part. Nafion<sup>®</sup> solution ( $1.44 \text{ mg Nafion in } 1 \text{ ml water}$ ) was used as a binder for fixing the catalyst on the GC. A rough porous well dispersed film was obtained with Nafion binder. Nafion layer thickness ( $20 \mu\text{l}$  used) was made sufficiently thin (less than  $0.2 \mu\text{m}$  as calculated from a covered electrode area of  $0.196 \text{ cm}^2$  and apparent film density of  $2.0 \text{ g cm}^{-3}$ ) so that the film diffusion resistance becomes negligible.[43] The electrode was then dried at  $190 \text{ }^\circ\text{C}$ . After cooling the electrode, the distribution of the particles on the surface of GC was examined by an optical microscope and finally installed in the measuring set up.

### 5.2.2. Electrochemical characterization

For RRDE and CV measurements, a setup consisting of a Pine bipotentiostat, rotor (Pine Research Instrumentation, Pennsylvania, USA) and three-electrode glass cell was used. The working electrode (WE) consisted of the modified GC disc (5 mm diameter surrounded radially by a platinum ring electrode of 6.5 mm internal diameter and 7.5 mm outer diameter), which was mounted to the RRDE Teflon Tip. Prior to use, the ring electrode was polished with 0.05 μm alumina slurry and then washed by Milli-Q water under sonication. The disc was inserted in, and afterwards the ring-disc electrode was screwed into a PEEK shaft which was fed through a Teflon stopper to the cell. The counter electrode was a Pt sheet immersed in a glass tube connected to the cell via a glass frit. The reference electrode was a reversible hydrogen electrode in the base electrolyte (RHE) and was placed very close to the WE via a Luggin capillary. A bipotentiostat (model AFCBP 1, Pine Research Instrumentation, Pennsylvania, USA), which has a built-in function generator, and a LabVIEW software (National Instruments GmbH, Munich, Germany) were used. The lower cycling potential limit was chosen -0.2 V vs. RHE to reduce any Ag species in the catalyst. The ring potential was kept constant at 1.2 V vs. RHE. The electrolytes were continuously purged with O<sub>2</sub> or Ar before and during the measurements. All experiments were conducted at room temperature, 25 ± 1°. Pb-UPD experiments were carried out in a separate three-electrode glass cell to avoid any Pb contaminations that might affect the activity. Pb-UPD was conducted in 0.1 M LiOH containing 125 μM Pb(NO<sub>3</sub>)<sub>2</sub> and holding the potential at 0.24 V for 180 s, and sweeping to 0.7 V at 100 mV s<sup>-1</sup>. The anodic stripping voltammograms were then integrated to estimate the surface area. Details of RRDE calculations are given in the supporting information.

### 5.2.3. Ex-situ and in-situ catalyst characterization

The morphology of the catalyst was examined by SEM (Zeiss dual-beam NVISION 40 with an operating voltage of 5-30 kV) at the University of Ulm by S. Eswara. The EDX data was obtained for the mixed catalyst after cycling using AMETEK EDAX, type Genesis APEX2. XPS experiments were done by C. Bondue (Uni. Bonn). XPS spectra were collected in the main chamber of a UVH-system with an attached Omicron EA125 hemispheric electron energy analyzer and an X-ray tube with a magnesium anode. Schematic illustration of the electrochemical-XPS instrument is shown in Fig. S1. After the electrochemical experiment in the ante-chamber, the electrolyte was replaced with 10<sup>-4</sup> M LiOH solution. The electrode was dipped into this solution under potential control for several times in order to remove excess amounts of conducting salt, that would cover the electrode, after the solvent was evaporated under UHV conditions.[44] The manipulator facilitates positioning of the working electrode during electrochemical measurements in the Ante-chamber and the XPS in the main chamber (see details in the supporting information). Due to stepper motors at the manipulator, it was possible to approach the identical position in each experiment.

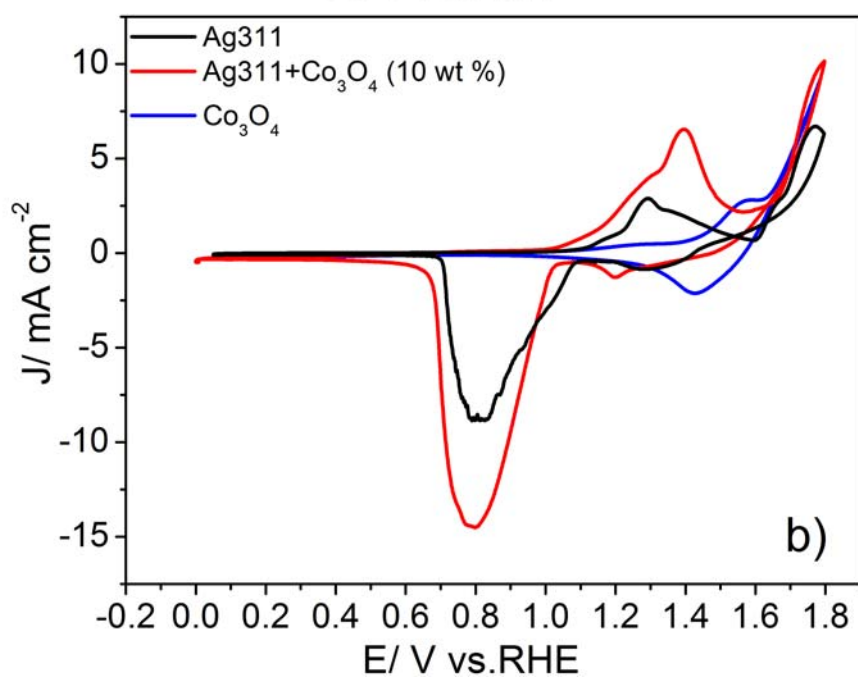
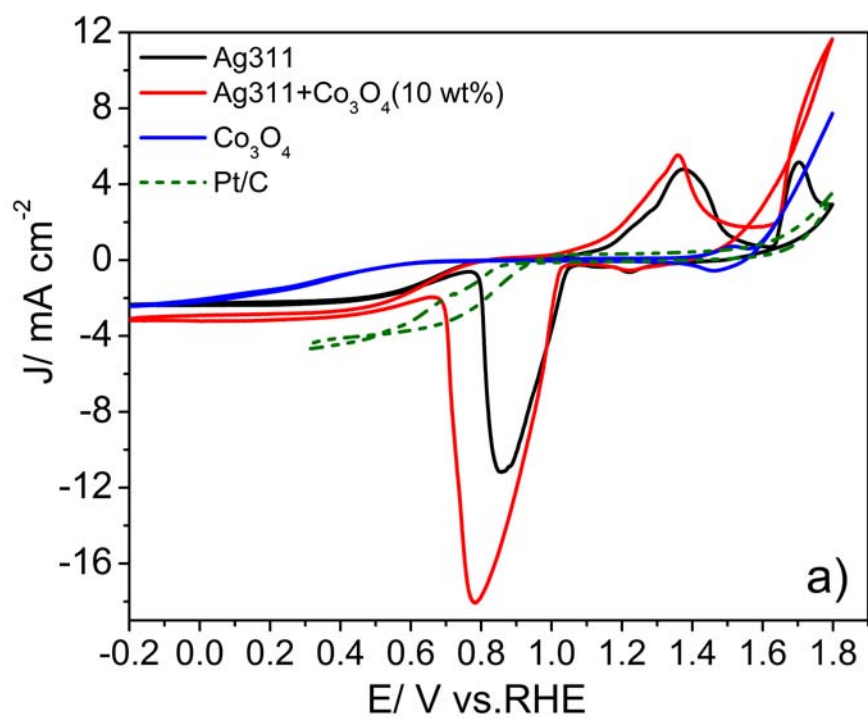
## 5.3. Results

### 5.3.1. Electrochemical performance of the catalyst

The catalytic activity of the mixed Ag<sub>311</sub>+Co<sub>3</sub>O<sub>4</sub> catalyst for ORR was characterized by cyclic voltammetry (CV) in O<sub>2</sub>-saturated 0.1 M LiOH solution and compared with its components (the same mass loading of 1 mg cm<sup>-2</sup> for all catalysts was used) using a RRDE at a rotation rate of 960 rpm and a scan rate of 10 mV s<sup>-1</sup>, see Fig. 1a. Diffusion limited currents

should theoretically coincide for the various catalysts (theoretically  $3.6 \text{ mA cm}^{-2}$  at 960 rpm for 4e-process), practically; they do not because of the low loading, parts of the electrode remain uncovered by catalyst. The redox peaks in the polarization curves are due to the different oxidation and reduction states of Ag and Co and their oxides, and also seen in Ar-saturated electrolyte, Fig. 1b; Ag oxidation and reduction is a reversible process. Although the peak at ca. 1.3 V in Fig. 1b is not identical in intensity to that in Fig. 1a, it is always higher in presence of  $\text{Co}_3\text{O}_4$ . The rate of the ORR is given by the current in the anodic sweep, which is not influenced by surface oxidation or reduction. Fig. 1c shows the curves for ORR after correction for the  $iR$ -drop and the capacitive current. ORR was observed at lower overpotentials with higher currents at the mixed 10% catalyst compared to the pure components (20 mV versus Ag and 330 mV versus  $\text{Co}_3\text{O}_4$  at  $1 \text{ mA cm}^{-2}$ ), see Fig. 1c. For ORR, the half-wave potential of the hybrid Ag311+ $\text{Co}_3\text{O}_4$  (10 wt%) bimetallic catalyst was similar to that of Ag and about 350 mV more positive than  $\text{Co}_3\text{O}_4$ , but about 200 mV less positive than that of Pt/C. The current density of the mixed catalyst at 0.7V was 1.3 times higher than that of pure Ag catalyst ( $0.93$  compared to  $0.71 \text{ mA cm}^{-2}$ , respectively). For OER, our previous report showed that the current in the negative-going scan corresponds to OER activity, whereas the positive-going scan is dominated by the formation of silver oxide. The steady-state experiments done for 3 minutes revealed that the currents are mostly stable for the mixed and pure  $\text{Co}_3\text{O}_4$  catalysts, but not for pure Ag.[37] For OER, the onset potential of the mixed catalyst was the same as that of  $\text{Co}_3\text{O}_4$  (ca. 1.55 V); however, it showed current enhancement by about 150% compared to  $\text{Co}_3\text{O}_4$  at 1.8 V. Pure Ag311 showed a negligible activity to OER. For comparison, Pt/C catalyst was tested and the data show the superior activity for OER of the mixed catalyst with respect to the Pt, see Fig. 1a. The potential gap between ORR and OER was about 0.85 V at  $1 \text{ mA cm}^{-2}$  for both reactions at the mixed catalyst.

Tafel plots (currents were corrected for diffusion, see details in experimental section) of the corresponding curves in Fig. 1a are shown in Fig. 1d and 1e for ORR and OER, respectively. Interestingly, Ag and the mixed catalysts showed the same Tafel slope for ORR ( $90 \text{ mV dec}^{-1}$ ) at lower overpotential (0.7-0.9 V), whereas ca.  $180 \text{ mV dec}^{-1}$  was obtained for  $\text{Co}_3\text{O}_4$ . This suggests that the catalytic performance for ORR is dominated by Ag in the mixed catalysts. Ag exists at OER potentials as Ag-oxide and is reduced at lower potentials to metallic Ag which is effective for ORR. For OER, Tafel slopes of 100, 214 and  $153 \text{ mV dec}^{-1}$  were obtained at lower potentials for  $\text{Co}_3\text{O}_4$ , Ag and mixed catalysts, respectively. The same Tafel slope of  $183 \text{ mV dec}^{-1}$  was obtained at higher potentials for both  $\text{Co}_3\text{O}_4$  and the mixed catalyst, implying that  $\text{Co}_3\text{O}_4$  is the dominant factor in OER activity in the mixed catalyst. This assesses the interplay between Ag and  $\text{Co}_3\text{O}_4$  in their mixture in the two different processes. Additionally, the overall number of electrons transferred ( $n$ ) was determined from the ring currents and found to be 3.9-4.0 for both Ag311 and the mixed 10% catalysts over the potential range of ORR, and  $\sim 3.5$  for the spinel  $\text{Co}_3\text{O}_4$ , Fig. 1f. Therefore, ORR on the mixed catalyst obeys the 4-electron pathway with negligible peroxide formation. Moreover, ORR is controlled by diffusion of  $\text{O}_2$  to the electrode surface since the dependence of current density on the rotation rate (K-L plots) reveals a straight line passing through the origin.



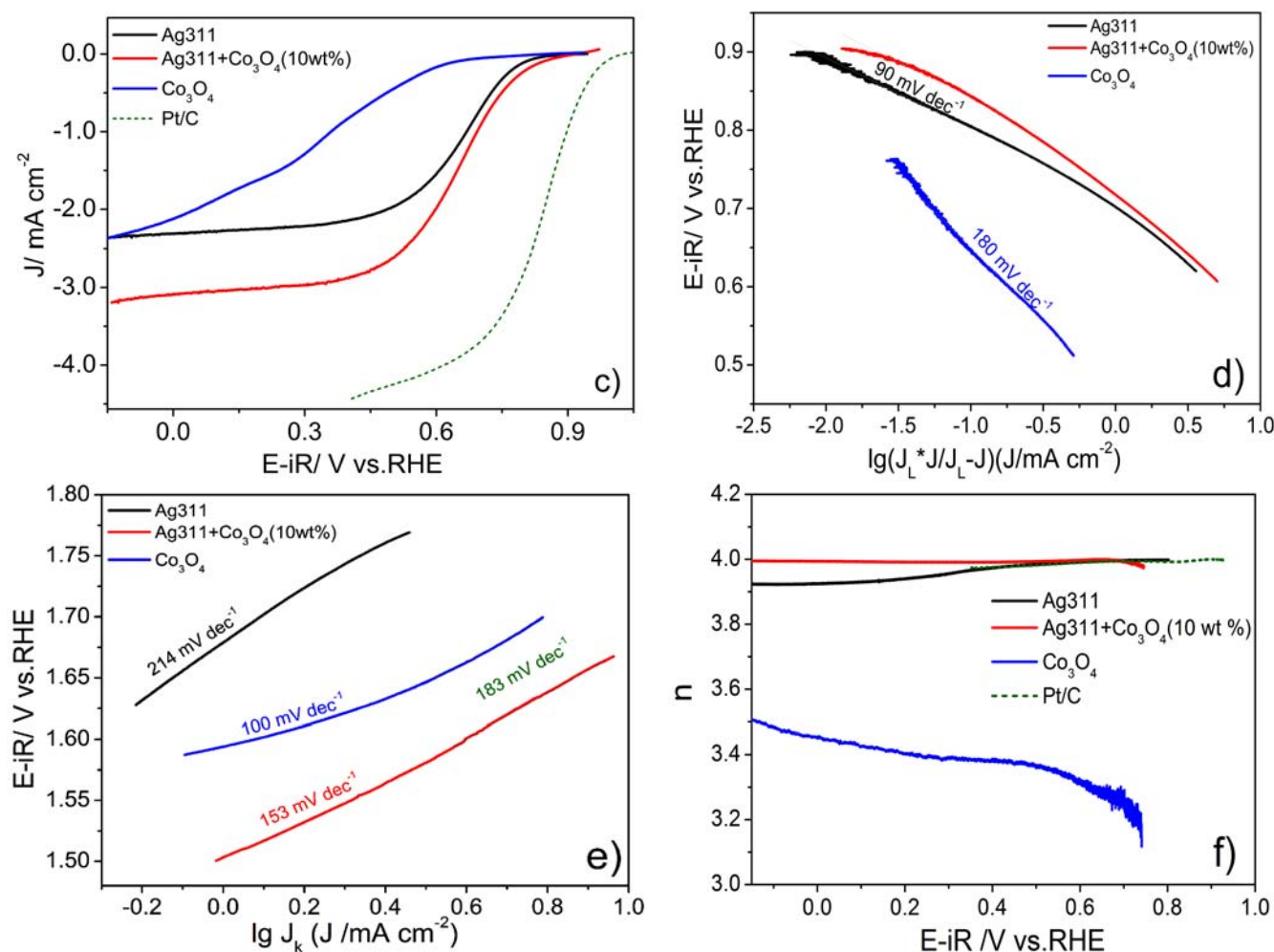


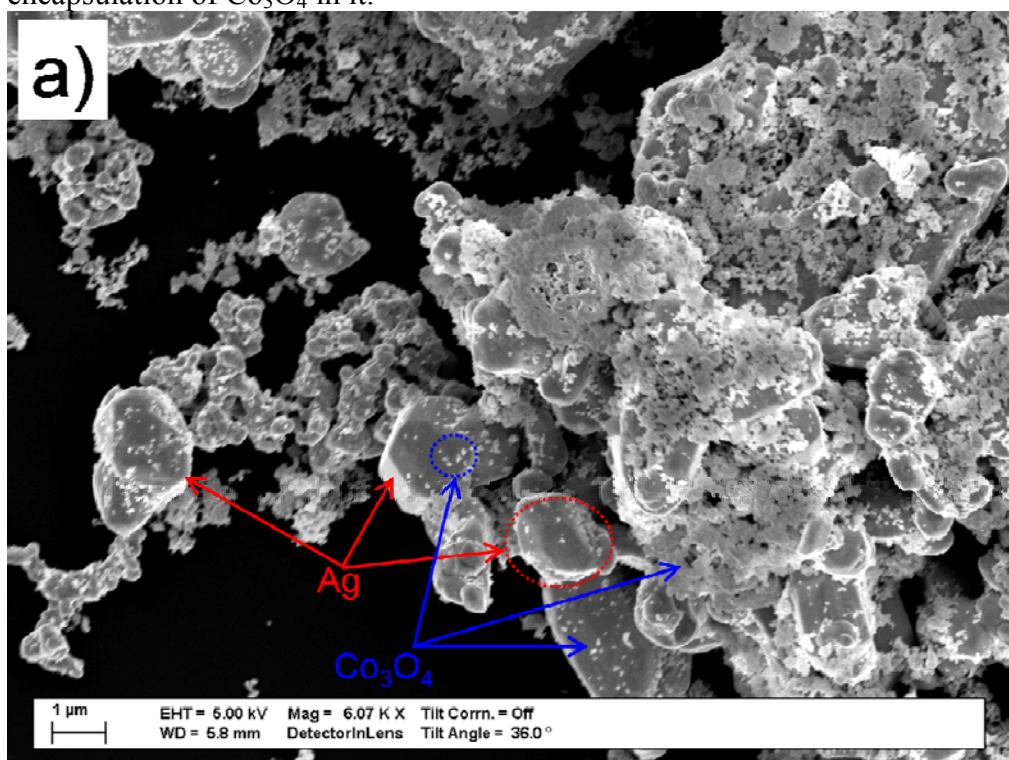
Fig. 1. a) CV curves of Ag311, Ag311+Co<sub>3</sub>O<sub>4</sub>(10 wt%), Co<sub>3</sub>O<sub>4</sub> and Pt catalysts (1 mg cm<sup>-2</sup>) on GC electrode in O<sub>2</sub>-saturated 0.1M LiOH solution at a rotation rate of 960 rpm with a scan rate of 10 mV s<sup>-1</sup>. b) polarization curves of various catalysts in Ar-saturated 0.1M LiOH solution with a scan rate of 50 mV s<sup>-1</sup>. Catalysts in a) and b) are different preparations. c) iR and capacitive current-corrected polarization curves derived from anodic scan in Fig. 1a. d) The corresponding mass-transport corrected Tafel plots for ORR and e) for OER. f) Electron transfer number ( $n$ ) derived from the corresponding RRDE data in Fig. 1c at various potentials.

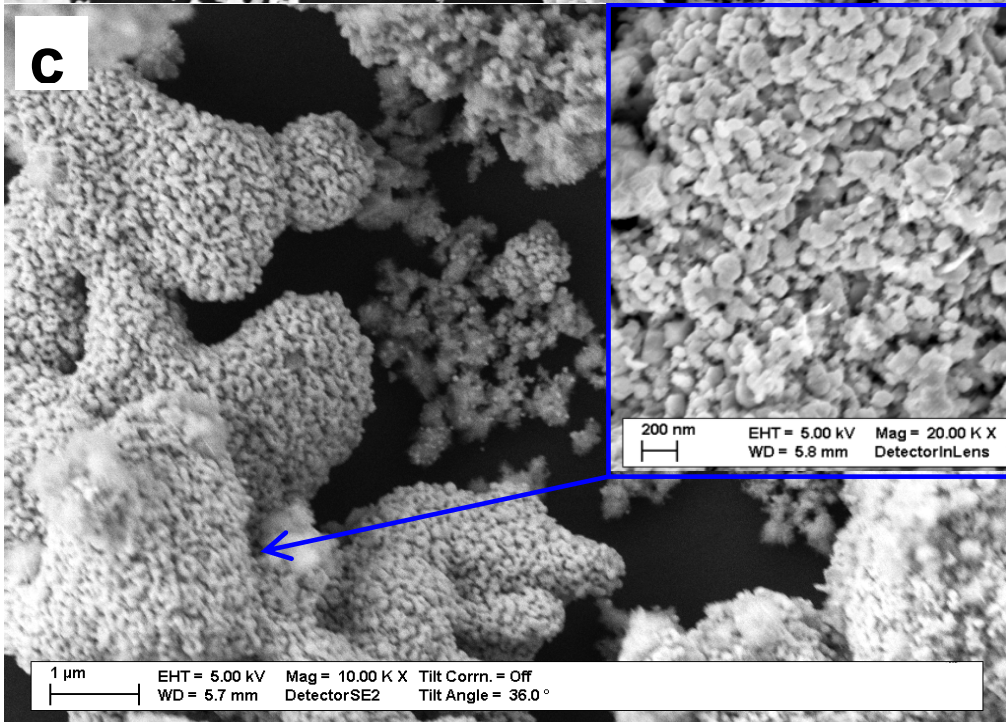
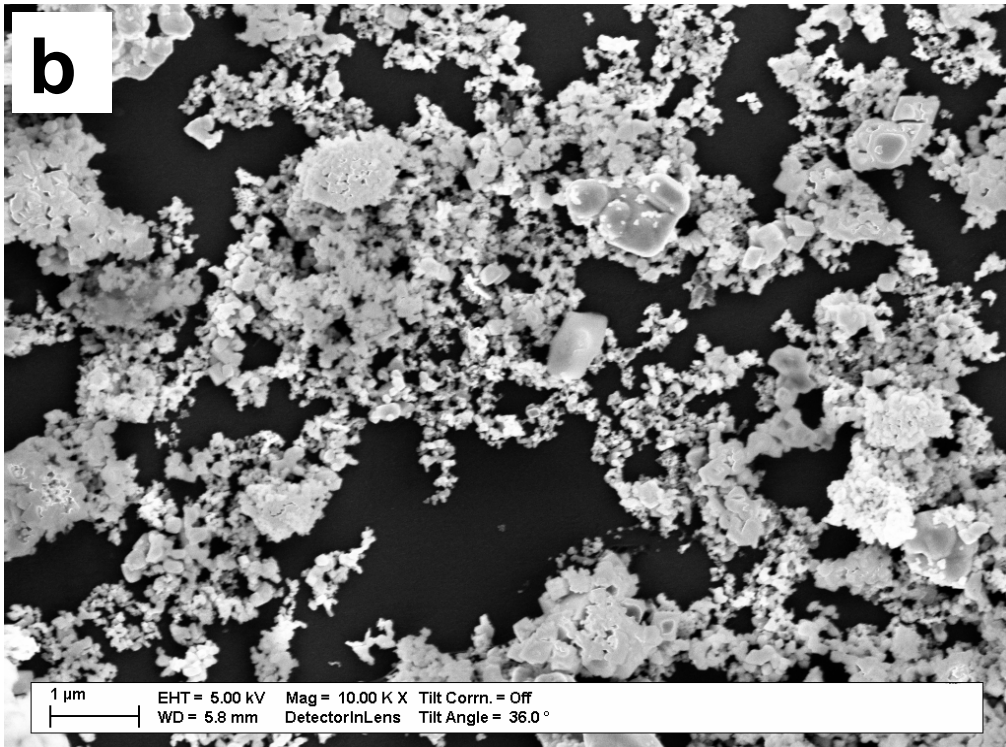
Long-term stability measurements have been done in our previous report on a GDE for the same catalysts and showed good durability for 200 successive cycles at OER and OER potentials.[38] Only slight decay was observed in the first 50 cycles of OER, but remains stable afterwards. For model electrodes such as those used in this study, the quasi-steady state currents for ORR were only slightly less than the current in the cathodic-going scan in the CV.[37] This was obtained by holding the potential for few minutes at different potentials and recording the current. For OER, Ag-containing catalysts exhibited current decay in the first minute where this high current involves the continuation of Ag-oxide formation, and afterwards stable currents are obtained for pure OER. Co<sub>3</sub>O<sub>4</sub> and the mixed catalysts showed good stability after one minute, and the very small decay is due to blocking of some active sites with evolved oxygen bubbles. On the other hand, Ag catalysts showed large decay and

less activity for OER.[37, 38] For ORR, There is no significant decay in the current in the potentiostatic experiment.

### 5.3.2. Ex-situ and in-situ surface characterization: SEM, EDX and XPS

Furthermore, the morphology and distribution of the catalyst were examined by scanning electron microscope (SEM). To get better resolution for SEM, we also imaged the surface without Nafion (Fig. 2a) in addition to the one containing Nafion (Fig. 2b) before electrochemical processes. In Fig. 2a, the composite consists of particles of two different contrasts. The individual Co<sub>3</sub>O<sub>4</sub> can be clearly identified as bright spots with ca. 50 nm size partially covering and attached to the darker ca. 1 μm Ag particles. The identification of the particles has been done by EDX data on the same catalyst in our previous report.[37] Co<sub>3</sub>O<sub>4</sub> nanoparticles are dispersed as a 2D layer on the larger Ag particles; 3D agglomerates are not observed (Fig. 2b). The catalyst with Nafion shows a quite better distribution and no or reduced aggregates but slightly blurred images. The coexistence of Co<sub>3</sub>O<sub>4</sub> in contact with Ag seems to provide stable anchor sites to keep the particles separated and prevent migration and coalescence during electrochemical cycling. Therefore, exposing the appropriate loading of the catalyst on GC does not induce significant mobility of the particles on the surface. SEM micrograph of the mixed catalyst with Nafion after several OER and ORR cycles is shown in Fig. 2c. After oxidation and reduction of the mixed catalyst, larger structures are noticed (ca. 100 nm), which cover most of Ag particles, see inset of Fig. 2c. These morphological changes observed on the surface after ORR/OER cycles might be due to enhanced roughness of the surface linked to Ag oxidation, which also will lead to a stronger contact of the Co<sub>3</sub>O<sub>4</sub> nanoparticles with Ag. EDX spectra showed the coexistence of Ag and Co<sub>3</sub>O<sub>4</sub> after several cycles, and it seems that large particles are thoroughly covered by small particles, as shown in Fig. 2d. It is possibly that rearrangement and growth of Ag could occur with partial encapsulation of Co<sub>3</sub>O<sub>4</sub> in it.





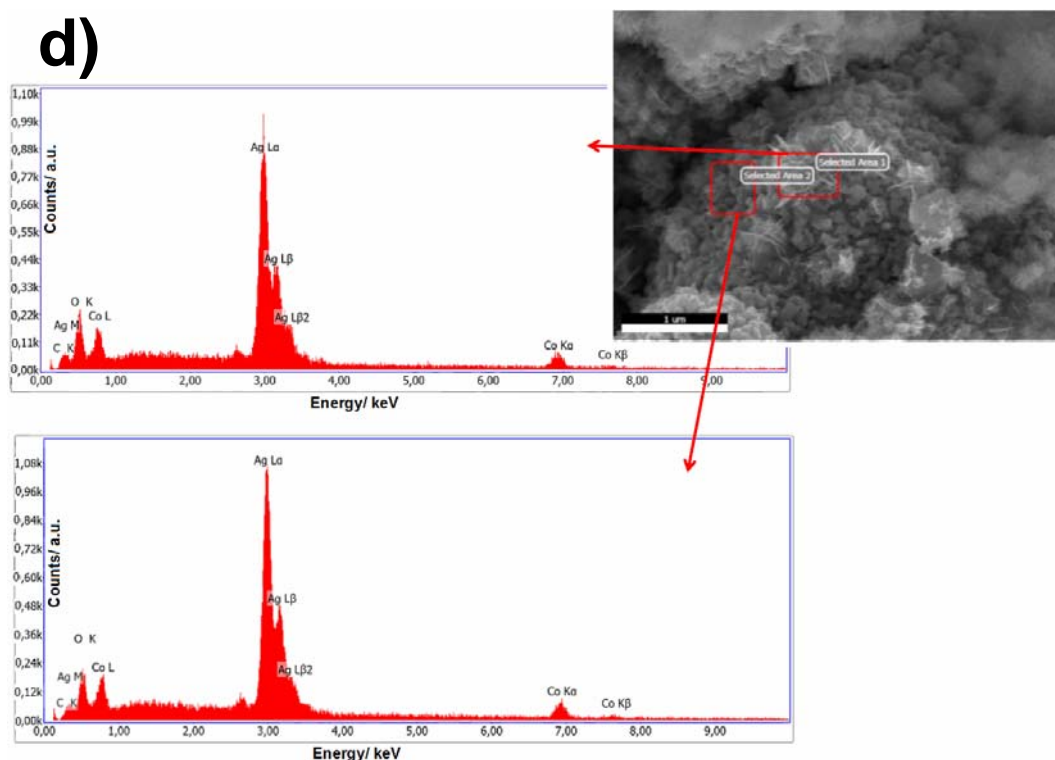
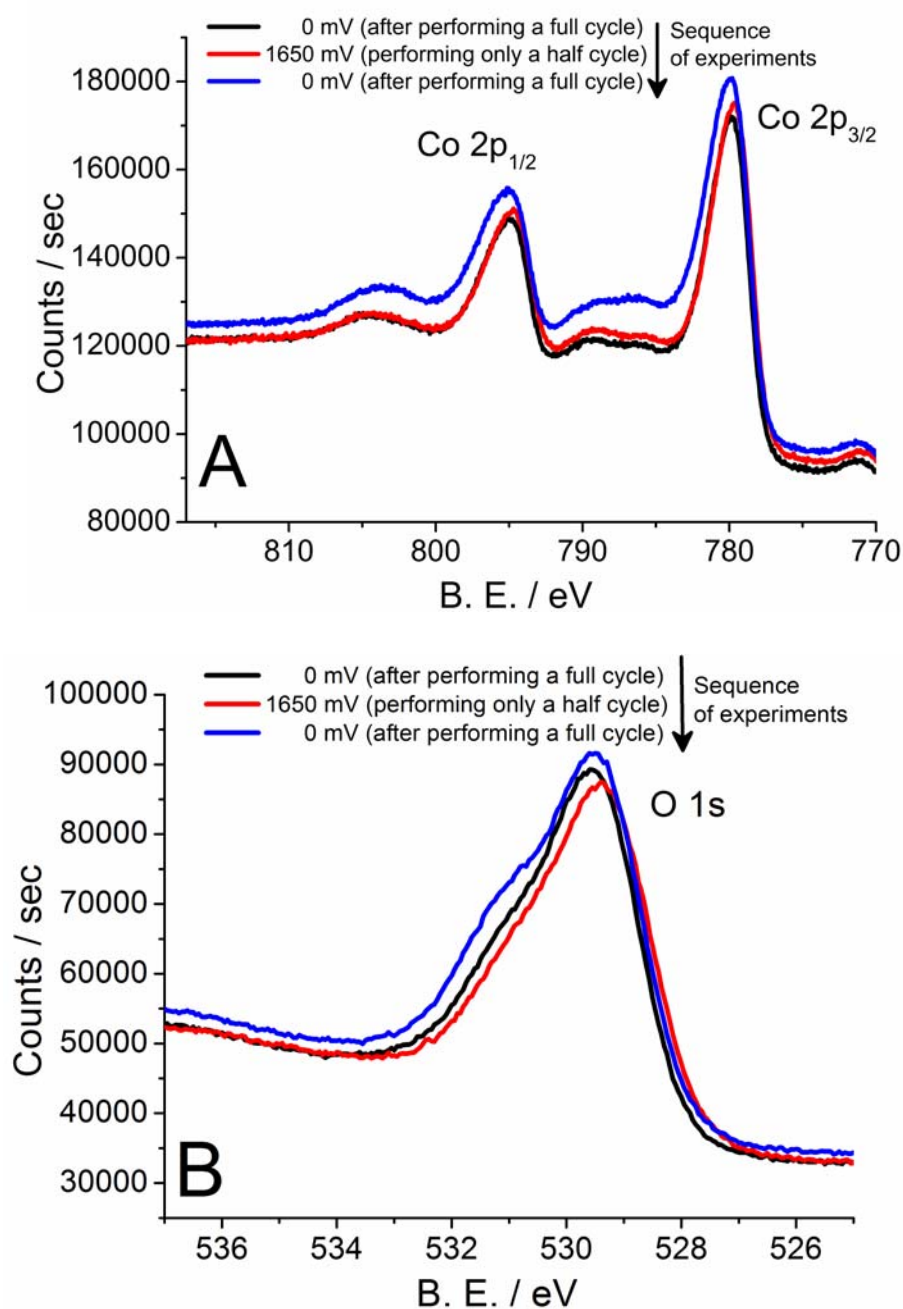


Fig. 2. SEM images of the  $1\text{ mg cm}^{-2}$  mixed Ag+Co<sub>3</sub>O<sub>4</sub> (10wt%) a) without Nafion and b) with Nafion before OER/ORR cycling, while c) with Nafion emersed at 1.0 V after cycling (oxidation and reduction). Inset is a zoom-in of part of the surface. d) EDX spectra of a part of the surface of the mixed catalyst after cycling.

In order to examine the catalyst more closely, XPS measurements of the 10% mixed catalyst and of the Co<sub>3</sub>O<sub>4</sub> particles alone were performed. For technical reasons, a polycrystalline Ag substrate was used in both cases; the total catalyst loading was  $400\ \mu\text{g cm}^{-2}$ . In the case of the pure Co<sub>3</sub>O<sub>4</sub> catalyst, which will be discussed first, this amount of Co<sub>3</sub>O<sub>4</sub> corresponds roughly to 20 layers of nanoparticles (assuming sphere shaped Co<sub>3</sub>O<sub>4</sub> particles forming a close-packed layer). Since the investigation of the Ag/Co<sub>3</sub>O<sub>4</sub>-surface would be impossible, if it was covered with a Nafion binder, the nanoparticles were deposited from a suspension in water. Therefore, the particles stuck to the surface of the silver electrode by adhesion only. Fig. 3d displays the CV of this electrode and indicates the sequence of the experiment: In each experiment, the electrode is immersed at 0 V into an electrolyte of 0.1 M LiOH and cycled to the indicated potential. In the first (black curve in Fig. 3) and in the third (blue curve in Fig. 3) experiment the electrode performed a full cycle in the potential range from 0 to 1.70 V. The electrode was immersed at 0 V and transferred to the main chamber, where the XP-spectrum was collected. In the second experiment only a half cycle was performed, and the electrode was immersed at 1.65 V.

Fig. 3 shows the highly resolved XP spectra of the Co 2p-line (A), the O 1s-line (B) as well as Ag 3d-line (C). According to the Pourbaix diagrams published by Chivot *et al.*[45] cobalt forms either Co<sub>3</sub>O<sub>4</sub> or CoOOH at 1.65 V. Although the positions of the Co 2p-lines are not very sensitive to the oxidation state of cobalt, the shown spectra are assigned to the Co<sub>3</sub>O<sub>4</sub> phase as they resemble those spectra shown by Biesinger *et al.* for Co<sub>3</sub>O<sub>4</sub>. [46] The phase was identified by the faint shake up satellites of the 2p-lines, which are somewhat different in

shape for  $\text{CoO}(\text{OH})$ [47]. In addition the O 1s line in Fig. 3B points to the presence of  $\text{Co}_3\text{O}_4$  rather than  $\text{CoO}(\text{OH})$ . Although the line position of the O 1s line is at 529.5 eV and thereby shifted by 0.5 eV to lower binding energies than reported by Yang *et al.* for  $\text{Co}_3\text{O}_4$ [47] it is still a single peak rather than an unresolved doublet, which is expected for  $\text{CoO}(\text{OH})$ . [47] It also does not change with potential. The formation of silver oxide at high potentials does not affect the shape or position of the O 1s peak because the surface is largely covered by  $\text{Co}_3\text{O}_4$  nanoparticles. The XP-spectra in Fig. 3 show that  $\text{Co}_3\text{O}_4$  is present at the surface both at 1.65 V and at 0 V. From thermodynamics it is expected that the  $\text{Co}_3\text{O}_4$ -particles do not undergo any phase transition at 1.65 V.[45] However, no  $\text{Co}(\text{OH})_2$  forms at 0 V although this would be the stable phase according to the Pourbaix-diagram of cobalt at this potential.[45]



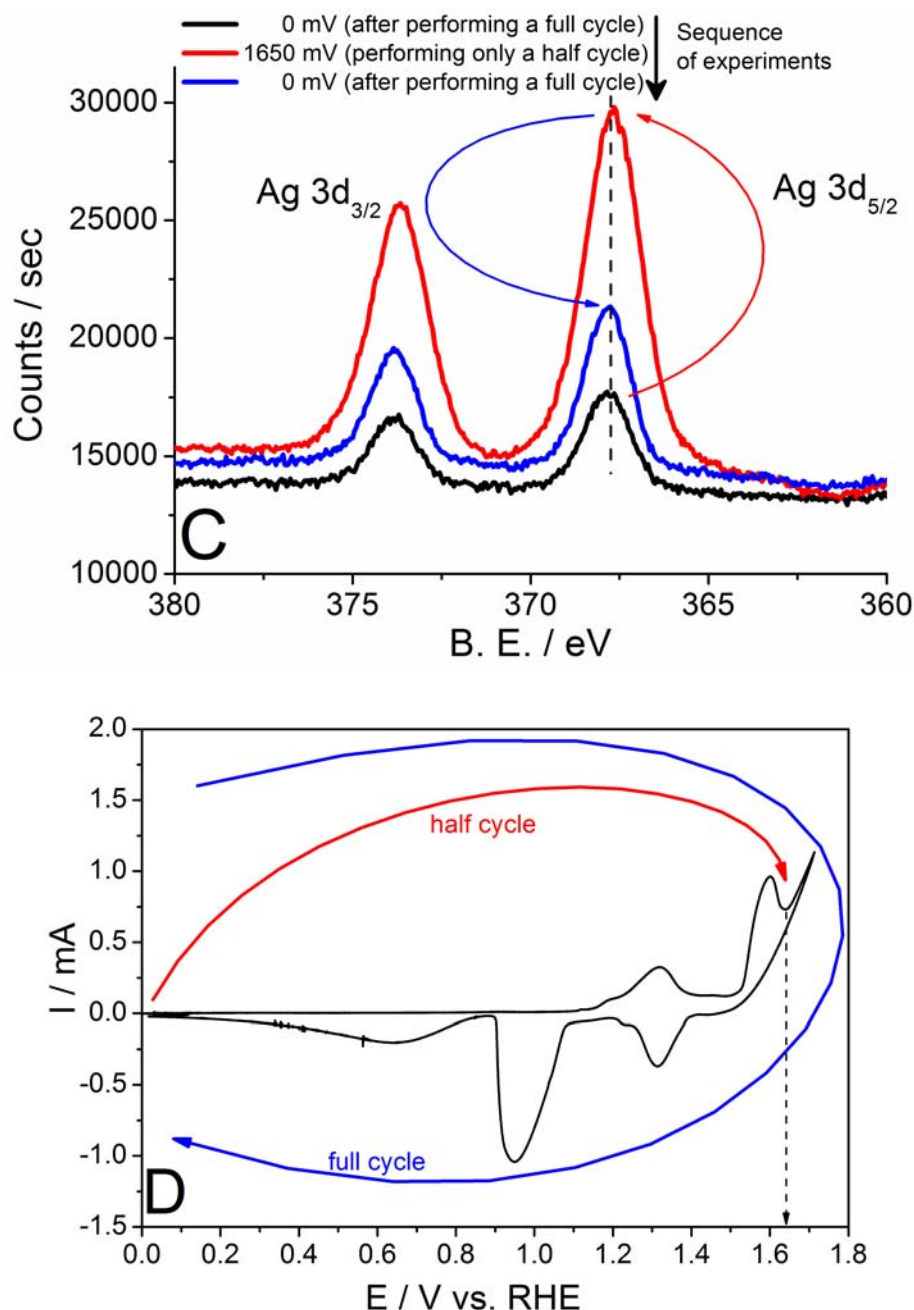


Fig. 3. XP-spectra of a polycrystalline silver electrode covered with  $400 \mu\text{g cm}^{-2}$   $\text{Co}_3\text{O}_4$  nanoparticles after electrochemical polarization to the indicated potentials (vs RHE) in an electrolyte of 0.1 M LiOH, A) Co 2p-lines; B) O 1s-line; C) Ag 3d-lines. D) CV of this electrode. The experiment was conducted as indicated: Starting from 0 V the electrode was cycled to either 1.65 V or back to 0 V where the transfer to the UHV chamber was conducted. Sweep rate:  $\nu = 5 \text{ mV s}^{-1}$

The positions of the silver 3d-lines remain unaltered regardless of the applied potential. In a control experiment we have polarized a polycrystalline silver electrode in the same electrolyte to several potentials in the absence of any  $\text{Co}_3\text{O}_4$ . The prominent peaks in anodic direction at 1.3 V and at 1.6 V are due to the oxidation of silver.[37] These experiments have shown that the Ag 3d-lines are insensitive to the oxidation state of silver. This finding is in contrast to an earlier report, where the authors found a decrease of the binding energy upon oxidation of

silver.[39] However, a reduced binding energy at higher oxidation states is rather unusual. We can observe changes in the less intense Ag MNN lines, which indicate the formation of Ag<sub>2</sub>O in the first oxidation peak. The Ag MNN lines were not investigated in [39]. Further changes in the Ag MNN lines do not appear as the potential is increased to 1.72 V where AgO is formed[48] (*i.e.* more precisely Ag<sup>I</sup>Ag<sup>III</sup>O<sub>2</sub>, since Ag<sup>II</sup>O is not known to exist [39, 49]). The XP-spectra of the Ag-3d and the Ag-MNN-lines as well as that of the O 1s-line can be found in Fig. S2 to S4 in the supporting information. Regardless of the actual product of oxidation at 1.72 V we assume that this product is not stable under UHV-conditions where the oxygen partial pressure is approaching zero. This is supported by the fact that the open circuit potential of the electrode after its back transfer is at 1.12 V and therefore, more cathodic than 1.30 V where a peak due to the reduction of Ag<sup>I</sup>Ag<sup>III</sup>O<sub>2</sub> appears. However, regardless of the oxidation state of the polycrystalline silver, the intensity of the Ag 3d lines remained unaltered in all control experiments.

In Fig. 3 the overall intensity of the silver lines is very low, as most of the silver surface is covered with Co<sub>3</sub>O<sub>4</sub>-nanoparticles. However, when the electrode is transferred after polarization to 1.65 V the intensity is increased compared to the experiment where the electrode is transferred after polarization to 0 V. In order to quantify the effect, the relative atom-% for cobalt, silver and oxygen was calculated according to eq. 5.1 [50] and listed in Table 1.

$$W_x = \frac{I_x / ASF_x}{\sum_i I_i / ASF_i} \quad \text{eq. 5.1}$$

In eq. 5.1,  $W_x$  is the portion of the element in question in the surface.  $I_x$  is the intensity of the respective line in the XP-spectrum as determined by integration after baseline subtraction, which needs to be weighted by the atomic sensitivity factor ( $ASF_x$ ). The weighted signal intensity is divided by the sum of the weighted intensity of all elements in the surface.

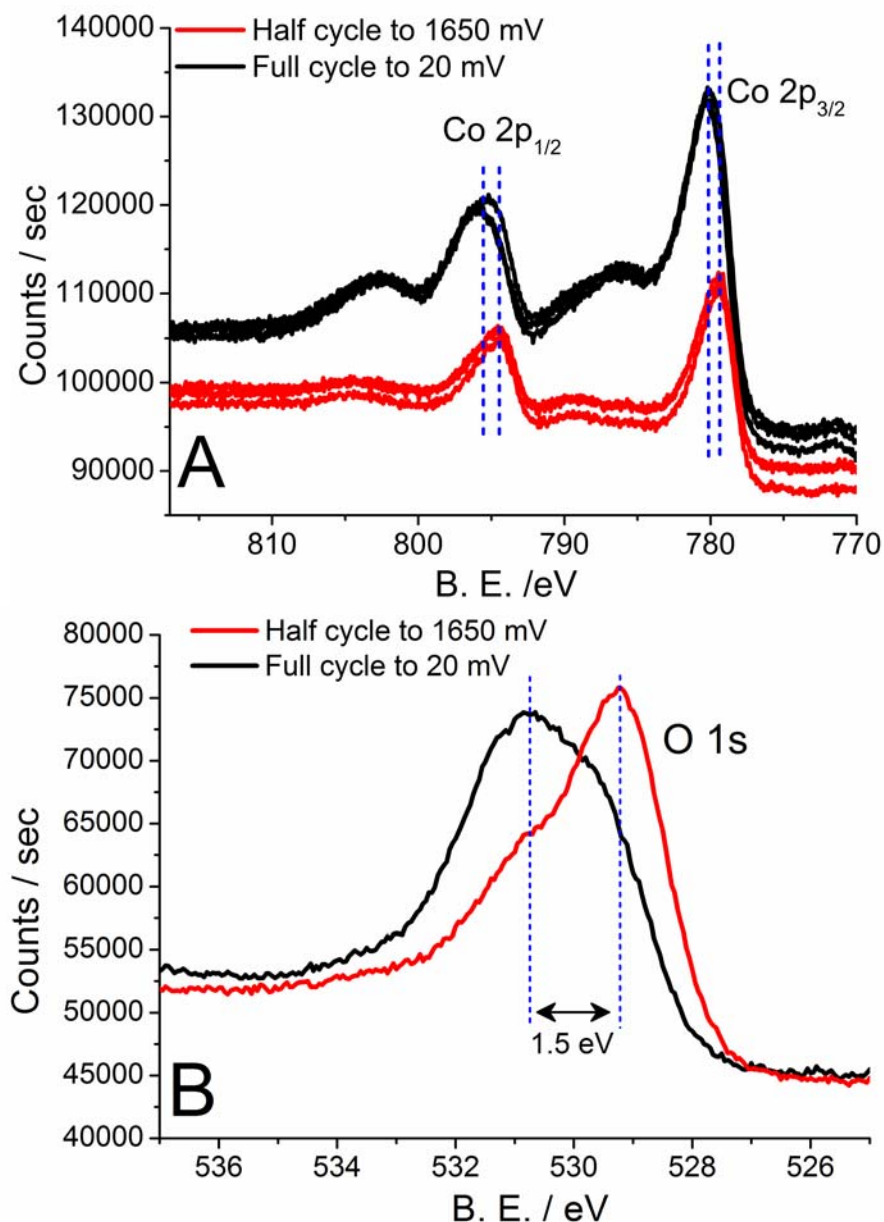
	rel. atom-% oxygen (theoretical)	rel. atom-% cobalt	rel. atom-% silver
<b>Co<sub>3</sub>O<sub>4</sub> / Ag (pc)</b>			
<b>1<sup>st</sup> Full cycle</b>	67.1 (44)	31.9	1.1
<b>Half cycle</b>	61.0 (47)	34.6	4.3
<b>2<sup>nd</sup> Full cycle</b>	62.4 (48)	36.3	1.3
<b>Ag311+Co<sub>3</sub>O<sub>4</sub> (~10wt%) /Ag (pc)</b>			
<b>1<sup>st</sup> Full cycle</b>	36.5 (34.6)	17.3	46.2
<b>Half cycle</b>	39 (37)	9	52

Table 1: relative atom-% of oxygen, cobalt and silver in a surface of a polycrystalline silver electrode covered with either 400 μg cm<sup>-2</sup> of Co<sub>3</sub>O<sub>4</sub> nanoparticles or 400 μg cm<sup>-2</sup> Ag311 and 50 μg cm<sup>-2</sup> of Co<sub>3</sub>O<sub>4</sub> after polarization to various potentials. The values were calculated according to eq. 5.1. The required values were obtained by integration of the curves shown in Fig. 3 and 4 after baseline subtraction.

According to Table 1(upper section) the relative amount of silver in the surface is low at all potentials for the Co<sub>3</sub>O<sub>4</sub> catalyst on Ag(pc), but it increases significantly, when the electrode

is polarized to 1.65 V. Although the formation of silver oxide is expected at this potential, this has little influence on the overall intensity of the oxygen O1s line as the relative amount of silver oxide in the surface is low. The process that leads to the increased amount of silver in the surface is at least partially reversible. This is shown qualitatively by the blue curve in Fig. 3 and quantitatively by the relative atom-% of silver in the surface listed in Table 1. An increased intensity of the Ag 3d lines means that more silver is exposed to the spectrometer: The expansion of Ag<sub>2</sub>O in volume during oxidation that pushes more silver through the over layer of Co<sub>3</sub>O<sub>4</sub>-particles to the surface is the most probable explanation and is supported by the SEM data shown above.

The contact area between silver and Co<sub>3</sub>O<sub>4</sub> is increased in the mixed catalyst. Therefore, the same experiments as shown in Fig. 3 were done with an Ag-electrode covered with 50 μg cm<sup>-2</sup> of Co<sub>3</sub>O<sub>4</sub> nanoparticles and 400 μg cm<sup>-2</sup> of Ag311 particles (Ag311+Co<sub>3</sub>O<sub>4</sub> (~10wt%))/Ag. The resulting XP-spectra are shown in Fig. 4. In this experiment, no significant changes in the Ag 3d intensity appear. Given that already most of the exposed material is silver this is expected.



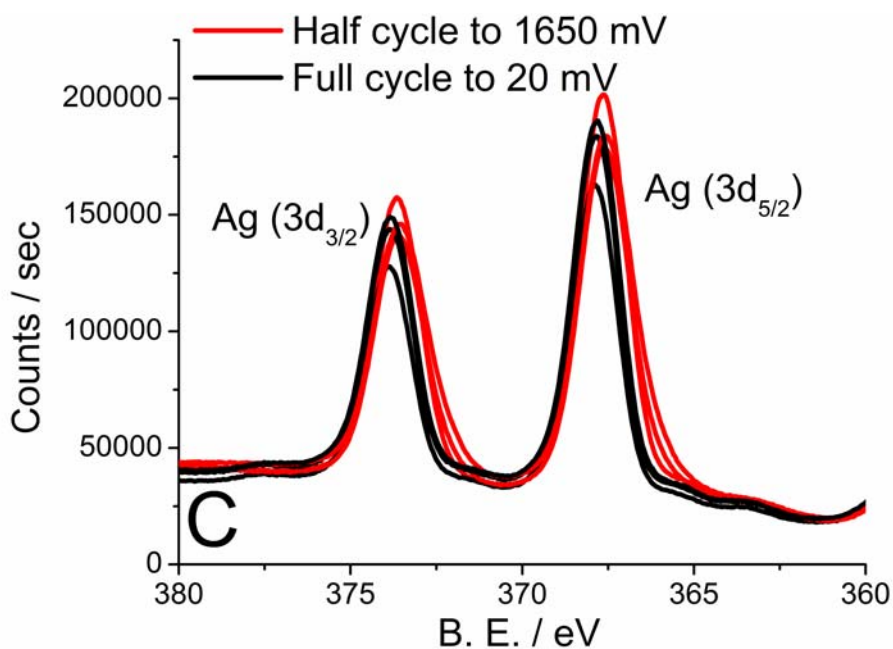


Fig. 4. XP-spectra of a polycrystalline silver electrode covered with  $50 \mu\text{g cm}^{-2}$   $\text{Co}_3\text{O}_4$  nanoparticles and  $400 \mu\text{g cm}^{-2}$  Ag311 particles after electrochemical polarization to the indicated potentials (vs RHE) in an electrolyte of 0.1 M LiOH. A) Co 2p-lines; B) O 1s-line; C) Ag 3d-lines. Both for Silver and Cobalt three spectra were collected at each potential. The spectra were collected on a rotating basis, after polarizing to 0.02V and 1.65 V, respectively.

From the XP-spectra in Fig. 4A it is clear that the Co 2p peaks are shifted to a lower binding energy and the shake up satellites change both their form and intensity as the electrode is polarized to 0.02 V compared to the spectra that were obtained after polarizing to 1.65 V. While at 1.65 V still  $\text{Co}_3\text{O}_4$  is present and the spectra obtained at 0.02 V resemble those shown by Biesinger *et al.* for the CoO or the  $\text{Co}(\text{OH})_2$ -Phase.[46] This is different from the experiment where a polycrystalline silver electrode was covered with  $\text{Co}_3\text{O}_4$  at all potentials (*c.f.* Fig. 3A): irrespective of the applied potential no reduction of the spinel occurred. However, when the electrode was only dipped into the electrolyte at 0.02 V without ever being polarized to 1.65 V in a previous experiment, the observed  $\text{Co}_3\text{O}_4$  phase was not reduced (*c.f.* Fig. S5 of the supporting information). Once the electrode was polarized to 1.65 V the formation of a Co(II)-phase was observed at 0.02 V. This process is reversible as shown by the switching between the phases in the six spectra for cobalt and silver in Fig. 4A and 4C. After polarization to 0.02V both  $\text{Ag}_2\text{O}$  and  $\text{Co}_3\text{O}_4$  are reduced. Any oxygen left on the surface belongs to the reduced Co/O-phase and the O 1s-line at 530.7 eV provides information on the nature of the reduced Co/O-phase: the observed value of 530.7 eV is close to the value of 531.07 eV reported for  $\text{Co}(\text{OH})_2$  by Biesinger *et al.*, whereas the reported value for the O 1s-line in CoO is 529.79 eV.[46] Hence at 0.02 V  $\text{Co}_3\text{O}_4$  is reduced to  $\text{Co}(\text{OH})_2$  rather than CoO. This is supported by the oxygen content (*cf.* Table 1), which is twice the value of Co.

It is clear from the CV in Fig. 2d and the XP-spectra of the Ag-MNN lines in Fig. S3 that the silver surface is oxidized at 1.65 V. From the curves shown in Fig. 4 the relative atom-% were calculated according to eq. 5.1 for the mixed catalyst and are also listed in Table 1 (lower section). At 1.65 V the relative cobalt content in the surface is 9% while that of silver is 52%.

A relative oxygen content of 39% ( $(4/3) \times 9\% + (1/2) \times 52\%$ ) at a potential, where Co exists as Co<sub>3</sub>O<sub>4</sub> is only explicable when Ag is oxidized to Ag<sub>2</sub>O. The XP-spectra of the O 1s-line obtained at this potential should reflect the oxidation state of silver, since 2/3 of the oxygen should exist as Ag<sub>2</sub>O. Indeed, the O 1s line of the oxidized surface is located at 529.2 eV in Fig. 4B. This is close to the O 1s line position of 529.5 eV expected for Ag<sub>2</sub>O.[51] Since this value is close to that reported for Co<sub>3</sub>O<sub>4</sub> (530 eV [46]) it is not expected that the difference between the oxygen atoms in both phases is resolved. However, the O 1s-line of the oxidized surface in Fig. 4B is shifted by 0.3 eV to lower binding energies as compared to the O 1s-line in Fig. 3B where Co<sub>3</sub>O<sub>4</sub> is the dominant phase in the surface.

As compared to the reduced surface the relative cobalt content is reduced by half at the oxidized surface. The decrease of the relative cobalt content signifies some shielding by Ag<sub>2</sub>O at high potential, due to the same effect as the increase of the Ag 3d-peaks in Fig. 3C. At 0.02 V the ratio of oxygen to cobalt is 2 : 1, which is expected for Co(OH)<sub>2</sub>. At this potential, silver should not be covered with an oxide over layer that would contribute to the relative amount of oxygen in the surface.

Co<sub>3</sub>O<sub>4</sub> (spinel-type) has a cubic-closed packed anion lattice, whereas Co(OH)<sub>2</sub> crystallizes in the CdI<sub>2</sub>-structure, which is a layered and hexagonal structure. Solid-state reactions like these in general involve large activation barriers. That is why the kinetic stability of the well crystallized Co<sub>3</sub>O<sub>4</sub> phase at a potential where CoO or Co(OH)<sub>2</sub> would be thermodynamically favored is expected. The kinetic stability of Co<sub>3</sub>O<sub>4</sub> at low overpotentials is lifted, when the relative contact area between Ag and Co<sub>3</sub>O<sub>4</sub> increases: Redox switching is only observed on a silver surface with 50 μg cm<sup>-2</sup> Co<sub>3</sub>O<sub>4</sub> and 400 μg cm<sup>-2</sup> Ag<sub>311</sub>. On Ag(pc) no such effect is observed when 400 μg cm<sup>-2</sup> of Co<sub>3</sub>O<sub>4</sub> cover a Ag(pc) substrate. However, since the formation of Co(OH)<sub>2</sub> is not observed when the electrode is only dipped at 0.02 V, but requires the polarization to 1.65 V in a previous experiment, the presence of metallic silver is not responsible for the facilitated redox switching of cobalt. Although we cannot offer any mechanism that would explain the observed behavior, the need to polarize to large potentials where oxidation of silver occurs suggests that the presence of silver cations is required in order to reduce the Co<sub>3</sub>O<sub>4</sub> phase at low potentials. Previously, the activity of ceramic catalysts for oxidation reactions has been assigned to the ability of the metal cation to change its oxidation state.[52-54] Since the presence of Ag facilitates the redox switching in Co<sub>3</sub>O<sub>4</sub>, this might be the reason for the enhanced activity of the Co<sub>3</sub>O<sub>4</sub>/Ag-electrode over the pure Co<sub>3</sub>O<sub>4</sub> phase for OER.

The increased activity of the Ag/Co<sub>3</sub>O<sub>4</sub> catalyst in the oxygen reduction region might be due to the formation of silver oxide, too. Fig. 3 shows that at high potentials the silver signal increases as Ag<sub>2</sub>O particles push through the layer of Co<sub>3</sub>O<sub>4</sub> particles. After reduction of silver oxide, the silver is distributed differently in the surfaces and has partially buried Co<sub>3</sub>O<sub>4</sub> particles as supported by SEM data. Fu *et al.* have shown in a thorough study on the oxidation of CO at a catalyst of FeO<sub>1-x</sub> islands on Pt(111) that the reactivity of CO linearly depends on the islands' periphery density (*e.g.* the overall length of the periphery per unit area) since dissociative adsorption of oxygen takes place preferentially at those sites.[55] Furthermore, similar effects of the role of the phase boundary have been shown for hydrogen evolution at Pd-modified gold single crystals[56] and for CO-electrooxidation at Ru- and Sn-modified

Pt(111) single crystals.[57-60] In the same way the activity of the Ag/Co<sub>3</sub>O<sub>4</sub> electrode might depend on the presence of phase boundaries between Ag and Co<sub>3</sub>O<sub>4</sub>.

### 5.3.3. Electrochemically surface area estimation

The electrochemically accessible area of Ag on the catalyst surface was determined by lead-underpotential deposition (Pb-UPD).[40-42] This is shown in the inset of Fig. 5 for pure Ag311 and several mixed catalysts on GC. A monolayer of Pb is deposited onto the Ag surface at potentials more positive than that of the expected equilibrium bulk deposition. Several stripping experiments have been conducted on Ag electrode by varying the deposition potential ( $E_d$ ) and time ( $t_d$ ) to reach optimum conditions for monolayer deposition.  $E_d$  of 0.24 V vs. RHE and  $t_d$  of 180 s were found to be optimum for our Ag311 and mixed Ag+Co<sub>3</sub>O<sub>4</sub> hybrid catalysts, where a maximum stripping charge reached without any bulk deposition. As shown in the CVs, the reversible peak in the region from 0.25 V to 0.5 V is due to the reduction of Pb<sup>II</sup> to Pb<sub>UPD</sub> and oxidation of Pb<sub>UPD</sub> to Pb<sup>II</sup> in the cathodic and anodic scans, respectively.[41] Monolayer coverage of Pb<sub>UPD</sub> requires 260  $\mu\text{C cm}^{-2}$  for a smooth surface.[40, 41] Thus, for the pure Ag catalyst, a stripping charge density of 1.5  $\text{mC cm}^{-2}$  is calculated corresponding to an apparent roughness factor of about 6 (i.e. surface area for Ag:  $\sim 5.8\text{cm}^2$  per  $\text{cm}^2$  geometric area). For the 10% catalyst, the active Ag area was 0.8  $\text{cm}^2$  per  $\text{cm}^2$  geometric area. Scanning to more negative potentials leads to Pb-alloy formation and an additional anodic peak at 0.2 V, as can be seen in the dashed line of inset of Fig. 5. By insertion of the nano Co<sub>3</sub>O<sub>4</sub> particles in the mixed catalyst, the surface area of the Ag particles exposed to Pb-UPD is reduced, as shown by the reduced stripping charge for Pb (Fig. 5): 88% blocking of the Ag surface area was achieved by insertion of 10 wt% of Co<sub>3</sub>O<sub>4</sub> in the hybrid, in qualitative agreement with the SEM shown in Fig. 2. A nearly complete blocking with Co<sub>3</sub>O<sub>4</sub> nanoparticles is achieved by dispersion of 20 wt% of Co<sub>3</sub>O<sub>4</sub> or more in the catalyst mixture. This is also the composition with a lower activity for ORR than Ag.

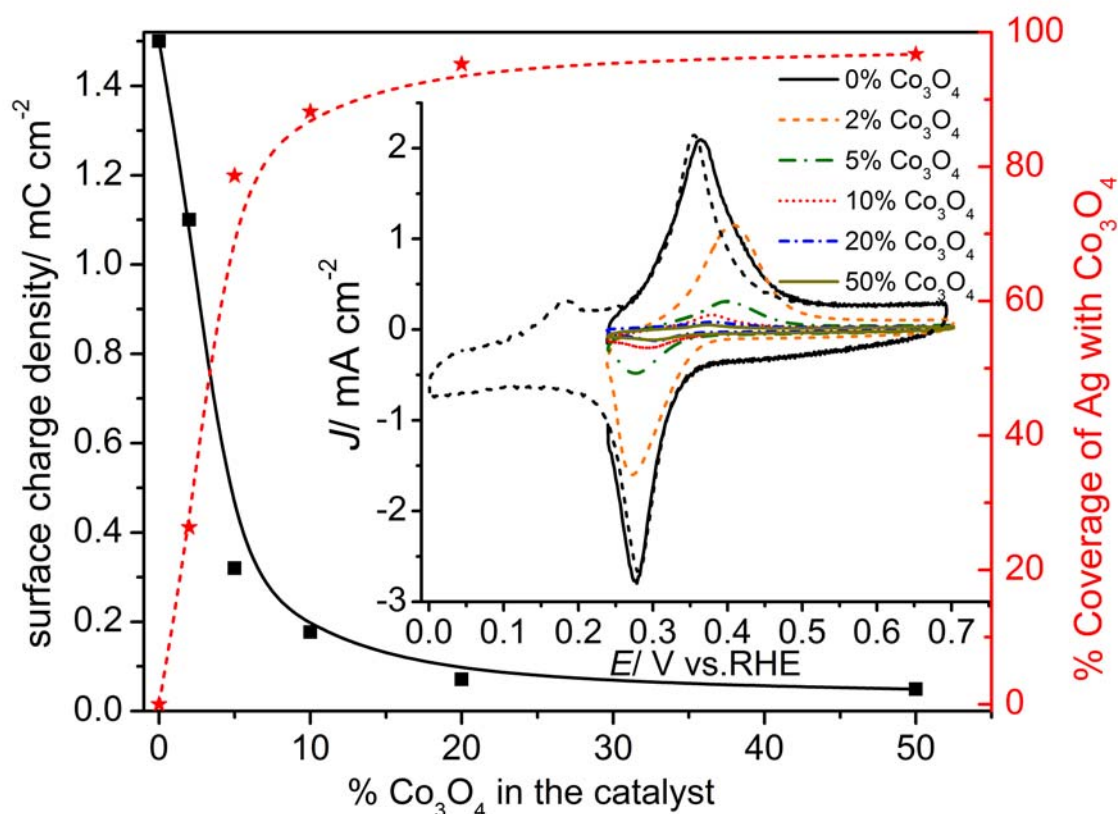


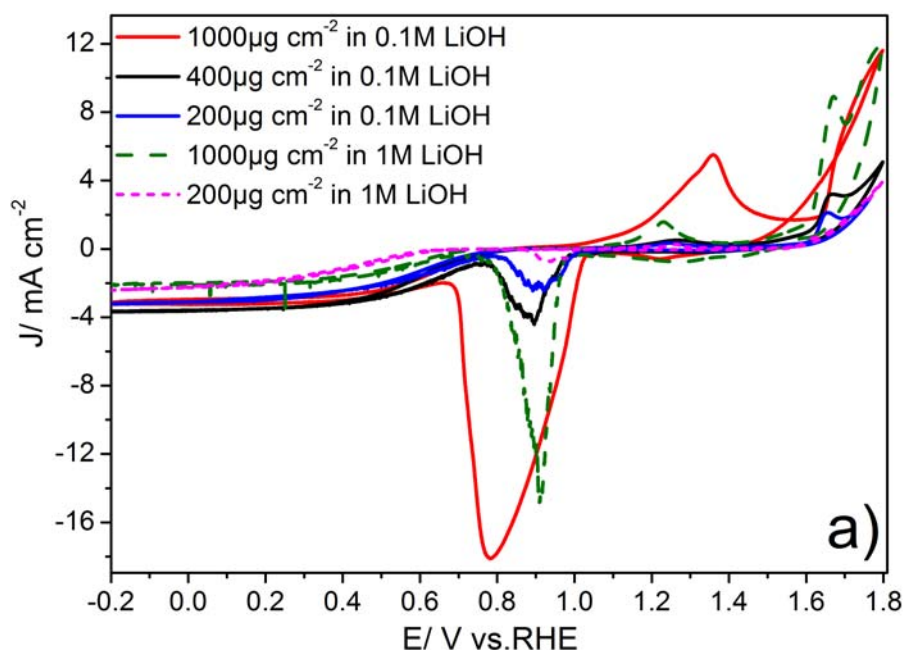
Fig. 5. Results of Pb-UPD on Ag<sub>311</sub>+Co<sub>3</sub>O<sub>4</sub>(10 wt%) in Ar-saturated 125 μM Pb(NO<sub>3</sub>)<sub>2</sub>+0.1M LiOH solution. The inset is the stripping CVs obtained after t<sub>d</sub> of 180 s and at E<sub>d</sub> of 0.24 V with a scan rate of 100 mV s<sup>-1</sup>(solid line), and a consecutive CV with more negative potential limit was recorded for Ag<sub>311</sub>(dashed line). Catalyst loading: 1 mg cm<sup>-2</sup>. The surface charge density was obtained by integration of the stripping anodic peak of the corresponding CV in the inset.

A simple ball model explains this finding: assuming a homogeneous radius of 0.5 μm for Ag particles, the number of particles and their total surface area can be calculated leading to a total surface area of 5.7 cm<sup>2</sup> per cm<sup>2</sup> of the substrate, in agreement with the above value of 6 for the apparent roughness factor. Similarly, for a uniform diameter of the Co<sub>3</sub>O<sub>4</sub> particles and assuming that each particle blocks a section of  $\pi r^2 = \pi(25 \text{ nm})^2$  of the Ag surface (i.e. the area underneath the particles is not accessible), a blocked area of 4.9 cm<sup>2</sup> of Co<sub>3</sub>O<sub>4</sub> per cm<sup>2</sup> of the GC substrate is obtained for the 10% Co<sub>3</sub>O<sub>4</sub> catalyst, corresponding to 86% of the Ag surface area (to be compared to the experimental value of 88%). We conclude: a catalyst with an Ag area exposed to the solution of only 12% of that of the pure Ag catalyst has an activity for O<sub>2</sub>-reduction, which is nearly twice as large. On the other hand, the catalyst with only 10% or 20% Co<sub>3</sub>O<sub>4</sub> (which could be thought to be responsible for O<sub>2</sub> evolution) has the same (or even a higher) activity than pure Co<sub>3</sub>O<sub>4</sub>.

### 5.3.4. Influence of catalyst loading and electrolyte concentration

The catalyst loading has a strong impact on the detection of HO<sub>2</sub><sup>-</sup> at the ring of RRDE, and therefore, on the catalytic activity and ORR mechanism. Poux et. al have investigated the loading effect on perovskite catalyst and concluded that ORR follows predominantly the series 2e+2e pathway through formation of HO<sub>2</sub><sup>-</sup> intermediate.[61] The extent of escape of

this intermediate from the surface depends strongly on the catalyst loading.[61] Here, we studied the loading effect of the Ag<sub>3</sub>11+Co<sub>3</sub>O<sub>4</sub>(10 wt%) catalyst on GC substrate. Three different loadings of the catalyst on the substrate were compared in Fig. 6. The onset and polarization curves of ORR shifted to more positive potentials as the loading increased (Fig. 6a). A decrease in the catalyst loading leads to a decrease in the disc currents, an increase in the ring currents, and consequently, an increase of HO<sub>2</sub><sup>-</sup> yield (Fig. 6b and c). The 1000 μg cm<sup>-2</sup> loading of the mixed catalyst in 0.1M LiOH has negligible peroxide formation, compared to about 8 % and 28 % for 400 and 200 μg cm<sup>-2</sup> loadings, respectively. This means the role of loading is significant. The decrease of the HO<sub>2</sub><sup>-</sup> yield with increased loading may be due to the higher chance for a HO<sub>2</sub><sup>-</sup> ion for being further reduced to OH<sup>-</sup> before diffusing out of the catalyst layer, as suggested in [61] (30 to 130 μg cm<sup>-2</sup> loading range there). Another possibility (more probable) is that for low loadings large parts of the GC substrate are uncovered, at these parts O<sub>2</sub> reduction follows a 2e-mechanism (this may also be true for[61]). Lower onset potential and higher current densities for OER are also observed for higher loading of 1 mg cm<sup>-2</sup>. The kinetic currents are calculated for different catalyst loadings from the measured thin-film RRDE experiments of Fig. 6a, then they are iR-corrected, and are used to establish Tafel plots as shown in Fig. 6c. The curves are almost parallel with Tafel slope of ca. 95 mV dec<sup>-1</sup> and 160-170 mV dec<sup>-1</sup> at low and high overpotentials, respectively. The kinetic current density increases with loading increase until a uniform thin layer covering the GC substrate is reached, which is important for reasonable RRDE analysis.



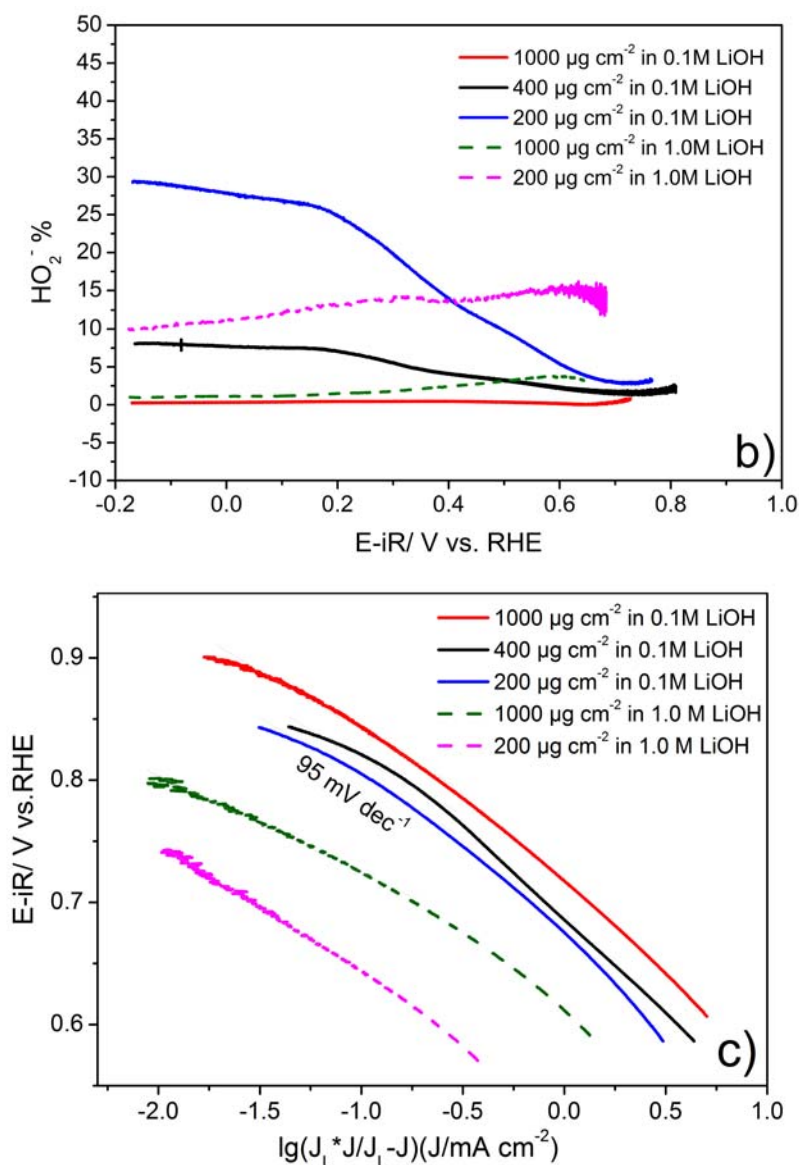


Fig. 6. a) Polarization curves obtained in O<sub>2</sub>-saturated LiOH solution with 10 mV s<sup>-1</sup> and at 960 rpm for Ag<sub>311</sub>+Co<sub>3</sub>O<sub>4</sub> (10 wt%) catalyst with 200, 400 and 1000 μg cm<sup>-2</sup> loadings. b) The corresponding H<sub>2</sub>O<sub>2</sub><sup>-</sup> % obtained when the ring kept at 1.2 V. c) Mass-transport corrected Tafel plots obtained from the polarization curves shown in Fig. 6a.

The trend of ORR/OER activity for two electrolyte concentrations has also been studied, Fig. 6a. For ORR, the current densities decrease in the studied potential range as the LiOH concentration increases due to the reduced O<sub>2</sub>-solubility. Tafel slopes were similar and have a value of ca. 90-100 mV dec<sup>-1</sup>, indicating no change in the ORR mechanism in these solutions, Fig. 6c. The results showed also that the overall electron transfer numbers in ORR do not alter much with electrolyte concentration variation, and were all close to 4 in case of 1000 μg cm<sup>-2</sup> loading. The peroxide species yields were as well comparable and very small (< 2% for 1 mg cm<sup>2</sup>) over the entire potential range for different concentrations, suggesting the 4-electron pathway for ORR at this catalyst, Fig. 6b.

## 5.4. Discussion

To monitor the overall bifunctionality of the catalysts, the potential difference ( $\Delta E$ ) between ORR at  $-1.5 \text{ mA cm}^{-2}$  and the OER at  $4 \text{ mA cm}^{-2}$  were calculated and listed in Table 2. The smaller the potential gap, the more reversible is the electrode. Based on some electrochemical parameters, which reflect the bifunctional activity, it is clear that the mixed catalyst (10%) has superior activity to OER and comparable activity to the commercial Pt for ORR. This carbon-free mixed catalyst exhibited similar onset potentials for ORR and OER to that of  $\text{Li}_x\text{Co}_2\text{O}_2$  loaded on carbon.[26] The electrochemical parameters for ORR and OER are also compared to the best carbon-free bifunctional catalysts in literature, as represented in Table 2.

Thus, the interaction between Ag and  $\text{Co}_3\text{O}_4$  leads to a synergistic effect and improvement in the catalytic activity for both OER and ORR. As demonstrated by the determination of the accessible Ag surface area by Pb-UPD, for ORR this effect is far beyond what might be expected by simply adding the activities of both components. Our XPS results show, that a reduction of the  $\text{Co}_3\text{O}_4$  to  $\text{Co}(\text{OH})_2$  is only achieved when an intimate contact between Ag and the Co-oxide is given, suggesting a catalytic effect of Ag on the redox switching in the Co-oxide. On the other hand, the increased charge of the Ag-oxide peaks in the mixed catalyst indicates also a catalytic effect of the  $\text{Co}_3\text{O}_4$  on the oxidation of Ag. It can be anticipated that this mutual catalysis of the redox switching also plays a role in the synergistic effect for OER and ORR of the two catalysts.

In summary, and as in part already discussed in our previous paper.[37] Possible reasons for this synergetic interaction are:

- a) Agglomeration, particularly of Ag particles, is prevented or at least reduced when they are covered by  $\text{Co}_3\text{O}_4$  particles, which leads to better distribution of the particles and a larger surface area.
- b) From SEM images, Ag particles are rougher after several electrochemical cycles. This roughened surface seems to remain stable, which might be due to a stabilization of the roughened Ag by  $\text{Co}_3\text{O}_4$  when they are in contact in the mixture.
- c) An electronic effect: the interaction between Ag and  $\text{Co}_3\text{O}_4$  modifies the electronic properties of the Ag and cobalt-oxide and changes the electron density and binding energy. Such an effect often has been reported for bimetallic catalysts,[62] and was also reported for combinations of oxides with metals, such as in the case of Pt-BSCF oxide.[15] For a Pd- $\text{WO}_3/\text{C}$  catalyst, XPS results also showed strong interaction and a shift in the  $\text{Pd}_{3d}$  peak. Cobalt was also found to perturb the Ag surface sites in their alloy according to DFT and CV study.[21, 36]
- d) A spillover mechanism: Here, e.g. Ag facilitates O–O bond breaking; then the adsorbed oxygen species spills over to  $\text{Co}_3\text{O}_4$ , where the electroreduction takes place, which release more active sites on Ag surface for further molecules to react. Thus, an improved activity is obtained for ORR. This mechanism is demonstrated in the cartoon shown in Fig. 7. Similarly, for OER,  $\text{OH}^-$  adsorbs and then diffuses to Ag-oxide where OER takes place. Therefore, the two components may be active for two different reaction steps: Ag is predominant in O–O bond splitting in ORR and  $\text{Co}_3\text{O}_4$  dominates in the oxidation of water (OER). The combination of two metals for two steps has also been used for design of bimetallic Pd-Co catalyst for ORR.[63]

e) As shown by the XPS results, the presence of Ag facilitates potential induced redox switching in Co<sub>3</sub>O<sub>4</sub> to Co(II) and therefore, also most probably the redox switching in the catalytic cycle during OER and ORR similar to the case of Pt with MoO<sub>x</sub>[64] and as well other oxides.[52, 53] On the other hand, the presence of Co not only leads to an increased stability of the silver oxide, as shown by the shift of the silver oxide reduction peak to a lower potential in the mixed catalyst compared to the pure Ag, but also to an increased amount of silver oxide (*cf.* Fig. 1a and b). This indicates a stronger adsorbed-oxygen interaction with Ag in the mixed catalyst. Therefore, Ag catalyzes the redox switching of Co, and Co catalyzes the redox switching of Ag.

f) The O<sub>2</sub> molecule reacts (or is formed) directly at the interphase boundary line between Ag and Co<sub>3</sub>O<sub>4</sub> with a simultaneous binding to both surfaces. Therefore, O<sub>2</sub> dissociation process could have lower reaction barriers on the triple phase boundary (TPB) at mixed catalyst than on the double phase boundary (DPB) at pure Ag. So, O<sub>2</sub> molecules prefer being reduced at TPB than on DPB. A partial burying of the Co<sub>3</sub>O<sub>4</sub> into the surface leads to an increased interphase boundary.

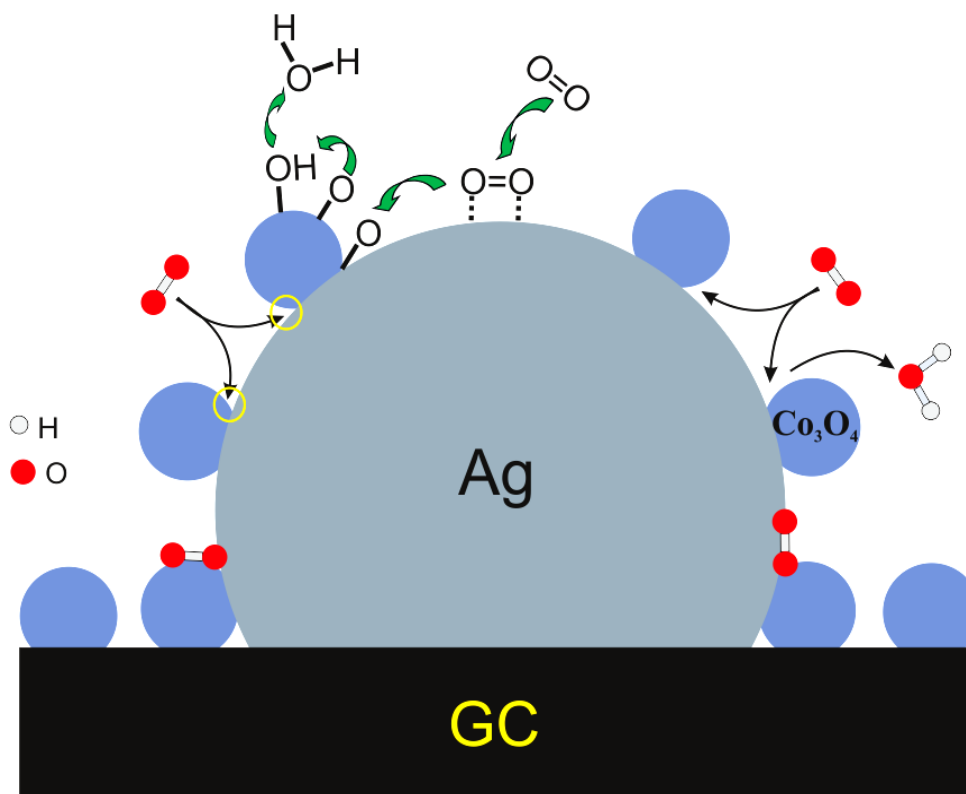


Fig. 7. Schematic illustration of the proposed mechanism of ORR and OER at bimetallic Ag<sub>311</sub>+Co<sub>3</sub>O<sub>4</sub> mixed catalyst.

Catalyst material	Electrolyte	ORR					OER				
		$E_{1/2}/V_{RHE}$	Onset Pot./ $V_{RHE}$	J/mA $cm^{-2}$ @ $0.8V_{RHE}$	Tafel slope at low overpot./ $mVdec^{-1}$	E/ V @1.5 $mA cm^{-2}$	Onset Pot./ $V_{RHE}$ * from DEMS <sup>[37]</sup>	J/mA $cm^{-2}$ @ $1.7V_{RHE}$	Tafel Slope	E/ V @ $4 mA cm^{-2}$	$\Delta E/V$
Ag311	0.1M LiOH	0.65	~0.87	0.11	90	0.61	>1.65*	1.1	--	>1.8	>1.19
Co <sub>3</sub> O <sub>4</sub>	0.1M LiOH	0.33	~0.71	0.00	~180	0.24	~1.55*	4.0	~70	1.70	1.46
Ag311+Co <sub>3</sub> O <sub>4</sub> (10wt%)	0.1M LiOH	0.65	~0.91	0.22	92	0.65	~1.55*	6.5	~115	1.64	0.99
Ba <sub>0.9</sub> Co <sub>0.5</sub> Fe <sub>0.4</sub> Nb <sub>0.1</sub> O <sub>3-<math>\delta</math></sub> [34]	0.1M KOH	0.64	0.75	Nil	--	0.65	1.55	6.2	--	1.63	0.98
Ag-MnO <sub>2</sub> <sup>[35]</sup>	0.1M KOH	0.64	~0.85	~0.29	77	0.63	~1.67	0.55	94	1.85	1.22
Ag-Co alloy <sup>[36]</sup>	0.1M NaOH	~0.81	~0.8	2.0	~40	0.82	OER not reported				
20 wt%Pt/C <sup>[37]</sup>	0.1M LiOH	0.87	~1.02	4.35	58	0.91	>1.58	1.67	--	1.77	0.86

Table 2. Summary of the electrochemical parameters for ORR and OER for our mixed catalyst and comparison to catalysts from literature.

## 5.5. Conclusion

We presented a facile procedure for the design of a bifunctional catalyst with promising electrocatalytic activity. A hybrid of Co<sub>3</sub>O<sub>4</sub> with superior OER activity and Ag with superior ORR activity was prepared by ultrasonic mixing. This mixed catalyst showed better activity to ORR than the pure Ag and better activity to OER than Co<sub>3</sub>O<sub>4</sub> alone. Furthermore, surface analysis revealed the effectiveness of the unique morphology of the composite to oxygen activity. Addition of only 10 wt% of Co<sub>3</sub>O<sub>4</sub> to Ag in the mixture leads to 88% coverage of the Ag surface by the oxide, and despite that it leads to a higher activity than pure Ag. Moreover, this catalyst with only 10% Co<sub>3</sub>O<sub>4</sub> has a higher activity for OER than a 100% Co<sub>3</sub>O<sub>4</sub> catalyst of the same loading. This activity improvement could be attributed to a synergistic effect between Co<sub>3</sub>O<sub>4</sub> and Ag, which could originate from redox switching effect, electronic effect and spillover effect. Silver particles were not only able to offer a synergistic effect by geometrically and electronically modifying the Co<sub>3</sub>O<sub>4</sub>, but also provide a large amount of highly active sites and more three-phase boundaries, which improved the catalytic activity of the mixed Ag<sub>311</sub>+Co<sub>3</sub>O<sub>4</sub> bimetallic catalyst towards OER and ORR in alkaline media. XPS results showed that the presence of Ag cation in contact with Co<sub>3</sub>O<sub>4</sub> facilitates the redox switching in Co<sub>3</sub>O<sub>4</sub>, which leads to an enhanced catalytic activity. This Carbon-free inexpensive composite exhibited good ORR activity comparable to the best-known precious Pt catalyst, but with superior activity and stability for OER. Such a catalyst is a valuable candidate for ORR/OER that could be applied in alkaline fuel cells and metal air batteries.

## 5.6. References

- [1] B. Scrosati, J. Garche, *Journal of Power Sources* 195 (2010) 2419-2430.
- [2] J.-S. Lee, S. Tai Kim, R. Cao, N.-S. Choi, M. Liu, K.T. Lee, J. Cho, *Advanced Energy Materials* 1 (2011) 34-50.
- [3] D. Safanama, D. Damiano, R.P. Rao, S. Adams, *Solid State Ionics* 262 (2014) 211-215.
- [4] G. Girishkumar, B. McCloskey, A.C. Luntz, S. Swanson, W. Wilcke, *The Journal of Physical Chemistry Letters* 1 (2010) 2193-2203.
- [5] Z.Y. Liu, J.S. Wainright, M.H. Litt, R.F. Savinell, *Electrochimica Acta* 51 (2006) 3914-3923.
- [6] J.S. Spendelow, A. Wieckowski, *Physical Chemistry Chemical Physics* 6 (2004) 5094-5118.
- [7] K.A. Striebel, F.R. McLarnon, E.J. Cairns, *Journal of The Electrochemical Society* 137 (1990) 3351-3359.
- [8] J.B. Henry, A. Maljusch, M. Huang, W. Schuhmann, A.S. Bondarenko, *ACS Catalysis* 2 (2012) 1457-1460.
- [9] N. Bogolowski, T. Nagel, B. Lanova, S. Ernst, H. Baltruschat, K. Nagabhushana, H. Boennemann, *Journal of Applied Electrochemistry* 37 (2007) 1485 - 1494.
- [10] P.K. Babu, A. Lewera, J.H. Chung, R. Hunger, W. Jaegermann, N. Alonso-Vante, A. Wieckowski, E. Oldfield, *Journal of the American Chemical Society* 129 (2007) 15140-15141.
- [11] T. Toda, H. Igarashi, H. Uchida, M. Watanabe, *Journal of the Electrochemical Society* 146 (1999) 3750-3756.
- [12] V.R. Stamenkovic, B. Fowler, B.S. Mun, G. Wang, P.N. Ross, C.A. Lucas, N.M. Markovic, *Science* 315 (2007) 493-497.

- [13] L.R. Merte, F. Behafarid, D.J. Miller, D. Friebel, S. Cho, F. Mbuga, D. Sokaras, R. Alonso-Mori, T.-C. Weng, D. Nordlund, A. Nilsson, B. Roldan Cuenya, *ACS Catalysis* 2 (2012) 2371-2376.
- [14] L. gan, C. Cui, S. Rudi, P. Strasser, *Topics in Catalysis* 57 (2014) 236-244.
- [15] Y. Zhu, C. Su, X. Xu, W. Zhou, R. Ran, Z. Shao, *Chemistry – A European Journal* 20 (2014) 15533-15542.
- [16] N.I. Andersen, A. Serov, P. Atanassov, *Applied Catalysis B: Environmental* 163 (2015) 623-627.
- [17] W. Yang, J. Salim, S. Li, C. Sun, L. Chen, J.B. Goodenough, Y. Kim, *Journal of Materials Chemistry* 22 (2012) 18902-18907.
- [18] S. Trasatti, *Electrodes of conductive metallic oxides*, Elsevier Scientific Pub.Co., Amsterdam, 1980.
- [19] Y. Zhan, C. Xu, M. Lu, Z. Liu, J.Y. Lee, *Journal of Materials Chemistry A* 2 (2014) 16217-16223.
- [20] Q. Tang, L. Jiang, J. Qi, Q. Jiang, S. Wang, G. Sun, *Applied Catalysis B: Environmental* 104 (2011) 337-345.
- [21] Y. Wang, X. Lu, Y. Liu, Y. Deng, *Electrochemistry Communications* 31 (2013) 108-111.
- [22] S. Zhuang, K. Huang, C. Huang, H. Huang, S. Liu, M. Fan, *Journal of Power Sources* 196 (2011) 4019-4025.
- [23] Y. Liang, H. Liang, J. Wang, Y. Zhou, J. Li, T. Wang, H. Regier, Dai, *Journal of the American Chemical Society* 134 (2012) 3517-3523.
- [24] Y.J. Sa, K. Kwon, J.Y. Cheon, F. Kleitz, S.H. Joo, *Journal of Materials Chemistry A* 1 (2013) 9992-10001.
- [25] T.Y. Ma, S. Dai, M. Jaroniec, S.Z. Qiao, *Journal of the American Chemical Society* 136 (2014) 13925-13931.
- [26] T. Maiyalagan, K.A. Jarvis, S. Therese, P.J. Ferreira, A. Manthiram, *Nat Commun* 5 (2014).
- [27] A. Zadick, L. Dubau, N. Sergent, G. Berthome, M. Chatenet, *ACS Catalysis* 5 (2015) 4819-4824.
- [28] S. Velraj, J.H. Zhu, *Journal of Electroanalytical Chemistry* 736 (2015) 76-82.
- [29] Y. Liang, Y. Li, H. Wang, J. Zhou, J. Wang, T. Regier, H. Dai, *Nature Materials* 10 (2011) 780-786.
- [30] J.-J. Han, N. Li, T.-Y. Zhang, *Journal of Power Sources* 193 (2009) 885-889.
- [31] B.B. Blizanac, P.N. Ross, N.M. Markovic, *Journal of Physical Chemistry B* 110 (2006) 4735-4741.
- [32] S. Kumar, C. Selvaraj, L.G. Scanlon, N. Munichandraiah, *Physical Chemistry Chemical Physics* 16 (2014) 22830-22840.
- [33] M. De Koninck, B. Marsan, *Electrochimica Acta* 53 (2008) 7012-7021.
- [34] C. Jin, Z. Yang, X. Cao, F. Lu, R. Yang, *International Journal of Hydrogen Energy* 39 (2014) 2526-2530.
- [35] F.W.T. Goh, Z. Liu, X. Ge, Y. Zong, G. Du, T.S.A. Hor, *Electrochimica Acta* 114 (2013) 598-604.
- [36] A. Holewinski, J.-C. Idrobo, S. Linic, *Nat. Chem.* 6 (2014) 828-834.
- [37] H.M.A. Amin, H. Baltruschat, D. Wittmaier, K.A. Friedrich, *Electrochimica Acta* 151 (2015) 332-339.
- [38] D. Wittmaier, N. Wagner, K.A. Friedrich, H.M.A. Amin, H. Baltruschat, *Journal of Power Sources* 265 (2014) 299-308.
- [39] D. Wittmaier, N.A. Cañas, I. Biswas, K.A. Friedrich, *Advanced Energy Materials* 5 (2015) 1500763-1500771.

- [40] E. Kirowa-Eisner, Y. Bonfil, D. Tzur, E. Gileadi, *Journal of Electroanalytical Chemistry* 552 (2003) 171-183.
- [41] M. Hepel, S. Bruckenstein, *Electrochimica Acta* 34 (1989) 1499-1504.
- [42] G.K.H. Wiberg, K.J.J. Mayrhofer, M. Arenz, *Fuel Cells* 10 (2010) 575-581.
- [43] T.J. Schmidt, H.A. Gasteiger, G.D. Stab, P.M. Urban, D.M. Kolb, R.J. Behm, *Journal of the Electrochemical Society* 145 (1998) 2354-2358.
- [44] F. Lu, G.N. Salaita, H. Baltruschat, A.T. Hubbard, *Journal of Electroanalytical Chemistry* 222 (1987) 305-320.
- [45] J. Chivot, L. Mendoza, C. Mansour, T. Pauporté, M. Cassir, *Corrosion Science* 50 (2008) 62-69.
- [46] M.C. Biesinger, B.P. Payne, A.P. Grosvenor, L.W.M. Lau, A.R. Gerson, R.S.C. Smart, *Applied Surface Science* 257 (2011) 2717-2730.
- [47] J. Yang, H. Liu, W.N. Martens, R.L. Frost, *The Journal of Physical Chemistry C* 114 (2009) 111-119.
- [48] H. Göhr, A. Breitenstein, *Electrochimica Acta* 13 (1968) 1377-1388.
- [49] A.F. Holleman, E. Wiberg, *Lehrbuch der Anorganischen Chemie*, 33 ed., Walter de Gruyter, Berlin, 1985.
- [50] C.D. Wagner, W.M. Riggs, L.E. Davis, J.F. Moulder, G.E. Muilenberg, *HANDBOOK OF X-RAY PHOTOELECTRON SPECTROSCOPY*, Perkin-Elmer Corporation, Eden Prairie, 1979.
- [51] V.K. Kaushik, *Journal of Electron Spectroscopy and Related Phenomena* 56 (1991) 273-277.
- [52] L.I. Krishtalik, *Electrochimica Acta* 26 (1981) 329-337.
- [53] A.C.C. Tseung, S. Jasem, *Electrochimica Acta* 22 (1977) 31-34.
- [54] J.L. Fernández, M.R. Gennero de Chialvo, A.C. Chialvo, *Electrochimica Acta* 47 (2002) 1145-1152.
- [55] Q. Fu, W.-X. Li, Y. Yao, H. Liu, H.-Y. Su, D. Ma, X.-K. Gu, L. Chen, Z. Wang, H. Zhang, B. Wang, X. Bao, *Science* 328 (2010) 1141-1144.
- [56] F. Hernandez, H. Baltruschat, *Langmuir* 22 (2006) 4877-4884.
- [57] Z. Jusys, H. Massong, H. Baltruschat, *Journal of the Electrochemical Society* 146 (1999) 1093.
- [58] G. Samjeské, X.-Y. Xiao, H. Baltruschat, *Langmuir* 18 (2002) 4659-4666.
- [59] H. Massong, S. Tillmann, T. Langkau, E.A. Abd El Meguid, H. Baltruschat, *Electrochimica Acta* 44 (1998) 1379-1388.
- [60] J. Suntivich, K.J. May, H.A. Gasteiger, J.B. Goodenough, Y. Shao-Horn, *Science* 334 (2011) 1383-1385.
- [61] T. Poux, A. Bonnefont, G. Kéranguéven, G.A. Tsirlina, E.R. Savinova, *ChemPhysChem* 15 (2014) 2108-2120.
- [62] H. Baltruschat, S. Ernst, N. Bogolowski, in: E. Santos, W. Schmickler (Eds.), *Catalysis in Electrochemistry*, Wiley, 2011, pp. 297-337.
- [63] J.L. Fernandez, D.A. Walsh, A.J. Bard, *Journal of the American Chemical Society* 127 (2005) 357-365.
- [64] R. Vellacheri, S.M. Unni, S. Nahire, U.K. Kharul, S. Kurungot, *Electrochimica Acta* 55 (2010) 2878-2887.

## Supporting Information

### XPS measurements

For the electrochemical preparation, the electrode was transferred into an ante-chamber, separated from the main chamber by a gate valve. The latter was closed, and the chamber filled with argon. The electrochemical cell was introduced into the ante-chamber through a second gate valve connected to bellows that were purged with argon for at least one hour prior to the experiment. The end of the bellows was closed with a Teflon body that contained a pin hole through which a glass capillary was passed. The electrolyte was pressed into the cell from a storage vessel outside the UHV-chamber through the capillary that also connects the cell to the reference electrode. The counter electrode was a long platinum wire that was connected to a steel pin, pressed into the Teflon body. The working electrode was connected via a feed through at the manipulator, which was also used to ground the sample during the XPS-measurement.

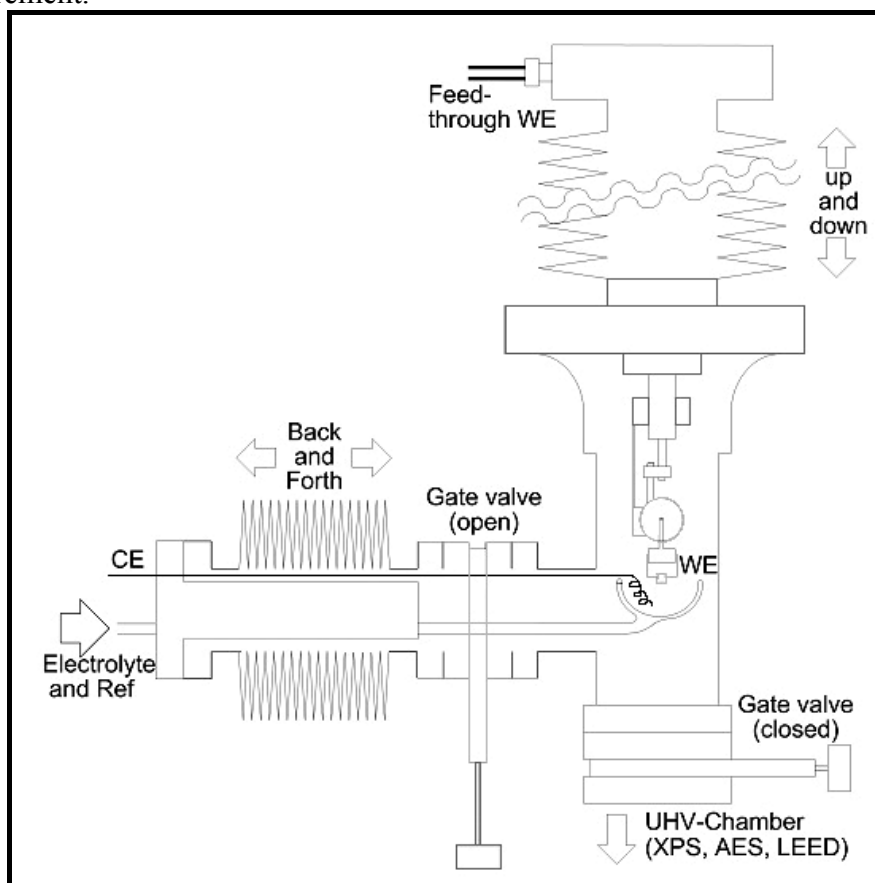


Fig. S1. Schematic of EC-XPS system permitting sample transport between aqueous media and UHV.

In order to start the electrochemical measurement, the manipulator and the electrode with it was descended until a contact to the electrolyte was made. In order to bring the electrode in a hanging meniscus arrangement the electrode was retracted again, and the electrochemical run was conducted. After the electrochemical experiment, the electrolyte was replaced with  $10^{-4}$  M LiOH solution. The electrode was dipped into this solution under potential control for several times in order to remove excess amounts of conducting salt, which would cover the electrode, after the solvent was evaporated under UHV conditions. The electrochemical cell

then was removed from the ante-chamber, the gate valve to the bellows was closed and the ante-chamber was evacuated. By opening the gate valve to the main chamber a connection was made and the electrode was placed in front of the spectrometer.

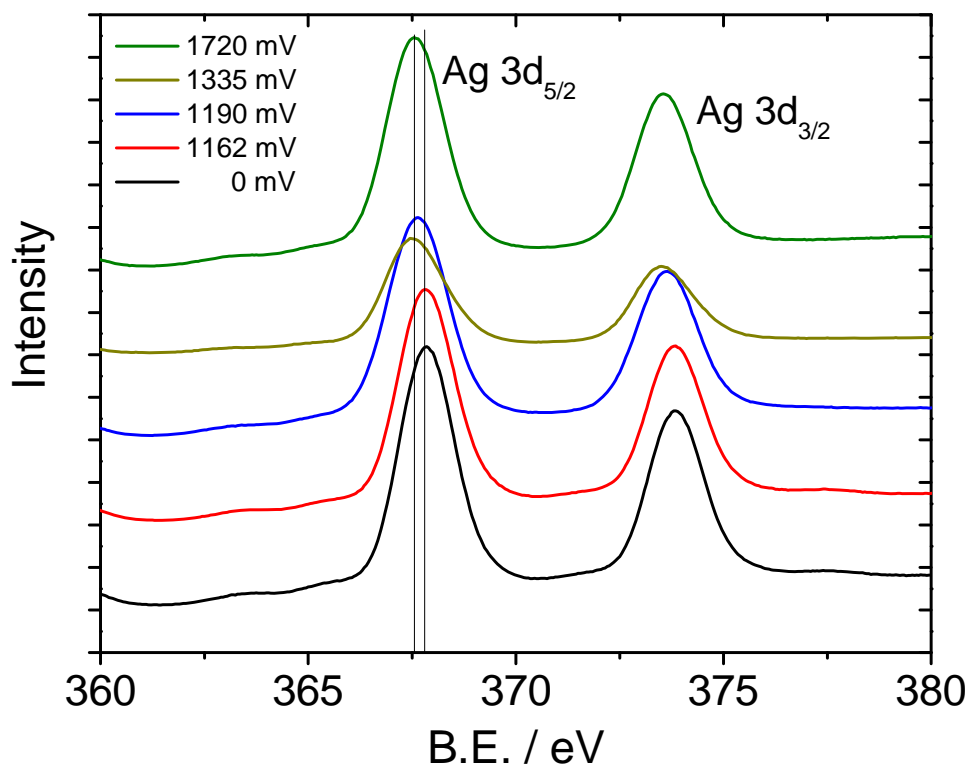


Fig. S2: XP-Spectrum of the Ag 3d-lines after polarising a polycrystalline silver electrode in an electrolyte of 0.1 M LiOH to the indicated potentials.

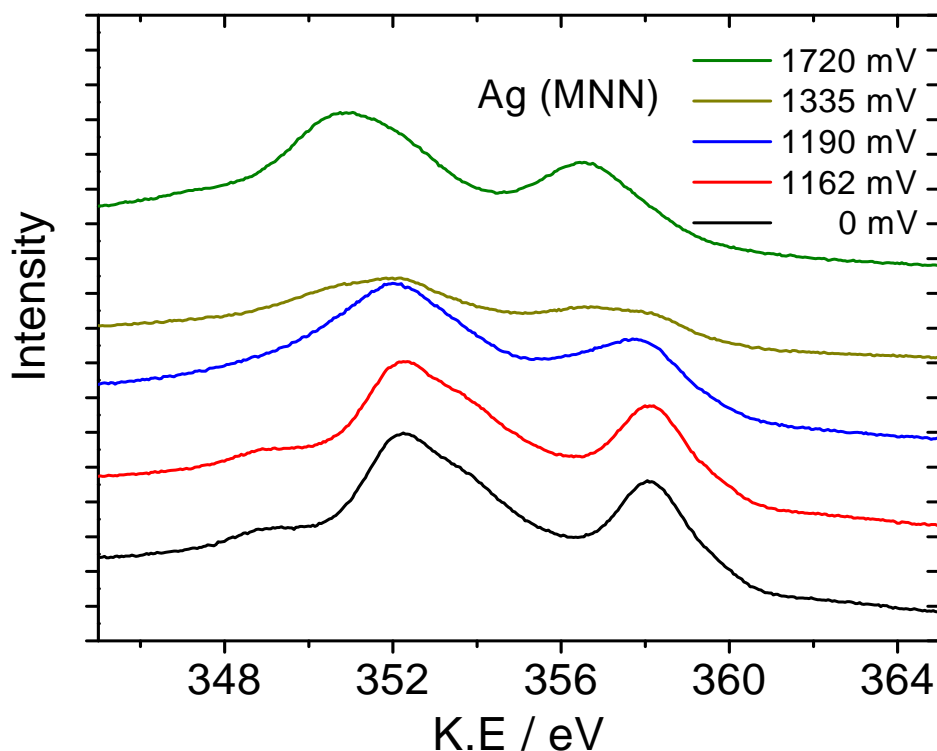


Fig. S3: XP-Spectrum of the Ag MNN-lines after polarising a polycrystalline silver electrode in an electrolyte of 0.1 M LiOH to the indicated potentials.

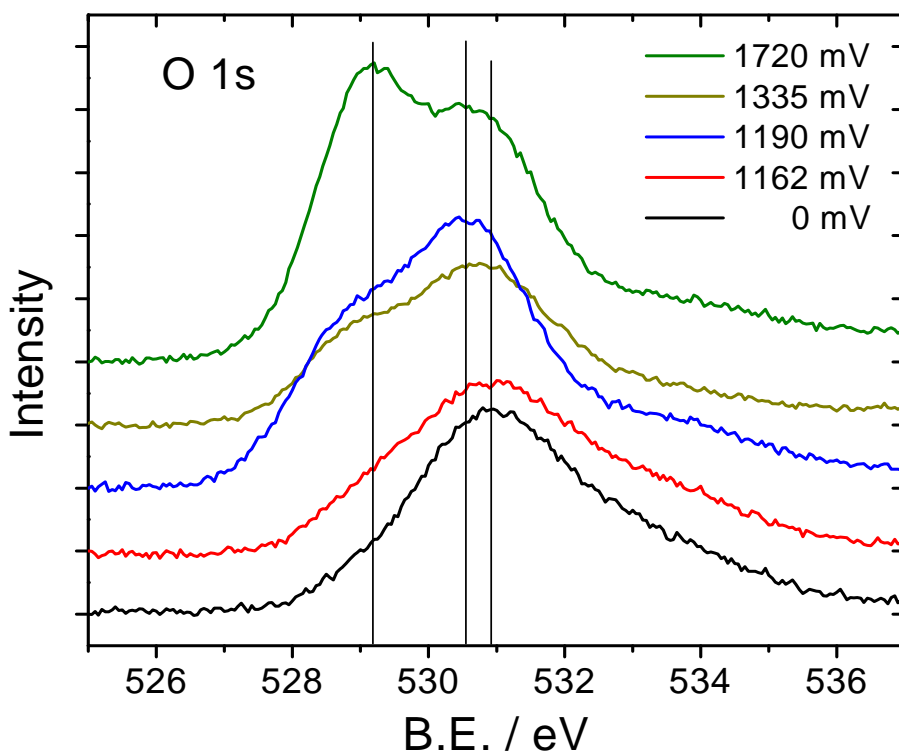


Fig. S4: XP-Spectrum of the O 1s-line after polarising a polycrystalline silver electrode in an electrolyte of 0.1 M LiOH to the indicated potentials. (Contributions at higher binding energies are to oxygen containing carbon contaminants. Their contribution is reduced as the electrode is polarised to higher potentials).

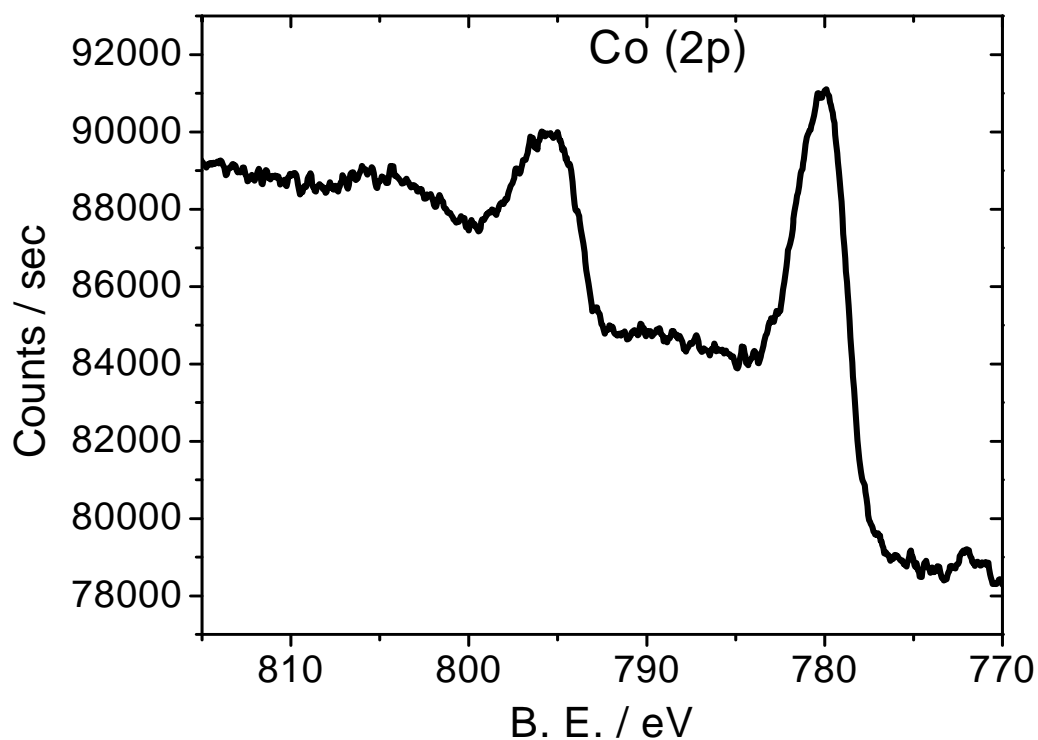


Fig. S5: XP-Spectrum of the Co 2p-lines after dipping a polycrystalline silver electrode covered with  $50 \mu\text{g cm}^{-2}$   $\text{Co}_3\text{O}_4$  nanoparticles and  $400 \mu\text{g cm}^{-2}$  Ag311 into an electrolyte of 0.1 M LiOH at 0.02 V.



## 6. Further investigation of various non-precious catalysts in alkaline media: Explorative study

### 6.1. Introduction

In this chapter, we present an explorative study on the catalytic activity of different catalysts towards ORR/OER. The results of this screening helped us to achieve an enhanced activity at the promising catalyst Ag+Co<sub>3</sub>O<sub>4</sub>, which is described in the previous two chapters. Here, additional experiments and results on different catalysts are presented. Ag is known as an active material towards ORR in alkaline media.[1-4] DFT calculations concluded that on the surface of Pt and Ag, oxygen absorbed on the surface shifts the activity to weak binding regions, thus enhances the ORR activity in alkaline media.[5] Therefore, we studied the activity of different Ag catalysts to get information on behavior of each and compare them. Co<sub>3</sub>O<sub>4</sub> is also known as a good material for OER. Thus, we aimed at mixing it with Ag to get a synergistic effect and enhanced activity. However, the mixed Ag/CoO bimetallic catalyst showed instability and lower ORR activity than single Ag. This could be due to agglomeration of the Ag flakes used. Therefore, we extended our investigations to study some factors, which influence the performance: different particle sizes of Ag and Co-oxide are studied. The loading effect of the catalyst onto the substrate is found to affect the activity. Also, the electrolyte concentration and nature of cationic species alter the activity of the catalyst. By the end, and after optimization of the composition, we achieved an improved activity on Ag311+Co<sub>3</sub>O<sub>4</sub> (10 wt%) mixed catalyst. This catalyst revealed also a good stability, which makes it a potential candidate for oxygen electrodes.

To test this synergistic effect with other oxides such as the perovskite, Ag311+LSF catalyst is examined, and it exhibited an enhanced activity (in particular, for OER), although it is lower than Ag311+Co<sub>3</sub>O<sub>4</sub> catalyst. Moreover, replacing Ag with Ni in Ni+Co<sub>3</sub>O<sub>4</sub> mixed catalyst showed insignificant improvement compared to pure Ni or Co<sub>3</sub>O<sub>4</sub>, and lower activity than Ag+Co<sub>3</sub>O<sub>4</sub> (in particular, for ORR), implying the effective role of Ag over Ni. This might be due to the lower electric conductivity of Ni than Ag. Surface analyses (SEM and EDX) of the catalysts were carried out to better characterize the morphology and composition of the surface.

### 6.2. Investigation of Ag catalysts in alkaline media

#### 6.2.1. Electrochemical behavior of Ag catalyst

Ag polycrystalline (pc) electrode is firstly characterized by CV. Fig. 1a shows the CVs of pure Ag in Ar-saturated 0.1 and 1.0M LiOH solution. Three oxidation peaks (A<sub>1</sub>, A<sub>2</sub> and A<sub>3</sub> at 1.22, 1.32 and 1.62 V, respectively) and two reduction peaks (C<sub>3</sub> at 1.35V and C<sub>2</sub> at 1.04V) for Ag in 0.1M LiOH are observed. The peaks A<sub>1</sub>, A<sub>2</sub> and A<sub>3</sub> are assigned to the oxidation of Ag to Ag(OH)<sub>2</sub><sup>-</sup>, afterwards to Ag<sub>2</sub><sup>I</sup>O and then to Ag<sup>I</sup>Ag<sup>III</sup>O<sub>2</sub>, respectively, as reported in our previous paper.[1] Cathodic peaks C<sub>3</sub> and C<sub>2</sub> are assigned to reduction of the oxides formed at A<sub>3</sub> and A<sub>2</sub>, respectively. At higher concentration, the peaks A<sub>1</sub>, A<sub>2</sub>, C<sub>3</sub> and C<sub>2</sub> are shifted by ca. 30 mV to more positive potential, whereas the peak A<sub>3</sub> is shifted by the same extent to more negative potential.

It is interesting to know how deep the oxide layer is grown on the Ag surface. From the calculation of the charge corresponding to Ag<sup>I</sup> oxidation (Peak A<sub>2</sub>) in the different Ag catalysts, the number of monolayers, and in turn the thickness of the oxide is estimated.

Different thicknesses are obtained (see different peak charges in Fig. 1b): the charges obtained are 4.3, 2.2, 11.2  $\text{mC cm}^{-2}_{\text{tr}}$  for Ag (pc), Ag311 (1  $\mu\text{m}$ ) and Ag (40  $\mu\text{m}$ ) catalysts, respectively, with respect to the true surface area of Ag, which is obtained below from Pb-UPD method. Taking the value of 260  $\mu\text{C cm}^{-2}$  for a monolayer, thus we obtain 17, 9 and 43 monolayers (i.e. roughly 85, 45 and 215 nm thick considering 5 nm as monolayer thickness) for the catalysts, respectively. In case of the mixed Ag331+Co<sub>3</sub>O<sub>4</sub> (10 w%) catalyst, 33  $\text{mC cm}^{-2}$  is obtained (i.e. 127 monolayers), which is more than that obtained in pure Ag311. This suggests that Co<sub>3</sub>O<sub>4</sub> could catalyze the oxidation of Ag in their mixture. Therefore, the depth of oxidation of the Ag surface is dependent on the particle size and the morphology of the Ag material.

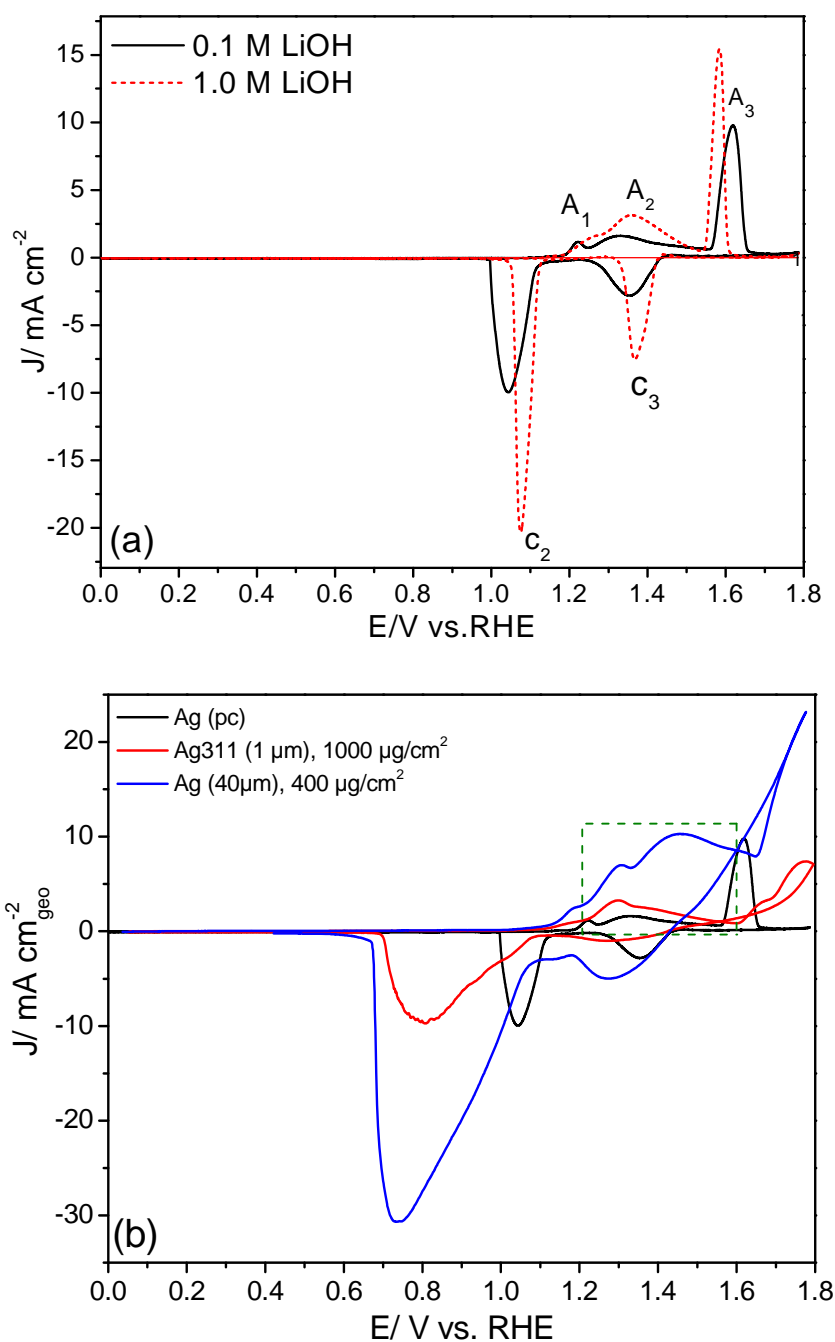


Fig. 1. (a) CVs of bare Ag (pc) in Ar-saturated 0.1M and 1M LiOH solution with sweep rate of 50  $\text{mV s}^{-1}$ . (b) CVs in Ar-saturated 0.1M LiOH solution with 50  $\text{mV s}^{-1}$ , and the loading is indicated in the graph.

### 6.2.2. Electrochemical surface area determination using Pb-UPD

Determination of *the electrochemically active surface area (ECA)* is important for proper comparison of the activities of different catalysts. However, there is no general standard method for all catalysts. For Pt-based catalysts, ECA is determined by stripping of underpotential deposited hydrogen (H-UPD) or adsorption of CO monolayer.[6] For non-platinum catalysts, these methods are not possible since the materials are inactive towards these reactions. As an alternative, Trasatti et al. suggested metal-UPD method.[7] This method has been successively applied: for example, Cu-UPD for Ru or Se on Pt electrodes.[6] For Ag-based catalysts, Pb-UPD[8] or Tl-UPD[9] are proper methods for ECA determination. Here, Pb<sub>UPD</sub> is applied in alkaline media for the determination of the electrochemically accessible active sites on Ag (pc) and Ag particles/GC electrodes. In this method, a lead monolayer is underpotentially deposited, and then stripped off the catalyst via a linear potential scan. The mechanism of Pb-UPD has been described elsewhere.[8, 10] The mechanism of Pb-UPD involves the reduction of adsorbed lead species on Ag to Pb<sub>UPD</sub>, and OH<sup>-</sup> is expelled from the surface at lower potentials (around 0.23V vs. RHE) according to eq. 6.1



At more negative potentials, surface coverage of adsorbed Pb<sup>II</sup> is reached after equilibrium, and dissolved lead species are reduced to Pb<sub>bulk</sub> according to eq. 6.2:



In addition, Pb can react slowly with Ag electrode, and forms Pb-Ag alloy, depending on the number of cycles.

Stripping of the Pb-UPD follows the reverse of eq. 6.1. A monolayer of Pb is deposited on Ag surface at potentials more positive than the equilibrium bulk deposition potential. The optimum potential is as negative as possible, while also it should avoid multilayer deposition.[3] Deposition of multilayers (bulk deposition) appears in the stripping voltammogram as a pre-peak (at ca. 0.25V), leading to an overestimation of the surface area. Different deposition potentials ( $E_d=0.17V$  to  $0.25V$ ) for a time of  $t_d=180$  s were examined in Ar-saturated  $125\mu M Pb(NO_3)_2+0.1M LiOH$  solution with  $100 mV s^{-1}$  to obtain the optimal potential for Pb-UPD on Ag(pc), as shown in Fig. 2a. Similar procedure has been reported in KOH solution.[3] The optimized condition obtained for our Ag(pc) electrode is  $E_d=0.24V$  for  $t_d=180$  s, where the stripping charge is the largest and no pre-peak for bulk deposition is observed. These values might slightly differ at Ag nanoparticles catalyst. The optimized stripping CVs of Pb-UPD formed on Ag(pc) at  $E_d=+0.24V$  for 180 s are depicted in Fig. 2b. Scanning to more negative potentials (dashed line) leads to bulk deposition and Pb-Ag alloy formation with an additional anodic peak at ca. 0.25V. The continuation of a negative current in the cathodic scan is a sign of the bulk deposition. The adsorption of Pb on Ag is incommensurate, because the diameter of the Pb atom is larger than the distance between adjacent Ag sites. Accordingly, the maximum charge per unit surface area is  $260 \mu C cm^{-2}$  for silver. This corresponds to the occupation of about 2/3 of the sites on Ag.[8] Pb-stripping from UPD resulted in a surface charge density of  $380-410 \mu C cm^{-2}$ , which is corresponding to a roughness factor of 1.5, which is reasonable for smooth Ag (pc) surface, and is consistent with the results reported in literature of  $400 \mu C cm^{-2}$  for Ag(pc).[8]

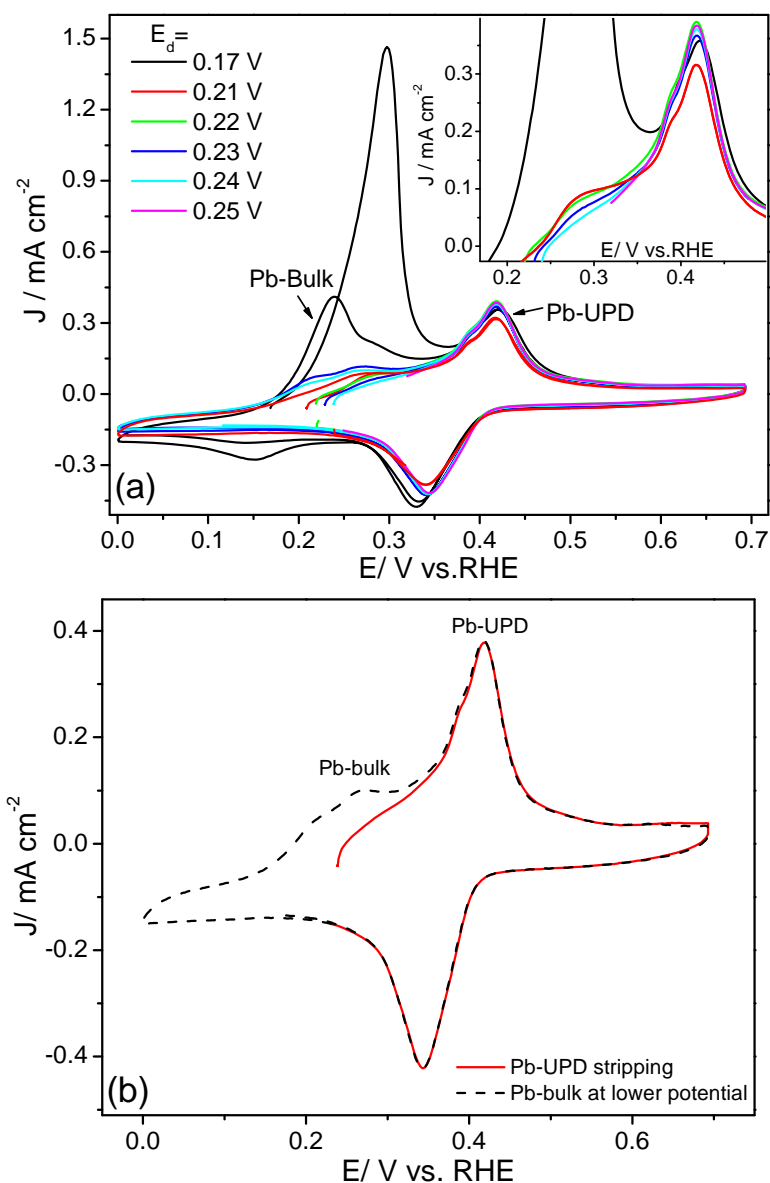


Fig. 2. (a) CV stripping of Pb-UPD on Ag(pc) electrode in Ar-saturated  $125\mu\text{M Pb}(\text{NO}_3)_2 + 0.1\text{M LiOH}$  solution with  $100\text{ mV s}^{-1}$  after  $t_d = 180\text{ s}$  and at different deposition times ( $E_d$ ), and the consecutive cycle with more negative potential limit. Inset is an expansion of the stripping peak. (b) Stripping CVs of Pb-UPD formed on Ag at  $E_d = +0.24\text{V}$  for  $180\text{ s}$ , (solid line) and consecutive CV with more negative potential limit (dashed line).

Analogous to the procedure of Pb-UPD used for Ag(pc), ECA of Ag ( $40\ \mu\text{m}$ ) catalyst is estimated using similar conditions (described in the caption of Fig. 3). The ECA is determined before and after ORR/OER cycles in LiOH, and the curves are depicted in Fig. 3. The surface stripping charge obtained pre-cycling at this Ag microparticles/GC electrode is  $\sim 1.6\text{ mC cm}^{-2}$  (this corresponds to a roughness factor of about 6), while that obtained post-cycling is  $1.3\text{ mC cm}^{-2}$ . The decrease of the real surface area after several cycles ( $\sim 17\%$  loss) could be due to a partial detachment of Ag particles from the electrode during electrolyte exchange step or during rotation in the electrochemical cycling.

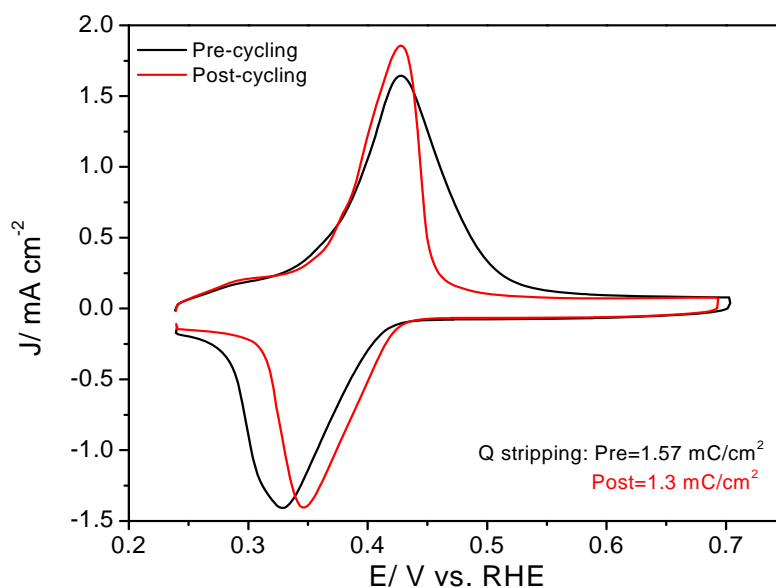


Fig. 3. CV stripping of Pb-UPD on Ag(40  $\mu\text{m}$ )/GC electrode in Ar-saturated 125  $\mu\text{M}$   $\text{Pb}(\text{NO}_3)_2$ +0.1M LiOH solution with  $100 \text{ mV s}^{-1}$  after deposition at  $E_d=0.24 \text{ V}$  for  $t_d=180 \text{ s}$ . Loading:  $200 \mu\text{g cm}^{-2}$ . Black curve: pre-cycling, and the red curve: post-cycling.

For Ag311 catalyst, a stripping charge of  $1.5 \text{ mC cm}^{-2}$  is obtained. Thus, the Ag particles are more roughened than the Ag (pc) surface. Comparison of the results is shown in Table 1.

Catalyst	Roughness factor	Area/mass	Specific activity@0.75V/ $\text{mA cm}^{-2}_{\text{tr}}$
Ag (pc)	1.5	--	0.12
Ag flakes (40 $\mu\text{m}$ )	6.0	$1.1/39=0.03 \text{ cm}^2/\mu\text{g}$	0.32
Ag311 (1 $\mu\text{m}$ )	5.8	$1.1/196=0.006 \text{ cm}^2/\mu\text{g}$	0.21

Table 1. Roughness factor and specific activity at different Ag catalysts (obtained from curves of Fig. 4b, and using the true surface area).

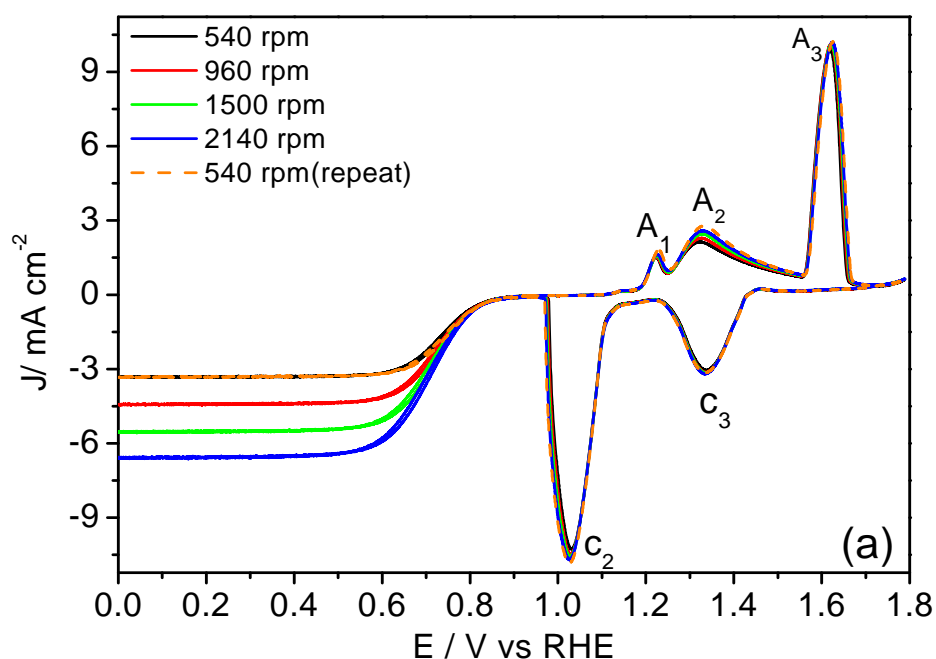
### 6.2.3. Catalytic activity towards ORR and OER: influence of particle size

Using RRDE, typical CVs of Ag (pc) with various rotation speeds were recorded, as shown in Fig. 4a. The onset potential for ORR is at ca. 0.9V for all rotation speeds. The redox peaks are reversible. Below 0.6V, well developed plateau is observed, indicating the pure diffusion-limited currents. The limiting current is directly proportional to the square route of scan rate, suggesting a diffusion limited process. Control experiment shows that with cycling the ORR and OER currents do not decay, indicating that the Ag surface is still active, and the silver oxide does not block the electrode surface. The electrode roughness increased slightly with cycling, as can be noticed from the slight increase of redox peak currents.

The performance of Ag catalyst towards ORR depends on the nature and size of Ag. Here, various Ag catalysts are investigated. The polarization curves of Ag(40  $\mu\text{m}$ ), Ag311(1 $\mu\text{m}$ ) and Ag(pc) electrodes are compared in Fig. 4b. Ag flakes (40  $\mu\text{m}$ )/GC electrode shows the highest ORR activity, where the overpotential is about 50 mV less than that of Ag311, and ca. 170 mV less than that of Ag (pc). For proper comparison, the specific activity (activity per true surface area) is plotted, as shown in the inset of Fig. 4b. The activity at the potential of interest (0.75V) at the three catalysts is shown in Table 1. Ag particles catalyst has significantly higher currents than Ag (pc). Thus, Ag microparticles are more active than the

polycrystalline electrode. This is attributed to the higher surface area, larger roughness and larger number of active sites on microparticles. This effect is in agreement with previous results comparing Ag NPs and Ag(pc).[3] On the other hand, Ag flakes are not stable, which might be due to their agglomeration during long-term cycling. Therefore, Ag311 is used in the development of our efficient bifunctional catalyst, as will be discussed below. At potentials below 0.4V, the current is limited by the pure diffusion process, as observed by the plateau. The diffusion-limited currents for these different electrodes are similar, and are close to the theoretical value for 4e-ORR at 960 rpm. Bare GC is known to have negligible effect on the ORR polarization curves of Ag/GC electrodes since GC has no current at potentials above 0.7V.

It is noteworthy to mention here that, also for  $\text{Co}_3\text{O}_4$  spinel; the activity depends on its particle size. Two different sizes (50 nm and 10  $\mu\text{m}$ ) are investigated, and they showed a clear difference: the smaller particle size catalyst is more active for both OER and ORR than the larger particles' catalyst of the same material and loading, see SI of chapter 7 for details.



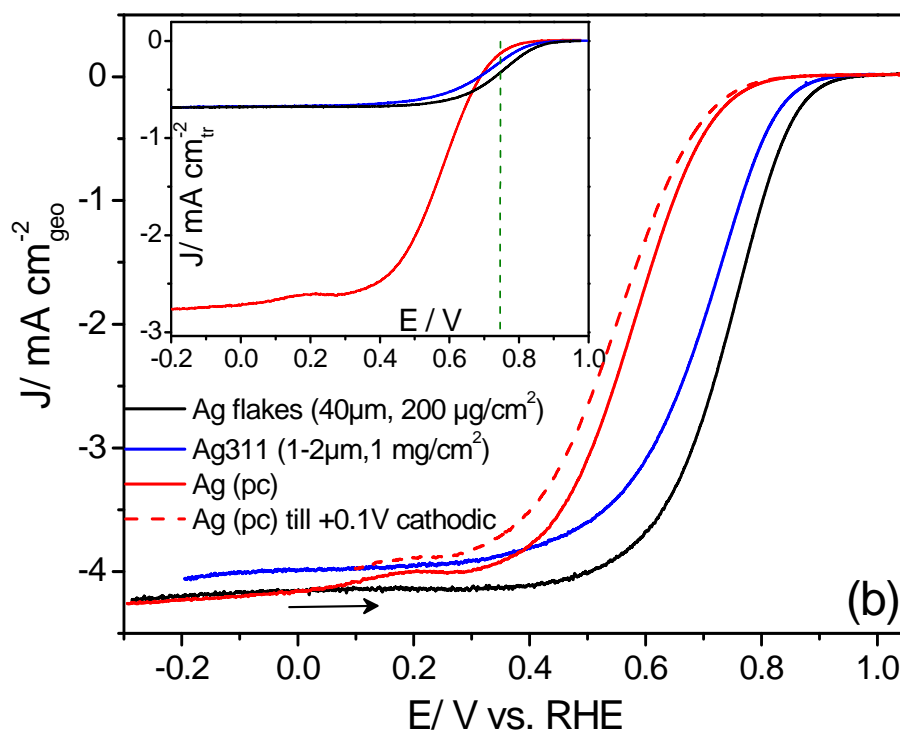


Fig. 4. (a) RRDE voltammograms for ORR at Ag (pc) with  $10 \text{ mV s}^{-1}$  in  $\text{O}_2$ -saturated 0.1M LiOH at different rotation rates. (b) RRDE measurements on Ag (pc), Ag flakes and Ag311 electrodes in  $\text{O}_2$ -saturated 0.1M LiOH solution at 960 rpm with  $10 \text{ mV s}^{-1}$ , upper potential limit was 1V except for Ag311 was 1.8V, the anodic scan is shown. Inset is the same curves corrected to the real surface area, which is obtained from Pb-UPD. The used loading is indicated in the graph.

### 6.3. Effect of catalyst loading

The influence of catalyst loading on the activity of ORR and the electrochemical behavior of Ag is also assessed. The polarization curves of three different loadings of Ag(40  $\mu\text{m}$ ) on GC are compared in Fig. 5a. It can be noticed that as the catalyst loading is increased, the polarization curves in ORR region are shifted to higher potentials, indicating higher activity. Moreover, for lower loading (100  $\mu\text{g cm}^{-2}$ ), the diffusion-limited current is lower, which is attributed to the incomplete coverage of the GC substrate. Surface redox peaks currents increase as the loading increases, which is due to the increase of the number of surface accessible sites. The charge of the oxidation/reduction peaks increases monotonically with the loading increase, but it is non-linear. The deviation from linearity (in particular, for the oxidation peaks) could be due to the fact that the same amount of Nafion binder is used for all loadings, which could facilitate agglomeration and reduce the exposed surface area in case of lower loading, leading to a smaller redox peak current than expected.

Furthermore, as the loading increases, the ring current decreases, and in turn the peroxide yield decreases, as shown in Fig. 5b and c. Peroxide amount of less than 4% is obtained for the 400  $\mu\text{g cm}^{-2}$  loading, suggesting the dominance of the 4e-pathway for ORR at this Ag/GC electrode. A similar effect has been previously reported on Ag nanoparticles.[3] The decrease of the  $\text{HO}_2^-$  yield with increased loading may be due to the higher chance of  $\text{HO}_2^-$  ion for being further reduced to  $\text{OH}^-$  before diffusing out of the catalyst layer at higher loadings, as suggested in [11] for perovskite (there the loading was between 30 to 130  $\mu\text{g cm}^{-2}$ ). Another

possibility (more probable) is that for low loadings, large parts of the GC substrate are uncovered. Consequently, at these parts,  $O_2$  reduction follows a 2e-mechanism (this may also be true for [11]). The influence of catalyst loading on the activity is studied in this work for other catalysts too (such as  $Co_3O_4$  (50 nm), Ag/CoO bimetallic catalyst and Ag+ $Co_3O_4$ ). Similar results are obtained, see Appendix A.

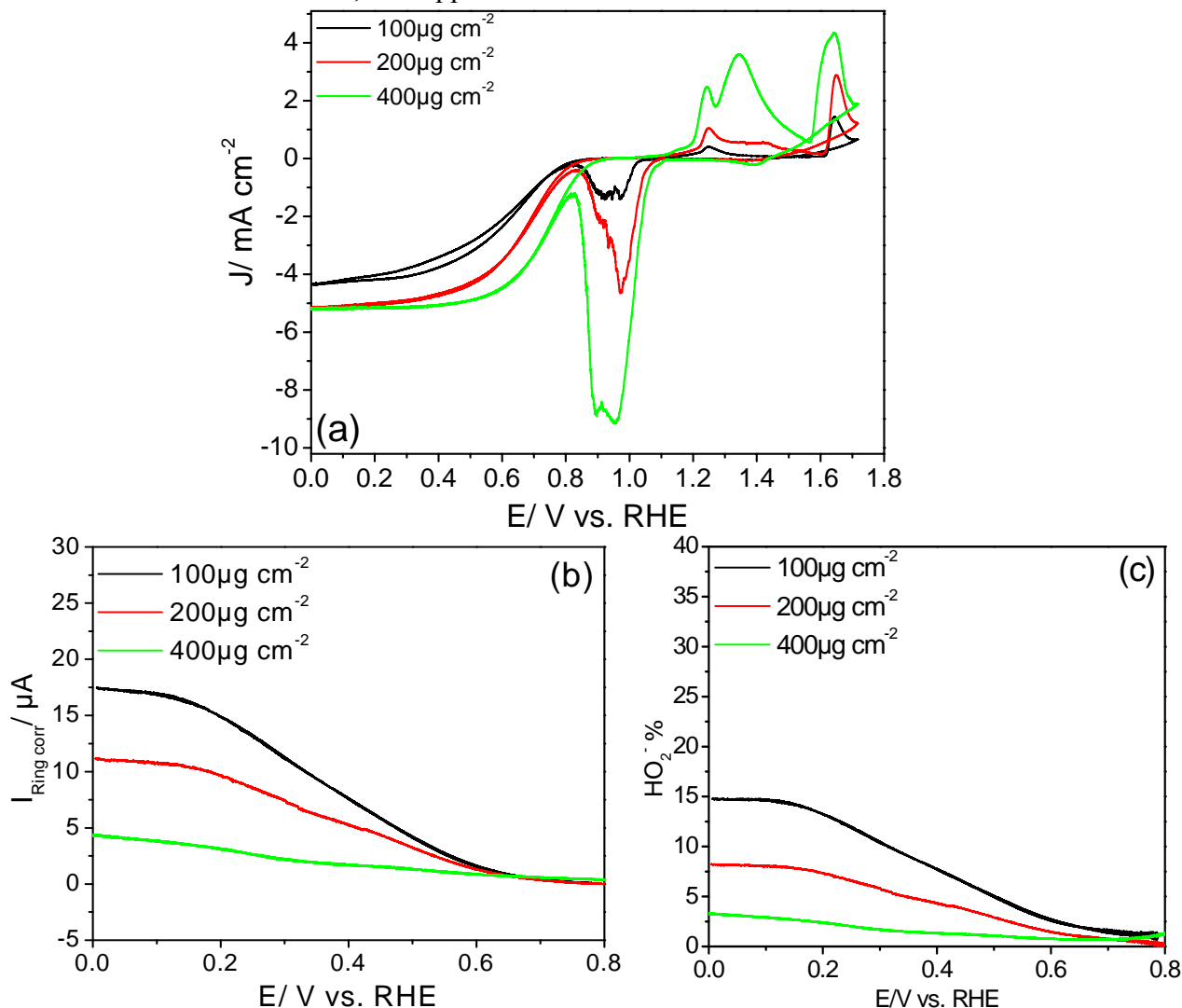


Fig. 5. (a) RRDE measurements on Ag (40µm)/GC electrode with different loadings in  $O_2$ -saturated 0.1M LiOH solution at 1500 rpm with 5 mV s<sup>-1</sup>. (b) Corresponding ring currents (anodic scan), when the ring is held at 1.2V. (c)  $HO_2^-$  % in ORR region.

#### 6.4. Effect of concentration and nature of cationic species of the electrolyte on activity

The effect of electrolyte concentration on the catalytic activity of Ag(40 µm) particles/GC is studied: two different concentrations of LiOH (0.1 M and 2.5 M) were examined for ORR/OER on Ag (40µm)/GC electrode, as shown in Fig. 6. The current densities and the ORR activity decrease as the concentration increases from 0.1M to 2.5M. The potential of ORR is significantly shifted to higher values (less overpotential) in 0.1M LiOH solution. This is attributed to the reduced oxygen solubility and the increased solution viscosity in solution with higher concentration. For OER, no significant change is observed for the two concentrations. The Ag redox peaks become less intense as the concentration increases, Fig.

6. RRDE results showed that the peroxide amount is lower (less than 10%) in 0.1M LiOH solution than in 1.0M LiOH, and the number of electrons transferred over the entire ORR potential range are very close to 4 ( $\sim 3.8$ ) for lower concentration, illustrating a dominant 4e-pathway. As the loading increases, the diffusion-limited current increases, and the redox currents increase. The same trend is also observed for another catalyst loading, see Fig. 6.

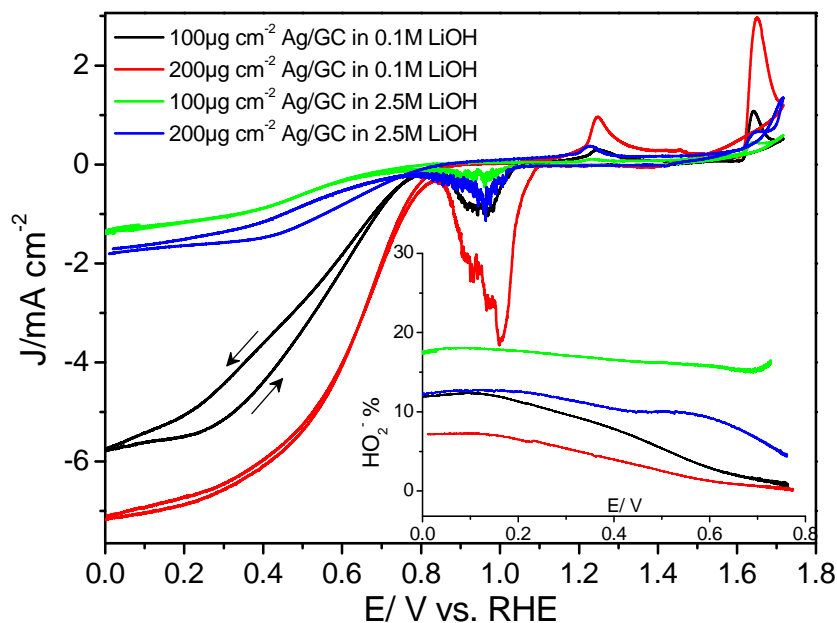


Fig. 6. RRDE measurements on Ag ( $40 \mu\text{m}$ )/GC electrode with two loadings in 0.1M and 2.5M LiOH solution at 2940 rpm with  $5 \text{ mV s}^{-1}$ . Inset: Corresponding  $\text{HO}_2^-$  % versus potential (anodic scan).

#### *Electrolyte effect on the activity of Ag<sub>3</sub>11+Co<sub>3</sub>O<sub>4</sub> (10 w%)*

The influence of the cationic species on the activity is investigated using RRDE on the mixed Ag<sub>3</sub>11+Co<sub>3</sub>O<sub>4</sub> (10 wt%) catalyst in alkaline media. The role of the cation on ORR activity of Pt[12] and other metals [13] has been studied. The same effect on OER at transition metal oxides (only on perovskites and IrO<sub>2</sub>) has been recently revisited.[14] There is no study on the effect of cation on the activity of mixed Ag+Co<sub>3</sub>O<sub>4</sub> catalyst for ORR/OER in alkaline media. Here, the activities in Li<sup>+</sup> and K<sup>+</sup>-containing electrolytes are compared, as depicted in Fig. 7. The catalyst showed higher activity in KOH than in LiOH, where the  $E_{1/2}$  for ORR is  $\sim 50$  mV more positive, and the current density is higher in KOH (Fig. 7a). The peroxide amount produced in KOH solution ( $< 8\%$ ) is less than that in LiOH ( $< 2\%$ ) at 960 rpm (Fig. 7b). Tafel plots were constructed to further analyze this effect (Fig. 7c). The kinetic currents increase as the size of the cation increases at the same potential. Moreover, Tafel slope in KOH electrolyte ( $\sim 56 \text{ mV dec}^{-1}$ ) is slightly lower than in LiOH ( $\sim 67 \text{ mV dec}^{-1}$ ) at lower overpotentials, while both exhibit comparable slopes ( $\sim 180 \text{ mV dec}^{-1}$ ) at higher overpotentials. The same trend is observed for OER, where OER started earlier, and higher currents are observed in KOH compared to LiOH solutions.

Two different prospects have been described to rationalize the decrease in activity without shut off as the cation's size decreases ( $\text{Li}^+ < \text{K}^+$ ). The first prospect attributed this effect to the non-covalent interaction between the cation and oxygenated species on the metal, forming an  $\text{OH}_{\text{ad}}-\text{Li}^+(\text{H}_2\text{O})_x$  cluster, which blocks the active sites.[12] According to this mechanism, we

should expect a deactivation of the Ag+Co<sub>3</sub>O<sub>4</sub> catalyst in LiOH since the surface is all oxygen-terminated instead of some free-metal sites as in the case of Pt surface. Notwithstanding, the results showed that Ag<sub>3</sub>11+Co<sub>3</sub>O<sub>4</sub> (10 wt%) catalyst has a good activity in Li<sup>+</sup> containing electrolyte, indicating the ability of the reactant to access the catalyst active sites. Thus, such activity contradicts the blocking mechanism. The second prospect is based on the interaction of the cation with the negatively charged reaction intermediates. This interaction modifies the energy barrier of ORR/OER.[14] Our results for Ag+Co<sub>3</sub>O<sub>4</sub> bimetallic catalyst agree with the second possibility. The strong electrostatic interaction of Li<sup>+</sup> (compared to K<sup>+</sup>) with OER/ORR intermediates affects the rate determining step. Thereby, it increases the reaction energy, and lowers the reactivity and reaction kinetics. Thus, the kinetics in KOH is faster than in LiOH.

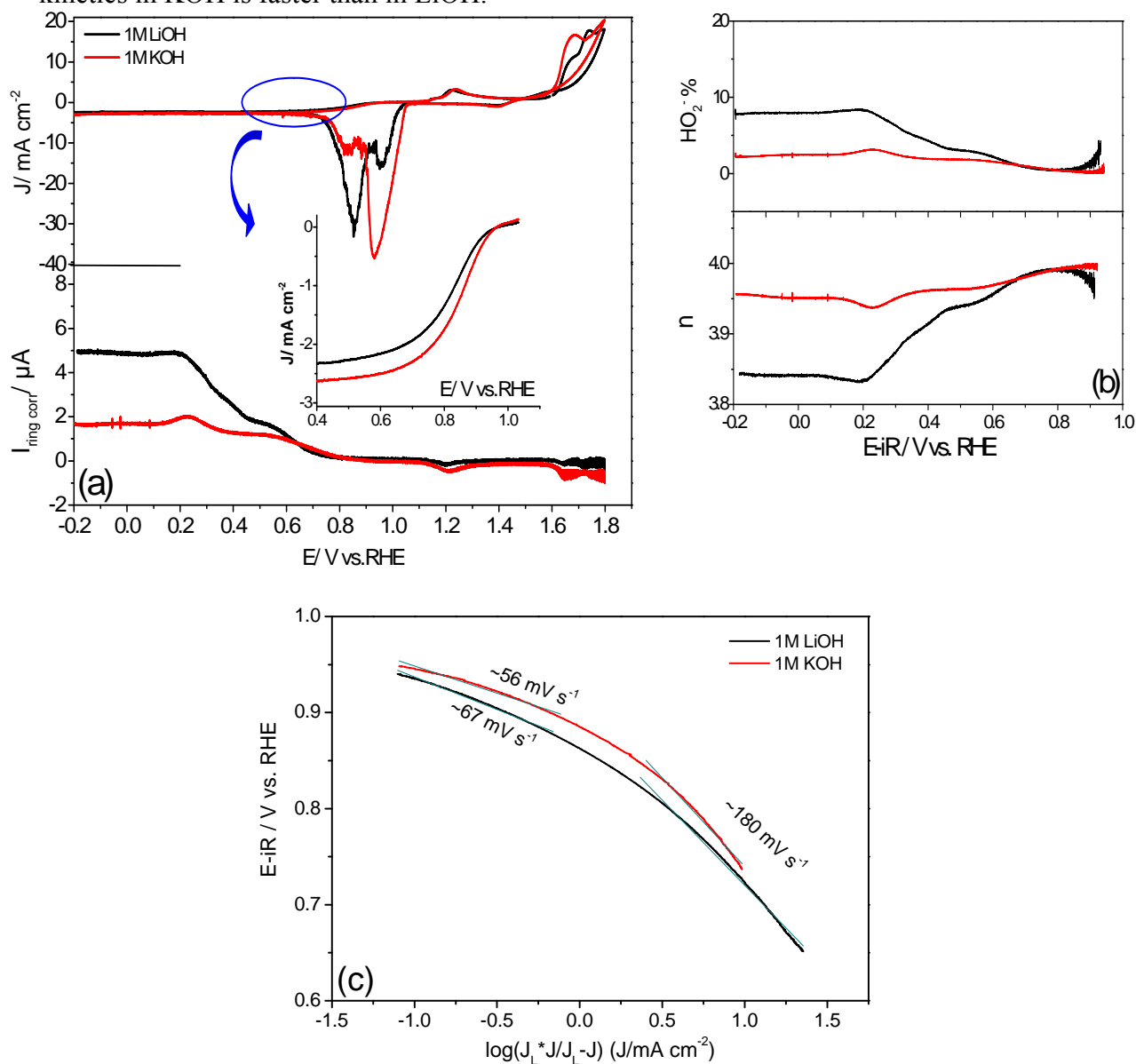


Fig. 7. (a) CVs of Ag<sub>3</sub>11+Co<sub>3</sub>O<sub>4</sub> (10 wt%) catalyst at 960 rpm and  $10 \text{ mV s}^{-1}$  in O<sub>2</sub>-saturated 1M LiOH and 1M KOH electrolytes (top panel). Inset: a magnification of the ORR region of interest. Ring currents are shown in the bottom of the graph. (b) The respective HO<sub>2</sub><sup>-</sup>% (top panel) and electron transfer number ( $n$ ) (bottom panel) at various potentials. (c) The corresponding mass-transport corrected Tafel plots for ORR.

Also, the solubility of oxygen in KOH is higher than in LiOH because the solvation of  $K^+$  is different from  $Li^+$  (since the size of  $Li^+ < K^+$ ). Therefore, in KOH, higher currents are obtained. These observations emphasize the role of the cation on the activity.

The influence of electrolyte nature and concentration is studied also for other catalysts such as Ag/CoO bimetallic catalyst, see Appendix A. Similar behavior is observed.

### 6.5. ORR and OER on bimetallic Ag/CoO (50/50 wt%) catalyst

From our results, we found that Ag is a good catalyst for ORR, while Co-oxide is good for OER (see Appendix A). Therefore, we mixed the two components (Ag + Co-oxide) in one catalyst to combine the best properties of each in one composite. The first measurements were carried out on bimetallic Ag/CoO(50 w%) catalyst. This catalyst is a physical mixture of Ag flakes ( $\sim 40 \mu\text{m}$ ) with CoO ( $20\text{-}30\mu\text{m}$ ). Fig. 8 depicts the polarization curves of pure Ag, pure CoO and Ag/CoO catalysts in the full potential range at  $5 \text{ mV s}^{-1}$  and 540 rpm. Noticeably, the diffusion-limited current should be the same for the different catalysts. However, some differences are observed due to the incomplete coverage of GC with catalyst. For OER, although Ag/CoO shows higher activity than Ag, it has lower activity than pure CoO (with only half of the loading is CoO). On the other hand, for ORR, higher activity (with respect to current and overpotential) is obtained on Ag than on the bimetallic Ag/CoO electrode, which showed higher activity than CoO. Moreover, the Ag/CoO catalyst was not stable. Unfortunately, these results were not the desired expectation. Therefore, we investigated another mixed catalyst, Ag<sub>311</sub>+Co<sub>3</sub>O<sub>4</sub>, which showed improved activity. Although the components in the Ag<sub>311</sub>+Co<sub>3</sub>O<sub>4</sub> mixture are similar to Ag/CoO catalyst, the particle size and morphology are different, and Co<sup>II</sup>O instead of Co<sub>3</sub>O<sub>4</sub> spinel was used, which could be one of the reasons of the lower activity. The other reason for the lack of the desired synergistic effect between Ag and CoO in their hybrid might be the aggregation of the particles, in particular Ag flakes, and the lower number of triple phase boundaries between Ag and CoO since they have similar particle size (few tens of  $\mu\text{m}$ ). It is noticeable that the Ag redox peaks currents in Ag/CoO catalyst are significantly smaller than in pure Ag catalyst, indicating lower Ag surface sites in the bimetallic catalyst, which could be due to major coverage of Ag surface with CoO particles or agglomeration of Ag particles.

The ring currents also support this interpretation since the amount of detected  $\text{HO}_2^-$  is close to that in CoO and larger than that in Ag, indicating major coverage of Ag with CoO such that the 2e-reduction at CoO prevails, see Fig. 8b and c. The peroxide anion percentage detected on the ring is up to 50%, on cobalt-containing electrodes, while less than 10% is obtained for pure Ag, see Fig 8c. From these results, we conclude that the Ag/CoO composite catalyst is inefficient as a bifunctional catalyst. Therefore, based on the explorative study of some factors such as the particle size of the components and the mixing ratio, the mixed Ag<sub>311</sub>+Co<sub>3</sub>O<sub>4</sub> catalyst was examined, and showed a synergistic effect and a higher activity, as discussed in chapters 4 and 5, and continue below.

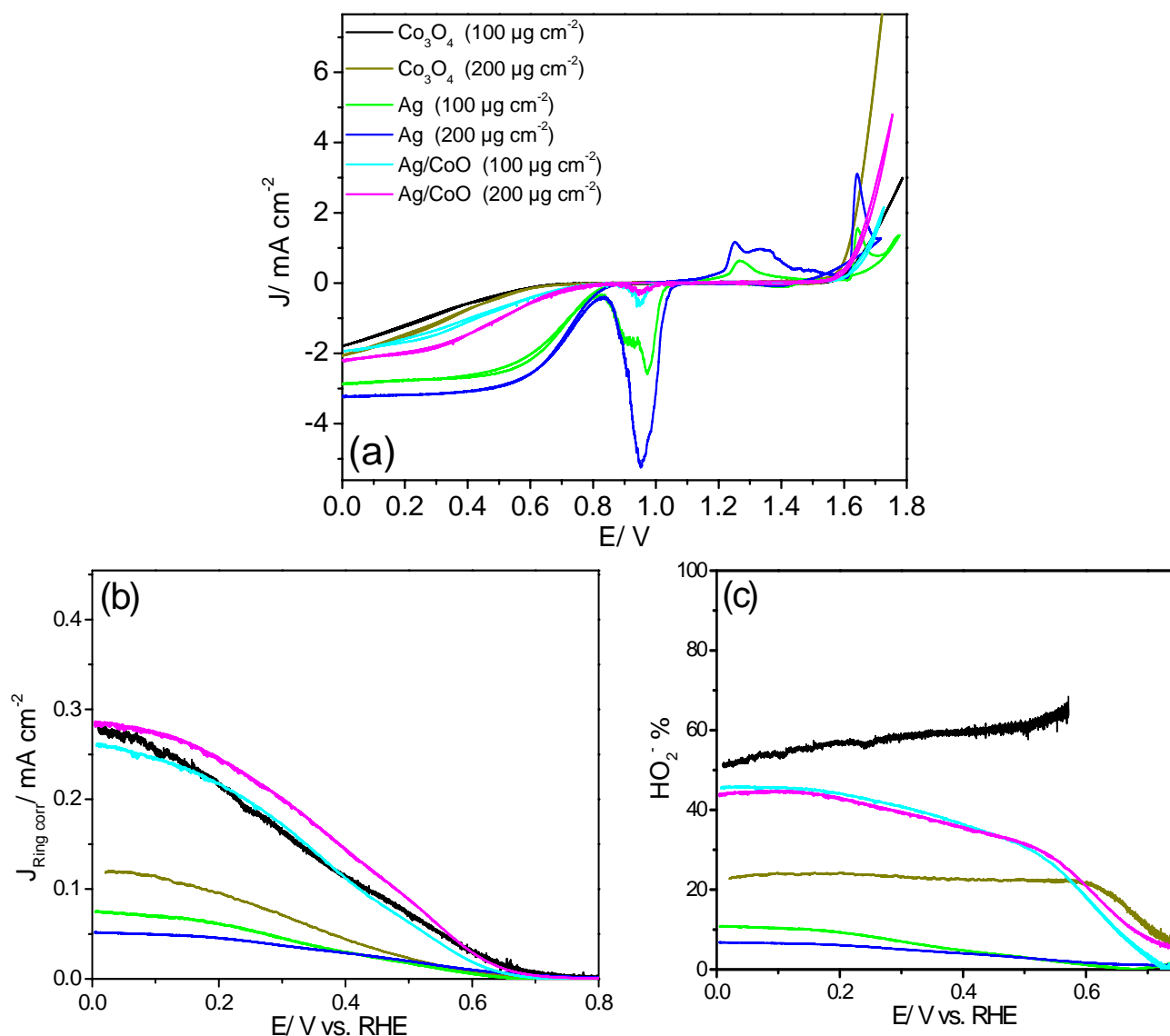


Fig. 8. (a) RRDE measurements on  $\text{Co}_3\text{O}_4$  (40  $\mu\text{m}$ ), Ag (40  $\mu\text{m}$ ) and bimetallic Ag/CoO (50 wt%) supported on GC electrodes in  $\text{O}_2$ -saturated 0.1M LiOH solution at 540 rpm with  $5 \text{ mV s}^{-1}$ . (b) Ring currents in the anodic scan of ORR region. (c) Corresponding peroxide yield.

### 6.6. Synergistic bifunctional activity of Ag+ $\text{Co}_3\text{O}_4$ mixed catalyst in alkaline media: kinetics and mechanism

#### *Catalytic activity of the mixed catalyst:*

A mixed composite based on a combination of  $\text{Co}_3\text{O}_4$  (50 nm) with Ag311 particles is investigated in order to develop an efficient carbon-free bifunctional catalyst. This mixed catalyst displayed a better activity than its individual components, and exhibited good stability. The enhanced activity is due to a synergistic effect between Ag and  $\text{Co}_3\text{O}_4$ . Better understanding of the origin of synergism is achieved by several methods. Such synergistic interaction is far beyond what might be expected by simply adding the activities of both components, as discussed below and with XPS analysis in chapter 5.

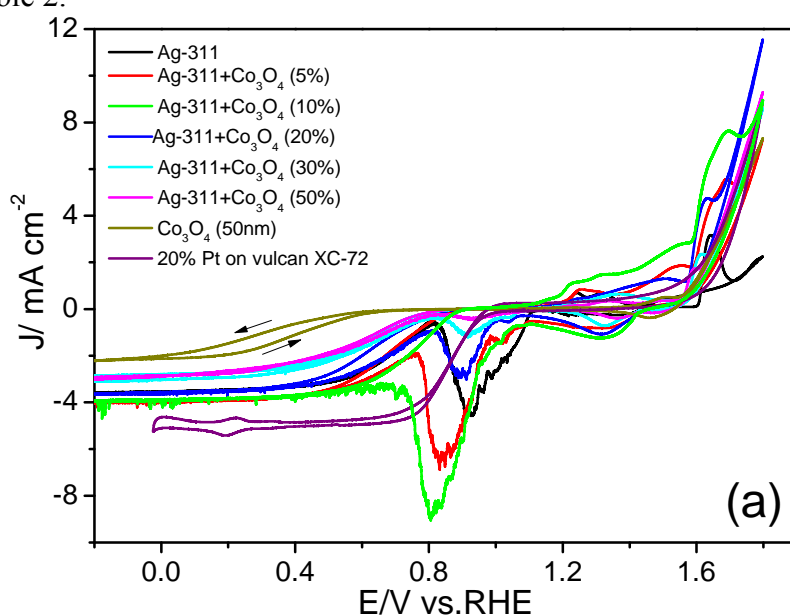
To assess the intrinsic electrocatalytic activity of these promising catalysts, Fig. 9a shows the performance of the different catalysts towards OER and ORR between -0.2V and 1.8V. The commercial 20 w% Pt/Vulcan XC-72 catalyst is also studied for comparison. For ORR, the currents in the positive-going sweep correspond to the true activity since in the negative-

going scan, Ag oxides and adsorbed hydroxides are still being reduced. For OER, the negative-going scan represents the true or steady-state currents since in the anodic scan, Ag and Co oxidations are superimposed to the OER currents. Optimization of the composition ratio is achieved: Ag311+Co<sub>3</sub>O<sub>4</sub> (10 wt%) catalyst outperformed the other compositions in terms of half-wave potential ( $E_{1/2}$ ) and current density, although the 20% mixture has slightly higher OER currents. Onset of ORR is at 0.9V for the 10% catalyst, which is about 50 mV more positive than that of pure Ag311. The  $E_{1/2}$  on the 10% mixed catalyst is ca. 0.74V, which is ~100 mV less positive than that of the commercial Pt/C, and ~50mV more positive than that of Ag. Noticeably, the diffusion-limited current of the different catalysts is different, which is not ideal behavior. These values are lower than the expected values from K-L equation (3.6 mA cm<sup>-2</sup> for 960 rpm in 0.1M LiOH). This could be due to the fact that parts of GC are uncovered with the catalyst, so that contribution of GC takes place. However, this feature has no obvious effect on the observed trend of activity.

Therefore, a proper way to compare the catalysts is to plot the normalized ORR currents with respect to their respective diffusion-limited currents ( $I_{disc}/I_{lim}$ ), as shown in Fig. 9b. For ORR, the curve of the 10% mixed catalyst is negatively shifted by ca. 100 mV from that of Pt/C. On the other hand, 10w% mixed catalyst is better by ca. 40 mV from Ag/C, and by >300 mV from Co<sub>3</sub>O<sub>4</sub>. Other compositions showed lower activities, but still better than the pure Co<sub>3</sub>O<sub>4</sub>. For OER, the activities of mixed catalysts are comparable, although 10-20% of Co<sub>3</sub>O<sub>4</sub> in the mixture exhibits the best activity, see Fig. 9c. The OER activity of the Ag311+Co<sub>3</sub>O<sub>4</sub> is two times higher than the commercial Pt/C, and Ag alone is mostly inactive towards OER. These results imply the superior activity of the bifunctional Ag+Co<sub>3</sub>O<sub>4</sub> catalyst over the single Ag or Co<sub>3</sub>O<sub>4</sub> catalysts.

From RRDE measurements on Ag311+Co<sub>3</sub>O<sub>4</sub> (10 %) and Pt/C, the peroxide anion amount is not large. On the other hand, for other compositions, < 8% HO<sub>2</sub><sup>-</sup> is obtained over the entire ORR potential range (see Fig. 12b in Appendix A). The number of electrons transferred is 3.99 for both Pt and 10% mixed catalysts, and the other mixed catalysts have values above 3.9, inferring that these composites follow the 4e-pathway for ORR.

Comparison of the kinetic parameters of our catalyst with other catalysts from literature is shown in Table 2.



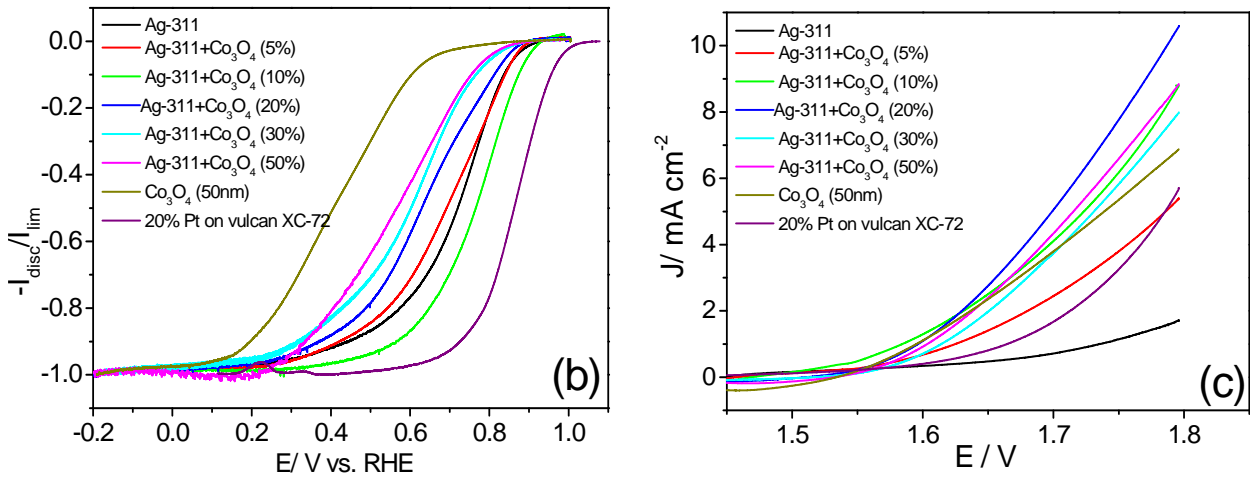


Fig. 9. RRDE measurements for ORR/OER on Ag<sub>311</sub>+Co<sub>3</sub>O<sub>4</sub> (x %)/GC electrodes in O<sub>2</sub>-saturated 0.1M LiOH solution at 960 rpm with 5 mV s<sup>-1</sup>. Loading for all catalysts: 1 mg cm<sup>-2</sup>. (b) Normalized ORR currents to the diffusion limited current, anodic scan. (c) Expansion of OER region in the cathodic scan.

*Effect of scan rate (diffusion in Ag-oxide film) and potential window:*

The effect of scan rate is used to investigate the diffusion of oxygen in the Ag-oxide layer in two different catalysts, Ag (40 μm) and Ag<sub>311</sub>+Co<sub>3</sub>O<sub>4</sub> catalysts. Fig. 10a depicts the variation of scan rate at Ag<sub>311</sub>+Co<sub>3</sub>O<sub>4</sub> (30 wt%). As the scan rate increases (from 10 to 200 mV s<sup>-1</sup>), the oxidation and reduction peak currents of Ag increase, see Fig. 10b and c. A linear relationship between the peak current of the second oxidation peak (corresponding to Ag<sup>I</sup> oxidation), and the square route of scan rate (i.e. Randles-Sevcik equation) is obtained. This linearity provides an evidence for a chemically reversible redox process, and indicates a surface-confined electron transfer mechanism, see Fig. 10b. This implies that the transport of oxygen in the oxide layer is diffusion limited. For Ag (40μm) single catalyst, the effect of scan rate is shown in Fig. 5 of Appendix A. Similar trend is observed. The slope of the linear plot is used to calculate the term  $D^{1/2}C$ , and values of  $4.3 \times 10^{-8}$  and  $1.1 \times 10^{-7}$  mol cm<sup>-2</sup> s<sup>-1/2</sup> are obtained for the mixed catalyst and pure Ag (40 μm), respectively. For comparison, the diffusion coefficient of oxygen atoms in silver oxide (AgO) is  $2.5 \times 10^{-13}$  cm<sup>2</sup>/s at 298 K.[15] This means that oxygen atoms are able to penetrate with higher rate in our AgO particles. Interestingly, the rate of diffusion of oxygen in Ag-oxide layer of Ag (40μm) is higher than the oxide layer of the mixed Ag+Co<sub>3</sub>O<sub>4</sub> catalyst.

Variation of the upper potential limit of scanning at Ag<sub>311</sub>+Co<sub>3</sub>O<sub>4</sub> (10 wt%)/GC electrode is shown in Fig. 10d. Three anodic peaks and two cathodic peaks are observed in the full range of sweep. Opening the upper limit to higher potentials leads to an increase of the consecutive peak of reduction of Ag<sub>2</sub>O, with a negative potential shift in the peak position.

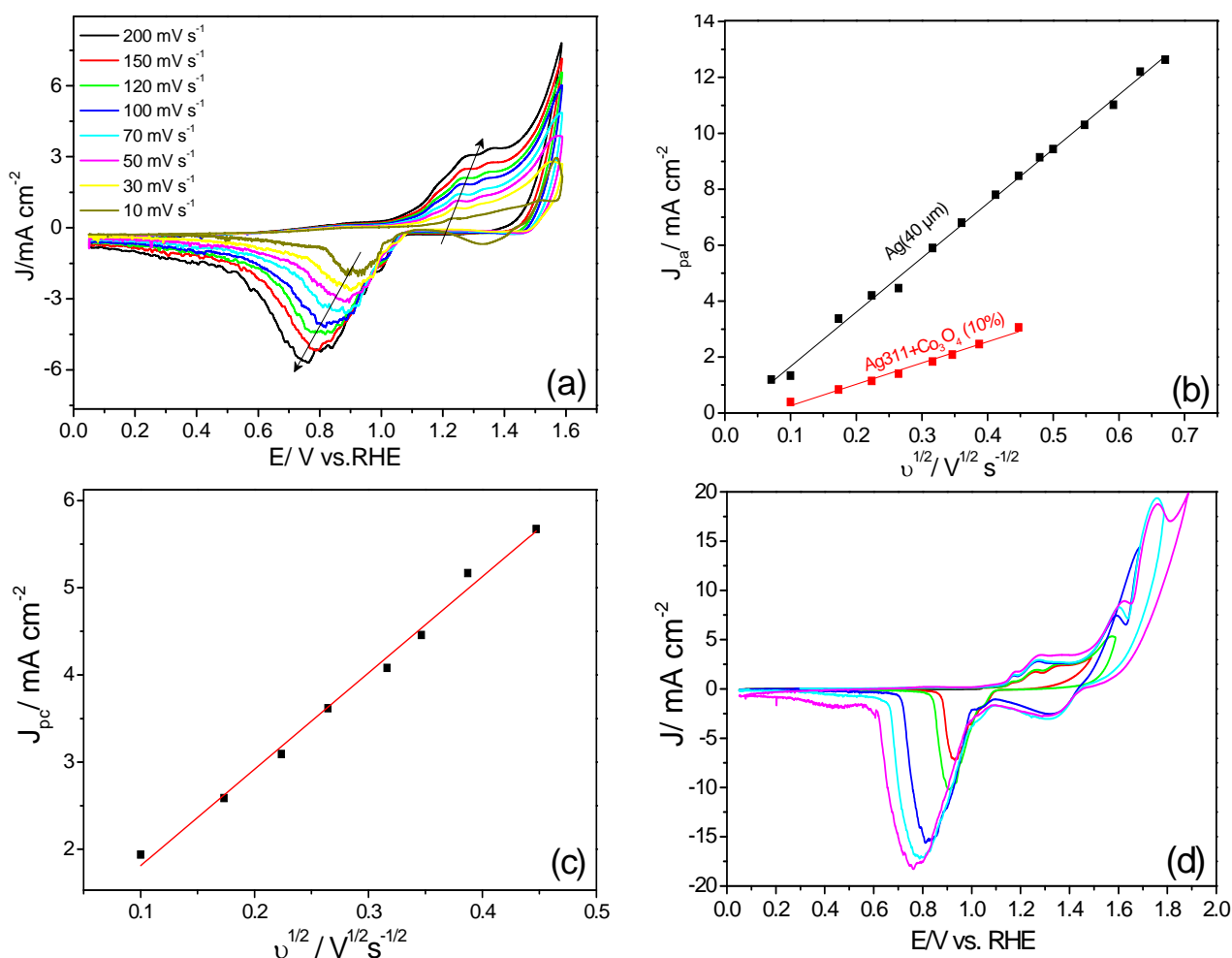


Fig. 10. (a) CVs on Ag<sub>311</sub>+Co<sub>3</sub>O<sub>4</sub> (30 wt%) electrode (1 mg cm<sup>-2</sup>) in O<sub>2</sub>-saturated 0.1M LiOH at different scan rates. Plot of  $J_p$  vs.  $v^{1/2}$  for anodic peak (b), and cathodic peak (c). (d) CVs of Ag<sub>311</sub>+Co<sub>3</sub>O<sub>4</sub> (10 wt%)/GC with loading of 1mg cm<sup>-2</sup> in Ar-saturated 0.1M LiOH, 50 mV s<sup>-1</sup> at different upper potential limits.

### 6.7. Stability of the catalysts

Since the stability of the bifunctional catalyst is a critical factor in commercial applications, steady-state experiments were conducted, as shown in Fig. 11. For ORR, the potential was held at 0.7V for 5 minutes at different catalysts, see Fig. 11a. Excellent stability is observed, with very small current decay from the initial values. For OER, steady-state currents were obtained by holding the potential at 1.7V for few minutes under rotation, see Fig. 11b. The fast decay, which is observed in the mixed catalysts, at the beginning (first 10 s) is due to continuation of oxide formation, and then the current becomes stable during pure OER. The mixed catalysts and pure Co<sub>3</sub>O<sub>4</sub> catalyst showed good stability, while Ag and Pt are not stable for OER. Furthermore, long-term stability tests on the same catalysts were carried by our project partners using GDE, and the results showed good stability, as reported in our paper.[16] Durability of Co<sub>3</sub>O<sub>4</sub> catalyst for OER is also investigated by performing 600 consecutive cycles between 0.05V and 1.8V with 200 mV s<sup>-1</sup>, and in between cycles with 10 mV s<sup>-1</sup> were recorded, and plotted in Fig. 11c. The OER currents at 1.8V are plotted at  $n^{\text{th}}$  cycles, see inset of Fig. 11c. The results show stable performance for 600 consecutive cycles, suggesting this catalyst to be promising candidate for O<sub>2</sub>-electrodes.

Comparison of the activity at the three electrodes at potential of ORR and OER is shown in Fig. 11d. The mixed catalyst outperformed the individual catalysts made of its own components.

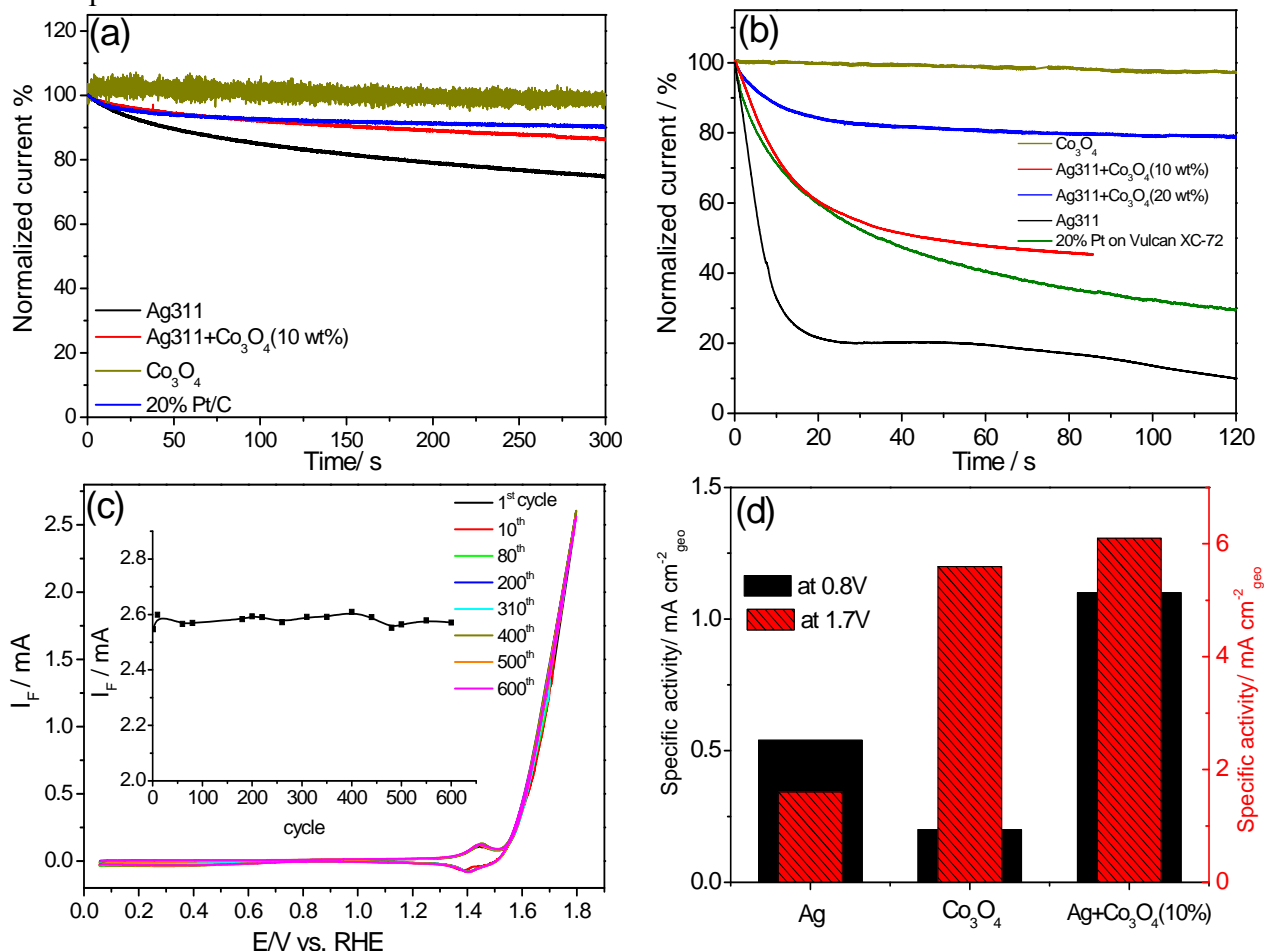


Fig. 11. Stability tests (normalized current to initial value) for different catalysts ( $1 \text{ mg cm}^{-2}$ ) in  $\text{O}_2$ -saturated  $0.1 \text{ M LiOH}$  solution at  $2160 \text{ rpm}$ , the potential is held at (a)  $0.7 \text{ V}$ , and (b)  $1.7 \text{ V}$ . (c) Long-term stability for OER at  $\text{Co}_3\text{O}_4$  ( $1 \text{ mg cm}^{-2}$ ) in Ar-saturated  $1 \text{ M LiOH}$  solutions in dual thin layer cell with flow rate  $5 \mu\text{l/s}$ . Cycling was with  $200 \text{ mV/s}$ , and in between cycles with  $10 \text{ mV/s}$  were recorded, and shown in this figure; inset: current at  $1.8 \text{ V}$  vs. cycle number. (d) Specific activity at  $0.8 \text{ V}$  and  $1.7 \text{ V}$  for the three catalysts in  $0.1 \text{ M LiOH}$  from data of Fig. 9a.

### 6.8. Surface characterization of the catalyst

In order to examine the microscopic structure of the mixed  $\text{Ag}+\text{Co}_3\text{O}_4$  catalyst, SEM together with EDX analyses were carried out. As shown in Fig. 12a,  $\text{Co}_3\text{O}_4$  nanoparticles cover most of the large Ag particles. Whereas, in between the Ag particles, the small  $\text{Co}_3\text{O}_4$  particles are predominant. This is proved by conducting EDX analysis in these two regions. EDX spectra proved the presence of Ag and Co signals confirming the coexistence of both on the uppermost surface. From the EDX spectra, it is found that in area 1, Ag signals are larger, while cobalt signals are smaller, indicating the presence of  $\text{Co}_3\text{O}_4$ -supported on Ag. On the other hand, Co signals are dominant in area 2, which is the area between Ag particles. Moreover, SEM images after several OER/ORR cycles showed slight morphological changes,

see Fig. 12b. However, the EDX spectra did not change significantly, indicating no alteration in the composition, but may be reorientation took place.

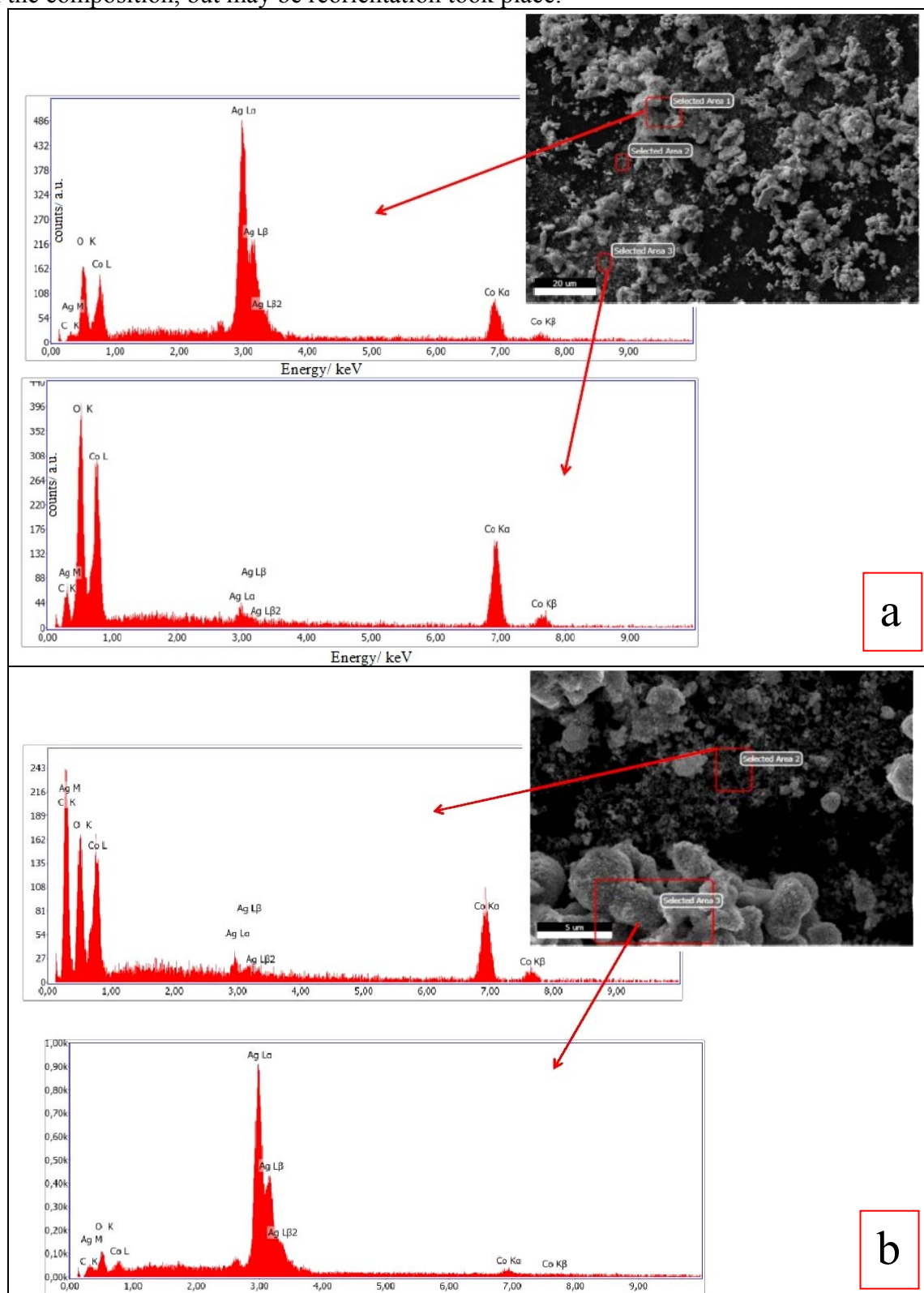


Fig. 12. SEM and EDX spectra of Ag<sub>311</sub>+Co<sub>3</sub>O<sub>4</sub> (10%)/GC catalyst with 1 mg cm<sup>-2</sup> with Nafion (a) before, and (b) after ORR/OER cycles.

BET data and XRD of Co<sub>3</sub>O<sub>4</sub> catalyst, and additional SEM images of the mixed catalyst are presented in the SI of chapter 7. These surface analyses, besides RRDE, XPS and XRD

reported in our publications[1, 16] explain the synergistic effect between Ag and  $\text{Co}_3\text{O}_4$ , and provide better understanding of the origin of this effect, which leads to enhanced activity, as discussed in details in chapter 5.

Catalyst	Electrolyte	ORR			OER			Ref.
		Onset Pot./ $V_{\text{RHE}}$	$E_{1/2}/V_{\text{RHE}}$	Tafel slope at lower pot./mV/dec	Onset Pot./ $V_{\text{RHE}}$	$J/\text{mA cm}^{-2}$ @ 1.58 $V_{\text{RHE}}$	Tafel Slope	
$\text{Mn}_{0.6}\text{Cu}_{0.4}\text{Co}_2\text{O}_4/\text{C}$	1M KOH	0.96	0.90 @1000 rpm	40 and 80 at high pot	1.50	0.015	--	[17]
LCCO-0.03Ag/XC-72R GDE	6MKOH	0.87	--	~70 and >400 at high pot.	~1.50	~32	--	[18]
Mn oxide	0.1MKOH	0.88	0.72 @1600 rpm	--	<1.45	2.4	--	[19]
Mesoporous LSCO+ AC nanowires	0.1MKOH	0.87	~0.73 @1000 rpm	--	1.65	<1	--	[20]
$\text{Co}_3\text{O}_4/\text{NrmGO}$	0.1MKOH	~0.91	0.84 @900 rpm	42	1.54	38 at carbon fiber paper	67	[21]
$\text{MnCo}_2\text{O}_4/\text{N-rmGO}$	1MKOH	~0.92	~0.87 @900 rpm	36	~1.53	18 at carbon fiber paper	--	[22]
Ag nanopowder	6MKOH	0.86	0.49 @1000 rpm	-- n=3.7	1.63	Nil, 2mA/cm <sup>2</sup> @1.64V	--	[23]
Ag-MnO <sub>2</sub>	0.1MKOH	0.89	0.67 @900 rpm	77	>1.71	Nil, 2mA/cm <sup>2</sup> @1.8V	94	[24]
$\text{Ba}_{0.9}\text{Co}_{0.5}\text{Fe}_{0.4}\text{Nb}_{0.1}\text{O}_{3.6}$	0.1MKOH	0.78	0.68 @900 rpm	n=3.8-3.9	1.59	<2	--	[25]
$\text{Mn}_{0.9}\text{Co}_{2.1}\text{O}_4$	1MKOH	0.95	0.83 @900 rpm	n=3.7-4	1.53	0.9	--	[26]
Ag-Co/C	1.0MKOH	0.89	0.76 @1600 rpm	50 and 80 at high	No OER mentioned			[27]
Bulk Ag	0.1MKOH	~0.9	0.75 @900 rpm	90	No OER mentioned			[3, 28]
Ag311+ $\text{Co}_3\text{O}_4$ (10 wt%)	0.1MLiOH	0.96	0.78 @960 rpm	76	~1.55	0.8	~80	Our work

Table 2. Summary of the electrochemical parameters at different catalysts from literature, and comparison to our catalyst.

### 6.9. Synergistic bifunctional activity at Ag+perovskite catalyst: role of the oxide

To verify whether the observed synergistic effect in Ag311+ $\text{Co}_3\text{O}_4$  mixed catalyst can be achieved in perovskites, lanthanum strontium ferrite (LSF) perovskite is mixed with Ag311,

and its activity is investigated. Interestingly, this mixture showed an enhanced bifunctional activity compared to its single components. This supports our proposal that a sort of interaction takes place between Ag and the oxide, and consequently, changes the electronic properties of the two components, and thus enhances the activity, as will be described in the electrochemical characterization below. SEM images of Ag311+LSF (10 wt%) were captured before (Fig. 13a and b) and after (Fig. 13c and d) performing several OER/ORR cycles. Magnified images are also shown, in which one can see the larger Ag particles (blue circle) with a defined shape are partially covered by the smaller LSF particles (red circle). The elemental composition is proved by the EDX spectra, see Fig. 14. The SEM images show that the presence of LSF in contact with Ag particles prevents/reduces the particles' agglomeration. After several oxidation and reduction cycles, slight morphological changes occur: LSF tends to cover more Ag sites; the surface microstructure smoothes out after cycling experiments; and the roughness of the surface increases.

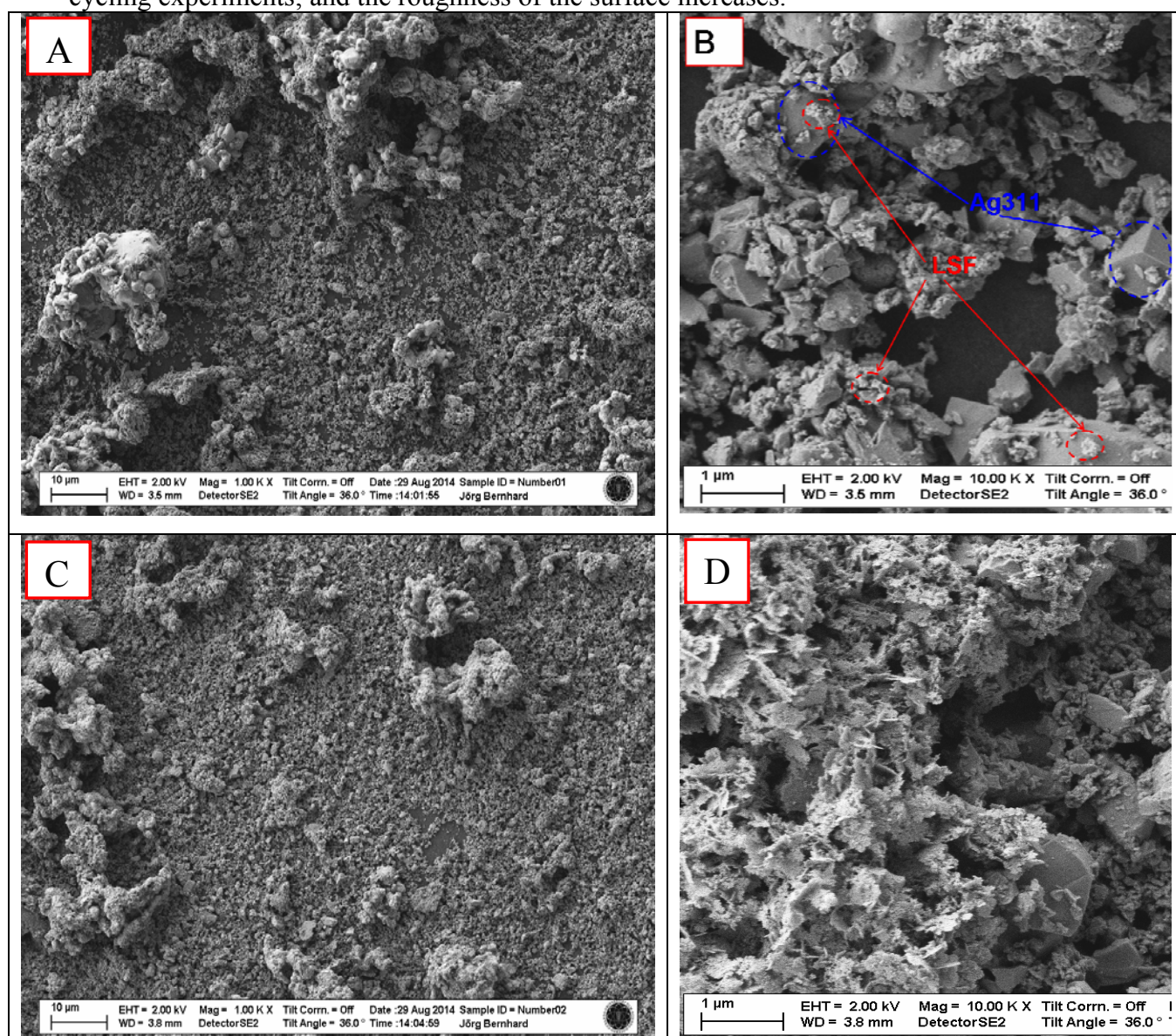


Fig. 13. SEM images of Ag311+LSF (10 wt%)/GC catalyst with  $1 \text{ mg cm}^{-2}$  loading (A) before, and (C) after cycling experiments. (B) and (D) are magnified views of (A) and (C), respectively.

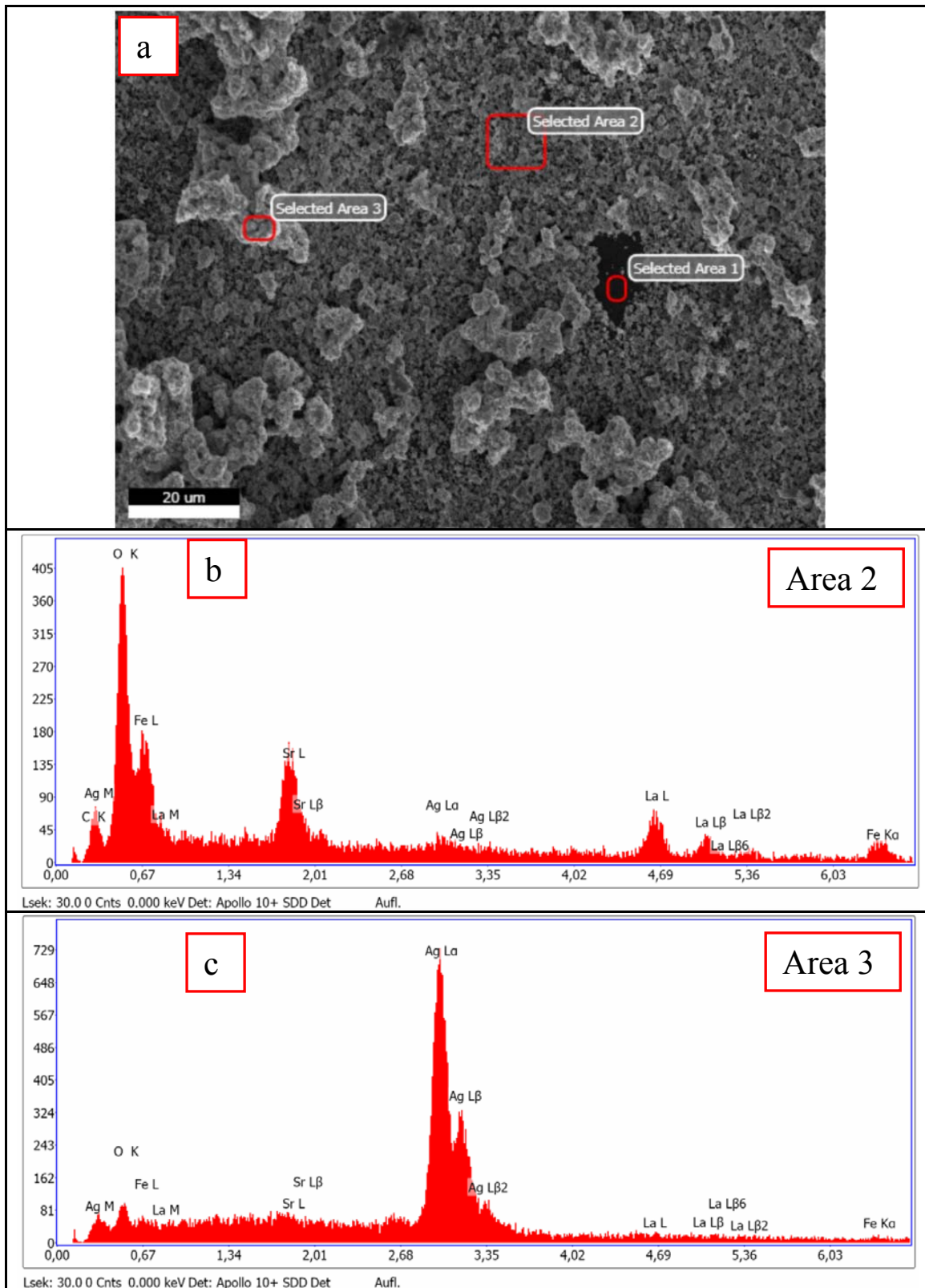


Fig. 14. (a) SEM images of Ag<sub>311</sub>+LSF (10 wt%) catalyst with 1 mg cm<sup>-2</sup> loading after several cycles. (b) and (c) EDX spectra of two different regions on the catalyst surface.

Fig. 14. depicts the SEM of Ag<sub>311</sub>+LSF (10 wt%) with a loading of 1 mg cm<sup>-2</sup> after cycling experiments and the corresponding EDX spectra at different regions on the surface. EDX profile confirms the presence of typical peaks for the existing metals in the catalyst (Ag, La,

Sr, Fe). In *area 2* of the surface, fine LSF particles dominate with coexistence of some Ag particles. While in *area 3*, large Ag particles are major, and are partially covered with LSF particles. The created phase boundaries between Ag and LSF provide more active sites, and thus increase the activity of the catalyst. *Area 1* shows a part of bare GC substrate.

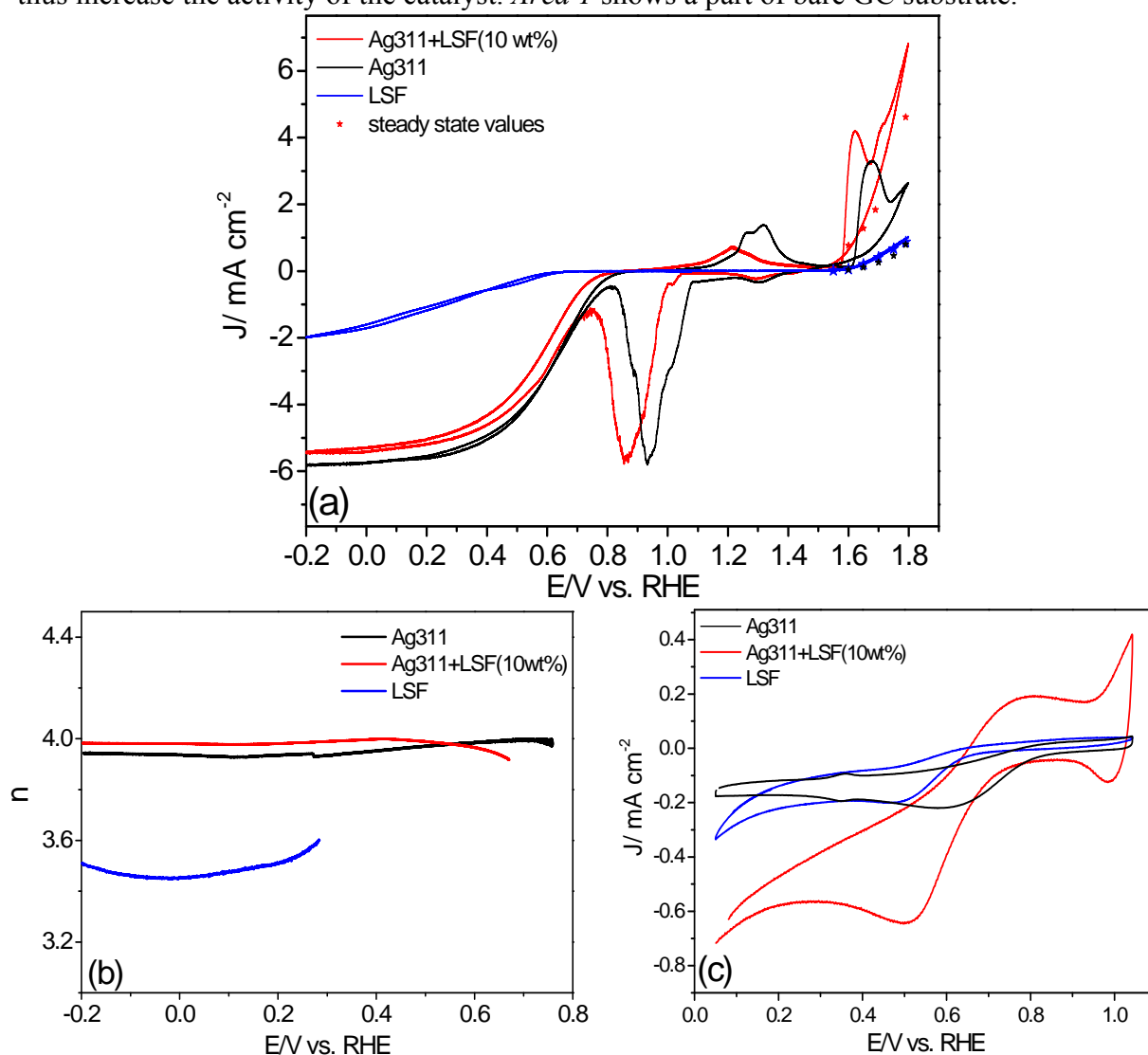


Fig. 15. (a) Polarization curves of Ag311, LSF and Ag311+LSF(10 wt%) catalyst electrodes in O<sub>2</sub>-saturated 0.1M LiOH solution with 5 mV s<sup>-1</sup>. (b) The number of electrons transferred ( $n$ ) in ORR region. (c) CVs in a stagnant solution with 50 mV s<sup>-1</sup>. Loading is 1 mg cm<sup>-2</sup> for all.

For their electrochemical characterization, Fig. 15c shows the CVs of LSF, Ag311 and their mixture Ag311+LSF (10 %) in a stagnant solution of 0.1M LiOH with 50 mV s<sup>-1</sup>. The mixed Ag311+LSF catalyst shows better ORR activity than its single components in terms of current density of oxygen reduction peak. However, CV is not an effective method for studying the catalytic activity since the anodic scan has significantly lower currents than the cathodic scan. Therefore, RRDE measurements were conducted, and are displayed in Fig. 15a, in which the reaction is under defined hydrodynamics. Thus, the current in both anodic and cathodic scans is similar (see the curves in a and c). The composite Ag311+LSF (10 wt%) exhibited comparable activity for ORR to Ag and better than LSF. However, it shows superior OER

activity (i.e. higher current and lower overpotential) over Ag<sub>311</sub> and LSF catalysts. The data points in the graph represent the steady-state currents obtained by holding the potential for a short time (1 min.) at different potentials under rotation. The decay of OER currents from the initial values is not significantly large at LSF and the mixed catalysts, indicating good stability. On the other hand, Ag revealed instability.

Negligible peroxide amount is detected based on the ring currents. The number of electrons (*n*) transferred during ORR is 4-*e*s for the Ag and the mixed catalyst, while a lower value of 3.5 for pure LSF is obtained, as shown in Fig. 15b. This indicates that the mixed and Ag catalysts follow the 4-*e*s pathway for ORR. From these results, a synergistic effect is achieved also at Ag+LSF catalyst, although the improvement is not large as in Ag+Co<sub>3</sub>O<sub>4</sub> catalyst. This suggests an effective role of the interaction between the two catalysts in their mixture, which is dependent on the nature of the two components (here, Co<sub>3</sub>O<sub>4</sub> is more effective and active than LSF, when they are combined with Ag).

#### 6.10. Synergistic effect in Ni+Co<sub>3</sub>O<sub>4</sub> mixed catalyst: role of the metal as a support

Cobalt and nickel are transition metals with incomplete d-orbital, and are known to have good catalytic activity for OER. NiO<sub>x</sub> has been reported to have better ORR activity than CoO<sub>x</sub> in alkaline media.[29] The OER activity of cobalt oxide supported on Au substrate is significantly higher than that of bulk cobalt oxide in KOH solution, indicating the significant role of the support.[30] The activity of this Co-oxide deposited on different metals decreased monotonically in the order of Au>Pt>Pd>Cu>Co, paralleling the decrease in the electronegativity of the metal. This emphasizes the role of the electronic properties of the metal in the synergistic effect, although it is investigated for only OER activity. Moreover, Co and Ni metals have been combined in a catalyst for ORR in acidic media, and showed better activity than their single metals.[31] As a bifunctional catalyst, Lithium cobalt oxide/C was also reported for both ORR and OER.[32] Mn and Co co-substituted Fe<sub>3</sub>O<sub>4</sub> nanoparticles on nitrogen-doped reduced graphene oxide showed enhanced synergistic effect in OER and ORR.[33] We showed in this work the enhanced activity of our mixed Ag+Co<sub>3</sub>O<sub>4</sub> catalyst,[1] and the synergism in Ag+LSF catalyst. And from the information of the above survey, we extended our work to investigate the effect of replacing Ag with Ni in the mixture with Co<sub>3</sub>O<sub>4</sub> to check how the nature of the metal is critical. Nickel is relatively inexpensive and possesses better electronic conductivity than cobalt. Therefore, combination between Ni and Co<sub>3</sub>O<sub>4</sub> should enhance the performance of the mixed catalyst. Here, we study the kinetics and mechanism using RRDE, although a gas diffusion electrode made of this composite was characterized in a parallel study by our project partner, and showed good long-term stability.[34]

Firstly, spinel Co<sub>3</sub>O<sub>4</sub>, metallic Ni particles and their mixed Ni+Co<sub>3</sub>O<sub>4</sub> catalysts were examined for ORR in a stagnant solution of 0.1M LiOH with 50 mV s<sup>-1</sup>, as shown in Fig. 16a. The mixed Ni+Co<sub>3</sub>O<sub>4</sub> catalysts show lower overpotential (i.e. better activity) than their single component catalysts. To assess the bifunctional catalytic activity, RRDE measurements were conducted and the results are displayed in Fig. 16b. The catalysts have the same loading of 1 mg cm<sup>-2</sup>. The different catalysts showed comparable activities for ORR and OER, although the mixed catalyst showed slightly higher activity than the pure catalysts (in particular, for OER, see Fig. 16b, d. Onset potential for ORR is about 0.65 V, whereas for OER is 1.55V.

The Ni+Co<sub>3</sub>O<sub>4</sub> (10 %) mixed catalyst exhibited better OER activity with 5.3 mA cm<sup>-2</sup> at 1.65V compared to 3.1 or 2.9 mA cm<sup>-2</sup> for the single Co<sub>3</sub>O<sub>4</sub> or Ni catalysts, respectively. OER curves are shifted by ca. 50 mV to lower overpotentials compared to pure Ni or Co<sub>3</sub>O<sub>4</sub>, see Fig. 16b. The higher OER activity could be attributed to the increase of the Co<sup>IV</sup> cations (a state that is believed to be determinant in OER) since Ni might catalyze the transition of Co<sup>III</sup> to Co<sup>IV</sup> when it is in contact with Co<sub>3</sub>O<sub>4</sub>. Steady-state current values are also presented as asterisks in the polarization curves, which showed good stability of the catalysts.

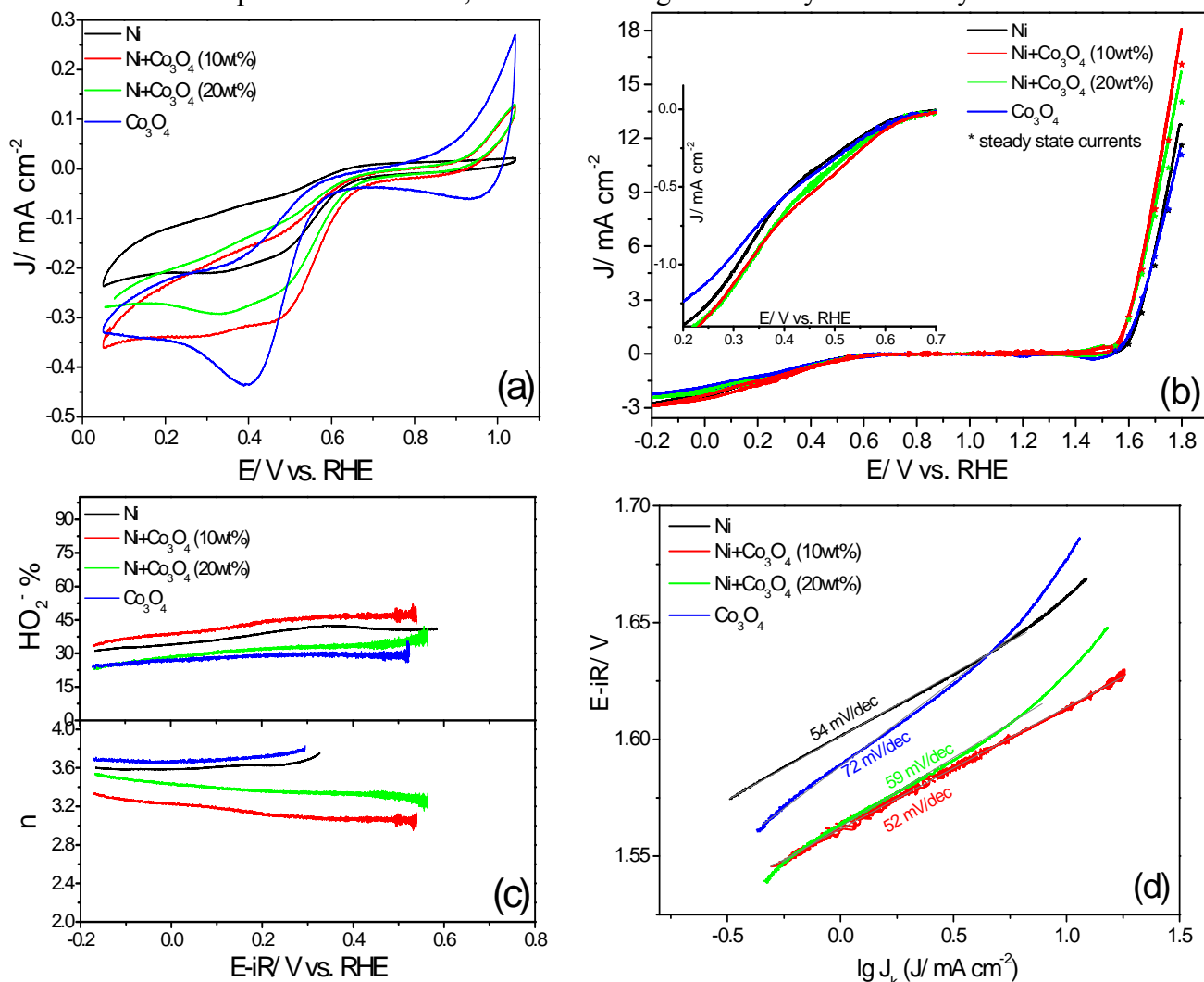


Fig. 16. (a) Polarization curves of Ni, Ni+Co<sub>3</sub>O<sub>4</sub> (10 wt%), Ni+Co<sub>3</sub>O<sub>4</sub> (20 wt%) and Co<sub>3</sub>O<sub>4</sub> catalysts electrodes in a stagnant O<sub>2</sub>-saturated 0.1M LiOH solution with 50 mV s<sup>-1</sup> and (b) at a rotation of 2160 rpm with 5 mV s<sup>-1</sup>. Inset: expansion of ORR region. (c) HO<sub>2</sub><sup>-</sup>% (upper panel), and the number of electrons transferred (*n*) (lower panel). (d) Tafel plots for OER.

The amount of peroxide anion intermediate detected on the ring is in the range of 25-45%, as shown in Fig. 16c. The overall number of electrons transferred is in the range of 3.2 to 3.7. This suggests that ORR on these four catalysts proceeds via both two-electron and four-electron pathways. IR-corrected Tafel plots for OER are constructed from the corresponding data, see Fig. 16d. Ni+Co<sub>3</sub>O<sub>4</sub> (10 wt%) catalyst has the lowest Tafel slope of 52 mV dec<sup>-1</sup>, indicating the higher reaction rate. Nevertheless, comparable Tafel slopes in the range of 52-72 mV dec<sup>-1</sup> are obtained for all catalysts, which are close to the 60 mV dec<sup>-1</sup>, indicating that

the different catalysts follow the same mechanism for OER. This also indicates that the rate determining step is the cleavage of M–O or M–O<sub>2</sub><sup>-</sup>.

The main difference between Ni and Ag when they are separately mixed with Co<sub>3</sub>O<sub>4</sub> is that pure Ni catalyst showed high OER activity (as good as that of Co<sub>3</sub>O<sub>4</sub>), while Ag has very small OER activity. On the other hand, Ag is more active for ORR than Ni, thus its combination with Co<sub>3</sub>O<sub>4</sub> is effective and creates enhanced activity for ORR. These results infer that the metal (as a support) plays a critical role in the activity improvement: Ni is not effective as Ag for ORR. This could be due to the higher electric conductivity of Ag than Ni (about 4 times higher), and possibly the oxide state of both metals behaves differently over the applied potential (i.e. different activity of Ni-oxide and Ag-oxide during OER).

From the above, the proper selection of the two components of the mixed catalyst is critical for achieving synergistic effect.

### 6.11. EIS Investigations on Ag, Co<sub>3</sub>O<sub>4</sub> and Ag+Co<sub>3</sub>O<sub>4</sub> (10 %) catalysts

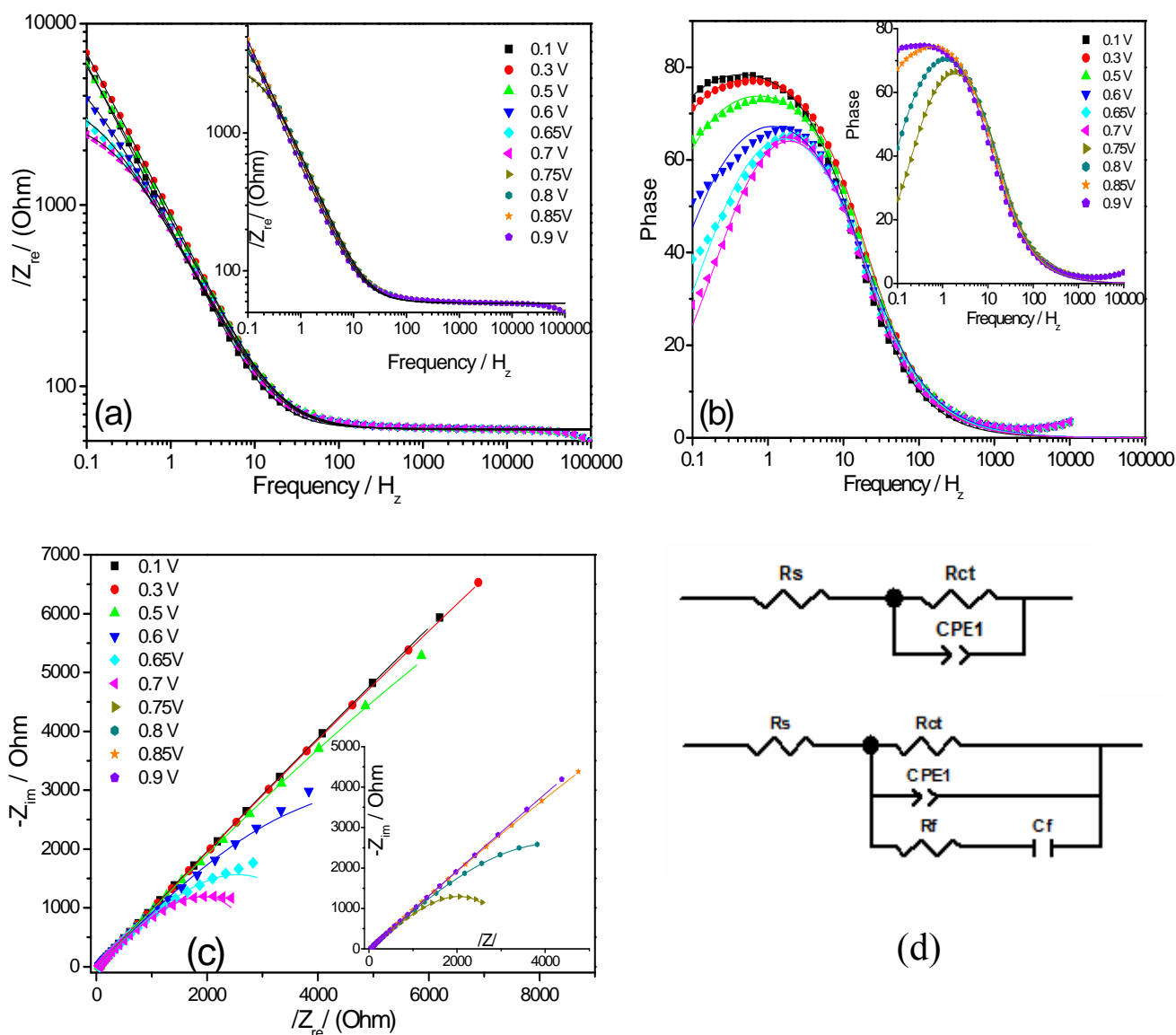


Fig. 17. (a) Bode plots for Ag<sub>311</sub>+Co<sub>3</sub>O<sub>4</sub> (10 %) in a stagnant O<sub>2</sub>-saturated 0.1M LiOH solution at different potentials in ORR region. (b) Bode plots for phase. (c) Nyquist plots. (d) The used equivalent circuits (upper for ORR, and lower for OER). Symbols: measured data; lines: fitted results.

To get information on the electrode/electrolyte interface, EIS measurements on the mixed catalyst were carried out at different DC potentials. Fig. 17 shows the Bode and Nyquist plots at different potentials in the ORR region. The Nyquist plots show a single time-constant arc, where its diameter can be correlated to the total impedance in the system. EIS data are fitted according to the equivalent circuit shown in Fig. 17d. This circuit is a modification of the known Randles-circuit. The circuit, which is applied for ORR potentials, consists of uncompensated solution resistance ( $R_s$ ) in series with a parallel set of charge transfer resistance ( $R_{ct}$ ) and constant phase element (CPE), which represents the double layer capacitance.

The double layer behaves more like a CPE than a perfect capacitor due to several factors such as the roughness and non-homogeneity effect, adsorption of species on the surface or distortion of the double layer by faradaic reactions at the interface. The impedance of a CPE is  $Z_{CPE}=1/Q(j\omega)^n$ , where  $j$  is the imaginary number,  $\omega$  is the frequency,  $Q$  is CPE coefficient and  $n$  varies between 0 and 1. A capacitor is a CPE with a constant phase angle of 90 degrees (thus,  $n=1$ ). Therefore, CPE reveals a depressed semicircle instead of a perfect semicircle in the Nyquist plot.

In ORR potential region, as the potential increases from 0.1V to 0.7V, the radius of the arc decreases (Fig. 17c), and thus the charge transfer resistance decreases due to the enhanced electrochemical kinetics. However, further increase to 0.9V leads again to larger resistances, as shown in the fitting parameters in Table 3. At lower potentials of ORR, the Nyquist plot is dominated by the diffusion process as can be observed from the straight line instead of an arc (Fig. 17c), and thus higher  $R_{ct}$  is obtained. Thereby, the change of the resistance at 0.7V could be due to the transition from a mass-transport controlled process to a kinetic controlled process.

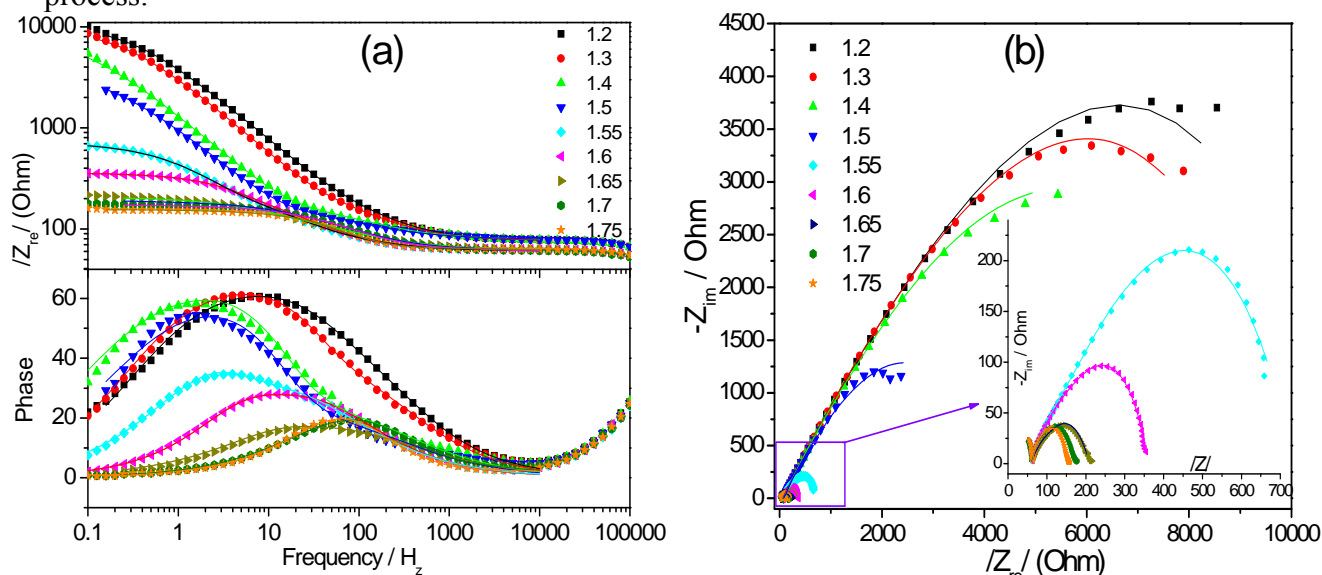


Fig. 18. (a) Bode plots for Ag<sub>311</sub>+Co<sub>3</sub>O<sub>4</sub>(10 %) in O<sub>2</sub>-saturated 0.1M LiOH solution at different potentials (above 1.2V, the measurements were at 2160 rpm to avoid the evolved O<sub>2</sub> bubbles). (b) Nyquist plots. Symbols: measured data; lines: fitted results.

Examining the EIS spectra at potentials of Ag oxidation is important to follow up the oxidation process. Fig. 18 shows the spectra for potentials between 1.2 and 1.75V. Here, a

modification of the equivalent circuit was done to account for the formed Ag-oxide film, namely, a film resistance ( $R_f$ ) and capacitance ( $C_f$ ) were added to the first circuit, as shown in the inset of Fig. 18d. The fitted results are in a very good agreement with the measured values. At potentials above 1.2 V, Ag is oxidized to  $\text{Ag}_2\text{O}$ , which has less electric conductivity than Ag. Further oxidation to  $\text{Ag}^{\text{I}}\text{Ag}^{\text{III}}\text{O}_2$ , which has higher conductivity than  $\text{Ag}_2\text{O}$ , takes place at higher potentials. Although it is difficult to separate between both resistances in the spectra, the overall resistance has a trend: as the potential increases from 1.2V to 1.75V, the total impedance decreases (i.e.  $R_{ct}$  and  $R_f$  decrease, whereas the film capacitance increases), which agrees with the oxidation of Ag, see Table 3. It is noted that at potentials above 1.55V, the resistance is significantly smaller than that below 1.5V.

Catalyst	Potential/ V vs.RHE	$R_s/\Omega$	$R_{ct}/\Omega$	CPE-T/ F	CPE-P	$R_f/\Omega$	$C_f/ F$
Ag311+Co <sub>3</sub> O <sub>4</sub> (10%)	<b>ORR region</b>						
	0.1	58.4	3.98E+04	2.49E-04	0.92	--	--
	0.3	58.0	3.72E+04	2.14 E-04	0.91	--	--
	0.5	57.8	1.95E+04	2.37 E-04	0.89	--	--
	0.6	57.4	7.29E+03	2.85 E-04	0.85	--	--
	0.65	57.5	3.91E+03	2.85 E-04	0.86	--	--
	0.7	57.9	2.88E+03	2.71 E-04	0.88	--	--
	0.75	58.2	3.06E+03	2.66E-04	0.89	--	--
	0.8	58.3	6.09E+03	2.79E-04	0.89	--	--
	0.85	58.3	2.09E+04	3.05E-04	0.89	--	--
	0.9	58.4	4.47E+04	3.47E-04	0.88	--	--
	<b>Ag oxidation region</b>						
	1.2	76.1	1.09E+04	5.28E-05	0.76	1172	1.74E-06
	1.3	76.2	9.87E+03	6.49E-05	0.75	437	6.32E-06
	1.4	77.9	9.11E+03	1.59E-04	0.68	182	3.18E-05
	1.5	78.5	4.07E+03	2.22E-04	0.67	155	4.08E-05
	<b>OER region</b>						
	1.55	60.5	6.71E+02	3.87E-04	0.68	635	4.38E-05
	1.60	61.4	2.99E+02	2.44E-04	0.73	748	2.18E-05
	1.65	60.3	1.49E+02	4.17E-04	0.61	697	1.03E-05
1.68	59.3	1.32E+02	2.66E-04	0.64	43	3.32E-06	
1.71	58.1	1.16E+02	2.03E-04	0.65	20	7.38E-06	
1.75	58.3	0.98E+02	1.92E-04	0.61	10	2.42E-05	

Table 3. Fitting parameters of 10% mixed catalyst at different anodic and cathodic potentials in O<sub>2</sub>-saturated 0.1M LiOH.

### Comparison of EIS of different catalysts:

EIS spectra of Ag,  $\text{Co}_3\text{O}_4$  and their mixture electrodes are compared in Fig. 19. At 0.7V (large points), the mixed catalyst shows the smallest impedance with the smallest arc, see Fig. 19b. While at 1.6V,  $\text{Co}_3\text{O}_4$  showed the smallest resistance. The fitting parameters, which are obtained according to the respective equivalent circuit, are shown in Table 4.

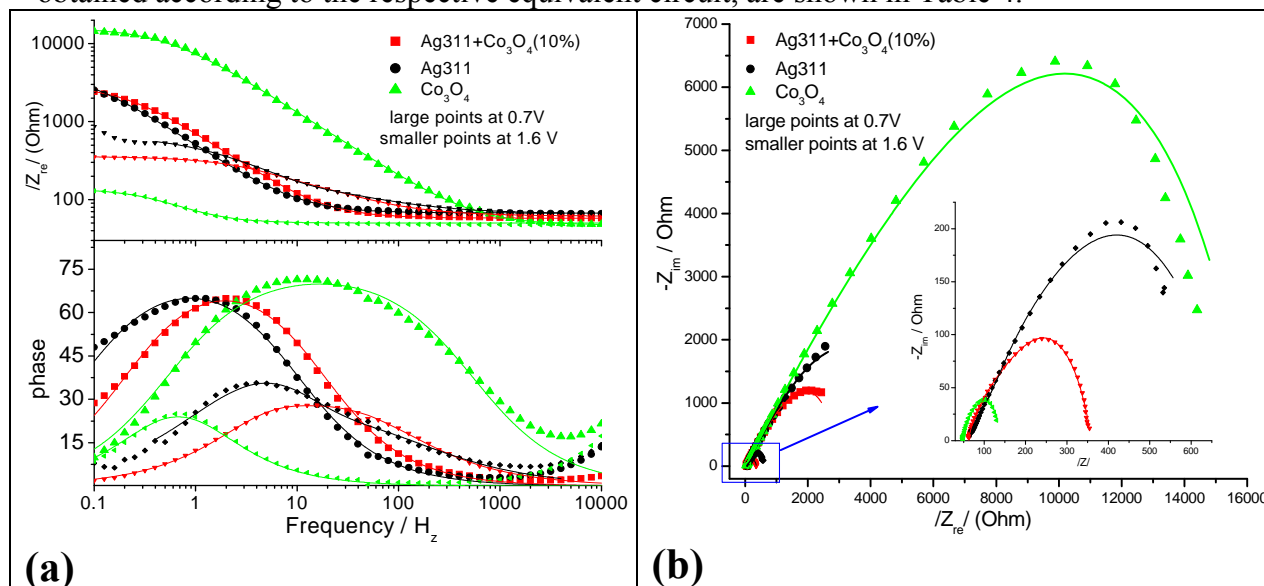


Fig. 19. (a) Bode plots for Ag311,  $\text{Co}_3\text{O}_4$ , Ag311+ $\text{Co}_3\text{O}_4$  (10 %) in  $\text{O}_2$ -saturated 0.1M LiOH solution at 0.7V and 1.6V. (b) Nyquist plots. Symbols: measured data; lines: fitted results.

Catalyst	$R_s / \Omega$	$R_{ct} / \Omega$	CPE-T/F	CPE-P	$R_f / \Omega$	$C_f / F$
<i>ORR @0.7 V vs. RHE</i>						
<b>Ag311</b>	67.4	4.55E+03	4.11 E-04	0.87	--	--
<b><math>\text{Co}_3\text{O}_4</math></b>	46.9	1.60E+04	2.29 E-05	0.84	--	--
<b>Ag311+<math>\text{Co}_3\text{O}_4</math>(10%)</b>	57.9	2.88E+03	2.71 E-04	0.88	--	--
<i>OER@1.6 V vs. RHE</i>						
<b>Ag311</b>	65.7	6.24E+02	3.43E-04	0.66	246	3.62E-05
<b><math>\text{Co}_3\text{O}_4</math></b>	50.0	0.88E+02	5.03E-03	0.90	40	9.56E-05
<b>Ag311+<math>\text{Co}_3\text{O}_4</math>(10%)</b>	61.4	2.99E+02	2.44E-04	0.73	748	2.18E-05

Table 4. Fitting parameters of Ag,  $\text{Co}_3\text{O}_4$  and mixed Ag+ $\text{Co}_3\text{O}_4$  (10%) mixed catalyst at 0.7V and 1.6V in 0.1M LiOH ( $\text{O}_2$ -sat.).

**Effect of electrolyte:**

EIS is a typical method to determine the solution resistance. From the Nyquist plot, it is clear that the impedance increases as the concentration of LiOH increases, where the radius of the semicircle increases, see in Fig. 20. The trend is the same at 0.7V and 1.6V. The solution resistance decreases from  $\sim 58 \Omega$  to  $16 \Omega$  as the concentration increases from 0.1M to 2.5M LiOH, which is expected since the conductivity increases in higher concentrations.  $R_{ct}$  increases with the concentration increase, see Table 5.

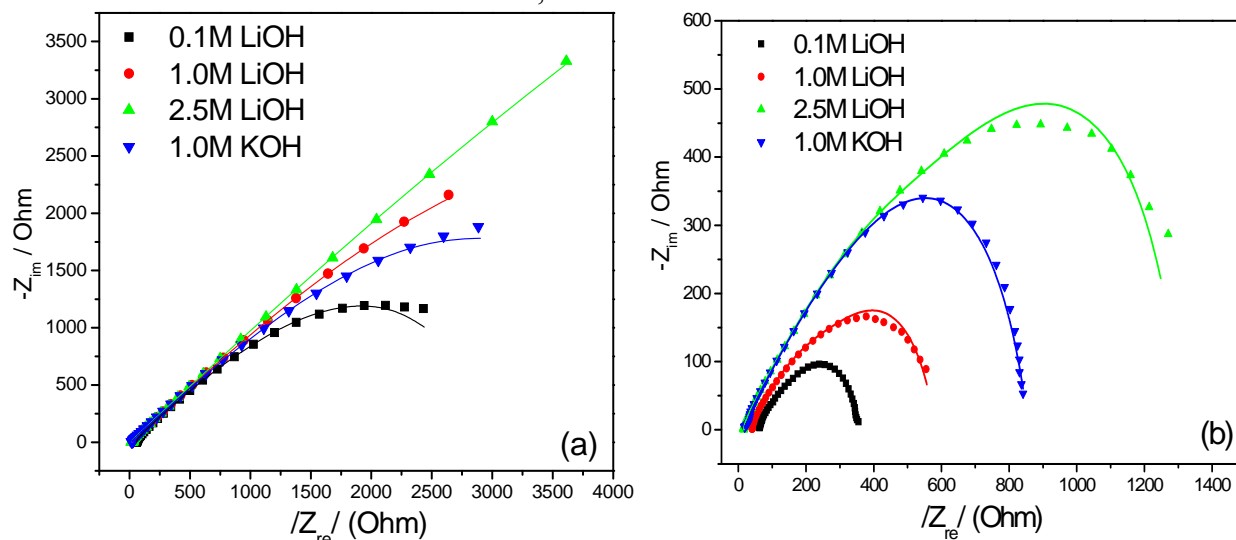


Fig. 20. Nyquist plots for Ag311+Co<sub>3</sub>O<sub>4</sub> (10 %) in different concentrations of LiOH solution at 0.7V (a) and 1.6V (b), and comparison to KOH is shown. Symbols: measured data; lines: fitted results.

Catalyst	Conc. of LiOH /M	$R_s / \Omega$	$R_{ct} / \Omega$	CPE-T/ F	CPE-P	$R_f / \Omega$	$C_f / F$
<b>ORR @0.7 V vs.RHE</b>							
Ag311+Co <sub>3</sub> O <sub>4</sub> (10%)	0.1	57.9	2.88E+03	2.71 E-04	0.88	--	--
	1.0	24.2	5.76E+03	3.81 E-04	0.90	--	--
	2.5	19.3	1.30E+04	3.94 E-04	0.91	--	--
	1.0 KOH	20.8	4.32E+03	2.68 E-04	0.88	--	--
<b>OER@1.6 V vs.RHE</b>							
	0.1	61.4	2.99E+02	2.44E-04	0.73	748	2.18E-05
	1.0	39.9	5.44E+02	3.01E-04	0.77	1360	8.06E-05
	2.5	15.9	1.29E+03	1.17E-04	0.89	1859	6.69E-05
	1.0 KOH	17.3	8.41E+02	1.11E-04	0.83	32	2.54E-05

Table 5. Fitting parameters of 10% mixed catalyst at 0.7V and 1.6V in different concentrations of LiOH (O<sub>2</sub>-sat.), and comparison to KOH.

**6.12. Conclusion**

In this chapter, we presented an explorative study of different catalysts to find out the best bifunctional activity. From the results of catalyst screening and variation of the composition and components of the mixed catalyst, we conclude that both components (Ag and Co<sub>3</sub>O<sub>4</sub>) in the mixture contribute effectively to the activity, and consequently, their properties (e.g.

conductivity, electronic structure, size) influence differently ORR/OER processes: Ag is more active than Ni for ORR, thus Ag showed significant enhancement when it is combined with  $\text{Co}_3\text{O}_4$ ; also  $\text{Co}_3\text{O}_4$  is more active than LSF when they are combined with Ag. Therefore, the mixture of Ag+ $\text{Co}_3\text{O}_4$  reveals the best activity in the studied mixed catalysts. The size and structure of the catalyst play a crucial role in the ORR/OER activity (as revealed from the study of different sizes of Ag and  $\text{Co}_3\text{O}_4$  separately). The origins of the synergistic effect are discussed in this chapter and in the previous two chapters based on SEM, XPS, XRD data. Briefly, several reasons lead to the synergistic effect and enhanced activity: reduced agglomeration; spillover effect and redox switching in  $\text{Co}_3\text{O}_4$ . The obtained activity and stability make the Ag+ $\text{Co}_3\text{O}_4$  (10-20%) mixed catalyst as a potential candidate for application in  $\text{O}_2$ -electrodes.

### 6.13. References

- [1] H.M.A. Amin, H. Baltruschat, D. Wittmaier, K.A. Friedrich, *Electrochimica Acta* 151 (2015) 332-339.
- [2] D. Šepa, M. Vojnović, A. Damjanovic, *Electrochimica Acta* 15 (1970) 1355-1366.
- [3] G.K.H. Wiberg, K.J.J. Mayrhofer, M. Arenz, *Fuel Cells* 10 (2010) 575-581.
- [4] J.-J. Han, N. Li, T.-Y. Zhang, *Journal of Power Sources* 193 (2009) 885-889.
- [5] H.A. Hansen, J. Rossmeisl, J.K. Nørskov, *Physical Chemistry Chemical Physics* 10 (2008) 3722-3730.
- [6] T. Nagel, N. Bogolowski, H. Baltruschat, *Journal of Applied Electrochemistry* 36 (2006) 1297-1306.
- [7] S. Trasatti, O.A. Petrii, *Pure and Applied Chemistry* 63 (1991) 711-734.
- [8] E. Kirowa-Eisner, Y. Bonfil, D. Tzur, E. Gileadi, *Journal of Electroanalytical Chemistry* 552 (2003) 171-183.
- [9] V. Daujotis, E. Gaidamauskas, *Journal of Electroanalytical Chemistry* 446 (1998) 151-157.
- [10] M. Hepel, S. Bruckenstein, *Electrochimica Acta* 34 (1989) 1499-1504.
- [11] T. Poux, A. Bonnefont, G. Kéranguéven, G.A. Tsirlina, E.R. Savinova, *ChemPhysChem* 15 (2014) 2108-2120.
- [12] D. Strmcnik, K. Kodama, D. van der Vliet, J. Greeley, V.R. Stamenkovic, N.M. Markovic, *Nat Chem* 1 (2009) 466-472.
- [13] D. Strmcnik, D.F. van der Vliet, K.C. Chang, V. Komanicky, K. Kodama, H. You, V.R. Stamenkovic, N.M. Markovic, *The Journal of Physical Chemistry Letters* 2 (2011) 2733-2736.
- [14] J. Suntivich, E.E. Perry, H.A. Gasteiger, Y. Shao-Horn, *Electrocatalysis* 4 (2013) 49-55.
- [15] M.A. Henderson, Y. Zhou, J.M. White, C.A. Mims, *Journal of Physical Chemistry* 93 (1989) 3688-3694.
- [16] D. Wittmaier, N. Wagner, K.A. Friedrich, H.M.A. Amin, H. Baltruschat, *Journal of Power Sources* 265 (2014) 299-308.
- [17] M. De Koninck, B. Marsan, *Electrochimica Acta* 53 (2008) 7012-7021.
- [18] S. Zhuang, K. Huang, C. Huang, H. Huang, S. Liu, M. Fan, *Journal of Power Sources* 196 (2011) 4019-4025.

- [19] Y. Gorlin, T.F. Jaramillo, *Journal of the American Chemical Society* 132 (2010) 13612-13614.
- [20] Y. Zhao, L. Xu, L. Mai, C. Han, Q. An, X. Xu, X. Liu, Q. Zhang, *Proc. Nat. Acad. Sci. USA* 109 (2012) 19569-19574.
- [21] Y. Liang, Y. Li, H. Wang, J. Zhou, J. Wang, T. Regier, H. Dai, *Nature Materials* 10 (2011) 780-786.
- [22] Y. Liang, H. Liang, J. Wang, Y. Zhou, J. Li, T. Wang, H. Regier, Dai, *Journal of the American Chemical Society* 134 (2012) 3517-3523.
- [23] N. Sasikala, K. Ramya, K.S. Dhathathreyan, *Energy Conversion and Management* 77 (2014) 545-549.
- [24] F.W.T. Goh, Z. Liu, X. Ge, Y. Zong, G. Du, T.S.A. Hor, *Electrochimica Acta* 114 (2013) 598-604.
- [25] C. Jin, Z. Yang, X. Cao, F. Lu, R. Yang, *International Journal of Hydrogen Energy* 39 (2014) 2526-2530.
- [26] X. Wu, K. Scott, *Journal of Power Sources* 206 (2012) 14-19.
- [27] F.H.B. Lima, J.F.R. de Castro, E.A. Ticianelli, *Journal of Power Sources* 161 (2006) 806-812.
- [28] B.B. Blizanac, P.N. Ross, N.M. Markovic, *Journal of Physical Chemistry B* 110 (2006) 4735-4741.
- [29] S.N.S. Goubert-Renaudin, A. Wieckowski, *Journal of Electroanalytical Chemistry* 652 (2011) 44-51.
- [30] B.S. Yeo, A.T. Bell, *Journal of the American Chemical Society* 133 (2011) 5587-5593.
- [31] J.L. Fernandez, D.A. Walsh, A.J. Bard, *Journal of the American Chemical Society* 127 (2005) 357-365.
- [32] T. Maiyalagan, K.A. Jarvis, S. Therese, P.J. Ferreira, A. Manthiram, *Nat. Commun.* 5 (2014).
- [33] Y. Zhan, C. Xu, M. Lu, Z. Liu, J.Y. Lee, *Journal of Materials Chemistry A* 2 (2014) 16217-16223.
- [34] D. Wittmaier, S. Aisenbrey, N. Wagner, K.A. Friedrich, *Electrochimica Acta* 149 (2014) 355-363.

## 7. Do oxygen atoms in $\text{Co}_3\text{O}_4$ spinel take part in oxygen evolution reaction? Isotope labeling together with a new DEMS cell approach

### Abstract

The mechanism of oxygen evolution reaction (OER) on a  $\text{Co}_3\text{O}_4$  spinel catalyst is investigated in alkaline media using  $^{18}\text{O}$  labeling combined with differential electrochemical mass spectrometry (DEMS). For the first time, a new small-volume DEMS cell, which allows the use of disc electrodes and  $<0.5$  ml electrolyte, is presented in this work. The quality of the cell is demonstrated by OER. This cell shows high sensitivity. It is shown that in  $\text{H}_2^{18}\text{O}$ -containing electrolyte the amount of  $^{18}\text{O}^{16}\text{O}$  evolved increases from cycle to cycle together with a concomitant decrease of the amount of  $^{16}\text{O}_2$  with each cycle before reaching a steady-state value.  $^{18}\text{O}^{16}\text{O}$  is also evolved from a  $\text{H}_2^{16}\text{O}$  solution on  $\text{Co}_3\text{O}_4$  electrode pre-treated in  $\text{H}_2^{18}\text{O}$  solution, indicating the formation of  $^{18}\text{O}$ -labelled oxide in the previous step. Consequently, the oxide layer takes part in the OER via an oxygen exchange mechanism. This effect is reproducible with different catalyst loadings and different particle sizes.

The total number of oxygen atoms of the oxide participating in OER is about 0.2% of the total oxide loading (for  $\text{Co}_3\text{O}_4$ , 50 nm), which corresponds to about 24% of the surface atoms. This indicates that only the outer few monolayers participate in OER and represent the catalytically active sites. The real surface area of the catalyst is estimated using different methods (namely ball model, double layer capacitance, redox peak, isotope exchange) and is compared to BET data. The areas from BET and ball model show consistency for small size  $\text{Co}_3\text{O}_4$ , and are roughly 3-times higher than that of the redox peak method. Interestingly, the amount of oxygen exchanged is higher on the mixed  $\text{Ag}+\text{Co}_3\text{O}_4$  catalyst compared to the single  $\text{Co}_3\text{O}_4$ , which could illustrate the improved electrocatalytic activity previously reported on the mixed catalyst.

### 7.1. Introduction

Oxygen evolution reaction (OER) is one of the most important technological reactions for renewable energy storage systems as water electrolysis, fuel cells and metal-air batteries. The best OER catalysts are  $\text{RuO}_2$  and  $\text{IrO}_2$ , but they are rather expensive. Transition metal oxides have recently attracted much attention due to their good electrocatalytic activity for OER. The catalytic performance of these catalysts has been intensively studied. However, the mechanism of OER at metal oxides is a matter of controversy and is still not well-understood. Many mechanisms for OER were suggested in literature.[1, 2] Recently, quantum calculations showed that the mechanism of OER on  $\text{Co}_3\text{O}_4$  could involve a single Co-site or dual-Co sites forming the oxo-ligands which then undergo subsequent reactions to generate  $\text{O}_2$ . [3] It was also shown that the preferred site depends on the structure and the applied potential. A generalized scheme for OER at metal oxides in alkaline media is presented in Fig. 1. OER involves four consecutive one-electron oxidation steps and transition of the metal between higher and lower oxidation states. The first step is the adsorption of  $\text{OH}^-$  species at the metal oxide  $\text{MO}_x$  surface (step 1). The next step depends on the nature of interaction between the adsorbed hydroxyl group and the oxide: If the hydroxyl is chemisorbed on the surface it interacts with the oxide forming a higher oxidation state oxide via deprotonation of the hydroxyl group (step 2); a parallel pathway is also indicated in the scheme if hydroxyl species are physisorbed and are oxidized to oxygen (step 2'). The following step is the formation of O–O bond in the OOH adsorbate (step 3). In step (3) the "oxygen exchange process" would

take place where original "black" O-atoms are indistinguishable from the "red" O-atoms bound to the metal atom in step 1. The peroxide is formed from hydroxide, then the O<sub>2</sub> molecule is formed either of the "red" or "black" oxygen atoms and their combinations. The terminal step involves also the disproportionation of higher valent oxide to lower valent oxide, and thus releasing oxygen (step 4).

The proposed mechanism in alkaline media (Fig. 1) is in agreement with Rossmeisl et al.[4] for perovskites in alkaline media, and the model proposed by Comninellis et al. for metal oxides in acidic media,[5] however, the mechanism contradicts the reaction sequences proposed in [6] and [7] in acidic media in which O<sub>2</sub> is formed directly from two OM-O units without peroxide intermediate. Many researchers tend to favor the assumption that OER occurs via transition between higher and lower valent metal oxides.[2, 8-11] However, there are only few direct experimental proofs for this assumption. Trasatti[12] assessed that the OER can only proceed when the electrode potential is higher than the potential of the metal/metal oxide couple or the lower metal oxide/higher metal oxide couple. Thus, the ideal couple will be the one which has a potential lower or similar to the theoretical potential of the OER (1.23 V<sub>RHE</sub> in acidic media). In other words, the "oxygen exchange mechanism" involves the release of oxygen atoms originated from the lattice atoms of the oxide catalyst.

To experimentally answer the question: does the oxide layer of metal oxide take part in OER? Wohlfahrt-Mehrens et al. performed the first experiments on RuO<sub>2</sub> electrode in H<sub>2</sub>SO<sub>4</sub> solution using <sup>18</sup>O isotope labeling and DEMS.[13] They confirmed qualitatively that the oxygen atoms of the oxide layer are exchanged during the oxygen evolution process. On Pt, however, no such oxygen exchange reaction is observed in both acidic and alkaline media.[14] On the other hand, the mechanism in which the oxide participates in OER is operating on other metal oxides. Two decades later, Baltruschat, Comninellis and their co-workers demonstrated in similar, but quantitative measurements, that IrO<sub>2</sub> layer takes part in oxygen evolution[15] and formic acid oxidation.[16, 17] Krtil and co-workers demonstrated the dependence of oxygen exchange mechanism on potential.[18] To date, this mechanism has only been studied on the noble metal catalysts, namely RuO<sub>2</sub> and IrO<sub>2</sub>.

Cobalt oxides (Co<sub>3</sub>O<sub>4</sub>) and Co-based materials are known to act as efficient non-precious bifunctional catalysts in alkaline media.[19-21] Co<sub>3</sub>O<sub>4</sub> belongs to the normal spinel crystal structure based on a close-packed face centered cubic configuration of O<sup>2-</sup> ions, in which Co<sup>2+</sup> ions occupy one-eighth of the tetrahedral A-sites while Co<sup>3+</sup> ions occupy one half of the octahedral B-sites.[22] Co<sub>3</sub>O<sub>4</sub> spinel has the form Co<sup>II</sup>[Co<sup>III</sup><sub>2</sub>]O<sub>4</sub> and exists as tetrahedral[octahedral]O<sub>4</sub>. Thus, Co<sub>3</sub>O<sub>4</sub> and Co-based spinel oxides have a considerable potential as efficient oxygen electrodes. Isotope exchange measurements have not yet been done on spinel oxides, e.g. Co<sub>3</sub>O<sub>4</sub>. Therefore, in this work, a similar procedure as in [13-17] is employed for the Co<sub>3</sub>O<sub>4</sub> as well as for a Ag+Co<sub>3</sub>O<sub>4</sub> mixed catalyst to investigate whether the lattice oxygen participates in oxygen evolution and to what extent they are taking part in the oxygen exchange process.

A new DEMS cell with an electrolyte volume of ≤0.5 ml is developed and is called *small-volume DEMS cell* and is presented in this work for the first time. In essence, this is a thin layer cell similar to that of [23], but the thin layer gap is variable and the electrolyte in this layer gap can be more easily exchanged. In this approach, the major advantages are the use of small disc electrodes (5 mm) and small electrolyte volume. These functions were not possible

in the classical cell, which employs a metal-sputtered membrane as the working electrode onto which nanoparticles casting is difficult,[24] and not similar to the dual thin layer flow cell, which requires a large amount of solution. The proof-of-concept of the cell for OER is examined by the delay time, the ionic current signals corresponding to  $O_2$  evolution, the reproducibility of  $K^*$  and the characteristic features of CV and MSCV. The main characteristic feature of the cell is the very short delay time ( $\leq 2s$ ).

Determination of the real surface area of metal oxides is not trivial as for Pt. The real surface area of the metal oxide catalyst is here estimated using different methods, namely ball model, double layer capacitance,[25] redox peak method and isotope exchange method. The results are then compared to BET data. These models can be further applied for other oxides.

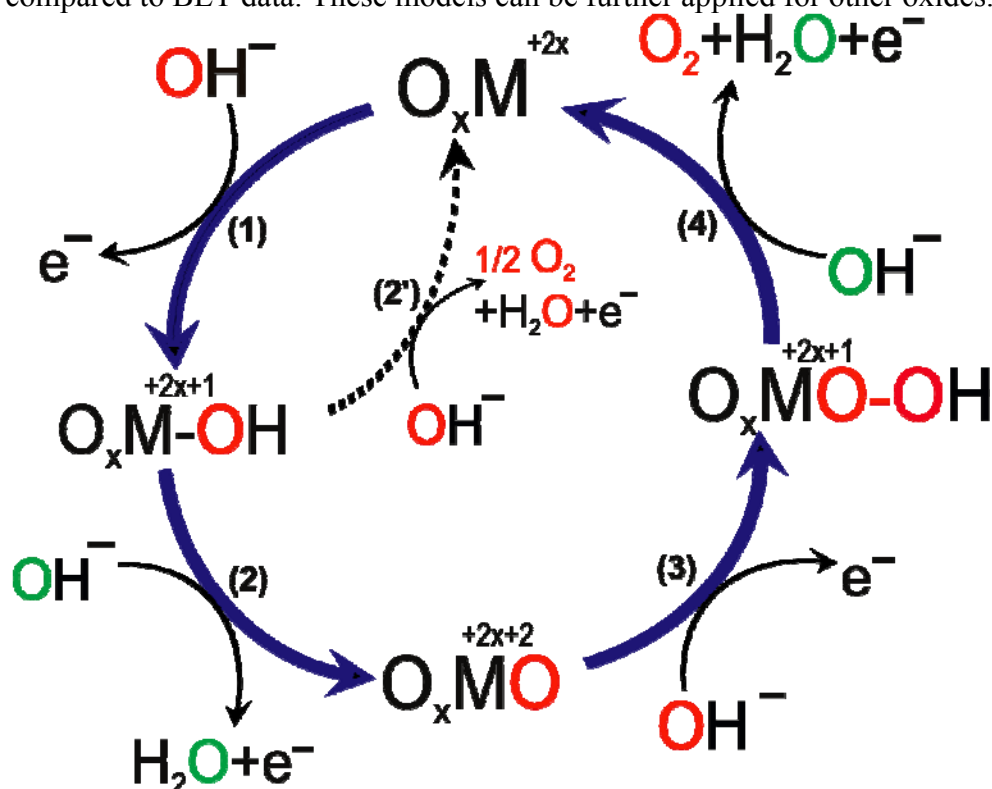


Fig. 1. Proposed scheme for oxygen evolution reaction on metal oxides in alkaline media, modified after [4].

## 7.2. Experimental

**Chemicals and electrode preparation:** Spinel  $Co_3O_4$  nanoparticles ( $\leq 50$  nm, 99.5%),  $Co_3O_4$  microparticles ( $< 10$   $\mu m$ ), Nafion<sup>®</sup> 117 (5% in a mixture of aliphatic alcohol and water), LiOH,  $H_2O$  (99%), KOH were purchased from Sigma-Aldrich, Germany.  $Co_3O_4$  ( $\sim 40$   $\mu m$ ,  $> 99.5\%$ ) was provided from Cerac Inc., and silver Ag311 catalyst (1  $\mu m$ ) from Ferro GmbH, Germany. Ultra-high pure Ar (99.999%, Air Liquide) and Milli-Q water (18.2 M $\Omega$  cm, 5 ppm TOC, Millipore Germany) were used. Prior to catalyst loading on GC electrode, the electrode was polished to mirror finish as described elsewhere.[26] The procedure of catalyst loading on GC is described in details in [26]. Briefly, an appropriate amount of catalyst suspension (ultrasonic dispersion of catalyst with ethylene glycol) was drop-cast onto the GC electrode to give the required loading, and then dried at 190  $^{\circ}C$  for 20 minutes in the oven. 20  $\mu l$  for 0.5 cm disc electrode (or 30  $\mu l$  for 1 cm disc) of Nafion solution (as a binder) were pipetted on the electrode and left to dry at 190  $^{\circ}C$  for 30 minutes. Finally, the electrode was installed slightly

warm in the shaft and left to cool. All experiments were carried out at room temperature ( $25 \pm 1$  °C). All potentials in this work are referred to RHE.

*DEMS technique:* DEMS measurements were firstly conducted in *the dual thin layer flow cell* which consists of two compartments: the volatile products (i.e.  $O_2$  in OER) generated in the electrochemical compartment diffuse through a porous Teflon membrane (Gore Tex<sup>®</sup>, Germany) to the mass spectrometer compartment (Balzer QMG-422, Pfeiffer Vacuum) under effect of electrolyte flow ( $5 \mu\text{l/s}$ ) then to the outlet. The faradaic currents and the ionic currents of volatile species are simultaneously recorded. A GC electrode with an exposed geometric area of  $0.283 \text{ cm}^2$  was used in this setup, and the electrolyte volume was defined by a thin porous Teflon ring spacers ( $50 \mu\text{m}$  each) underneath the disc electrode. Two Pt wires at the inlet and outlet of electrolyte were used as counter electrodes to minimize the ohmic resistance of solution in the cell. More details about DEMS and this cell are given elsewhere.[24, 27] The electrolyte was saturated with Ar for about 10 minutes prior to the experiment. A home-made potentiostat has been used to record the CV. A LabVIEW software is used for data collection.

*New DEMS cell:* A schematic drawing of this cell and detailed description are presented in chapter 2 (Experimental). An actual photo of the used setup is shown in Fig. 2.

The ionic currents for ions of  $m/z = 32, 34$  and  $36$  were recorded versus the electrode potential (MSCV) together with the faradaic current (CV).

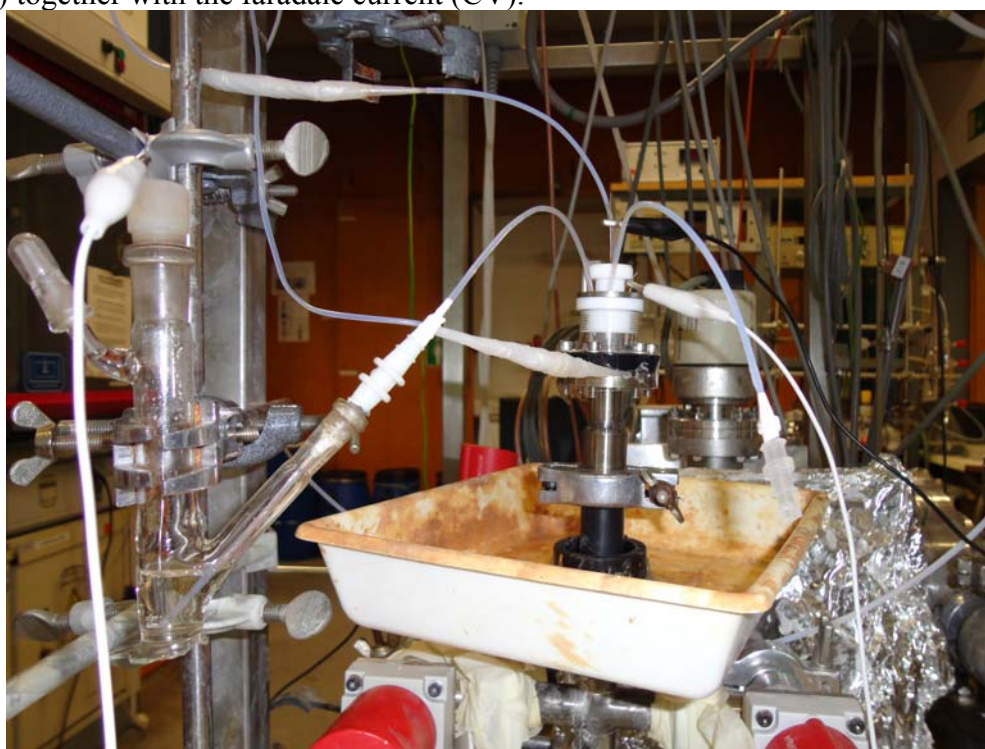


Fig. 2. Actual photo of the new *small-volume DEMS cell*.

To obtain quantitative information from the ionic currents (e.g. faradaic current if the peak is not that clear in the CV), it is necessary to determine the calibration constant ( $K^*$ ). This was done by conducting a potentiostatic experiment in the respective cell, where the potential was held at a certain value in the OER region, and the faradaic and ionic currents were simultaneously recorded. A plateau was obtained for current transient. From the ratio of the faradaic and ionic currents (or charges),  $K^*$  can be obtained according to the equation:  $K^* =$

$z \cdot I_i / I_F = z \cdot Q_i / Q_F$ , where,  $z$  is the number of electrons transferred,  $I$  is the current and  $Q$  is the charge. Due to some uncertainties in the calibration constant, base line correction and integration of signals, it is therefore fair to assume an error of  $\pm 10\%$  on the DEMS results.

### 7.3. Results

Typical voltammograms of  $\text{Co}_3\text{O}_4/\text{GC}$  with a loading of  $100 \mu\text{g cm}^{-2}$  in Ar-saturated 0.5M KOH are shown in Fig. 3. The CVs were recorded in the dual thin layer cell at a flow rate of  $5 \mu\text{l s}^{-1}$  and at 10 and 50  $\text{mV s}^{-1}$ . Bare GC is also shown for comparison, and revealed no significant currents since GC is not active for OER. The CV of  $\text{Co}_3\text{O}_4$  is characterized by the main pair of redox peaks: an anodic at  $E = 1.48 \text{ V}$  (Epa2) and a cathodic at  $E = 1.4 \text{ V}$  (Epc2), prior to oxygen evolution (around 1.53V) as depicted in Fig. 3. During the positive-going scan, the current increases until a small peak (Epa1) is seen at 1.2V and by reversing the scan the corresponding cathodic peak (Epc1) appears at ca. 1.1V. As the scan rate increases, the peaks get more defined, and their currents increase.

The first broad redox peak (Ep1) is assigned to the following reaction in agreement with [28, 29]:



While the main peak (Ep2), just prior to oxygen evolution or superimposed on it, is attributed to the reaction [30]:



The ratio of the charge of Ep1:Ep2 is approximately 1:3, which is consistent with the fact that in the first one-electron process, three cobalt atoms are involved ( $\text{Co}_3\text{O}_4$ ) while in the second process only one cobalt atom ( $\text{CoOOH}$ ).

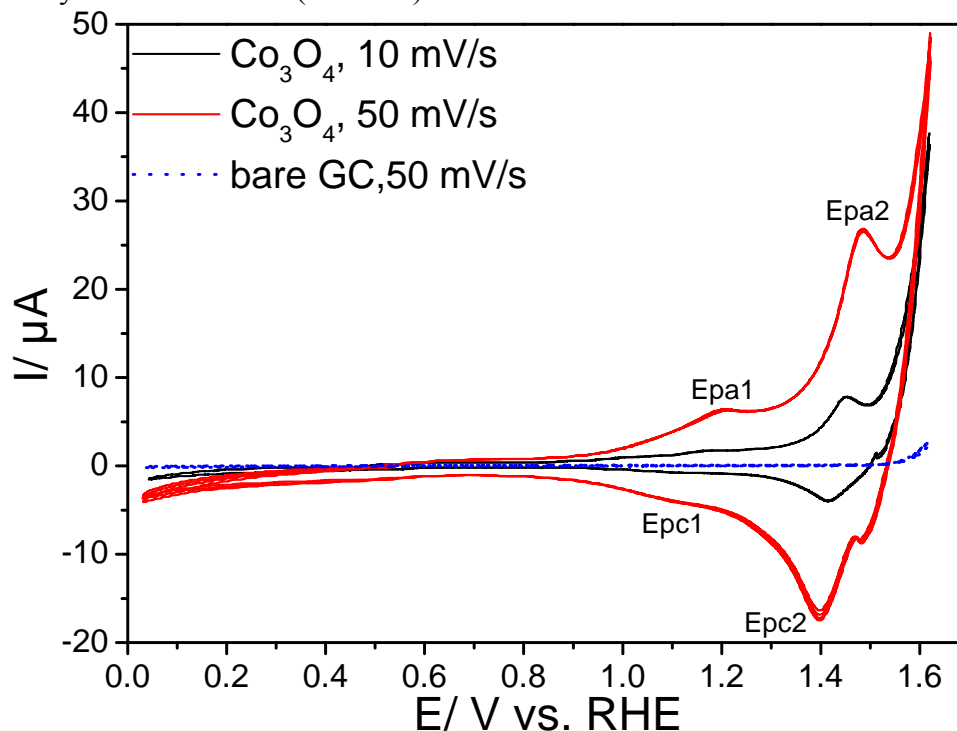


Fig. 3. CVs of  $\text{Co}_3\text{O}_4/\text{GC}$  electrode in 0.5M KOH (Ar-saturated) in the dual thin layer cell with a flow rate of  $5 \mu\text{l s}^{-1}$  and at 10 and 50  $\text{mV s}^{-1}$ . Catalyst ( $40 \mu\text{m}$  size) loading:  $100 \mu\text{g cm}^{-2}$ .

### 7.3.1. Co<sub>3</sub>O<sub>4</sub> (40 μm) catalyst with 100 μg cm<sup>-2</sup> loading in 0.1M LiOH

Basically, two series of experiments (*series A and B*) have been conducted. In the first series A, we aimed to mark the oxygen of Co<sub>3</sub>O<sub>4</sub> with <sup>18</sup>O atoms by treatment with H<sub>2</sub><sup>18</sup>O containing solution and obtain information on the extent of isotope exchange from the relative amount of <sup>16</sup>O<sup>18</sup>O evolved. While in the second series B, the labeled oxide was used to evolve oxygen in H<sub>2</sub><sup>16</sup>O containing electrolyte. By monitoring the ion signals of masses 32, 34 and 36 (corresponding to <sup>16</sup>O<sub>2</sub>, <sup>16</sup>O<sup>18</sup>O and <sup>18</sup>O<sub>2</sub>, respectively), one can examine if the labeled <sup>18</sup>O is transferred from the Co<sub>3</sub>O<sub>4</sub> lattice to the evolved oxygen. In the first two measurements, the DEMS dual thin layer cell was used until the new cell was developed.

#### *Series A:*

In this series, the DEMS dual thin layer cell was filled continuously (flow rate: 5 μl/s) with Ar-saturated 0.5M KOH containing 2 w% of marked water (H<sub>2</sub><sup>18</sup>O). The working electrode consists of 100 μg cm<sup>-2</sup> Co<sub>3</sub>O<sub>4</sub>/GC. Co<sub>3</sub>O<sub>4</sub> in this experiment was of 40 μm particle size. Several successive scans were applied with 10 mV s<sup>-1</sup> between 0.05V and 1.62V (vs. RHE), and the faradaic currents were recorded together with the ionic currents for <sup>16</sup>O<sub>2</sub>, <sup>16</sup>O<sup>18</sup>O and <sup>18</sup>O<sub>2</sub> for each scan. The respective diagrams obtained during the consecutive scans are depicted in Fig. 4a.

Signals for ionic currents corresponding to <sup>16</sup>O<sub>2</sub> and <sup>16</sup>O<sup>18</sup>O were observed in the MSCV for the consecutive cycles. Ionic currents for <sup>18</sup>O<sub>2</sub> were not large enough to be observed since only 2 w% H<sub>2</sub><sup>18</sup>O were used in solution. The small hysteresis observed in the cathodic sweep is due to the slow transport from the upper to the lower compartment of the dual thin layer cell leading to a delay time of 2s. As can be seen from MSCV, there is no ionic current at potentials less than 1.45V while faradaic currents are noticeable, which are due to the surface oxidation and reduction reactions of the oxide as explained above. To elucidate the extent of oxygen exchange in the formed O<sub>2</sub>, the mole fraction (*X*) of <sup>16</sup>O<sub>2</sub> and <sup>16</sup>O<sup>18</sup>O gases was calculated as follows (and plotted in Fig. 5a):

$$X_i = \frac{Q_i}{\sum_j Q_j} \quad \text{eq. 7.1}$$

Here, *Q<sub>i</sub>* is the ionic charge of the m/z 34 or 32 and  $\sum Q_j = Q_{32} + Q_{34} + Q_{36}$  is the total ionic charge related to the formation of oxygen <sup>16</sup>O<sub>2</sub> + <sup>16</sup>O<sup>18</sup>O + <sup>18</sup>O<sub>2</sub>. The charge is obtained by integration of the mass signals from MSCV. The predicted value obtained from the concentration of H<sub>2</sub><sup>18</sup>O in the solution is also plotted in Fig. 5a. The amount of <sup>16</sup>O<sub>2</sub> decreases gradually with an attendant increase of the amount of <sup>16</sup>O<sup>18</sup>O after each cycle, reaching a steady-state value of H<sub>2</sub><sup>18</sup>O in solution (corresponds to the expected value) at the fifth cycle. The continuous flow of the electrolyte through the cell and at the working electrode ascertains a homogeneous constant amount of marked water in the solution. Thus, the increase of <sup>16</sup>O<sup>18</sup>O associated with the decrease of <sup>16</sup>O<sub>2</sub> after each scan proves directly that the oxide layer participates in the oxygen evolution reaction. The lattice oxygen <sup>16</sup>O of the oxide is replaced with <sup>18</sup>O from solution, which leads to labeling of the oxide with <sup>18</sup>O. The highest mole fraction of <sup>16</sup>O<sub>2</sub> is obtained in the first scan because Co<sub>3</sub>O<sub>4</sub> originally contains mainly <sup>16</sup>O, which contributes more in oxygen evolution in the first cycle.

After some cycles the isotope content in the oxide (or better at the surface of the oxide) is similar to that in the electrolyte, and no further exchange takes place; the isotopic composition

of the O<sub>2</sub> formed (<sup>16</sup>O<sup>18</sup>O: <sup>16</sup>O<sub>2</sub>= 0.04:0.96) corresponds to that expected from the electrolyte composition (H<sub>2</sub><sup>18</sup>O: H<sub>2</sub><sup>16</sup>O= 0.02:0.98).

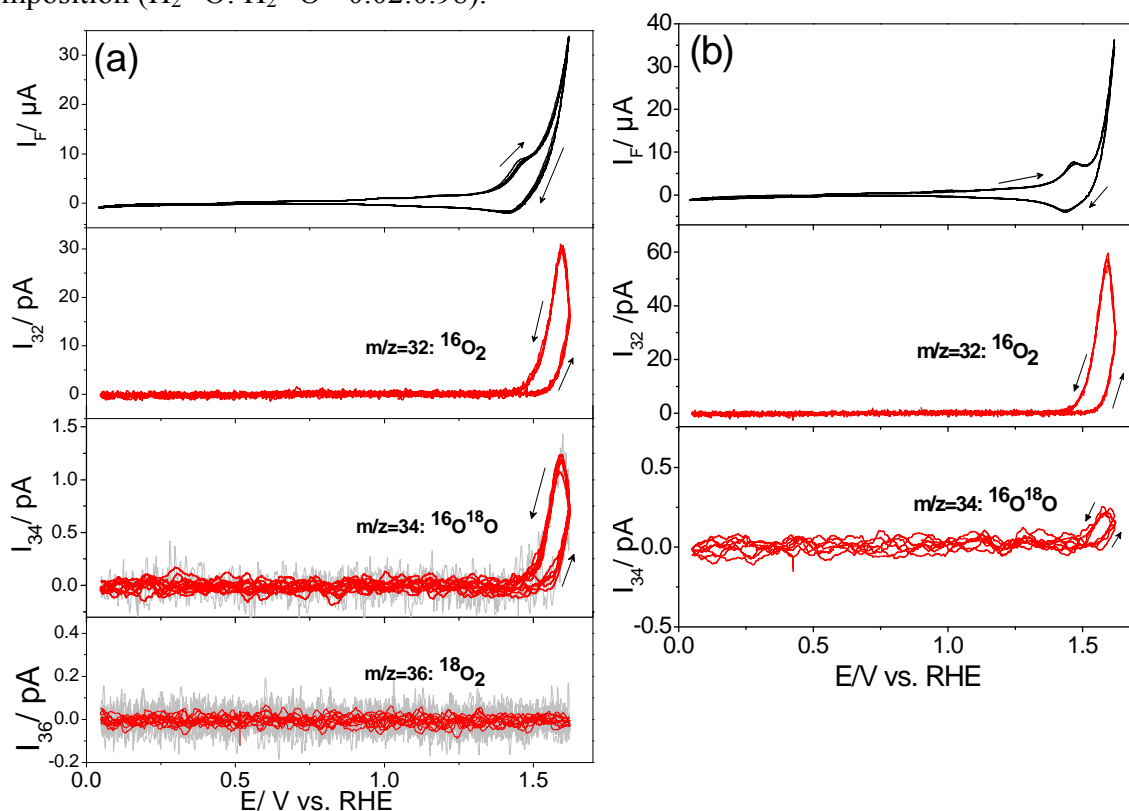


Fig. 4. DEMS results for OER at Co<sub>3</sub>O<sub>4</sub> (100 $\mu\text{g}/\text{cm}^2$ , 40 $\mu\text{m}$  size)/GC electrode in (a) Ar-saturated 0.5M KOH solution containing 2% (w/w) of marked H<sub>2</sub><sup>18</sup>O, scan rate=10 mV/s and flow rate 5 $\mu\text{l}/\text{s}$ , and (b) in 0.5M KOH/H<sub>2</sub><sup>16</sup>O, the electrode has been pre-treated in 0.5M KOH/H<sub>2</sub><sup>18</sup>O. The upper panel displays the faradaic current, while the lower ones represent the ionic currents for m/z 32, 34 and 36.

To quantitatively estimate the amount of lattice oxygen involved in the oxygen exchange process of the total catalyst loading, evaluations from CV and MSCV data are done. The number of moles ( $n$  in mol/cm<sup>2</sup>) and the corresponding number of the <sup>16</sup>O lattice oxygen atoms ( $N$ ) which are exchanged to <sup>18</sup>O per unit electrode geometric area for each scan (of the first four scans in this case) is calculated according to Faraday's law as follows (eq. 7.2):

$$n = \frac{1}{2} f \frac{\Delta Q_{34}}{\sum_j Q_j} \frac{Q_F}{zF} = \frac{1}{2} f \gamma \frac{Q_F}{2F} \quad \text{where,} \quad \gamma = \frac{\Delta Q_{34}}{\sum_j Q_j} \quad \text{eq. 7.2}$$

$$N = n \cdot N_A$$

where,  $\gamma$  is the excess ratio (with respect to the steady state value of the 5<sup>th</sup> scan in this case) related to the incorporation of <sup>18</sup>O into the oxide lattice; and  $\Delta Q_{34}$  is the difference of ionic charge for each scan to the steady state value of the 5<sup>th</sup> scan;  $\sum Q_j$  is the total ionic charge;  $N_A$  is Avogadro's constant;  $Q_F$  is the faradaic charge related to the formation of oxygen (C/cm<sup>2</sup>) and can be obtained by integration of faradaic current corresponding to oxygen evolution from CV or from the sum of ionic charges for oxygen ( $\sum Q_j$ ) using the relation:  $Q_F = z \cdot \sum Q_j / K^*$

where,  $K^*$  is a calibration factor of the DEMS cell[24];  $F$  is the Faraday's constant; and  $z$  is the number of electrons involved in the OER ( $z = 2$  per oxygen atom).

In this formula, the factor of  $1/2$  accounts for the fact that the concentration of  $^{18}\text{O}^{16}\text{O}$  in dioxygen is double that of the atomic concentration of  $^{18}\text{O}$  referred to the total number of oxygen atoms. The factor ( $f$ ) in our formula accounts for the low isotopic content of the water used here and is the reciprocal of the concentration of  $\text{H}_2^{18}\text{O}$  in solution:

$$\frac{1}{f} = \frac{X(\text{H}_2^{18}\text{O})}{X(\text{H}_2^{16}\text{O}) + X(\text{H}_2^{18}\text{O})} \quad \text{eq. 7.3}$$

For the isotopic content of 2 w%  $\text{H}_2^{18}\text{O}$  thus  $f=50$ .

From the experimental data of oxygen exchange of Fig. 4a, we calculated  $\gamma$  of  $^{16}\text{O}^{18}\text{O}$  for each scan, also the faradaic current was calculated from CV. Using equation 7.2 and the values obtained for  $\gamma$  and  $Q_F$ ,  $n$  can be calculated for each scan. The total amount of  $^{18}\text{O}$  atoms exchanged during the successive scans are calculated by summation of contribution of each cycle ( $\sum n = 1.34 \text{ nmol/cm}^2$ ).

- To get the number of moles of oxygen atoms in the total  $\text{Co}_3\text{O}_4$  loading  $n_t(\text{O}^{2-})$ , eq. 7.4 was used:

$$n_t(\text{O}^{2-}) = 4 \cdot \frac{m_{\text{Co}_3\text{O}_4}}{M_{\text{Co}_3\text{O}_4}} \quad \text{eq. 7.4}$$

where,  $m$  is the mass of catalyst loaded on GC,  $M$  is the molar mass of  $\text{Co}_3\text{O}_4$ , and the factor 4 refers to the number of oxygen atoms per  $\text{Co}_3\text{O}_4$  unit. The loading of the catalyst used here was  $100 \mu\text{g/cm}^2$  (i.e.  $n_t(\text{O}^{2-}) = 4 \times 100 / 241 \mu\text{mol/cm}^2 = 1660 \text{ nmol/cm}^2$  of oxygen atoms).

Thus, the ratio of the amount of exchanged lattice oxygen to the total loading is  $r_{\text{exch}}$ :

$$r_{\text{exch}} = \frac{n_{\text{O-exch}}}{n_t(\text{O}^{2-})} \quad \text{eq. 7.5}$$

where,  $n_{\text{O-exch}}$  is obtained from isotope exchange experiment and  $n_t(\text{O}^{2-})$  from the loading. Thus,  $r_{\text{exch}} = 1.34 / 1660 = 0.08\%$  are exchanged of total oxygen atoms in the loading. This implies that only few monolayers of the oxide participate in OER. The deeper parts of the oxide are blocked by the evolved oxygen and thus are excluded for further oxygen reactions.

To get an estimate of the surface active sites, the number of exchanged oxygen atoms is compared with the amount of surface atoms which are in contact with the solution. By integration of the anodic faradaic current of the CV (Fig. 4a) of the catalyst between 1.36 and 1.51V (i.e. between the minima, without further background subtraction), which is assumed to be due to surface charge  $Q_s$  (redox couple  $\text{Co}^{3+}/\text{Co}^{4+}$  of the catalyst), a charge of  $0.53 \text{ mC/cm}^2$  is obtained. Thus, the amount of surface active redox sites  $n_{\text{surf}}$ , which is in contact with solution, is obtained as follows:

$$n_{\text{surf}} = \frac{Q_s}{zF} \quad \text{eq. 7.6}$$

where,  $Q_s$  is the surface charge of the redox process. Thus,  $n_{\text{surf}} = 0.53 / 1 \times 96500 \text{ mmol/cm}^2 = 5.5 \text{ nmol/cm}^2$  active cobalt surface atoms.

The amount of cobalt atoms on the surface to the total amount of oxygen atoms in the catalyst loading =  $5.5 / 1660 = 0.33\%$ . If only a part of the  $\text{Co}_3\text{O}_4$  of the surface is oxidized, the number of cobalt atoms is even larger, if the charge is in part due to double layer charging it is

smaller. The amount of exchanged oxygen atoms to the surface atoms  $y_{exch}$  is given as follows:

$$y_{exch} = \frac{n_{O-exch}}{n_{surf}} \quad \text{eq. 7.7}$$

This gives a value of  $y_{exch} = 1.34/5.5 = 0.24$  (i.e. 24% of the surface atoms are active and participate in the oxygen exchange reaction).

Further analyses of the real surface area of the catalyst using the ball model, DL capacitance model, isotope exchange method and redox peak model are done:

- Assuming the exposed surface of the Co /Co-spinel is the (111) surface orientation, then 4 oxygen atoms are located within a unit cell with an area of  $\sim 0.36 \text{ nm}^2$ . [31] Based on this model the number of moles of oxygen atoms at surface per  $\text{cm}^2_{\text{geo}}$  is  $S$  and is given by:

$$S = \frac{4}{0.36 \text{ nm}^2 \cdot N_A} = 1.85 \text{ nmol/cm}^2_{\text{geo}} \quad \text{eq. 7.8}$$

- *Isotope exchange model*: the true surface area  $A_{tr}$  according to this model equals:

$$A_{tr} = \frac{n_{O-exch}}{S} \quad \text{eq. 7.9}$$

Thus,  $A_{tr} = 1.34 \text{ (nmol/cm}^2) / 1.85 \text{ (nmol/cm}^2_{\text{geo}}) = 0.72 \text{ cm}^2$ .

- A simple *ball model* is also applied to estimate the true surface area of  $\text{Co}_3\text{O}_4$  catalyst: assuming a homogeneous radius of  $20 \text{ }\mu\text{m}$  for  $\text{Co}_3\text{O}_4$ , the number of particles and their total surface area is calculated leading to a total surface area of  $11 \text{ cm}^2$  as follows:

$$V(\text{Co}_3\text{O}_4) = \frac{m}{\rho} \quad \text{eq. 7.10}$$

where,  $V(\text{Co}_3\text{O}_4)$  is the volume of the catalyst used,  $\rho$  is the density of  $\text{Co}_3\text{O}_4$  ( $\rho = 6.11 \text{ g/cm}^3$ ) and  $m$  is the mass of catalyst used ( $28.3 \text{ }\mu\text{g}$ ), thus  $V(\text{Co}_3\text{O}_4) = 4.63 \times 10^6 \text{ }\mu\text{m}^3$ .

Considering one particle as a ball, then the volume and area of each ball are given by:

$$V(r = 20 \text{ }\mu\text{m}) = \frac{4}{3} \pi r^3 \quad \text{eq. 7.11}$$

$$A(r = 20 \text{ }\mu\text{m}) = 4\pi r^2 \quad \text{eq. 7.12}$$

Where,  $r$  is the radius of the ball (in this case  $r = 20 \text{ }\mu\text{m}$ ). The number of particles in this volume  $N(r = 20 \text{ }\mu\text{m})$  is:

$$N(r = 50 \text{ nm}) = \frac{V(\text{Co}_3\text{O}_4)}{V(r = 20 \text{ }\mu\text{m})} \quad \text{eq. 7.13}$$

Here,  $N(r = 20 \text{ }\mu\text{m}) = 88$  particles. Thus the surface area which is calculated according to the ball model is called  $A_{tr}$ :

$$A_{tr} = N_{(r=50 \text{ nm})} \cdot A_{(r=50 \text{ nm})} \quad \text{eq. 7.14}$$

From this, the ball model results in  $A_{tr} = 0.0044 \text{ cm}^2$  or  $0.0044 \text{ cm}^2 / 0.283 \text{ cm}^2 = 0.016 \text{ cm}^2_{\text{tr}} / \text{cm}^2_{\text{geo}}$ .

The number of moles of active atoms  $= \frac{A_{tr}}{A_{\text{geo}}} \cdot S$  eq. 7.15

A value of  $0.016 (\text{cm}^2 / \text{cm}^2) \times 1.85 \text{ (nmol / cm}^2_{\text{geo}}) = 0.03 \text{ nmol / cm}^2_{\text{geo}}$ .

- Based on the unit cell of Co-oxide in [31] mentioned above, the number of moles of oxygen atoms, which are located in the calculated true surface area  $n_{tr}$  is:

$$n_{tr} = \frac{4 \cdot A_{tr}}{(0.36 \text{ nm}^2) \cdot N_A} \quad \text{eq. 7.16}$$

This gives  $n_{tr} = 8.1 \times 10^{-12}$  moles of O-atoms per  $\text{cm}^2_{tr}$ . The number of moles of oxygen atoms per  $\text{cm}^2$  in the total loading is calculated above  $n_t (\text{O}^{2-}) = 1660 \text{ nmol}/\text{cm}^2$ . Since 0.08% of the total oxygen atoms are being exchanged (from the isotope exchange experiment), this corresponds to  $1.3 \times 10^{-9}$  moles of oxygen atoms are being exchanged. According to eq. 7.5, the fraction of oxygen exchanged of total loading  $r_{\text{exch}} = 1.3 \times 10^{-9} / 8.1 \times 10^{-12} = 160$ . This high value could be due to the large roughness of each particle in the loading. However, for nanoparticles it gives a reasonable value since the roughness is reduced.

The surface area from this model ( $A_{tr}$ ) can be calculated according to the following eq.:

$$A_{tr} = \frac{r_{\text{exch}} \cdot A_{\text{geo}}}{m_{\text{Co}_3\text{O}_4}} \quad \text{eq. 7.17}$$

$$A_{tr} = 1.6 \times 10^{16} \times 0.283 \text{ cm}^2 / 28.3 \mu\text{g} = 1.6 \times 10^{16} \text{ m}^2/\text{g}.$$

- Using *double layer (DL) capacitance*: for oxide surfaces, a value of  $60 \mu\text{F}/\text{cm}^2$  is taken as a reference.[25, 32] However, this typical value was reported to have 100% degree of uncertainty.[25] The DL capacitance between 0.5 and 0.8V was about  $0.71 \text{ mF}/\text{cm}^2$ . Consequently,  $A_{tr}/A_{\text{geo}}$  is obtained as follows:

$$\frac{A_{tr}}{A_{\text{geo}}} = \frac{C_{dl} (\mu\text{F cm}^{-2})}{60 \mu\text{F cm}^{-2}} \quad \text{eq. 7.18}$$

This yields  $12 \text{ cm}^2/\text{cm}^2$ . According to eq. 7.15, the number of moles of active atoms =  $12 (\text{cm}^2/\text{cm}^2) \times 1.85 \text{ nmol}/\text{cm}^2_{\text{geo}} = 22 \text{ nmol}/\text{cm}^2_{\text{geo}}$ .

Using the roughness factor of 22 obtained from DL capacitance assumption, we obtain  $A_{tr} = 12 \times 0.283 \text{ cm}^2 / 28.3 \mu\text{g} = 12 \text{ m}^2/\text{g}$ , i.e.  $3.4 \text{ cm}^2$ .

- *Redox peak model*: the number of moles of active atoms obtained from the charge under the redox peak corresponding to the transition  $\text{Co}^{\text{III}}/\text{Co}^{\text{IV}} = 5.5 \text{ nmol}/\text{cm}^2$  (as calculated above).

- The true surface area per geometric surface area is obtained from eq. 7.15 and gives  $A_{tr}/A_{\text{geo}} = 5.5 (\text{nmol}/\text{cm}^2) / 1.85 (\text{nmol}/\text{cm}^2_{\text{geo}}) = 3 \text{ cm}^2/\text{cm}^2_{\text{geo}}$ .

These results show that this ball model does not fit for large particles ( $40 \mu\text{m}$ ) while redox peak method reveals comparable data to isotope exchange method. The results are compared in Table 1.

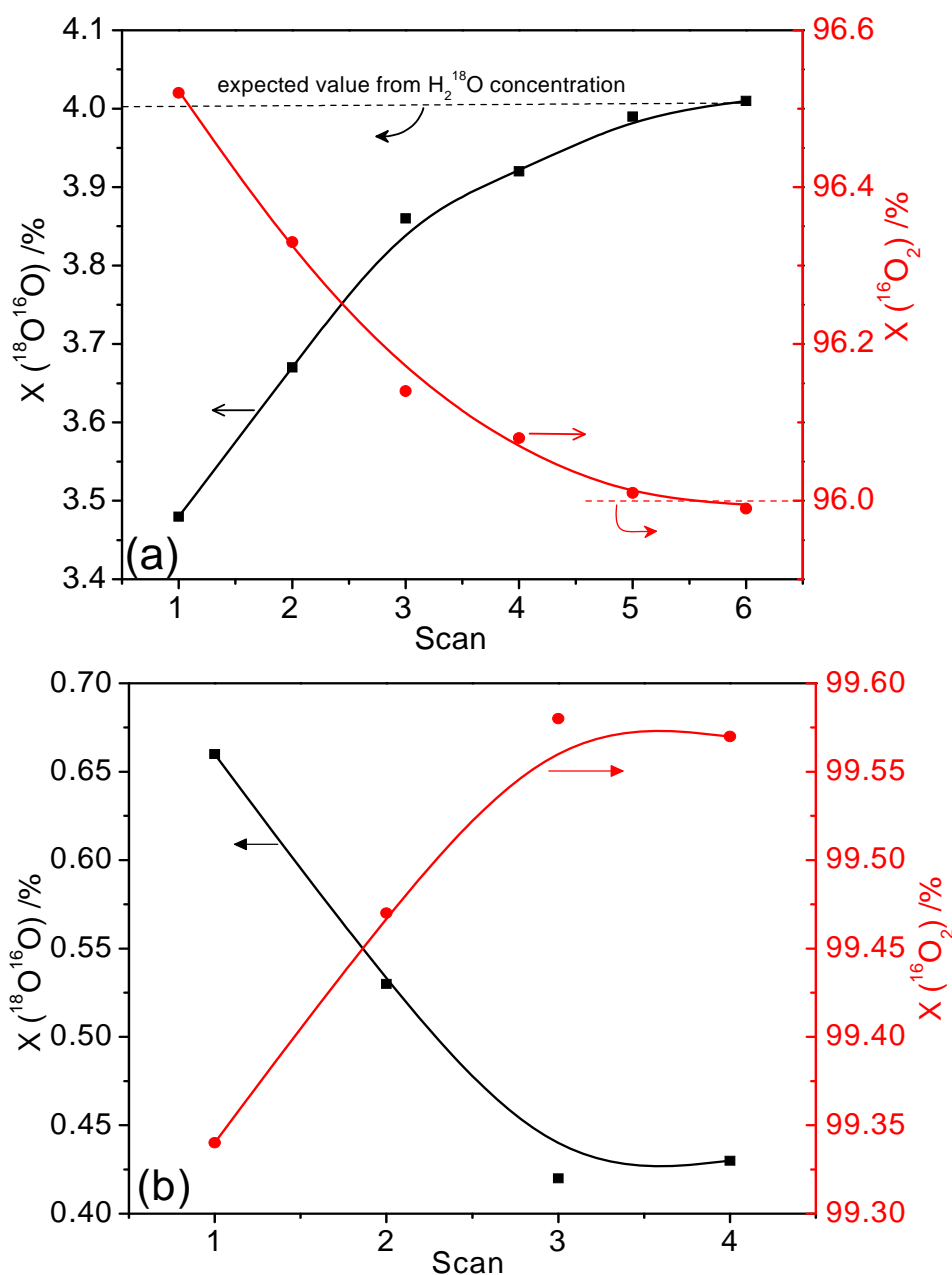


Fig. 5. plot of the isotopic content as a function of scan number for OER on  $\text{Co}_3\text{O}_4$  ( $100\mu\text{g}/\text{cm}^2$ )/GC with scan rate of 10 mV/s in (a) 0.5M KOH/ $\text{H}_2^{18}\text{O}$ , (b) 0.5M KOH/ $\text{H}_2^{16}\text{O}$ , the electrode was pre-treated in 0.5M KOH/ $\text{H}_2^{18}\text{O}$ . Data were taken from the experiment shown in Fig. 4.

#### Series B:

In this series of measurements, after obtaining the labeled  $\text{Co}_3\text{O}_4$  oxide in the experiments of *series A*, the potential was stopped at 0.5V during the cathodic sweep to exchange the electrolyte: The  $^{18}\text{O}$ -containing electrolyte was withdrawn from the cell; the cell was carefully washed with 0.5M KOH/ $\text{H}_2^{16}\text{O}$  solution, then the cell was refilled with fresh 0.5M KOH/ $\text{H}_2^{16}\text{O}$  solution while keeping the potential constant. Again, the potential was scanned up to 1.62V in the fresh electrolyte for several cycles. Fig. 4b depicts the respective CVs together with the ionic currents of  $^{16}\text{O}_2$  and  $^{16}\text{O}^{18}\text{O}$ . This figure shows the formation of  $^{16}\text{O}^{18}\text{O}$  in  $\text{H}_2^{16}\text{O}$  containing electrolyte. The signal of mass 32 is the strongest as to be expected for

OER from  $\text{H}_2^{16}\text{O}$ . The measured concentrations of  $^{16}\text{O}^{18}\text{O}$  and  $^{16}\text{O}_2$  obtained for the four successive scans are plotted in Fig. 5b. One can clearly see that the concentration of  $^{16}\text{O}^{18}\text{O}$  decreases in parallel with the  $^{16}\text{O}_2$  concentration increase with each scan reaching a steady value in the third cycle. The steady-state value  $X(^{16}\text{O}^{18}\text{O})$  in the last cycle was about 0.43%, which corresponds to a concentration of 0.21% of atomic  $^{18}\text{O}$ , which is very close to the natural abundance of  $^{18}\text{O}$  (0.2 %).

This trend indicates that some of the evolved oxygen molecules originate from the oxide. This illustrates that the  $^{18}\text{O}$ -containing oxide layer (previously formed in series A) was replaced by its  $^{16}\text{O}$  analogue via isotope exchange reaction in  $\text{H}_2^{16}\text{O}$  electrolyte. Thus, it proves again that the oxide layer takes part in oxygen evolution reaction. We conclude that oxygen evolution occurs via redox transitions in the oxide. Surface redox transitions in the oxide layer appear also at the onset potential of oxygen evolution and at lower potentials, as seen in Fig. 5.

According to Faraday's law and the previous equations applied in *series A*, the amount of  $^{18}\text{O}$  atoms in the oxide which are exchanged with  $^{16}\text{O}$  equals  $0.51 \text{ nmol/cm}^2$  (i.e. only 0.03% of the total catalyst loading). These are about one-third of the amount obtained in *Series A*. This difference might be due to some loss of  $^{18}\text{O}$  from oxide during the washing procedure (electrolyte exchange) or interdiffusion of  $^{18}\text{O}$  into the bulk of  $\text{Co}_3\text{O}_4$  lattice.[15] The amount of oxygen exchanged was about 13% of the surface oxygen atoms.

It might be argued that the electrolyte was not completely exchanged in the cell or in the pores of the membrane. This can be ruled out since the solution is continuously swept away from the thin layer flow cell.

### 7.3.2. $\text{Co}_3\text{O}_4$ (50 nm) catalyst with $200 \mu\text{g cm}^{-2}$ loading in 0.1M LiOH

Similar procedure as above was applied for other  $\text{Co}_3\text{O}_4$  particles of smaller size (50 nm) and higher marked water content of 10 w% in the same dual thin layer cell was used. The catalyst loading here was  $200 \mu\text{g cm}^{-2}$  on GC. In *Series A*, the DEMS measurements were done in Ar-saturated 0.1M LiOH solution containing 10% (w/w) of marked  $\text{H}_2^{18}\text{O}$  with  $10 \text{ mV s}^{-1}$  and  $5 \mu\text{l s}^{-1}$ . Several consecutive cycles ( 8 scans) were applied to a potential limit of 1.8V as shown in Fig. 6a. The upper potential applied here was higher than that in the previous experiment due to the lower conductivity of the 0.1M LiOH than that of 0.5M KOH. This leads to higher ohmic drop, thus a positive potential shift of the redox peaks (ca. 150 mV) and delay of the oxygen evolution can be noticed in Fig. 6. The hysteresis between anodic and cathodic scans is slightly larger. However, the same features of the voltammograms were observed as above. Similar behavior has been obtained as in case of  $\text{Co}_3\text{O}_4$  with larger size. The signals corresponding to  $^{16}\text{O}_2$ ,  $^{16}\text{O}^{18}\text{O}$  and  $^{18}\text{O}_2$  can be clearly observed. Fig. 7a shows the increase of the concentration of  $^{16}\text{O}^{18}\text{O}$  with each successive cycle associated with a decrease in  $^{16}\text{O}_2$  concentration until a steady state value after the 6<sup>th</sup> scan is reached. The steady state value equals the expected value from the concentration of  $\text{H}_2^{18}\text{O}$  in water (here 18% for  $^{16}\text{O}^{18}\text{O}$  for 10w% marked water). Steady state was reached one or two cycles later compared to the  $\text{Co}_3\text{O}_4$  (40  $\mu\text{m}$ ). In *series B*, after the solution is being exchanged with 0.1M LiOH/ $\text{H}_2^{16}\text{O}$  electrolyte the labeled oxide was scanned for 10 cycles in this unmarked solution as shown in Fig. 6b. Oxygen is partly evolved from the lattice oxygen of the oxide, thus the amount of  $^{16}\text{O}^{18}\text{O}$  decreases with cycling, implying the contribution of the oxide in the OER, see Fig. 7b.

Using the same evaluations as above, we obtain a total of  $7.3 \text{ nmol/cm}^2$  oxygen atoms exchanged, corresponding to 0.22% of the total  $\text{Co}_3\text{O}_4$  loading. Since the faradaic current for OER is superimposed on oxide oxidation currents, it is more proper to get the faradaic charge from the ionic charge using  $K^*$  according to equation:  $Q_F = z \cdot Q_i / K^*$  as mentioned above. Comparing this value to the amount of oxygen atoms, which forms the surface (i.e.  $5.7 \text{ mC/cm}^2$  between 1.39 - 1.7V), we found that 12% of surface atoms participate in the oxygen exchange mechanism.

From series B, an amount of  $3.4 \text{ nmol/cm}^2$  oxygen is replaced, which represents 0.1% of the total  $\text{Co}_3\text{O}_4$  loading or maximum 8.5% of the surface atoms.

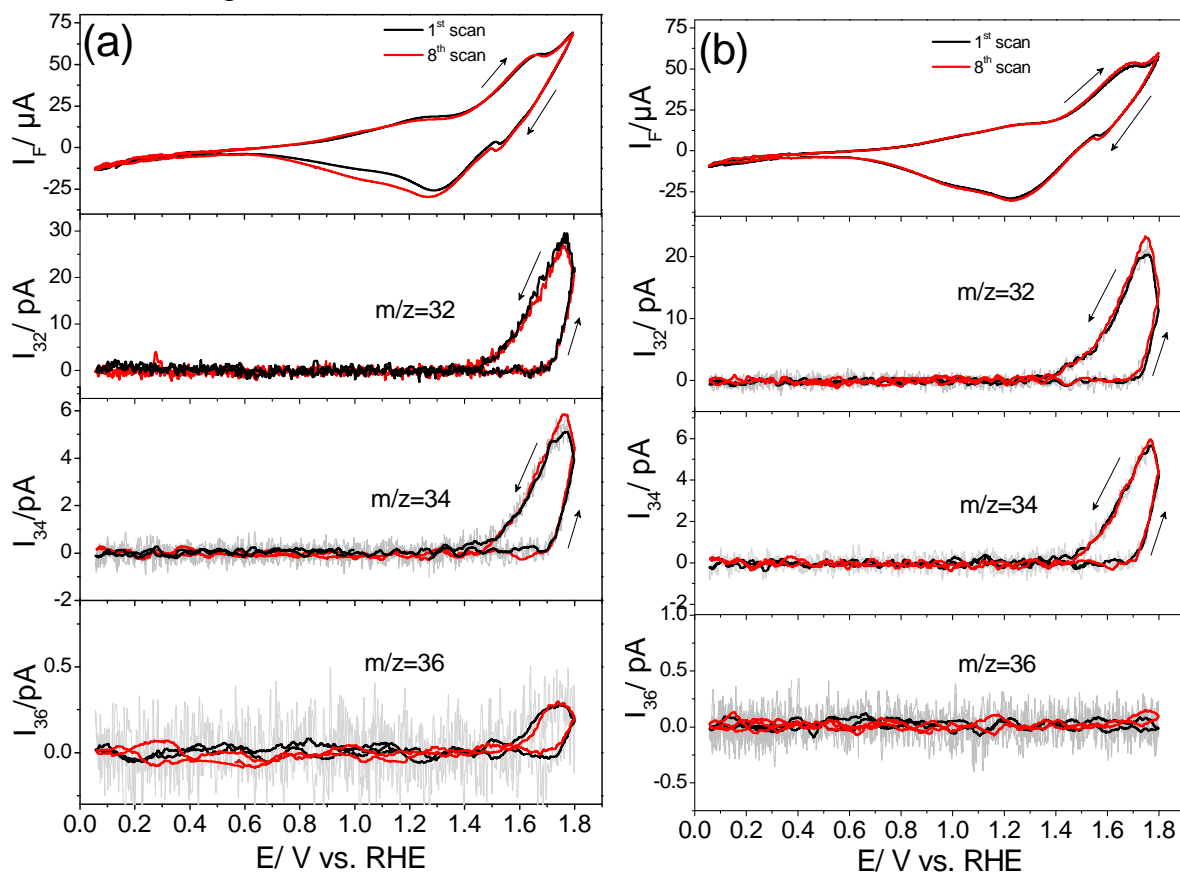


Fig. 6. DEMS results for OER at  $\text{Co}_3\text{O}_4$  ( $200 \mu\text{g/cm}^2$  of 50 nm size)/GC electrode in (a) Ar-saturated 0.1M LiOH solution containing 10% (w/w) of marked  $\text{H}_2^{18}\text{O}$ , scan rate=10 mV/s and flow rate  $5 \mu\text{l/s}$ . (b) in 0.1M LiOH/ $\text{H}_2^{16}\text{O}$ , the electrode has been pre-treated in 0.1M LiOH/ $\text{H}_2^{18}\text{O}$ . The upper panel displays the faradaic current, while the lower ones represent the ionic currents for m/z 32, 34 and 36 in the second scan.

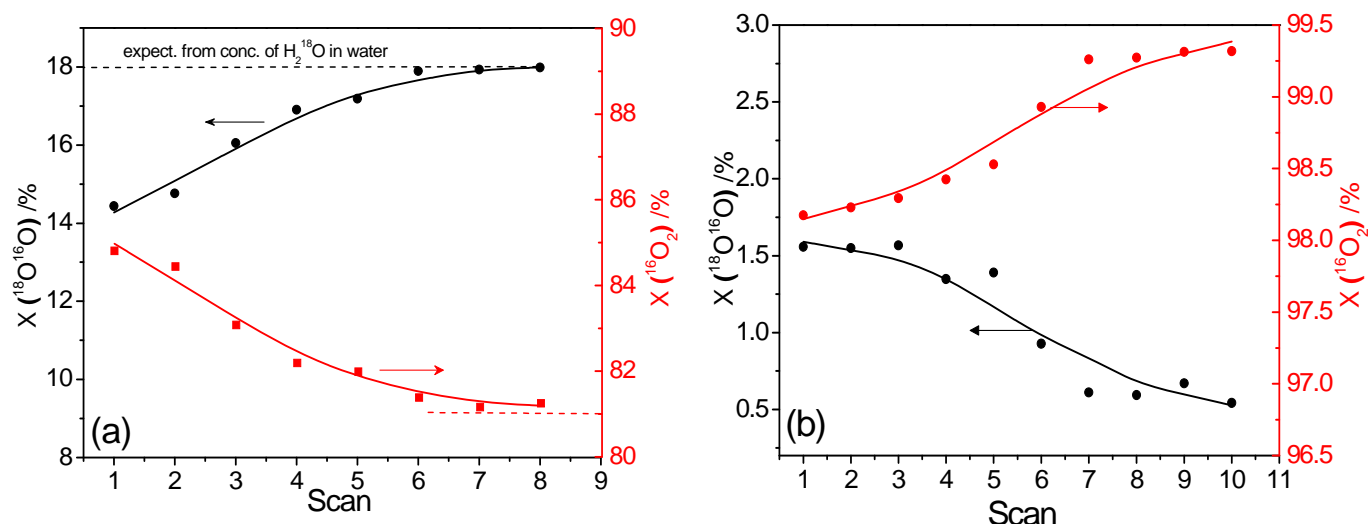


Fig. 7. Plot of the isotopic content as a function of scan number for OER on  $\text{Co}_3\text{O}_4$  ( $200\mu\text{g}/\text{cm}^2$ )/GC with scan rate=10mV/s in (a) 0.1M LiOH/ $\text{H}_2^{18}\text{O}$ , (b) 0.1M LiOH/ $\text{H}_2^{16}\text{O}$ , the electrode has been pre-treated in 0.1M LiOH/ $\text{H}_2^{18}\text{O}$ . Data were taken from the experiment shown in Fig. 5.

The data are evaluated according to the previous equations and results are summarized in Table 1. In addition, the BET data are also compared here: BET data was analyzed and a real surface area of  $16.5\text{ m}^2/\text{g}$  was obtained, which corresponds to  $9.3\text{ cm}^2$ . Therefore,  $A_{tr}/A_{geo} = 9.3\text{ cm}^2/0.283\text{ cm}^2 = 33\text{ cm}^2/\text{cm}^2_{geo}$ .

These results illustrate that the ball model and redox peak method are in agreement with the BET data for this catalyst.

### 7.3.3. New small-volume DEMS cell: $\text{Co}_3\text{O}_4$ (50 nm) in 20% marked $\text{H}_2^{18}\text{O}$ solution

In this part, we present the good performance of the new cell for quantitative and qualitative analysis of volatile products. The  $\text{Co}_3\text{O}_4$  catalyst ink has been loaded on a GC disc electrode to yield a coverage of  $400\mu\text{g cm}^{-2}$ , afterwards the disc was carefully inserted in the shaft which was next installed in the cell. The cell was filled with 0.8M LiOH solution containing 20% (w/w) of marked  $\text{H}_2^{18}\text{O}$  from the electrolyte reservoir using a Teflon tube inlet. In *series A* of experiments, the potential was scanned for 6 cycles between 0.05V and 1.6V, while the CVs and MSCVs were recorded together, then the potential was stopped at 0.4V for electrolyte exchange. Fig. 8a shows the respective voltammograms for the first 3 cycles. The ionic currents corresponding to  $^{16}\text{O}_2$ ,  $^{16}\text{O}^{18}\text{O}$  and  $^{18}\text{O}_2$  gases are clearly noticeable. Interestingly, there is no significant hysteresis between anodic and cathodic scans in the MSCV, compared to the dual thin layer cell[16] or to the Kel-F cell used by Krtil et al.[18] The delay time in this cell was very short (1-2s) as can be seen from the CVs and MSCVs. The results show that similar trend has been observed: the increase of concentration of  $^{16}\text{O}^{18}\text{O}$  with a concomitant decrease in concentration of  $^{18}\text{O}_2$  with each cycle as shown in Fig. 9a. This indicates that the oxide participates, to some extent, in the oxygen evolution reaction. In *series B*, the marked solution has been withdrawn from the cell under constant potential of 0.4V using a syringe. The electrolyte was replaced gradually to keep a little of solution over the membrane, this process was repeated several times to ascertain the substitution of all the marked solution with  $\text{H}_2^{16}\text{O}$  solution. The pre-labeled oxide was then scanned in the fresh

0.8M LiOH/H<sub>2</sub><sup>16</sup>O solution for 7 cycles, as shown in Fig. 8b. The amount of <sup>16</sup>O<sup>18</sup>O decreases with cycles. This proves the oxygen exchange mechanism, see Fig. 9b. The steady-state values were reached after the 4<sup>th</sup> or the 5<sup>th</sup> cycle. The expected values of the steady state were matching a concentration of 16.5 w% H<sub>2</sub><sup>18</sup>O instead of the apparent 20% called in *Series A*. This could be due to some loss on the walls of the syringe during transfer and dilution of the marked solution by the rest of water on the walls and membrane of the cell before the begin of the experiment.

From the above equations, here a total of 13.5 nmol/cm<sup>2</sup> oxygen atoms are exchanged, which correspond to  $r_{\text{exch}} = 0.2\%$  of the total oxygen atoms in Co<sub>3</sub>O<sub>4</sub> loading. This can be compared to the surface atoms, where  $y_{\text{exch}} = 25\%$  of the surface atoms are active and participate in the oxygen exchange process. Further analyses of the real surface area of the catalyst using the ball model, DL capacitance assumption and redox peak were done and compared to BET data. The results are given in Table 1. Detailed calculations for this catalyst are in SI.

The results illustrate that the ball model and DL capacitance method are comparable to the BET data for this catalyst. The same series of experiments on Co<sub>3</sub>O<sub>4</sub> (50 nm) were done with a higher anodic potential limit of 1.65V and comparable results are obtained, where 0.33% of the total oxide is exchanged. The data are presented in Table 1 (between brackets), and the corresponding CVs and MSCVs are displayed in SI (Fig. S 1,2).

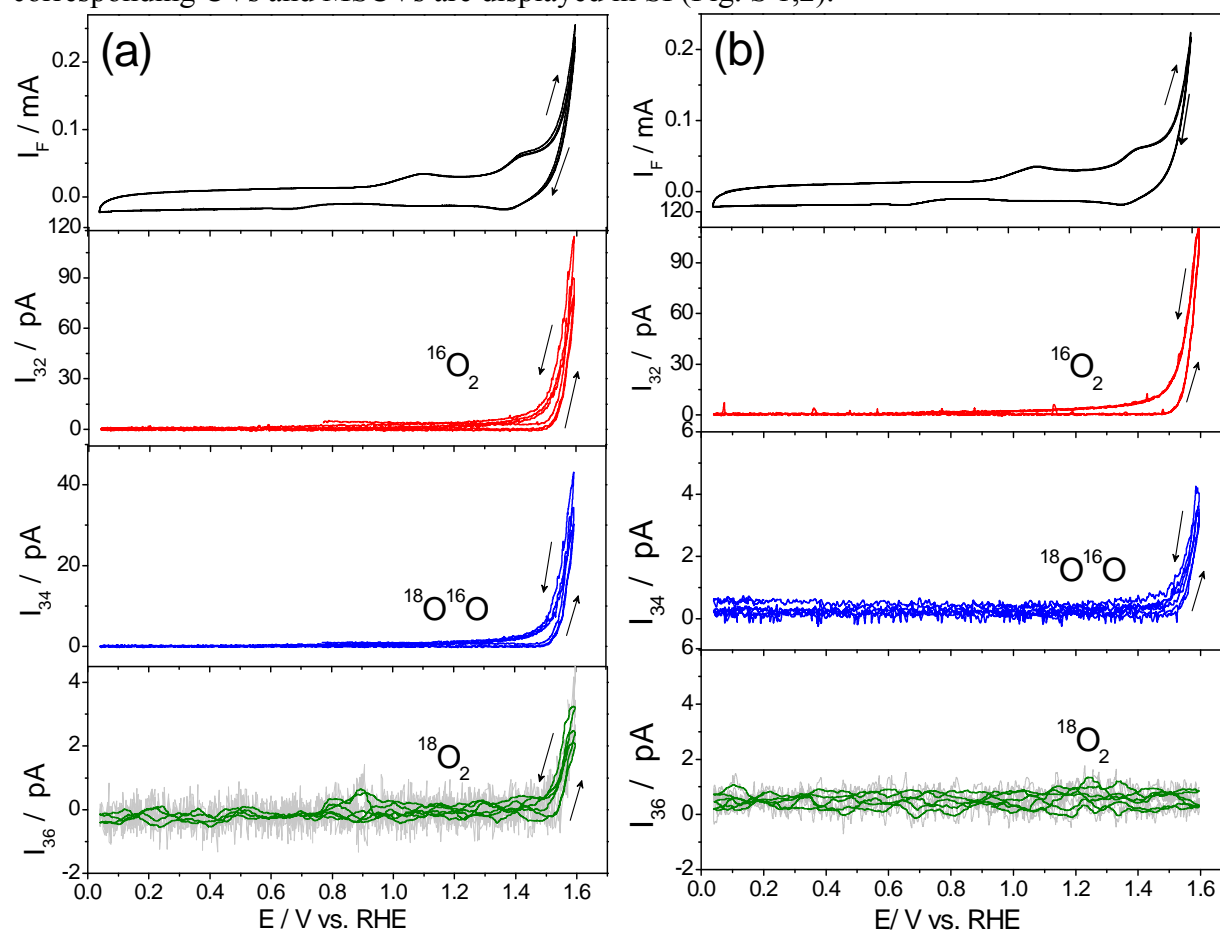


Fig. 8. DEMS results for 6 cycles of OER at Co<sub>3</sub>O<sub>4</sub> (400 μg/cm<sup>2</sup> of 50 nm size)/GC electrode in the new small volume DEMS cell in (a) Ar-saturated 0.8M LiOH solution containing 20% (w/w) of marked H<sub>2</sub><sup>18</sup>O, scan rate=10 mV/s. (b) in 0.8M LiOH/H<sub>2</sub><sup>16</sup>O, the electrode has been

pre-treated in 0.8M LiOH/H<sub>2</sub><sup>18</sup>O. The upper panel displays the faradaic current, while the lower ones represent the ionic currents for m/z 32, 34 and 36.

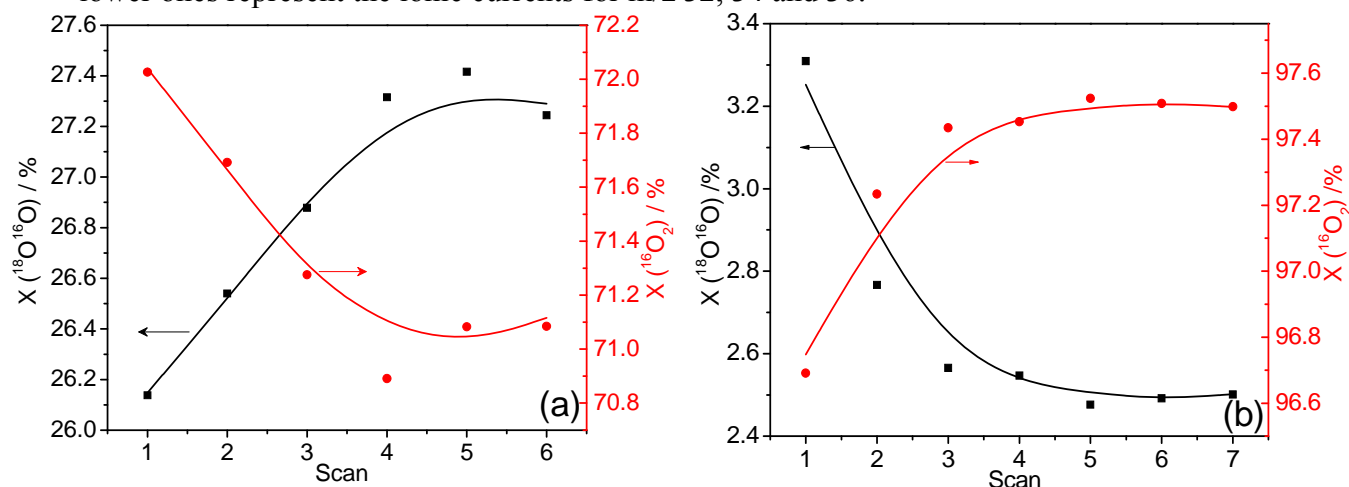


Fig. 9. Plot of the isotopic content as a function of scan number for OER on Co<sub>3</sub>O<sub>4</sub> (400 μg/cm<sup>2</sup>)/GC with scan rate=10mV/s in (a) 0.8M LiOH/(20 w%)H<sub>2</sub><sup>18</sup>O, (b) 0.8M LiOH/H<sub>2</sub><sup>16</sup>O, the electrode has been pre-treated in 0.8M LiOH/H<sub>2</sub><sup>18</sup>O. Data were taken from the experiment shown in Fig. 7.

#### 7.3.4. Co<sub>3</sub>O<sub>4</sub> (50 nm) in 50% marked H<sub>2</sub><sup>18</sup>O solution using the new small volume DEMS cell:

Similar results are obtained when higher upper potential limit (to 1.65V) and higher H<sub>2</sub><sup>18</sup>O concentration in the solution (50 w%) was used, as shown in Fig. 10 and 11. The onset of OER is the same as observed above, and the signal for mass 36 is obvious. The dependence of the isotope exchange ratio on the potential limit of scanning is not significant. The amount of oxygen, which is exchanged with the marked solution, is about 0.15% of the total catalyst loading, which corresponds to about 23% of the Co<sub>3</sub>O<sub>4</sub> surface atoms. These results demonstrate that the oxygen exchange process and the contribution of the oxide in OER are reproducible (i.e. with different loadings, particle sizes and isotopic water percentage). Further evaluation of the true surface area and comparison of the different methods on this catalyst is presented in Table. 1. Similar oxygen exchange values and surface areas are obtained compared to the previous experiment in 20% marked solution. Remarkably, even if the total amount of exchanged oxygen is higher by increasing the loading or opening the potential window, the fraction of Co<sub>3</sub>O<sub>4</sub> participating in the oxygen evolution remains close to 0.2% of the total loading or around 24% of the surface atoms.

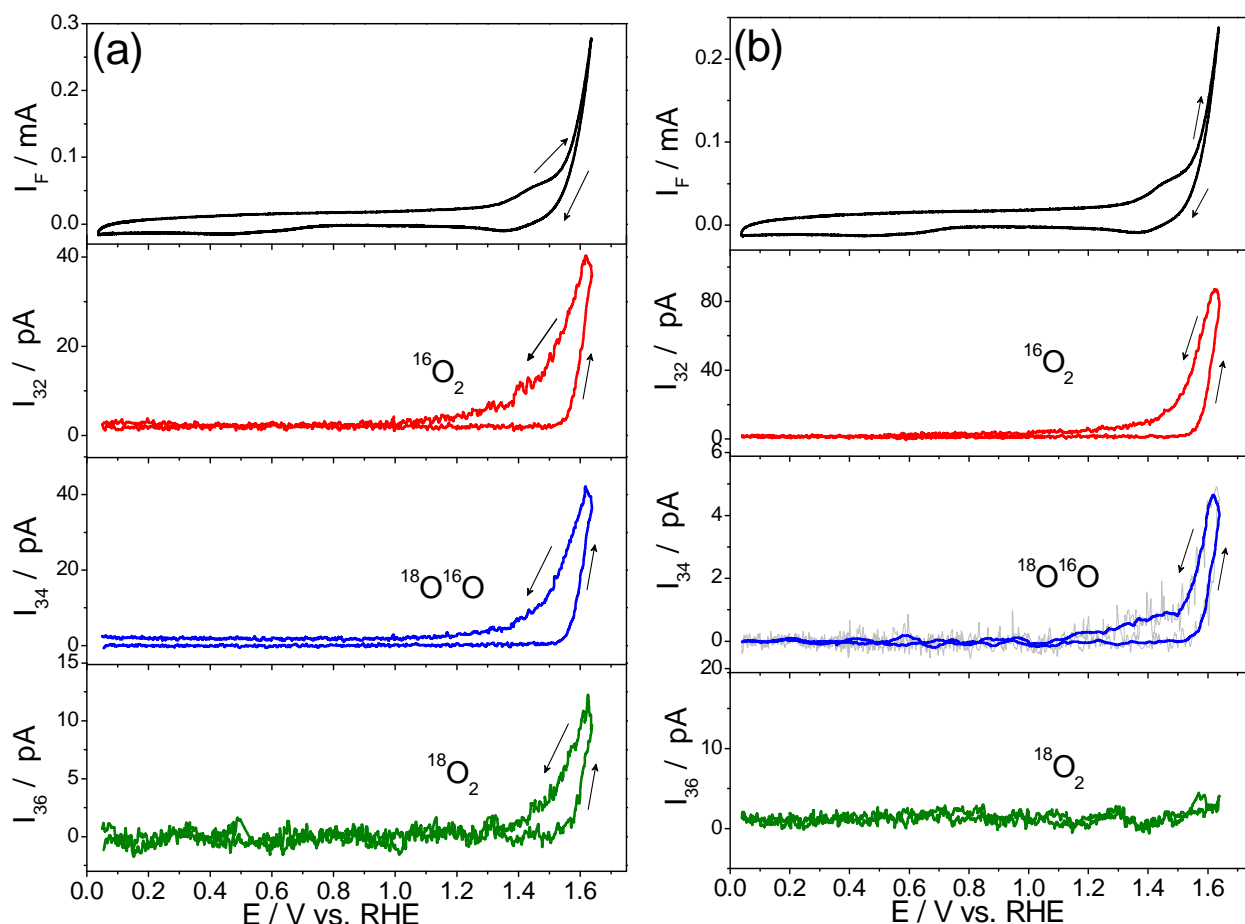


Fig. 10. DEMS results for OER (first cycle) at  $\text{Co}_3\text{O}_4$  ( $400\mu\text{g}/\text{cm}^2$  of  $50\text{nm}$  size)/GC electrode in the new small volume DEMS cell in (a) Ar-saturated  $0.5\text{M}$  LiOH solution containing  $50\%$  (w/w) of marked  $\text{H}_2^{18}\text{O}$ , scan rate= $10\text{ mV}/\text{s}$ . (b) in  $0.5\text{M}$  LiOH/ $\text{H}_2^{16}\text{O}$ , the electrode has been pre-treated in  $0.5\text{M}$  LiOH/ $\text{H}_2^{18}\text{O}$ . The upper panel displays the faradaic current, while the lower ones represent the ionic currents for  $m/z$  32, 34 and 36. The potential was scanned between  $0.05$  to  $1.65\text{V}$ .

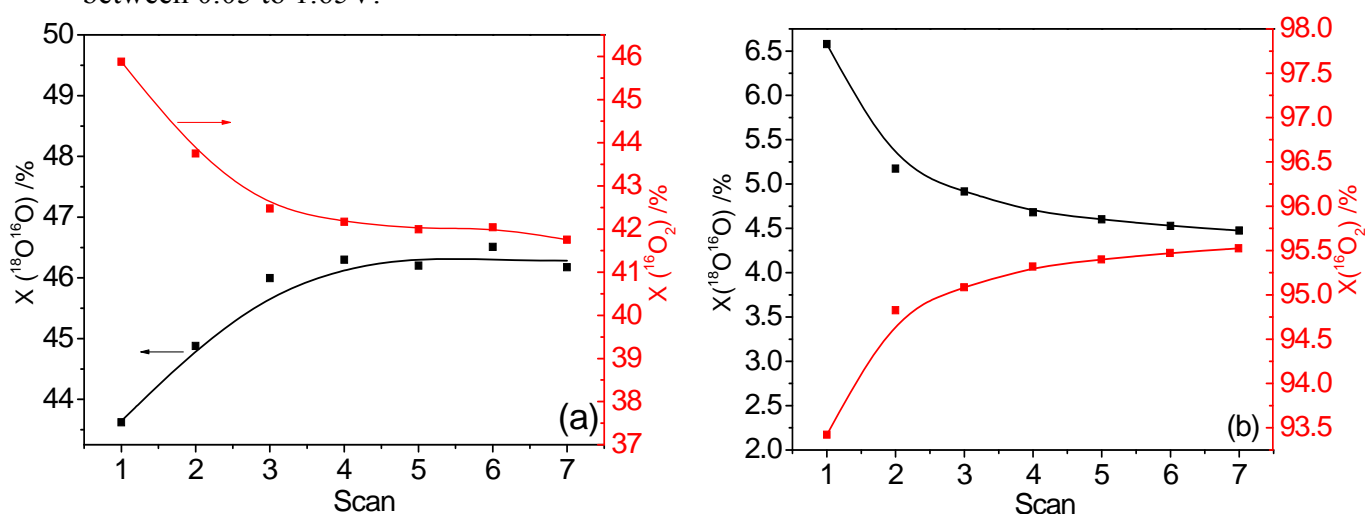


Fig. 11. Plot of the isotopic content as a function of scan number for OER on  $\text{Co}_3\text{O}_4$  ( $400\mu\text{g}/\text{cm}^2$ )/GC with scan rate= $10\text{ mV}/\text{s}$  in (a)  $0.5\text{M}$  LiOH/ $(50\text{ w}\%)\text{H}_2^{18}\text{O}$ , (b)  $0.5\text{M}$  LiOH/ $\text{H}_2^{16}\text{O}$ , the electrode has been pre-treated in  $0.5\text{M}$  LiOH/ $\text{H}_2^{18}\text{O}$ . Data were taken from the experiment shown in Fig. 10.

### 7.3.5. $\text{Co}_3\text{O}_4$ (10 $\mu\text{m}$ ) in 20% marked $\text{H}_2^{18}\text{O}$ solution using the new small volume DEMS cell:

Larger size of  $\text{Co}_3\text{O}_4$  (10  $\mu\text{m}$ ) has been examined and showed also isotopic exchange mechanism. The same trend of oxygen concentration change with each cycle has been noticed as shown in Fig. 12 for *Series A and B*. The amount of oxygen exchange was about 0.03% of the total loading. The amount of oxygen exchanged is close to that obtained in case of 40  $\mu\text{m}$   $\text{Co}_3\text{O}_4$  catalyst, but less than that obtained in case of the 50 nm  $\text{Co}_3\text{O}_4$  particles. The smaller the size of the particles the larger the number of accessible sites exposed to solution, and the larger the amount of oxygen exchange. The results show that the ball model does not fit well to BET data or other models in case of larger particles, namely 10  $\mu\text{m}$  and 40  $\mu\text{m}$ . This could be due to the non-homogeneity and absence of uniform distribution of the surface. Estimation of the number of active sites on the catalyst has been done, and are compared in Table 1. As expected, the larger  $\text{Co}_3\text{O}_4$  (10 $\mu\text{m}$ ) catalyst revealed smaller real surface area compared to that of 50 nm  $\text{Co}_3\text{O}_4$  as obtained from different methods (except for isotope exchange method).

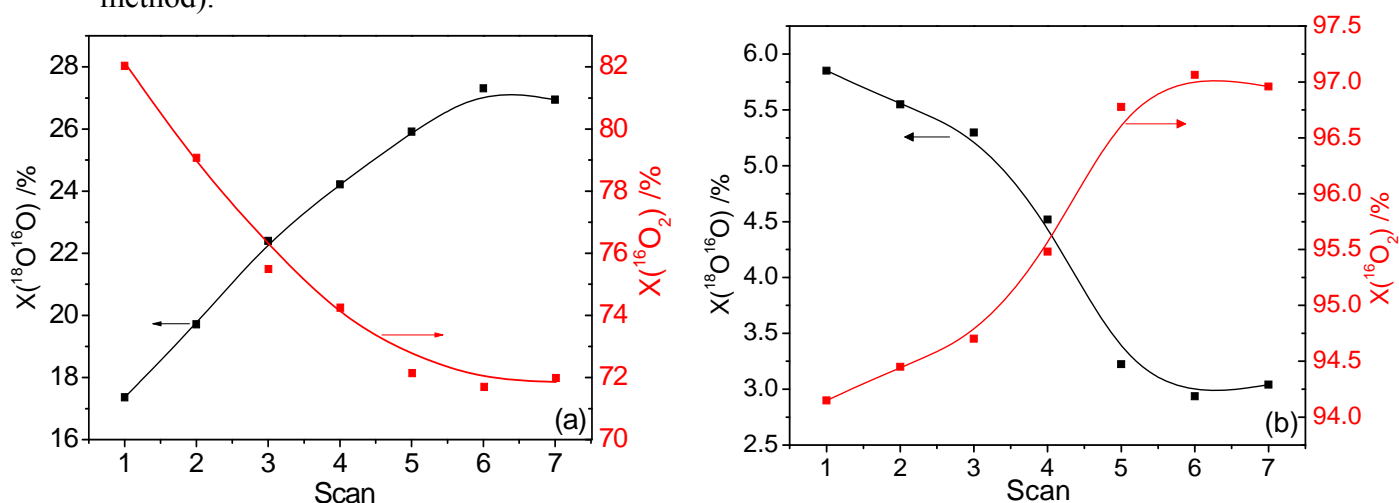


Fig. 12. Plot of the isotopic content as a function of scan number for OER on  $\text{Co}_3\text{O}_4$  (10  $\mu\text{m}$  size) with (600 $\mu\text{g}/\text{cm}^2$ )/GC with scan rate=10mV/s in (a) 0.8M LiOH/(20 w%) $\text{H}_2^{18}\text{O}$ , (b) 0.8M LiOH/ $\text{H}_2^{16}\text{O}$ , the electrode has been pre-treated in 0.8M LiOH/ $\text{H}_2^{18}\text{O}$ .

### 7.3.6. Ag+ $\text{Co}_3\text{O}_4$ (10 w%) mixed catalyst in 50% marked $\text{H}_2^{18}\text{O}$ solution using new small volume DEMS cell

We have shown in our previous reports, that the mixed Ag+ $\text{Co}_3\text{O}_4$  catalyst has a marked catalytic activity for OER and ORR in alkaline media.[26, 33] This enhanced bifunctionality was attributed to a sort of synergistic effect between the two components of the composite. XPS results showed also a change in the electronic properties of cobalt-oxide when it is in contact with Ag. Furthermore, the results showed that the presence of Ag cation in contact with  $\text{Co}_3\text{O}_4$  facilitates the redox switching in  $\text{Co}_3\text{O}_4$  (i.e. transitions between  $\text{Co}_3\text{O}_4$  and  $\text{Co}(\text{OH})_2$ ), which could be the reason for the enhanced activity (see chapter 5). Therefore, the disproportionation of higher valent oxide to lower valent oxide via an oxygen exchange process between the oxide and the solution is involved in the oxygen evolution reaction. Here, we investigate OER on a mixed catalyst based on Ag311 (1 $\mu\text{m}$ )+ $\text{Co}_3\text{O}_4$  (50 nm) 10 w% in 0.5M LiOH solution containing 50% (w/w) of marked  $\text{H}_2^{18}\text{O}$ , as shown in Fig. 13a. The redox

peaks observed in CV of Fig. 13 are assigned to oxidation and reduction of Ag and cobalt and their oxides. Ag is oxidized to  $\text{Ag}_2\text{O}$  and then further oxidized to  $\text{Ag}^{\text{I}}\text{Ag}^{\text{III}}\text{O}_2$  as explained previously.[26] In *Series A* of experiments on the mixed catalyst, an increase of  $^{16}\text{O}^{18}\text{O}$  concentration with a concomitant decrease of  $^{16}\text{O}_2$  concentration with consecutive scans has been observed (Fig. 14a). While in *Series B* of the experiment, a decrease of concentration of  $^{16}\text{O}^{18}\text{O}$  with a concomitant increase in  $^{16}\text{O}_2$  concentration with each cycle has been noticed, see Fig. 14b. This behavior is similar to that observed on pure  $\text{Co}_3\text{O}_4$  catalyst. This proves again the contribution of the oxide, and could be also the Ag-oxide since it is oxidized at higher potentials, in the oxygen exchange process. According to the above equations, the total amount of  $^{18}\text{O}$  atoms exchanged during the successive scans equals  $6.6 \text{ nmol cm}^{-2}$ , which corresponds to 1% of the total loading with respect to only  $\text{Co}_3\text{O}_4$  mass since Ag is mostly inactive for OER. In *series B*, 0.3% is obtained, which is less than that in *series A*. This might be due to  $^{18}\text{O}$  interdiffusion or loss upon rinsing, as discussed above.

The above results show that the amount of cobalt atoms in the mixed  $\text{Ag}+\text{Co}_3\text{O}_4$  catalyst taking part in the oxygen exchange mechanism are higher than that observed on pure  $\text{Co}_3\text{O}_4$  catalyst (1% for the mixed catalyst compared to 0.2% for the single catalyst). Therefore, the surface of the mixed catalyst is more active than that of single  $\text{Co}_3\text{O}_4$ . This suggests that OER takes place at the interphase between  $\text{Co}_3\text{O}_4$  and Ag particles, which exists in case of the mixed catalyst. This explains the improved catalytic activity observed on the mixed catalyst. For this composite catalyst, it is more reasonable to compare different methods for surface area determination. The results from BET, ball model, Redox peak model and isotope exchange model revealed good agreement and similar true surface area, as displayed in Table 1. This illustrates the suitability and validation of the used methods for the characterization of our catalysts. However, the results based on the DL capacitance method deviate from the other methods because part of the exposed surface is oxide, and the rest is metallic Ag, and  $60 \mu\text{F cm}^{-2}$  is only for oxides.

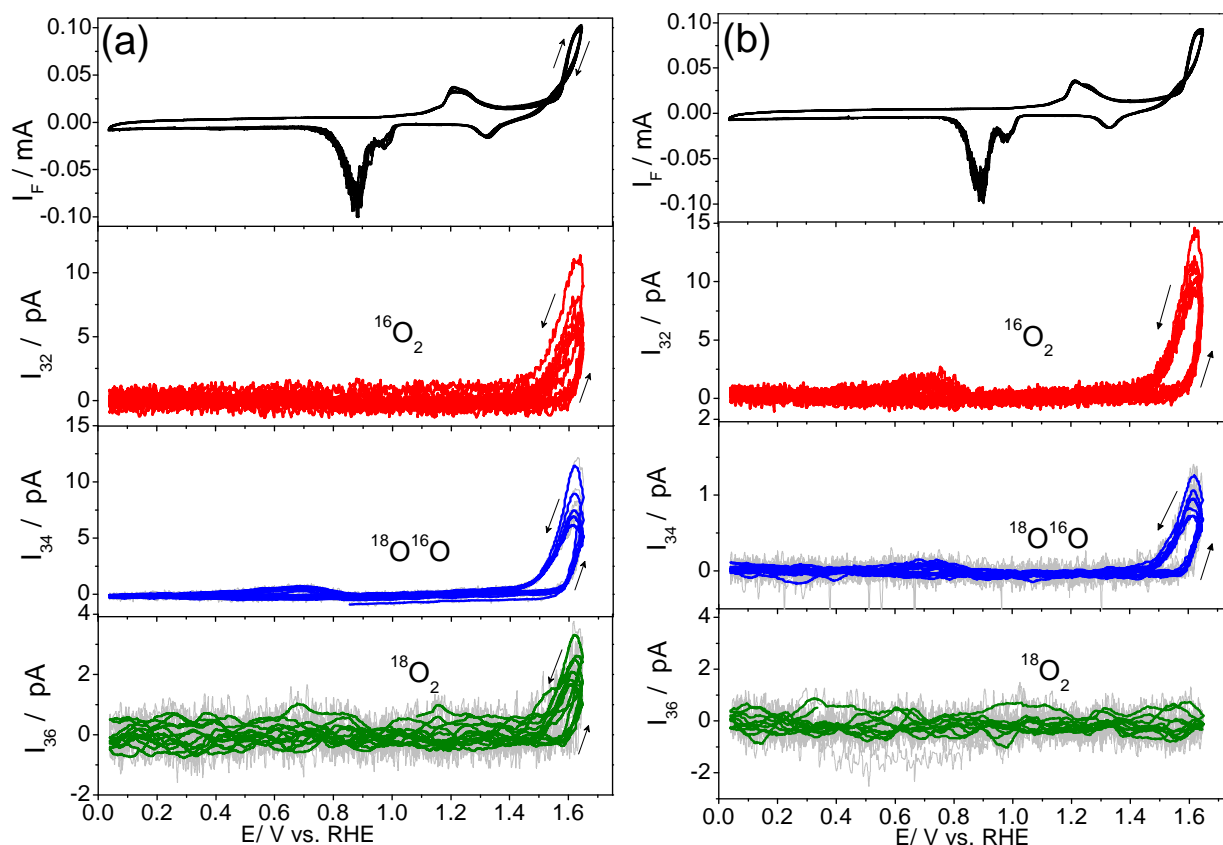


Fig. 13. DEMS results for 6 cycles OER at Ag+Co<sub>3</sub>O<sub>4</sub> (10w%) (400μg/cm<sup>2</sup>)/GC electrode in the new small volume DEMS cell in (a) Ar-saturated 0.5M LiOH solution containing 50% (w/w) of marked H<sub>2</sub><sup>18</sup>O, scan rate=10 mV/s. (b) in 0.5M LiOH/H<sub>2</sub><sup>16</sup>O, the electrode has been pre-treated in 0.5M LiOH/H<sub>2</sub><sup>18</sup>O. The upper panel displays the faradaic current, while the lower ones represent the ionic currents for m/z 32, 34 and 36. The potential was scanned between 0.05 to 1.65V.

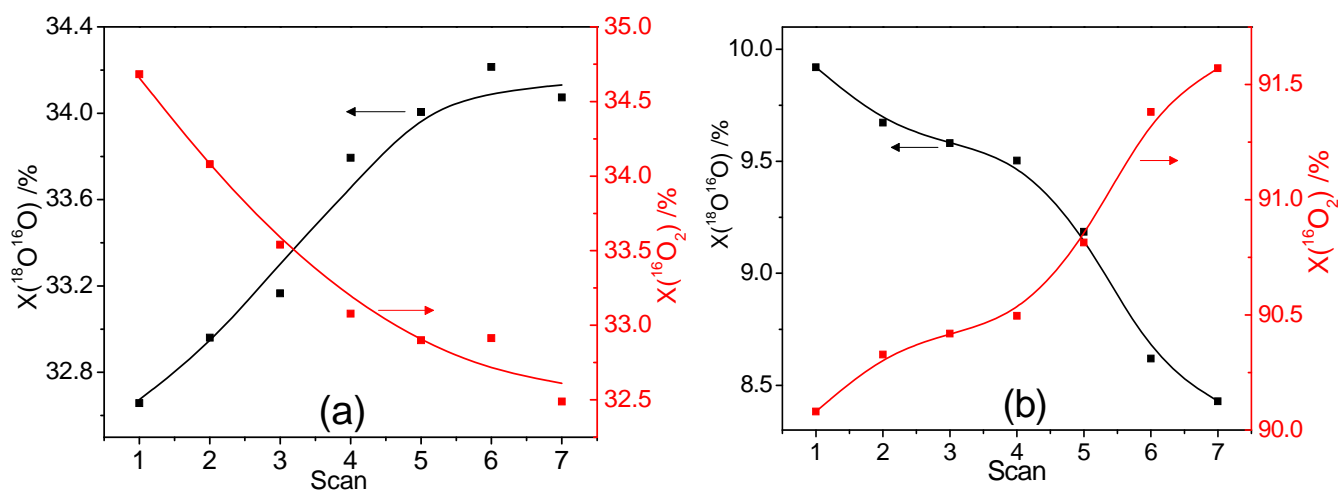


Fig. 14. Plot of the isotopic content as a function of scan number for OER on Ag+Co<sub>3</sub>O<sub>4</sub> (10w%) with (400μg/cm<sup>2</sup>)/GC with scan rate=10mV/s in (a) 0.5M LiOH/(50 w/w)H<sub>2</sub><sup>18</sup>O, (b) 0.5M LiOH/H<sub>2</sub><sup>16</sup>O, the electrode has been pre-treated in 0.5M LiOH/H<sub>2</sub><sup>18</sup>O. Data were taken from the experiment shown in Fig. 13.

#### 7.4. Discussion

Comparison of the amount of exchanged oxygen ( $n$ ) on different catalyst loadings of  $\text{Co}_3\text{O}_4$  and also different potential limits on different catalysts are shown in Table 1. As can be noticed from the values, the area (roughness factor) obtained from redox peak method for  $\text{Co}_3\text{O}_4$  (50nm) is roughly one-third to half of the BET value, indicating that a part of the surface is active. Exception is the experiment in 0.1M LiOH in thin layer cell where the ohmic resistance was high so that the peaks are not well separated and expanded (*cf.* Fig. 6), thus the uncertainty in peak charge could be high. In a separate experiment at  $\text{Co}_3\text{O}_4$  (50 nm) with  $1 \text{ mg cm}^{-2}$  and  $50 \text{ mV s}^{-1}$  in RRDE cell, the area calculated using redox peak method is roughly one-third of the BET value. This ratio is similar to the results in our new cell (see Table 1). BET and ball model show relatively good consistency for small size particles (50 nm), although they deviate for larger size particles. Moreover, the true surface area obtained from isotope exchange method is a fraction (roughly 25%) of the area obtained from redox method, indicating that only a part of the surface atoms are exchanged. No significant effect of particle size and loading on the amount of exchanged oxygen of the total catalyst is observed. However, larger surface area is obtained (from isotope exchange experiments) as the particle size decreases: 0.72, 3.4 and 4-7  $\text{cm}^2/\text{cm}^2_{\text{geo}}$  are for 40  $\mu\text{m}$ , 10  $\mu\text{m}$  and 50 nm particle sizes of  $\text{Co}_3\text{O}_4$ . Additionally, the true surface area (from isotope experiment) increases as the loading of the catalyst increases, but from DL capacitance and redox peak methods, it is lower, which could be due to roughening of the surface. The fraction of oxygen atoms of the catalyst participating in oxygen exchange mechanism approaches 0.2% of the total loading, independent of the loading. The true surface areas determined using the ball model and BET data are also included. The true surface area of different sizes of  $\text{Co}_3\text{O}_4$  was in the order: 50 nm > 10  $\mu\text{m}$  > 40  $\mu\text{m}$  which is reasonable as depicted in Table 1.

The transition of higher oxidation state oxide to lower oxidation state oxide, and thus releasing oxygen, occur on  $\text{Co}_3\text{O}_4$ . This could be via the exchange reaction between lattice oxygen atoms of the oxide and an oxygen atom from the solution. A scheme correlating oxygen evolution reaction and the redox transitions in  $\text{Co}_3\text{O}_4$  catalyst is proposed in Fig. 15. In this scheme, adsorption of  $\text{OH}^-$  species via one electron transfer is the first step, then followed by the formation of O-O bond in the OOH group. The terminal step involves the disproportionation of higher valent oxide ( $\text{CoO}_2$ ) to lower valent oxide ( $\text{CoO}$ ), and thus releasing oxygen. Further employment of this procedure to other catalysts and systematic investigation of the potential effect on the exchange process could help to draw a full and universal image of the mechanism. The application of the new cell for other purposes could be promising.

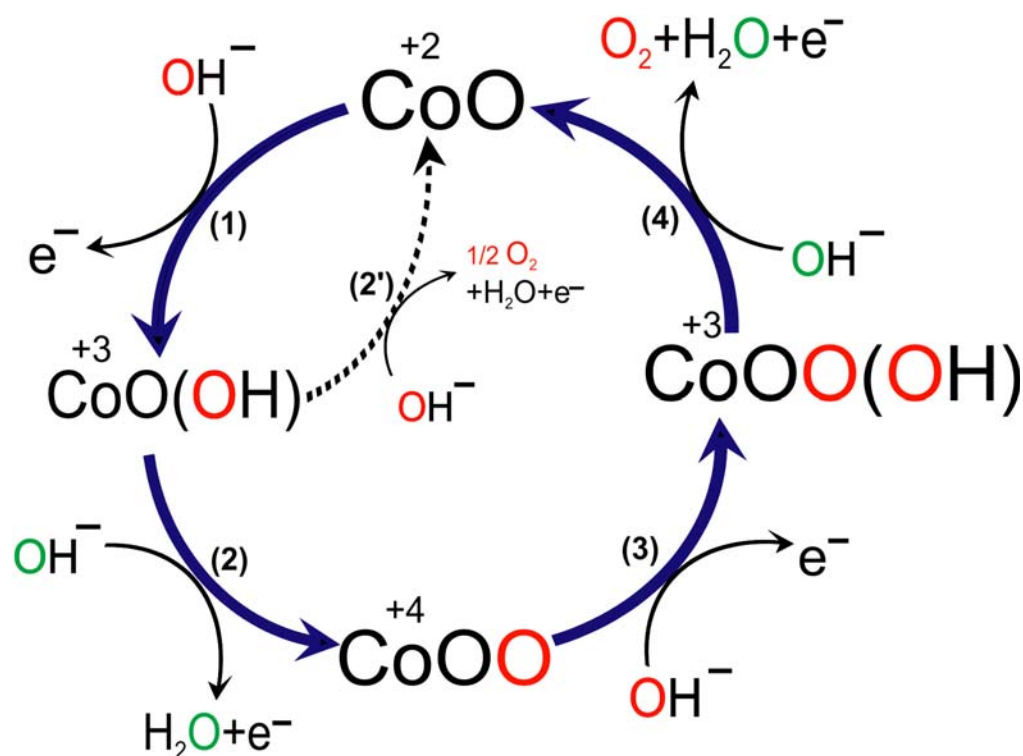


Fig. 15. Proposed scheme for oxygen evolution reaction on cobalt-containing oxide catalyst in alkaline media.

### 7.5. Conclusion

Oxygen evolution reaction has been studied using  $^{18}\text{O}$  isotope labeling together with DEMS measurements. The results showed that the amount of  $^{18}\text{O}^{16}\text{O}$  increases with each cycle in  $\text{H}_2^{18}\text{O}$  containing electrolyte, with a concomitant decrease of the amount of  $^{16}\text{O}_2$ . While in  $\text{H}_2^{16}\text{O}$  containing electrolyte, the pre-treated (labeled) oxide electrode showed evolution of  $^{18}\text{O}^{16}\text{O}$ , and its concentration decreases parallel to an increase of  $^{16}\text{O}_2$  concentration with consecutive cycling. These results prove that the oxide takes part in the oxygen evolution reaction via an oxygen exchange mechanism. This mechanism is reproducible with different catalyst loadings and different particle sizes. Therefore, we infer that these sites (about 24% of the surface atoms) are the catalytically active sites for OER. Interestingly, the amount of oxygen exchanged is higher on the mixed  $\text{Ag}+\text{Co}_3\text{O}_4$  catalyst compared to the single  $\text{Co}_3\text{O}_4$ , illustrating the improved electrocatalytic activity previously observed on the mixed catalyst. The amount of lattice oxygen participating in the oxygen exchange mechanism is close to 0.2% of the total catalyst loading, which shows the high sensitivity of this method. Therefore, only the interfacial part of the catalyst takes part in the oxygen evolution reaction.

A new DEMS cell is developed and showed good performance for OER with 1-2 s delay time and consumes only  $\leq 0.5$  ml electrolyte.

A simple ball model, DL capacitance assumption, redox peak model, and isotope exchange method have been employed to estimate the true surface area of the catalyst and the number of active sites. The different methods have been compared to the BET data. Comparable results have been obtained in most of the models.

Table 1. Summary of results of oxygen exchange experiments and estimation of true surface area of different catalysts and loadings using different methods.

Method	Co <sub>3</sub> O <sub>4</sub> (40μm) 100μg/cm <sup>2</sup> in 0.5M KOH using dual thin-layer cell with 2% isotope till 1.62V		Co <sub>3</sub> O <sub>4</sub> (50nm) 200μg/cm <sup>2</sup> in 0.1M LiOH using dual thin layer cell with 10% isotope till 1.8V		Co <sub>3</sub> O <sub>4</sub> (50nm) 400μg/cm <sup>2</sup> in 0.5M LiOH using new cell with 50% isotope till 1.65V (1.6 V)"		Co <sub>3</sub> O <sub>4</sub> (50nm) 400μg/cm <sup>2</sup> in 0.8M LiOH using new cell with 20% isotope till 1.6V (1.65 V)"		Co <sub>3</sub> O <sub>4</sub> (10 μm) 600μg/cm <sup>2</sup> in 0.8M LiOH using new cell with 20% isotope till 1.61V		*Ag+Co <sub>3</sub> O <sub>4</sub> (10wt%) 400μg/cm <sup>2</sup> in 0.5M (0.8M) <sup>§</sup> LiOH using new cell with 50% (20%) <sup>§</sup> isotope till 1.65V		
	A <sub>tr</sub> / cm <sup>2</sup> <sub>geo</sub>	n/ nmol/cm <sup>2</sup> <sub>geo</sub>	A <sub>tr</sub> / cm <sup>2</sup> <sub>geo</sub>	n/ nmol/cm <sup>2</sup> <sub>geo</sub>	A <sub>tr</sub> / cm <sup>2</sup> <sub>geo</sub>	n/ nmol/cm <sup>2</sup> <sub>geo</sub>	A <sub>tr</sub> / cm <sup>2</sup> <sub>geo</sub>	n/ nmol/cm <sup>2</sup> <sub>geo</sub>	A <sub>tr</sub> / cm <sup>2</sup> <sub>geo</sub>	n/ nmol/cm <sup>2</sup> <sub>geo</sub>	A <sub>tr</sub> / cm <sup>2</sup> <sub>geo</sub>	n/ nmol/cm <sup>2</sup> <sub>geo</sub>	A <sub>tr</sub> / cm <sup>2</sup> <sub>geo</sub>
<b>Ball model</b>	0.016	0.03	39	72	78.6	145	78.6	145	0.59	1.03	7.9 (11.6)	14.5 (21.5)	
<b>BET</b>	--	--	33	61	63	116	63	116	13.6	25.2	6.3 (9.7)	11.6 (17.9)	
<b>DL-cap. assumption</b>	12	22	140	255	105 (89)	194 (165)	68	126	25	45	77 (44)	142 (81)	
<b>Isotope exchange exp. A</b>	0.72	1.34	3.9	7.3	5.2 (8)	9.7 (15)	7.3 (10.9)	13.5 (20.2)	3.4	6.2	3.6 (3.8)	6.6 (7.1)	
<b>Redox peak method</b>	3.0	5.5	32	59	23 (22)	42 (41)	29	53	--	--	--	--	
<b>Isotope exchange exp. B<sup>#</sup></b>	0.28	0.51	1.8	3.4	2.4 (0.7)	4.5 (1.3)	1.8 (3)	3.4 (5.5)	1.3	2.4	0.9	1.6	
<b>r<sub>exch</sub>/ %<sup>a</sup></b>	0.08		0.22		0.15 (0.2)		0.2 (0.33)		0.03		1.0 (0.7)		
<b>y<sub>exch</sub>/ %<sup>a</sup></b>	24		12		23 (22)		25		--		55 (26)		
<b>r<sub>exch</sub>/ %<sup>#</sup></b>	0.03		0.1		0.07 (0.1)		0.05		0.02		0.3		
<b>y<sub>exch</sub>/ %<sup>#</sup></b>	13		8.5		11 (3)		6.4		--		13		
<b>Exp No.</b>	h2205203		h13062804		h15041703 (h15041704)"		h14123101 (h15040803)"		h15031901		h15041601 (h15031801) <sup>§</sup>		

# Isotope exchange in H<sub>2</sub><sup>18</sup>O-free solution after Co<sub>3</sub>O<sub>4</sub> labeling (series B)

<sup>a</sup> exchanged oxygen atoms to the total oxygen atoms in the catalyst loading ( $r_{\text{exch}}$ ) or to the oxygen atoms on the surface, obtained from redox peak, ( $y_{\text{exch}}$ ) in *series A* experiments

\* calculations were done with respect to only the amount of Co<sub>3</sub>O<sub>4</sub> (50 nm) component in the mixed catalyst

§ repeated experiments with 20% marked solution

" repeated experiments with different upper potential limit are displayed between brackets

## 7.6. References

- [1] J. Suntivich, K.J. May, H.A. Gasteiger, J.B. Goodenough, Y. Shao-Horn, *Science* 334 (2011) 1383-1385.
- [2] H.-Y. Su, Y. Gorlin, I.C. Man, F. Calle-Vallejo, J.K. Nørskov, T.F. Jaramillo, J. Rossmeisl, *Physical Chemistry Chemical Physics* 14 (2012) 14010-14022.
- [3] C.P. Plaisance, R.A. van Santen, *Journal of the American Chemical Society* 137 (2015) 14660-14672.
- [4] I.C. Man, H.-Y. Su, F. Calle-Vallejo, H.A. Hansen, J.I. Martínez, N.G. Inoglu, J. Kitchin, T.F. Jaramillo, J.K. Nørskov, J. Rossmeisl, *ChemCatChem* 3 (2011) 1159-1165.
- [5] G. Foti, D. Gandini, C. Comninellis, *Current Topics in Electrochemistry* 5 (1997) 71-91.
- [6] J. Rossmeisl, Z.W. Qu, H. Zhu, G.J. Kroes, J.K. Nørskov, *Journal of Electroanalytical Chemistry* 607 (2007) 83-89.
- [7] G. Lodi, E. Sivieri, A. De Battisti, S. Trasatti, *Journal of Applied Electrochemistry* 8 (1978) 135-143.
- [8] E. Rios, J. Gautier, G. Poillerat, P. Chartier, *Electrochimica Acta* 44 (1998) 1491-1497.
- [9] M. De Koninck, B. Marsan, *Electrochimica Acta* 53 (2008) 7012-7021.
- [10] Y. Gorlin, T.F. Jaramillo, *Journal of the American Chemical Society* 132 (2010) 13612-13614.
- [11] L.I. Krishtalik, *Electrochimica Acta* 26 (1981) 329-337.
- [12] S. Trasatti, *Electrochimica Acta* 36 (1991) 225-241.
- [13] M. Wohlfahrt-Mehrens, J. Heitbaum, *Journal of Electroanalytical Chemistry* 237 (1987) 251-260.
- [14] J. Willsau, O. Wolter, J. Heitbaum, *Journal of Electroanalytical Chemistry* 195 (1985) 299-306.
- [15] S. Fierro, T. Nagel, H. Baltruschat, C. Comninellis, *Electrochemistry Communications* 9 (2007) 1969-1974.
- [16] S. Fierro, T. Nagel, H. Baltruschat, C. Comninellis, *Electrochemical and Solid State Letters* 11 (2008) E20-E23.
- [17] S. Fierro, L. Ouattara, E.H. Calderon, E. Passas-Lagos, H. Baltruschat, C. Comninellis, *Electrochimica Acta* 54 (2009) 2053-2061.
- [18] K. Macounova, M. Makarova, P. Krtil, *Electrochemistry Communications* 11 (2009) 1865-1868.
- [19] Y. Liang, Y. Li, H. Wang, J. Zhou, J. Wang, T. Regier, H. Dai, *Nature Materials* 10 (2011) 780-786.
- [20] K.-N. Jung, S.M. Hwang, M.-S. Park, K.J. Kim, J.-G. Kim, S.X. Dou, J.H. Kim, J.-W. Lee, *Scientific Reports* 5 (2014) 7665.
- [21] J. Hu, L. Wang, L. Shi, H. Huang, *Electrochimica Acta* 161 (2015) 115-123.
- [22] A. Restovic, E. Ríos, S. Barbato, J. Ortiz, J.L. Gautier, *Journal of Electroanalytical Chemistry* 522 (2002) 141-151.
- [23] T. Hartung, H. Baltruschat, *Langmuir* 6 (1990) 953-957.
- [24] H. Baltruschat, *Journal of the American Society for Mass Spectrometry* 15 (2004) 1693-1706.
- [25] J.O.M. Bockris, T. Otagawa, *Journal of The Electrochemical Society* 131 (1984) 290-302.
- [26] H.M.A. Amin, H. Baltruschat, D. Wittmaier, K.A. Friedrich, *Electrochimica Acta* 151 (2015) 332-339.
- [27] Z. Jusys, H. Massong, H. Baltruschat, *Journal of the Electrochemical Society* 146 (1999) 1093.
- [28] J.A. Koza, Z. He, A.S. Miller, J.A. Switzer, *Chemistry of Materials* 24 (2012) 3567-3573.

- [29] M. Pourbaix, Atlas d'Équilibres Electrochimiques - Atlas of Eh-pH diagrams, Paris (Gauthier-Villars & Cie ), 1963.
- [30] M. Hamdani, R.N. Singh, P. Chartier, Co<sub>3</sub>O<sub>4</sub> and Co- Based Spinel Oxides Bifunctional Oxygen Electrodes, Int. J. Electrochem. Sci., 2010, pp. 556-577.
- [31] W.M.a.K.B.a.M.G.a.L.H.a.K. Heinz, Journal of Physics: Condensed Matter 20 (2008) 265011.
- [32] S. Levine, A.L. Smith, Discussions of the Faraday Society 52 (1971) 290-301.
- [33] D. Wittmaier, N. Wagner, K.A. Friedrich, H.M.A. Amin, H. Baltruschat, Journal of Power Sources 265 (2014) 299-308.
- [34] T. Poux, A. Bonnefont, G. Kéranguéven, G.A. Tsirlina, E.R. Savinova, ChemPhysChem 15 (2014) 2108-2120.

## Supplementary Information

### Calculations for the Co<sub>3</sub>O<sub>4</sub> (50 nm) catalyst with 200 μg cm<sup>-2</sup> loading in 0.1M LiOH (upper limit is 1.8V):

Analyses of the real surface area of the catalyst using the ball model, DL-capacitance assumption model and redox peak model were done and compared to BET data:

- Based on the model used in eq. 7.8,  $S=4/0.36/6.02 \times 10^{23}=1.85 \text{ nmol/cm}^2_{\text{geo}}$ .

*Isotope exchange model:*

$\sum n=7.3 \text{ nmol/cm}^2$ , and from eq. 7.9,  $A_{tr}=7.3 \text{ (nmol/cm}^2)/1.85 \text{ (nmol/cm}^2_{\text{geo}})=3.9 \text{ cm}^2$ .

- According to eq. 7.4,  $n_t(\text{O}^{2-})=4 \times 200 \text{ (}\mu\text{g/cm}^2) / 241 \text{ (g/mol)}=3320 \text{ nmol/cm}^2$

- Thus,  $r_{\text{exch}}=7.3 \text{ (nmol/cm}^2)/3320 \text{ (nmol/cm}^2)=0.22\%$ .

*ball model:*

- For  $r=25 \text{ nm}$ ,  $m(\text{Co}_3\text{O}_4)=56.6 \mu\text{g}$ ,  $A_{tr}=11 \text{ cm}^2$ .

$A_{tr}/A_{\text{geo}}=11 \text{ cm}^2/0.283 \text{ cm}^2=39 \text{ cm}^2_{\text{tr}}/\text{cm}^2_{\text{geo}}$ .

This gives moles of active atoms= $39 \text{ (cm}^2/\text{cm}^2) \times 1.85 \text{ (nmol/cm}^2)=72 \text{ nmol/cm}^2_{\text{geo}}$ .

-According to eq. 7.16,  $n_{tr}=2.04 \times 10^{-8}$  moles of O-atoms per  $\text{cm}^2_{\text{tr}}$ .

Since 0.22% of the total oxygen atoms are being exchanged (from the isotope exchange experiment), this corresponds to  $0.22 \times 3320 \text{ nmol/cm}^2=7.3 \times 10^{-9} \text{ mol/cm}^2$  of oxygen atoms are exchanged. This gives a factor = $7.3 \times 10^{-9}/2.04 \times 10^{-8}=0.35$  (35%).

- According to eq. 7.17:  $A_{tr}=0.35 \times 0.283 \text{ cm}^2/56.6 \mu\text{g}=0.18 \text{ m}^2/\text{g}$ .

*DL capacitance assumption for oxide:*

In between 0.76 to 1.39V, eq. 7.18 gives  $A_{tr}/A_{\text{geo}}=140 \text{ cm}^2/\text{cm}^2$ .

Thus,  $A_{tr}=140 \times 0.283 \text{ cm}^2/56.6 \mu\text{g}=70 \text{ m}^2/\text{g}$ , i.e.  $39 \text{ cm}^2$ .

From eq. 7.15, the number of moles of active atoms= $140 \text{ (cm}^2/\text{cm}^2) \times 1.85 \text{ nmol/cm}^2_{\text{geo}}=255 \text{ nmol/cm}^2_{\text{geo}}$ .

*Redox peak model:*

- The charge under the redox peak corresponding to the transition  $\text{Co}^{\text{III}}/\text{Co}^{\text{IV}}=5.7 \text{ mC/cm}^2$ .

- $n_{\text{surf}}=5.7/(1.F) \text{ nmol/cm}^2=59 \text{ nmol/cm}^2$ , thus  $y_{\text{exch}}=12\%$

-Eq. 7.15 gives  $A_{tr}/A_{\text{geo}}=59 \text{ (nmol/cm}^2)/1.85 \text{ (nmol/cm}^2_{\text{geo}})=32 \text{ cm}^2/\text{cm}^2_{\text{geo}}$ .

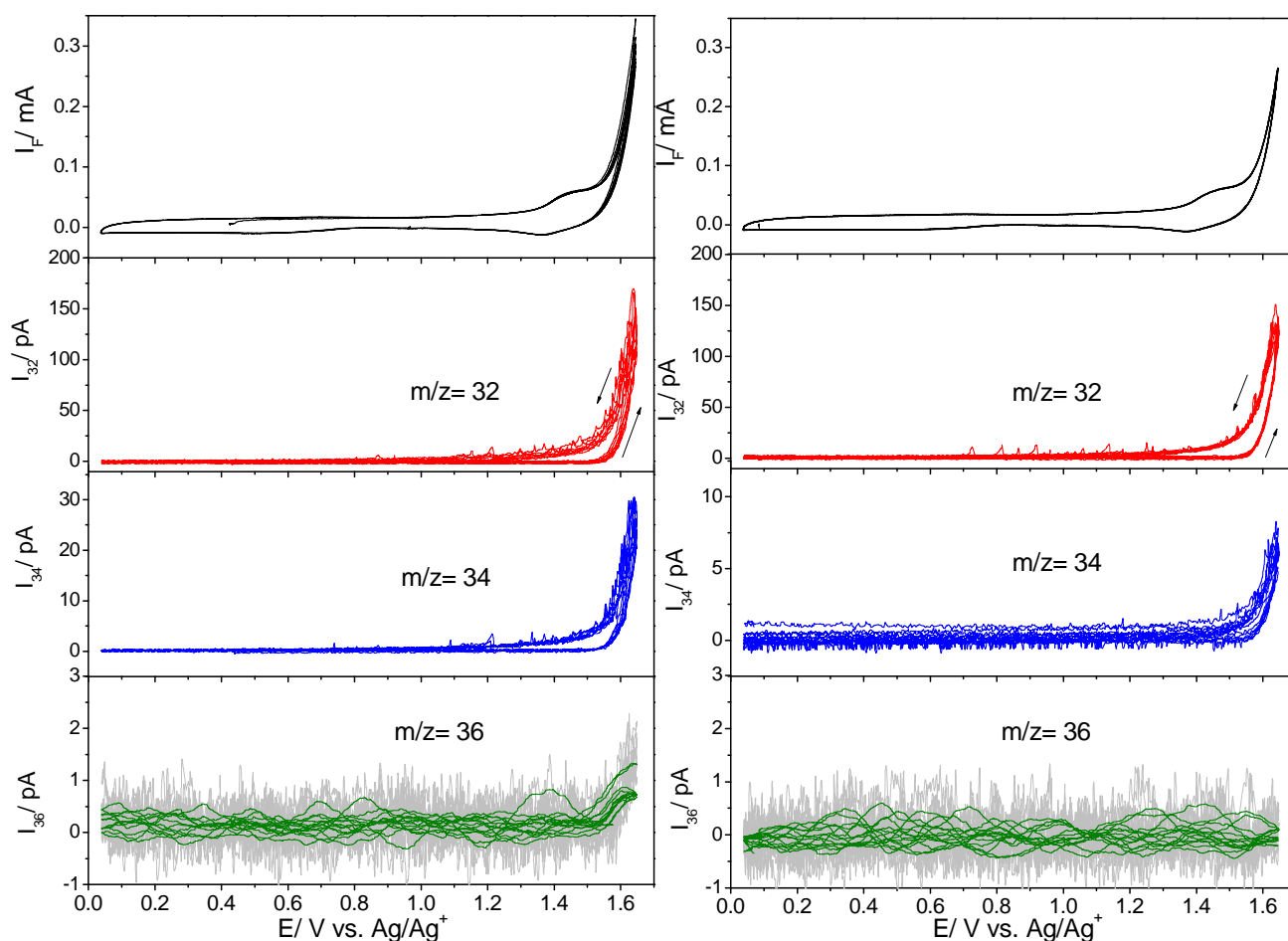


Fig. S1. DEMS results for 7 cycles of OER at  $\text{Co}_3\text{O}_4$  ( $400\mu\text{g}/\text{cm}^2$  of 50 nm size)/GC electrode in the small-volume DEMS cell in (a) Ar-saturated 0.8M LiOH solution containing 20% (w/w) of marked  $\text{H}_2^{18}\text{O}$ , scan rate=10 mV/s and upper potential limit is 1.65V. (b) in 0.8M LiOH/ $\text{H}_2^{16}\text{O}$ , the electrode has been pre-treated in 0.8M LiOH/ $\text{H}_2^{18}\text{O}$ . The upper panel displays the faradaic current, while the lower ones represent the ionic currents for m/z 32, 34 and 36.

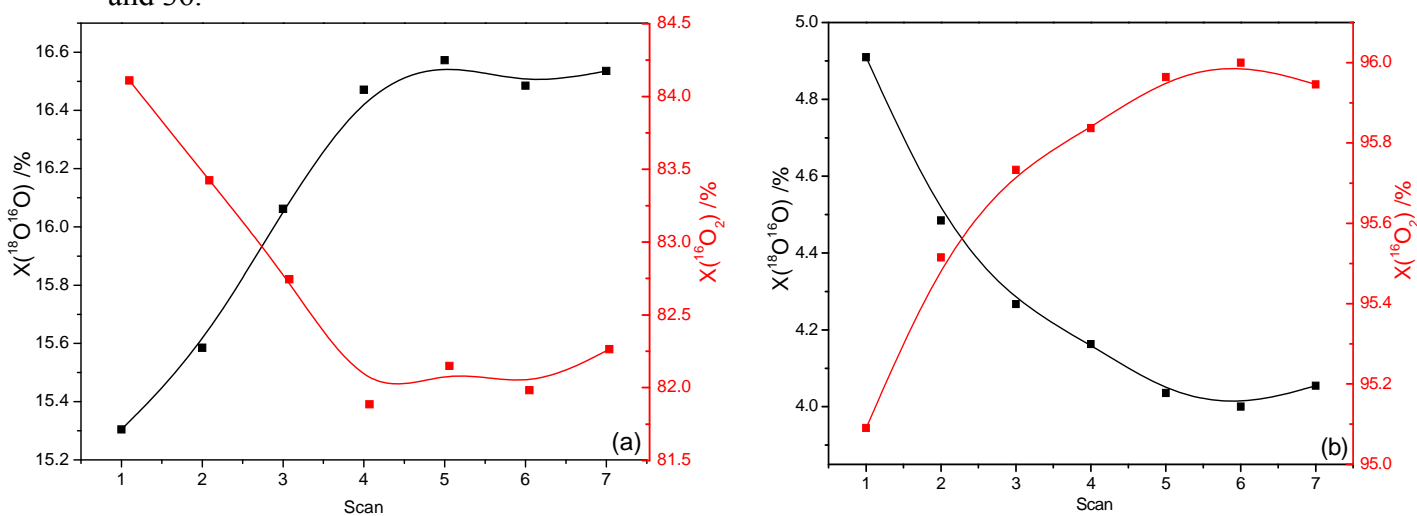


Fig. S2. Plot of the isotopic content as a function of scan number for OER on  $\text{Co}_3\text{O}_4$  ( $400\mu\text{g}/\text{cm}^2$ )/GC with scan rate=10 mV/s in (a) 0.8M LiOH/(20 w%) $\text{H}_2^{18}\text{O}$ , (b) 0.8M LiOH/ $\text{H}_2^{16}\text{O}$ , the electrode has been pre-treated in 0.8M LiOH/ $\text{H}_2^{18}\text{O}$ . Data were taken from the experiment shown in Fig. S1.

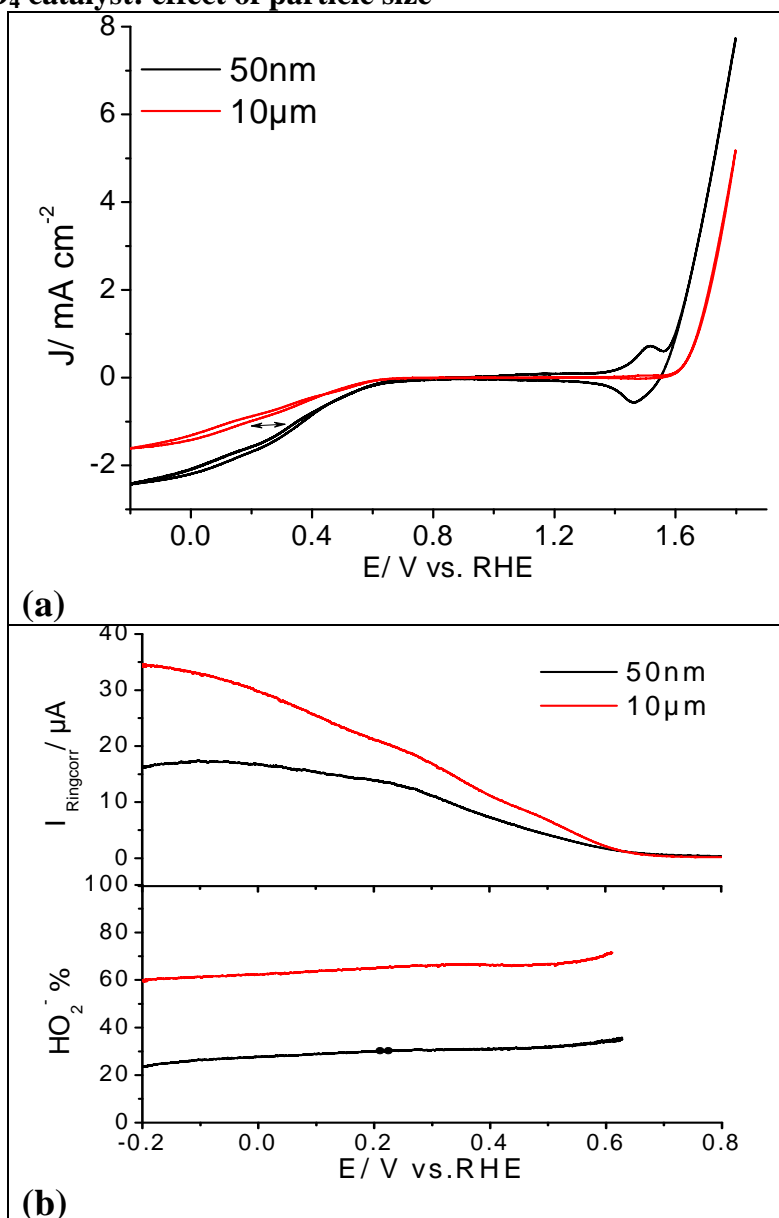
**RRDE on  $\text{Co}_3\text{O}_4$  catalyst: effect of particle size**


Fig. S3.(a) RRDE measurements on  $\text{Co}_3\text{O}_4$  with two particle sizes loaded on GC electrode ( $1\text{mg cm}^{-2}$ ) in different solutions at 960 rpm with  $10\text{ mV s}^{-1}$ . (b) Corresponding ring currents and peroxide anion amount in the anodic scan when ring hold at 1.2V.

It is well believed that the electrocatalytic activity of nanoparticle-catalysts is related to their morphology. To assess the role of particle size on the activity and in order to explore a more active catalyst, two particle sizes of  $\text{Co}_3\text{O}_4$  spinel has been studied: 50 nm and 10  $\mu\text{m}$ . The electrocatalytic activity of  $\text{Co}_3\text{O}_4$  varies with the particle size change, as shown in Fig. S3. RRDE technique has been used to assess this effect on two different sizes of the same material. For OER,  $\text{Co}_3\text{O}_4$  (50 nm) exhibited about 80 mV less overpotential compared to the 10  $\mu\text{m}$   $\text{Co}_3\text{O}_4$  catalyst. For OER, the smaller size catalyst showed  $\sim 100$  mV less overpotential and about 4 times higher current density at 1.65V. Furthermore, it revealed higher ORR activity: the currents are shifted by ca. 100 mV to more positive potentials on the 50 nm catalyst. This could be attributed to the larger surface area of the smaller particle size. The  $\text{Co}^{\text{III}}/\text{Co}^{\text{IV}}$  redox peak at about 1.5V gets smaller in large particle size  $\text{Co}_3\text{O}_4$  electrode, as shown in Fig. S4.

This has also been observed in 40 $\mu\text{m}$   $\text{Co}_3\text{O}_4$  catalyst (not shown here). This could be due to the fact that the same amount of binder has been used which leads to smaller exposed surface area on larger particles, so that the surface redox reactions are less. In RRDE technique, the ring can be held at a potential at which peroxide intermediate can be oxidized so that the yield of peroxide anion and the mechanism of ORR can be determined. The amount of peroxide anion detected on the ring was about 30% for 50 nm size catalyst, whereas a higher value of 60 % was obtained on the 10  $\mu\text{m}$  catalyst, as shown in Fig. S3b. This suggests that ORR at the small size tends to proceed via both the 2e and the 4e-pathways, while the larger particles follow mostly the 2e-pathway for ORR. Therefore,  $\text{Co}_3\text{O}_4$  (50 nm) is better and is expected to be efficient together with Ag311 in one mixture.

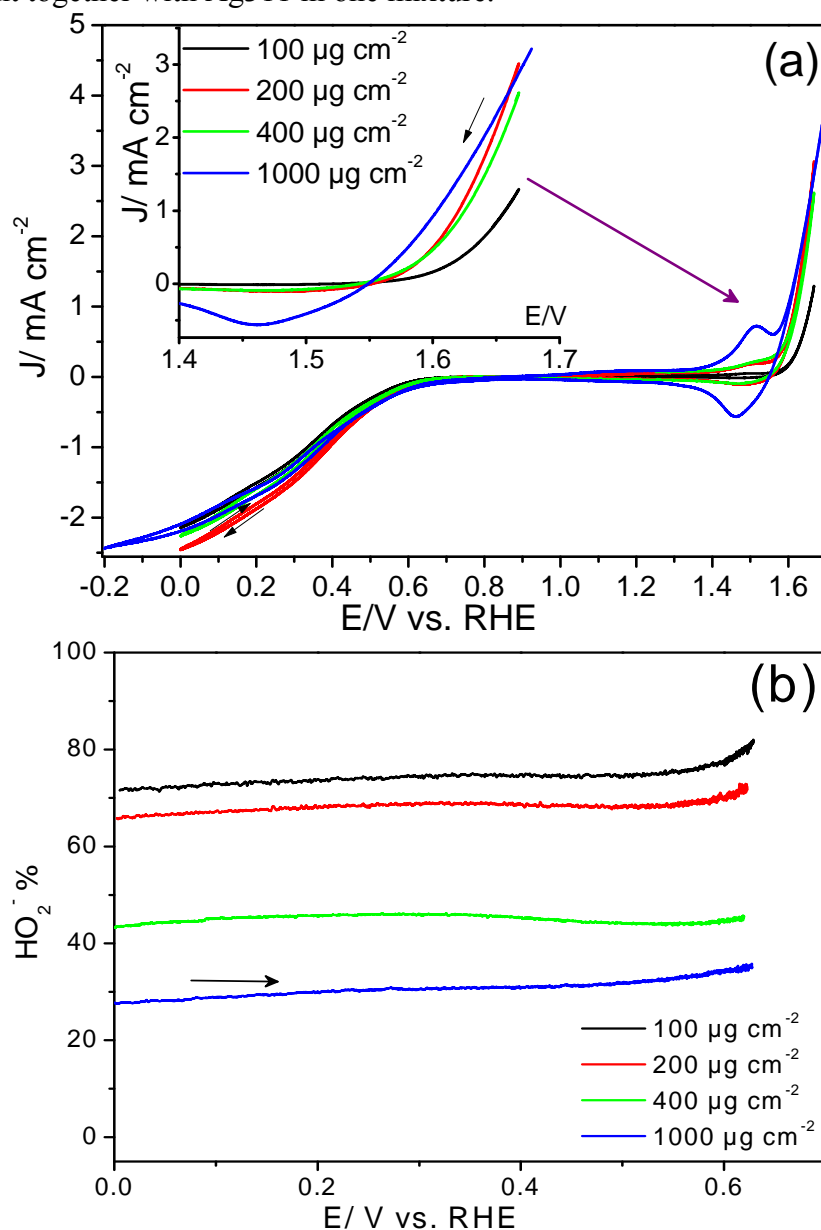


Fig. S4. (a) RRDE measurements on  $\text{Co}_3\text{O}_4$  (50 nm)/GC with different loadings on GC electrode in 0.1M LiOH solution with 1500 rpm with  $10 \text{ mV s}^{-1}$ . Inset is an expansion of the OER in the negative-going scan. (b) Corresponding peroxide anion amount in the anodic scan when ring was hold at 1.2V.

The loading effect on the activity of OER has been investigated using RRDE, as shown in Fig. S4a. Various loadings of  $\text{Co}_3\text{O}_4$  (50 nm) were examined, and their activities are compared. The onset and the polarization curves are shifted to less positive potentials (i.e. lower overpotentials) as the loading increases. This could be due to the higher number of active sites and surface area on high loadings. It is noticeable that the  $\text{Co}^{3+/4+}$  peak is larger at higher loadings. This effect is not significant here for ORR activity on this catalyst, although it has a strong impact on the detected peroxide anion amount at the ring, as shown in Fig. S4b. The ring current increases and consequently, the peroxide yield increases as the loading increases: 30% of  $\text{HO}_2^-$  is detected for the  $1\text{ mg cm}^{-2}$  loading, while 75% for  $100\ \mu\text{g cm}^{-2}$  loading, Fig. S4b. This might be due to the higher probability of further reduction of peroxide intermediate to  $\text{OH}^-$  on higher loadings before diffusing away from the catalyst surface[34] or also probably for low loadings, parts of the GC substrate are not covered with catalyst and thus ORR follows the 2e-pathway on these parts.

### Surface characterization of the catalyst

BET plot and adsorption/desorption isotherms for  $\text{Co}_3\text{O}_4$  catalyst are depicted in Fig. S5 a, b. The specific surface area obtained for 50 nm  $\text{Co}_3\text{O}_4$  catalyst is  $16.5\ \text{m}^2\ \text{g}^{-1}$ , while that for the  $10\ \mu\text{m}$  catalyst is  $2.3\ \text{m}^2\ \text{g}^{-1}$ , which is reasonable. The particle size distribution of  $\text{Co}_3\text{O}_4$  was analyzed and the average particle size (assuming that the particles are spherical and non-porous) was determined from BET data. An average particle diameter of 40 nm was found as shown in Fig. S5c, which is consistent with the value given from the manufacturer data sheet. XRD patterns (supplied from the manufacturer) of  $\text{Co}_3\text{O}_4$  (50 nm) catalyst are shown in Fig. S5d. The signals are then analyzed and assigned to the different phases of cobalt oxide. The graph exhibits intense and sharp diffraction peaks which are characteristic of the  $\text{Co}_3\text{O}_4$  cubic spinel crystalline structure. The signals of  $\text{Co}_3\text{O}_4$  agreed perfectly with XRD standard data (JCPDS card number: 9-418) and are in a good agreement with literature values.[33] The oxide is highly pure since no peaks of any impurity phase could be observed from this pattern. Fig. S6 (upper panel) shows low-magnification SEM image of Ag311+  $\text{Co}_3\text{O}_4$  (10 w%) with a loading of  $1\ \text{mg cm}^{-2}$  on GC without Nafion binder. The inset of the image is a higher magnification of a part of the surface, which shows the  $\text{Co}_3\text{O}_4$  nanoparticles with the light contrast supported on the dark large Ag microparticles.  $\text{Co}_3\text{O}_4$  particle size is about 40 nm while Ag has roughly  $1\ \mu\text{m}$  size. On the other hand, addition of Nafion is important to fix the catalyst on the substrate with no obvious electrochemical difference and allows long time measurements under rotation. Better distribution of the catalyst can be observed when Nafion is used, as shown in Fig. S6 (lower panel).

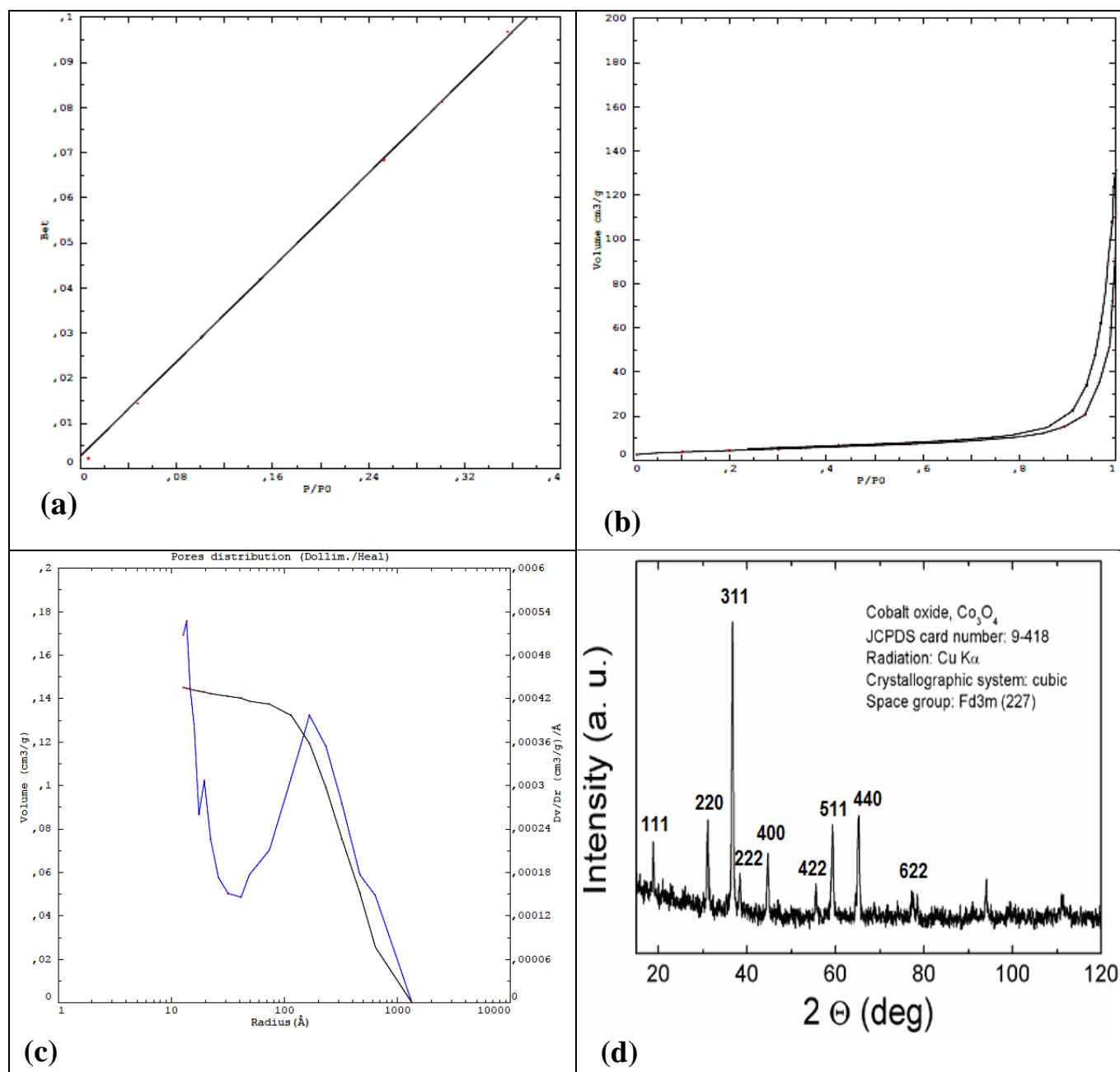


Fig. S5. (a) BET plot of  $\text{Co}_3\text{O}_4$  (50 nm) catalyst. (b) Adsorption/desorption isotherms on the catalyst. (c) Particle size distribution of the corresponding catalyst. (d) XRD patterns of  $\text{Co}_3\text{O}_4$ .

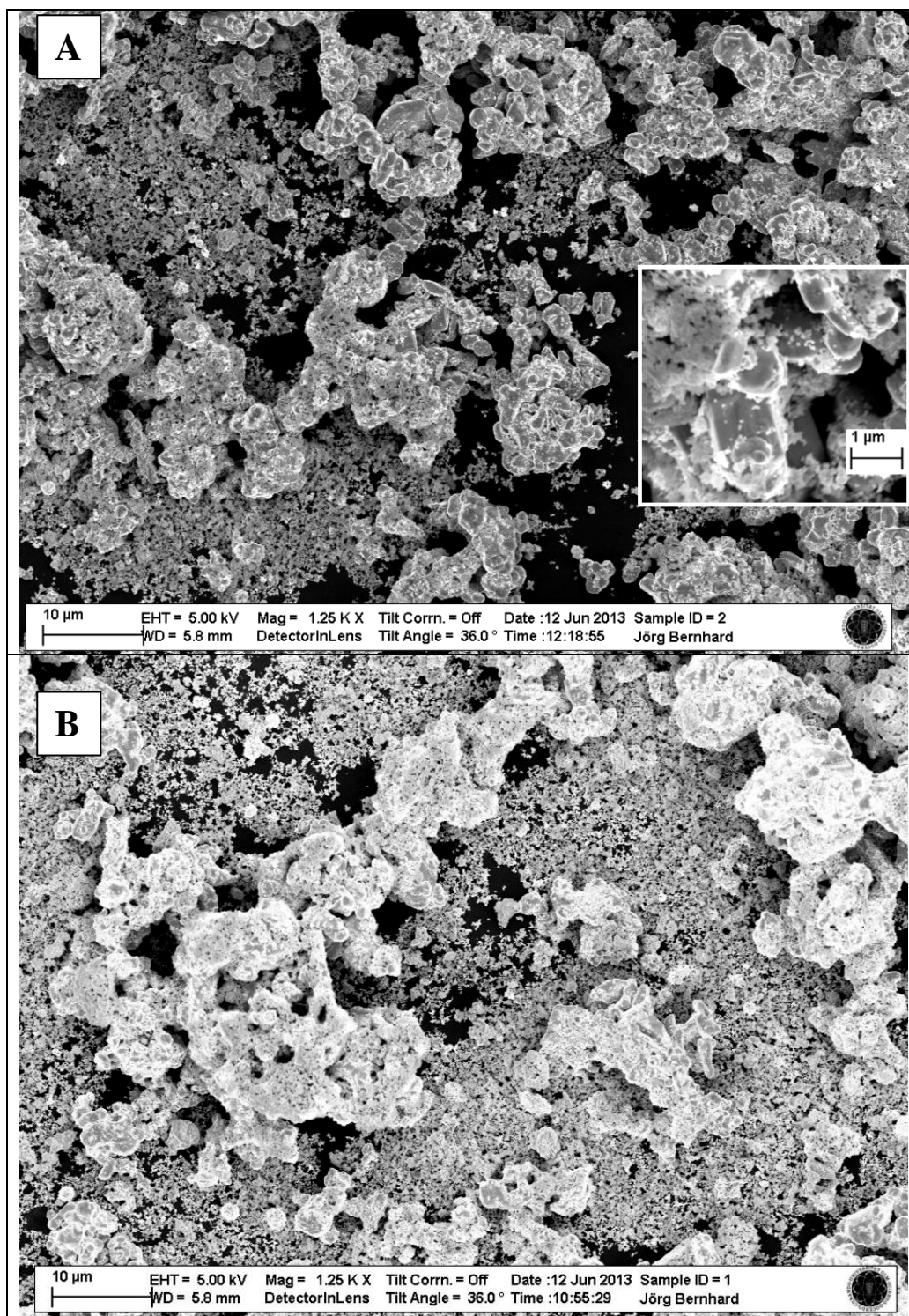


Fig. S6. (A) SEM of Ag<sup>+</sup> Co<sub>3</sub>O<sub>4</sub> (50 nm) mixed catalyst loaded on GC without Nafion (1 mg/cm<sup>2</sup>), inset is part of the sample with higher magnification. (B) same sample with Nafion binder.



## 8. Quantitative and mechanistic insights into ORR and OER in DMSO, Tetraglyme and their mixture electrolyte for Li-O<sub>2</sub>

### 8.1. Introduction

Li-air batteries are promising candidates for rechargeable systems due to their extremely high theoretical specific energy.[1, 2] It would be a breakthrough in energy storage even if only half of its theoretical value, which still would exceed by ca. 4-orders of magnitude the currently Li-ion batteries, and is comparable to the usable energy density of gasoline 1.7 (kWh kg<sup>-1</sup>), could be realized.[2-4] Therefore, they attract worldwide interest.[5, 6] Despite the intensive efforts, which have been done so far, the realization of this principle in the batteries industry has not been achieved yet. This arises from the necessary use of an organic electrolyte, which is in contact with the lithium metal, and the electrochemical reactions namely oxygen reduction (ORR) and evolution (OER) reaction in these types of electrolytes were hardly studied in the past.

Despite the rechargeability of Abraham's first Li-O<sub>2</sub> cell for few cycles, the poor cyclability stimulated researchers to find out other electrode materials and electrolytes.[1] The discharge products (namely Li<sub>2</sub>O<sub>2</sub>) cause blocking of the surface sites in carbonate-based electrolytes, and also they (in particular, LiO<sub>2</sub>) attack the solvents, thus reduce the cyclability of the cell.[7] Therefore, electrochemical stability of the electrolyte and fundamental understanding the role of the electrolyte in the reversibility and ORR mechanism are key challenges for practical Li-air batteries.[8, 9]

Organic carbonate-based electrolytes were chosen as first candidates, but unfortunately they showed to decompose irreversibly.[5, 8, 10, 11] Read suggested ether-based electrolytes to perform well in the Li/O<sub>2</sub> cell due to both good stability and excellent rate capability.[12] In recent years, Tetraglyme (G4) suitability is questionable: Laoire et al. reported the formation of Li<sub>2</sub>O<sub>2</sub> in LiPF<sub>6</sub>/G4, but with capacity decay;[13] Bruce and coworkers also demonstrated the decomposition of G4 in Li-O<sub>2</sub> cells using spectroscopy[14]. On the other hand, the Scrosati group reported that G4 is a suitable solvent, and their cell delivered a capacity of 1000 mAh g<sup>-1</sup> for at least 100 cycles.[15] As an alternative, DMSO was suggested as a convenient solvent with low potential gap, stability against superoxide and good performance.[9, 16, 17] A DMSO-based electrolyte showed apparently 95% capacity retention for 100 cycles.[17] Our group showed previously the reversible formation of Li<sub>2</sub>O<sub>2</sub> in DMSO-based electrolyte using DEMS.[18] However, an XPS study showed recently the decomposition of DMSO to carbonate or other species when it is in contact with Li<sub>2</sub>O<sub>2</sub> for long time.[19] These formed species might, on the other hand, act as a protective film against further attack. Moreover, LiOH is reported to form by a chemical reaction of the superoxide with DMSO.[20] Although DMSO has lower O<sub>2</sub>-solubility and higher volatility, it is more prone to be relatively stable with higher capacity and kinetically favorable for ORR and OER than G4 due to its higher ionic conductivity and O<sub>2</sub>-diffusivity.[9, 21]

It is admitted now in these systems, particularly ether-based ones, that Li<sub>2</sub>O is not the reduction product, but Li<sub>2</sub>O<sub>2</sub>. [22-24] However, this discharge product is insoluble in most of nonaqueous electrolytes, and therefore, deposits on the air electrode and blocks the active sites, and hence hinders the battery from reaching a reasonable portion of its potential capacity. The nature of the solvent plays a critical role in Li<sub>2</sub>O<sub>2</sub> product and/or LiO<sub>2</sub> intermediate formation.[25] Laoire et al. have reported for the first time that ORR mechanism

depends significantly on the donor number (DN) of the solvent used.[9] Furthermore, the solubility of  $\text{LiO}_2$  influences significantly the ORR mechanism and cell performance.[26] Most recently, Peng et al. have reported a mechanism of ORR using Raman spectroscopy, and concluded that the formation of  $\text{O}_2^-$  and  $\text{LiO}_2$  in DMSO is potential dependent: at low overpotentials, the adsorbed  $\text{O}_2^-$  diffuses into solution and forms toroid-shaped  $\text{Li}_2\text{O}_2$  particles via a solution-mediated disproportionation pathway; while at higher overpotentials a surface-mediated pathway via  $\text{LiO}_2$  intermediate is prevailed.[27] However, the limited reversibility and the overall processes remain incompletely understood. Electrolyte properties, such as  $\text{O}_2$ -solubility, viscosity and conductivity were reported to affect the discharge capacity.[12, 28] Therefore, selection of a solvent that stabilizes  $\text{Li}^+$  in solution and hinders passivation of the electrode is important for capacity improvement of the battery.

Here, combining the unique properties of two solvents in a mixed electrolyte is one of the scenarios to enhance the performance of the electrolyte and by varying the ratio of the two solvents; one could get more information on the determinant criteria that direct the mechanism. This idea of using mixed electrolytes has been reported to improve the cycle life the cell, but they mainly contain an ionic liquid which has high viscosity and lower diffusion coefficient (slow kinetics).[29, 30] Nevertheless, G4-DMSO blended electrolyte was proposed as a promising electrolyte and showed an improved cyclability and lower potential gap than the single G4 or DMSO, although 80 wt% DMSO was used in this mixture, which already possesses high performance, and also no kinetic or mechanistic studies were reported.[31]

We examined different electrolytes based on DMSO, G4 and their mixtures. The kinetics and mechanistics of OER and ORR in the single and mixed solvents are studied using RRDE technique. Moreover, the diffusion coefficient of superoxide in DMSO is successfully determined using RRDE combined with chronoamperometry. Also, the effect of electrode material on the kinetics is investigated. The catalytic activity of  $\text{Co}_3\text{O}_4$  nanoparticles is demonstrated in DMSO-based electrolyte. For a proper characterization of the cell rechargeability, quantitative analysis of the gas evolved and consumed is coupled with a determination of the faradaic charge. DEMS has become a versatile tool for quantitative and qualitative detection of volatile products and intermediates.[5, 10, 32, 33] DEMS is used to determine the true coulombic efficiency (based on the oxygen amount) as a proper criterion for rechargeability rather than the apparent coulombic efficiency (based on faradaic charges) for different electrolytes. More importantly, DEMS is used to identify the side products and the number of electrons transferred. A reduction products-induced decomposition of the electrolyte is illustrated. Previous reports found  $2e^-/\text{O}_2$  in DME[23] or DMSO solvents[34] using DEMS. Here, variation of the ratio of the two solvents in the mixed electrolyte is investigated, and its influence on the performance and discharge products is discussed. Gas diffusion electrode (GDE) is employed to mimic a breathing battery; in which the electrode breathes in air upon discharge and breathes it out upon charge. The GDE uses a 50 nm Au-sputtered porous membrane as the working electrode and as the electrolyte-vacuum interface. A schematic of the setup was reported previously[34] and in the experimental chapter. Finally, our main goal is better understanding of the role of solvent on the mechanism and reduction products and studying novel electrolyte formulations, which are important aspects in the development of Li-air batteries.

## 8.2. Experimental

### *Chemicals and materials*

LiClO<sub>4</sub> (battery grade, Sigma-Aldrich), extra dry DMSO (99.7% over molecular sieves, Acros Organics), Tetrabutylammonium trifluoromethanesulfonate (TBAOTf, Sigma-Aldrich) and AgNO<sub>3</sub> (AppliChem, *p.a grade*) were used as received. Extra dry tetraglyme (Sigma-Aldrich) was dried over molecular sieves for a week. KClO<sub>4</sub> (99%, Sigma-Aldrich) was dried at 180 °C under reduced pressure. Highly pure Ar (99.999%, Air Liquide) and oxygen (99.9995 %, Air Liquide) were used for purging or as the source of oxygen, respectively.

Coulometric Karl-Fischer Titrator (C20, Metler Toledo) with a diaphragm electrode was used to determine the water content in the electrolyte. All electrolytes were prepared in a glove box (MBraun), in which the H<sub>2</sub>O and O<sub>2</sub> contents do not exceed 0.5 ppm. The prepared electrolytes were kept in closed vials inside the glove box and used within a week for DEMS or freshly prepared on the same day for RRDE experiments. The water contents of the as-prepared electrolytes were ~20 ppm for G4 or G4+DMSO 5% and 50% electrolytes, ~20 ppm for KClO<sub>4</sub>/G4, ~30 ppm for TBAOTf/G4 and ~100 ppm for LiClO<sub>4</sub>/DMSO. The major source of water comes from the salt since pure solvents have lower water contents. The electrolyte picks up some water (up to double the amount of the as-prepared) during transfer from the glove box to the cell.

### *Co<sub>3</sub>O<sub>4</sub> modified GC electrode preparation*

Spinel Co<sub>3</sub>O<sub>4</sub> nanoparticles (50 nm, Aldrich) and Ag311 (1 μm, Ferro GmbH) were used for catalyst ink preparation. The catalyst ink was loaded on a glassy carbon substrate. GC (and also Au) electrodes (0.196 cm<sup>2</sup>) were polished to a mirror finish, with the help of 0.05 μm alumina slurry on a polishing cloth (Microcloth PSA 2, Buehler). The electrodes were then cleaned from the suspension residues and adhering impurities with acetone (99.5%, Sigma-Aldrich) and Milli-Q water. Finally, the electrodes were cleaned with Milli-Q water in an ultrasonic bath (VWR<sup>®</sup>, Germany) for 5 minutes and then dried with KIMTECH wipes and coated with the respective catalyst suspension. The procedure for preparing the modified GC electrode was mentioned in our previous paper.[35] Briefly, an appropriate amount of the catalyst suspension (catalyst dispersed in ethylene glycol) was drop-cast onto the surface of the GC electrode by Eppendorf-Pipette yielding the required loading, and afterwards dried for 10 minutes at 190 °C in an oven. Nafion<sup>®</sup> (5%, Aldrich) solution was used as a binder for fixing the catalyst on the GC. Nafion layer thickness (20 μl was pipetted) was made sufficiently thin (less than 0.2 μm as calculated from a covered electrode area of 0.196 cm<sup>2</sup> and apparent film density of 2.0 g cm<sup>-3</sup>) so that the film diffusion resistance becomes negligible.[36] The electrode was then dried at 190 °C. After cooling the electrode, the distribution of the particles on the surface of GC was examined by an optical microscope and finally installed in the measuring set up.

### *RRDE measurements*

For RRDE and CV measurements, a setup consisting of a Pine bipotentiostat, rotor (Pine) and three-electrode glass cell was used. The working electrode (WE) consisted of the disc or coated disc (5mm diameter surrounded radially by a platinum ring of 6.5mm ID and 7.5mm OD, and in between a Teflon cup), which was mounted to the RRDE Teflon Tip. All CVs of Pt were done using Pt ring as the WE instead of using a disc electrode of Pt. Prior to use, the Pt ring electrode was polished with 0.05 μm alumina slurry and then washed by Milli-Q water

under sonication, the disc was inserted, and then the ring-disc tip was screwed into a PEEK shaft which was fed through a Teflon stopper to the cell. The counter electrode was a Pt sheet, which was immersed in a glass tube connected to the cell via a glass frit. The reference electrode was Ag/0.1M AgNO<sub>3</sub> in DMSO since AgNO<sub>3</sub> is not soluble in G4. For RRDE cell, the silver containing solution was in a separate compartment which was connected to the working electrolyte via a glass stop cock. The conductivity was achieved through the wetted walls of the stop cock. A bipotentiostat (model AFCBP 1, Pine Research Instrumentation, Pennsylvania, USA), which has a built-in function generator, and a LabVIEW software (National Instruments GmbH, Munich, Germany) were used for RRDE, while a home-made potentiostat was used for DEMS system. The electrolytes were continuously purged with O<sub>2</sub> - or Ar prior the experiment or over the electrolyte during the measurements. All experiments were conducted at room temperature, 25±1°.

#### *DEMS measurements*

The classical cell for DEMS was used here. Details about this setup are reported elsewhere.[37] Au-nanoparticles modified electrodes have shown an enhancement in cyclability over carbon electrodes.[38, 39] Thus, the working electrode here is Au-sputtered (50 nm) Teflon membrane, which was supported onto a stainless steel holder containing steel frit in the centre and connected to the mass spectrometer. The membrane acts also as an interface between liquid and vacuum and as a working electrode. The hydrophobic nature of the membrane prevents the passage of the liquid electrolyte, but allows volatile species to permeate. The cell needs an electrolyte of about 1 ml. The counter electrode was a gold wire inserted in the cell. The reference electrode was Ag/0.1M AgNO<sub>3</sub> in DMSO. For DEMS setup, contact of RE to the electrolyte was done by filling a Teflon tube with the Ag<sup>+</sup> containing solution and was ended with a glass bead and inserted into the working electrolyte. The other end was inserted in the silver-containing solution. This reference electrode has a potential of +3.89V vs. Li/Li<sup>+</sup> according to the values given in [40]. The electrolyte was continuously purged with Ar for 10 minutes prior to the experiment or with O<sub>2</sub> during ORR. A calibration leak experiment is performed to determine the value of K<sup>o</sup>, which is used to calculate the z-value, as mentioned previously.[34] The calibration experiment was performed under the same conditions of the main experiment, and the corresponding K<sup>o</sup> value is used. More details and an example of the calibration leak experiment are given in chapter 3 experimental.

#### *Determination of electrolyte resistance by galvanostatic pulse method*

The galvanostatic pulse experiment was conducted prior to or after the RRDE experiments in the same cell and with the same electrodes. A current pulse of 100 μA was applied for about 2 ms using a constant current galvanostat and at the same time the voltage difference between the reference and the working electrodes is recorded. The voltage transient in LiClO<sub>4</sub>/DMSO electrolyte, for example, is shown in Fig. 1. The voltage jump in the curve corresponds to the ohmic resistance (R<sub>s</sub>) and is found to be in the range of 70-100 Ω depending on the electrolyte and the distance between the Luggin capillary and the working electrode. The iR-correction is not considered in every evaluation since the ohmic loss is not significant at the measured currents; while for Tafel plots, it is applied.

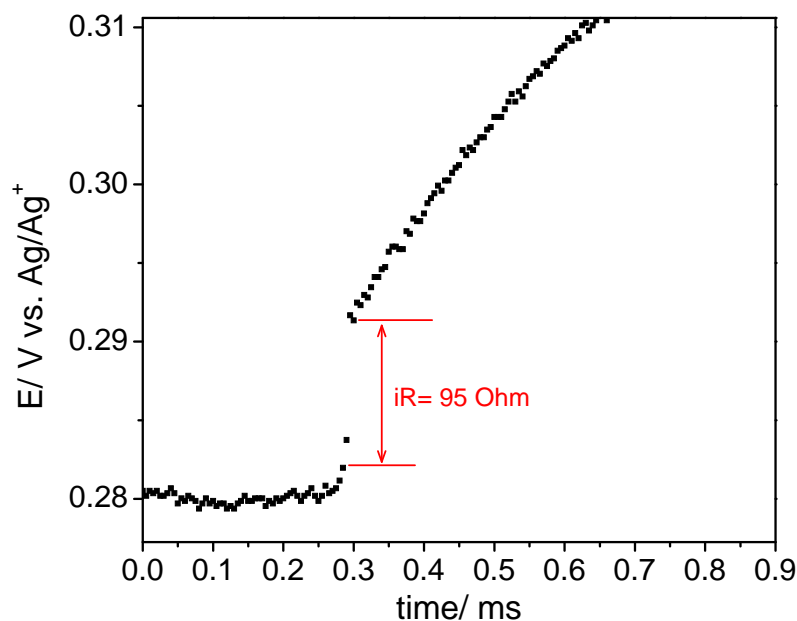


Fig. 1. Voltage transients recorded with a current pulse of 100  $\mu\text{A}$ . Distance between RE and WE: 3 mm.

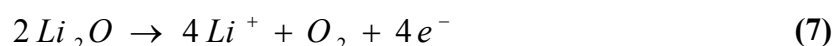
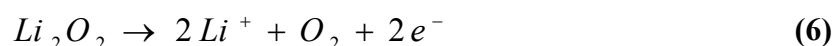
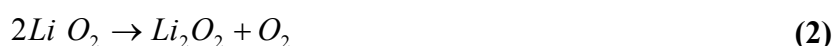
### 8.3. Results and Discussion

#### 8.3.1. Elucidation of the reaction mechanism of ORR /OER in DMSO-based electrolyte

Upon discharge, ORR products (predominantly insoluble and insulating  $\text{Li}_2\text{O}_2$ ) passivate the electrode surface by blocking the active sites. Some reports avoid this problem by limiting the discharge capacity depth to get several cycles.[5, 41] However, an appropriate polar solvent is essential to dissolve the possible reduction products ( $\text{LiO}_2$ ,  $\text{Li}_2\text{O}_2$ ,  $\text{Li}_2\text{O}$ ). DMSO has been shown to stabilize the superoxide as seen in the reverse oxidation scan when the cathodic potential is limited where  $\text{LiO}_2$  is formed (see. Fig. 3) or by detecting currents of superoxide oxidation at the RRDE ring.[9, 20] This is attributed to the stability of superoxide in DMSO where the high DN solvent forms ( $\text{Li}^+(\text{DMSO})-\text{O}_2^-$ ) complex, which stabilizes the superoxide in solution instead of  $\text{Li}^+\text{O}_2^-$  ion pair as in low DN solvents.. As a result, the detection of ORR products is feasible. In low DN solvents (e.g. acetonitrile or tetraglyme), superoxide is not stable since it might have a short life and further reacts to insoluble  $\text{Li}_2\text{O}_2$  and thus blocks the electrode. Here, we present a mechanistic kinetic study of ORR in DMSO, G4 and their mixed solvent. RRDE is a useful hydrodynamic tool since the disc can be used for CV and RDE scans and it decouples the mass transport loss (mass transport is by convection).

Firstly, electrochemical behavior and kinetics in sole  $\text{Li}^+$ /DMSO electrolyte are discussed. Fig. 2 shows the CVs in  $\text{O}_2$ -saturated 0.1M  $\text{LiClO}_4$ /DMSO at GC and Pt electrodes. The CV in Ar-saturated solution is also plotted. Both GC and Pt electrodes show a reasonable stability and cyclability for consecutive cycles, see Fig. 3 and S1. Stable cycling is achieved by sweeping to higher potentials (1V vs.  $\text{Ag}/\text{Ag}^+$ ). In Fig. 2, two reduction peaks and two oxidation peaks are observed at GC. A general reaction mechanism for OER/ORR is shown in scheme 1 and Fig. 21. The initial cathodic peak (pc1, appears as a shoulder) is attributed to the reduction of  $\text{O}_2$  to  $\text{LiO}_2$  ( reaction 1), where  $\text{O}_2$  first adsorbs on surface and then is reduced to  $\text{O}_2^-$  which reacts with  $\text{Li}^+$  in solution forming  $\text{LiO}_2$ , which may be further

disproportionate chemically to  $\text{Li}_2\text{O}_2$  (reaction 2). The second reduction peak (pc2) is a further reduction of  $\text{LiO}_2$  electrochemically to  $\text{Li}_2\text{O}_2$  (reaction 3). Consecutive reduction to  $\text{Li}_2\text{O}$  is thermodynamically possible (reaction 4) but kinetically improbable. The second peak is convoluted with the first reduction process. The reversible anodic peak (pa1) is due to oxidation of the formed  $\text{Li}_2\text{O}_2$  (reactions 6), while pa2 could be due to oxidation of  $\text{Li}_2\text{O}_2$  deposited on  $\text{Li}_2\text{O}_2$  particles layer (and not on substrate) or, improbably, to the oxidation of  $\text{Li}_2\text{O}$  (reaction 7). Reaction 5 occurs if the cathodic scan is limited to the first peak so that  $\text{LiO}_2$  is oxidized in the reverse scan, as discussed below.



Scheme 1: ORR and OER mechanism in aprotic electrolyte

The nature of the electrode material and its roughness play a critical role on the mechanism of ORR and the formation of  $\text{Li}_2\text{O}_2$ . [18, 42] At Pt (as a ring electrode), a single anodic peak is observed in contrast to GC (as a disc) (Fig. 2), which is assigned to a direct 2e-oxidation of  $\text{Li}_2\text{O}_2$ . This difference in peak shape at Pt is due to the different interactions and adsorption of the reduction products at the surface. This could be attributed to the stabilization and stronger adsorption of  $\text{O}_2^-$  or  $\text{Li}_2\text{O}_2$  at GC more than at Pt, and thus keeping more peroxide, which is reoxidized in the anodic scan at lower potentials prior to the second oxidation. Pt is more active towards OER than GC. OER occurs at Pt ca. 150 mV earlier than that at GC and with higher anodic peak currents (Fig. 3 and S1), indicating its catalytic effect in OER. However, similar ORR activity is observed for GC and Pt: the onset of ORR is the same; similar half-peak potential (1.01V) on both electrodes with higher peak currents on the Pt is observed..

In high DN solvents,  $\text{LiO}_2$  is stable in solution; therefore, the nature of electrode surface and electrocatalysis will not play a big role.

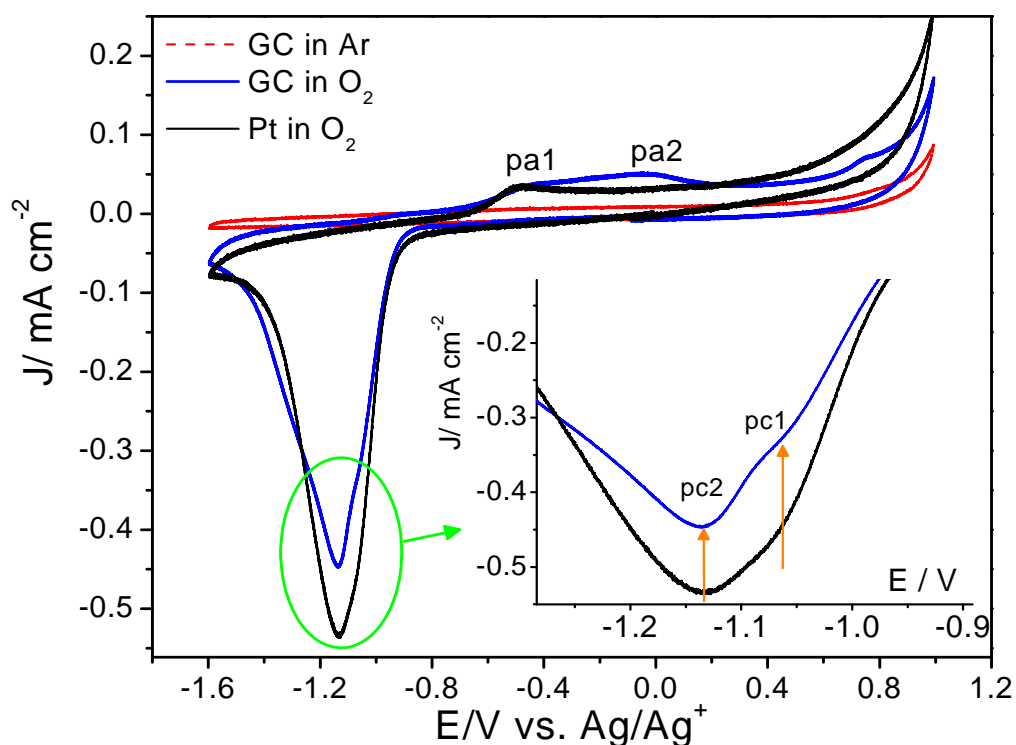


Fig. 2. CVs of GC disc and Pt ring electrodes in both are cycled in a stagnant  $O_2$ -sat. 0.1M  $LiClO_4/DMSO$  with a scan rate of 10 mV/s. Dashed line: in Ar-saturated solution. Inset: a magnification of ORR region.

Superoxide detection is governed by the operating potential window. Fig. 3 shows detailed CVs obtained at GC with different lower potential limits. As the lower limit was restricted to -1.1V (just before the first cathodic peak), only one anodic peak at -0.9V is observed at GC or with a little contribution of the second anodic peak at Pt. Extending the scan to the first peak potential pc1 (-1.2V) creates two anodic peaks in the reverse scan (pa0, pa1). Scanning further in the negative-going direction increases the current of the consecutive anodic peaks, then sweeping to more lower potentials (till -1.35V) results in decreasing of pa1 current together with increasing of pa1 current. The dominance of the first anodic peak upon scanning to lower potentials and its disappearance and appearance of the second anodic peak imply that superoxide is involved as intermediate in first the reduction step. This illustrates also that  $O_2/O_2^-$  couple is reversible and  $LiO_2$  is formed at lower overpotentials.  $LiO_2$  further disproportionates to  $Li_2O_2$ . The presence of two distinct anodic peaks (while the potential still did not reach the pc2 peak) supports the disproportionation mechanism (reaction 2). Scanning further to lower values produces a second reduction peak (-1.4V), which means another electrochemical process. By reversing the scan, superoxide oxidation peak (pa0) disappears and pa1 current increases. This confirms that the second electron transfer process and reduction of  $LiO_2$  to  $Li_2O_2$  at more negative potentials. Reversing the potential at lower potentials (-1.6V) produces  $Li_2O_2$  oxidation peak (pa1) and a very small broad peak (pa2), which could be due to the oxidation of  $Li_2O_2$  adlayers. From DEMS results (discussed below),  $2e^-/O_2$  is obtained over the entire ORR range, indicating that also the second electron reduction to  $Li_2O_2$  occurs at lower overpotential. Thus, both the direct and indirect pathways

of formation of  $\text{Li}_2\text{O}_2$  occur at low overpotentials, while at higher overpotentials the direct reduction to peroxide prevails.

Furthermore, the current ratios of  $\text{pa}0/\text{pa}1$  are higher on GC than on Pt, when the cathodic potential is limited to  $-1.2\text{V}$ , indicating the stability of superoxide on GC than on Pt. Again, the superoxide oxidation peak appears at lower overpotentials at GC. This is an indicative of the stronger interaction of superoxide on GC than on Pt. Consequently, the two reduction peaks are better resolved on GC, see Fig. 3. This is in agreement with previous DEMS experiments, which showed that  $\text{Li}_2\text{O}_2$  formation ( $z$ -value was  $2e^-/\text{O}_2$ ) is predominant at Pt. The catalytic effect of Pt in OER in DMSO can be explained from the shift of overpotential of peroxide peak ( $\text{pa}1$ ) to lower values at Pt than on GC, Fig. 3.

Noticeably, here the oxidation peak ( $\text{pa}1$ ) at Pt electrode is different (stronger) from that in Fig. 2 due to the higher scan rate. At higher scan rates, there is more convection, thus the oxidation rate is higher, leading to a single sharper peak which is similar to the case where a thin layer flow cell is used where also convection takes place.[18] At GC, two anodic peaks are observed at lower scan rate (discussed below with capacity calculations).

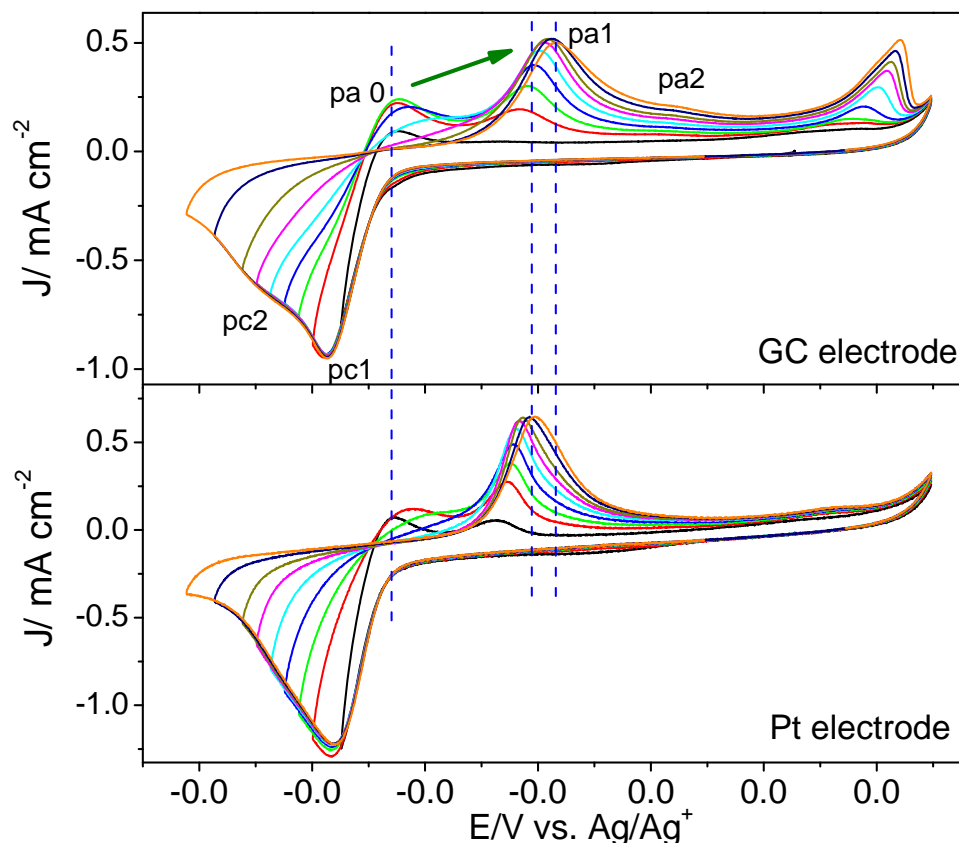


Fig. 3. CVs of GC (upper panel) and Pt (lower panel) electrodes in  $\text{O}_2$ -sat.  $0.1\text{M}$   $\text{LiClO}_4/\text{DMSO}$  at various cathodic limits with  $100\text{ mV/s}$ .

Further investigations of ORR process were conducted using RRDE technique at GC with different rotation rates, see Fig. 4a. By sweeping the potential to the negative direction, the disc currents increase reaching a maximum instead of the expected plateau (which is a typical feature for pure diffusion limited process). After the peak, the disc current decreases and deactivation occurs. This is due to the formation of insoluble  $\text{Li}_2\text{O}_2$  at higher overpotentials (while at lower potentials toroid-shaped  $\text{Li}_2\text{O}_2$  in solution is formed), which blocks the surface

and hinders further O<sub>2</sub> molecules to react. The soluble superoxide generated at the disc transfers to the ring and can be detected if the ring was held at a potential that assures oxidation of superoxide (0 V). Disc and ring currents increase with the rotation rate increase. The limiting peak currents are below the theoretical diffusion-limiting currents for a 2e-process, as analyzed by Koutecky-Levich (K-L) plots (eq. 8.1).[43]

$$\frac{1}{I} = \frac{1}{I_k} + \frac{1}{I_L} \quad \text{eq. 8.1}$$

where:  $I_L = 0.62nFAD_o^{2/3}\omega^{1/2}C_o\nu^{-1/6}$   
 $I_k = nFAkC_o$

where,  $I_L$  (A) is the Levich current for the electrode reaction of a reactive species by a diffusion-controlled process;  $I_k$  (A) is the kinetic current;  $n$  (mol<sup>-1</sup>) is the electron transfer number per mole of a reactive species;  $F$  (A s) is the Faraday constant,  $A$  (cm<sup>2</sup>) is the electrode area;  $k$  (cm mol<sup>-1</sup> s<sup>-1</sup>) is the kinetic rate constant;  $C_o$  (mol cm<sup>-3</sup>) is the bulk concentration of the reactive species;  $D_o$  (cm<sup>2</sup> s<sup>-1</sup>) is their diffusion coefficient;  $\nu$  (cm<sup>2</sup> s<sup>-1</sup>) is the kinematic viscosity (cm<sup>2</sup> s<sup>-1</sup>), and  $\omega$  is the angular velocity ( $\omega=2\pi f$ ,  $f$  is the linear rotation speed in rpm). Plotting the experimental peak limiting current vs.  $\omega^{1/2}$  (see inset of Fig. 4a) shows a nearly straight line with a slope closer to or even less than the theoretical slope for  $n=1$  rather than for  $n=2$ , indicating that this maximum current is related to an O<sub>2</sub> transport-controlled process at the interface. Nevertheless, these peak currents do not reach the theoretical diffusion limited current for  $n=2$ , and slightly below  $n=1$ .

Noticeably, fraction of superoxide generated at the disc is lost during transfer to ring (loss ca. 5% at higher rotations), considering the theoretical collection efficiency  $N_o=0.25$  and all reduction products are soluble. This loss could be due to reaction of superoxide with traces of water forming H<sub>2</sub>O<sub>2</sub>,[44] or reaction of superoxide with electrolyte.[45] The ratio of collection efficiency to the theoretical collection efficiency ( $N/N_o$ ) is plotted versus ORR potential at different rotation speeds, Fig. 4b. The collection efficiency  $N$  ( $N=I_R/I_D$ ) depends on the ring and disc geometry, diffusion coefficient of superoxide and rotation rate.  $N$  increases at higher  $\omega$  because of the shorter transient time which minders the side reactions of superoxide radical, providing more superoxide to the ring.

In addition, the oxidation of peroxide at the disc at ca. -0.5V in the anodic scan is not associated with any ring current (while ring was kept at 0V), confirming the mechanism of oxidation of peroxide directly to O<sub>2</sub> without superoxide intermediate, see Fig. 4a.

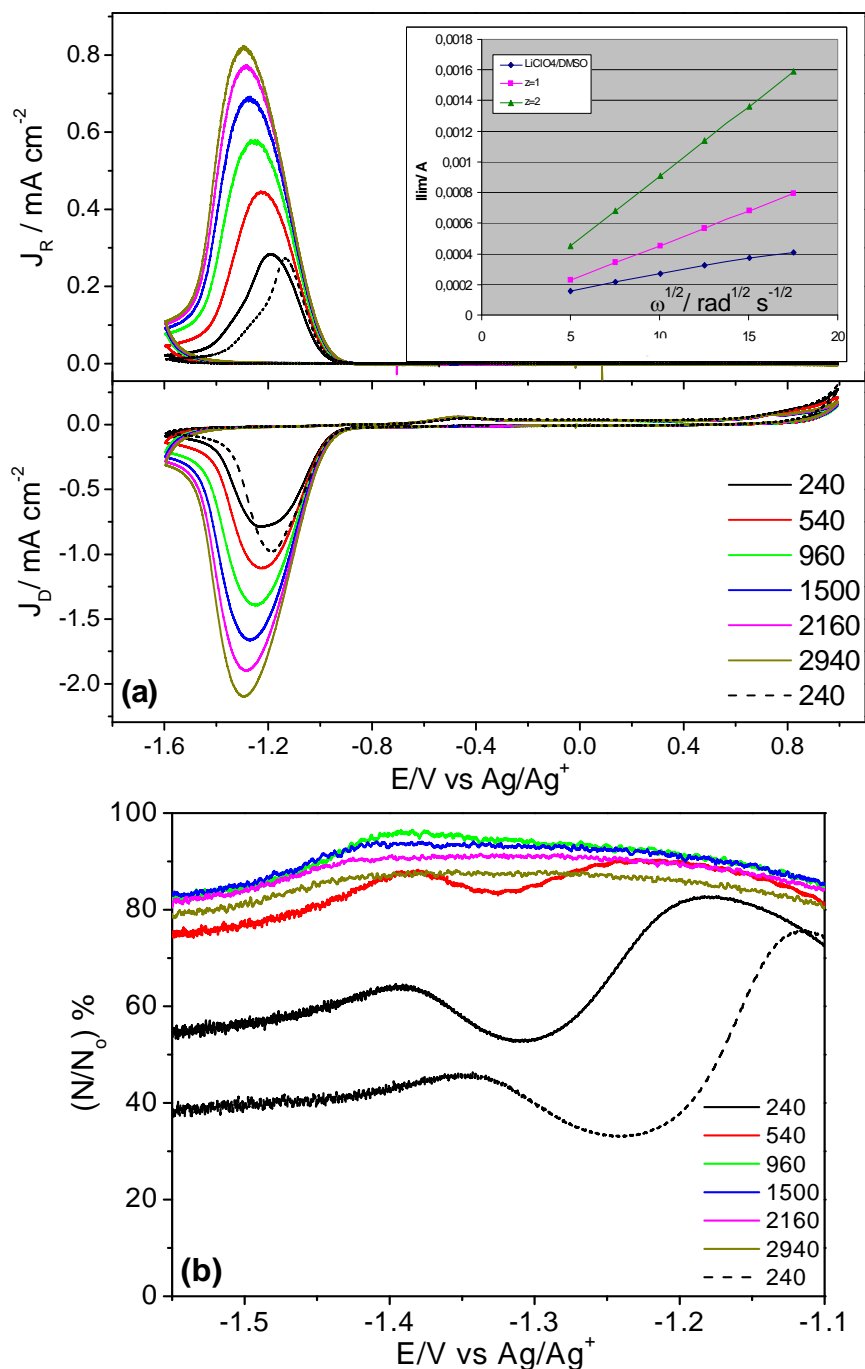


Fig. 4. (a) RRDE voltammograms obtained at GC with  $10 \text{ mV s}^{-1}$  in  $\text{O}_2$ -sat.  $0.1 \text{ M LiClO}_4/\text{DMSO}$  with different rotation rates (240-2940 rpm), Upper panel: ring currents at  $E_R = 0 \text{ V}$ , lower panel: disc current. Inset is the theoretical Levich plot for  $n=1$  and 2 and the experimental peak current. (b)  $N/N_0$  percentage vs. potential at different rotation speeds obtained from (a).

The influence of scan rate on ORR under convective-diffusion control is studied here using RRDE, see Fig. 5. GC electrode was scanned under rotation of 1500 rpm with various scan rates, while the ring was kept at 0 V. At higher scan rates, the disc currents become flat and a semi-plateau occurs, indicating less passivation and reduced blocking. Thus, the oxidation peak at  $-0.3 \text{ V}$  increases with the scan rate increase. The disc peak current is proportional to the scan rate, and the Nicholson-Shain relationship (eq. 8.2), in which the reduction peak

current ( $I_p$ ) versus  $v^{1/2}$ , shows a plausible linearity, see inset of Fig. 5. Nicholson-Shain relationship can be applied for irreversible systems (eq. 8.2).[43]

$$I_p = 2.99 \times 10^5 n(n^* \alpha)^{1/2} A D^{1/2} C v^{1/2} \quad \text{eq. 8.2}$$

where,  $I_p$  is the peak current (A);  $n$  is the number of electrons transferred;  $n^*$  is the number of electrons transferred in the rate determining step;  $\alpha$  is the transfer coefficient;  $A$  is the electrode surface area;  $C$  is the solubility of oxygen;  $D$  is the diffusion coefficient of oxygen and  $v$  is the scan rate.

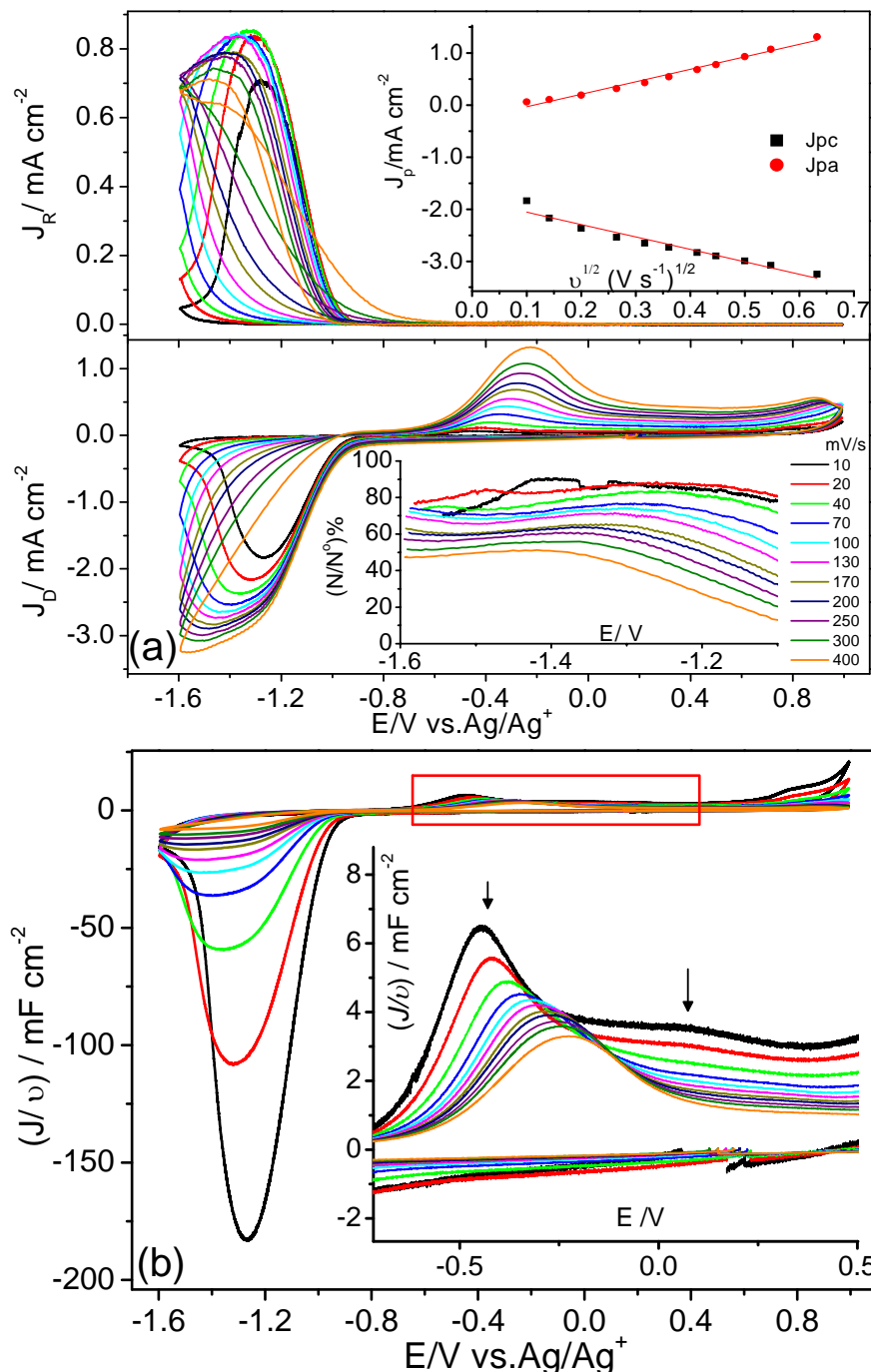


Fig. 5. (a) RRDE results at GC-disc and Pt-ring in O<sub>2</sub>-sat. 0.1M LiClO<sub>4</sub>/DMSO at 1500 rpm with various scan rates, ring was held at 0V; inset: plot of  $J_p$  vs.  $v^{1/2}$ . (b)  $J/v$  at the disc at various scan rates obtained from CVs in (a); inset is a magnification of oxidation peak.

The linearity suggests a mass-transport controlled process, although one should not expect such behavior when rotating. However, the reason of such behavior could be the formation of a passivating film on the electrode surface (mainly  $\text{Li}_2\text{O}_2$ ) which generates additional transport limitation. This film must be porous so that the transport of  $\text{O}_2$  through the film is diffusion-limited. The number of electrons transferred ( $n$ ) is calculated from the slope of relationship, although  $D$  and  $C$  of  $\text{O}_2$  in DMSO solution are used, which might differ from that of diffusion in a film. Taking the value of  $D=1.67 \times 10^{-5} \text{ cm}^2 \text{ s}^{-1}$  and  $C=2.1 \times 10^{-6} \text{ mol cm}^{-3}$ , [9, 46] the best theoretical fit for  $n=1$  is obtained using  $\alpha=0.9$ , which agrees with irreversible system and blocking feature. Moreover, the amount of  $\text{Li}_2\text{O}_2$  detected at the ring ( $N/N_0$ ) decreases with the scan rate increase (not shown).

Interestingly, from the plot of the capacity ( $I/v$ ) vs. potential (inset of Fig. 5b), at lower scan rates, two oxidation peaks are observed while at higher scan rates only one peak appears at shifted potential. This is because at slow scan rates, there is much time for formation of more  $\text{Li}_2\text{O}_2$  on the electrode, leading to the formation of a second layer of  $\text{Li}_2\text{O}_2$  during reduction. Thus, during oxidation two peaks corresponding to oxidation of two layers appear. This supports our proposed mechanism of sequential formation of monolayers.

#### *Tafel slope:*

Kinetic currents can be extracted from the intercept of K-L plots, which are then used to built up Tafel plots and give more details about the mechanism. Fig. 6a shows K-L plots at GC at different potentials. The lines are reasonably straight and parallel in the mixed kinetic-diffusion controlled region, indicating a first-order reaction with respect to dissolved  $\text{O}_2$  concentration. The average slope of K-L plots was used to calculate the number of electrons transferred. Knowing  $D$  and  $C$  in this solution and using eq. 8.1,  $n=0.9$  is obtained, suggesting a one electron transfer process in the first step, although DEMS data showed nearly  $2e^-/\text{O}_2$  over all ORR potential range. This contrast could arise from the use of different  $\text{O}_2$ -concentration and convection in a different type of cells. At  $-1.22 \text{ V}$  (diffusion control region) the intercept should be zero. However, it does not pass through the origin due to an additional current limitation ( $I_A$ ). This limitation is assumed to be related to a heterogeneous process (possibly diffusion through a porous film on the surface). Therefore, a correction has to be made in eq. 8.1 to match this transport limitation according to eq. 8.3.

$$\frac{1}{I} = \frac{1}{I_k} + \frac{1}{I_L} + \frac{1}{I_A} \quad \text{eq. 8.3}$$

If the current  $I_A$  is independent of  $E$  and  $\omega$ , the kinetic current ( $I_k$ ) can be obtained by first determining  $I_A$  by extrapolation of  $I^1$  to  $\omega^{-1/2}$  at peak potential and according to eq. 8.3 this value is taken as an offset for the intercept obtained at other potentials. However, we should mention that different film thicknesses are formed at different rotations.

Tafel plots corrected for additional current limitations revealed a slope (134 mV/dec) close to 120 mV/dec for ORR, while the plots without this correction show a higher value of 186 mV/dec (Fig. 6b), suggesting the need for such correction. This indicates that the one-electron reduction to superoxide is the rate determining step. Tafel plots for ORR obtained from stagnant solution (CV from Fig. 2) show slopes of 119 and 122 mV/dec at lower overpotentials at Pt and GC, respectively, which are slightly lower than the former values due to iR-correction. In this method, the additional limitation current is inherent in the measured

current in the CV (i.e. no need for correction of current to the diffusion current). For OER, a Tafel slope of 114 mV/dec is obtained at Pt which is quite similar to that of ORR, illustrating the reversibility of the first electron transfer process where first electron transfer is too slow while the second is too fast, see Fig. 6d. However, higher slope is obtained at GC. The standard rate constant ( $k$ ) was calculated from eq. 8.1 and is found to range from  $3 \times 10^{-3}$  to  $2.3 \times 10^{-2} \text{ cm s}^{-1} \text{ mol}^{-1}$  for ORR.

From these results, we conclude that  $\text{O}_2$  is firstly reduced to superoxide which further undergoes a simultaneous disproportionation to peroxide (namely, at lower overpotential), while at higher overpotentials peroxide is formed via the direct pathway. Upon charge, peroxide is oxidized to  $\text{O}_2$  without detection of  $\text{LiO}_2$  intermediate (as shown by the absence of ring currents at potentials of peroxide oxidation on the disc, cf. Fig. 5)

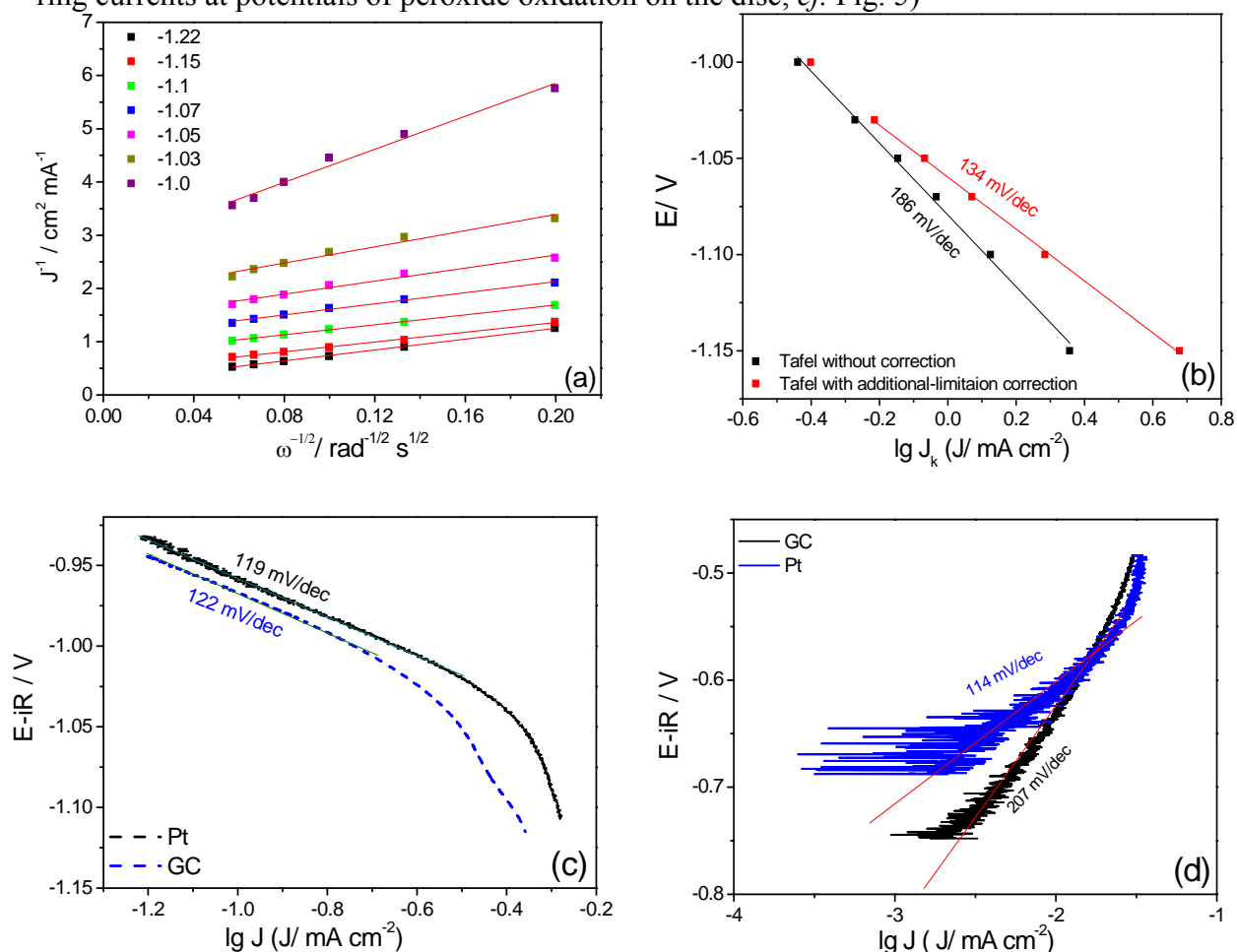


Fig. 6. (a) K-L plots obtained from the CVs in Fig. 4a at GC at different potentials. (b) non- $iR$ -corrected Tafel plots in which the kinetic current was obtained from the intercept of corresponding K-L graph of (a) with and without additional limitation correction. Capacitive and  $iR$ -corrected Tafel plots obtained from the CVs of Fig. 2 at 10 mV/s at GC and Pt electrodes for ORR (c), and for OER (d).

### 8.3.2. Determination of diffusion coefficient of superoxide radical $D(\text{O}_2^{\cdot-})$ using RRDE chronoamperometry

RRDE Chronoamperometry technique was applied here to deconvolute time and potential effects, since they are not elaborated in cyclic voltammetry. Since the collection efficiency depends on RRDE geometry, rotation rate, kinematic viscosity, and diffusion coefficient of

superoxide  $D(O_2^{\bullet-})$ , estimation of  $D(O_2^{\bullet-})$  is important. RRDE can be used to quantify  $D(O_2^{\bullet-})$  using potential step procedure, firstly introduced by Bruckenstein et. al in 1965[47] and later applied by Gan et al.[48] This method has the advantages of being rapid, reproducible and simple in calculations, which make it probably more accurate than the microelectrode method, where natural convection or disturbances could lead to a large error.[48] The disc potential was stepped from 0 V (where no electrochemical reactions take place) to -1.25V (where ORR is diffusion limited), while the ring was kept at 0 V( at which superoxide oxidation is diffusion limited). Superoxide generated at the disc transfers to the Pt ring where it is back-oxidized to  $O_2$  producing current transients as shown in Fig. 7a. The disc current decays with time, while the ring current shows a peak at short times. This decay is due to blocking of the surface with  $Li_2O_2$ . The maximum of the ring peak shifts to longer time at lower rotations together with a faster blocking of the disc. The delay time between the disc potential step and superoxide oxidation at the ring is the transit time ( $T_s$ ) for superoxide.  $T_s$  is inversely proportional to the rotation speed, see inset of Fig. 7a.  $T_s$  is less than 1s in this solution, therefore, there is no obvious delay in the ring response in the CVs. The variation of  $T_s$  with rotation rate is shown in Fig. 7b and can be used to determine  $D$  according to eq. 8.4:[48]

$$T_s = K \left( \frac{\nu}{D} \right)^{1/3} \omega^{-1} \quad \text{eq. 8.4}$$

where,  $K$  is a factor characteristic of the RRDE geometry. For ideal RRDE,  $K$  can be theoretically calculated accord. to eq. 8.5:

$$K = 43.1 \left( \log \frac{r_2}{r_1} \right)^{2/3} \quad \text{eq. 8.5}$$

where,  $r_2$  is the inner radius of the ring (3.25 mm), and  $r_1$  is the radius of the disc (2.5 mm). Here, this theoretical value of 10.1 rpm.s for  $K$  is obtained. From the slope of  $T_s$  vs.  $\omega^{-1}$  and considering kinematic viscosity ( $\nu = 0.002 \text{ cm}^2 \text{ s}^{-1}$ ) for this solution, the  $D(O_2^{\bullet-})$  in 0.1M  $LiClO_4/DMSO$  is estimated to be  $4.2 \times 10^{-7} \text{ cm}^2 \text{ s}^{-1}$ . An overall experimental error in  $D$  of  $\pm 31\%$  could also be considered, which is estimated by taking the finite differences of the logarithm of eq. 8.4.[45, 48] Our  $D(O_2^{\bullet-})$  value is very different from the only available value for DMSO that was reported by Sawyer et al. ( $1.1 \times 10^{-5} \text{ cm}^2 \text{ s}^{-1}$ ),[49] but they used chronopotentiometric titration in a different salt ( $Et$ ) $_4NClO_4$  with possible large uncertainty in end point detection and overestimation of  $O_2$  solubility using Winkler's method. Our value of  $D(O_2^{\bullet-})$  in  $Li^+/DMSO$  is 20 times lower than that in  $TBA^+/ACN$  ( $8.4 \times 10^{-8} \text{ cm}^2 \text{ s}^{-1}$  obtained from Randles-Sevcik).[50] On the other hand, our value is comparable to that in literature obtained using CV fitting for  $[N_{6222}][N(Tf)_2]$  ( $1.5 \times 10^{-7} \text{ cm}^2 \text{ s}^{-1}$ ),  $Pyr_{14}N(Tf)_2$  ( $3.4 \times 10^{-7} \text{ cm}^2 \text{ s}^{-1}$ )[51] or using a similar procedure for  $Pyr_{14}TFSI$  ( $1.1 \times 10^{-7} \text{ cm}^2 \text{ s}^{-1}$ )[45]. The derivation of eq. 8.4 assumes implicitly a perfectly smooth surface[47], and thus the presence of higher surface roughness and large depth of irregularities in the disc surface leads to higher slope ( $\omega T_s$ ) since additional time is possibly consumed for diffusion of a species from bottom to top of a scratch on the surface. Remarkably, the diffusion coefficient of superoxide is much smaller than that of oxygen ( $1.67 \times 10^{-5} \text{ cm}^2 \text{ s}^{-1}$ ), which is attributed to the extensive solvation of superoxide or the formation of an ion pair with  $Li^+$ . [49] The ratio of oxygen to superoxide diffusivity  $D(O_2)/D(O_2^{\bullet-})$  in DMSO is  $\sim 41$ , which is comparable to that reported in literature for  $[N_{6,2,2,2}][NTf_2]$  (ratio=56).[52] For comparison,  $TBA^+/PC$  has a ratio of  $\sim 4$  which is related to

the 10 times higher  $D(O_2^{\bullet-})$ ,[45] and thus causes  $\sim 10$ -fold higher ratio in PC compared to DMSO. The ratio is  $\sim 3$  in TBA<sup>+</sup>/ACN.[50] Nevertheless, a comparison should be done in a similar solvent since these electrolytes have different viscosities, but the data are not available.

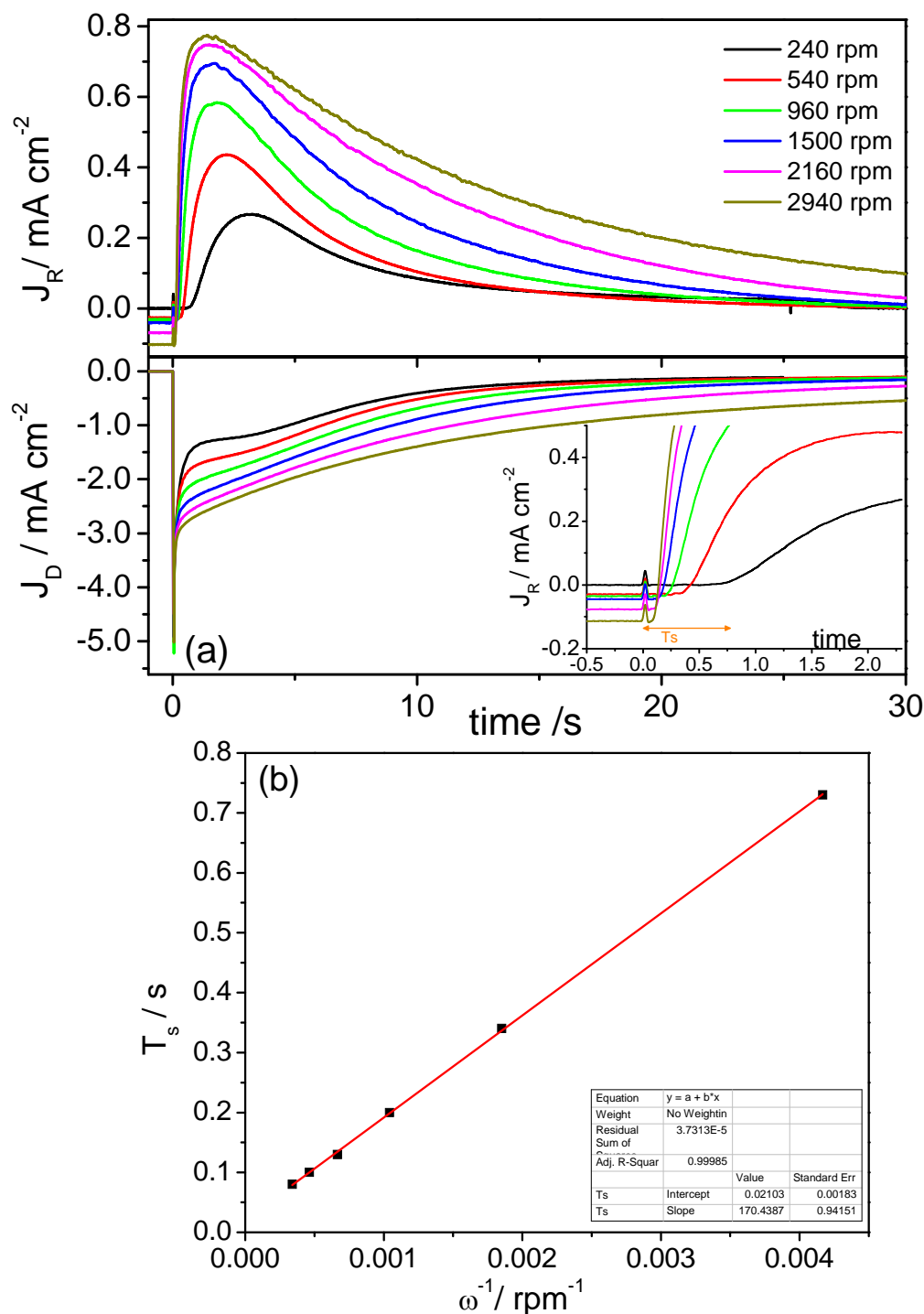


Fig. 7. (a) Current transients for GC disc and Pt ring for ORR in 0.1M LiClO<sub>4</sub>/DMSO, where the disc potential was stepped from 0V to -1.25V while the ring potential was held at 0 V. The step was for 30s at different rotation rates. Inset is a magnification of ring transient at short times. (b) Plot of  $T_s$  vs.  $\omega^{-1}$  in the previous solution to get  $D(O_2^{\bullet-})$  from the slope.

### 8.3.3. ORR in TBA(OTf)/ G4

Here, we investigate the kinetics in TBA<sup>+</sup>/G4, for the first time to the best of our knowledge, where superoxide is the only expected product. Since not all of TBA<sup>+</sup> salts can be dissolved in G4, the large ion OTf as a counter-ion is used, but the conductivity of the solution is low resulting in a higher ohmic drop as can be observed in the CVs of Fig 8. CVs in O<sub>2</sub>-saturated 0.2 M TBA(OTf)/G4 with 100 mV s<sup>-1</sup> at GC, Au and Pt electrodes are presented in Fig. 8a. CV in Ar-saturated solution indicates no countable current since no other electroactive species are present in solution. The reversible redox (O<sub>2</sub>/O<sub>2</sub><sup>-</sup>) peaks are clearly observable. The activity of the three surfaces towards both ORR and OER in terms of overpotential and current is in the order: Pt>Au≈GC. This assesses the effective role of catalyst in superoxide formation/decomposition. From the ring currents, only ca. 50% of the theoretical collection efficiency of superoxide is obtained at lower potentials, indicating the consumption of a part of the produced superoxide by its reaction with G4 or lost in solution, which could be a reason for the instability of G4 solvent against superoxide. The apparent reversibility at Pt electrode is about 50% from the CV. Au electrode shows slightly better activity than GC under rotation mode, Fig. 8b.

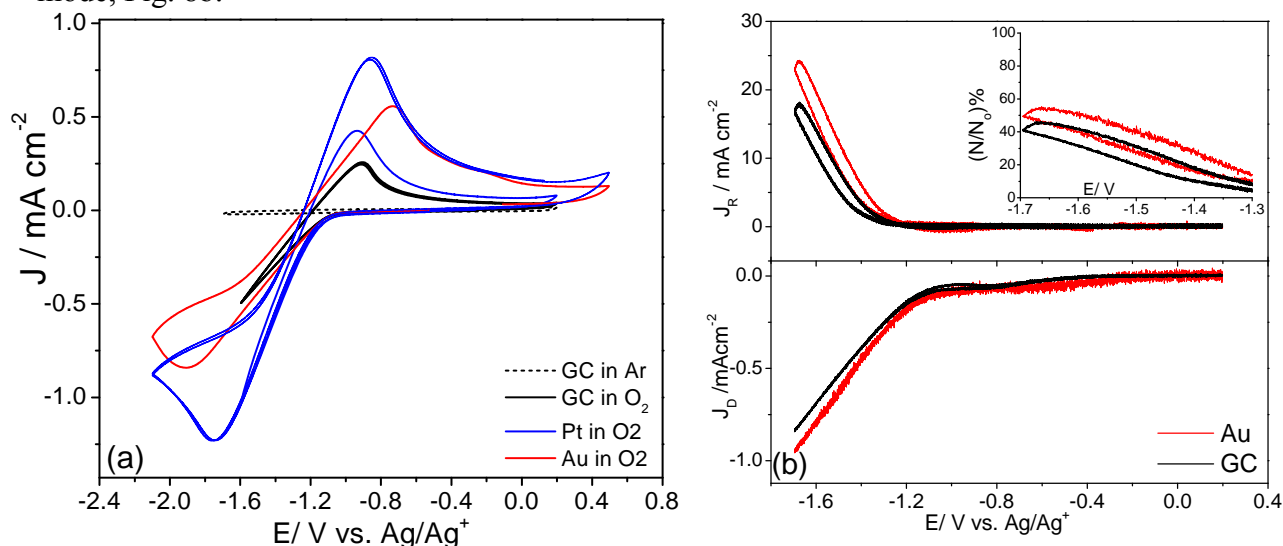


Fig. 8. (a) CVs in O<sub>2</sub>-sat. 0.2M TBA(OTf)/G4 recorded at GC disc, Pt ring and Au disc electrodes with a scan rate of 100 mV/s. (b) Disc and ring currents at GC and Au with 20mV/s and the Pt ring potential was held at +0.2V. Inset is the (N/N<sub>0</sub>)% at both electrodes vs. ORR potential.

### 8.3.4. ORR and OER in a blended Li<sup>+</sup>/G4-DMSO-based electrolyte

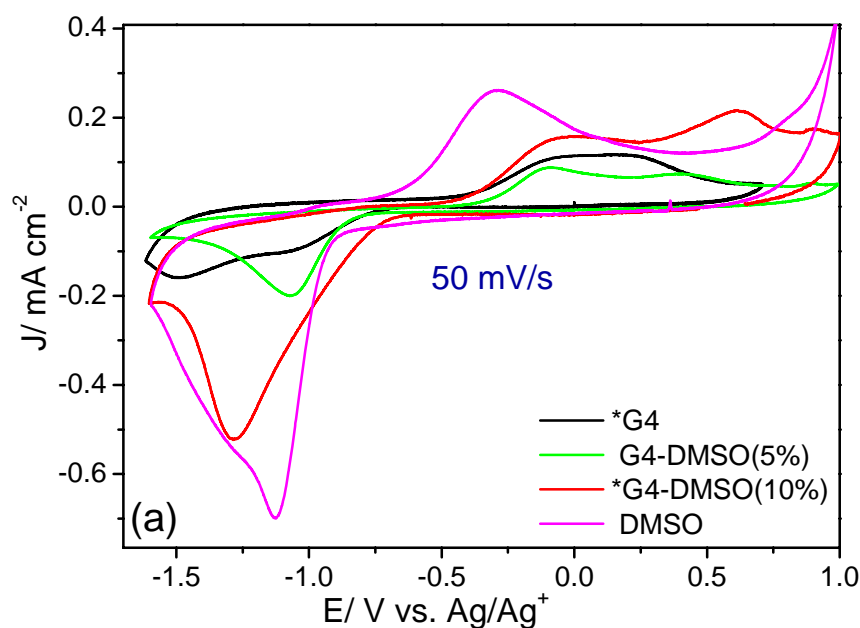
In order to investigate the effect of the solvent on the mechanism, and the influence of the composition ratio in a mixed electrolyte on the superoxide stability, we compared ORR/OER in G4, DMSO and mixtures of G4+DMSO solvents (Fig. 9). Here, the two solvents, which form the mixed electrolyte, have different properties (in particular, the donor number which is possibly related to the solvation strength of the solvent): a DMSO solvent with high DN, higher conductivity and O<sub>2</sub>-diffusivity; a G4 solvent with low DN, higher O<sub>2</sub>-solubility, as shown in the properties of solvents in Table 1. Moreover, we aim to achieve better stability and enhanced activity by a combination of the unique properties of each solvent in one

mixture. Fig. 9a shows the CVs without rotation in different mixtures. The solvent has an influence on the oxygen reaction kinetics. OER is more active (less overpotential) in DMSO electrolyte, while ORR seems to have lower overpotential in G4, and the mixtures have activity in between both single solvents. The pre-peak at the onset of ORR (in G4-containing solvents) is related to the history of the electrode. It appears if the electrode is cycled many times in G4. This is also observed in the mixtures using DEMS technique (discussed below). In the inset of Fig. 9b, the  $\text{Li}_2\text{O}_2$  oxidation peak is shifted to lower overpotential in DMSO than in G4. Also, the addition of DMSO in the mixture increases the oxidation and reduction currents compared to single G4. To investigate the mechanism, the amount of soluble  $\text{LiO}_2$  is detected at the ring using RRDE (Fig. 9b). Interestingly, in G4 solvent the soluble  $\text{LiO}_2$  intermediate is very little due to the smaller stabilization by solvation of  $\text{Li}^+$  in G4 and thus faster reduction of  $\text{LiO}_2$  to insoluble  $\text{Li}_2\text{O}_2$ , causing blocking of the electrode surface. Therefore, no significant ring currents corresponding to superoxide oxidation are detected (black curve). Also, the low  $\text{O}_2$ -diffusion coefficient and ionic conductivity in G4 cause mass transport limitations and reduce the ORR kinetics. By addition of DMSO to G4 in one mixture, the amount of soluble  $\text{LiO}_2$  intermediate increases, see Fig. 9c. On the other hand, in single DMSO solvent (pink curve), mostly all  $\text{LiO}_2$  (90%) is detected in solution (in contrast to G4). Thus, the mechanism of ORR and the stability of superoxide in solution depend mainly on the solvation strength of the solvent.

Table 1. Properties of solvents and their Li salts.

Solvent	Donor Number/ kcal mol <sup>-1</sup>	$\epsilon$ at 25°C	BP/ °C	Viscosity/ cP	Conductivity/ mS cm <sup>-1</sup>	$\text{O}_2$ solubility / mM cm <sup>-3</sup>	$\text{O}_2$ diffusion Coefficient/ Cm <sup>2</sup> s <sup>-1</sup>
DMSO	29.8 <sup>a</sup>	48	189	1.9	2.11 <sup>b</sup>	2.1 <sup>c</sup>	1.67x10 <sup>-6</sup> <sup>b</sup>
Tetraglyme	16.6 <sup>b</sup>	8	275	4.0	0.30 <sup>b</sup>	4.4 <sup>d</sup>	0.22x10 <sup>-6</sup> <sup>b</sup>

<sup>a</sup>Gutmann; [53] <sup>b</sup>Laoire et al.;[9] <sup>c</sup>Sawyer et al.;[46] <sup>d</sup>Read[54]



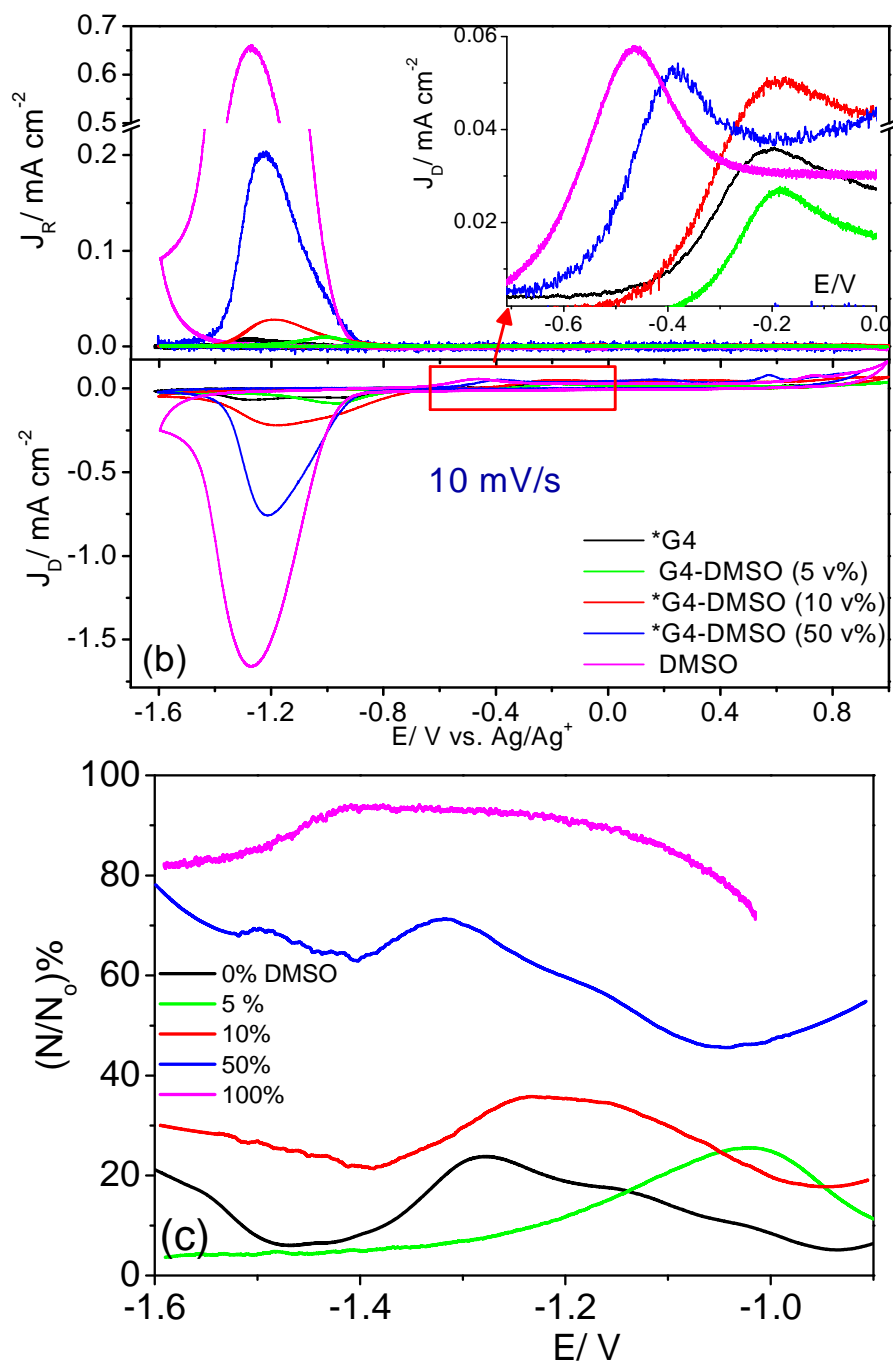


Fig. 9. (a) CVs in stagnant O<sub>2</sub>-sat. 0.1M LiClO<sub>4</sub> in different solvents recorded at Au electrode with a scan rate of 50 mV/s (third cycle is shown). (b) Disc and ring currents recorded at Au disc with 10 mV/s and ring potential was held at +0.3V. Inset: magnification of the oxidation peak at disc. (c) the (N/N<sub>0</sub>)% vs. ORR potential. The experiments marked with \* were kindly supplied by my colleague C. Molls (Diss. in preparation, Bonn Uni. 2016).

A scheme of the mechanism and the two possible pathways of ORR is shown in Fig. 21. In G4 (low DN solvent), Li<sup>+</sup>-O<sub>2</sub><sup>-</sup> ion pair is less solvated, thus remains adsorbed on the electrode surface and a "surface-mediated pathway" takes place, in which LiO<sub>2</sub> is further reduced to Li<sub>2</sub>O<sub>2</sub>, blocking and deactivating the surface, and in turn very little superoxide is detected under convection. In DMSO (high DN), LiO<sub>2</sub> is stabilized in solution, and superoxide is

detected on ring, thus, a "solution-mediated pathway" prevails, in which  $\text{LiO}_2$  disproportionates forming  $\text{Li}_2\text{O}_2$  toroids in solution.

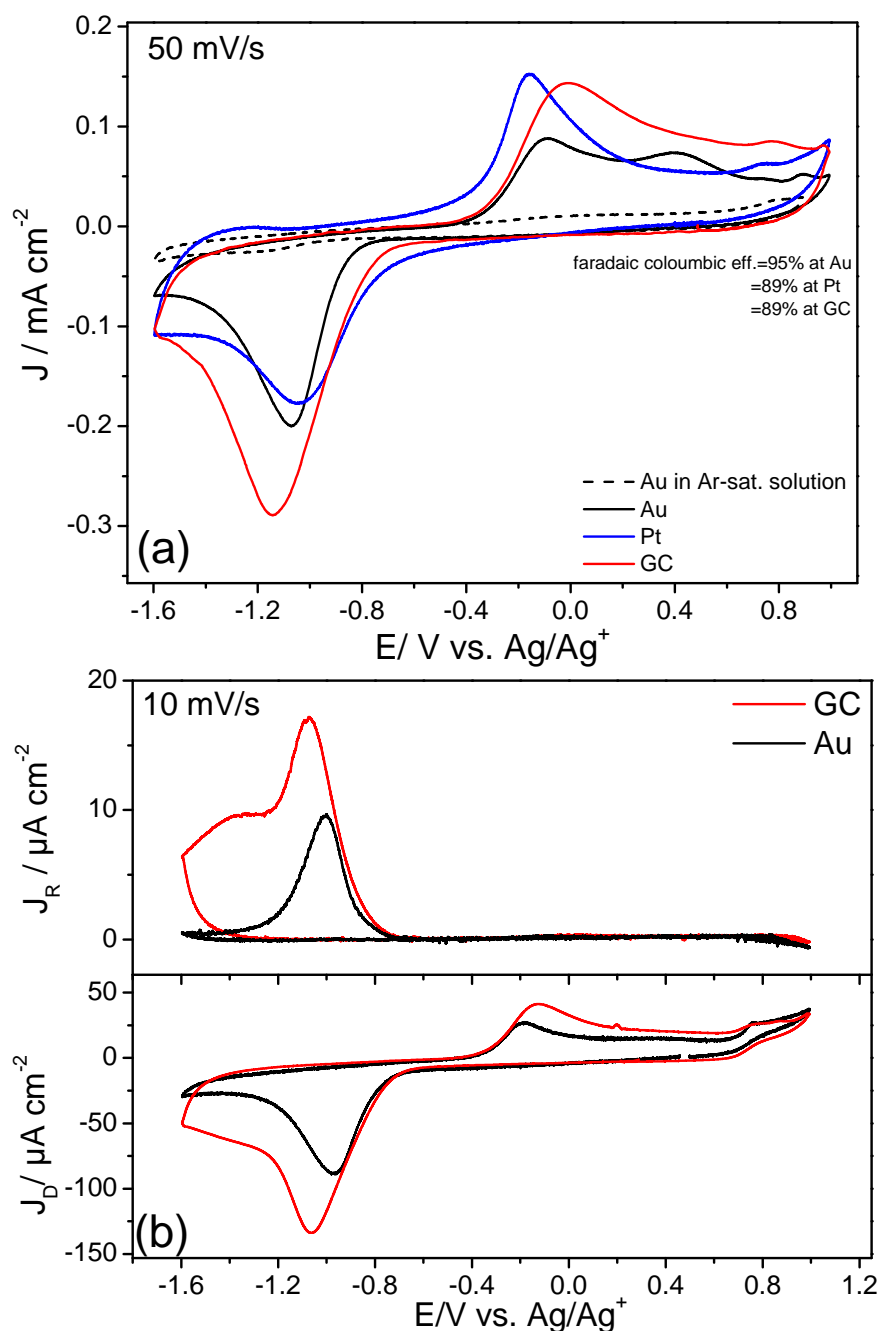


Fig. 10. (a) CVs at GC, Au and Pt electrodes in stagnant  $\text{O}_2$ -sat. 0.1M  $\text{LiClO}_4/\text{G4-DMSO}$  (5 v%) recorded with a scan rate of 50  $\text{mV/s}$ . (b) RRDE curves at GC and Au with 10  $\text{mV/s}$  and 1500 rpm in the same electrolyte. Ring was held at 0 V.

One mixed electrolyte is studied here in details, namely G4+DMSO (5 v%). The catalytic effect of three different electrodes (GC, Au, Pt) is clear in this solution, as shown in Fig. 10a. The charge transfer in ORR/OER in this case is sensitive to the catalyst, where the oxygen species are strongly bound to surfaces of metals like Pt. Thus, a catalyst here lowers the activation energy of reactions and in turn the overpotential. Although the mixture contains mainly the low DN solvent (G4), the process is complex since  $\text{LiO}_2$  is better solvated in DMSO than in G4, accordingly a competition for solvation between the two solvents might

occur. Thus, some superoxide is stabilized in the mixture and can be detected at the ring as shown in Fig. 10b. For OER, the largest current density ( $153 \mu\text{A cm}^{-2}$ ) is observed at Pt, while lower values of 143 and  $87 \mu\text{A cm}^{-2}$  are obtained at GC and Au, respectively, as in Fig. 10a. Pt>GC>Au is the trend of activity especially for OER. Not only higher currents, but also  $\sim 40$  mV lower overpotential (at  $E_{1/2}$ ) is achieved at Pt compared to Au. For ORR, the outperformance of Pt is also noticeable via 90 mV positive shift in potential at  $E_{1/2}$ . Au electrode shows one-step reduction and two-steps oxidation, while Pt shows only one-step reduction and oxidation.

Improvement of the coulombic efficiency in the mixed G4-DMSO solvent (89% @Pt and GC, 95% @ Au from charges in CVs) is obtained compared to the single DMSO electrolyte (60% @GC, *cf.* Fig. 2 and S1). This indicates that G4 improves the rechargeability in the mixture, although 100% reversibility still has not been reached. However, the presence of only 5 v% G4 in the mixture reduced the ORR current to about half of that in DMSO and slightly higher than that in G4. This is due to the lower conductivity in the mixture and the easier blocking of the active sites with  $\text{Li}_2\text{O}_2$ . RRDE experiments were performed to detect the superoxide amount at the ring as shown in Fig. 10b. The transition from 1e to 2e-reduction is remarkable on Au, as seen from the shoulder at potentials more negative to  $-1.2\text{V}$  in Fig. 10b. Interestingly, ca. 30% soluble superoxide in this mixed electrolyte reach the ring from the total flux at the disc (compared to  $<10\%$  in G4 but still less than the 90% in DMSO), implying the effect of solvent on the stability of  $\text{LiO}_2$  intermediate and thus on the mechanism. Even in a very large amount of G4 in the mixture,  $\text{Li}^+$  prefers to be solvated by DMSO forming a stable  $\text{Li}^+-\text{O}_2^-$  complex rather than decomposition to  $\text{Li}_2\text{O}_2$ , raising the amount of  $\text{LiO}_2$  in the mixture than in pure G4. But at more negative potentials,  $\text{LiO}_2$  follows a second electron reduction to  $\text{Li}_2\text{O}_2$  and hence lower ring currents, and passivation are observed. Remarkably, the anodic peak at  $\sim 0.2\text{V}$  is not accompanied by ring currents, indicating the direct oxidation of  $\text{Li}_2\text{O}_2$  to  $\text{O}_2$  without superoxide intermediate.

RRDE measurements in G4-DMSO (5 v%) solvent at GC with  $10 \text{ mVs}^{-1}$  at different rotation speeds were conducted, see Fig. 11a. The disc and ring currents increase slightly with the rotation rate increase; however, the change is not as large as in pure DMSO. A deactivation is observed as a plateau-like shape at potentials more negative to  $-1.2\text{V}$ , indicating blocking with  $\text{Li}_2\text{O}_2$ . The collection efficiency at the ring increases with the rotation speed increase, but still less than that in single DMSO, inset of Fig. 11a. This can be understood by the major formation of  $\text{Li}_2\text{O}_2$ , which is not soluble, and loss of some superoxide during transfer to ring. At higher rotation frequencies, the deactivation is less, and the transport of the products to the ring is faster, so that the superoxide yield at the ring increases. For ORR peak, there is ca. 200 mV positive potential shift in the mixed electrolyte than in the pure DMSO. For OER, there is ca. 200 mV positive shift (*cf.* Fig. 4) which is undesired and could be related to a surface blocking or sluggish kinetics due to ohmic losses.

Basically, the ring current is held at a potential at which superoxide oxidation is diffusion limited or more to ensure complete oxidation. The ring potential is found to strongly affect the superoxide yield at ring, as shown in Fig. 11b. As the ring potential increases from  $-0.6\text{V}$  to  $-0.3\text{V}$ , the superoxide amount increases then reaches almost constant value above  $-0.3\text{V}$ , where all superoxide can be oxidized, inset of Fig. 11b. That is why we selected 0V as the ring potential in most of our experiments to oxidize all ORR products. The need of higher potentials than that expected to oxidize all superoxide at ring could be attributed to the

additional oxidation of the reaction products of the "escaped"  $O_2^-$  ( $LiO_2$  and/or  $Li_2O_2$ ).[27] This escaped  $O_2^-$  was reported also by others.[25].

The effect of scan rate under rotation condition is also investigated in this mixed electrolyte and similar results are obtained compared to the single DMSO solvent, see Fig. S5.

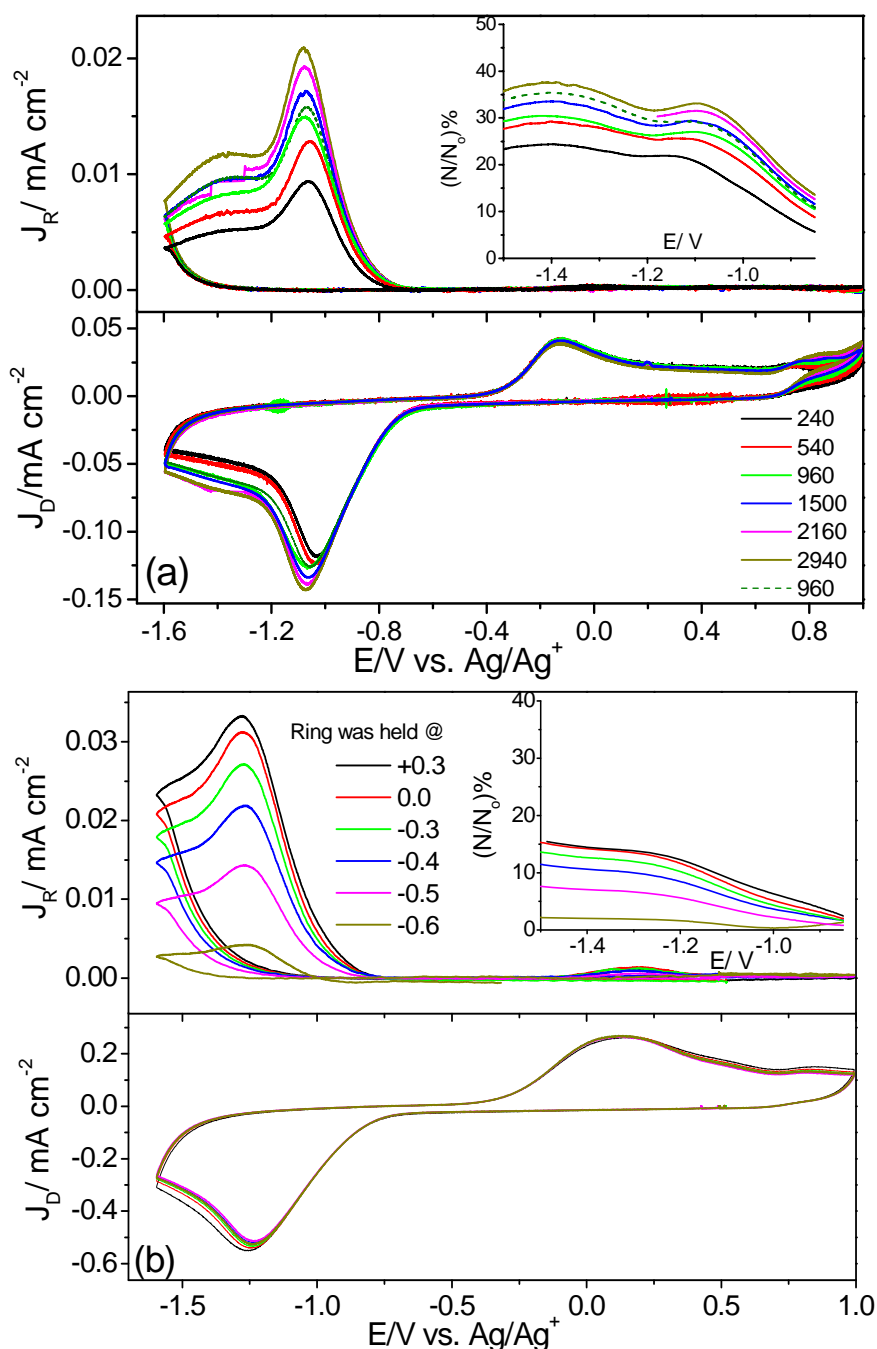


Fig. 11. (a) RRDE curves at GC with 10 mV/s in  $O_2$ -sat. 0.1M  $LiClO_4$ /G4-DMSO (5 v%) electrolyte at different rotation rates. Ring was held at 0V. (b) RRDE curves at GC with 100 mV/s and 1500 rpm in the same solution and at different ring potentials. Inset is the  $(N/N_0)\%$  vs. ORR potential.

### 8.3.5. The role of catalyst in ORR/OER in DMSO-based electrolyte: $Co_3O_4$ bifunctional catalyst

Despite the great efforts done on electrocatalysis in organic electrolytes, the role and the benefits of the catalyst in aprotic electrolytes are incompletely clarified. Porous carbon

exhibits a limited round trip efficiency, and promotes electrolyte degradation.[55] Therefore, a catalyst should be expected to reduce the overpotential of ORR/OER and facilitate the removal of discharge products. DMSO solvent was found to be kinetically favorable and stable when combined with noble metals like Pt and Pd than G4. This synergy between the catalyst and DMSO enhanced the capacity and performance of the cell.[21] Metal oxides were also found to improve the cycle stability:  $\text{Co}_3\text{O}_4$  showed enhanced charge/discharge performance and reduced discharge overpotential in G4 compared to the pure carbon electrode, although no kinetic or RRDE studies were shown.[56]  $\text{Co}_3\text{O}_4$  nanofibers (1D) were immobilized on graphene nanoflakes and showed superior cyclability and high capacity (10500 mAh/g) in G4. This was attributed to the large surface area and fast  $\text{O}_2$  diffusion through graphene and  $\text{Co}_3\text{O}_4$ . [57]  $\text{Co}_3\text{O}_4$  showed as well good compromise between initial capacity (2000 mAh  $\text{g}^{-1}$ ) and capacity retention and with less charging voltage in propylene carbonate-based electrolyte, but without mechanistic study.[58] Manganese oxides were investigated in DMSO and revealed an enhanced activity over carbon in terms of onset potential.[59] Our previous report discussed in details the effect of different noble metals on the reaction mechanism and reduction products in DMSO.[18] Thus, proper co-selection of a catalyst and electrolyte is essential to achieve the synergistic effect.

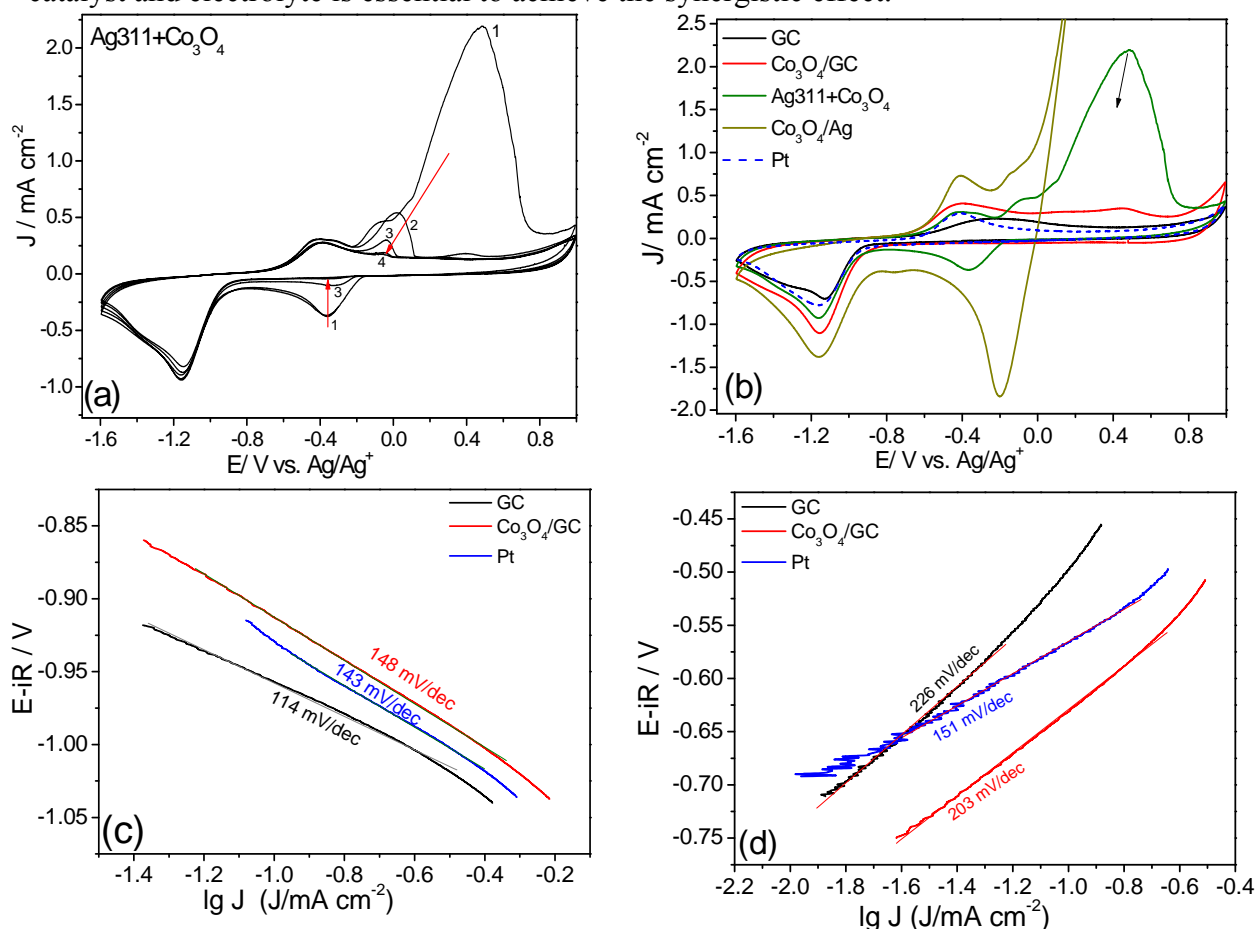


Fig. 12. (a) Consecutive CVs of  $\text{Ag311+Co}_3\text{O}_4$  (10 w%)/GC electrode in a stagnant  $\text{O}_2$ -sat. 0.1M  $\text{LiClO}_4/\text{DMSO}$  with  $50 \text{ mV s}^{-1}$ . (b) First CVs at different catalysts in stagnant  $\text{O}_2$ -sat. 0.1M  $\text{LiClO}_4/\text{DMSO}$  with  $50 \text{ mV s}^{-1}$ . (c) Capacitive current- and  $iR$ -corrected Tafel plots derived from (b) at different electrodes for ORR and (d) for OER.

Here, we present the catalytic behavior of a nonprecious  $\text{Co}_3\text{O}_4$  nanoparticles catalyst in DMSO based electrolyte. This catalyst was recently shown to be active, particularly for OER in alkaline media. Noteworthy, we started our measurements with the mixed  $\text{Ag}+\text{Co}_3\text{O}_4$  catalyst, which showed superior performance in alkaline media,[35] but failed to work in DMSO electrolyte due to the rapid dissolution of Ag in DMSO containing electrolyte. This results in undefined electrode composition and solution. The dissolution is observed in all Ag-containing catalysts. One example is shown in Fig. 12a for  $\text{Ag}_{311}+\text{Co}_3\text{O}_4$  (10 w%)/GC catalyst. The anodic peaks above -0.2V are assigned to Ag oxidation and dissolution, and they decrease with cycling till most of Ag are bleached from the surface. The cathodic peak at -0.35V is the reduction of Ag oxide formed at higher potentials.

Fig. 12b compares the electrochemical behavior of different catalysts in the first cycle (Pt,  $\text{Co}_3\text{O}_4/\text{GC}$ ,  $\text{Ag}+\text{Co}_3\text{O}_4/\text{GC}$  and  $\text{Co}_3\text{O}_4/\text{Ag}$ ) to that of bare GC. The catalyst loading was  $400 \mu\text{g cm}^{-2}$ . Although Ag-containing catalysts exhibit apparently higher currents, they are unstable. Therefore, the focus is on  $\text{Co}_3\text{O}_4$  (50nm). The kinetic parameters for GC and  $\text{Co}_3\text{O}_4/\text{GC}$  electrodes derived from Fig. 12b are summarized in Table 2. For ORR,  $\text{Co}_3\text{O}_4$  catalyst exhibits a positive shift in onset potential (ca. 70 mV) compared to GC. This enhancement in activity is also clear in the ORR Tafel plots where higher kinetic currents are observed for  $\text{Co}_3\text{O}_4$ , see Fig. 12c. For OER, about two-fold current density is achieved at  $\text{Co}_3\text{O}_4$  compared to GC and with ca. 150 mV lower overpotential (Table 2). Pt as a standard material is compared. It shows slightly higher activity (less overpotential and higher current) for ORR and OER than GC, but is less active than  $\text{Co}_3\text{O}_4$ . Furthermore, the coulombic efficiency, calculated from oxidation and reduction faradaic charges, increases significantly from 60% at GC to 89% at  $\text{Co}_3\text{O}_4$  catalyst, demonstrating enhanced reversibility. This indicates the bifunctionality of the catalyst for ORR and OER. Tafel plots are depicted in Fig. 12c,d. Typical Tafel slope close to 120 mV/dec is obtained for ORR at GC, indicating one-electron reduction of  $\text{O}_2$  to superoxide as the rds, with subsequent  $\text{Li}_2\text{O}_2$  formation. The increase of Tafel slope at  $\text{Co}_3\text{O}_4$  nanoparticles might be due to a change in the reaction mechanism where  $(\text{LiO})_{\text{ad}}$  species could be formed on the more active sites of  $\text{Co}_3\text{O}_4$  nanoparticles (GC has less adsorption strength). This was also proposed by others for  $\text{Mn}_3\text{O}_4$  catalyst.[59]

These results demonstrate the improvement in the activity significantly in OER and to some extent, in ORR at  $\text{Co}_3\text{O}_4$  catalyst compared to GC.

Table 2. Kinetic parameters derived from CVs at  $50 \text{ mV s}^{-1}$  in Fig. 12b for GC and  $\text{Co}_3\text{O}_4/\text{GC}$  electrodes in DMSO.

Electrode	ORR				OER			
	$E_{\text{onset}}$ / V	$E_{1/2}$ / V	I @-1.05V / $\mu\text{A cm}^{-2}$	Tafel Slope/ $\text{mVdec}^{-1}$	$E_{\text{pa}}$ /V	I@ -0.46V / $\mu\text{Acm}^{-2}$	Tafel slope/ $\text{mVdec}^{-1}$	Coulombic Efficiency $Q_{\text{OER}}/Q_{\text{ORR}}$
GC	-0.87	-1.03	479	114	-0.26	138	226	60
$\text{Co}_3\text{O}_4/\text{GC}$	-0.80	-1.03	694	148	-0.41	281	203	89

The RRDE results comparing  $\text{Co}_3\text{O}_4/\text{GC}$  electrode to bare GC at  $10 \text{ mV s}^{-1}$  and 1500 rpm are depicted in Fig. 13. Differences are observed on the catalyzed electrode. The first significant impact of  $\text{Co}_3\text{O}_4$  catalyst is the lower amount of detected superoxide, emphasizing the role of

the catalyst on the reaction pathway. Indeed, there is no significant change in ORR activity at  $\text{Co}_3\text{O}_4$  compared to GC, while significant changes in the ring currents are observed regarding peak magnitude and onset potential. For GC, earlier onset of ORR and higher ring currents are observed, see upper panel of Fig. 13. The delay in ring response might be due to slow diffusion of superoxide in the  $\text{Co}_3\text{O}_4$  film. Superoxide yield from theoretical value of disc flux ( $N/N_0$ ) is ca. 50% at  $\text{Co}_3\text{O}_4$  catalyst compared to ca. 95% at the bare GC electrode, as shown in the inset of Fig. 13. This supports the mechanism proposed for formation of oxygenated lithium species adsorbed on  $\text{Co}_3\text{O}_4$  nanoparticles, which possess larger surface area and more active centers for adsorption than GC. Superoxide is adsorbed on  $\text{Co}_3\text{O}_4$  catalyst in the inner Helmholtz plane promoting further electrochemical reduction to  $\text{Li}_2\text{O}_2$  and less  $\text{LiO}_2$  (i.e. lower ring currents).

The second important effect of the catalyst is its higher OER activity and synergistic effect: higher oxidation currents are observed, see inset of Fig. 13.  $\text{Co}_3\text{O}_4$  facilitates the charge transport to  $\text{Li}_2\text{O}_2$ , thus catalyzes the oxidation of  $\text{Li}_2\text{O}_2$  predeposited on it. Radin et al. have reported that the performance of Li-O<sub>2</sub> batteries is limited by the sluggish charge transport within  $\text{Li}_2\text{O}_2$ . [60] According to their theoretical calculations, the incorporation of traces of Co into  $\text{Li}_2\text{O}_2$  can enhance the charge transport. This enhanced charge transport could rationalize the improved performance observed in  $\text{Co}_3\text{O}_4$ -modified electrode, in particular, during charging. Therefore,  $\text{Co}_3\text{O}_4$  is a good candidate for Li-O<sub>2</sub> batteries.

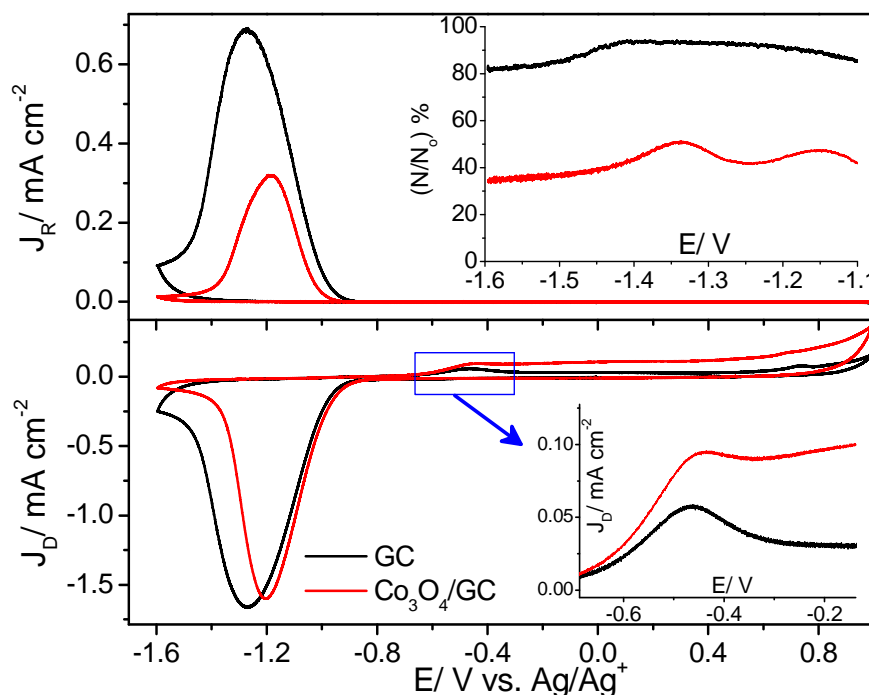


Fig. 13. RRDE curves for oxygen reactions at  $\text{Co}_3\text{O}_4/\text{GC}$  ( $400 \mu\text{g cm}^{-2}$ ) and bare GC electrodes at  $10 \text{ mV s}^{-1}$  and 1500 rpm in 0.1M  $\text{LiClO}_4/\text{DMSO}$ , Ring was kept at 0 V. Inset is  $N/N_0$  percentage at ORR range.

RRDE results at different rotation rates and various scan rates on this catalyst are also discussed in the SI. Ring potential is found to affect the amount of superoxide detected as in case of GC.

From these results, we conclude that  $\text{Co}_3\text{O}_4$  is a stable bifunctional material for OER and ORR in DMSO solvent. The catalyst showed improved OER activity and enhanced

reversibility and round trip efficiency. This could be attributed to the synergy between the catalyst and the solvent. The nature of the solvent is a crucial factor in the mechanism. Whether the catalyst plays a significant or little role is dependent on the degree of solvation of  $\text{Li}^+$  in the electrolyte (i.e. DN of the solvent) and the adsorption of intermediates on the catalyst. Thus, further investigating the activity of  $\text{Co}_3\text{O}_4$  in a low DN solvent could be reasonable to get a clearer image on this criterion.

### 8.3.6. Quantitative investigation of ORR and OER in G4 and mixed G4-DMSO electrolyte: DEMS insight

#### 8.3.6.1. One-electron transfer ORR and OER in $\text{TBA}^+$ -and $\text{K}^+$ -containing electrolyte: Calibration of DEMS for $\text{O}_2$

In DEMS, mass resolved detection of volatile educts, reaction products or intermediates is achieved by mass spectrometry (MS) with very short delay time. The rate of formation or consumption of a species can be monitored by measuring the corresponding ionic current by MS. Therefore, online CV will be recorded simultaneously with the mass spectrometric cyclic voltammogram (MSCV). The ion intensity ( $I_i$ ) determined spectrometrically is directly proportional to the flow of species entering the mass spectrometer ( $dn/dt$ ). The proportionality constant is the calibration constant ( $K^o$ ), eq. 8.6:

$$I_i = K^o \left( \frac{dn}{dt} \right) \quad \text{eq. 8.6}$$

Since the transfer of the products into the mass spectrometer is not complete and the ionization probability of the species alters with the age of the filament, calibration of the mass spectrometer is necessary. Since, the incoming flow can be expressed by the faradaic current;  $dn/dt = I_F/zF$  assuming 100% current transfer efficiency. Thus, the correlation between the faradaic current ( $I_F$ ), which can be extracted from CV, and the ionic current ( $I_i$ ), which is detected by mass spectrometry, is defined according to eq. 8.7. Using  $K^o$  for oxygen, the number of electrons transferred per oxygen molecule ( $z$ ) upon oxidation or reduction can be calculated:

$$z = \frac{K^o \times I_F}{F \times I_i} \quad \text{eq. 8.7}$$

where,  $F$  is the faradaic constant.  $K^o$  is determined using a calibration leak experiment, as discussed in experimental section.

To validate our setup and demonstrate the reasonable value of  $K^o$ , DEMS experiments were first performed in an electrochemical reaction with a known value of  $z=1$  as superoxide is formed, namely ORR in  $\text{TBA}^+/\text{G4}$  and  $\text{K}^+/\text{G4}$ . Fig. 14a shows CV and MSCV in 0.1M  $\text{TBA}(\text{OTf})$  in G4 with  $20 \text{ mV s}^{-1}$  starting from 0V in the cathodic direction. The solution was continuously purged with  $\text{O}_2$ . Basically, upon reduction oxygen is consumed, so the decrease in  $I_{32}$  is expected because the reduction products are not volatile, and fewer oxygen molecules diffuse to the mass spectrometer.  $\text{O}_2$  started reduction at ca. -1.1V and then reoxidized in the positive-going scan evolving  $\text{O}_2$  as a peak at -1.06V. Since the flow of  $\text{O}_2$  from the electrolyte into the vacuum is steady and any  $\text{O}_2$  from leakage or residual gas in the system causes a change in the base line, a correction for baseline of  $I_{32}$  was basically done. DEMS is a quantitative tool to measure the amount of oxygen evolved (as positive ionic current) and consumed (as negative ionic current). We found that  $0.91 \text{ e}^-/\text{O}_2$  is consumed during ORR and  $1.05 \text{ e}^-/\text{O}_2$  is produced upon oxidation in  $\text{TBA}^+/\text{G4}$  electrolyte according to eq. 8.7, see Fig.

14b. This  $z=1$  value indicates that only the one-electron process is present and other reduction products as peroxide are improbable. In addition, no additional OER peaks are noticed. This means that oxygen is reduced to superoxide, which is then re-oxidized to oxygen in  $\text{TBA}^+/\text{G4}$  electrolyte. The ratio of  $z(\text{OER})/z(\text{ORR})$  is  $\sim$ one, indicating that side reactions with  $\text{O}_2$  are unlikely to occur.

Since the formed soluble superoxide is mainly transported to the bulk solution by convection, only fraction of superoxide can be reoxidized to  $\text{O}_2$  on the surface so that low reversibility is observed. Furthermore, a small amount of mass 44 was observed, which could be  $\text{CO}_2$  evolution at potentials beyond OER region. Possibly, this is caused by electrolyte decomposition or other side reactions with electrolyte and superoxide. Nevertheless, the oxidation and reduction processes are stable for several cycles as shown for the first two scans in Fig. 13b. Data for  $\text{K}^+/\text{G4}$  show a  $\sim 1\text{e}^-/\text{O}_2$ , implying also that one electron reduction process takes place, see SI.

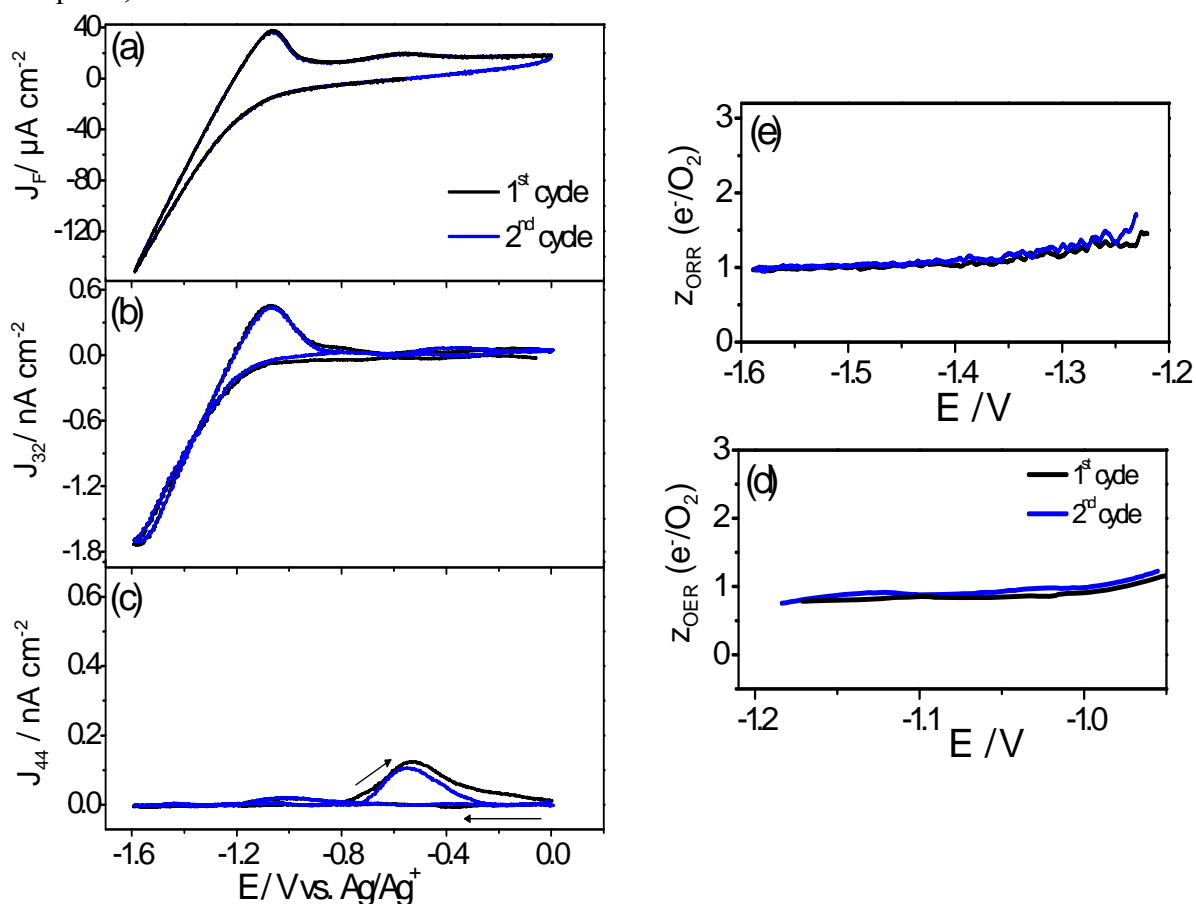


Fig. 14. CVs (a) and MSCVs recorded simultaneously at Au-sputtered membrane electrode for ORR and OER in  $\text{O}_2$ -saturated 0.1M  $\text{TBA}(\text{OTf})$  in G4 with  $20 \text{ mV s}^{-1}$ . (d) number of electrons transferred per oxygen molecule ( $z$ ) obtained during ORR and (e) OER from the corresponding curves.

### 8.3.6.2. ORR and OER in $\text{LiClO}_4/\text{G4}$ : Deactivation and reactivation of the electrode

During sweeping between  $-1.7\text{V}$  to  $+0.1\text{V}$ , progressive deactivation of the electrode takes place (see SI). To better understand the source of deactivation, the effect of the upper potential limit is examined, see Fig. 15. The reduction peak at ca.  $-1.3\text{V}$  is assigned to

peroxide formation, while the anodic peak at ca. 0V is assigned to the oxidation of peroxide to oxygen. The second oxidation peak appeared above +0.5V is due to electrolyte decomposition and is associated with CO<sub>2</sub> evolution as will be discussed below. It is obvious also in the coming CVs, that several peaks appear higher potentials and are larger in G4-containing electrolytes. It is also seen in RRDE experiment (*cf.* Fig. 9a). The peak potential separation between reduction and oxidation is about 1.3 V, which is ca. 500 mV less than that observed in literature although GC and higher scan rate 100 mV s<sup>-1</sup> were used there.[13] Onset of oxygen reduction is at -0.7V and OER onset is at ca. -0.35V. In the first 6 cycles, a wide potential window up to +1.0V was applied. The cathodic currents in the reduction region are simultaneously accompanied with decrease in the ionic current, indicating that ORR surely takes place. The faradaic and ionic currents are stable upon cycling with no deactivation. Once the anodic scan was limited to lower potential of +0.4V in the consecutive 7<sup>th</sup> and 8<sup>th</sup> cycles (green curve), a clear deactivation is experienced. As soon as the potential window was re-opened to higher potentials (blue curve), a reasonable reactivation appears, and the currents restore mostly their initial values of the first CVs. We infer from these results that the blocking film formed upon reduction can be oxidized and removed from the active sites of the surface by sweeping to higher potential limit. Therefore, the full sweeping to higher potentials is needed to remove the passivating layer (see also SI for 3 consecutive cycles). The deactivation/reactivation process has been studied in DMSO electrolyte using only cyclic voltammetry experiments.[20]

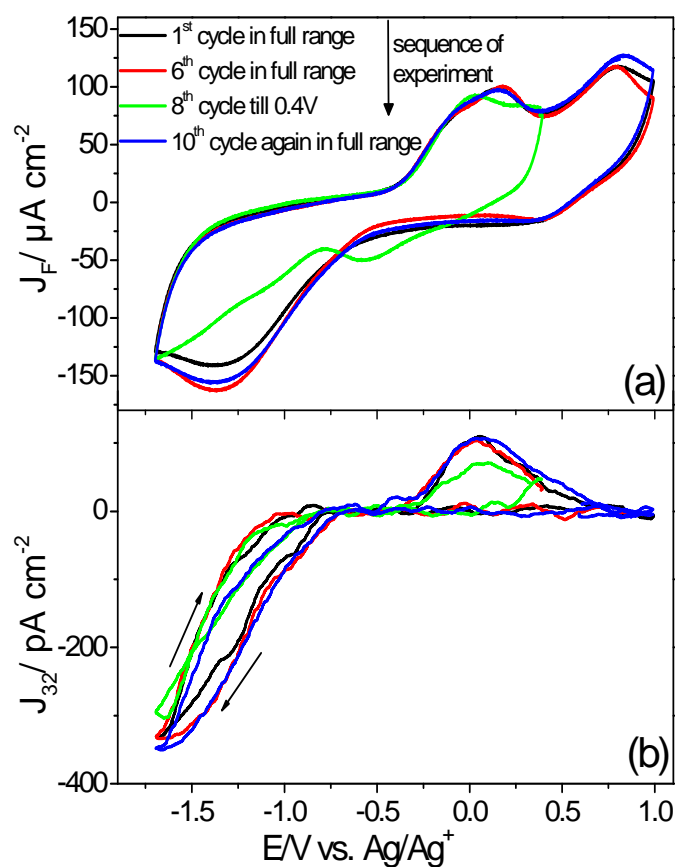


Fig. 15. CVs (a) and MSCVs (b) for mass 32 at Au-sputtered membrane electrode in O<sub>2</sub>-sat. 0.1M LiClO<sub>4</sub>/G4 electrolyte with 20 mV s<sup>-1</sup>. Current density is calculated with regard to geometric area.

To better understand whether a reduction products-induced decomposition takes place and if the amount of reduction products affects the decomposition, an experiment of lower potential limit opening was done as shown in Fig. 16. The shape of the oxidation peaks in  $\text{Li}^+/\text{G4}$  electrolyte depends on the nature, roughness and structure of the electrode. However, the main features are similar in all cases: one reduction peak and two or more oxidation peaks.[9, 13] Here, the onset potential difference between ORR and OER is ca. 350 mV (see Fig. 16a,b), while in Laoire et al. report[9, 13] higher overpotential ( $\sim 500$  mV) was observed. That might be due to a difference in electrode structure. The reduction peak is at about -1.3V, and its oxidation at -0.1V. The second anodic peak at +0.2V is partially for OER, but also the contribution from electrolyte decomposition. The third peak at +0.7V does not correspond to oxygen evolution but side reactions as can be seen from Fig. 16b. As the lower limit expands, higher anodic currents positive shift of anodic peak and more oxygen are obtained.

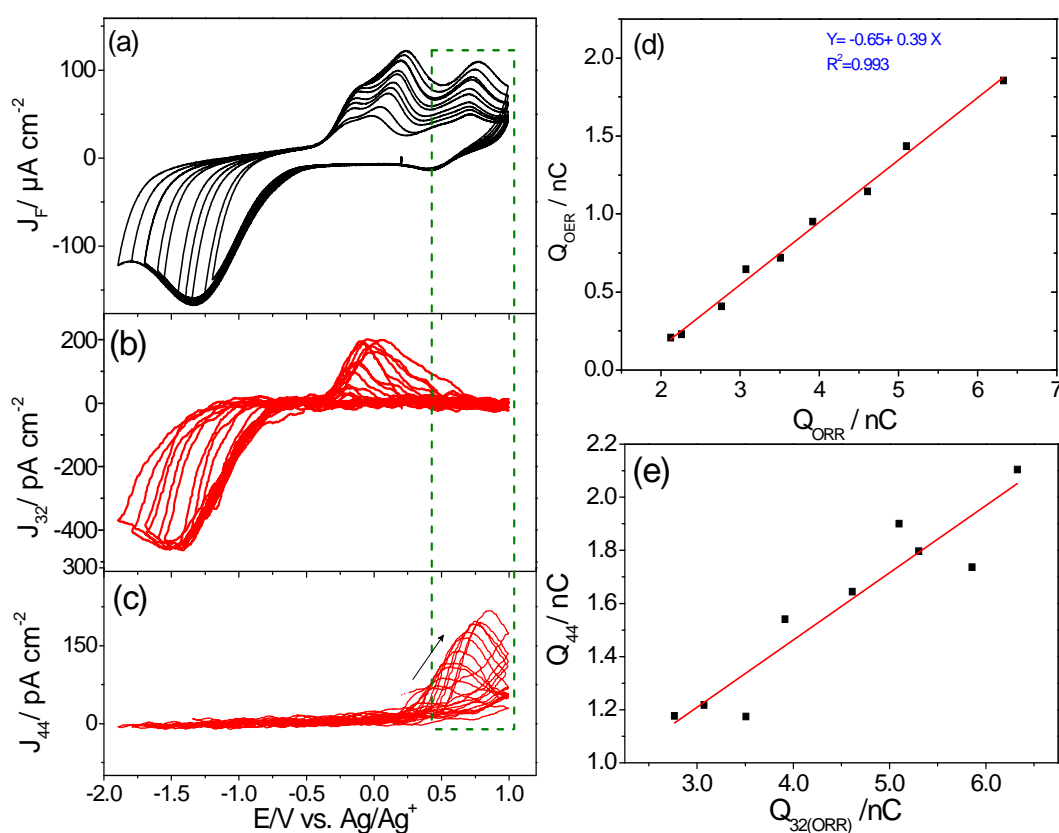


Fig. 16. CVs (a) and MSCVs for mass 32 (b) and mass 44 (c) at Au-sputtered membrane electrode in  $\text{O}_2$ -sat. 0.1M  $\text{LiClO}_4/\text{G4}$  with  $20 \text{ mV s}^{-1}$ . Current density is calculated with regard to geometric area. (d) plot of ionic charge of OER vs. ionic charge of ORR at various potential window. (e) Plot of  $Q_{44}$  vs.  $Q_{32}$  of ORR. Charges are obtained by integration of the curves in left panel.

The efficiency or rechargeability of the cell are critical factors in the development of Li-air battery. But the basis on which the rechargeability is calculated is also questionable. In most of the literature, the term "coulombic efficiency" has been widely used as an indication of the cyclability of the cell, but this is not proper since other faradaic processes for instance electrolyte decomposition could contribute. Thus, one has to distinguish between the "apparent coulombic efficiency" (the ratio of faradaic charges) and the "true coulombic

efficiency (the ratio of oxygen evolved/consumed). To date, all electrolytes tested exhibited a true coulombic efficiency below 90%.[61] For instance, Laoire et al. found 95% efficiency based on the faradaic charge in G4-LiPF<sub>6</sub> electrolyte,[13] whereas McCloskey et al. found 75% true coulombic efficiency based on the oxygen amount in the same electrolyte or less in others.[61] Triglyme revealed a yield of 75% while DMSO showed 50-60%.[13, 34] Here, the ionic charge of oxygen evolution of each cycle (from Fig. 16b) is plotted against the corresponding ionic charge of reduction as displayed in Fig. 16d. The slope of this linearity represents the true coulombic efficiency, which is found here to be about 40%. This infers that a portion of the reduced oxygen is not reproduced in each cycle. It is also noteworthy to mention that the straight line has a negative intercept of 650 pC, which indicates that a certain amount of reduced oxygen is not available in the consecutive anodic scan. Therefore, only about 25% efficiency can be obtained if this intercept is taken into account. This is consistent with the value obtained from oxidation and reduction charges of one cycle. To analyze this loss, we looked at the ionic currents of mass 44, which accounts for CO<sub>2</sub>. Since the only source of carbon in the cell is the solvent G4, we expected that CO<sub>2</sub> evolution at higher potentials is generated from G4 decomposition. This is supported by the fact that CO<sub>2</sub> is produced parallel to the faradaic peaks above +0.3V, where no oxygen is observed. If the anodic potential is limited to +0.3V, no CO<sub>2</sub> evolution appears and deactivation takes place.

It is interesting to notice that the CO<sub>2</sub> evolution increases as the amount of reduced oxygen increases (e.g. by successively reducing the lower limit). The anodic ionic charge of CO<sub>2</sub> is plotted against the amount of oxygen reduced in each previous cycle, as shown in Fig. 16e. A linear proportionality is found. This observation suggests that a discharge products-induced chemical decomposition of electrolyte takes place, leading to formation of a deactivating film on the surface upon reduction, and is only removed by oxidation at higher potentials. This finding has also been found for DMSO electrolyte, although the reversibility is higher in DMSO than in G4.[62] CO<sub>2</sub> evolution associated with electrolyte decomposition was also observed in DME.[8] Bruce group confirmed the decomposition of G4 using XRD, FTIR and Raman techniques and pointed out some side products[14], which is consistent with our results. Electrochemical reaction of discharge products with the solvent is improbable since about 2e<sup>-</sup>/O<sub>2</sub> were consumed, but chemically it is possible.

It is also reasonable to estimate the number of Li<sub>2</sub>O<sub>2</sub> monolayers (i.e. thickness of the film) formed on the surface upon full discharge. Only one monolayer (~sub nanometer thickness) of Li<sub>2</sub>O<sub>2</sub> per surface Au atom is obtained (~6 nC is obtained from ionic currents upon cycling to -1.7V, then using eq. 8.7 for charge, we obtain the faradaic charge and from which the number of monolayers). Therefore, a very thin film of Li<sub>2</sub>O<sub>2</sub> can effectively block the electrode surface.

The formation of peroxide upon reduction was confirmed by z-values close to 2e<sup>-</sup>/O<sub>2</sub> at different cathodic limits, while values of 2.5 to 3.5 e<sup>-</sup>/O<sub>2</sub> are obtained for OER, as shown in Fig. S11. In agreement with literature, post-mortem analyses like XRD and SEM were carried out on a fully discharged electrode after cell disassembly, and showed that Li<sub>2</sub>O<sub>2</sub> is the dominant reduction product in G4 electrolyte.[13, 31, 41] The z-value increases with each cycle by extending the lower limit, as shown in Fig. S11a. This behavior can be understood by the gradual increase of side products.

### 8.3.6.3. ORR and OER in LiClO<sub>4</sub> in G4-DMSO mixed electrolyte: DEMS

CVs and MSCVs for two mixed G4-DMSO based electrolytes (5 and 50 v% DMSO) at Au-sputtered membrane electrode are shown in Fig. 17. In CVs, only the first anodic peak corresponds to oxygen evolution. The additional peaks above 0V in the anodic scan and the hump at -0.2V in the cathodic scan are due to electrolyte decomposition. Here, an effect of the solvent on oxygen reduction and evolution kinetics. DMSO is more active for OER while G4 is more active for ORR. This effect is also observed in RRDE results in Fig. 9. In the mixture containing much G4, the overpotential for reduction decreases, while the mixture containing much DMSO shows reduced overpotential for oxidation. This is consistent with RRDE results, which showed the higher activity for OER in DMSO, while higher activity for ORR in G4 (*cf.* Fig. 9). Thus, each solvent is preferred for different process. In both mixtures, OER has lower overpotential (100 or 400 mV) than in pure G4 (*cf.* Fig. 15). In the 50 v% mixture, a shift of anodic peak ca. 250 mV more negative is observed and the reduction peak is shifted by about 160 mV to more negative compared to the 5% mixed electrolyte. The oxidation currents in the 50% electrolyte were improved by about two-folds compared to the 5% solution, as shown in Fig. 17 a,b. This suggests the effectiveness of DMSO in the mixture, which could be due to its higher oxygen diffusivity (10-fold) and ionic conductivity than G4. However, the reversibility in 5 v% mixture is higher than that in 50 v%. CO<sub>2</sub> was evolved in both electrolytes, but the contribution of G4 in this CO<sub>2</sub> is larger than DMSO since our previous report showed less amount of CO<sub>2</sub> in pure DMSO electrolyte.[18]

The number of electrons transferred upon reduction is 1.6 to 2.2 e<sup>-</sup>/O<sub>2</sub> in both electrolytes. For OER, about 2 e<sup>-</sup>/O<sub>2</sub> is delivered in 50% based electrolyte, and this value increased to 4 e<sup>-</sup>/O<sub>2</sub> in 5% DMSO electrolyte due to electrolyte decomposition and more contributions of G4, Fig. 17 d,e,f. We conclude that the reduction products react more effectively with G4 than with DMSO, causing more decomposition. Therefore, incorporation of G4 with DMSO in one mixture is a good alternative. This supports the results obtained with a GDE where higher discharge capacity and long life cycle were obtained in the mixed electrolyte compared to pure G4.[56] This was attributed to the enhancement of mass-transport due to the improved ionic conductivity and higher O<sub>2</sub> solubility in the mixture.

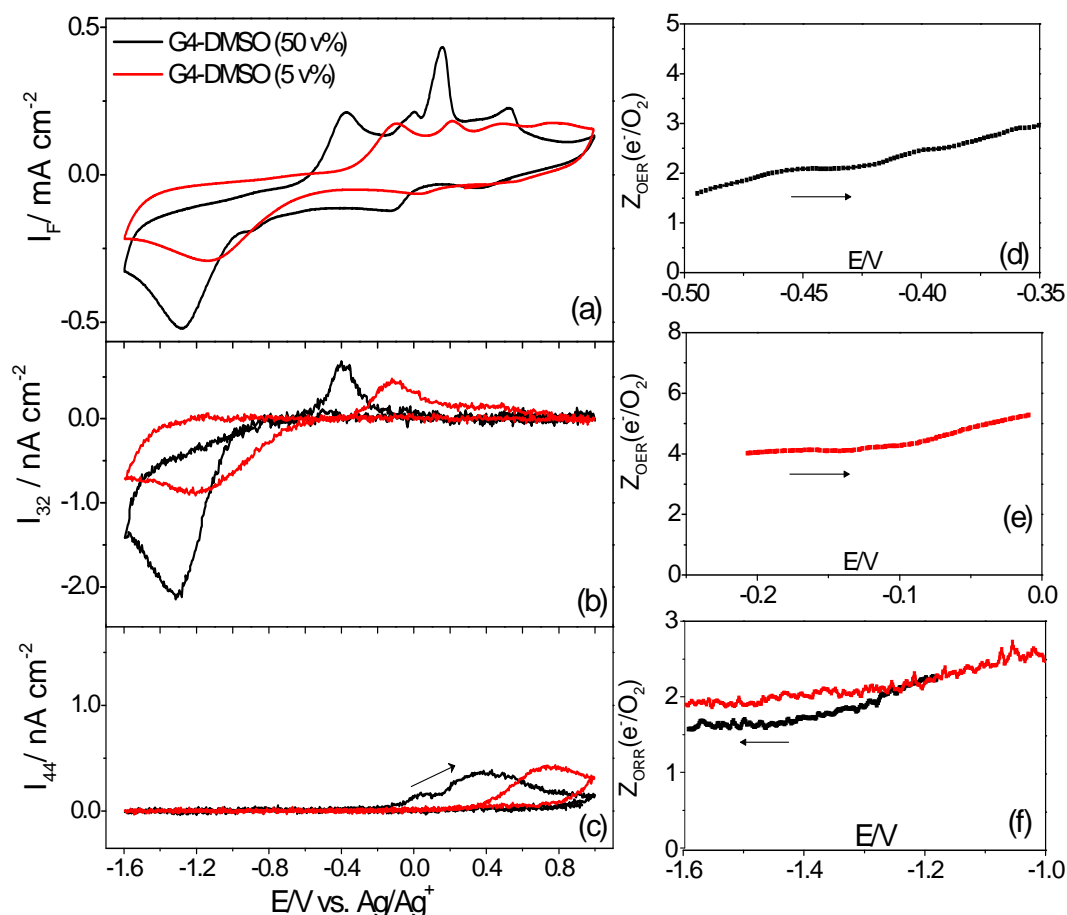


Fig. 17. CVs (a) and MSCVs for mass 32 (b) and mass 44 (c) in the second cycle at Au-sputtered membrane electrode in  $\text{O}_2$ -sat. 0.1M  $\text{LiClO}_4/\text{G4}+\text{DMSO}$  with  $20 \text{ mV s}^{-1}$ . (d) z-value for OER in 50% solution. (e) z-value for OER in 5 v% DMSO solution. (f) z-values for ORR, cathodic scan, in both solutions.

The stability and the reactivation effect in the mixed solvent-based electrolyte (5 v%) are depicted in Fig. 18. The first 5 cycles were recorded in a full range (-1.6 to +1.0V) and show a good stability. As the potential window was limited to +0.2V in the consecutive 3 cycles, gradual decrease in reduction as well as oxidation currents is noticed, as shown in Fig. 18. Deactivation of the electrode is due to formation of a blocking layer. This suggests that the blocking layer accumulates on the surface and its thickness increases with each cycle as long as no higher potentials were applied to the electrode to get rid of this passive film. The deactivation is associated with large z-values for OER due to contribution of side reactions despite peroxide formation on the discharge (around  $2e^-/\text{O}_2$ ), see 8<sup>th</sup> cycle in Fig. 18d. Expansion of the upper limit to +1V in the 9<sup>th</sup> and 10<sup>th</sup> cycles restores the reduction currents, but not completely (see the blue curve). As can be seen from mass 44 signal, the reduction product-induced side reactions formed in the first cathodic sweep lead to a higher  $\text{CO}_2$  signal, which decreases with cycling due to gradual removal of the deactivating layer. The incomplete reactivation of the surface might be due to removal of only the outermost layer of the blocking film, and a part of the film remains sticking to the surface. Similar behavior of deactivation and reactivation is also observed in the electrolyte containing 50 v% DMSO, see SI. This leads to a continuous increase in the z-value with each cycle, see Fig. S12,13.

However, this value for ORR does not exceed  $3.5 e^-/O_2$ . The true coulombic efficiency is found to be 15-20% for G4-DMSO (50%) and about 25-30% for G4-DMSO (5%) electrolyte.

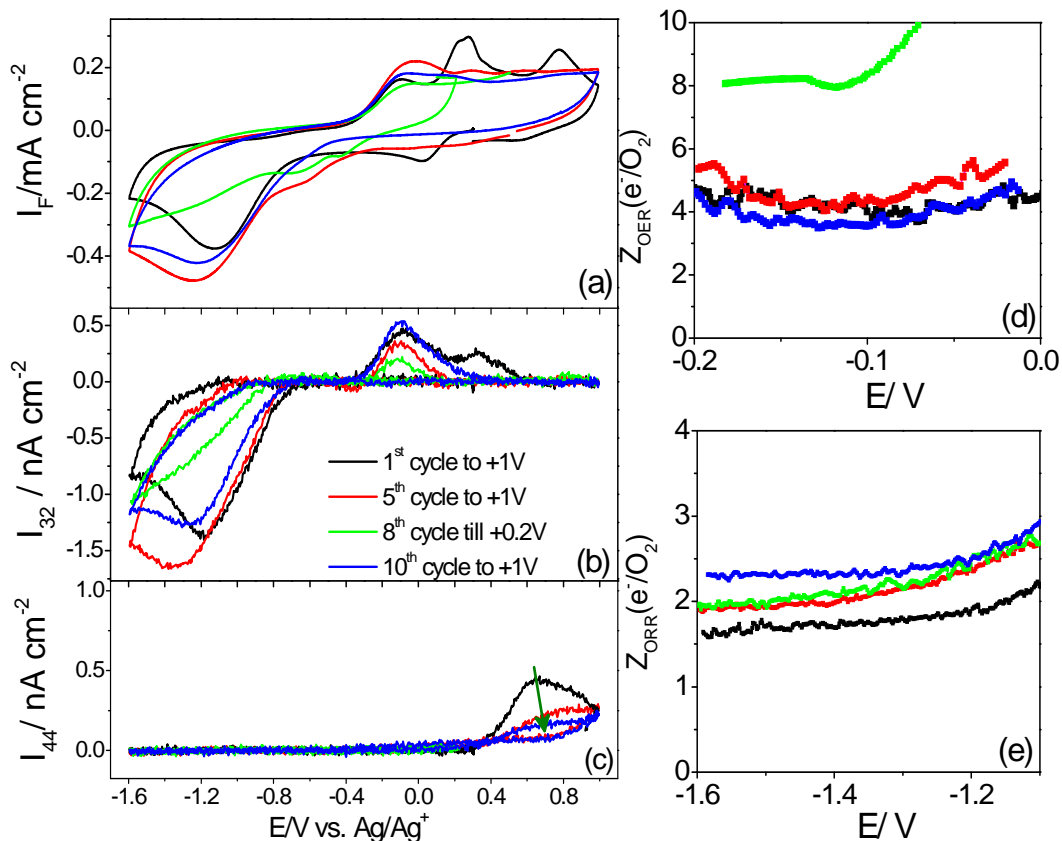


Fig. 18. CVs (a) and MSCVs for mass 32 (b) and mass 44 (c) at Au-sputtered membrane electrode in  $O_2$ -sat. 0.1M  $LiClO_4/G4+DMSO$  (5 v%) with  $20 mV s^{-1}$ . (d) z-value for the first 4 cycles for OER, and (e) for ORR.

#### 8.3.6.4. Gas diffusion electrode (GDE) as a breathing battery

In principle, the lithium ion should react with oxygen from air forming lithium peroxide in a real battery. Here, we present firstly the suitability of the Au-sputtered membrane electrode, as a GDE in the mixed electrolyte, where pure  $O_2$  from a gas cylinder was supplied to the membrane at its back side (i.e. not the electrolyte side). In this setup, which has been previously described by our group,[34] the volume underneath the membrane was firstly evacuated to remove any remaining gases. Afterwards, the angle valve between the vacuum and the electrochemical cell was closed, and the dosing valve connecting the volume underneath the membrane to the oxygen inlet was opened to introduce  $O_2$  under pressure of 450 mbar through the steel frit reaching the membrane working electrode. Subsequently, a first cathodic sweep was applied in which the potential was scanned from 0V in the negative direction to -1.3V in 0.1M  $LiClO_4/G4-DMSO$  (50 v%) electrolyte and was held for one minute while the electrolyte is purged with Ar. ORR starts at -0.9 V reaching a peak at  $\sim -1.3V$ . Only CV is recorded since the mass spectrometer is not connected (blue curve in Fig. 19a). The volume underneath the electrode was then evacuated by opening the angle valve to the mass spectrometer so that the cell is again connected to the mass spectrometer. The current drops to zero as the oxygen supply was cut off. The pre-formed  $Li_2O_2$  on the electrode is reoxidized and oxygen is evolved (at -0.6V) as evidenced by recording MS signal of oxygen (m/z 32) in the Ar-saturated solution, see the red curve of Fig. 19b. In the second

sweep, oxygen was supplied from solution so that the dissolved oxygen is reduced and oxidized as in typical experiments.

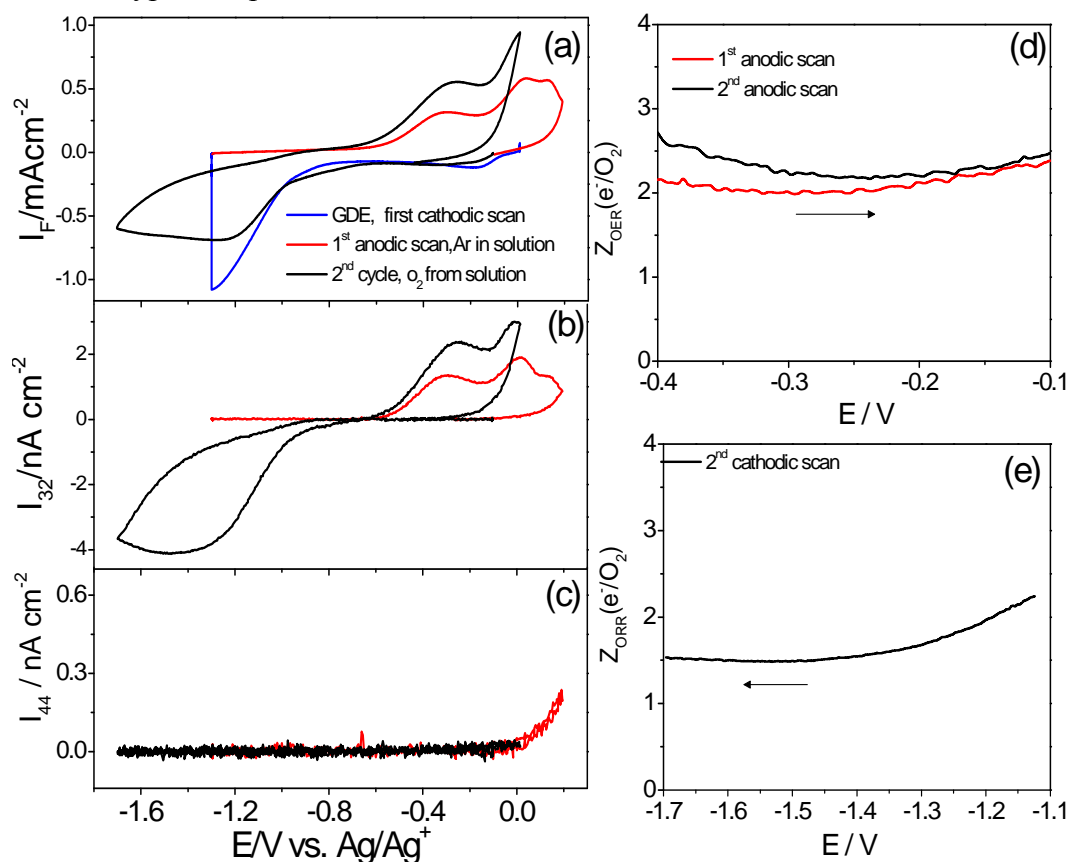


Fig. 19. Simultaneous CVs (a) and MSCVs for mass 32 (b) and mass 44 (c) during oxygen reduction and evolution reactions on Au-sputtered membrane as GDE electrode in 0.1M  $\text{LiClO}_4/\text{G4-DMSO}$ (50 v%) mixed electrolyte with 20 mV/s. In the first cathodic sweep oxygen was supplied from the gas side of the membrane under pressure of 450 mbar while solution was purged with Ar (blue curve) and potential was held for 1 minute; First anodic sweep: only Ar saturated solution (red); second sweep:  $\text{O}_2$  was purged in solution (black). (d) z-values for OER and (e) for ORR.

The second anodic peak in the CV and MSCV appearing at potentials higher than 0V is associated with  $\text{CO}_2$  evolution. The only source of  $\text{CO}_2$  here is the solvent. In addition, there are no  $\text{O}_2$  or  $\text{CO}_2$  evolutions when the electrode was cycled in an Ar-saturated solution. Hence oxygen evolution in the second peak may be due to oxidation of organic peroxide and thus associated with  $\text{O}_2$  and  $\text{CO}_2$  or oxidation of peroxide deposits formed on the decomposition products. The removal of these decomposition products is accompanied by  $\text{CO}_2$  evolution so that peroxide deposits restore its contact with the electrode and can be oxidized at the same time. Another possible reason is the reaction of reduction products with the solvent. z-values of  $1.5$  to  $2.1e^-/\text{O}_2$  during reduction and  $2.2 e^-/\text{O}_2$  during oxidation are found when the electrode was used as GDE in the previous sweep or slightly higher value of  $2.4e^-/\text{O}_2$  when oxygen was supplied to the electrode from the solution, indicating the reversible formation and decomposition of  $\text{Li}_2\text{O}_2$  in this process, Fig. 19d,e. Thus, Au-sputtered membrane electrode showed suitability as a model for GDE with z-values fit well to the reduction and oxidation of oxygen to peroxide and vice versa.

Interesting is that much larger current density at the peak is achieved when the electrode is employed as a GDE (ca.  $1.1 \text{ mA cm}^{-2}$ ) compared to the typical oxygen-saturated solution experiment ( $700 \mu\text{A cm}^{-2}$ ). This is attributed to the more efficient oxygen transport from the gas phase to the electrode than oxygen diffusion in solution to the electrode.

There is a peak shift of OER of ca. 50 mV to more positive potential when oxygen was supplied from solution, as observed in CV and MSCV of Fig. 19. This could be due to formation of much  $\text{Li}_2\text{O}_2$  during the preceding reduction. This effect is similar to that observed in Fig. 16 for pure G4. Also, some side reactions other than oxygen evolution could occur and increase the overpotential and interfere with oxygen evolution and therefore, increase the z-value, as can be seen in the black curve.

A difference between 50% mixed electrolyte and pure G4 electrolyte (*cf.* Fig. S14) is that larger currents are observed in 50% mixed electrolyte than G4. Also, slightly larger z-values are obtained in 50% than in G4. This is consistent with RRDE results where higher currents are obtained in DMSO than in G4 electrolyte (see Fig. 9).

GDE was also examined under ambient conditions (i.e. atmospheric humid air). Here, as an example  $\text{O}_2$ -saturated 0.1M  $\text{LiClO}_4/\text{G4}$  was exposed to lab air from the gas side instead of pure oxygen used in the previous experiment, see Fig. 20. Briefly, the angle valve to the mass spectrometer was closed, the blind flange down to the membrane was opened to allow atmospheric air entering the volume underneath the membrane and potential was scanned to -1.4V and then was held (blue curve). After that, the blind flange was directly re-assembled, and the volume underneath the cell was evacuated (current drops to zero) and mass spectrometer was reconnected. Upon sweeping the potential in the anodic direction, OER starts at ca. -0.3V with evolution of  $\text{O}_2$  signal in the MSCV (red curve). In the following cycle, the amount of dissolved oxygen in the electrolyte decreased since there is no more supply of oxygen from the gas side (black curve). Hence, the anodic ionic currents of the second and third cycles are lower than those in the first cycle in which oxygen was supplied from the gas side to the electrode.

$\text{Li}_2\text{O}_2$  formation is proved from the z-value which is close to  $2 e^-/\text{O}_2$ , as shown in Fig. 20e. For OER, a z-value close to  $3e^-/\text{O}_2$  is obtained when oxygen was delivered from the gas side, however, higher values of  $4\text{-}5 e^-/\text{O}_2$  are transferred when oxygen was supplied to the electrode from solution (Fig. 20d). These values are far from the typical  $2 e^-/\text{O}_2$  expected for  $\text{Li}_2\text{O}_2$  oxidation, indicating the contribution from other parasitic reactions during charging. This might be due to humidity or reaction of  $\text{CO}_2$  with the electrolyte. When oxygen is reduced from the gas phase, larger amounts of peroxide are formed, leading to more decomposition byproducts than in the case of less peroxide amounts (when oxygen was supplied from solution). This can be clearly seen from the evolution of more  $\text{CO}_2$  in the first anodic scan where the electrode was set as a GDE in the previous cathodic scan. The amount of  $\text{CO}_2$  decreases in the following cycles, see Fig. 20c. The difference between the experiment with air and a similar experiment with pure  $\text{O}_2$  (Fig. S14) is that higher currents are obtained and thus more  $\text{Li}_2\text{O}_2$  is formed when air was the source of  $\text{O}_2$ . However, more decomposition (influence of  $\text{CO}_2$  and humidity in air) occurs as seen from the larger amount of  $\text{CO}_2$  evolved in Fig. 20c. This decomposition is however, lower in the consecutive cycles. From these measurements we managed to observe oxygen reduction and evolution under ambient

conditions without the use of oxygen-selective membrane. This boosts the feasibility of air as an oxygen source in Li-air batteries.

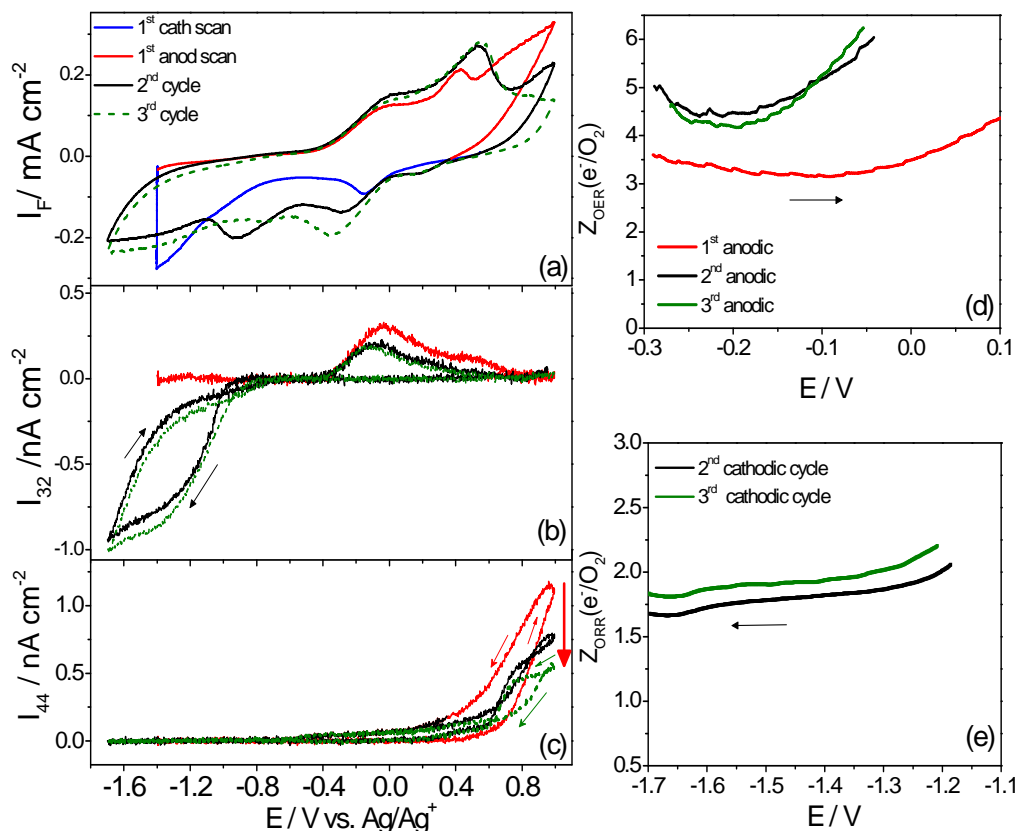


Fig. 20. Simultaneous CVs (a) and MSCVs for mass 32 (b) and mass 44 (c) during oxygen reduction and evolution reactions on Au-sputtered membrane as GDE electrode in 0.1M LiClO<sub>4</sub>/G4 electrolyte with 10 mV/s. In the first cathodic sweep: oxygen source was the atmospheric air from the gas side of the membrane while solution was purged with O<sub>2</sub> (blue curve); First anodic sweep: O<sub>2</sub> in solution (red); second (black) and third (green) sweep: O<sub>2</sub> was supplied from solution. (d) z-values for OER and (e) for ORR.

#### 8.4. Conclusion

From the above results, a schematic of the proposed generalized mechanism is presented in Fig. 21. Two pathways are assumed for Li<sub>2</sub>O<sub>2</sub> formation: solution pathway and surface pathway. In both of them, O<sub>2</sub> has to be adsorbed, and then further reduced to superoxide. In the surface pathway, superoxide undergoes electrochemical second reduction to Li<sub>2</sub>O<sub>2</sub> on the surface. While in the solution pathway, LiO<sub>2</sub> is stable in solution, and afterwards Li<sub>2</sub>O<sub>2</sub> is formed in solution near to surface as well as few on the surface depending on the potential. The lifetime of the intermediate LiO<sub>2</sub> and the mechanism depend on the solvation strength of the solvent (It is possibly related to the DN). In low DN solvents (e.g. G4), superoxide is very short-lived intermediate and instable in solution (small amount is detected in solution), thus it is further reduced to Li<sub>2</sub>O<sub>2</sub> on the surface. On the other hand, in high DN solvents (e.g. DMSO), superoxide is stable in solution, and consequently it further disproportionates to Li<sub>2</sub>O<sub>2</sub> in solution, which can precipitate and also blocks the electrode. Therefore, the amount of detected superoxide increases monotonically as the amount of DMSO to G4 in the mixture increases. The solvent also exerts an influence on the kinetics: DMSO is more active for OER than G4. The addition of a little amount of DMSO to G4 in one blended electrolyte enhances

the reversibility, and the overpotential of oxidation compared to pure G4.  $\text{Co}_3\text{O}_4$  catalyst shows a catalytic activity in DMSO-based electrolyte, in particular, for OER. This catalyst facilitates charge transport for oxidation and a clear effect of  $\text{Co}_3\text{O}_4$  on superoxide formation is observed. DEMS results assessed the origin of electrolyte decomposition and the role of the operating potential window. In most cases, roughly  $2 e^-/\text{O}_2$  is found upon discharge, implying  $\text{Li}_2\text{O}_2$  formation.

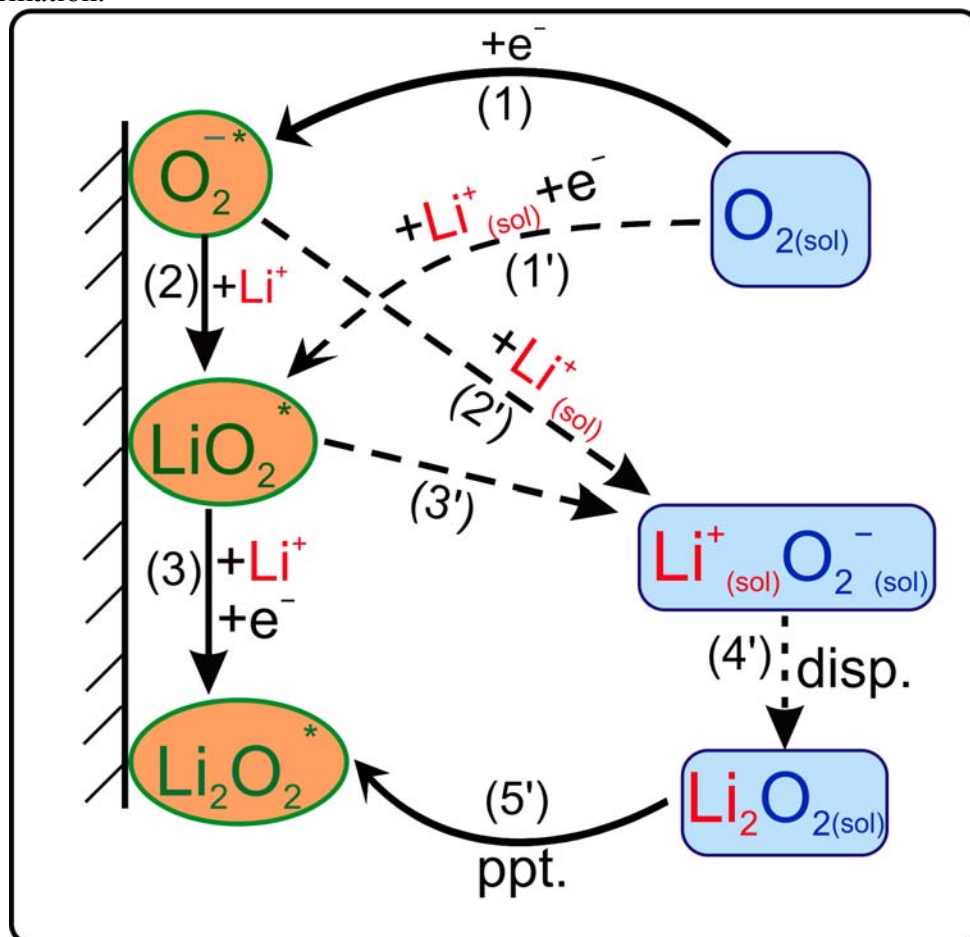


Fig. 21. Schematic of the proposed ORR mechanism in aprotic electrolytes. Low DN solvents follow the surface pathway (orange), while high DN solvents follow the solution pathway (blue).

### 8.5. References

- [1] K.M. Abraham, Z. Jiang, *Journal of the Electrochemical Society* 143 (1996) 1-5.
- [2] P.G. Bruce, S.A. Freunberger, L.J. Hardwick, J.-M. Tarascon, *Nat Mater* 11 (2012) 19-29.
- [3] G. Girishkumar, B. McCloskey, A.C. Luntz, S. Swanson, W. Wilcke, *J. Phys. Chem. Lett.* 1 (2010) 2193-2203.
- [4] N. Garcia-Araez, P. Novák, *Journal of Solid State Electrochemistry* 17 (2013) 1793-1807.
- [5] T. Ogasawara, A. Débart, M. Holzapfel, P. Novák, P.G. Bruce, *Journal of the American Chemical Society* 128 (2006) 1390-1393.
- [6] Y.-C. Lu, Z. Xu, H.A. Gasteiger, S. Chen, K. Hamad-Schifferli, Y. Shao-Horn, *Journal of the American Chemical Society* 132 (2010) 12170-12171.
- [7] S.A. Freunberger, Y. Chen, Z. Peng, J.M. Griffin, L.J. Hardwick, F. Barde, P. Novak, P.G. Bruce, *Journal of the American Chemical Society* 133 (2011) 8040-8047.

- [8] B.D. McCloskey, D.S. Bethune, R.M. Shelby, G. Girishkumar, A.C. Luntz, *J. Phys. Chem. Lett.* 2 (2011) 1161-1166.
- [9] C.O. Laoire, S. Mukerjee, K.M. Abraham, E.J. Plichta, M.A. Hendrickson, *Journal of Physical Chemistry C* 114 (2010) 9178-9186.
- [10] R. Imhof, P. Novak, *Journal of the Electrochemical Society* 146 (1999) 1702-1706.
- [11] M. Holzappel, A. Wursig, W. Scheifele, J. Vetter, P. Novak, *Journal of Power Sources* 174 (2007) 1156-1160.
- [12] J. Read, *Journal of the Electrochemical Society* 153 (2006) A96-A100.
- [13] C.O. Laoire, S. Mukerjee, E.J. Plichta, M.A. Hendrickson, K.M. Abraham, *Journal of the Electrochemical Society* 158 (2011) A302-A308.
- [14] S.A. Freunberger, Y. Chen, N.E. Drewett, L.J. Hardwick, F. Barde, P.G. Bruce, *Angewandte Chemie-International Edition* 50 (2011) 8609-8613.
- [15] H.-G. Jung, J. Hassoun, J.-B. Park, Y.-K. Sun, B. Scrosati, *Nature Chemistry* 4 (2012) 579-585.
- [16] D. Xu, Z.-l. Wang, J.-j. Xu, L.-l. Zhang, X.-b. Zhang, *Chem. Commun.* 48 (2012) 6948-6950.
- [17] Z. Peng, S.A. Freunberger, Y. Chen, P.G. Bruce, *Science* 337 (2012) 563-566.
- [18] C. Bondue, P. Reinsberg, A.-E.-A.A. Abd-El-Latif, H. Baltruschat, *Phys. Chem. Chem. Phys.* 17 (2015) 25593-25606.
- [19] R. Younesi, P. Norby, T. Vegge, *ECS Electrochemistry Letters* 3 (2014) A15-A18.
- [20] M.J. Trahan, S. Mukerjee, E.J. Plichta, M.A. Hendrickson, K.M. Abraham, *Journal of the Electrochemical Society* 160 (2013) A259-A267.
- [21] F.S. Gittleston, R.C. Sekol, G. Doubek, M. Linardi, A.D. Taylor, *Phys. Chem. Chem. Phys.* 16 (2014) 3230-3237.
- [22] B.D. Adams, C. Radtke, R. Black, M.L. Trudeau, K. Zaghbi, L.F. Nazar, *Energy Environ. Sci.* 6 (2013) 1772-1778.
- [23] B.D. McCloskey, R. Scheffler, A. Speidel, G. Girishkumar, A.C. Luntz, *Journal of Physical Chemistry C* 116 (2012) 23897-23905.
- [24] R.R. Mitchell, B.M. Gallant, Y. Shao-Horn, C.V. Thompson, *The Journal of Physical Chemistry Letters* 4 (2013) 1060-1064.
- [25] L. Johnson, C. Li, Z. Liu, Y. Chen, S.A. Freunberger, P.C. Ashok, B.B. Praveen, K. Dholakia, J.-M. Tarascon, P.G. Bruce, *Nat Chem* 6 (2014) 1091-1099.
- [26] J. Read, *Journal of The Electrochemical Society* 149 (2002) A1190-A1195.
- [27] Y. Zhang, X. Zhang, J. Wang, W.C. McKee, Y. Xu, Z. Peng, *The Journal of Physical Chemistry C* 120 (2016) 3690-3698.
- [28] J. Read, K. Mutolo, M. Ervin, W. Behl, J. Wolfenstine, A. Driedger, D. Foster, *Journal of the Electrochemical Society* 150 (2003) A1351-A1356.
- [29] L. Cecchetto, M. Salomon, B. Scrosati, F. Croce, *Journal of Power Sources* 213 (2012) 233-238.
- [30] A. Khan, C. Zhao, *Electrochem. Commun.* 49 (2014) 1-4.
- [31] J. Zeng, C. Francia, S. Bodoardo, N. penazzi, *Rsc Advances* 5 (2013) 83056-83064.
- [32] H. Baltruschat, *Journal of the American Society for Mass Spectrometry* 15 (2004) 1693-1706.
- [33] P. Novak, J.C. Panitz, F. Joho, M. Lanz, R. Imhof, M. Coluccia, *Journal of Power Sources* 90 (2000) 52-58.
- [34] C.J. Bondue, A.A. Abd-El-Latif, P. Hegemann, H. Baltruschat, *Journal of the Electrochemical Society* 162 (2015) A479-A487.
- [35] H.M.A. Amin, H. Baltruschat, D. Wittmaier, K.A. Friedrich, *Electrochimica Acta* 151 (2015) 332-339.
- [36] T.J. Schmidt, H.A. Gasteiger, G.D. Stab, P.M. Urban, D.M. Kolb, R.J. Behm, *Journal of the Electrochemical Society* 145 (1998) 2354-2358.

- [37] H. Baltruschat, *Journal of the American Society for Mass Spectrometry* 15 (2004) 1693-1706.
- [38] C.J. Barile, A.A. Gewirth, *Journal of the Electrochemical Society* 160 (2013) A549-A552.
- [39] M. Marinaro, U. Riek, S.K. Eswara Moorthy, J. Bernhard, U. Kaiser, M. Wohlfahrt-Mehrens, L. Jörissen, *Electrochem. Commun.* 37 (2013) 53-56.
- [40] G. Gritzner, *Journal of Molecular Liquids* 156 (2010) 103-108.
- [41] M. Marinaro, S. Theil, L. Jörissen, M. Wohlfahrt-Mehrens, *Electrochimica Acta* 108 (2013) 795-800.
- [42] C. Bondue, P. Reinsberg, A.-E.-A.A. Abd-El-Latif, H. Baltruschat, *Physical Chemistry Chemical Physics* (2015) DOI: 10.1039/c1035cp04356e.
- [43] A.J. Bard, L.R. Faulkner, *Electrochemical Methods: Fundamentals and Applications*, 2nd ed., John Wiley & Sons Inc., New York, Weinheim, 2001.
- [44] E.J. Calvo, N. Mozhzhukhina, *Electrochem. Commun.* 31 (2013) 56-58.
- [45] J. Herranz, A. Garsuch, H.A. Gasteiger, *Journal of Physical Chemistry C* 116 (2012) 19084-19094.
- [46] D.T. Sawyer, G. Chlericato, C.T. Angelis, E.J. Nanni, T. Tsuchiya, *Analytical Chemistry* 54 (1982) 1720-1724.
- [47] S. Bruckenstein, G.A. Feldman, *Journal of Electroanalytical Chemistry* 9 (1965) 395-399.
- [48] F. Gan, D.T. Chin, *Journal of Applied Electrochemistry* 23 (1993) 452-455.
- [49] D.T. Sawyer, J.L. Roberts, *Journal of Electroanalytical Chemistry* (1959) 12 (1966) 90-101.
- [50] C.O. Laoire, S. Mukerjee, K.M. Abraham, E.J. Plichta, M.A. Hendrickson, *Journal of Physical Chemistry C* 113 (2009) 20127-20134.
- [51] R.G. Evans, O.V. Klymenko, S.A. Saddoughi, C. Hardacre, R.G. Compton, *Journal of Physical Chemistry B* 108 (2004) 7878-7886.
- [52] E.I. Rogers, X.-J. Huang, E.J.F. Dickinson, C. Hardacre, R.G. Compton, *The Journal of Physical Chemistry C* 113 (2009) 17811-17823.
- [53] V. Gutmann, *Coord. Chem. Rev.* 18 (1976) 225-255.
- [54] S.S. Zhang, D. Foster, J. Read, *Journal of Power Sources* 195 (2010) 1235-1240.
- [55] M.M. Ottakam Thotiyil, S.A. Freunberger, Z. Peng, P.G. Bruce, *Journal of the American Chemical Society* 135 (2013) 494-500.
- [56] J. Zeng, C. Francia, J. Amici, S. Bodoardo, N. Penazzi, *Journal of Power Sources* 272 (2014) 1003-1009.
- [57] W.-H. Ryu, T.-H. Yoon, S.H. Song, S. Jeon, Y.-J. Park, I.-D. Kim, *Nano Letters* 13 (2013) 4190-4197.
- [58] A.I. D'Alba, J. Bao, G. Armstrong, P.G. Bruce, *Journal of Power Sources* 174 (2007) 1177-1182.
- [59] M. Augustin, O. Yezerska, D. Fenske, I. Bardenhagen, A. Westphal, M. Knipper, T. Plaggenborg, J. Kolny-Olesiak, J. Parisi, *Electrochimica Acta* 158 (2015) 383-389.
- [60] M.D. Radin, C.W. Monroe, D.J. Siegel, *Chem. Mat.* 27 (2014) 839-847.
- [61] B.D. McCloskey, D.S. Bethune, R.M. Shelby, T. Mori, R. Scheffler, A. Speidel, M. Sherwood, A.C. Luntz, *The Journal of Physical Chemistry Letters* 3 (2012) 3043-3047.
- [62] C.J. Bondue, M. Hegemann, C. Molls, E. Thome, H. Baltruschat, *Journal of The Electrochemical Society* 163 (2016) A1765-A1775.
- [63] V. Viswanathan, K.S. Thygesen, J.S. Hummelshoj, J.K. Nørskov, G. Girishkumar, B.D. McCloskey, A.C. Luntz, *Journal of Chemical Physics* 135 (2011) 10.
- [64] W. Torres, N. Mozhzhukhina, A.Y. Tesio, E.J. Calvo, *Journal of the Electrochemical Society* 161 (2014) A2204-A2209.

## Supplementary Information

### ORR/OER in Li<sup>+</sup>/DMSO electrolyte

The cyclability of the electrodes in DMSO-based electrolyte is shown in Fig. S1. The stability of the cycles is strongly dependent on the limits of potential sweep. Stable behavior is obtained when the potential is scanned to higher potentials, where any possible undesired products formed on the surface during reduction (namely from reaction with superoxide or peroxide) are oxidized at higher potentials, allowing free active sites for further ORR in the next cycle. This emphasizes the stable performance of DMSO in a full potential range of scan. The reversibility of this system is not 100%, since 55-60% of the reduced faradaic charge is regained upon oxidation at GC and ca. 36% at Pt at 50 mV s<sup>-1</sup>, as calculated from the CVs. This could be due to the formation of some irreversible reduction products on the electrode.

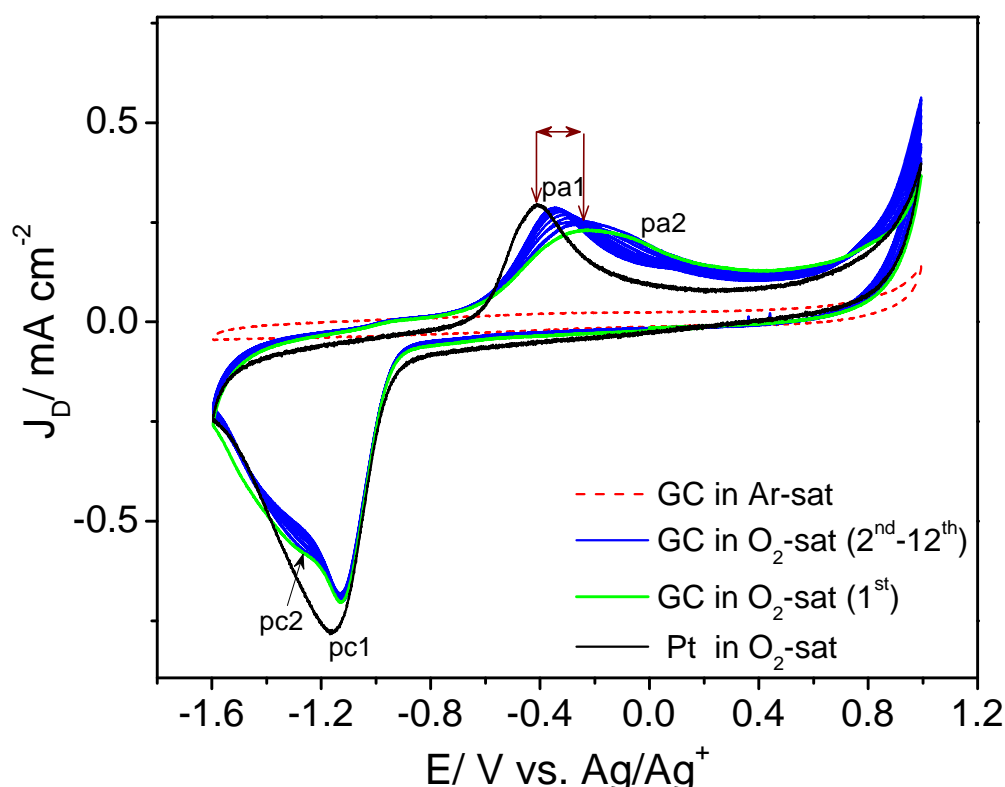


Fig. S1. CVs at GC and Pt electrodes in a stagnant O<sub>2</sub>-sat. 0.1M LiClO<sub>4</sub>/DMSO recorded with a scan rate of 50 mV/s. Dashed line is in Ar-saturated solution.

To estimate the number of electrons transferred during ORR, GC electrode potential was scanned with different scan rates, see Fig. S2. As shown, cathodic and anodic peak currents increase with the scan rate increase, accompanied with a negative shift in the cathodic peak and positive shift in the anodic peak, suggesting an irreversible process. Nicholson-Shain relationship (eq. 8.2)[43] shows a straight line, suggesting a diffusion-controlled process, inset of Fig. S2. Taking the value of  $D=1.67 \times 10^{-5} \text{ cm}^2 \text{ s}^{-1}$  and  $C=2.1 \times 10^{-6} \text{ mol cm}^{-3}$ , [9, 46] the best fit of the experimental data gives a value of  $n$  and  $n^*=1$  when setting  $\alpha=0.87$ , which is reasonable for an irreversible process and sluggish kinetics.[20] This is consistent with the first one-electron reduction of O<sub>2</sub> to LiO<sub>2</sub> process, as discussed above.

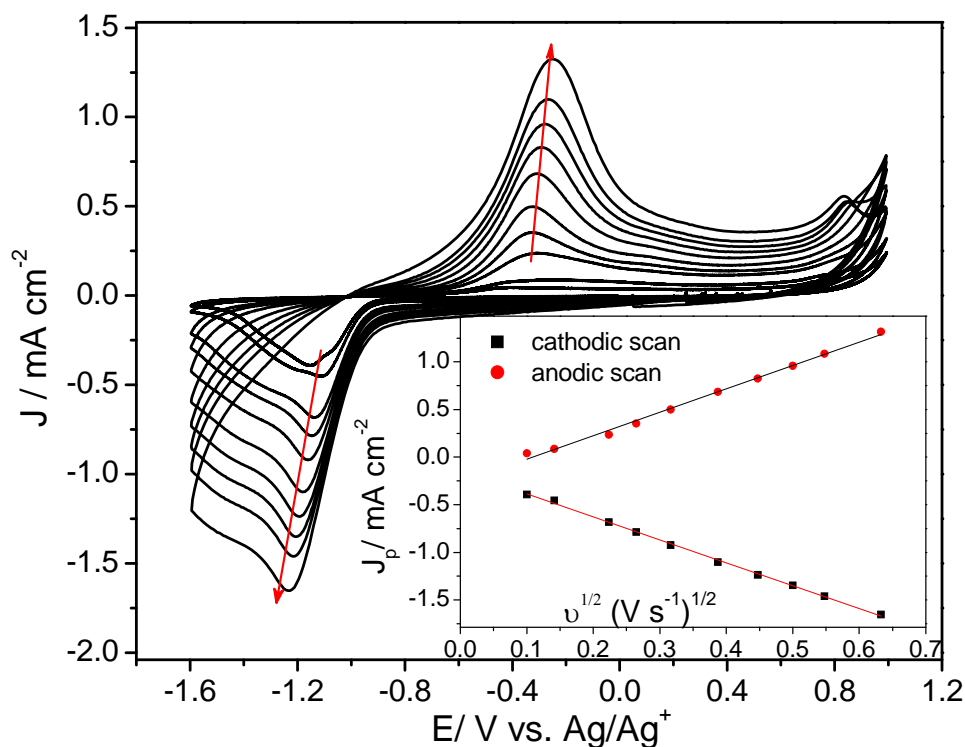


Fig. S2. CVs at GC electrode in O<sub>2</sub>-sat. 0.1M LiClO<sub>4</sub>/DMSO at various scan rates. Inset: cathodic and anodic peak current densities versus square route of scan rate.

### RRDE chronoamperometry

Current transients were recorded for 60s simultaneously at the disc and ring where the potential of the GC disc was stepped from 0V (where no electrochemical reductions take place) to different potentials in ORR range, and the Pt ring was held at 0V (where superoxide is fully oxidized), Fig. S3a. The experiment is performed under 960 rpm. Noticeably, the disc current drops as the surface is blocked by Li<sub>2</sub>O<sub>2</sub>, whereas the ring current shows a peak at short times. This confirms the spread away of superoxide from disc through the electrolyte to the ring.

The decay of the disc current with time illustrates that ORR takes place with the formation of insoluble Li<sub>2</sub>O<sub>2</sub>, which blocks the surface. Afterwards, ORR continues with a lower rate at Li<sub>2</sub>O<sub>2</sub> film until a critical film thickness is reached. Since Li<sub>2</sub>O<sub>2</sub> is a poor conductor, the charge transfer through this film is limiting the ORR.[63] Therefore, blocking of the electrode is faster at lower potentials, as shown in Fig. S3a. The ring currents are smaller than the expected theoretical values due to loss of some as LiO<sub>2</sub> or Li<sub>2</sub>O<sub>2</sub> in solution. Remarkably, the  $N/N_0$  ratio decreases with time due to blocking of the surface. The behavior depends on the disc potential, as seen in the inset of Fig. S3a. The peak current of the ring, which is recorded when different constant disc potentials are used, is dependent on the disc potential, and exhibits the same shape of ring currents observed in typical CV with a maxima at ca. -1.25V, Fig. S3b. Similar effect has been previously reported using Au ring.[64] This peak behavior of Fig. S3b could be related to the competition between superoxide formation and disproportionation at lower overpotentials or second reduction step at higher overpotentials, which is consistent with [64].

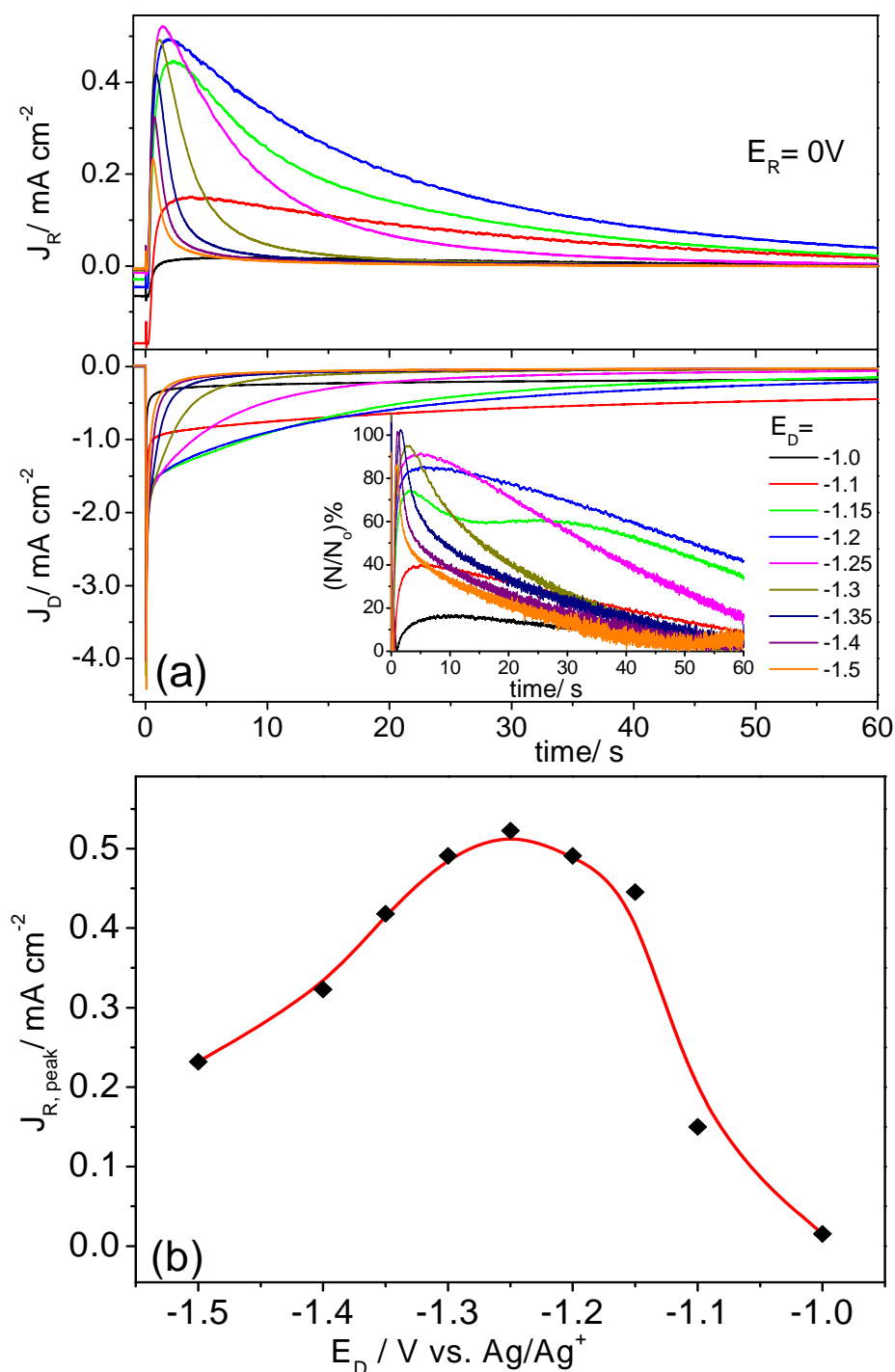


Fig. S3. (a) Current transients at GC disc and Pt ring for ORR in 0.1M LiClO<sub>4</sub>/DMSO, where GC disc was stepped from 0V to the mentioned disc values in ORR region and the ring potential was held at 0V, the experiment were done with 960 rpm. (b) Ring peak current vs. the constant disc potentials obtained from data in (a).

#### ORR/OER in TBA(OTf)/G4

The relationship between peak current and scan rate is defined in Nicholson-Shain equation (eq. 8.2) for irreversible systems. Fig. S4 shows CVs at GC and Pt at different scan rates. Similar behavior is observed on both electrodes. The Nicholson-Shain plot is linear with very small intercept (ca. 39 $\mu$ A), suggesting a diffusion-controlled electrochemical process, see inset of Fig. S4. The intercept could be due to additional transport limitation of the active

species through a film of decomposition products on the electrode, as discussed in  $\text{Li}^+$ /DMSO system. The theoretical fit for  $n=1$  matches well the experimental data when  $\alpha=0.75$ , implying one electron reduction to superoxide as limiting step.

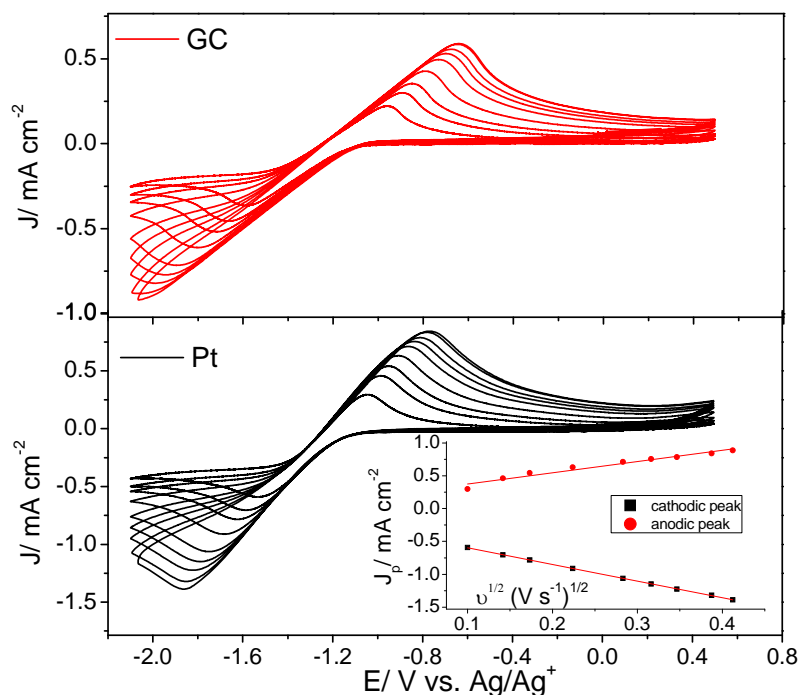


Fig. S4. CVs at GC and Pt electrodes in  $\text{O}_2$ -sat. 0.2M TBA(OTf)/G4 at various scan rates. Inset: cathodic and anodic peak current density vs. square root of scan rate at Pt.

### ORR/OER in mixed G4-DMSO based electrolyte

The effect of scan rate on the behavior of the electrode in the mixed G4-DMSO electrolyte is studied under convective-diffusion controlled conditions. The same effect is studied in single solvent in the main chapter. The electrode is scanned with different sweep rates at 1500 rpm and the ring was held at 0V, as shown in Fig. S5. Disc current increases anodically and cathodically with the scan rate increase. Ring currents also increase, but at higher scan rates they apparently decrease although the charge under ring peaks increases even under rotation. This is due to the delay in the response of the ring at higher scan rates as can be seen from the higher ring currents in the reverse scan. Moreover, less deactivation is observed at higher scan rates.  $J_p$  vs.  $\nu^{1/2}$  is represented by Nicholson-Shain plot as shown in inset of Fig. S5. A linear relationship passing through the origin is obtained, illustrating that the mass transport of  $\text{O}_2$  from bulk solution to the electrode surface is the limiting step. The best fit is found when setting  $\alpha=0.5$  and the number of electrons transferred is 1.2, which is close to the one-electron transport in first reduction reaction. The oxidation reaction is also diffusion limited.

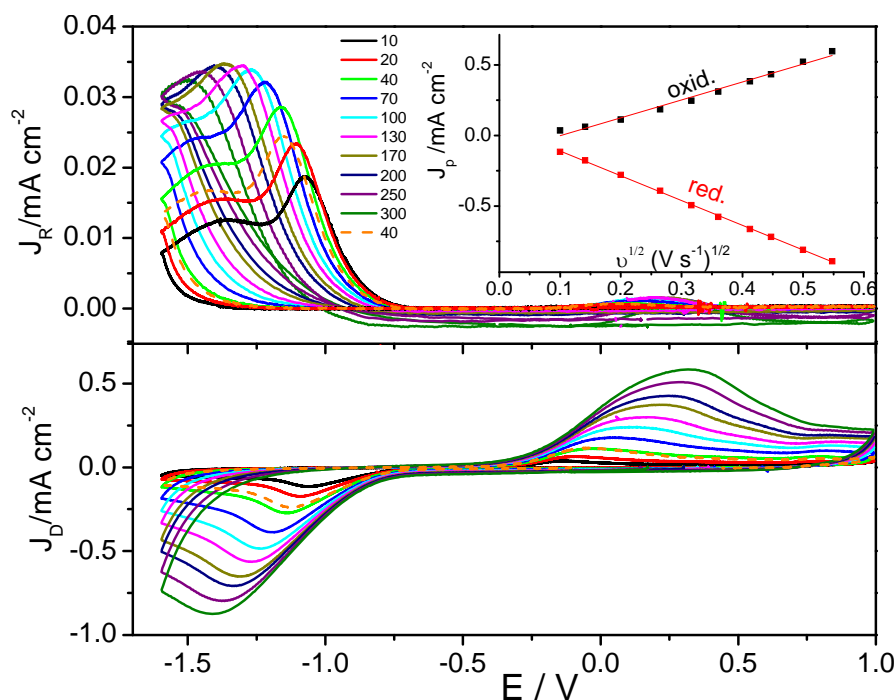


Fig. S5. CVs at GC-disc and Pt-ring in  $O_2$ -sat. 0.1M  $LiClO_4$ /G4-DMSO (5 v%) solution at 1500 rpm and various scan rates, ring was held at 0V. Inset:  $J_p$  vs.  $v^{1/2}$ .

### The role of $Co_3O_4$ catalyst in ORR/OER in DMSO-based electrolyte

Disc and ring currents at  $Co_3O_4$ /GC in  $O_2$ -saturated solution at different rotation rates are depicted in Fig. S6a. As rotation rate increases, ORR disc currents as well as ring currents increase. The amount of superoxide detected at the ring increases with the rotation rate increase due to the shorter transit time at higher speed rates, raising the probability of superoxide to arrive the ring, inset of Fig. S6a. Control experiments (i.e. repeated scan at the end of the series was done) exclude a significant "history" effect on the disc, as displayed with dashed lines in the graph, although a little decrease in the ring current is observed due to slight passivation of the electrode. Ring current depends on the potential at which the ring was held. Fig. S6b displays the behavior of the electrodes at different ring potentials with 1500 rpm and  $10\text{ mV s}^{-1}$ . At lower ring potentials (below  $-0.3\text{V}$ ), less superoxide yield was detected at the ring. While from  $-0.3\text{V}$  to  $+0.3\text{V}$  ring potentials, the same ring current and in turn superoxide amount was detected. The same effect is observed on bare GC.  $Co_3O_4$ /GC catalyst showed also reasonable stability in DMSO solvent, where ORR currents are nearly stable upon cycling at least for the 10 cycles shown.

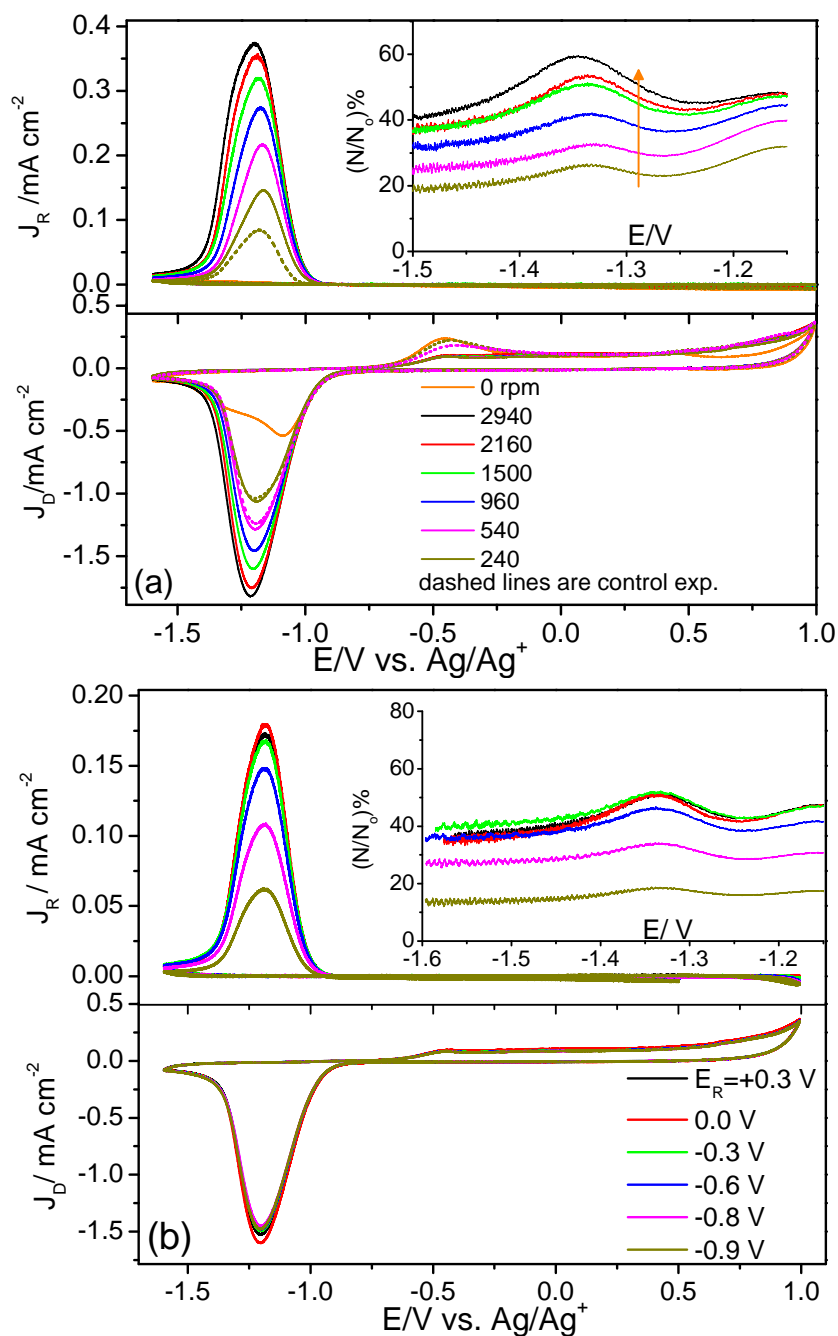


Fig. S6. (a) RRDE curves at  $\text{Co}_3\text{O}_4/\text{GC}$  disc electrode at  $10 \text{ mV s}^{-1}$  in  $0.1\text{M LiClO}_4/\text{DMSO}$  at different rotation rates, Pt-ring was kept at  $0\text{V}$ . (b) RRDE results of  $\text{Co}_3\text{O}_4/\text{GC}$  electrode with  $10 \text{ mV s}^{-1}$  and  $1500 \text{ rpm}$  at different ring potentials. Inset is  $(N/N_0)\%$  vs. potential.

The influence of scan rate on ORR at this catalyst under rotation is depicted in Fig. S7. As scan rate increases disc current increases cathodically and anodically with a potential shift. The ORR peak turns to being broader at higher sweep rates, and a semi-plateau is observed due to a reduced passivation. Ring charge corresponding to superoxide oxidation increases with scan rate increase. Plot of  $J_{pc}$  vs.  $v^{1/2}$  displays nearly a straight line, as shown in the inset of Fig. S7. This indicates that ORR is a diffusion-limited process at the interface despite rotation. Similar trend is found on bare GC. This could be due to diffusion of  $\text{O}_2$  through a pre-formed film on the surface, and mass-transport through this layer is the limiting process.

Therefore, the straight line in the inset of the graph has a y-axis intercept instead of passing through the origin.

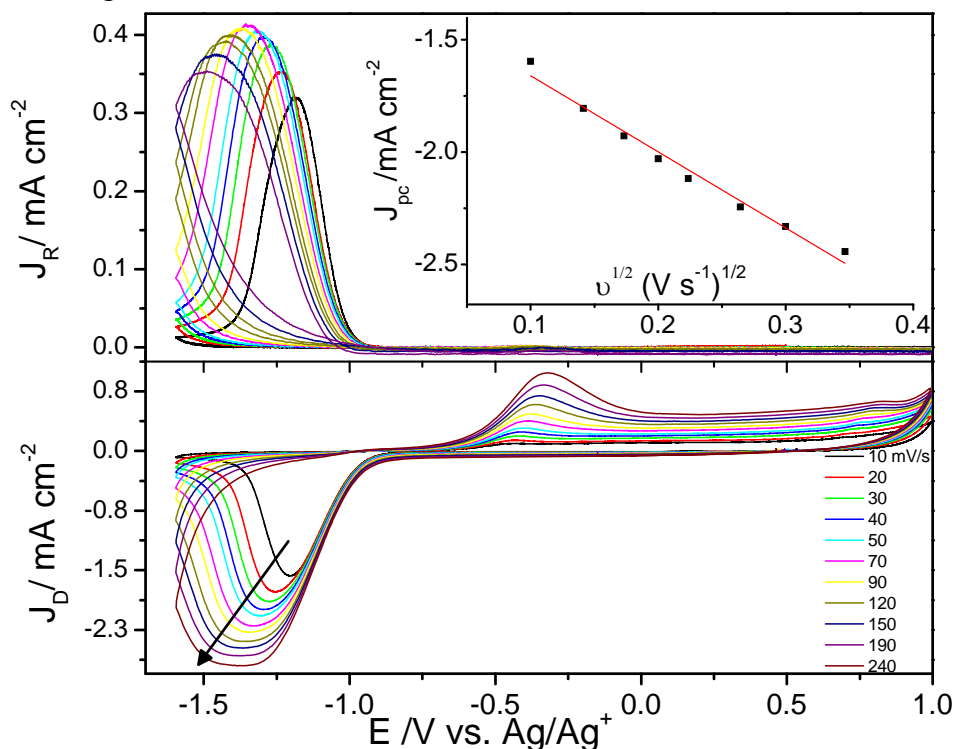


Fig. S7. RRDE CVs at  $\text{Co}_3\text{O}_4/\text{GC}$  disc and Pt-ring in  $\text{O}_2$ -sat. 0.1M  $\text{LiClO}_4/\text{DMSO}$  at 1500 rpm and various scan rates, ring was held at 0 V. Inset:  $J_{pc}$  vs.  $\nu^{1/2}$ .

## DEMS Investigations

### ORR/OER in $\text{K}^+/\text{G4}$ :

The effect of scan rate on the produced amount of superoxide is shown in Fig. S8a. As the scan rate decreases, the amount of produced superoxide decreases, and they partially diffuse into the electrolyte due to convection. Thus, at lower scan rates, they are no longer available for re-oxidation at the surface. Plot  $I_{pa}$  vs.  $\nu^{1/2}$  shows a linear relationship, suggesting a mass-transport limited process (inset of Fig. S8a). The number of electrons extracted from the analysis of Randles-Sevcik plot (for reversible system) does not exceed one, which exclude peroxide or other species. As the amount of superoxide increases, the decomposition of the electrolyte increases (see  $m/z$  44 signal).

ORR is also studied in 0.1M  $\text{KClO}_4/\text{G4}$  solution as presented in Fig. S8b. Here, ORR sets at ca. -0.9V, which is more positive than the value in  $\text{TBA}^+$  based electrolyte. This might be due to some impurities in TBA salt, different solution resistance and ohmic drop or high water content. Nevertheless,  $z$ -values of 0.91-1.16  $e^-/\text{O}_2$  is also obtained in  $\text{K}^+/\text{G4}$ , see inset of Fig. S8b, indicating only reduction to superoxide. The formed superoxide is directly soluble in the electrolyte so that no oxidation peak is observed as in case of  $\text{TBA}^+$  solution. These results validate our calibration method since it is also found in literature for other solvents containing  $\text{TBA}^+$  and  $\text{K}^+$  a value of  $1e^-/\text{O}_2$ . [9, 34]

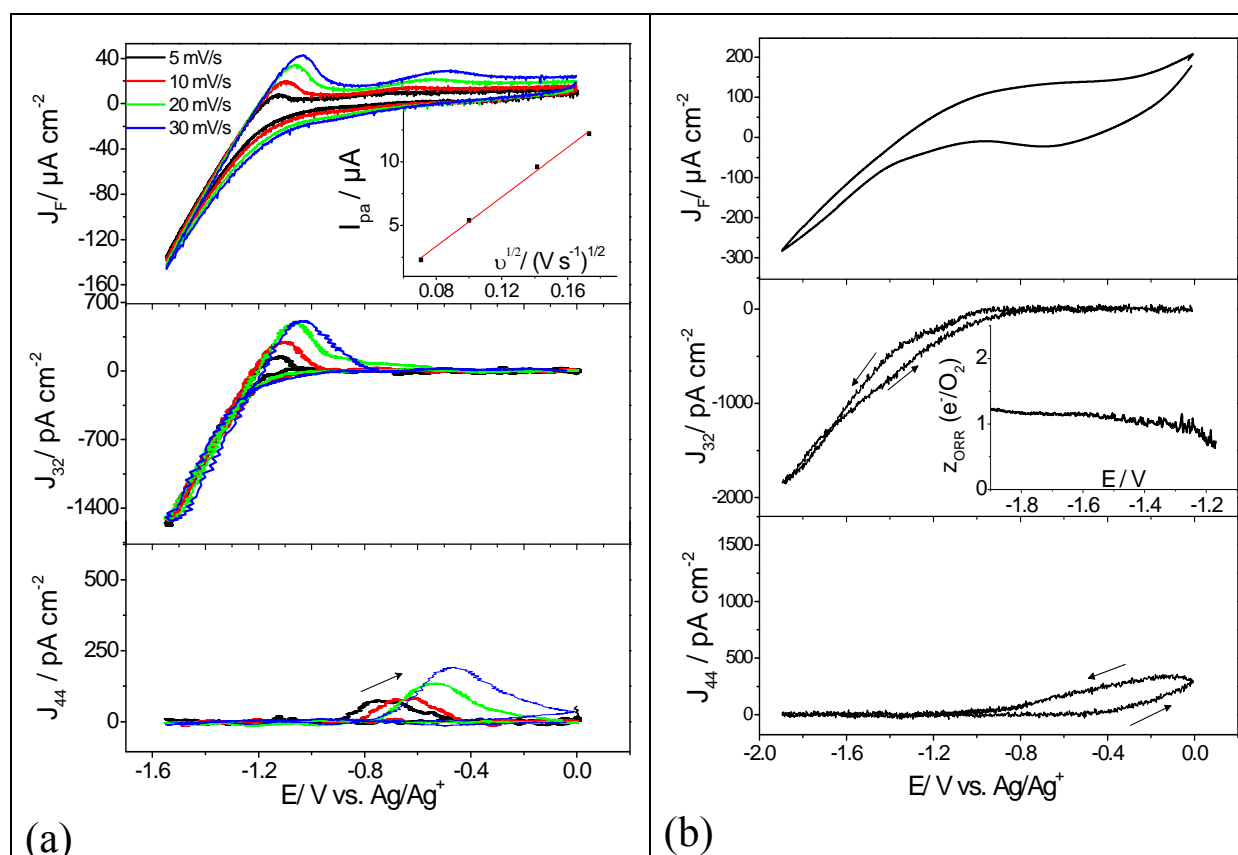


Fig. S8. (a) CVs and MSCVs recorded simultaneously at different scan rates at Au-sputtered membrane for ORR and OER in O<sub>2</sub>-saturated 0.1M TBA(OTf) in G4. Inset is plot of  $I_{pa}$  vs. sqrt of scan rate. (b) CVs and MSCVs recorded at Au-sputtered membrane for ORR and OER in O<sub>2</sub>-saturated 0.1M KClO<sub>4</sub> in G4 with 10 mV s<sup>-1</sup>. Inset is the number of electrons transferred ( $z$ ) per oxygen molecule for ORR.

#### ORR/OER in Li<sup>+</sup>/G4:

DEMS measurements in O<sub>2</sub>-saturated 0.1M LiClO<sub>4</sub>/G4 electrolyte are displayed in Fig. S9a. Upon cycling the electrode in the potential range from -1.7V to +0.1V, deactivation of the electrode is clearly observable. The faradaic as well as the ionic currents deteriorate from the first to the third cycle with no obvious evolution of currents for mass 44, see Fig. S9 a,b,c. The number of electrons transferred is calculated according to eq. 8.7 and  $\sim 2e^-/\text{O}_2$  is found for ORR while higher values above  $2e^-/\text{O}_2$  for OER, see Fig. S9 c,d. These values increase with cycling due to the progressive deactivation. A value of  $2e^-/\text{O}_2$  represents the reduction of oxygen to peroxide either directly or indirectly through the short-lived superoxide formation, while during the oxidation; side reactions take place beside peroxide oxidation. The deactivation is due to the reaction of reduction products with the electrolyte so that a deactivating film is irreversibly formed on the electrode and blocked it for further reduction. Therefore, the reversibility is obviously low.

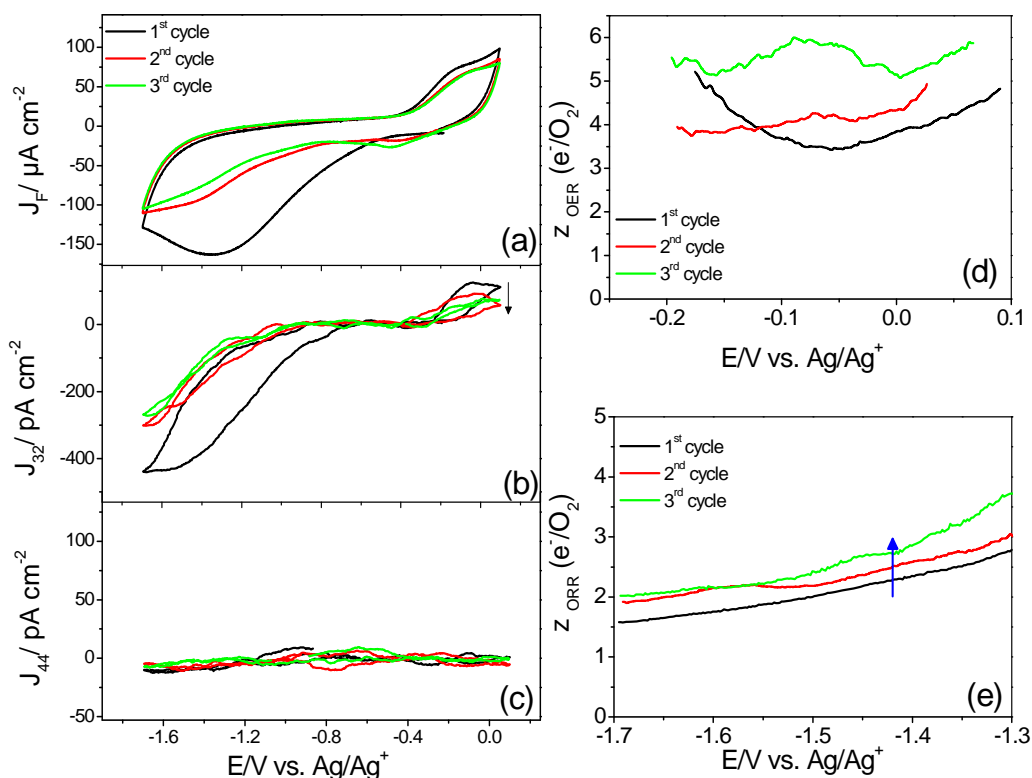


Fig. S9. CVs (a) and MSCVs for mass 32 (b) and mass 44 (c) at Au-sputtered membrane electrode in  $O_2$ -sat. 0.1M  $LiClO_4/G4$  with  $20\text{ mV s}^{-1}$ . Current density is calculated with regard to geometric area. The z-value for OER (d) and ORR (cathodic scan) (e) in the same experiment.

Three consecutive CVs for Au-sputtered electrode in a full potential range (up to +1V) are shown in Fig. S10. We can see the stability of the currents in the three cycles. From eq. 8.7, z-values are calculated for the three consecutive cycles as shown in Fig. S10d, e. Double layer charges are corrected and subtracted for z-value calculations. Roughly  $2e^-/O_2$  is obtained for ORR, and this is mostly unaltered in the three cycles. For OER, a z-value of about  $2.1 e^-/O_2$  is obtained at the oxidation peak (at -0.1V), whereas the z-value increases to about  $3e^-/O_2$  at higher potentials where the additional peaks are observed in the CV (Fig. S11). This suggests the oxidation of peroxide firstly, and afterwards some side reactions take place. The decomposition of electrolyte is associated with evolution of mass 44 starting from +0.3V. ORR sets in  $Li^+$ -electrolyte at potential similar to that in  $K^+$ -containing electrolyte, although in  $K^+$ -solution superoxide is formed and in  $Li^+$  solution peroxide is formed. This may support the notion that in  $Li^+$ -electrolyte the first reduction process to superoxide is the rate determining step as we found out in the kinetic analysis (Tafel slope) using RRDE.

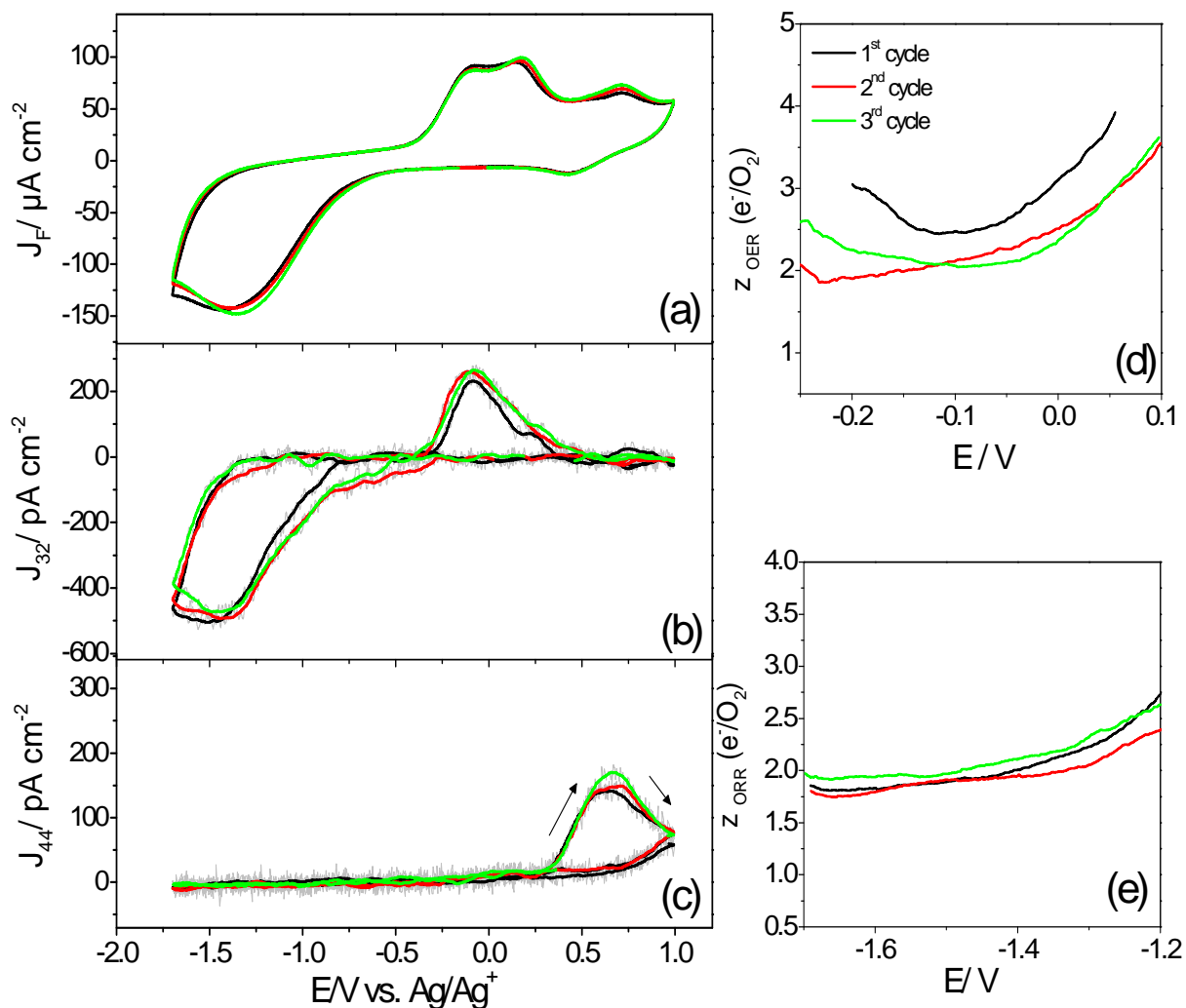


Fig. S10. CVs (a) and MSCVs for mass 32 (b) and mass 44 (c) at Au-sputtered membrane electrode in  $O_2$ -sat. 0.1M  $LiClO_4/G4$  with  $20 \text{ mV s}^{-1}$ . current density is calculated with regard to geometric area. The  $z$ -value during (d) OER, and ORR (cathodic scan) in the same experiment (e).

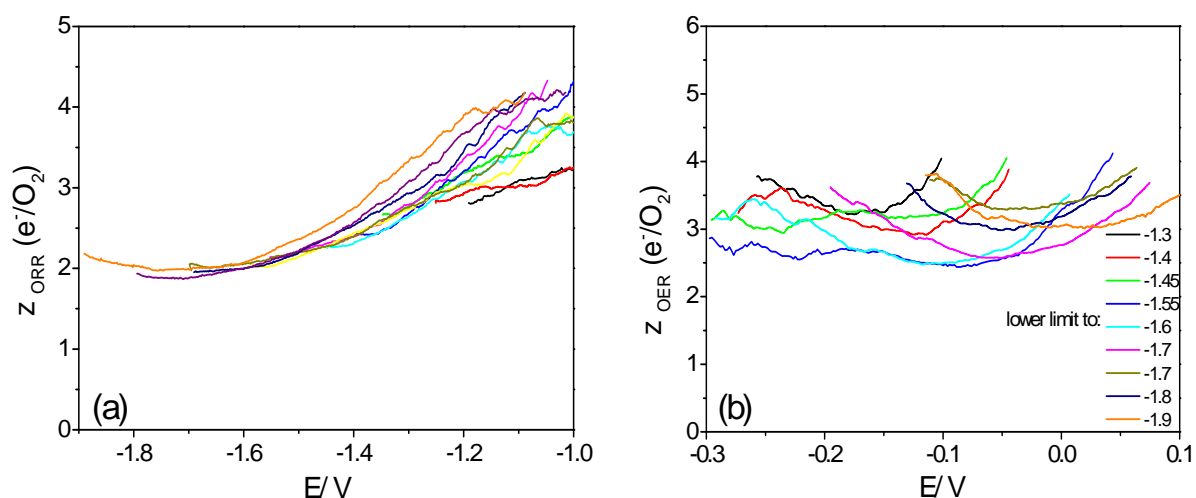


Fig. S11. The  $z$ -values for (a) ORR (cathodic scan), and (b) OER at different lower potential limits in 0.1M  $LiClO_4/G4$  at  $20 \text{ mV/s}$ .

The stability of the mixed electrolyte (50 v%) is depicted in Fig. S12. The first 4 cycles were recorded in a full potential range and show good stability. Only in the first cycle, a small shoulder in the anodic scan at ca. 0V appears in MSCV. This shoulder disappears in the following cycles and a slight increase in the reduction currents occurs, which could be attributed to the removal of the passive film formed in the first cycle. On the other hand, z-values of about 1.5 to 2  $e^-/O_2$  are obtained in the first 4 discharge cycles. The value of 2 to 3  $e^-/O_2$  evolved differs slightly from the ideal 2  $e^-/O_2$  for  $Li_2O_2$ , implying the presence of sort of side reactions.

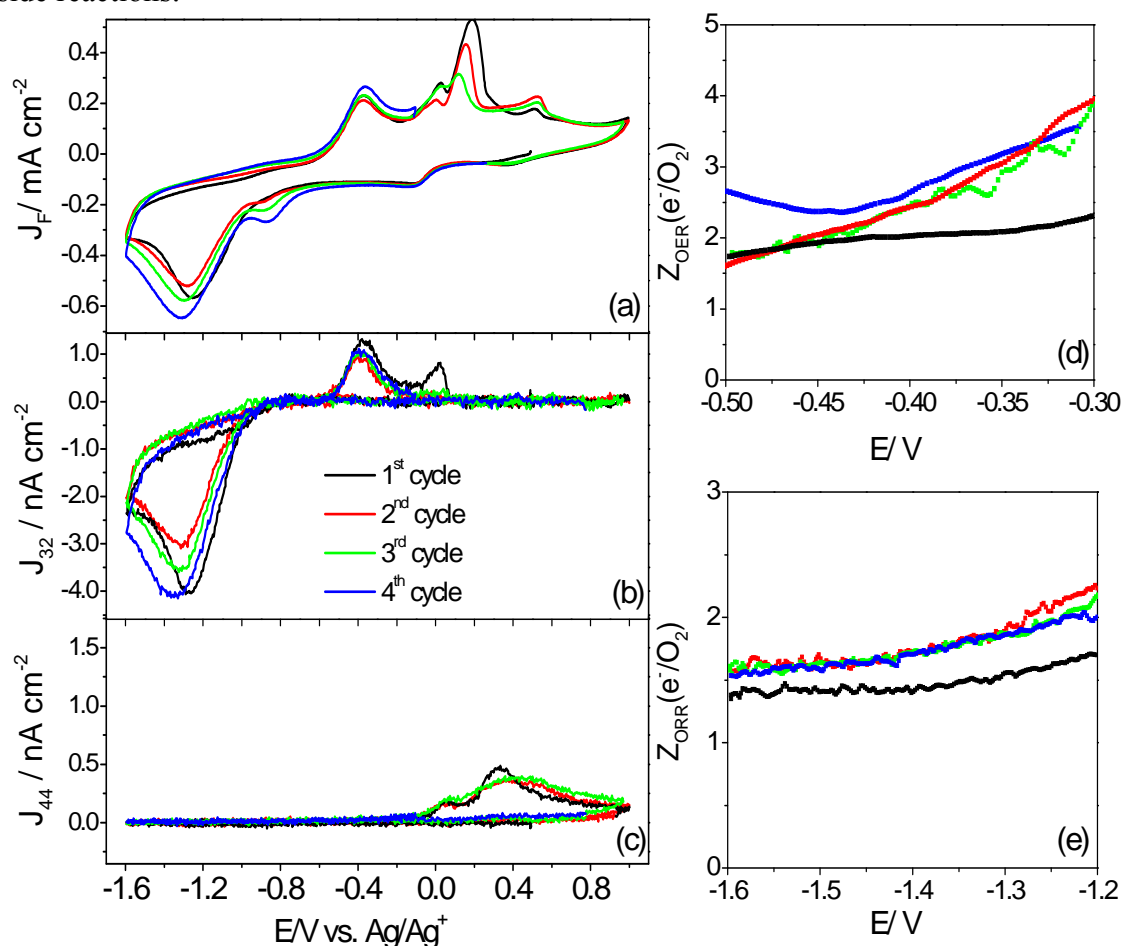


Fig. S12. CVs (a) and MSCVs for mass 32 (b) and mass 44 (c) in the second cycle at Au-sputtered membrane electrode in  $O_2$ -sat. 0.1M  $LiClO_4/G4+DMSO$  (50 v%) with  $20\text{ mV s}^{-1}$ . (d) z-value for the first 4 cycles for OER, and (e) for ORR.

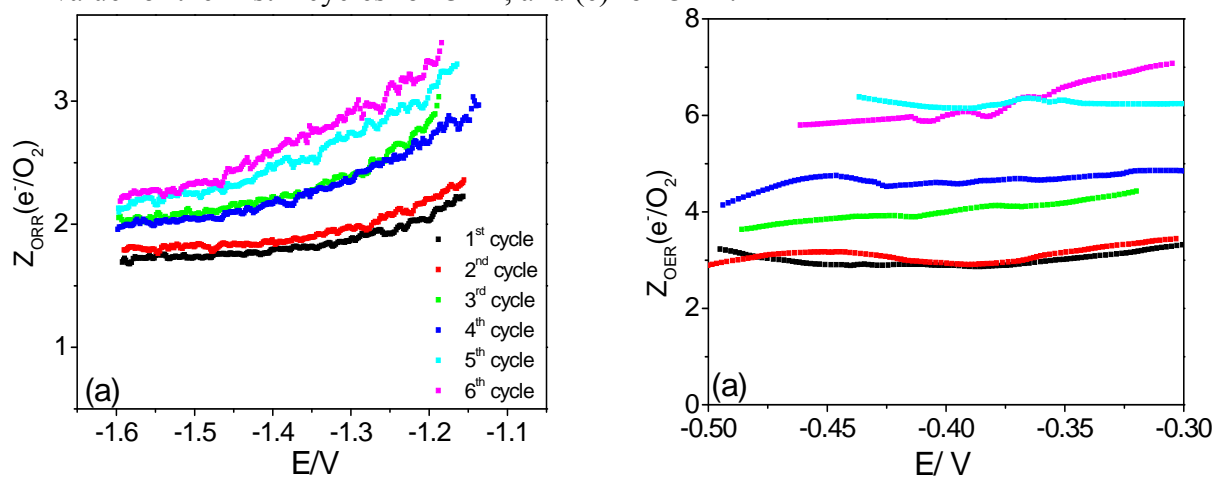


Fig. S13. The z-values for (a) ORR (cathodic scan), and (b) OER for consecutive cycles at Au-sputtered electrode in 0.1M Li<sup>+</sup>/G4-DMSO (50%) when potential was swept between -1.6 and -0.1V.

#### GDE experiments:

Here, GDE experiment was done in the single G4 electrolyte in a similar procedure, where in the first cathodic sweep, potential was held at -1.5V for 3 minutes, blue curve in Fig. S14a. In the first anodic sweep, potential was scanned to 1V. The reduction products pre-formed on the electrode are reoxidized and oxygen is evolved as shown in MSCV, red curve of Fig. S14b. In the second sweep, oxygen was supplied from solution side so that the dissolved oxygen is reduced and oxidized as in typical experiments. ORR takes place on GDE at the same potential (ca. -0.75V) of the typical experiment in which oxygen was supplied from solution (*cf.* Fig. S10).

The faradaic current efficiency in this GDE experiment is 50-60%. This low value is due to deactivation of the electrode and electrolyte decomposition. ORR proceeds via transfer of 2 electrons per oxygen molecule as shown in Fig. S14e. Thus oxygen is reduced as lithium peroxide, which blocks the surface. Z-value of 2.5 to 3.5 is observed during oxidation in the first and second cycles, as shown in Fig. S14d.

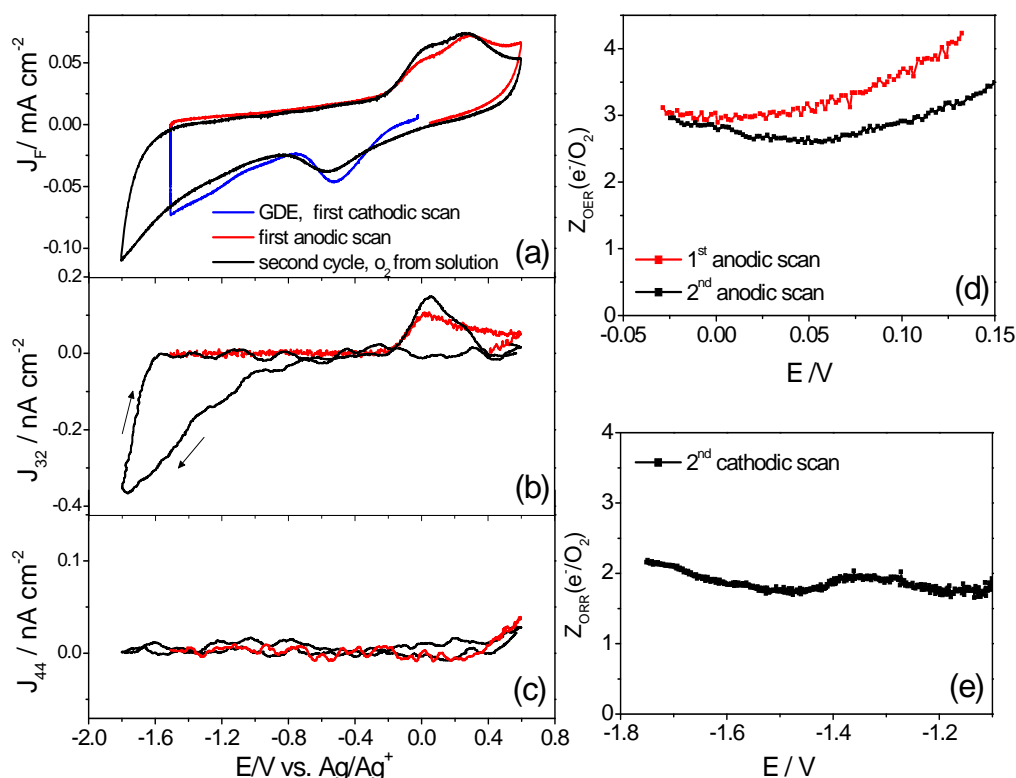


Fig. S14. Simultaneous CVs (a) and MSCVs for mass 32 (b) and mass 44 (c) during OER/ORR on Au-sputtered membrane as GDE electrode in 0.1M LiClO<sub>4</sub>/G4 electrolyte with 20 mV/s. In the first cathodic sweep oxygen was supplied from the gas side of the membrane under pressure of 500 mbar while solution was purged with Ar (blue curve); First anodic sweep: in Ar-saturated solution (red); Second cycle: O<sub>2</sub> was purged in solution (black). (d) z-values for OER and (e) for ORR.

## 9. A novel electrolyte based on DMI for oxygen reduction and evolution in Li-O<sub>2</sub> batteries: RRDE and DEMS insights

### Abstract

This work investigates the application of a novel organic electrolyte based on 1,3-dimethyl-2-imidazolidinone (DMI) for Li-O<sub>2</sub> cells. Here, for the first time, oxygen reduction (discharge) and evolution (charge) reactions in DMI-based electrolyte are characterized. The catalytic role of three electrode materials (GC, Au and Pt) as well as their electrochemical behavior are examined for ORR/OER using RRDE: GC is more active towards oxygen reduction than Au, in particular, for superoxide formation process; Pt exhibited ~360 and 250 mV less overpotentials for OER compared to GC and Au, respectively. The kinetics and the mechanism of ORR and OER in TBA<sup>+</sup> and Li<sup>+</sup>/DMI-based electrolytes are intensively investigated. Reversible formation of superoxide is elucidated in TBA<sup>+</sup>-salt. One-electron transfer process is found to be the rate determining step in ORR in Li<sup>+</sup>/DMI electrolyte. RRDE Chronoamperometry is applied here to deconvolute time and potential effects on the kinetics, while they are not separated in CV. Interestingly, ring current transients revealed a peak, and the ring peak currents at different disc potentials follow the same shape observed in CV. Quantitative analysis of the amount of oxygen consumed or evolved is conducted using DEMS technique. The results show the formation/decomposition of Li<sub>2</sub>O<sub>2</sub> as the major product upon reduction/oxidation in Li-salt with roughly 2e<sup>-</sup>/O<sub>2</sub>. On the other hand, a sort of electrolyte decomposition is observed, which is associated with CO<sub>2</sub> evolution at higher potentials. The true coulombic efficiency is about 35%. The possibility to use Au-sputtered membrane as a model for GDE is achieved and also shows the reduction of O<sub>2</sub> to Li<sub>2</sub>O<sub>2</sub> and its reoxidation. Although DMI is non-hazardous and possesses preferable physical and chemical properties, side reactions and decomposition of DMI-based electrolytes cause electrode deactivation and poor cycle life. Thus, further investigations (e.g. use mixture) to improve the solvent stability are needed.

### 9.1. Introduction

Li-air batteries have attracted great attention as a power source candidate for portable applications. They are promising because of their high theoretical energy density compared to the present Li-ion batteries.[1, 2] Development of a safe electrolyte is a prerequisite for commercialized energy systems. Therefore, one of the challenges is the identification of an aprotic electrolyte of good physical and chemical characteristics and decent stability during cycling. Several aprotic solvents have been reported for Li-O<sub>2</sub> battery applications and showed good capacities, in particular, ether-based ones.[3-7] However, to date there is no a stable electrolyte with outstanding performance and long life cycle. Electrolyte properties, such as O<sub>2</sub>-solubility, viscosity and conductivity were reported to affect the discharge capacity.[8, 9] Thereby, selection of a solvent that stabilizes Li<sup>+</sup> in solution and hinders passivation of the electrode is crucial in capacity improvement of the battery.

Carbonate-based electrolytes were early studied and showed to decompose.[3, 10] Read suggested ether-based electrolytes as potential candidates.[8] In recent years, Tetraglyme (G4) was extensively studied and its suitability is controversial: Scrosati et al. showed that G4 is a suitable solvent with a capacity of 1000 mAh g<sup>-1</sup> for at least 100 cycles,[11] while Laoire and Bruce and their co-workers demonstrated the decomposition of G4 despite Li<sub>2</sub>O<sub>2</sub>

formation.[12, 13] As an alternative, DMSO was suggested.[4, 14, 15] Bondue et al. showed by DEMS the reversible formation of Li<sub>2</sub>O<sub>2</sub> as the main product.[16] However, an XPS study showed recently the decomposition of DMSO to carbonate and other species when in contact with Li<sub>2</sub>O<sub>2</sub> for long time[17] or formation of LiOH upon reaction with superoxide.[18]

Theoretical calculations showed that N-alkyl lactams (e.g. N-methyl-2-pyrrolidone NMP) are stable against superoxide attack since nucleophilic substitution at any ring carbon is improbable and has high energy barriers.[19] Therefore, we thought of a novel electrolyte based on N,N-methyl substituted lactam. Few articles have recently studied ORR/OER in NMP-based electrolyte and showed good cycle performance despite of some electrolyte decomposition.[20, 21] DEMS data showed a maximum coulombic efficiency of 25% in NMP solvent.[22] In addition to the stability issue, some of the drawbacks for practical use are the high volatility and flammability of solvents and limited reversibility of the electrolyte.

1,3-dimethyl-2-imidazolidinone (DMI) is a non-ionic aprotic solvent with the structure shown in Fig. 1. It has promising properties over other solvents (as NMP or DMSO) such as the low melting point (8 °C), the high boiling point (225 °C), flash point of 120 °C (open method), the low flammability and the relatively low toxicity. It is a highly polar so that it can dissolve most of Li salts like LiClO<sub>4</sub> and LiTFSI. In particular, DMI possesses low viscosity (1.94 mPa s at 25 °C) and high dielectric constant (37.6 F m<sup>-1</sup> at 1MHz and 25 °C).[23] For safety concerns, it has been used as a substitute of the carcinogenic HMPA in some organic syntheses. Therefore, the above-mentioned features of DMI make it a potential candidate as a solvent for Li-O<sub>2</sub> cell. One more practical and industrial advantage is the insolubility of DMI in PTFE. DMI does not corrode metallic materials as steel, iron and others. In addition, DMI has a higher ionic conductivity (4.6 mS cm<sup>-1</sup> in 1M LiTFSI) than the unsubstituted ethyleneurea (0.26) or acetamide (0.8) due to its low viscosity.[24] This is correlated to the substitution of the hydrogen atoms on the nitrogen atom of the acylamino group with methyl. The acylamino group in DMI plays an important role in the solvation: C=O of the acylamino group coordinates with the cation, and N-CH<sub>3</sub> coordinates with anion forming a complex which leads to the higher boiling point. Hence, DMI has been used for Al electrodeposition.[25] Secondary amides are expected to be unstable toward superoxide due to the high acidity of the N-H group as in the case of aliphatic cyclic ketones.[26] However, NMP is reported according to theoretical energy calculations to be stable. Consequently, DMI is expected to have better stability against O<sub>2</sub><sup>•-</sup> in comparison to NMP because it contains two acylamino groups, which could alter the basicity of the solvent. The possible reduction products of oxygen in Li-salts are LiO<sub>2</sub>, Li<sub>2</sub>O<sub>2</sub> and Li<sub>2</sub>O, and they are polar. Thus, a highly polar solvent is required to dissolve them and prevent their precipitation and blocking of the electrode, and accordingly promote the rechargeability. Therefore, our aim is focused on the search for a novel electrolyte with such preferable properties.

To the best of our knowledge, the performance of DMI for Li-air batteries has not been reported yet. We first characterize ORR and OER in TBAClO<sub>4</sub>/DMI electrolyte on Au and GC electrodes. It is shown the reversible formation of superoxide, which is indicative of the relatively chemical stability of the solvent towards superoxide over the time scale of the scan at Au electrode. The kinetics and the mechanism of oxygen reactions are investigated in Li<sup>+</sup> containing DMI by RRDE and DEMS techniques. The role of electrode material as a catalyst on the kinetics is also explored. Au electrode was reported to be beneficial for oxidation

reactions as for example in EMITFSI ionic liquid.[27] Thus, we utilized Au-sputtered membrane as the working electrode in DEMS experiments, in addition to comparison with GC and Pt using RRDE. DMI has a quite high surface tension ( $33.6 \text{ dyne cm}^{-1}$ ), which is an important parameter for the suitability of a porous membrane as an interface in DEMS. In DEMS, the hydrophobic nature of the membrane prevents the passage of the liquid electrolyte, but allows volatile species to permeate. RRDE chronoamperometry is also applied to differentiate between time and potential effects on the kinetics. The ring currents are correlated to the amount of soluble superoxide collected at the ring. Quantitative analysis of the amount of oxygen consumed or evolved is done using DEMS. The number of electrons consumed/evolved per oxygen molecule upon reduction/oxidation is found from DEMS data to be roughly  $2e^-/\text{O}_2$ , indicating  $\text{Li}_2\text{O}_2$  formation. These results suggest that this class of solvents should be taken into account when developing new electrolytes for metal-air batteries.

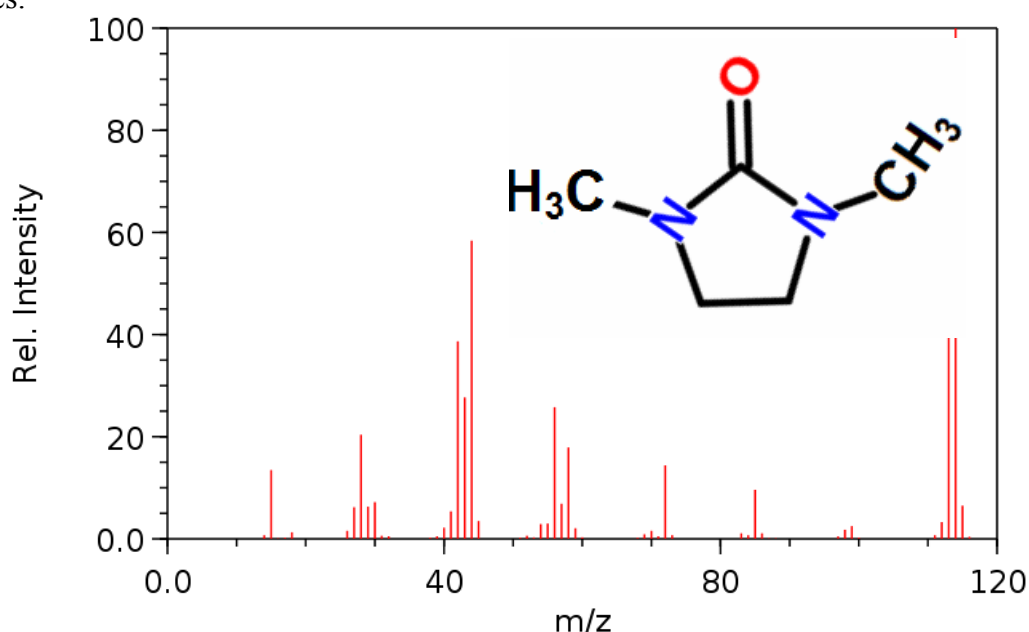


Fig. 1. Structural formula of 1,3-dimethyl-2-imidazolidinone (DMI) and its Mass spectrum (Spectra adapted from NIST Chemistry WebBook).

## 9.2. Experimental

### *Chemicals and materials*

Extra dry  $\text{LiClO}_4$  (battery grade, Sigma-Aldrich), Tetrabutylammonium perchlorate  $\text{TBAClO}_4$  (99%, Fluka) and  $\text{AgNO}_3$  (AppliChem, *p.a grade*) were used as received. 1,3-dimethyl-2-imidazolidinone DMI (absolute, over molecular sieves ( $\text{H}_2\text{O} \leq 0.04\%$ ,  $\geq 99.5\%$  GC, Sigma-Aldrich) was extra dried over molecular sieves  $4\text{A}^\circ$  in the glove box. Highly pure Ar for purging (99.999%, Air Liquide) and oxygen (99.9995 %, Air Liquide) were used.

Coulometric Karl-Fischer Titrator (C20, Metler Toledo) with a diaphragm electrode was used to determine the water content in the electrolyte. All electrolytes were prepared in a glove box (Labmaster, MBraun), where the  $\text{H}_2\text{O}$  and  $\text{O}_2$  contents do not exceed 0.5 ppm. The prepared electrolytes were kept in closed vials inside the glove box and used within a week for DEMS or prepared freshly on the same day for RRDE experiments. The water contents of the as-prepared electrolytes were  $\sim 30$  ppm for  $\text{TBAClO}_4/\text{DMI}$ ,  $\sim 70$  ppm for  $\text{LiClO}_4/\text{DMI}$  in DEMS. The electrolyte picks up some water (up to twice the amount of the as-prepared) during

transfer from the glove box to the DEMS cell. In RRDE measurements, 70-130 ppm were measured just before the experiments. The major source of water is the salt.

#### *RRDE measurements*

For RRDE and CV measurements, a setup consisting of a Pine bipotentiostat, rotor (Pine) and three-electrode glass cell was used. The working electrode (WE) consists of the disc (5 mm diameter surrounded radially by a platinum ring electrode of 6.5 mm inner diameter and 7.5 mm outer diameter) and they are separated by a Teflon cup. The disc was inserted into the tip, and then the tip was screwed into a PEEK shaft which was fed through a Teflon stopper to the cell. GC and Au discs have been used. The Pt ring was also used in some experiments as a working electrode to obtain the CV on Pt. Prior to use, the working electrodes were polished with 0.05 μm alumina slurry, and afterwards washed with acetone and then Milli-Q water under sonication and dried. The counter electrode was a Pt sheet immersed in a glass tube connected to the cell via a glass frit. The reference electrode was Ag/0.1M AgNO<sub>3</sub> in DMI. For this cell, the silver containing solution was in a separate compartment which was connected to the working electrolyte through a closed glass stop cock to prevent contamination of the working electrolyte with silver. The electrical contact was achieved through ion migration along the wetted walls of the stop cock. A bipotentiostat (model AFCBP 1, Pine Research Instrumentation, USA) with a built-in function generator and a LabVIEW software (National Instruments GmbH, Germany) were used for RRDE, while a home-made potentiostat was used for DEMS system. The electrolytes were continuously purged with O<sub>2</sub> or Ar prior each experiment or over the electrolyte during the measurements. All experiments were conducted at room temperature, 25 ± 1 °.

The electrolyte resistance in RDDE cell is determined by galvanostatic pulse method, in which a current pulse of 100 μA is applied for about 2 ms. The solution resistance ( $R_s$ ) was in range of 50-110 Ω depending on the electrolyte and on the distance between the Luggin capillary and the working electrode. *iR*-correction is not considered in every evaluation since the ohmic loss is not large at the measured currents, but is considered for Tafel plots.

#### *DEMS measurements*

In DEMS, mass resolved detection of volatile reactants, reaction products or intermediates of an electrochemical reaction is achieved by mass spectrometry with very short delay time. The separation between the liquid phase and the high vacuum phase is achieved by a microporous Teflon membrane, which is mechanically stabilized on a steel frit.[28] The penetrating species can be detected online by recording the ionic current of the corresponding mass with the mass spectrometer. Therefore, online CV will be recorded simultaneously with the mass spectrometric cyclic voltammogram (MSCV).

Here, the classical DEMS cell is used.[28] The working electrode is Au-sputtered (50 nm) Teflon membrane. This cell requires an electrolyte of about 1 ml. The counter electrode was a gold wire inserted in the cell. The reference electrode was Ag/0.1M AgNO<sub>3</sub> in DMI. The reference electrode was connected to the electrolyte through a salt bridge which was made by filling a Teflon tube with the Ag<sup>+</sup>-containing solution which was ended with a glass bead and inserted into working electrolyte. The other end was inserted in the Ag<sup>+</sup>-containing solution arm. This reference electrode has a potential around +3.8V vs. Li/Li<sup>+</sup> since this value was determined in NMP.[29] The electrolyte was continuously purged with Ar prior to the experiment or with O<sub>2</sub> during run. More details about this setup can be found elsewhere.[30]

The Au-membrane was used in some experiments as a GDE, where oxygen was supplied from the gas side underneath the membrane, while in a typical experiment, oxygen was provided from solution. The exact procedure is described below in the results. For quantitative analysis of DEMS data, a correction of the base line of ionic masses 32 and 44 is done, since the solvent DMI has a fragment at  $m/z$  44 with strong intensity (as can be seen from the mass spectrum of DMI obtained from NIST webbook, Fig. 1), which is independent of the applied potential in the cell.

#### *Calibration leak experiment*

The ion intensity ( $I_i$ ) determined spectrometrically is directly proportional to the flow of species entering the mass spectrometer ( $dn/dt$ ). The proportionality constant is the calibration constant ( $K^o$ ), eq. 9.1:

$$I_i = K^o \left( \frac{dn}{dt} \right) \quad \text{eq. 9.1}$$

Since the transfer of the products into the mass spectrometer is not complete, and the ionization probability of the species alters with the age of the filament, calibration of the mass spectrometer is necessary on the same day.  $K^o$  is used in DEMS for calculation of the number of electrons transferred ( $z$ ). Details of the calibration experiment are reported elsewhere.[22] Briefly, a certain volume underneath the membrane electrode was filled with  $O_2$ , and then a defined flow of the gas into the mass spectrometer was recorded together with the pressure drop from which the amount of substance consumed ( $dn/dt$ ) is calculated.

#### *Diffusion coefficient and solubility*

The diffusion coefficient and solubility of  $O_2$  in DMI-based electrolyte have not been empirically determined yet. Using the Stokes-Einstein equation (eq. 9.2)[31], it is possible to estimate the diffusion coefficient ( $D$ ). In this case, the fact that oxygen molecules are smaller than the solvent molecules, and that they are not located in a completely homogeneous medium is neglected.

$$D = \frac{kT}{6\pi\eta a} \quad \text{eq. 9.2}$$

where,  $k$  is Boltzmann constant,  $T$  is the temperature,  $\eta$  is the dynamic viscosity (1.94 mPa s) and  $a$  is the hydrodynamic radius of  $O_2$  and is here substituted with the  $O_2$  bond length of 121 pm.[9] A diffusion coefficient  $D$  for  $O_2$  in DMI of  $9.3 \times 10^{-6} \text{ cm}^2 \text{ s}^{-1}$  is obtained. This value is close to that obtained by a similar method in NMP ( $10.9 \times 10^{-6} \text{ cm}^2 \text{ s}^{-1}$ )[20] or half of the value obtained from a DEMS method in NMP ( $20 \times 10^{-6} \text{ cm}^2 \text{ s}^{-1}$ )[32] or other aprotic solvents such as DMSO ( $17 \times 10^{-6} \text{ cm}^2 \text{ s}^{-1}$ )[15, 32], since no data for DMI are available.

Also, the solubility in DMI has not been yet experimentally determined. Thus, the solubility is estimated here using the Hansen solubility parameters (HSPs) of oxygen and pure solvent. HSPs of oxygen are  $\delta_d = 6.7 \text{ MPa}^{1/2}$ ,  $\delta_p = 0.0 \text{ MPa}^{1/2}$ , and  $\delta_h = 3.8 \text{ MPa}^{1/2}$ , where d, p, and h stand for dispersion forces, dipole interaction, and hydrogen bonding, respectively. Solubility can be represented by  $R_a$  ( $\text{MPa}^{1/2}$ ), which is the distance between the HSPs of two substances in the three-dimensional (3D)-HSP diagram as follows:  $R_a = [4(\delta_{d1} - \delta_{d2})^2 + (\delta_{p1} - \delta_{p2})^2 + (\delta_{h1} - \delta_{h2})^2]^{1/2}$  where the subscripts 1 and 2 represent oxygen and DMI. The relationship between  $R_a$  and the logarithm of solubility ( $\log S$ ) for oxygen was reported with a high correlation coefficient (eq. 9.3)[33]:

$$\log S (\text{MP}_a^{1/2}) = (-8.89 \times 10^{-2}) R_a - 1.10 \quad \text{eq. 9.3}$$

HSPs for DMI were reported in literature;  $\delta_d = 18 \text{ MPa}^{1/2}$ ,  $\delta_p = 10.5 \text{ MPa}^{1/2}$ , and  $\delta_h = 9.7 \text{ MPa}^{1/2}$ . [34] From the above evaluations, the solubility in pure DMI solvent is estimated to be  $4.2 \times 10^{-4} \text{ mol L}^{-1}$ . The solubility in TBA<sup>+</sup>-solution ( $3.2 \times 10^{-3} \text{ mol L}^{-1}$ , determined below by RRDE) is higher than that in pure solvent, as in the case of most other solvents. [32] This value is very close to the value obtained in NMP ( $3.2 \times 10^{-3} \text{ mol L}^{-1}$ ). [32]

The thickness of the Nernstian diffusion layer ( $\delta$ ) can be also calculated according to eq. 9.4:

$$\delta = \frac{zFDAC}{I_L} \quad \text{eq. 9.4}$$

where,  $z$  is the number of transferred electrons,  $F$  is Faraday constant,  $C$  is the concentration of oxygen,  $A$  is the area of the electrode and  $I_L$  is the diffusion limiting current. The thickness of the diffusion layer was found to be  $181 \mu\text{m}$  at GC and  $140 \mu\text{m}$  at Au at 1500 rpm.

### 9.3. Results and Discussion

#### 9.3.1. Oxygen electrochemistry in TBAClO<sub>4</sub> in DMI electrolyte: RRDE investigations

Firstly, the electrochemistry of ORR and OER is examined in TBA<sup>+</sup>-based electrolyte. Fig. 2a depicts cyclic voltammograms (CVs) in O<sub>2</sub>-saturated 0.1M TBAClO<sub>4</sub>/DMI solution at three different electrodes (GC, Pt and Au). The potential scan started from 0 V in the negative-going direction until -1.8V with  $50 \text{ mV s}^{-1}$ . Clear cathodic peak is observed, corresponding to O<sub>2</sub> reduction to O<sub>2</sub><sup>•-</sup>. Upon reversing the scan direction, the formed superoxide reoxidizes to O<sub>2</sub> as can be seen from the anodic peak. In Ar-saturated solution (dashed line), there are no redox peaks, implying the absence of other electroactive species in solution. A clear effect of the electrode material on the kinetics of oxygen reaction is observed: the reversibility is higher at GC (~68%) than Au (~46%) and least on Pt (~30%), as can be noticed from the ratio of peak currents of oxidation to reduction in the CV. However, it is less than 100%, implying the reaction of superoxide, to some extent, with the electrolyte so that a small portion is not available for back oxidation in the anodic scan. Nevertheless, the process is reversible at least on GC and Au. ORR peak at GC appears ca. 100 mV and ca. 180 mV less negative to that on Au and Pt, respectively, although Au and Pt showed higher peak currents than GC only at higher overpotentials. However, onset of ORR is the same at Au and GC (at -1.2V). Remarkably, OER is also more active on GC than on Au and Pt, as shown from the negative potential shift of the anodic peak (Fig. 2a), indicating the enhanced oxidation kinetics on GC and Au with respect to Pt. These observations suggest that the superoxide could be more effectively reacted (adsorbed) on the surface of GC and Au (in the form Au···O<sub>2</sub><sup>•-</sup>) than on Pt, leading to lower overpotentials for oxidation and reduction. The activity of oxidation on the different electrode materials is in the following order: GC ≥ Au > Pt in terms of the overpotential. Therefore, the electrode material plays an electrocatalytic role in oxygen electrochemistry in this solution.

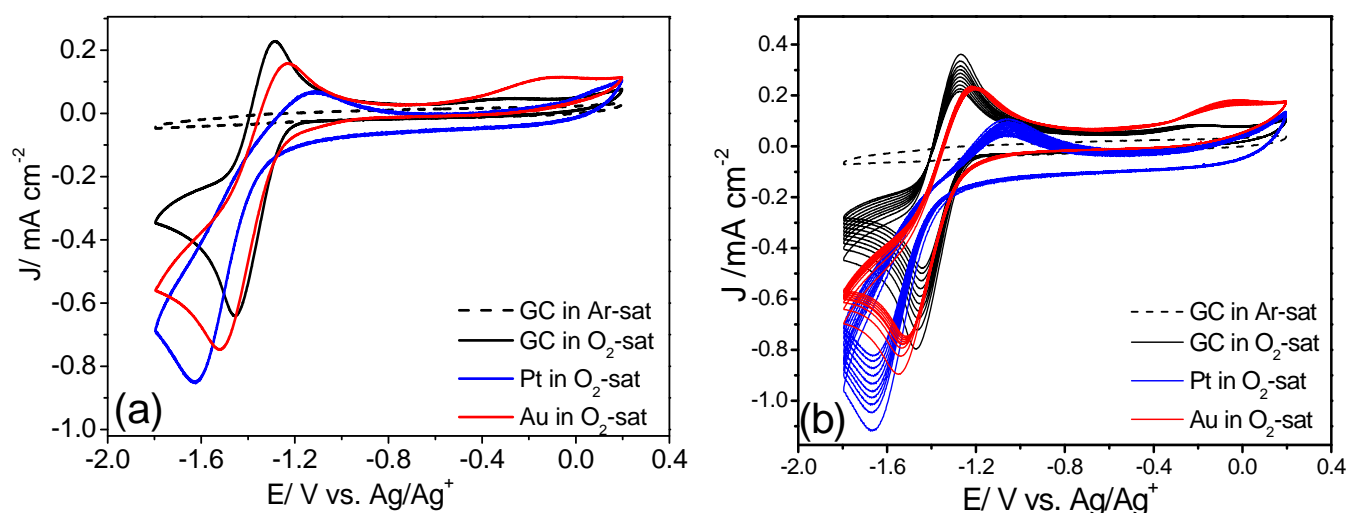


Fig. 2. CVs (2<sup>nd</sup> cycle) obtained at GC, Au and Pt electrodes in a stagnant  $\text{O}_2$ -sat. 0.1M  $\text{TBAClO}_4/\text{DMI}$  solution with 50  $\text{mV/s}$ . CVs on Pt were recorded on a Pt-ring. (b) 10 consecutive CVs at the three electrodes but with 100  $\text{mV/s}$  in the same solution.

To investigate the cyclability of ORR and OER in this solution, 10 consecutive CVs were performed on GC, Au and Pt electrodes with 100  $\text{mV s}^{-1}$ , as shown in Fig. 2b. On GC and Pt electrodes, continuous decrease of the anodic and cathodic peak currents is observed in each cycle until nearly stable behavior is reached. This could be attributed to the electrolyte decomposition and formation of side products, which form an undesired passivating film, partially blocking the electrode. The side reactions are associated with  $\text{CO}_2$  evolution as observed from DEMS (see Fig. 14). Nevertheless, only small amount of  $\text{O}_2$  is consumed in the side reactions, in particular, at Au. On Au, ORR showed better performance with little loss in the cathodic current (16% after 10 cycles), and no significant decrease in oxidation currents, demonstrating the higher stability on Au electrode. This observation implies the catalytic effect of Au on the processes, where Au could stabilize superoxide more effectively so that more superoxide is preserved on the surface and is further oxidized, as observed for another solvent.[27] Therefore, Au is a proper electrode material for this electrolyte since it enhances the oxidation kinetics.

The very small broad peak appeared around 0 V on Au is probably due to sort of solvent decomposition reactions. It is noticeable that the anodic and cathodic peak shapes are asymmetric on Pt, which could be due to blocking of the surface with side products where species can strongly adsorb on Pt. For comparison, oxygen reactions in  $\text{TBA}^+$  containing G4 or DMSO are more reversible and stable than in DMI.[15](for G4 see chapter 8).

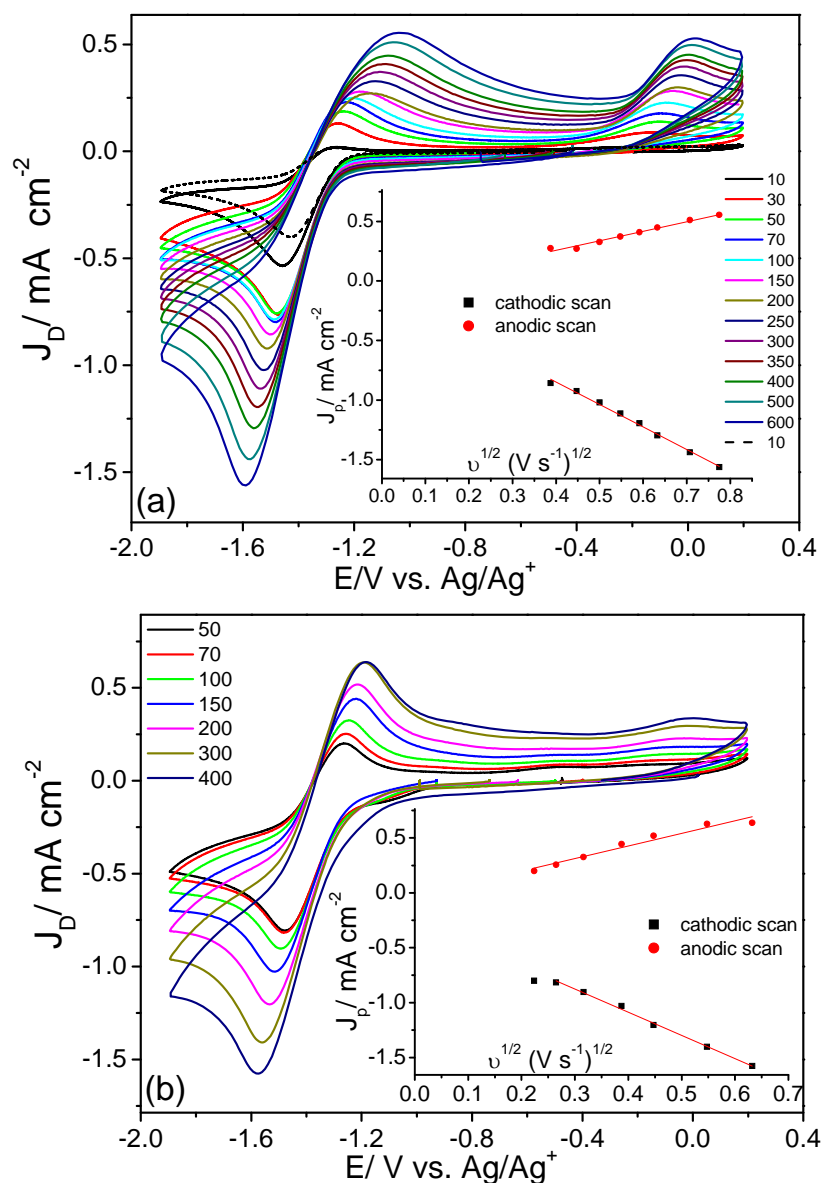


Fig. 3. Quiescent CVs at GC (a) and Au (b) electrodes in O<sub>2</sub>-sat. 0.1M TBAClO<sub>4</sub>/DMI at various scan rates. Inset: cathodic and anodic peak current density vs.  $v^{1/2}$ .

Fig. 3 portrays the CVs at various scan rates on GC and Au electrodes. Similar behavior is observed on both electrodes except the peak position as discussed above. The anodic peak at 0V is more affected by the reduction products on GC than on Au. Again, Au is more resistant to parasitic reactions than GC. The cathodic and anodic peak currents are proportional to the square root of scan rate, see inset of Fig. 3. A reasonable linear relationship between  $I_p$  and  $v^{1/2}$  (Randles-Sevcik plot, eq. 9.5 for reversible system) indicates a diffusion-limited process on Au and GC electrodes. The peak currents deviate slightly from linearity at lower scan rates (less than 100  $\text{mV s}^{-1}$ ) due to the blocking effect. The linear plot represents the data in the range of 100-600  $\text{mV s}^{-1}$ . The fitting of the straight line passes through, or very close to the origin.

$$I_p = 2.69 \times 10^5 n^{3/2} A D^{1/2} C v^{1/2} \quad \text{eq. 9.5}$$

where,  $I_p$  is the peak current,  $n$  is the number of electrons transferred,  $A$  is the electrode surface area,  $D$  is the diffusion coefficient of oxygen,  $C$  is the solubility of oxygen and  $v$  is the

scan rate. Taking the values in this solution of  $D = 9.3 \times 10^{-6} \text{ cm}^2 \text{ s}^{-1}$  (calculated from Stokes-Einstein equation) and  $C = 3.2 \times 10^{-6} \text{ mol cm}^{-3}$  (obtained from K-L plots below), the best fit of the experimental data for the cathodic peak gives a slope from which values of  $n = 0.8$  (on GC) and  $n = 0.86$  (on Au) are obtained. These values are close to one, indicating that the number of electrons transferred in the first reduction step is one. The deviation of  $n$  from one might be due to the sluggish kinetics.[18] The reduction of  $\text{O}_2$  to  $\text{O}_2^{\bullet -}$  in this solution is also quantitatively proven by DEMS (discussed below).

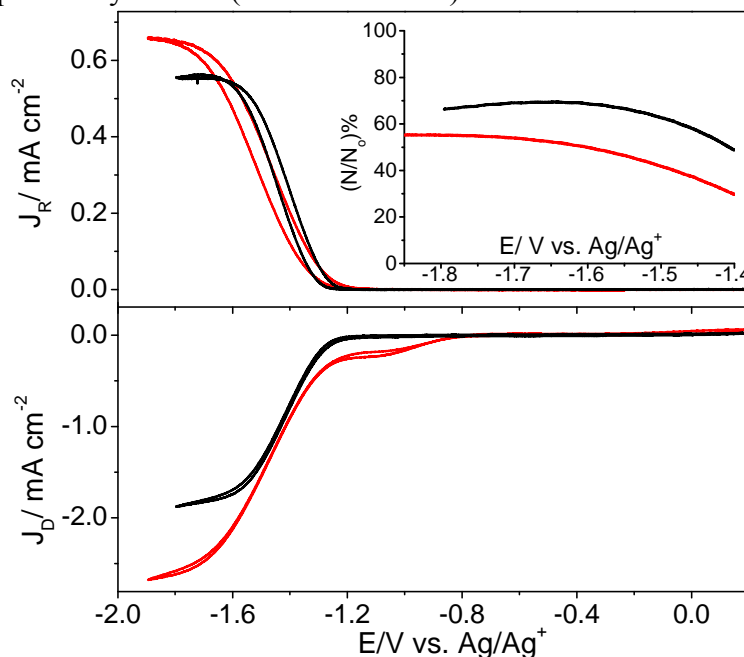


Fig. 4. RRDE results obtained at GC and Au discs (lower panel) and Pt-ring (upper panel) with 20 mV/s under 540 rpm in  $\text{O}_2$ -saturated 0.1M  $\text{TBAClO}_4/\text{DMI}$  and ring potential was held at  $-0.6\text{V}$  vs.  $\text{Ag}/\text{Ag}^+$ . Inset is the  $(N/N_0)\%$  vs. potential in the cathodic scan.

To examine the effect of electrode material on superoxide amount, RRDE is used. It enables the detection of soluble superoxide (which is generated at the disc electrode) at the ring. The Ring was biased at a potential of  $-0.6\text{V}$ , a potential at which superoxide oxidation is diffusion limited, and the disc was scanned starting from  $0\text{V}$  in the negative-going direction to  $-1.8\text{V}$  at  $20 \text{ mV s}^{-1}$ . Fig. 4 depicts the ORR disc currents in parallel to the superoxide oxidation ring currents at 540 rpm at GC and Au electrodes. ORR sets in at ca.  $-1.2\text{V}$  with a simultaneous increase in ring currents reaching a plateau at potentials more negative to  $-1.55\text{V}$ . This plateau is indicative of a diffusion-limited process at disc and superoxide is oxidized under convective-diffusion conditions (different from quiescent solution in Fig. 2). The collection efficiency ( $N$ ) in RRDE system is defined as the ratio of ring to disc currents ( $N = I_R/I_D$ ).  $N$  depends on the ring and disc geometry, diffusion coefficient of superoxide and rotation rate. The ratio of experimental  $N$  to the theoretical  $N_0$  ( $N/N_0$ ) is plotted versus potential in ORR region in the inset of Fig. 4. Only 70% of the expected value of superoxide is detected (in case of GC disc), considering the theoretical collection efficiency of this setup  $N_0 = 0.25$  and that all reduction products are soluble. This indicates that a fraction of the superoxide produced at the disc is lost through its transport to the ring. This loss could be due to reaction of superoxide with traces of water forming  $\text{H}_2\text{O}_2$ ,[35] or reaction of superoxide with electrolyte.[36] It is interesting that only 55% of superoxide was detected at Au. This infers that the stability of

superoxide on GC is different from that on Au. O<sub>2</sub><sup>•-</sup> is relatively stronger adsorbed on Au than on GC so that higher reduction currents are observed on Au, while more superoxide can be easily released from GC and transfer to the ring, yielding higher superoxide yield.

The pre-peak observed only at Au electrode at ca. -1.0V just prior to ORR is thought to be due to adsorption of O<sub>2</sub> as O<sub>2</sub><sup>-</sup> (see Fig. 4). However, its current increases with the scan rate increase, and it has large charge thus excluding this interpretation. Thus, this peak might be due to side reactions at the electrode.

The effect of rotation rate is described. RRDE measurements were performed on GC and Au electrodes using sweep rate of 20 mV s<sup>-1</sup> and rotation speeds ranging between 240 and 2940 rpm, see Fig. 5. The ring was set at -0.6V. Upon sweeping the potential in the cathodic direction, the disc and ring currents increase reaching the diffusion limitation region characterized by a plateau. Moreover, typical behavior of increasing the ring and disc currents with rotation rate is observed, as can be seen from Fig. 5a. The faster the electrode is rotated the thinner the stagnant layer in front of the electrode, and thus the more efficient the transport of oxygen to the electrode surface. Similar performance has been noticed on Au and GC discs and the same Pt ring except that slightly higher currents are observed on Au than on GC discs, see Fig. 5b. In a stagnant solution (0 rpm), lower disc currents are recorded and no superoxide is transported to the ring, thus no ring current is observed. Repeated cycling was done after each series as a control experiment (dashed curves), and a little change can be observed due to time or side effects. Higher amount of superoxide is obtained in case of GC disc (60-70% of the theoretical value) compared to the Au disc (45-55%), see insets of Fig. 5a,b.

Noticeably, the ring currents at GC at 240 rpm are delayed and a significant hysteresis between ring anodic and cathodic scans is noticed (Fig. 5a). The reason for this could be the long transition time of superoxide from disc to the ring at low rotation rates, and this feature vanishes at higher rotation speeds where the transit time of O<sub>2</sub><sup>•-</sup> is reduced. This effect may also be due to more blocking at lower speeds. This is as well correlated to the low diffusivity of superoxide so that positive currents are recorded at the disc in the anodic scan at ca. -1.3V corresponding to oxidation of the remaining superoxide that has not been removed away from the disc surface. This effect is in agreement with a previous report for ionic liquid.[36] The relation between the diffusion-limited current ( $I_L$ ) and the square route of rotation rate is represented in *Levich equation* ( $I_L = 0.62nFAD^{2/3}\nu^{-1/6}\omega^{1/2}$ ) which is a part of the *Koutecky-Levich equation K-L* (eq. 9.6).[37]

$$\frac{1}{I} = \frac{1}{I_k} + \frac{1}{I_L} = \frac{1}{nFAkC} + \frac{1}{0.62nFAD^{2/3}C\nu^{-1/6}\omega^{1/2}} \quad \text{eq. 9.6}$$

where,  $k$  is the rate constant,  $D$  ( $9.3 \times 10^{-6} \text{ cm}^2 \text{ s}^{-1}$ ) is the diffusion coefficient of oxygen,  $\nu$  is the kinematic viscosity ( $1.8 \times 10^{-3} \text{ cm}^2 \text{ s}^{-1}$  calculated from the dynamic viscosity of 1.94 mPa s),  $\omega$  is the angular rotation speed and the other parameters have their usual meaning as previous. Fig. 5c shows the Levich plots for both GC and Au electrodes from the data presented in Fig. 5a,b. The linearity of the plots indicates that the mass-transport of oxygen from bulk to the electrode surface controls the limiting current. There is an intercept of the plot at Au, while at GC it passes nearly through the origin. From the slope of Levich plot at GC and when  $n=1$ , the concentration of oxygen in 0.1M TBAClO<sub>4</sub>/DMI is determined to be

$3.2 \times 10^{-6} \text{ mol cm}^{-3}$ . This value is very close to previously reported values in NMP ( $3.2 \text{ mmol L}^{-1}$ )[20] and DMSO ( $2.1 \text{ mmol L}^{-1}$ ).[15]

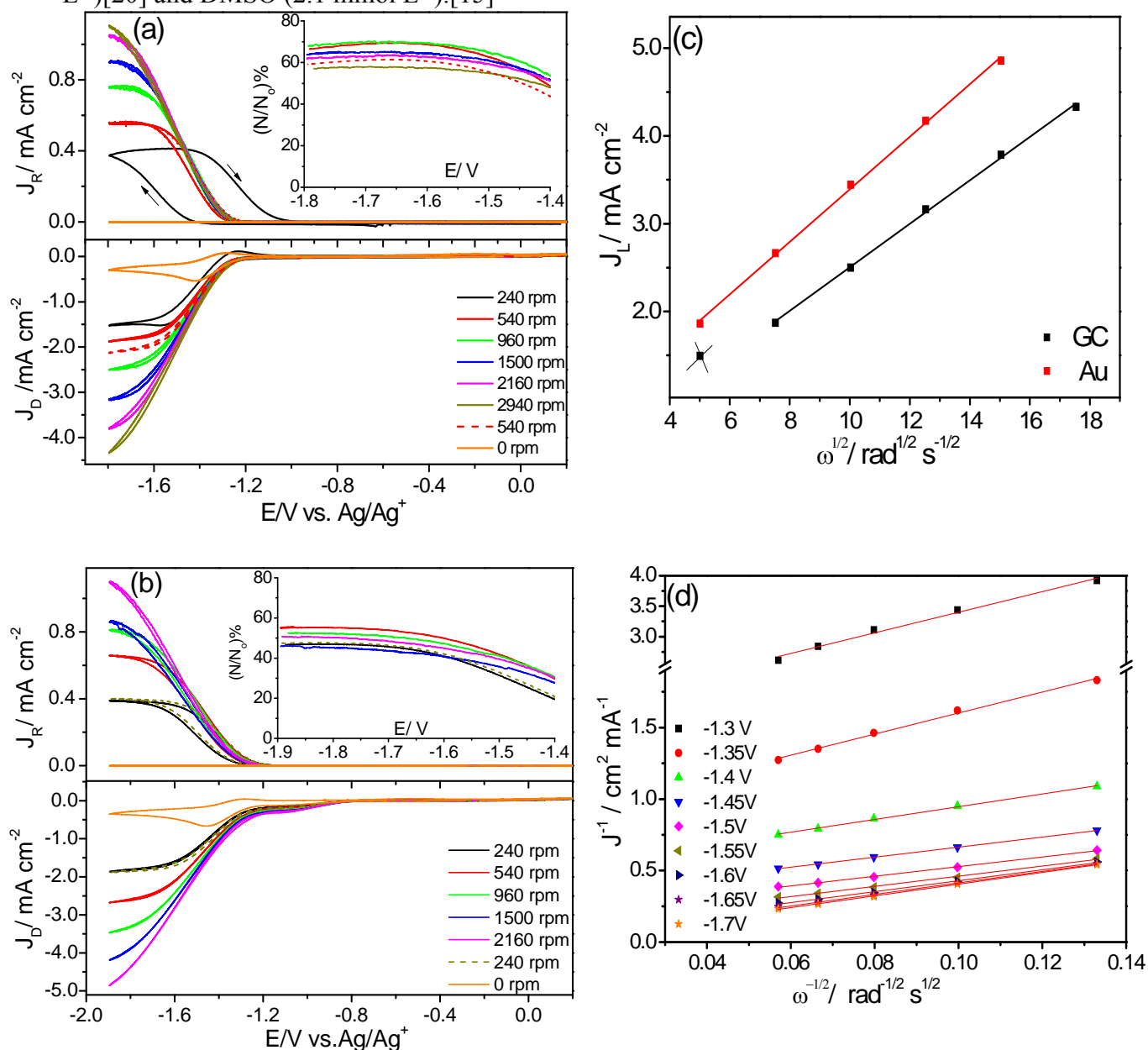


Fig. 5. (a) RRDE voltammograms obtained on (a) GC and (b) Au electrodes with  $20 \text{ mV s}^{-1}$  in  $\text{O}_2$ -sat.  $0.1 \text{ M TBAClO}_4/\text{DMI}$  with different rotation speeds (240-2940 rpm); Pt-ring was held at  $E_R = -0.6 \text{ V}$ . Inset is  $(N/N_0)\%$  at different rotations in the cathodic scan. (c) Levich Plot at GC and Au obtained from the data in (a) and (b). (d) K-L plots on GC at different potentials and  $20 \text{ mV/s}$ .

The kinetics of ORR on GC is further analyzed by constructing K-L plots at different potentials in the kinetic as well as in the diffusion-controlled regions, as shown in Fig. 5d. K-L data were extracted from the corresponding curves in Fig. 5a. Linear plots are obtained and are nearly parallel at various potentials, which agrees with a first-order reaction with respect to dissolved oxygen concentration. The intercept of the lines gives the reciprocal of the kinetic current at potentials of mixed diffusion-kinetic control, while at potentials of pure

diffusion control (negative to -1.7 V), the lines pass very close to the origin. The diffusion coefficient of oxygen is also calculated from the average slope of K-L plots: when  $n=1$  a value of  $9.7 \times 10^{-6} \text{ cm}^2 \text{ s}^{-1}$  is obtained, which is similar to the value obtained from Stokes-Einstein equation (although the later is for pure solvent not solution). The rate constant of ORR is calculated from the intercepts and ranges between  $2.6 \times 10^{-4}$  and  $3.2 \times 10^{-2} \text{ cm s}^{-1} \text{ mol}^{-1}$  at different potentials for TBA<sup>+</sup>/DMI solution.

The kinetic nature of the reaction is further analyzed using Tafel plots. Tafel plot at GC obtained from K-L Plots at various potentials is displayed in Fig. 6a. A very small intercept of K-L plots at -1.65V (diffusion-limited region) is observed, which arose from an additional current limitation, possibly diffusion and/or migration through an adsorbate passive layer on the electrode. Thereby, a correction is made in eq. 4.6 to match this undesired mass transport limitation according to eq. 9.7.

$$\frac{1}{I} = \frac{1}{I_k} + \frac{1}{I_L} + \frac{1}{I_A} \quad \text{eq. 9.7}$$

where,  $1/I_A$  contributes to the additional film hindrance. If the current  $I_A$  is independent of E and  $\omega$ , the kinetic current ( $I_k$ ) can be obtained by first determining  $I_A$  by extrapolation of  $I^{-1}$  to  $\omega^{-1/2}$  in the area of the diffusion-limited currents and this value is then taken as an offset for the intercept at other potentials according to eq. 4.7. After correction, a Tafel slope of 124 mV dec<sup>-1</sup> is obtained at low overpotentials, which is very close to 120 mV dec<sup>-1</sup>, implying a one electron transfer reduction to superoxide as the rate determining step. At higher overpotentials, larger Tafel slopes are obtained. Tafel data are iR-corrected and deviate from non-iR corrected at higher overpotentials as shown in Fig. 6a. In addition, Tafel plot at GC is obtained from the mass-transport correction of the measured current according to eq. 9.8.

$$J_k = \frac{J_L \times J}{J_L - J} \quad \text{eq. 9.8}$$

where,  $J$  is the current density,  $J_L$  is the diffusion-limited current density and  $J_k$  is the kinetic current density. Fig. 6b depicts the Tafel plot obtained from the corresponding data of Fig. 5a at 960 rpm. The Tafel slope of 117 mV dec<sup>-1</sup> obtained from this method is in a good agreement with that obtained from K-L plots, indicating consistent results. This slope is typical for the one-electron reduction to superoxide.

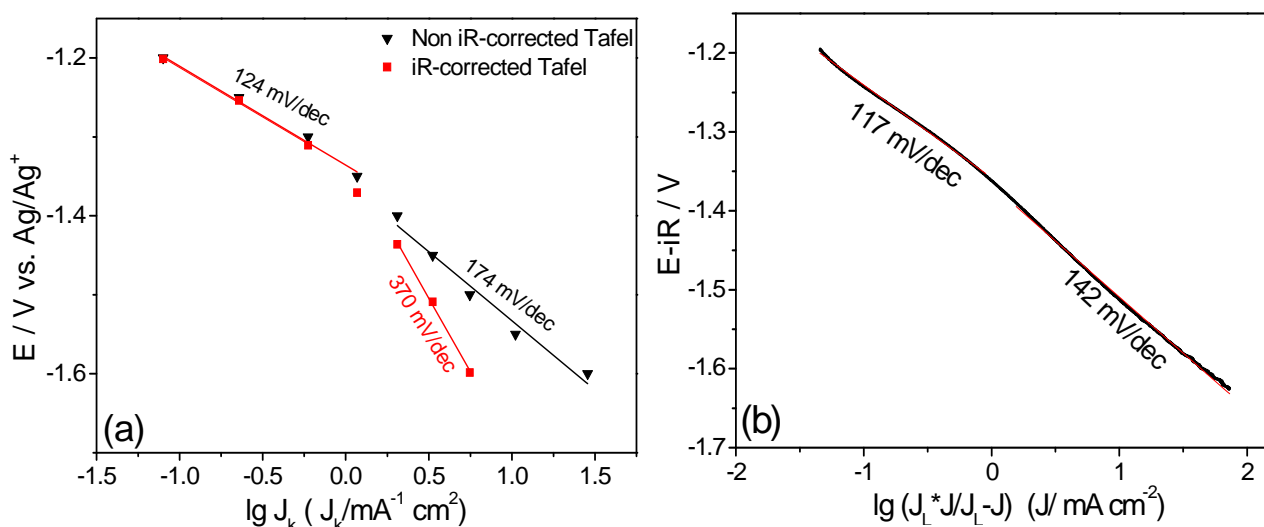


Fig. 6. (a) Tafel plots at GC obtained from K-L plots at different potentials of Fig. 5d with and without iR-correction. (b) iR-corrected Tafel plots obtained by mass-transport correction at GC at 960 rpm and 20 mV/s from Fig. 5a.

The potential at which the ring was held affects the amount of superoxide detected, as shown in Fig. S1. Basically, the ring current should be held at a potential at which superoxide oxidation is diffusion-limited. As the ring potential increases from -1.2V to 0V, the superoxide amount ( $N/N_0$ ) increases reaching the maximum value when ring potential is set above 0V. 80% of the theoretical value of superoxide is detected at higher ring potentials. Thus, higher potentials than the expected for superoxide oxidation are needed to oxidize all available superoxide at the ring. This could be due to oxidation of the "running away" reduction products ( $\text{LiO}_2$  or  $\text{Li}_2\text{O}_2$ ) which need higher potential or the reaction at ring might also include oxidation of undesired soluble reduction products at higher potentials.

### 9.3.2. Oxygen electrochemistry in $\text{LiClO}_4/\text{DMI}$ electrolyte: RRDE investigations

In this part of work, a clear effect of the electrode material on oxygen evolution kinetics is shown. After presenting the reactions in TBA-solution, here the mechanism and kinetics of ORR and OER in  $\text{Li}^+/\text{DMI}$ -based solution are investigated. Fig. 7a depicts the behavior of different electrodes, namely GC, Pt and Au, in the first two cycles. From the CV, only one reduction peak and one/two anodic peaks are observable. The cathodic peak is assigned to the reduction of  $\text{O}_2$  to  $\text{Li}_2\text{O}_2$  via direct and indirect pathways (discussed below in scheme 2). Upon reversing the potential scan, two anodic peaks are observed on Au and GC while only one peak on Pt, see Fig. 7b and c. The two anodic peaks are due to oxidation of two layers of  $\text{Li}_2\text{O}_2$ . This could be related to formation of much  $\text{Li}_2\text{O}_2$  upon reduction, and thus sequential formation of layers is probable. Single cathodic peak accompanied by two anodic peaks is an indication that chemical reactions are associated to the ORR as observed in another electrolyte  $\text{Li}^+/\text{EMITFSI}$ .<sup>[27]</sup>

Another significant observation from the CV is the effect of the electrode material on the activity and kinetics, Fig. 7a. ORR at GC electrode occurs at lower overpotentials (less negative) than on Au and Pt. The cathodic peak potentials are -1.48, -1.57 and -1.62V at GC, Au and Pt, respectively. The peak width (difference between peak potential and half peak

potential)( $E_{pc1}-E_{pc1/2}$ ) in this system at GC is  $\sim 190$  mV, which is higher than the 95 mV expected for the one-electron irreversible process, indicating the sluggish kinetics due to formation of a deactivating layer at the surface.

OER, in particular, is affected by the nature of the electrode: Pt reveals only a single oxidation peak whereas GC (also Au) displays two oxidation peaks as can be clearly seen in Fig. 7b,c. OER is more active on Pt than on GC electrode ( $\sim 370$  mV lower overpotential than GC and  $\sim 260$  mV in comparison to Au). This difference is due to different adsorption strength of the reduction products on the electrodes. The reduction product (mainly  $Li_2O_2$ ) seems to be strongly adsorbed on GC than on Pt, and can be reoxidized at higher potentials. We conclude that the activity for ORR is in the order:  $GC > Au \approx Pt$  which is similar to that in TBA-solution, while for OER  $Pt > GC \approx Au$ . The reversibility of this system does not reach 100%, since only 44% of the reduced faradaic charge can be regained upon oxidation at GC and ca. 41% at Pt and Au at  $100 \text{ mV s}^{-1}$ , implying blocking and side reactions with the discharge products. Our results are indicative of the catalytic role in reduction and oxidation reactions.

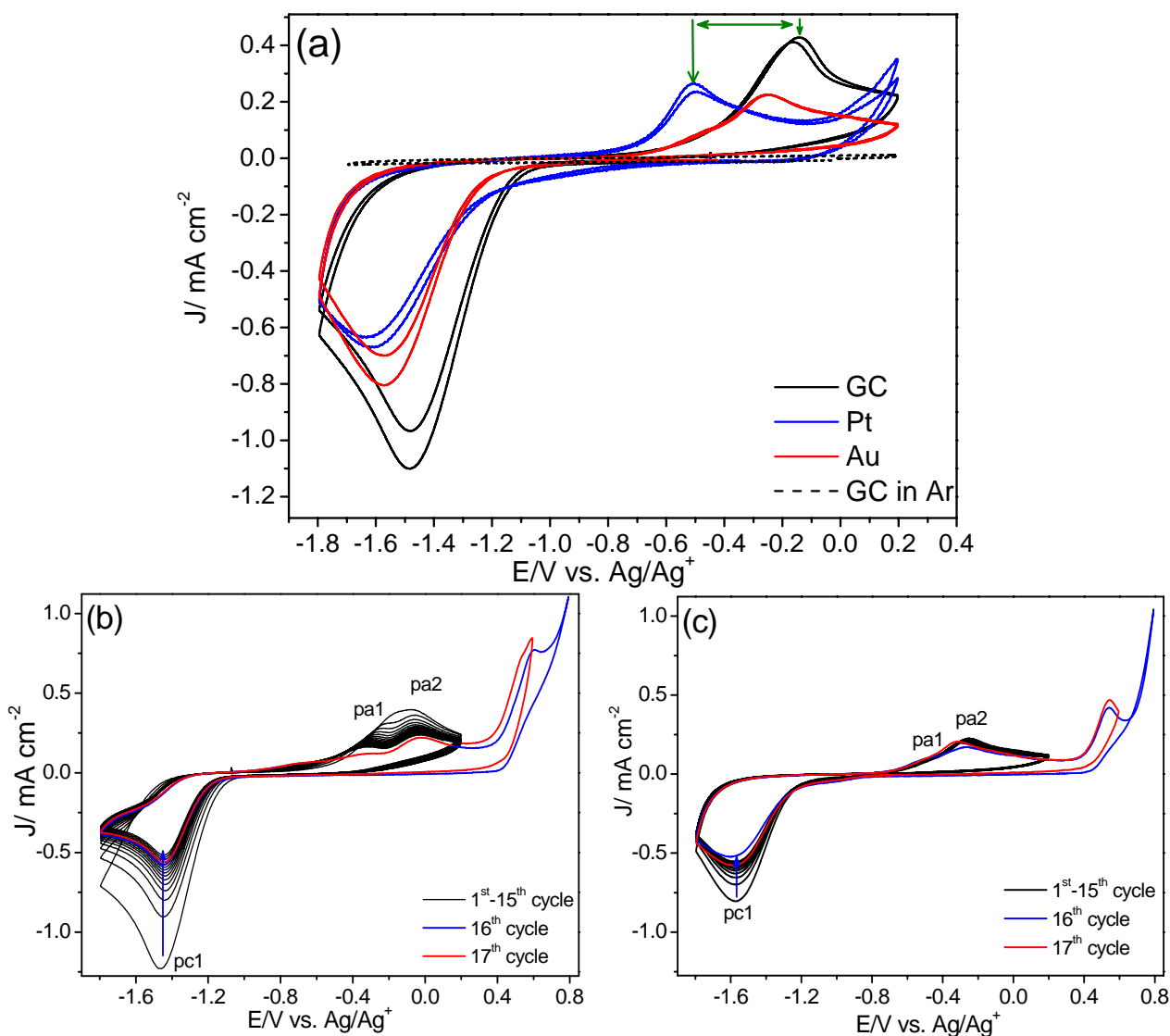


Fig. 7. (a) First two CVs at GC, Au and Pt electrodes in stagnant O<sub>2</sub>-sat. 0.1M LiClO<sub>4</sub>/DMI recorded with 100 mV/s, CVs of Pt were on the Pt-ring; dashed line is in Ar-saturated solution. Consecutive CVs (17 cycles) obtained with 100 mV/s at GC (b) and on Au (c).

The stability of GC and Au electrodes is studied by performing consecutive cycles with  $100 \text{ mV s}^{-1}$  as shown in Fig. 7b, c. Both electrodes showed a decrease of the cathodic peak currents which is indicative of surface deactivation. However, the decay of cathodic current is larger on GC than on Au, suggesting stronger adsorption of reduction products on GC and rapid blocking caused by acculation of reduction products and by-products. For OER, Au shows good stability with small current loss. Noteworthy, with cycling, in particular, on GC, the anodic peaks gradually split, illustrating two electrochemical reactions occurring at near potentials. The second peak could be correlated to the oxidation of peroxide deposited on previously formed peroxide in the former cycles, as mentioned above.

In contrast to DMSO, where the electrode can be reactivated due to the removal of the blocking layer by opening the upper potential limit to higher values[18], in DMI, the electrode cannot restore significant amount of its initial activity, as displayed in the 16<sup>th</sup> and 17<sup>th</sup> cycles in Fig. 7a,b. This is due to irreversible formation of side products, which block the surface. Therefore, the reactivation procedure at higher potentials is not effective in this electrolyte.

The nature of the reduction and oxidation products is affected the operating potential window. Fig. 8 shows detailed CVs recorded at GC, Au and Pt electrodes under different lower potential limits with  $100 \text{ mV s}^{-1}$ . Sweeping the potential cathodically to  $E_{1/2}$  of Epc leads to appearance of two overlapping anodic peaks in the reverse scan. Extending the scan to more negative potentials ( $-1.6\text{V}$ ) leads to splitting of the two anodic peaks (Epa1, Epa2). Scanning further cathodically leads to an increase of the current of the consecutive anodic peak (Epa2) together with a decrease of current of Epa1. In addition, the first anodic peak Epa1 (particularly on GC and Au) is shifted to more positive potentials when the cathodic limit is opened to more negative potentials. All this supports our mechanism of sequential formation of  $\text{Li}_2\text{O}_2$ . This suggests that both pathways exist even at lower potentials: Indirect pathway with disproportionation of  $\text{LiO}_2$  and direct formation of  $\text{Li}_2\text{O}_2$ .

The three electrodes show different features in ORR and OER regions in Fig. 8: on Au and GC, two anodic peaks (Epa1 and Epa2) are clearly observed, while on Pt only one anodic peak, as discussed above; the shape of the cathodic peak on Au and Pt is different (broader) from that on GC. Another interesting notion is that the current ratio of Epa1/Epa2 is higher on Au electrode than on GC. This current ratio decreases with expanding the potential limit until the current in the second peak gets equal or greater than that in the first peak. This effect can be explained in the way that by extending the cathodic limit, more reduction products (mainly  $\text{Li}_2\text{O}_2$ ) are deposited not only on the Au surface but also on the pre-formed  $\text{Li}_2\text{O}_2$  particles by nucleation mechanism and thus the oxidation of these over-layers of  $\text{Li}_2\text{O}_2$  requires higher overpotential, as can be noticed from the positive shift of the anodic peaks. Multilayer formation explains also the two oxidation peaks corresponding to different layers of  $\text{Li}_2\text{O}_2$ . However, another possibility could be that Au stabilizes the reduction products more effectively than GC[27], and consequently providing higher oxidation currents in the first peak on Au. At Pt electrode, the anodic peak is not significantly influenced by potential window broadening as in case of Au, indicating the catalytic effect of Pt in the oxidation process (lower oxidation overpotential).

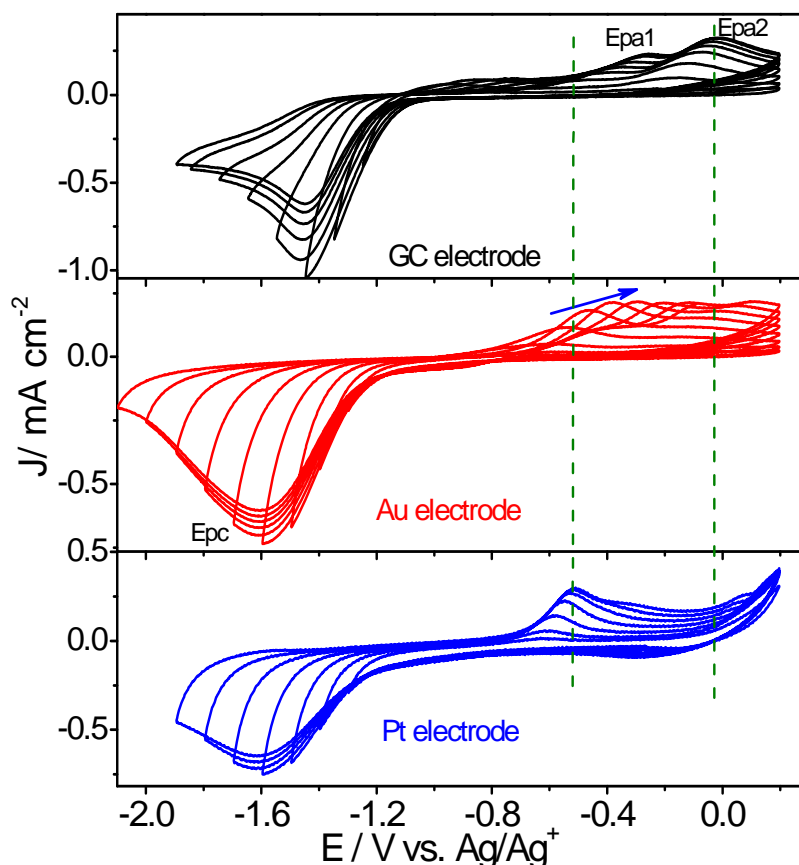


Fig. 8. CVs on GC, Au and Pt electrodes in stagnant O<sub>2</sub>-sat. 0.1M LiClO<sub>4</sub>/DMI at various cathodic potential limits with 100 mV/s.

The effect of scan rate is displayed in Fig. S2. The oxidation behavior on GC is different (shape of peak) from that on Au. As the scan rate increases, the cathodic peak shifts to more negative values on GC as well as on Au, suggesting irreversible ORR process. Noticeably, the anodic peak on Au electrode remains centered with increasing the scan rate (Fig. S2b), while on GC it shifts to higher potentials (Fig. S2a). This infers the catalytic role of Au in the oxidation process, where Au could stabilize the reduction products more effectively than GC. Nicholson-Shain relationship can be applied for irreversible systems (eq. 9.9).[37] The anodic and cathodic peak currents are directly proportional to the square route of scan rate. The plot reveals a straight line passing or very close to the origin on both GC and Au, suggesting a diffusion-controlled process, inset of Fig. S2a.

$$I_p = 2.99 \times 10^5 n(n^* \alpha)^{1/2} AD^{1/2} C \nu^{1/2} \quad \text{eq. 9.9}$$

where,  $n$  is the number of electrons transferred,  $n^*$  is the number of electrons transferred in the rate determining step, and other parameters have the same meaning as above. Taking the value of  $D = 9.3 \times 10^{-6} \text{ cm}^2 \text{ s}^{-1}$  (from Stokes equation), and considering  $n$  and  $n^*$  equal one; the best fit of the experimental straight line gives a value for  $C = 3.9 \times 10^{-6} \text{ cm}^2 \text{ s}^{-1}$  when  $\alpha = 0.7$ , which is reasonable for irreversible process. This is close to the value obtained in TBA-containing solution. GC and Au electrodes revealed a similar slope for the cathodic peak, whereas a change in the slope for the anodic peak is observed, see Fig. S2a inset.

The nature and solvation strength of the solvent influence significantly the stability of the LiO<sub>2</sub>: DMSO has been shown to stabilize the superoxide in solution so that it is detected at the ring, while in acetonitrile the superoxide is not stable (no ring currents were detected) and

rather  $\text{Li}_2\text{O}_2$  is formed.[15, 18] RRDE enables us to detect the soluble superoxide at the ring in  $\text{Li}^+$ /DMI, as shown in Fig. 9, where the ring was held at 0.0 V, a potential at which superoxide oxidation is diffusion limited. Inset of Fig. 9 shows that 40-75% of the theoretical collection efficiency of superoxide detection is obtained depending on the discharge potential, indicating that a part of the total ORR charge goes for the production of insoluble components (i.e.  $\text{Li}_2\text{O}_2$ ). The amount of detected superoxide increases at higher overpotentials.  $\text{LiO}_2$  amount in DMI is slightly lower than that in DMSO (~90%), but is higher than that in DME (20%).[38] This indicates that  $\text{LiO}_2$  is more soluble in DMSO than DMI than in DME. On the other hand, no soluble  $\text{LiO}_2$  was detected in acetonitrile.[39] Therefore, the solvation strength of the solvent governs the stability and the amount of soluble  $\text{LiO}_2$  intermediate. GC shows also better activity than Au under rotation mode, see Fig. 9. Although the ORR currents on GC are much higher than on Au, the percentage of superoxide at the ring from the GC disc is not so large compared to the Au disc, indicating the stability of superoxide on Au.

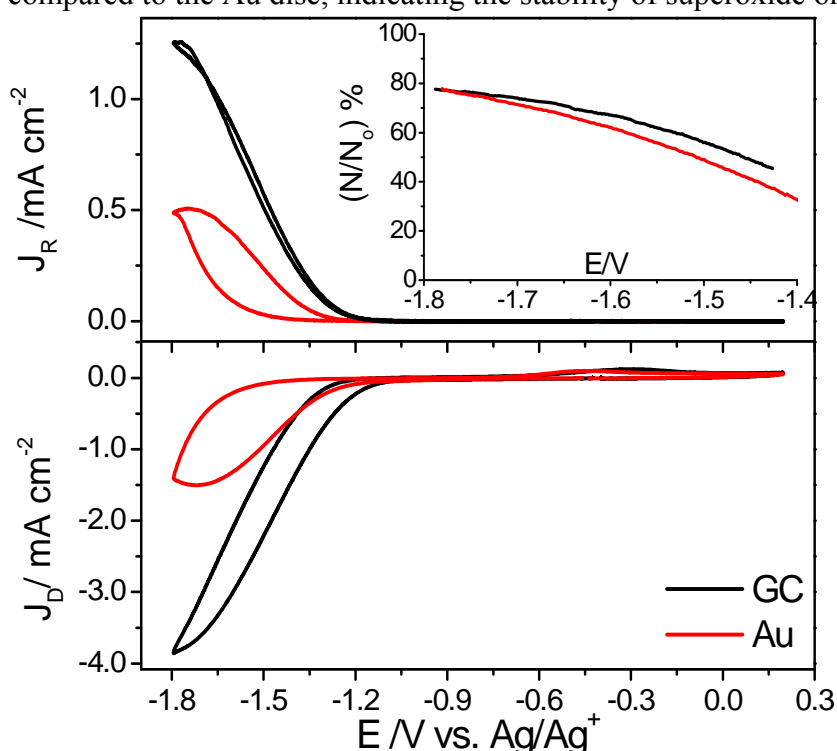


Fig. 9. RRDE results at GC and Au electrodes (lower panel) and Pt-ring (upper panel) recorded in  $\text{O}_2$ -sat. 0.1M  $\text{LiClO}_4$ /DMI with 100 mV/s and 1500 rpm and Pt-ring potential was held at 0.0V. Inset is the  $(N/N_0)\%$  in the cathodic scan.

Further investigations are done at GC and Au electrodes by applying different rotation rates and  $100 \text{ mV s}^{-1}$  as shown in Fig. 10. Higher scan rate is used to avoid fast deactivation of the electrode during measurements. Typical behavior is observed: disc and ring currents increase with the rotation rate increase. Semi-plateau is observed at the diffusion-limited current region. However, deactivation of the electrode occurs as can be noticed from the hysteresis between the anodic and cathodic scans in the ORR region. This is attributed to the formation of a deactivating layer of  $\text{Li}_2\text{O}_2$ , which blocks the active sites on the surface.

The soluble superoxide generated at the disc transfers to the ring. However, some superoxide generated at the disc are lost during transfer (loss ca. 20% at higher rotations and -1.7V), considering the theoretical collection efficiency  $N_0=0.25$  and all reduction products are

soluble. This loss could be due to reaction of superoxide with traces of water forming H<sub>2</sub>O<sub>2</sub>[35] or reaction of superoxide with electrolyte.[36] The ratio of collection efficiency to the theoretical collection efficiency ( $N/N_0$ ) is plotted at different rotation speeds versus the potential as shown in Fig. 10 c, d. The superoxide yield  $N/N_0$  increases at higher rotation speeds because of the short transient time.

It is noteworthy to mention that the anodic peak between -0.6 to -0.2V on both GC and Au discs is not accompanied with any ring current, indicating the oxidation of Li<sub>2</sub>O<sub>2</sub> directly to O<sub>2</sub> without passing through superoxide intermediate, see Fig. 10 a,b. This supports our interpretation of the two anodic peaks observed above.

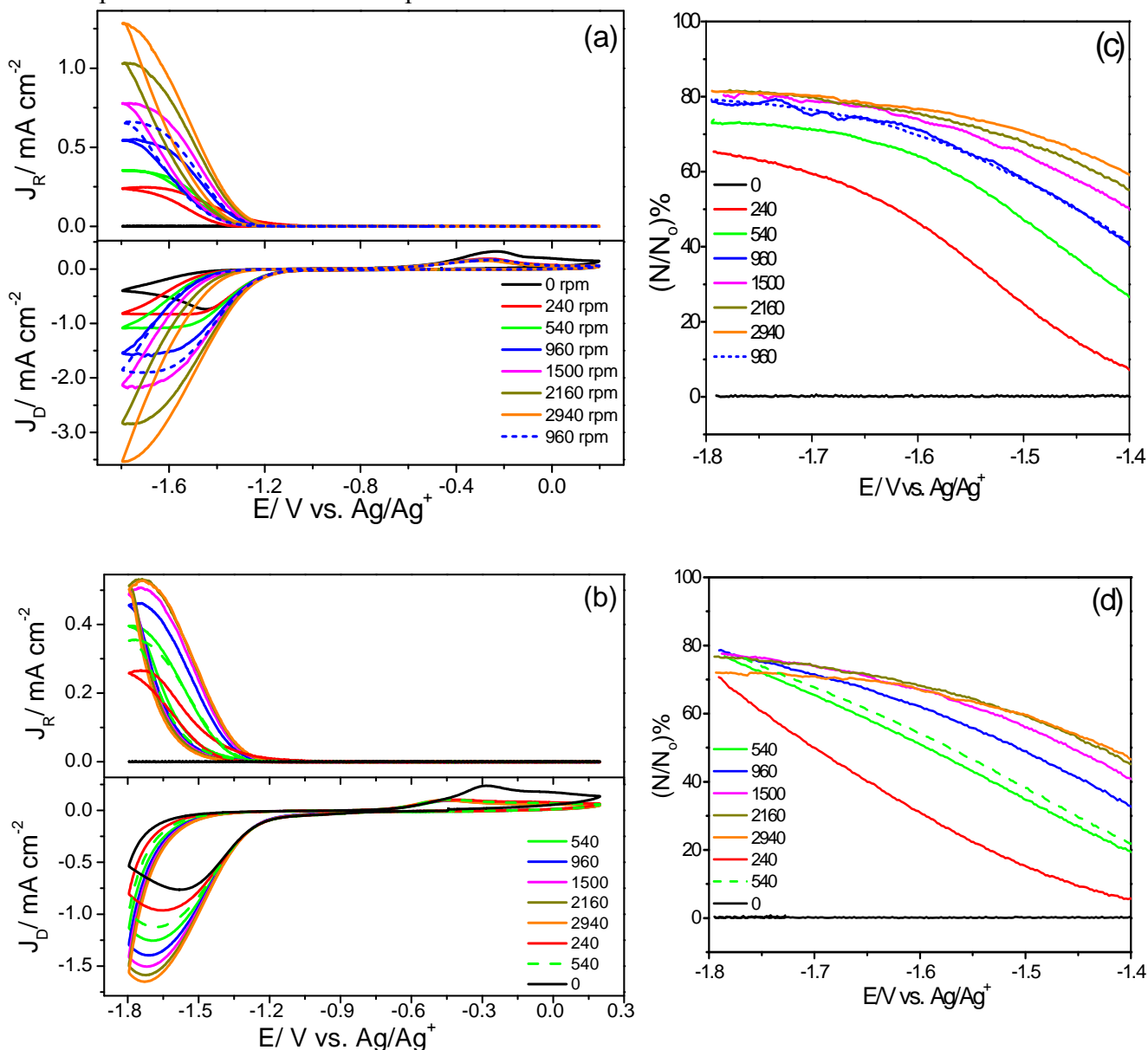


Fig. 10. RRDE voltammograms obtained at GC (a) and Au (b) electrodes with 100 mV s<sup>-1</sup> in O<sub>2</sub>-sat. 0.1M LiClO<sub>4</sub>/DMI with different rotation rates (240-2940 rpm), ring was held at  $E_R=0V$ . The  $(N/N_0)\%$  at different rotation speeds vs. ORR potential for GC (c) and for Au (d) electrodes.

### 9.3.3. Tafel slope and RRDE chronoamperometry

Evaluation of the diffusion-limiting current using Levich plot is done at GC electrode from the data of Fig. 10a and is portrayed in Fig. 11a. The limiting current is directly proportional to the square route of the rotation speed. This suggests that the plateau in ORR region is correlated to O<sub>2</sub>-transport controlled process at the interface. The measured limiting current for ORR is below the expected theoretical value for a 2e-process according to eq. 9.6. Using the values of D ( $9.3 \times 10^{-6} \text{ cm}^2 \text{ s}^{-1}$ ) and C ( $3.2 \times 10^{-6} \text{ mol cm}^{-3}$ ) a value of  $n=1$  is obtained.

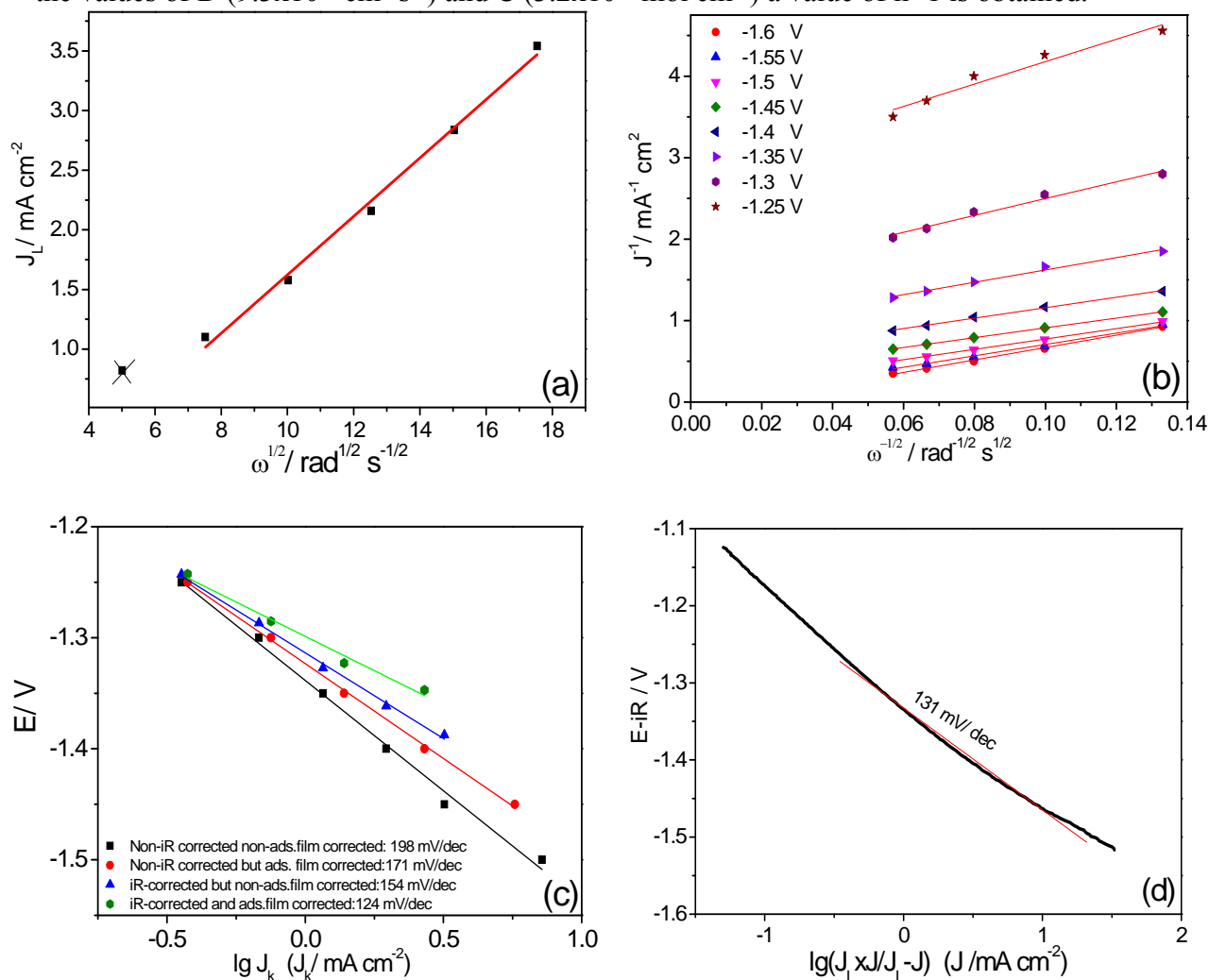


Fig. 11. (a) Levich Plot and (b) K-L plots at GC electrode obtained from the corresponding data in Fig. 10a at various rotations in O<sub>2</sub>-sat. 0.1M LiClO<sub>4</sub>/DMI solution. (c) Tafel plots from the intercepts of K-L plots at GC obtained at different potentials. (d) mass-transport corrected Tafel plots obtained at GC at 540 rpm and 100 mV/s from data in Fig. 10a.

K-L plots are constructed for GC electrode at different potentials from the data in Fig. 10a and are displayed in Fig. 11b. K-L plots are linear and quite parallel in the mixed kinetic-diffusion limited current region, suggesting a first-order reaction with respect to O<sub>2</sub> concentration. The number of electrons transferred during ORR can be calculated from the slope of K-L plots according to eq. 9.6. Considering D, C and the average slope of K-L plots in this solution,  $n=0.7$  is obtained according to eq. 9.6, which is close to one, indicating that the reduction peak currents are not the diffusion limited currents for  $n=2$  process which is

possibly due to formation of a blocking layer. However,  $2e^-/O_2$  is obtained from DEMS. K-L plots should ideally intercept zero at potentials in the diffusion-limited region. Nevertheless, a very small intercept is observed at potential of -1.6 and -1.55V. Thereby, a correction is made according to eq. 9.7 to get the kinetic current for Tafel plot.

Kinetic currents are obtained from the intercept of K-L plots, then are used to built-up Tafel plots. Fig. 11c shows Tafel plots at GC for the data corrected for  $iR$ -ohmic drop and compared to the plots without  $iR$ -correction. In addition, Tafel plots with and without correction for the additional limitations are displayed. The results indicate that higher Tafel slopes are obtained as long as no  $iR$ -correction or additional transport limitation correction are made. Therefore, these corrections are needed for such systems. After both corrections, a Tafel slope of  $124 \text{ mV dec}^{-1}$  is obtained, which is very close to the typical  $120 \text{ mV dec}^{-1}$ , suggesting that the one-electron reduction to superoxide is the rate determining step. Tafel plot is also obtained by mass-transport correction of the currents at GC from the CV of Fig. 10a at 540 rpm according to eq. 9.8 and shows  $131 \text{ mV dec}^{-1}$  for ORR in the same potential range, as shown in Fig. 11d. This illustrates the consistency of both methods.

The effect of ring potential is the same as in the case of  $TBA^+$  containing solution. Fig. 12 displays the behavior of the GC electrode at different ring potentials. At lower ring potentials (less than 0.0V), less superoxide amount is detected on the ring, while if the ring was held above -0.3 V, the maximum superoxide amount is detected, as shown in the inset of Fig. 12. That is why we selected 0V to be our ring potential in other experiments. The same trend is observed on Au electrode as shown in Fig. S3.

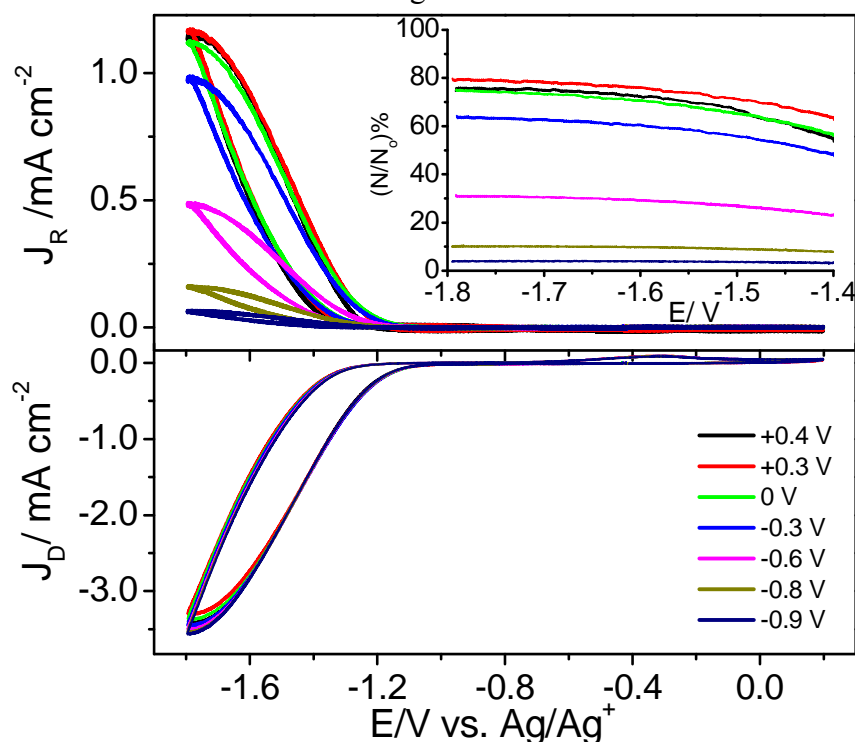


Fig. 12. RRDE curves at GC electrode obtained with 100 mV/s and 1500 rpm in  $O_2$ -sat. 0.1M  $LiClO_4/DMI$ . Ring was held at different potentials. Inset is the corresponding  $(N/N_0)\%$  vs. potential in cathodic scan.

Here, we present RRDE Chronoamperometric technique. The purpose of this experiment is to deconvolute time and potential effects on the kinetics since they are not separated in cyclic

voltammetry and usual RRDE experiments. In CV, more  $\text{Li}_2\text{O}_2$  is accumulated on the electrode upon potential sweeping and causes blocking. Consequently, it affects the rate of the reaction of the next reacting species. In contrast, in RRDE chronoamperometry a potential step is done, avoiding the "history effect" of the electrode. Therefore, superoxide which is reacting on a surface covered with  $\text{Li}_2\text{O}_2$  is different from that formed on  $\text{Li}_2\text{O}_2$ -free surface. Moreover, in CV the formation of  $\text{Li}_2\text{O}_2$  blocking layer could influence the r.d.s. and thus the amount of superoxide detected. This method also gives information on the rate of deactivation of the surface by  $\text{Li}_2\text{O}_2$ . A similar procedure has been recently applied in DME and DMSO solutions.[38, 40]

Here, the current transients at Au disc and Pt ring are recorded simultaneously under rotation of 1500 rpm where the potential of the disc was stepped from 0V (where no electrochemical reductions take place) to various disc potentials between -1.2 and -1.8V while the Pt ring was held at 0V (where superoxide is fully oxidized), see Fig. 13. At all set disc potentials, the disc current drops sharply as the electrode surface is blocked by the reduction products (mainly  $\text{Li}_2\text{O}_2$ ), while the ring current shows a peak at short times and decays slower, thus  $N/N_0$  ratio decreases with time. This implies the transport of superoxide generated at the disc to the ring where it is reoxidized.

The deactivation is faster at higher overpotentials as can be observed from the exponential current decay at the disc. This behavior was also observed for DMSO and DME.[38] The disc current decays with time until it reaches a nearly steady-state value, indicating the formation of insoluble  $\text{Li}_2\text{O}_2$  film, which passivates the surface. Afterwards, ORR still takes place even on  $\text{Li}_2\text{O}_2$  thin film, but with a lower rate until a critical layer is deposited, and shuts down the process, see Fig. 13. Since  $\text{Li}_2\text{O}_2$  is a poor conductor, the charge transfer through this film is limiting the ORR.[41] The ring currents are only a fraction of the expected theoretical values due to the loss in the form of  $\text{Li}_2\text{O}_2$  deposit via further reduction of  $\text{LiO}_2$  on the surface or loss in solution. The ring peak current recorded is dependent on the applied disc potential, and exhibits the same shape of ring currents observed in the typical CV (*cf.* Fig. 10) with a plateau starting at ca. -1.7V, inset of Fig. 13a, although in CV time is convoluted since the potential varies linearly with time. Similar behavior has been previously reported for DMSO-based electrolyte.[40] The amount of detected superoxide ( $N/N_0\%$ ) is higher at more negative potentials, see Fig. S5. In addition, the ring/disc charge ( $Q_R/Q_D$ ) increases with disc potential increase (from 2% at -1.2V to 15% at -1.7V) for Au disc. Thus, a large fraction of ORR charge is used to produce soluble  $\text{LiO}_2$  at more negative potentials, while at less negative potentials  $\text{Li}_2\text{O}_2$  formation prevails. At less negative potentials, there is a competition between superoxide formation and disproportionation or further reduction to peroxide so that less superoxide amount is detected. The amount of  $\text{LiO}_2$  detected ( $N/N_0$ ) from chronoamperometry method at different potentials (Fig. S5) is consistent with that obtained from usual RRDE experiment (*cf.* Fig. 9, 10). This demonstrates that the kinetics of ORR and  $\text{Li}_2\text{O}_2$  formation are functions of potential and not time.

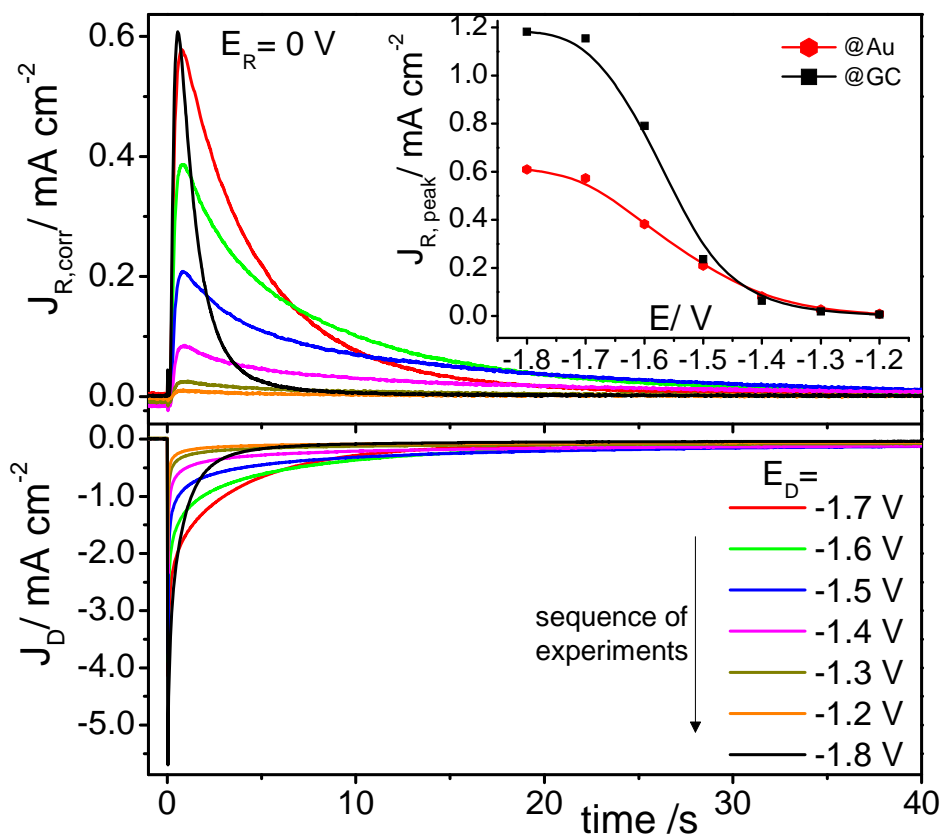


Fig. 13. Current transients for Au disc (lower panel) and Pt ring (upper panel) for ORR in 0.1M LiClO<sub>4</sub>/DMI, where the disc potential was stepped from 0V to the mentioned disc potentials in ORR region and kept for 40 s while the ring potential was held at 0V; the experiment was under 960 rpm. Inset: Ring peak currents for GC and Au discs obtained at different disc potentials from the corresponding ring data.

It is noticeable (in particular, for GC disc, Fig. S4) that the ring currents fall close to zero, while there are still disc currents at -1.4 and -1.5V. At the beginning of the ORR, superoxide is formed over the bare GC surface while at longer times, ORR still takes place on the pre-formed Li<sub>2</sub>O<sub>2</sub> particles so that the ring current vanishes and disc still records. Interestingly, Au and GC electrodes show similar behavior: the ring peak currents at different disc potentials follow the same peak shape of the ring currents observed in their respective CVs (see Fig. S4). Furthermore, larger amount of superoxide is detected for GC electrode than for Au electrode, see inset of Fig. 13a and as well Fig. 9 for comparison.

### 9.3.4. Quantitative investigation of ORR and OER in DMI-based electrolyte: DEMS insight

The incoming flow of a species can be expressed by the faradaic current;  $dn/dt = I_F/zF$  assuming 100% current transfer efficiency. Thus, the correlation between the faradaic current ( $I_F$ ), which is extracted from CV, and the ionic current ( $I_i$ ), which is detected by mass spectrometry, is defined according to eq. 9.10. Using  $K^o$ , the number of electrons transferred per oxygen molecule ( $z$ ) upon oxidation or reduction can be calculated from eq. 9.10.

$$z = \frac{K^o \times I_F}{F \times I_i} \quad \text{eq. 9.10}$$

where,  $K^o$  is a calibration constant determined using a calibration leak experiment.

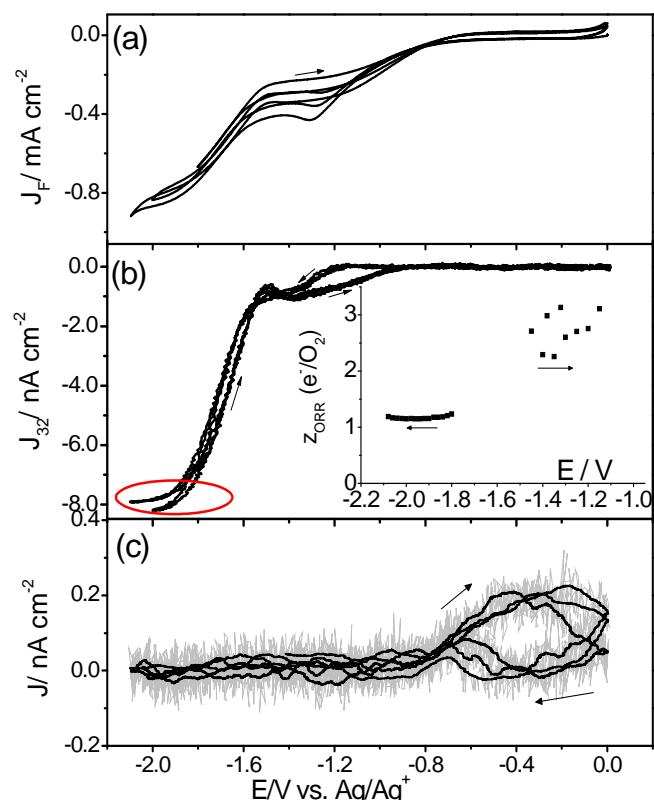


Fig. 14. CVs (a) and MSCVs for mass 32 (b) and mass 44 (c) recorded simultaneously at Au-sputtered membrane electrode for ORR and OER in  $O_2$ -saturated 0.1M TBAClO<sub>4</sub>/DMI with 20  $mV s^{-1}$ . Inset: z-value obtained during ORR, the arrows show the direction of scan.

To validate our cell with the employment of the membrane as an interface and to prove the reasonable value of  $K^o$ , an electrochemical reaction with an expected z-value of one is first characterized, namely ORR in TBA-solution. Fig. 14 shows the CVs and MSCVs recorded simultaneously for three cycles at the Au-sputtered membrane electrode in  $O_2$ -saturated 0.1M TBAClO<sub>4</sub>/DMI with 20  $mV s^{-1}$ . Upon cycling, ORR takes places as can be seen from the faradaic current increase in the negative scale. This is associated with decrease in  $I_{32}$ , which is expected since the reduction products are not volatile, and less oxygen is diffusing to the mass spectrometer. The observation of a plateau at more negative potentials (see the marked red circle, below -1.8V) is due to the diffusion-limited oxygen transport to the electrode caused by continuous bubbling with oxygen in solution. By reversing the scan direction, the reoxidation peak of superoxide is absent because the formed superoxide is soluble and under convection (by bubbling in the cell) it diffuses away from the electrode into the bulk solution. In contrast, the oxidation peak is observed in CV of Fig. 2 because there is no convection (stagnant solution). Small peak for mass 44 is observed at higher potential, corresponding to  $CO_2$  evolution (see Fig. 14c). Since the only source of  $CO_2$  is the electrolyte, this peak could be due to electrolyte decomposition. The decomposition could occur via attack of  $O_2^{\cdot-}$  on the ring  $CH_2$  of DMI, and forming  $CO_2$  by the end, in a similar way to that proposed for NMP.[20] This could be an interpretation of the low stability observed on the electrodes upon cycling in Fig. 2. The pre-peak at ca. -1.2V might be due to side reactions of the electrolyte or reduction to  $Li_2O_2$  from some  $Li^+$  salt residues in the cell since the z-value in this region is

~2.5 e<sup>-</sup>/O<sub>2</sub> but it is improbable since the potential is less than that of superoxide. Quantitative estimation of the amount of electrons consumed per oxygen molecule is done in the diffusion limited region according to eq. 9.10. An average of 1.1 e<sup>-</sup>/O<sub>2</sub> upon reduction is obtained, as shown in the inset of Fig. 14. The behavior of the electrode is quite stable at Au for the repeated three cycles.

DEMS measurements in O<sub>2</sub>-saturated Li<sup>+</sup>/DMI at the Au-sputtered membrane electrode with 20 mV s<sup>-1</sup> are shown in Fig. 15. Onset of ORR is at -1.1V and then the faradaic current increases in the negative direction parallel to a decrease in the ionic currents of mass 32 reaching a peak at about -1.4V after which the electrode is deactivated at -1.8V. In the anodic scan, OER starts at -0.85 V followed by two peaks in the CV, although only the first peak is associated with signal for mass 32 in MSCV. This suggests that the first anodic peak is assigned to the reoxidation of peroxide, and the second peak is attributed to electrolyte decomposition. This is confirmed by the evolution of ionic currents for mass 44 at higher potentials, see Fig. 15c. This could be due to CO<sub>2</sub> evolution and the only source of CO<sub>2</sub> in the system is the electrolyte. In a similar way to NMP, CO<sub>2</sub> can be evolved from DMI upon oxidation.[20]

It is also reasonable to estimate the number of Li<sub>2</sub>O<sub>2</sub> monolayers (i.e. thickness of the film) formed on the surface upon full discharge. The amount of oxygen consumed to form Li<sub>2</sub>O<sub>2</sub> (around 10 nC) corresponds to only two monolayers of Li<sub>2</sub>O<sub>2</sub> per surface Au atom. We suggest that a reduction products-induced electrolyte decomposition occurs during reduction, which leads to a deactivating layer, which is partially oxidized at higher potentials evolving CO<sub>2</sub>, as displayed in Fig. 15d. No CO<sub>2</sub> or O<sub>2</sub> evolutions are observed in Ar-saturated solution (see Fig. S6).

The number of electrons transferred upon ORR in the three cycles is 2 to 2.3 e<sup>-</sup>/O<sub>2</sub>, indicating the reduction of oxygen to Li<sub>2</sub>O<sub>2</sub> either directly or indirectly, see Fig. 15e. Roughly 2 e<sup>-</sup>/O<sub>2</sub> are determined for OER, Fig. 15d. The higher z-value at the peripheries of the oxidation peak could be due to contribution of some double layer charges in calculations. However, the z-values exclude the higher oxidation states of oxide. No significant change is observed among the three repeated cycles on this type of electrode.

Since the apparent coulombic efficiency is based only on the faradaic charge of charging and discharging in which other faradaic processes, for instance, electrolyte decomposition, may interfere, another criterion for rechargeability called the *true coulombic efficiency* is more proper. The true coulombic efficiency takes into account the amount of oxygen consumed and evolved upon oxygen reduction and evolution, respectively. A value of 35% is found for this electrolyte over the three cycles, which is lower than the ideal 100% due to deactivation and some side reactions.

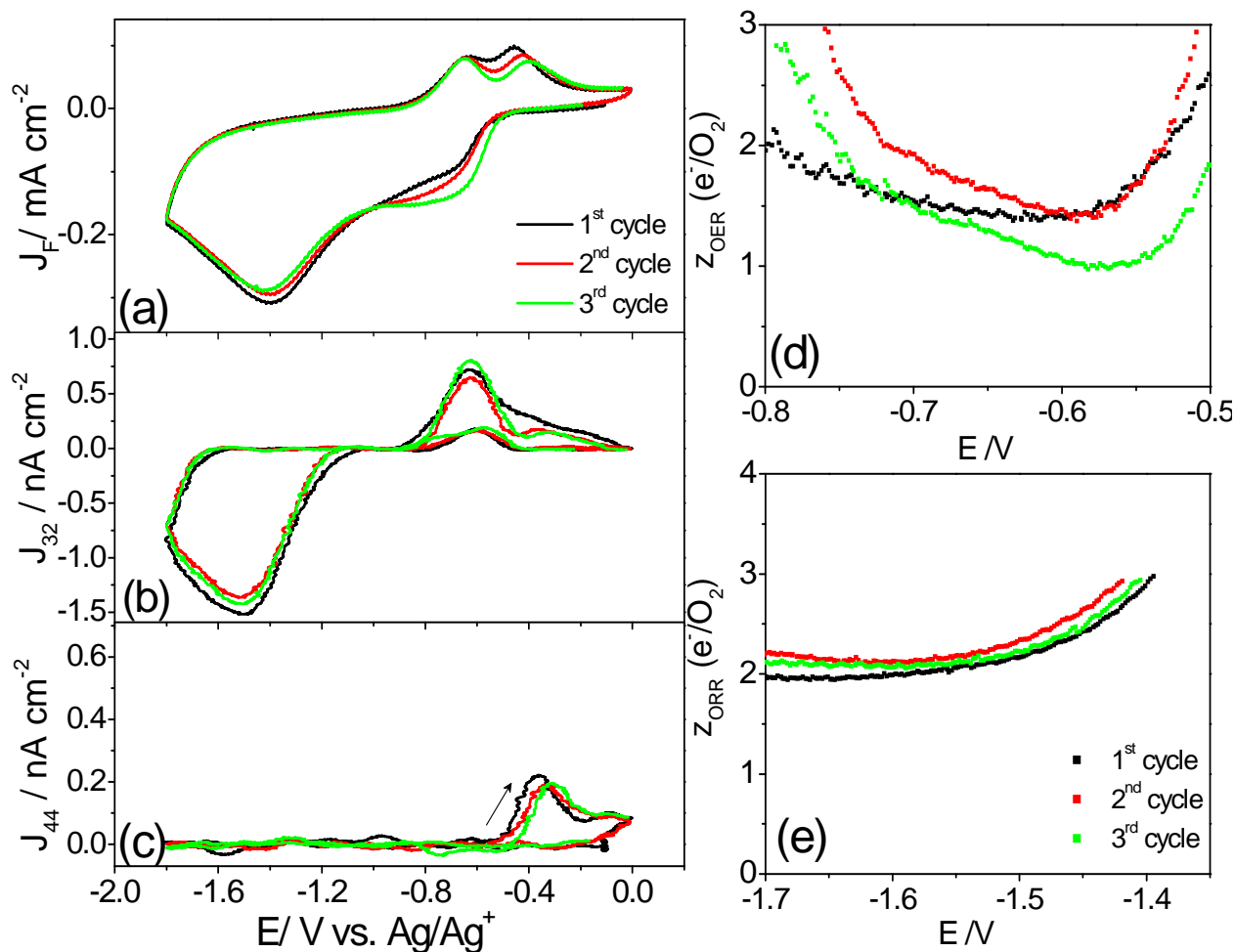
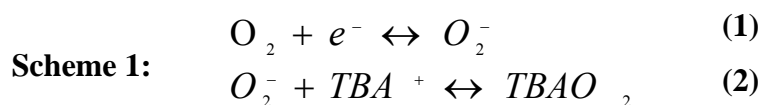


Fig. 15. CVs (a) and MSCVs for mass 32 (b) and mass 44 (c) at Au-sputtered membrane electrode in  $O_2$ -sat. 0.1M  $LiClO_4/DMI$  with  $20\text{ mV s}^{-1}$ . z-values during OER (d), and ORR (cathodic scan) (e) in the same experiment

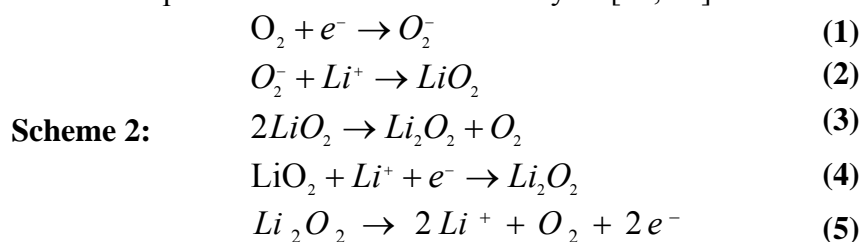
To sum up, from the above results, the ORR mechanism in  $TBA^+/DMI$  electrolyte can be described according to scheme 1, concluding a reversible one-electron reduction of  $O_2$  to superoxide.



The high dielectric constant of DMI could facilitate the solvation of TBA-superoxide. This could stabilize a complex formed upon reaction of  $O_2^{\bullet-}$  with solvated  $TBA^+$  and in turn afford reversibility of  $TBAO_2$ . This is also reported in DMSO.[15] From Randles-Sevcik relation,  $n=0.9$  is obtained, supporting the one-electron reduction mechanism. Nevertheless, part of  $O_2^-$  is consumed in side reactions during reduction. K-L plots agree with a first-order reaction with respect to  $O_2$  concentration. The D value obtained from K-L slope is in a good agreement with that obtained from Stokes-Einstein equation, although the later is for pure solvent and not solution. Tafel slopes close to  $120\text{ mV dec}^{-1}$  (from K-L plots and mass-transport correction) and  $1e^-/O_2$  from DEMS results support the mechanism of one-electron reduction to superoxide. Moreover, no OER peaks corresponding to peroxide or oxide are observed. This is in agreement with results for  $TBA^+/DMSO$ .[22]

In Li<sup>+</sup> containing electrolyte, the kinetics of oxygen reactions is affected by the electrode material. On GC, one reduction peak and two oxidation peaks are observed in CV (Fig. 7). The reduction is assigned to Li<sub>2</sub>O<sub>2</sub> formation (mostly via 2e<sup>-</sup>-reduction), while the two anodic peaks are due to direct oxidation of different layers of Li<sub>2</sub>O<sub>2</sub> on the electrode.

A proposed mechanism of ORR and OER in the Li<sup>+</sup>-containing DMI electrolyte is shown in scheme 2. A generalized scheme is also shown in chapter 8 (Fig. 21). Oxygen is first adsorbed on the electrode and reduced to O<sub>2</sub><sup>-</sup> (reaction 1) which then can follow both direct and indirect reduction pathways: O<sub>2</sub><sup>-</sup> reacts directly with Li<sup>+</sup> to LiO<sub>2</sub>, which is a short-lived intermediate (reaction 2). This superoxide is stabilized in solution and thus ca. 80% of LiO<sub>2</sub> are detected on the ring upon rotation. Subsequently, LiO<sub>2</sub> could either chemically disproportionate to Li<sub>2</sub>O<sub>2</sub> in solution and precipitate on the surface causing blocking (reaction 3), or undergo a second reduction to Li<sub>2</sub>O<sub>2</sub> on the surface (Epc1, reaction 4). This surface-mediated pathway is most probable in this electrolyte as evidenced by 2e<sup>-</sup>/O<sub>2</sub> from DEMS. The reactions in DMI are similar to that in DMSO but ~90% of LiO<sub>2</sub> was detected in DMSO in solution. The amount of superoxide depends on electrode material, potential window and the rotation rate. The first reduction step is shown to be kinetically the rate determining step. The oxidation of the formed peroxide is direct to O<sub>2</sub> without passing through LiO<sub>2</sub> (Epa1, Epa2 reaction 5) (since no ring current detected at potential of Li<sub>2</sub>O<sub>2</sub> oxidation). The reactions discussed here, and in scheme 2 are similar to previous ones in other electrolytes.[27, 42]



The electrode material influences the kinetics of oxygen reactions. In TBA-solution, GC and Au are more active than Pt, which might be due to formation of a polymeric layer of DMI near the surface and thus decreases the stability. In Li<sup>+</sup> solution, Pt shows better activity for oxidation than GC although GC is slightly better for reduction. Tafel slope close to 120 mV dec<sup>-1</sup> for reduction implies that a one-electron reduction to superoxide is the r.d.s., and the second reduction step is then faster. Thus, only one reduction peak is observed since the lifetime of superoxide is short. D of O<sub>2</sub> in Li-solution is close to that in TBA-solution considering n=1.

#### 9.4. Conclusion

In this study, a novel aprotic electrolyte based on DMI is introduced and characterized for the first time for ORR and OER for Li-O<sub>2</sub> battery application. The electrochemical performance of different electrode materials for ORR and OER in this new solvent is investigated. The mechanism and the kinetics of oxygen reactions in TBA<sup>+</sup> and Li<sup>+</sup>-DMI are elucidated using RRDE technique. Reversible superoxide formation is found in TBA<sup>+</sup>-solution. Both the direct and indirect pathways of Li<sub>2</sub>O<sub>2</sub> occur. The role of the electrode material is significant: ORR/OER activity is in the order GC ≥ Au > Pt in terms of overpotential in Li<sup>+</sup>-salt. Kinetic studies revealed a Tafel slope close to 120 mV/dec, suggesting that the one-electron reduction to superoxide is the rate determining step. A blocking layer of Li<sub>2</sub>O<sub>2</sub> is formed, which

influences the behavior in the consecutive cycles. RRDE chronoamperometry has a benefit of deconvolution of time and potential effects on the kinetics which are not separated in usual RRDE experiment. The results show that  $\text{Li}_2\text{O}_2$  formation is a function of potential and not time. Interestingly, ring current transients show a peak and the ring peak currents depend on the applied disc potential and follow the same shape observed in the typical CV. DEMS results show the formation and decomposition of  $\text{Li}_2\text{O}_2$  as the major product since roughly  $2e^-/\text{O}_2$  are obtained. However, side reactions occur. A true coulombic efficiency of about 35% is obtained. Thus, further improvement is required with better understanding of the surface structure of the formed  $\text{Li}_2\text{O}_2$ .

These results offer an important guideline for the development and characterization of an electrolyte with desired properties for metal-air batteries. Further investigations of the new electrolyte with real gas diffusion electrode under galvanostatic conditions are interesting to get the charge-discharge curves on a large surface area electrode. Testing mixtures of this solvent with others in a blend could also offer a promising performance.

## 9.5. References

- [1] K.M. Abraham, Z. Jiang, *Journal of the Electrochemical Society* 143 (1996) 1-5.
- [2] P.G. Bruce, S.A. Freunberger, L.J. Hardwick, J.-M. Tarascon, *Nat Mater* 11 (2012) 19-29.
- [3] B.D. McCloskey, D.S. Bethune, R.M. Shelby, G. Girishkumar, A.C. Luntz, *J. Phys. Chem. Lett.* 2 (2011) 1161-1166.
- [4] D. Xu, Z.-l. Wang, J.-j. Xu, L.-l. Zhang, X.-b. Zhang, *Chem. Commun.* 48 (2012) 6948-6950.
- [5] D.G. Kwabi, T.P. Batcho, C.V. Amanchukwu, N. Ortiz-Vitoriano, P. Hammond, C.V. Thompson, Y. Shao-Horn, *The Journal of Physical Chemistry Letters* 5 (2014) 2850-2856.
- [6] M. Marinaro, S. Theil, L. Jörissen, M. Wohlfahrt-Mehrens, *Electrochimica Acta* 108 (2013) 795-800.
- [7] F.S. Gittleson, R.C. Sekol, G. Doubek, M. Linardi, A.D. Taylor, *Phys. Chem. Chem. Phys.* 16 (2014) 3230-3237.
- [8] J. Read, *Journal of the Electrochemical Society* 153 (2006) A96-A100.
- [9] J. Read, K. Mutolo, M. Ervin, W. Behl, J. Wolfenstine, A. Driedger, D. Foster, *Journal of the Electrochemical Society* 150 (2003) A1351-A1356.
- [10] S.A. Freunberger, Y. Chen, Z. Peng, J.M. Griffin, L.J. Hardwick, F. Barde, P. Novak, P.G. Bruce, *Journal of the American Chemical Society* 133 (2011) 8040-8047.
- [11] H.-G. Jung, J. Hassoun, J.-B. Park, Y.-K. Sun, B. Scrosati, *Nature Chemistry* 4 (2012) 579-585.
- [12] C.O. Laoire, S. Mukerjee, E.J. Plichta, M.A. Hendrickson, K.M. Abraham, *Journal of the Electrochemical Society* 158 (2011) A302-A308.
- [13] S.A. Freunberger, Y. Chen, N.E. Drewett, L.J. Hardwick, F. Barde, P.G. Bruce, *Angewandte Chemie-International Edition* 50 (2011) 8609-8613.
- [14] Z. Peng, S.A. Freunberger, Y. Chen, P.G. Bruce, *Science* 337 (2012) 563-566.
- [15] C.O. Laoire, S. Mukerjee, K.M. Abraham, E.J. Plichta, M.A. Hendrickson, *Journal of Physical Chemistry C* 114 (2010) 9178-9186.
- [16] C. Bondue, P. Reinsberg, A.-E.-A.A. Abd-El-Latif, H. Baltruschat, *Phys. Chem. Chem. Phys.* 17 (2015) 25593-25606.
- [17] R. Younesi, P. Norby, T. Vegge, *ECS Electrochemistry Letters* 3 (2014) A15-A18.
- [18] M.J. Trahan, S. Mukerjee, E.J. Plichta, M.A. Hendrickson, K.M. Abraham, *Journal of the Electrochemical Society* 160 (2013) A259-A267.

- [19] V.S. Bryantsev, V. Giordani, W. Walker, M. Blanco, S. Zecevic, K. Sasaki, J. Uddin, D. Addison, G.V. Chase, *Journal of Physical Chemistry A* 115 (2011) 12399-12409.
- [20] H. Wang, K. Xie, L. Wang, Y. Han, *Journal of Power Sources* 219 (2012) 263-271.
- [21] Y.-M. Chen, A. Xie, Y. Zhu, *Chemelectrochem* 2 (2014) 208-212.
- [22] C.J. Bondue, A.A. Abd-El-Latif, P. Hegemann, H. Baltruschat, *Journal of the Electrochemical Society* 162 (2015) A479-A487.
- [23] M.C. America, <http://www.mitsuichemicals.com/dmi.htm>, Mitsui Chemicals Group, 2016.
- [24] R. Chen, F. Wu, H. Liang, L. Li, B. Xu, *Journal of The Electrochemical Society* 152 (2005) A1979-A1984.
- [25] A. Endo, M. Miyake, T. Hirato, *Electrochimica Acta* 137 (2014) 470-475.
- [26] M. Lissel, E.V. Dehmlow, *Tetrahedron Letters* 19 (1978) 3689-3690.
- [27] C.J. Allen, S. Mukerjee, E.J. Plichta, M.A. Hendrickson, K.M. Abraham, *J. Phys. Chem. Lett.* 2 (2011) 2420-2424.
- [28] H. Baltruschat, *Journal of the American Society for Mass Spectrometry* 15 (2004) 1693-1706.
- [29] G. Gritzner, *Journal of Molecular Liquids* 156 (2010) 103-108.
- [30] H. Baltruschat, *Journal of the American Society for Mass Spectrometry* 15 (2004) 1693-1706.
- [31] A. Sutherland, *philosophical Magazine* 9 (1905) 781-785.
- [32] M. Khodayari, P. Reinsberg, A.A. Abd-El-Latif, C. Merdon, J. Fuhrmann, H. Baltruschat, *CHEMPHYSICHEM* (2016).
- [33] T. Sato, Y. Hamada, M. Sumikawa, S. Araki, H. Yamamoto, *Industrial & Engineering Chemistry Research* 53 (2014) 19331-19337.
- [34] S.D. Bergin, Z. Sun, D. Rickard, P.V. Streich, J.P. Hamilton, J.N. Coleman, *ACS Nano* 3 (2009) 2340-2350.
- [35] E.J. Calvo, N. Mozhzhukhina, *Electrochem. Commun.* 31 (2013) 56-58.
- [36] J. Herranz, A. Garsuch, H.A. Gasteiger, *Journal of Physical Chemistry C* 116 (2012) 19084-19094.
- [37] A.J. Bard, L.R. Faulkner, *Electrochemical Methods: Fundamentals and Applications*, 2nd ed., John Wiley & Sons Inc., New York, Weinheim, 2001.
- [38] D.G. Kwabi, M. TuÅ, odziecki, N. Pour, D.M. Itkis, C.V. Thompson, Y. Shao-Horn, *The Journal of Physical Chemistry Letters* 7 (2016) 1204-1212.
- [39] M.J. Trahan, I. Gunasekara, S. Mukerjee, E.J. Plichta, M.A. Hendrickson, K.M. Abraham, *Journal of the Electrochemical Society* 161 (2014) A1706-A1715.
- [40] W. Torres, N. Mozhzhukhina, A.Y. Tesio, E.J. Calvo, *Journal of the Electrochemical Society* 161 (2014) A2204-A2209.
- [41] V. Viswanathan, K.S. Thygesen, J.S. Hummelshoj, J.K. Nørskov, G. Girishkumar, B.D. McCloskey, A.C. Luntz, *Journal of Chemical Physics* 135 (2011) 10.
- [42] Z. Peng, S.A. Freunberger, L.J. Hardwick, Y. Chen, V. Giordani, F. Bardé, P. Novák, D. Graham, J.-M. Tarascon, P.G. Bruce, *Angew. Chem.* 50 (2011) 6351-6355.

## Supporting Information

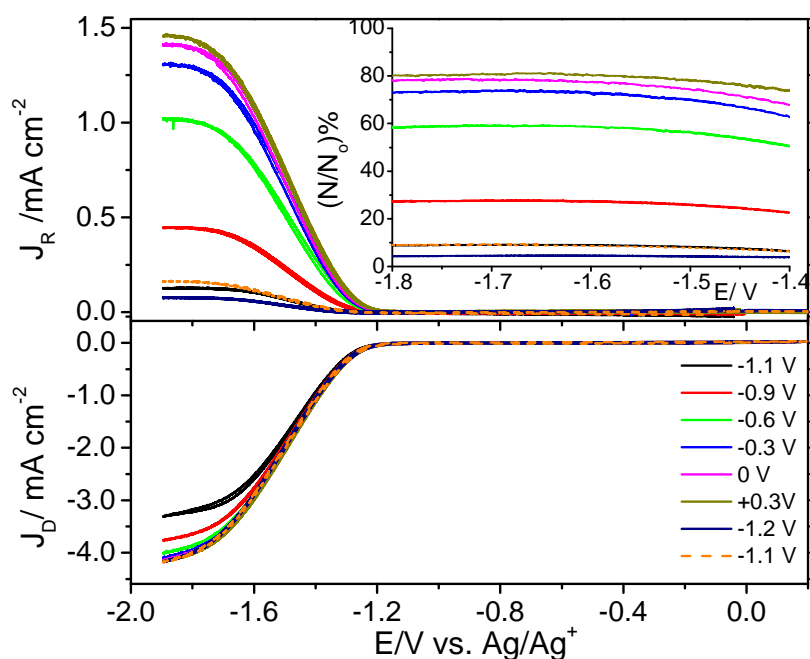
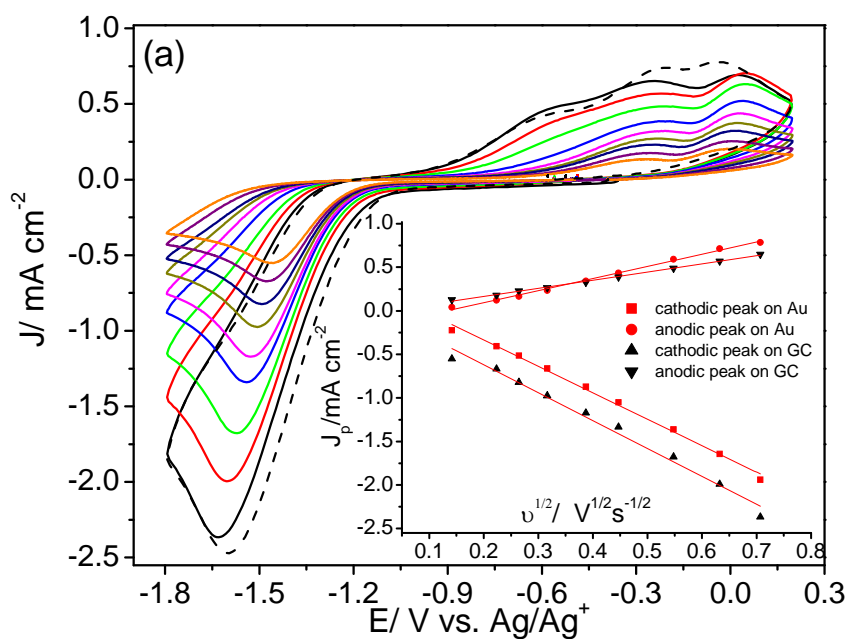


Fig. S1. RRDE curves at GC electrode with 20 mV/s and 1500 rpm in O<sub>2</sub>-sat. 0.1M TBAClO<sub>4</sub>/DMI. Ring was held at different potentials. Inset is the  $(N/N_0)\%$  at different rotation rates versus potential.



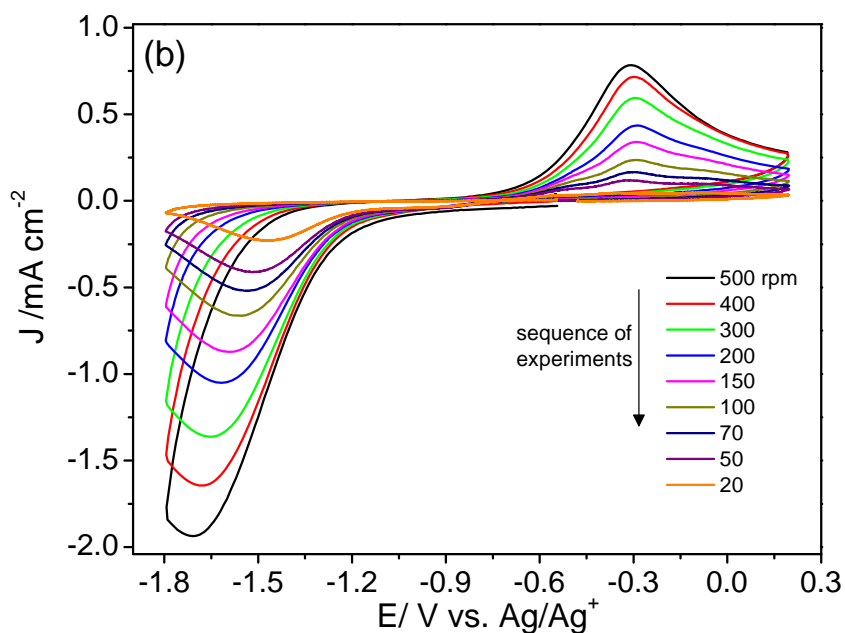


Fig. S2. CVs at GC (a) and Au (b) electrodes in O<sub>2</sub>-sat. 0.1M LiClO<sub>4</sub>/DMI at various scan rates. Inset: cathodic and anodic peak currents vs. square route of scan rate. Dashed line is repeated scan.

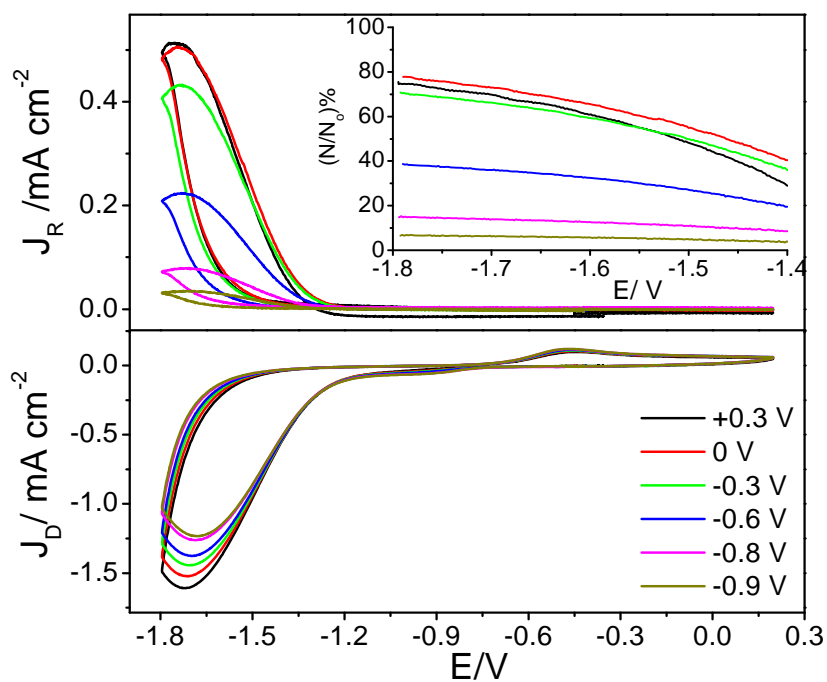


Fig. S3. RRDE curves at Au electrode obtained with 100 mV/s and 1500 rpm in O<sub>2</sub>-sat. 0.1M LiClO<sub>4</sub>/DMI. Ring was held at different potentials. Inset is the (N/N<sub>0</sub>)% vs. potential in the cathodic scan.

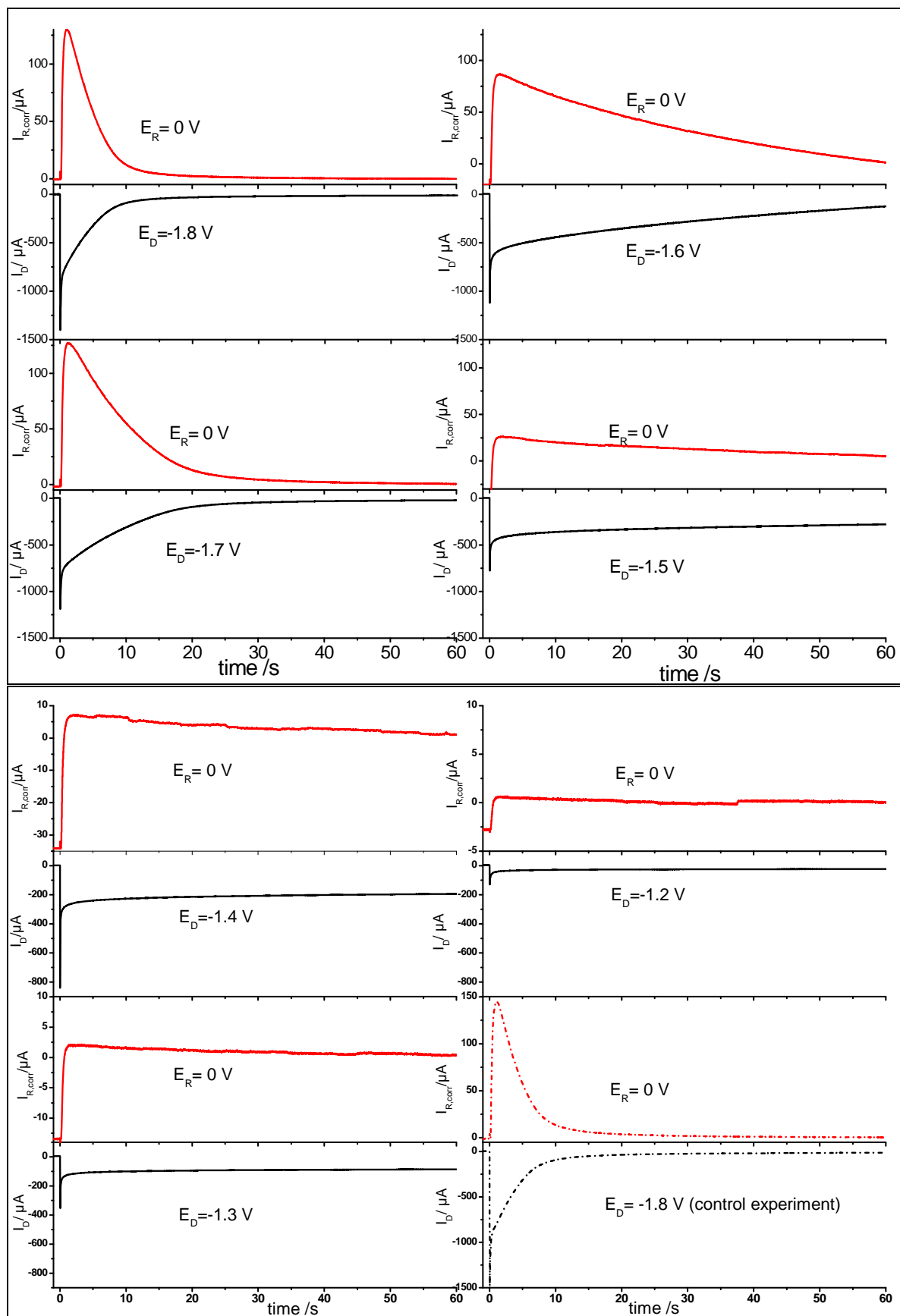


Fig. S4. Current transients at GC disc and Pt ring for ORR in 0.1M LiClO<sub>4</sub>/DMI, where the disc potential was stepped from 0V to the mentioned disc constant values in ORR region and kept for 60 s while the ring potential was held at 0V; the experiment was done under 960 rpm; Dashed graph is a control experiment for reproducibility.

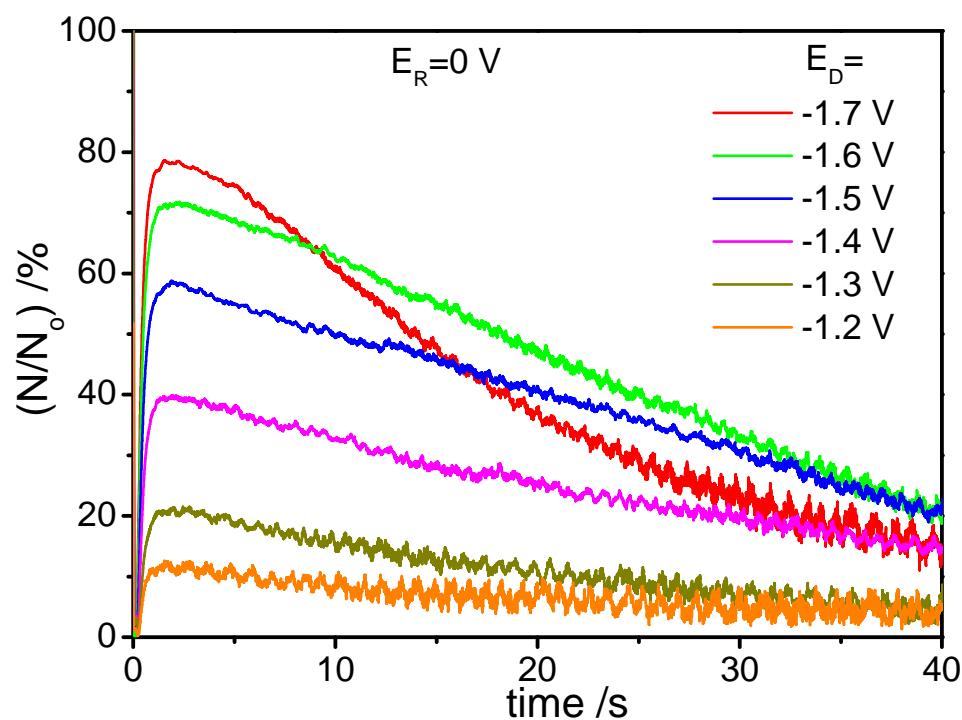


Fig. S5. The  $(N/N_0)$  percentage vs. time obtained at Au-disc and Pt-ring for the experiments shown in Fig. 13.

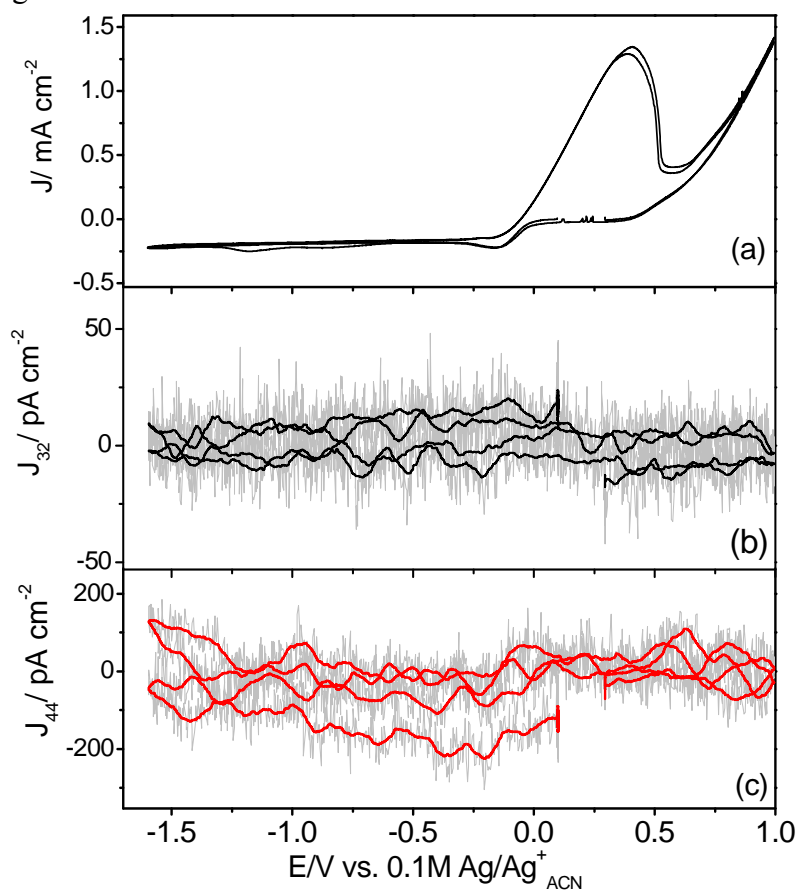


Fig. S6. CVs (a) and MSCVs for mass 32 (b) and mass 44 (c) at Au-sputtered membrane electrode in Ar-sat. 0.1M LiClO<sub>4</sub>/DMI with 20 mV s<sup>-1</sup>.

The suitability of Au-sputtered (50nm) membrane as a GDE in this solution is investigated: oxygen is supplied from the gas side of the membrane, and penetrates through the pores reaching the electrolyte phase; afterwards it reacts with  $\text{Li}^+$  forming  $\text{Li}_2\text{O}_2$ . In this setup, which has been previously described by our group,[22] the volume underneath the membrane was firstly evacuated. Then, the angle valve between the vacuum phase and the electrochemical cell was closed, and the dosing valve connecting the volume underneath the membrane electrode to the oxygen inlet was opened to introduce  $\text{O}_2$  under pressure of 470 mbar through the steel frit reaching the working electrode. In the first cathodic sweep, the potential was scanned from -0.1V to -1.42V in 0.1M  $\text{LiClO}_4/\text{DMI}$ , and afterwards it is stopped for 3 minutes at -1.42V, where ORR takes place while the electrolyte was purged with Ar. Only CV was recorded since the mass spectrometer is not connected (red curve in Fig. S7a). Then, the volume underneath the electrode was again evacuated, and next the mass spectrometer was connected. The current drops to zero as the oxygen supply was cut off. In the first anodic sweep, potential was scanned to 0V. The pre-reduced oxygen on the electrode is reoxidized and oxygen is evolved as recorded by CV and MSCV, see the blue curve of Fig. S7b. In the second sweep (black curve), oxygen was supplied from the solution so that the dissolved oxygen is reduced and oxidized as in typical experiments. ORR onset appears on GDE at similar potential (ca. -1.15V) of the typical experiment in which oxygen was supplied from solution (*cf.* Fig. 15). In MSCV, there is an oxygen evolution peak in the cathodic scan (black curve) at about -0.7V which is not well understood, but it might be that not all  $\text{Li}_2\text{O}_2$  was oxidized in the preceding anodic scan and thus is oxidized in the cathodic scan.

The  $z$ -value for ORR is calculated, and found to be 2.6, as shown in Fig. S7e. This indicates that ORR proceeds via the direct formation of  $\text{Li}_2\text{O}_2$  as the main reduction product through 2e-reduction process. However,  $z$ -value of 2-3.5 $e^-/\text{O}_2$  is obtained during OER after GDE experiment, and 1.5-2.5 in the consecutive cycle when oxygen is supplied from solution in the first cycle, as shown in Fig. S7d.

Therefore, Au-sputtered membrane electrode shows feasibility as a model for GDE with  $z$ -values fitting well to the reduction of oxygen to peroxide and vice versa. Interesting is that much larger current density during reduction is achieved when the electrode is employed as a GDE (ca. 0.45  $\text{mA cm}^{-2}$ ) compared to the normal oxygen-saturated solution (0.26  $\text{mA cm}^{-2}$ ) although the oxidation current is not larger, which might be due to more blocking when GDE is used. Larger ORR current is attributed to the more efficient oxygen transport from the gas phase to the electrode than oxygen diffusion in solution to the electrode. Noteworthy, there is ca. 60 mV positive potential shift of the oxidation peak when oxygen was reduced on the GDE in the preceding cathodic scan compared to that when oxygen was supplied from solution, see Fig. S7a, b. Thus, some side reactions other than oxygen evolution take place in the anodic sweep when oxygen was reduced in the previous cathodic sweep from the gas side. This reaction interferes with oxygen evolution and therefore increases the  $z$ -value and delays the oxidation to higher overpotentials, as can be noticed in the blue curve. The anodic peak at ca. -0.7V in MSCV in the black curve is also observed in the normal experiment, but is more obvious in the GDE experiment since more oxygen or  $\text{CO}_2$  are supplied through the pores of the electrode and hence more side products.

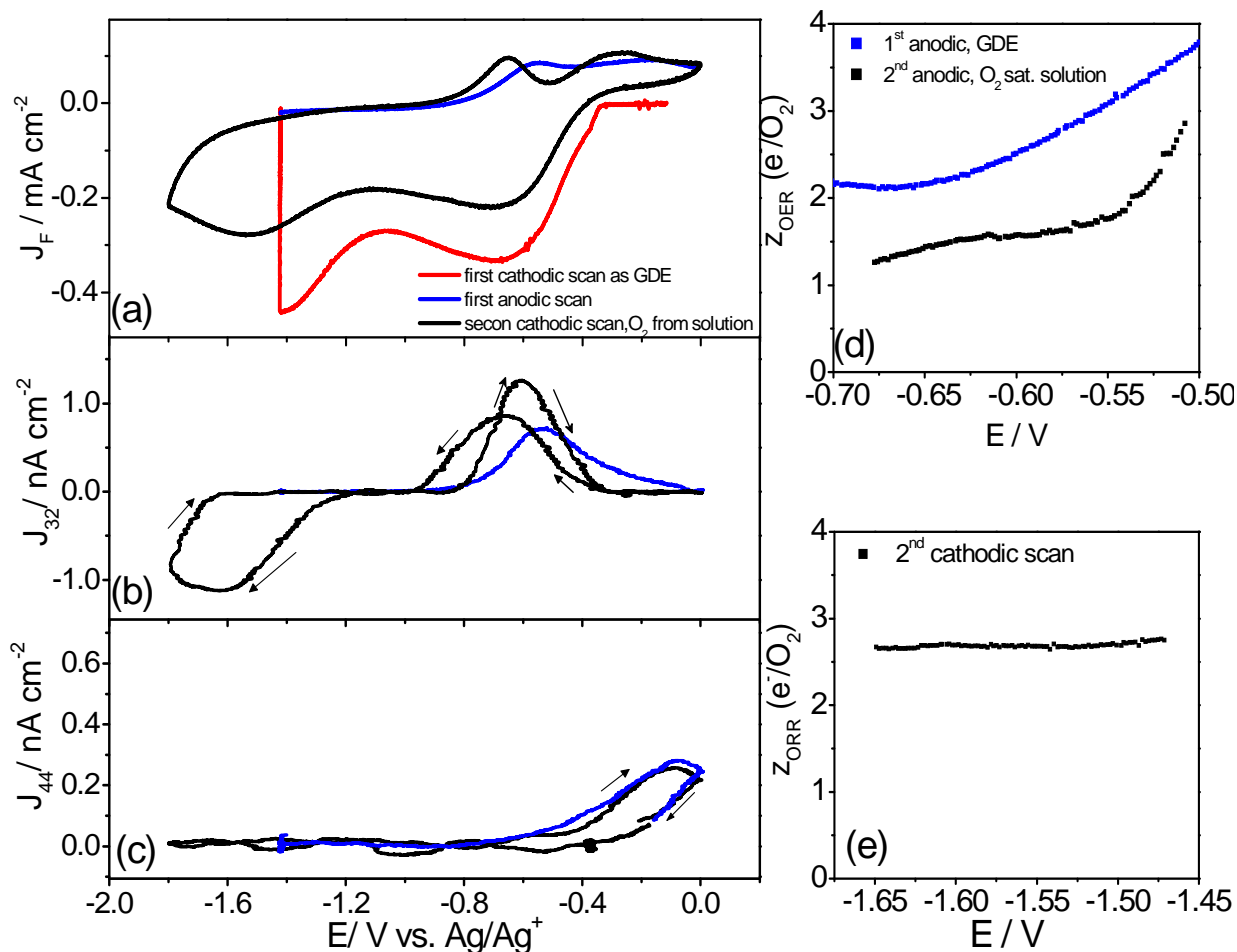


Fig. S7. Simultaneous CVs (a) and MSCVs for mass 32 (b) and mass 44 (c) during ORR/OER on Au-sputtered membrane as GDE electrode in 0.1M LiClO<sub>4</sub>/DMI electrolyte with 20 mV/s. In the first cathodic sweep oxygen was supplied from the gas side of the membrane under pressure of 470 mbar while solution was purged with Ar (red curve); First anodic sweep: in Ar-saturated in solution (blue); second sweep: O<sub>2</sub> was purged in solution (black). z-values for OER (d) and for ORR (e).

## 10. Summary and future directions

One of the major future tasks to power electric vehicles (EVs) and total electrification of transportation on a long-term basis is the development of advanced energy storage systems. The use of rechargeable batteries is one of the most promising solutions based on electrochemistry, and nowadays Lithium-ion batteries (LIBs) are part of our portable devices and EVs. The state-of-the-art LIBs provide long cycle life and the highest energy density available; however, their low specific energy (i.e. high weight) and high-cost limit their implementation on a full battery-powered EV. As an alternative, non-aqueous Li-air batteries, which are based on the reaction of lithium with oxygen, are expected to provide higher storage capabilities than LIBs (5-fold higher theoretical specific energy density).

Thus, if realized, the Li-air battery would be the system with the highest specific energy density (longer travel distance). Therefore, Li-air (Li-O<sub>2</sub>) batteries have captured the spotlight as a future class of energy storage systems. Despite the intensive research on the Li-air batteries, some obstacles are undermining their commercialization: sluggish kinetics of oxygen reduction (ORR) and evolution (OER) in the air electrode; high overpotentials; in addition to instability of organic electrolytes. These issues reduce the operational life time of the battery. Since the kinetics of oxygen reactions in alkaline media are known, one possible approach is the mixed aqueous-nonaqueous battery, in which the anode and cathode are separated by a Li<sup>+</sup>-ion conducting membrane. Consequently, in order to improve the kinetics in an alkaline media, a bifunctional catalyst has to be developed, which is the focus of the first part of this thesis.

In alkaline media, a bifunctional carbon-free mixed catalyst is developed and characterized. This catalyst is based on a combination of two non-precious components (Ag+Co<sub>3</sub>O<sub>4</sub>) being highly active towards both, ORR and OER, for alkaline media. Two main issues are addressed in this part: First, screening of several catalysts using RRDE technique to find the most efficient mixed catalyst composition and its optimization. Second, surface and spectroscopic characterization in order to better understand the origin of the enhanced activity and the synergistic effect. The conclusions that can be drawn from this part are:

- In this work, we completely substituted carbon (which causes corrosion problems) with Ag, which acts as a support of a metal oxide or perovskite in the mixed catalyst. Pure Ag showed a decent good ORR activity, whereas Co-oxide showed good OER activity. Thus, combination of the desired properties of Ag and Co-oxide in one blend is our applied scenario. Initial measurements on Ag/Co (50/50 wt %)/GC catalyst showed unsatisfied activity, and lower stability. This is attributed to the agglomeration of the used Ag flakes (40 μm), and the small surface area of the 40 μm Co particles. Therefore, other sizes and structures of each of the components are tested to get the optimized catalytic response.
- The loading of the catalyst has a clear effect not only on the diffusion-limited current, but also on the activity of the catalyst and the amount of peroxide anions generated. For example: higher loadings of Ag (40 μm) lead to higher current densities for OER and ORR, and less than 4% of HO<sub>2</sub><sup>-</sup>. The concentration of LiOH electrolyte also influences the activity of the catalysts, where in higher concentrations, less activities and lower diffusion currents are observed. The same effect is also observed on Co<sub>3</sub>O<sub>4</sub> and mixed Ag+Co<sub>3</sub>O<sub>4</sub> catalysts. The cations of the electrolyte affect the performance of the catalyst in alkaline media. KOH solution showed higher activity for ORR and OER than LiOH.

- The particle size exerts an influence on the activity: Ag311 (1  $\mu\text{m}$ ) showed comparable ORR activity to Ag (pc), and higher than that of Ag (40  $\mu\text{m}$ ) catalyst in terms of half-wave potentials ( $E_{1/2}$ ). Therefore, Ag311 is used for the further investigations.  $\text{Co}_3\text{O}_4$  (50 nm size) exhibited about 80 mV lower overpotential for ORR, and ca. two times higher current density for OER than the 10  $\mu\text{m}$ -catalyst due to the larger surface area. In addition, only 25% of peroxide is detected for the smaller particle size catalyst compared to 60% for the larger one, indicating different reaction pathways.
- From the screening results, the development of a carbon-free highly efficient bifunctional catalyst based on Ag311+ $\text{Co}_3\text{O}_4$  hybrid is achieved. The catalyst has been prepared by physical mixing of the two components. RRDE results showed that the mixed catalyst outperformed its single components. The weight ratio of Ag to  $\text{Co}_3\text{O}_4$  in the mixture affects the activity: Ag311+ $\text{Co}_3\text{O}_4$  (10 wt%) catalyst exhibited the best total activity, although 20 wt%  $\text{Co}_3\text{O}_4$  showed slightly higher OER activity. Thus, 10-20wt% is the optimum composition in our study. For ORR, this 10% mixed catalyst exhibited >300 mV lower overpotential than  $\text{Co}_3\text{O}_4$  alone, slightly lower overpotential than pure Ag311, and not much higher overpotential than the commercial Pt/C catalyst. For OER, the mixed catalyst showed 1.5 times and 4 times higher current density than that of  $\text{Co}_3\text{O}_4$  and Ag, respectively. The potential difference between ORR and OER at 1  $\text{mA cm}^{-2}$  is ca. 0.85V, which is comparable to that of the noble metal-based catalysts. The bifunctional catalyst showed good stability. A negligible peroxide anion formation suggests that the mixed catalyst follows the direct 4-electron ORR pathway with  $\text{OH}^-$  as the final product. Tafel slopes for ORR are similar for the Ag and the mixed catalyst ( $\sim 80 \text{ mV dec}^{-1}$ ), suggesting that ORR is dominated by Ag in the mixed catalyst. On the other hand, Tafel slopes for OER on  $\text{Co}_3\text{O}_4$  and mixed catalysts are similar, indicating that  $\text{Co}_3\text{O}_4$  is the dominant factor in OER activity of the mixed catalyst. Thus, the synergistic effect between Ag and  $\text{Co}_3\text{O}_4$  in mixed catalyst is the reason for the enhanced activity.
- Surface analysis demonstrated the influence of the morphology of the mixed catalyst on oxygen activity. SEM and EDX (done by S. Eswara, Ulm Univ.) showed that  $\text{Co}_3\text{O}_4$  nanoparticles partially cover the Ag microparticles. Pb-UPD is used to determine the real surface area of Ag-based catalysts. The results showed that addition of 10 wt% of  $\text{Co}_3\text{O}_4$  to Ag in the mixture leads to 88% coverage of the Ag surface by  $\text{Co}_3\text{O}_4$  and in despite of that leads to a higher ORR activity than pure Ag. This catalyst also showed higher OER activity than the 100%  $\text{Co}_3\text{O}_4$  catalyst of the same loading.
- EIS results of the mixed catalyst showed that the total impedance at oxidation potentials is significantly higher than at reduction potentials. Within the oxidation region, the impedance decreases as the potential increases from 1.2V to 1.75V due to the oxidization of Ag to  $\text{Ag}_2\text{O}$ . This is further oxidized to  $\text{Ag}^I\text{Ag}^{III}\text{O}_2$ , which has higher conductivity than  $\text{Ag}_2\text{O}$ . Moreover, the mixed 10 wt% catalyst displayed the smallest impedance at 0.7V (ORR) compared to its individual components. While at 1.6V,  $\text{Co}_3\text{O}_4$  catalyst reveals the smallest resistance.
- To better understand the origin of the synergistic interaction, XPS measurements (done by C. Bondue, Uni. Bonn) were carried out. XPS results demonstrated that a redox switching is taking place in  $\text{Co}_3\text{O}_4$  when it is in contact with Ag particles. This redox switching

process is not observed for pure  $\text{Co}_3\text{O}_4$ , suggesting that this process is a probable explanation of the improved catalytic activity in the mixed catalyst.

- A direct evidence for oxygen evolution at the catalysts is provided by DEMS. Results showed an onset of 1.55V for OER at single  $\text{Co}_3\text{O}_4$  and the mixed catalysts.
- To verify whether this synergistic effect can be achieved with other materials, and to determine, which is the most determinant component (Ag or the oxide), a mixed Ag+perovskite (LSF) is characterized. This catalyst showed high bifunctional activity, indicating a synergism in Ag+perovskites mixture as well. In another set of experiments, Ag is replaced with Ni (mixed Ni+ $\text{Co}_3\text{O}_4$  catalyst). However, this mixture showed lower activity than the Ag311+ $\text{Co}_3\text{O}_4$  catalyst, implying the effective role of the support in the enhanced bifunctional catalytic activity.
- The answer of the question: Do oxygen atoms in  $\text{Co}_3\text{O}_4$  spinel take part in OER? is drawn from the results of the isotope labeling together with DEMS. For this purpose, a novel small-volume DEMS cell is developed for the first time for  $\leq 0.5\text{ml}$  solution and disc electrodes. It showed a very short delay time and high sensitivity for oxygen. The results demonstrated that in  $\text{H}_2^{18}\text{O}$ -containing electrolyte, the lattice oxygen in the oxide is labeled with  $^{18}\text{O}$ . Consequently, the oxide layer takes part in oxygen evolution via an oxygen exchange mechanism. Further evaluation of the data revealed that the amount of lattice oxygen participating in the oxygen exchange mechanism is close to 0.2% from the total catalyst loading (for  $\text{Co}_3\text{O}_4$ , 50 nm) which corresponds to  $\sim 24\%$  of the surface atoms. Therefore, only the interfacial part of the catalyst takes part in oxygen evolution. This mechanism is reproducible with different catalyst loadings and different particle sizes. Interestingly, the amount of oxygen exchanged on the mixed Ag+ $\text{Co}_3\text{O}_4$  catalyst is higher than in the single  $\text{Co}_3\text{O}_4$  catalyst, which could support the improved electrocatalytic activity of the mixed catalyst. Several methods are applied to estimate the real surface area and the number of active sites of the catalyst: simple ball model, DL-capacitance model, redox peak model, and isotope exchange model. Comparable results are obtained from the different methods and are similar to BET data in most cases.
- Finally, the possible origins of the improved activity are: synergistic effect, which could be due to redox switching; electronic effect; spillover effect; reduced agglomeration of the particles and increased triple phase boundaries.

The work in organic electrolytes (in the second part of this thesis) aimed to better understand the electrochemical reactions taking place in Li- $\text{O}_2$  system. The research activities in this part are addressed towards:

- Deepening the knowledge on the mechanism and the kinetics of ORR/OER in aprotic electrolytes using RRDE since this issue was rarely investigated and is not well understood in literature.
- Quantitative analysis of the number of electrons consumed/evolved per oxygen molecule during discharge/charge, and consequently, the nature of the product ( $\text{LiO}_2$  or  $\text{Li}_2\text{O}_2$ ), in addition to identification of byproducts.
- Better understanding of the role of the solvent in the mechanism. To enhance the rechargeability, blends of electrolytes are investigated. This idea is based on combining the desired properties of two solvents in a mixed electrolyte.

iv) Developing a novel electrolyte which has promising physical properties and studying its behavior in Li-O<sub>2</sub> system.

The conclusions that can be drawn from the results of this part are:

- In the beginning, propylene carbonate PC (classical solvent for LIB) is studied with DEMS, and showed to decompose in Ar-saturated Li-solution with evolution of CO<sub>2</sub> as the main product. Other parasitic products like propene and propanal are detected. The stability potential window depends on the electrode material: BDD>GC>Au>Pt in terms of the potential window. Water facilitates the decomposition of PC. Thus, it is not suited as a stable electrolyte.
- Further investigations of the mechanism and kinetics are carried out on relatively stable electrolytes (G4 and DMSO-based electrolytes). Deactivation and reactivation of the electrode in G4 (and also in DMSO) are observed depending on the operational potential window. While, restricting the upper limit to lower potentials leads to deactivation. On the other hand, extending the potential to higher values causes reactivation. DEMS results showed the evolution of CO<sub>2</sub> at higher potentials. Thereby, we conclude that a passive film is formed during reduction from the reaction of the reduction products with the electrolyte. This deactivating film is oxidized, and partially removed at higher potentials evolving CO<sub>2</sub>. Some other undesired faradaic reactions might occur during OER. Thus, the number of electrons during OER is in some cases slightly higher than the ideal 2e<sup>-</sup>/O<sub>2</sub>.
- The electrode material has a clear effect on oxygen evolution kinetics: Pt is more active for OER than GC in DMSO, and also in mixed G4-DMSO. GC exhibited two peaks in each of oxidation and reduction, whereas Pt showed only one peak with higher currents.
- In DMSO-containing electrolyte, the short-lived LiO<sub>2</sub> intermediate is detected. Besides, its back oxidation is quasi-reversible as long as the cathodic potential is limited to a value before the second reduction to Li<sub>2</sub>O<sub>2</sub>. From the ring currents of RRDE, about 90% of the theoretical amount of LiO<sub>2</sub> is detected in Li<sup>+</sup>/DMSO. In addition, zero ring currents are observed at potentials of Li<sub>2</sub>O<sub>2</sub> oxidation, implying that peroxide is directly oxidized to O<sub>2</sub> without passing through superoxide intermediate. Tafel slopes for both ORR and OER at GC in DMSO are close to 120 mV dec<sup>-1</sup>, indicating that the first one-electron reduction of O<sub>2</sub> to LiO<sub>2</sub> is the rate determining step, which is followed by a fast reduction to Li<sub>2</sub>O<sub>2</sub>.
- The scan rate has an influence on ORR under rotation in DMSO. A linear relationship between peak current and  $v^{1/2}$  is obtained indicating a mass-transport limitation process, although one should not expect such behavior upon rotation. This effect is also observed in the G4-DMSO blended electrolyte. This limitation could be due to the formation of a porous passive layer of Li<sub>2</sub>O<sub>2</sub> on the electrode surface. At low scan rates, sequential formation of Li<sub>2</sub>O<sub>2</sub> layers takes place. Thus, during oxidation, two peaks appear on GC electrode corresponding to the oxidation of different layers, while at higher scan rates, only one oxidation peak is observed.
- More importantly, RRDE chronoamperometry is successful in deconvolution of time and potential effects, while in CV the time effect is not excluded. The disc current decays with time reaching a steady value, implying the gradual formation of Li<sub>2</sub>O<sub>2</sub> until a critical film thickness is reached, which blocks the surface. It is found that the deactivation is faster at higher overpotentials in DMSO. The ring peak current value is dependent on the applied disc potential. The ring peak current exhibits the same shape of ring currents observed in

typical CV with a maximum at ca. -1.25V. This phenomenon is observed on GC as well as on Au electrodes. Interestingly, RRDE chronoamperometry is used to determine the diffusion coefficient of superoxide in DMSO (which is not trivial or simple with other methods). It is based on the linear variation of transit time with rotation rate.

- Clear effect of the solvent on the mechanism of oxygen reduction is observed. The solvation strength of the solvent (may be the donor number (DN) as a characteristic) significantly influences the lifetime of  $\text{LiO}_2$ . In high DN solvents (e.g. DMSO), a "solution-mediated pathway" takes place, in which superoxide is stable in solution, thus it is further disproportionate to  $\text{Li}_2\text{O}_2$  in solution. On the other hand, in low DN solvents (e.g. G4), a "surface-mediated pathway" takes place, in which the superoxide is strongly adsorbed at the electrode, and thus it cannot be detected in solution rather it is further reduced on the electrode to  $\text{Li}_2\text{O}_2$ , blocking the surface. In a mixed G4+DMSO solvent, the amount of detected  $\text{LiO}_2$  increases monotonically as the ratio of DMSO in the mixture increases. In addition, the solvent exerts an effect on the kinetics of oxygen evolution, where DMSO is more active than G4. Mixed G4-DMSO based electrolyte showed a coulombic efficiency of about 90% compared to 60% in single DMSO electrolyte based on faradaic charges, supporting the enhancement of the rechargeability in the mixed electrolyte.
- The amount of detected  $\text{LiO}_2$  depends on the potential, at which the ring is held for pure DMSO and the mixed electrolytes. The superoxide yield increases at higher ring potentials until the maximum amount is detected when ring is set at -0.3V.
- Ag-containing catalysts are not suited for DMSO due to catalyst dissolution. However,  $\text{Co}_3\text{O}_4/\text{GC}$  catalyst showed better kinetics of oxidation than bare GC in DMSO. The coulombic efficiency is improved from 60 to 89%. Remarkably, a clear effect of  $\text{Co}_3\text{O}_4$  on superoxide formation is observed: only 50% of superoxide is detected for  $\text{Co}_3\text{O}_4$  catalyst compared to 90% for GC, which could be due to the stronger adsorption of superoxide on  $\text{Co}_3\text{O}_4$ .
- DEMS quantitative analysis revealed the formation of only superoxide in  $\text{TBA}^+$  or  $\text{K}^+$  containing G4. In  $\text{Li}^+$  solutions, the formation of peroxide during reduction is confirmed by DEMS, where a value close to  $2e^-/\text{O}_2$  is obtained, while values of 2.0 to 3.5  $e^-/\text{O}_2$  is obtained for oxygen evolution in pure G4, G4-DMSO (5%) and also 50% electrolytes.
- The true coulombic efficiency is determined from DEMS, and ~25% are obtained for G4 after considering  $\text{CO}_2$  byproducts, while 60% are previously reported for pure DMSO. This infers that portion of reduced oxygen is not reproduced in each cycle. It is also interesting to notice that the  $\text{CO}_2$  evolution (arise from electrolyte decomposition) increases as the amount of formed  $\text{Li}_2\text{O}_2$  increases. This suggests that a discharge products-induced chemical decomposition of the electrolyte leads to a deactivating film formation on the surface, which can be partially removed at higher potentials.
- The Au-sputtered membrane showed feasibility as a Gas diffusion electrode (GDE). The results showed the formation and decomposition of  $\text{Li}_2\text{O}_2$  in G4 as well as in the mixed electrolyte.
- For the first time, a novel organic electrolyte based on 1,3-dimethylimidazolidinone (DMI) is investigated for ORR and OER. DMI is a non-hazardous alternative to the carcinogenic HMPA. RRDE results showed a clear catalytic effect of different electrode

materials: GC is more active towards ORR, while Pt is more active for OER than GC and Au (as in case of DMSO). Formation and decomposition of  $\text{Li}_2\text{O}_2$  are demonstrated from DEMS results, which showed roughly  $2e^-/\text{O}_2$ . The  $\text{CO}_2$  evolution at higher potentials is observed due to electrolyte decomposition. True coulombic efficiency of about 35% is obtained. Superoxide formation is confirmed in TBA-containing electrolyte. One-electron transfer step is the rate determining step in Li-based solution. GDE measurements also showed the reduction of  $\text{O}_2$  to  $\text{Li}_2\text{O}_2$  and its reoxidation. This solvent could be a possible candidate for Li- $\text{O}_2$  battery applications due to its outstanding physical and chemical properties.

### *Future perspectives*

Having worked within the same field of research in four years naturally brings up many ideas for further research. I have here chosen the suggestions that I consider most interesting:

- Further optimization of the bifunctional Ag+Co<sub>3</sub>O<sub>4</sub> catalyst by systematic variation of the particle size of both components could bring more enhancements to the catalytic activity. Combination of either Ag or Co<sub>3</sub>O<sub>4</sub> with other components (e.g. Co<sub>3</sub>O<sub>4</sub>/Co or Co<sub>3</sub>O<sub>4</sub>-Pt) could improve the activity and stability. Synthesis of Ag core-Co shell structure and investigating its activity could be an interesting point. Further screening of other catalytic materials (e.g. LiCoO<sub>3</sub>) is required to avoid Pt and carbon in the commercial catalysts.
- Examining doped supports as Co or Ni-doped TiO<sub>2</sub> instead of carbon and testing its stability.
- Further investigation of Ag-containing electrolytes in Tetraglyme or mixed G4-DMSO since Ag does not dissolve in Tetraglyme in contrast to DMSO.
- Fundamental investigations with DEMS are recommended to test new electrolytes and materials, in particular, studying the effect and behavior of the system in presence of additives such as redox mediators (I<sub>2</sub>, TTF, TEMPO) is important.
- Testing the use of external Li<sub>2</sub>O<sub>2</sub> as a discharge product, and investigating the kinetics of OER to avoid the blocking layer formed upon *in-situ* reduction, and to distinguish the limitations of OER from ORR.
- Theoretical calculations of the potential energy curves for the mixed catalyst with ORR intermediates in alkaline media to confirm the synergism, and in case of an aprotic mixed electrolyte the theoretical calculations of the multiphase electron transfer reactions at an electrode/electrolyte interface could be an added value.
- Testing of different recipes of mixed solvents in order to get the desired properties. Combining the best properties of different solvents (high DN, low AN, low vapor pressure) in a one mixed electrolyte is a good strategy to solve the problem of electrode blocking and improve the cyclability. Performing charge/discharge cycles in DMI-based electrolyte in a gas-diffusion electrode with a coin cell set up can provide more information on its long-term performance.
- It would be interesting to look at other systems like Na-O<sub>2</sub> or Ca-O<sub>2</sub> with DEMS for comparison.



## Appendix A: Further investigations of non-precious bifunctional oxygen catalysts in alkaline media

### A.1. Performance of the commercial Pt/C catalyst as a benchmark catalyst

The quality of the Pt ring used in the RRDE setup was examined prior to each series of experiments. Pt (pc) ring was polished as in the standard procedure (alumina slurry, acetone and water), and then cycled for several cycles in Ar-saturated solution. Fig. 1 shows a typical CV of Pt in Ar- and O<sub>2</sub>-saturated 0.1M LiOH solution. In O<sub>2</sub>-saturated solution, ORR takes place with a cathodic current increase (blue curve). Under rotation, ORR current increases reaching the diffusion limited current plateau. This plateau ends with a hump at ~ 0.1V, where hydrogen adsorption takes place, and may hinder the cleavage of O-O bond, resulting in more peroxide intermediate, and blocking of the active sites, thus the peroxide amount increases in this region.

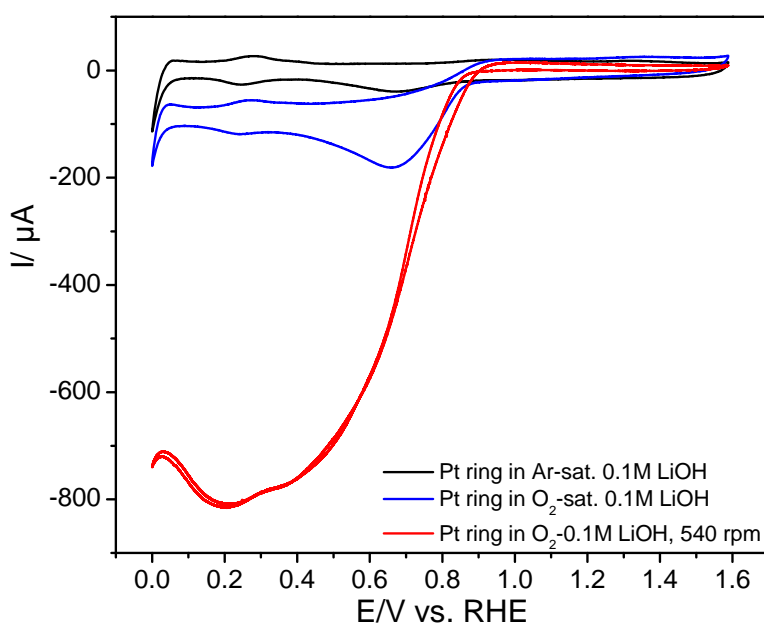


Fig. 1. CVs of the Pt-ring in 0.1M LiOH solution with  $50 \text{ mV s}^{-1}$  between 0 and 1.6V. ORR at Pt ring under rotation of 540 rpm and  $5 \text{ mV s}^{-1}$  is also shown.

Since Pt/C is the best-known commercial catalyst for ORR, its behavior is studied here in 0.1M LiOH solution for comparison. CV of the commercial 20% Pt/ Vulcan XC-72 carbon in O<sub>2</sub>-saturated 0.1M LiOH solution with  $50 \text{ mV s}^{-1}$  is shown in Fig. 2a. Typical features of Pt are observed: H-adsorption/desorption and O-adsorption/desorption peaks. The polarization curves of Pt/C at different rotation rates are presented in Fig. 2b. The diffusion currents increase with the rotation rate increase due to the more efficient contact of oxygen with Pt atoms at higher rotations. Onset potential of ORR is at ~1V in the anodic scan direction. OER currents decrease with each cycle, indicating the instability of Pt/C catalyst at higher potentials. Pt is known to follow the direct 4e-ORR pathway as confirmed here from the ring currents, which correspond to the oxidation of the produced peroxide anion. Very small ring currents were recorded, which is in agreement with previous studies,[1] as shown in Fig. 2c. The maximum peroxide yield is not more than 3%. In the negative-going scan, the ring currents, and consequently, the amount of peroxide anion increases gradually reaching a peak at about 0.74V vs. RHE, and then decrease, as shown in Fig. 2d. This peak is most likely due

to poisoning of the Pt surface or the adsorption of hydrogen on the Pt surface, inhibiting peroxide reduction.[2, 3] Peroxide anion formation in alkaline media occurs through an outer sphere electron transfer process, where  $\text{HO}_2^-$  is related to specifically adsorbed oxides on Pt as follows:



The generated peroxide anion is then oxidized at Pt ring (held at 1.2 V), leading to this cathodic peak in the graph at 0.73V according to the equation:



The number of electrons transferred during ORR is directly related to the  $\text{HO}_2^-$  yield, and 4es are obtained.

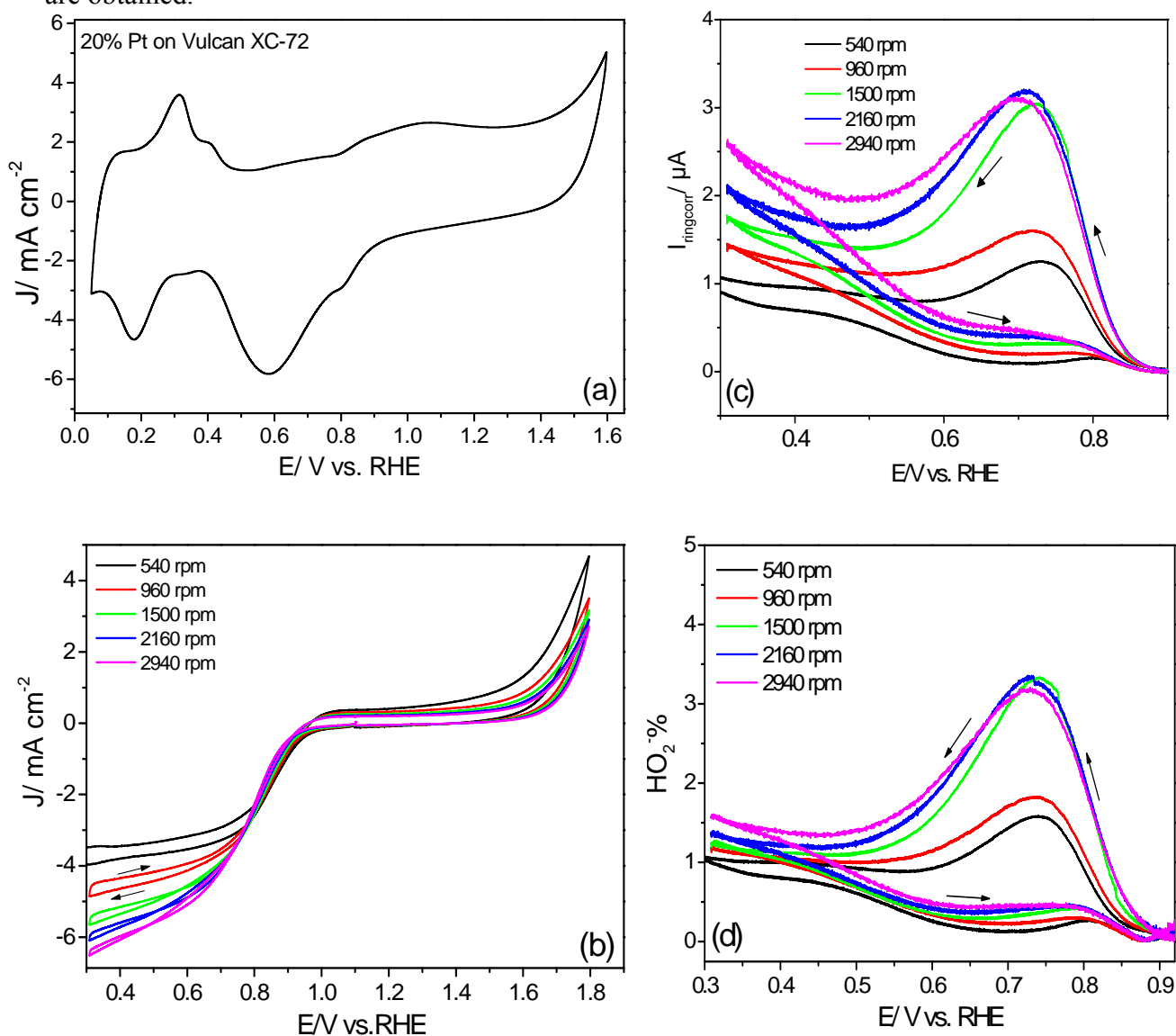


Fig. 2. (a) CV of 20% Pt/Vulcan XC-72 with loading  $1 \text{ mg cm}^{-2}$  on GC in  $\text{O}_2$ -saturated 0.1M LiOH,  $50 \text{ mV s}^{-1}$  without rotation. (b) RRDE measurements on the same electrode in  $\text{O}_2$ -saturated 0.1M LiOH solution with  $10 \text{ mV s}^{-1}$  at different rotations. (c) The corresponding corrected ring currents, where  $E_{\text{ring}}=1.2\text{V}$ . (d)  $\text{HO}_2^-$  % in ORR region at different rotations.

## A.2. Electrochemical behavior and activity of Ag catalysts in alkaline media

### Ag polycrystalline:

Since Ag has very low activity towards OER, we focused to characterize it for ORR. CVs of Ag (pc) electrode in a stagnant 0.1M LiOH solution with  $100 \text{ mV s}^{-1}$  are shown in Fig. 3a. The onset of ORR is at 0.84V, and ORR is noticeable by a peak at ca. 0.5V and a shoulder at 0.1V. Fig. 3b shows that cycling more negative to 0V leads to a positive shift of ORR curve, thus an increase of ORR activity. This could be attributed to the complete reduction of the Ag surface at more negative potentials.[4] In case of Ag particles electrode, this lower limit should at the same time be chosen not very low to avoid the Ag particles' detachment. Therefore, our lower limit in most of the experiments based on Ag particles-modified electrode, discussed below, was -0.2V. In the polarization curves of Fig. 3c, a hump at ca. 0.1V is observed. This might be due to presence of some contaminants.

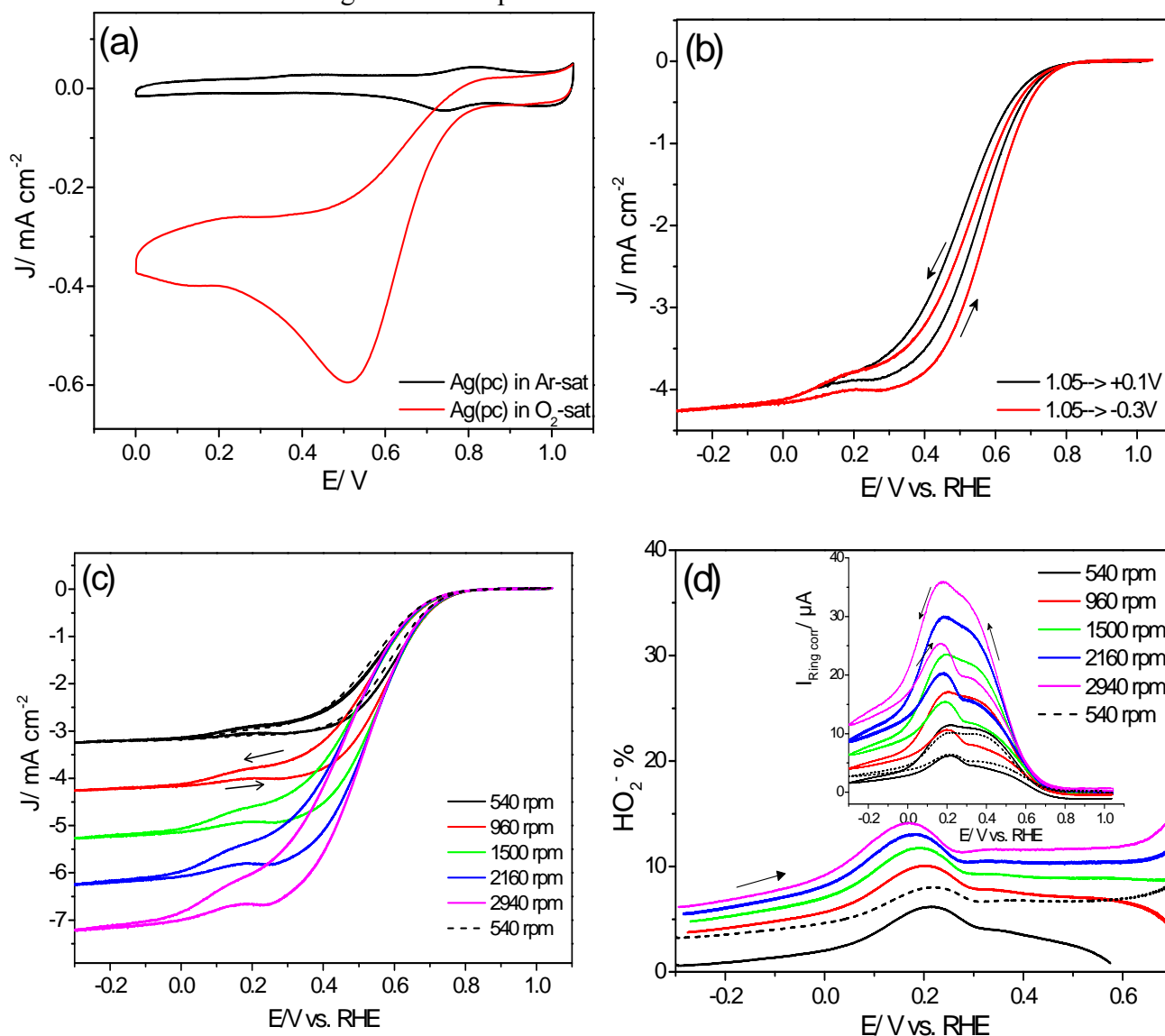


Fig. 3. (a) CV of Ag (pc) electrode in stagnant 0.1M LiOH at  $100 \text{ mV s}^{-1}$ . (b) RRDE measurements on Ag (pc) electrode in O<sub>2</sub>-saturated 0.1M LiOH solution at 960 rpm with  $10 \text{ mV s}^{-1}$  at two cathodic potential limits. (c) RRDE results on the same electrode with  $10 \text{ mV s}^{-1}$

<sup>1</sup> at different rotations. (d) Peroxide yield in ORR region at different rotations. Inset is the ring currents.  $E_{\text{ring}}=1.2\text{V}$ .

Hysteresis between the anodic and cathodic-going scans is observed when the electrode potential scan was limited between  $-0.3\text{V}$  and  $1.05\text{V}$ : higher currents are observed in the cathodic scan than in the anodic. This hysteresis is not observed (or is negligible) if the sweep is to higher potentials ( $1.8\text{V}$ ), *cf.* Fig. 4a in chapter 6. The hysteresis is also insignificant for other Ag particles, *cf.* Fig. 4. This suggests the need of reductively removal of the adsorbed OH-species to activate the electrode surface. This indicates the potential dependence on  $\text{OH}_{\text{ad}}$  surface coverage. RRDE results of Ag (pc) electrode at different rotation rates are shown in Fig. 3c. Disc currents increase as the rotation speed increases. The corresponding ring currents are small fractions of the disc currents, and consequently, the peroxide yield ( $<10\%$ ) is low, as shown in Fig. 3d, indicating that ORR proceeds mainly via the  $4e$ -pathway. The peak at ca.  $0.2\text{V}$  might be due to contaminants in solution or on the electrode surface during preparation since it disappeared in other experiments.

#### Ag (40 $\mu\text{m}$ ) microparticles catalyst

Here, Ag particles catalyst is presented. CVs on Ag ( $40\mu\text{m}$ )/GC electrode with a loading of  $200\ \mu\text{g cm}^{-2}$  at different rotation rates are displayed in Fig. 4a. The potential was scanned between  $-0.3\text{V}$  and  $1.05\text{V}$ . Typical diffusion limited currents at various rotations are observable. A control experiment (repeated CV at  $540\text{ rpm}$  after the series, see dashed black line) shows consistent results, indicating the stability over ORR region. Small ring currents are obtained, as shown in Fig. 4b, corresponding to  $4e$ s-pathway of ORR.

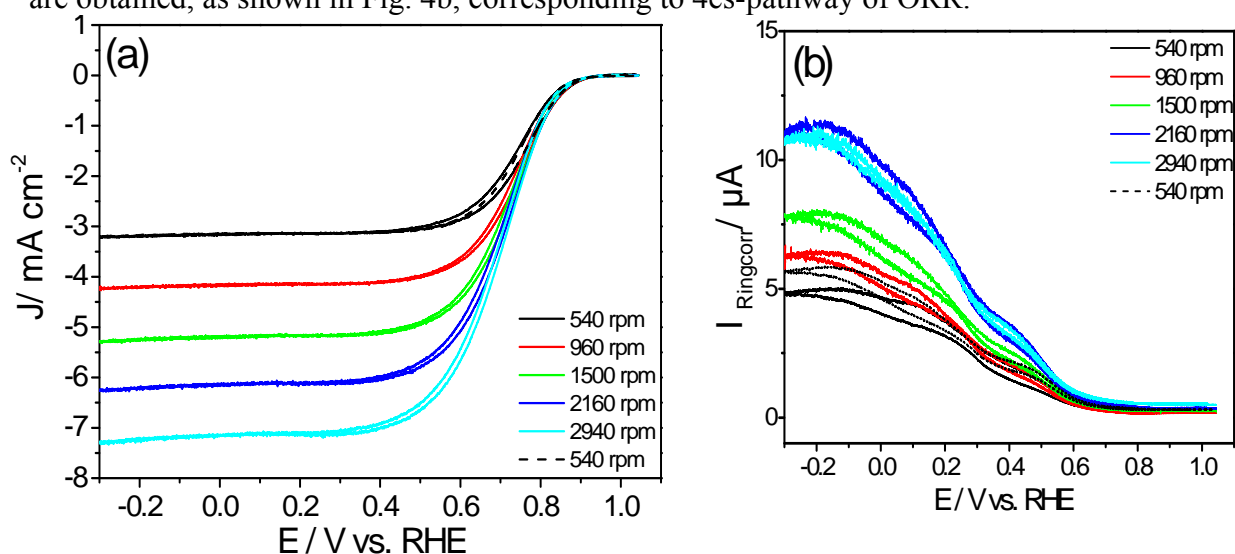


Fig. 4. (a) RRDE measurements on Ag ( $40\mu\text{m}$ )/GC electrode with  $200\ \mu\text{g cm}^{-2}$  loading in  $\text{O}_2$ -saturated  $0.1\text{M LiOH}$  solution at different rotations with  $10\ \text{mV s}^{-1}$ . (b) Corresponding ring currents when ring is held at  $1.2\text{V}$ .

Further characterization of Ag ( $40\mu\text{m}$ ) catalyst, and studying some effects (scan rate and potential window effects) are carried out using cyclic voltammetry. Fig. 5a shows the behavior of Ag( $40\ \mu\text{m}$ ) particles at different scan rates ( $5\text{--}450\ \text{mV s}^{-1}$ ). Surface oxidation and reduction peak currents increase as the scan rate increase, indicating mass-transport controlled

process. Also, a negative potential shift of the reduction peak is observed, while a positive shift of anodic peaks is observed with the scan rate increase.

The upper potential limit controls the state of oxidation of Ag and its oxides. If the potential is limited to only a value after the second anodic peak,  $\text{Ag}^{\text{I}}\text{Ag}^{\text{III}}\text{O}_2$  will not be formed, and consequently, the first cathodic peak at ca. 1.3V will not appear, see Fig. 5b. Extending the potential to higher values allows further oxidation of  $\text{Ag}^{\text{I}}$  to  $\text{Ag}^{\text{I+III}}$ , thus the peak at 1.3V appears. The second cathodic peak is shifted to more negative potentials with higher currents upon expanding the upper potential limit. Thus, these surface processes are potential sensitive. Stability of the redox peaks is examined by recording 15 repeated cycles. The results are shown in Fig. 5c, and infer the stability of the catalyst over the tested potential window. It is noteworthy to mention that almost no OER is observed in this potential range since it starts on this catalyst at potentials above 1.6 V.

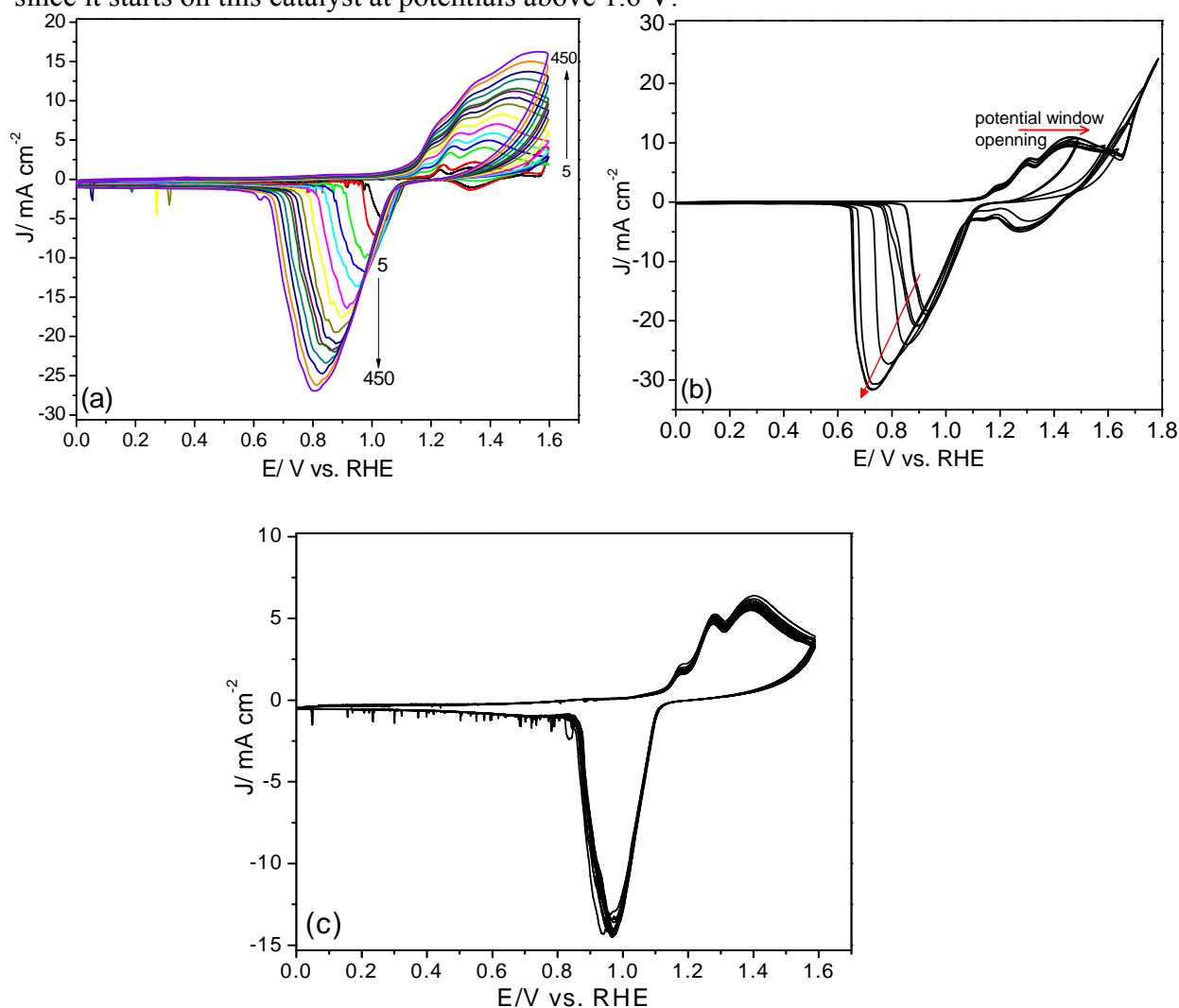


Fig. 5. (a) CVs of Ag particles (40 $\mu\text{m}$ )/GC electrode (400 $\mu\text{g cm}^{-2}$ ) in O<sub>2</sub>-saturated 0.1M LiOH solution at various scan rates (5-450 mV s<sup>-1</sup>). (b) CVs at different anodic potential limits with 50 mV s<sup>-1</sup> in Ar-saturated solution (c) 15 consecutive cycles in O<sub>2</sub>-saturated solution with 50 mV s<sup>-1</sup>.

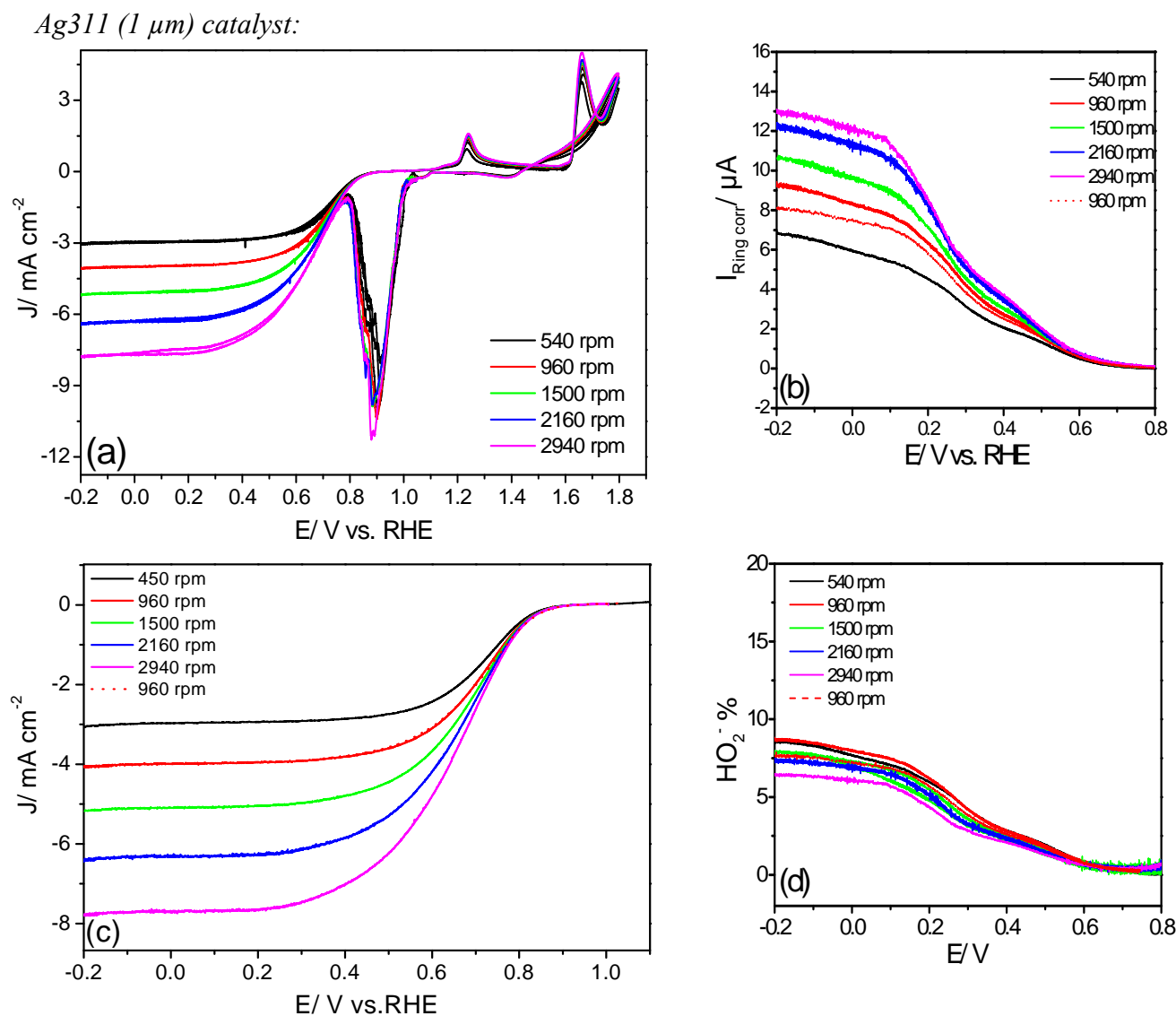


Fig. 6. (a) RRDE measurements on Ag311/GC electrode with  $1\text{ mg cm}^{-2}$  loading in  $\text{O}_2$ -saturated  $0.1\text{M LiOH}$  solution at different rotations with  $10\text{ mV s}^{-1}$ . (b) Anodic scan of ORR region. (c) Corresponding ring currents when  $E_{\text{ring}} = 1.2\text{V}$ . (d) The respective peroxide yield.

Another Ag microparticles catalyst, so-called Ag311 with a particle size of  $1\text{-}2\mu\text{m}$  obtained from Ferro GmbH, is examined. This Ag311 will be a component of our promising mixed catalyst, discussed in the main chapters, since it shows higher activity and performance than the Ag( $40\mu\text{m}$ ) flakes. Fig. 6a shows the polarization curves of Ag311/GC in  $\text{O}_2$ -saturated  $0.1\text{M LiOH}$  solution with  $10\text{ mV s}^{-1}$  at different rotations. The onset of the ORR is observed near  $0.9\text{ V}$ , with a diffusion limited behavior being achieved between  $0.6$  and  $-0.2\text{ V}$ . The anodic peaks at ca.  $1.25\text{ V}$  and  $1.65\text{ V}$  correspond to the oxidation of Ag to  $\text{Ag}_2\text{O}$  and  $\text{Ag}^{\text{I}}\text{Ag}^{\text{III}}\text{O}_2$ , respectively.[5] The cathodic peaks around  $1.4$  and  $0.9\text{V}$  are the respective reduction peaks. According to Savinova et al. Ag oxides are inactive for ORR, while Ag hydroxides are active. The shoulder in the strong reduction peak at ca.  $0.85\text{V}$  could be due to the reduction of  $\text{Ag-O}_{\text{ad}}$  to  $\text{Ag-OH}$ , which is ORR active. These redox peaks are independent of the rotation rate of the electrode, but it is slightly affected by the roughening of the surface with time. Zoomed-in graph of ORR region is shown in Fig. 6c. Few microamperes of current

are detected on the ring, corresponding to about 7% of peroxide anion, as shown in Fig. 6b, d. These results confirm the good activity of Ag311 catalyst for ORR in alkaline media.

### A.3. Activity of $\text{Co}_3\text{O}_4$ (50 nm) catalyst

Oxides of noble metals, in particular,  $\text{RuO}_2$  and  $\text{IrO}_2$ , have been proven to be highly active OER catalysts with overpotentials around 300 mV to reach a current density of  $10 \text{ mA/cm}^2$ . [6-8] However, they are expensive. Thus, oxides or hydroxides of transition metals are investigated as alternatives. [9, 10] Among all candidates, cobalt-based materials demonstrated decent activity, and thus gained considerable attention as water oxidation catalysts. [11, 12] On the other hand, their activity towards ORR is not superior. [13] Here, we study the activity of  $\text{Co}_3\text{O}_4$  based electrodes as a potential candidate in our mixed catalyst. Fig. 7 shows CVs of  $\text{Co}_3\text{O}_4$  (40  $\mu\text{m}$ )/GC electrode compared to Pt(pc) in 0.1M LiOH solution. The activity of ORR at  $\text{Co}_3\text{O}_4$  is very low compared to the Pt: ORR peak at  $\text{Co}_3\text{O}_4$  is observed near 0.5V, which is ca. 300 mV less positive to that at Pt; ORR onset is at ca. 0.7 V at  $\text{Co}_3\text{O}_4$ .

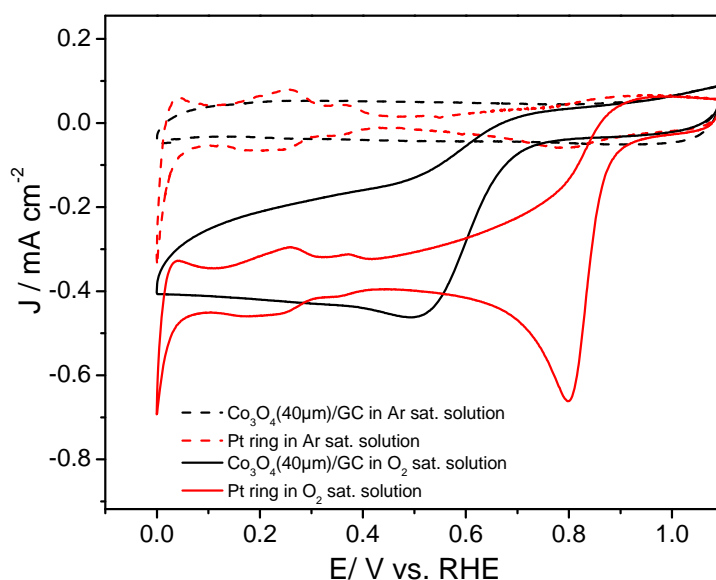


Fig. 7. CVs of  $\text{Co}_3\text{O}_4$ (40  $\mu\text{m}$ )/GC disc and Pt (pc) ring both scanned in 0.1M LiOH solution with 50 mV/s. Geometric area is considered. Loading:  $200 \mu\text{g cm}^{-2}$ .

Another size of  $\text{Co}_3\text{O}_4$  catalyst (50 nm) is also studied. Fig. 8 shows the RRDE curves at  $\text{Co}_3\text{O}_4$  (50 nm) with  $100 \mu\text{g cm}^{-2}$  loading at different rotation rates and  $10 \text{ mV s}^{-1}$  in 0.1M LiOH. Stable OER current densities are observed during consecutive cycling at various rotation speeds. The inset of Fig. 8 displays the corresponding ring currents. The yield of  $\text{HO}_2^-$  is in the range of 60-80%. This implies the dominance of the 2e-pathway over the 4e-pathway for ORR on  $\text{Co}_3\text{O}_4$  catalyst.

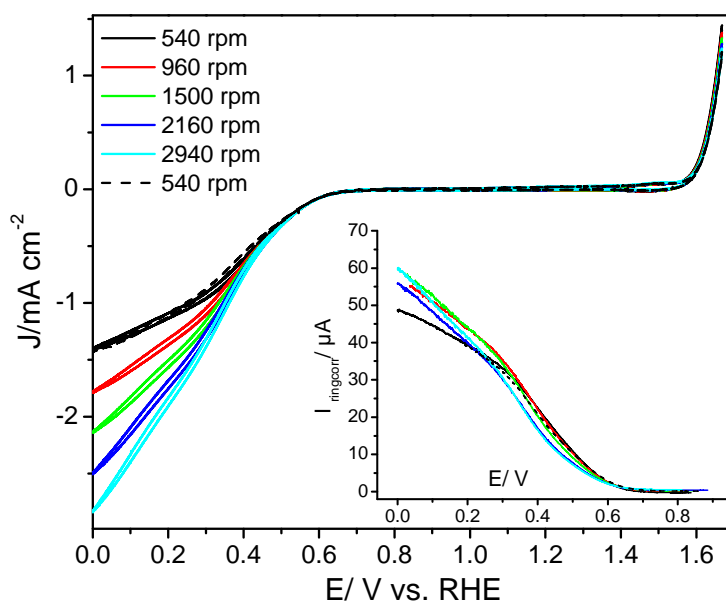


Fig. 8. (a) RRDE measurements on  $\text{Co}_3\text{O}_4$  (50 nm)/GC electrode ( $100 \mu\text{g cm}^{-2}$ ) in 0.1M LiOH at different rotations with  $10 \text{ mV s}^{-1}$ . Inset: Corresponding ring currents in the anodic scan when ring was held at 1.2V.

Potential window opening experiment is conducted to characterize the redox peaks of  $\text{Co}_3\text{O}_4$ . Fig. 9 shows the CVs of  $\text{Co}_3\text{O}_4$  (50 nm)/GC in Ar-saturated 0.1M LiOH solution, where the potential is scanned to different upper limits. When the scan is reversed just beyond the first anodic peak (at 1.25V), only one broad cathodic peak is observed (red curve). Upon extending the potential scan to higher potentials, the second main peak at ca. 1.5V appears prior to oxygen evolution reaction. The first peak is assigned to the transition of the redox couple  $\text{Co}^{\text{II}}/\text{Co}^{\text{III}}$  (eq. 4.5), whereas the second peak corresponds to the redox couple  $\text{Co}^{\text{III}}/\text{Co}^{\text{IV}}$  (eq. 4.6). This is in agreement with following reactions reported previously.[14]

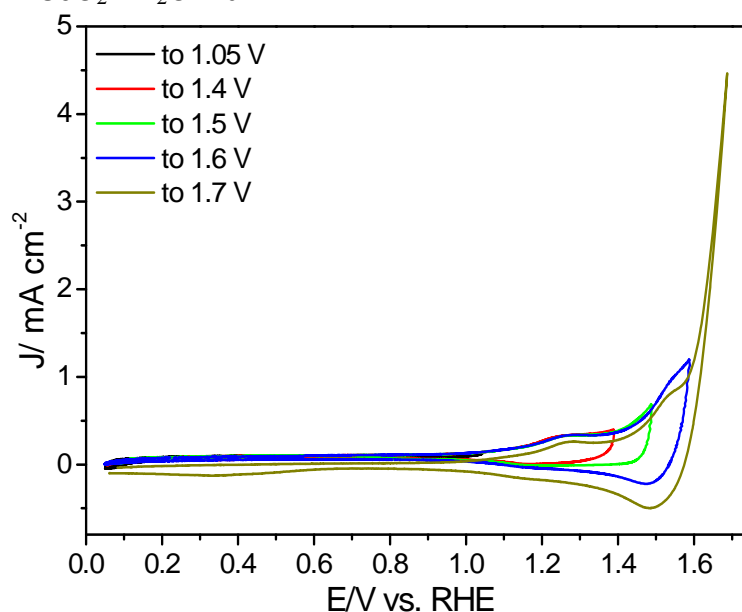


Fig. 9. CVs on  $\text{Co}_3\text{O}_4$  (50 nm)/GC electrode ( $200 \mu\text{g cm}^{-2}$ ) in Ar-saturated 0.1M LiOH at different anodic potential limits with  $50 \text{ mV s}^{-1}$ .

#### A.4. Ag/CoO bimetallic catalyst: effect of electrolyte and loading on activity

The influence of the electrolyte concentration is studied here at Ag/CoO bimetallic catalyst, see Fig. 10. The same behavior is observed as on other catalysts. Solution of 0.1M LiOH showed better ORR activity than 1.0M LiOH due to the higher O<sub>2</sub>-solubility. Moreover, the influence of the cationic species on OER/ORR activity of Ag/CoO catalyst in alkaline media is examined, as shown in Fig. 10. Specifically, Li<sup>+</sup> and K<sup>+</sup> containing electrolytes are compared. The catalyst showed higher ORR activity in KOH than in LiOH solution: the polarization curves are shifted by ca. 90 or 140 mV (for 100 or 200 μg cm<sup>-2</sup>, respectively) to more positive potentials in KOH than in LiOH. Higher OER currents are obtained for KOH compared to LiOH at 1.7V. This is consistent with previous results on perovskite and IrO<sub>2</sub>. [15] Lower ring currents and peroxide yield are obtained for 2.5M KOH than in 2.5M LiOH, see Fig. 10b. However, a different trend is found for 0.1M concentration, which might be due to a sort of uncleanliness of the Pt ring.

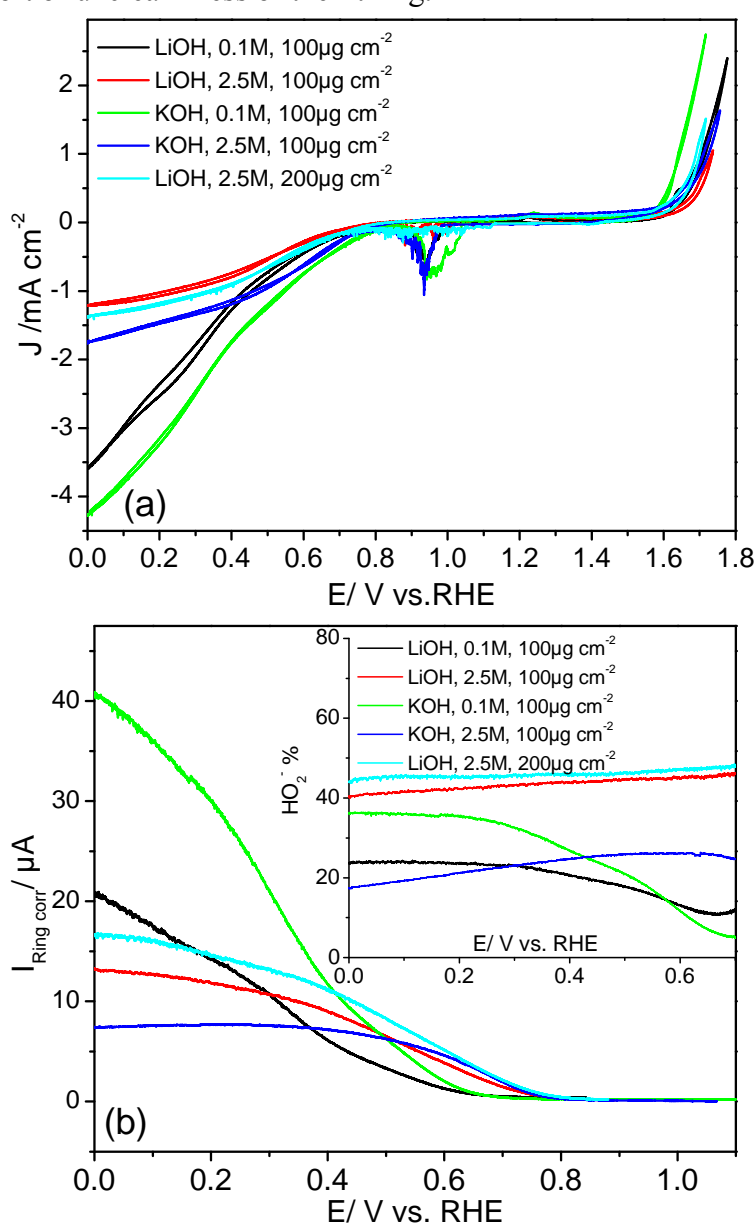
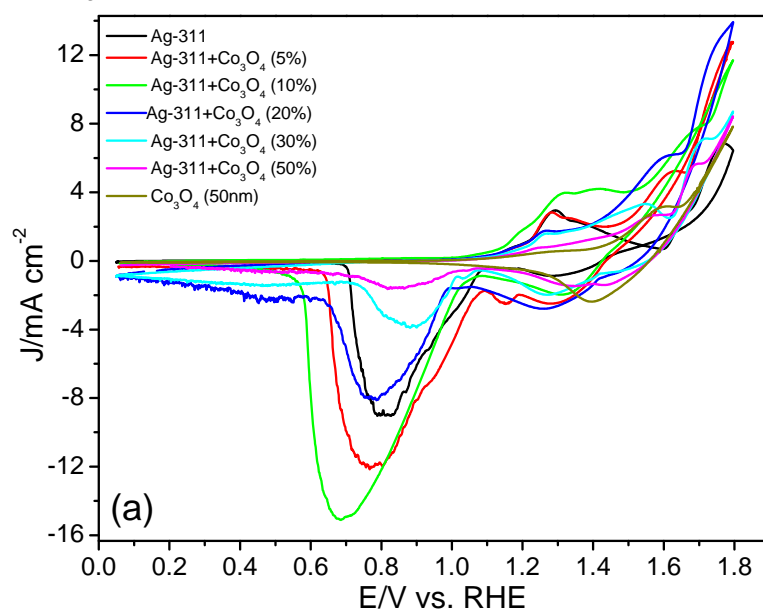


Fig. 10. (a) RRDE measurements on Ag/CoO (50 wt%) loaded on GC electrode in different solutions at 2940 rpm with 5 mV s<sup>-1</sup>. (b) Corresponding ring currents in the anodic scan when ring was held at 1.2V.

### A.5. Synergistic bifunctional activity of Ag+Co<sub>3</sub>O<sub>4</sub> mixed catalyst in alkaline media: kinetics and mechanism

Fig. 11a shows the CVs of Ag<sub>311</sub>+Co<sub>3</sub>O<sub>4</sub> catalyst with different compositions in Ar-saturated 0.1M LiOH solution at 50 mV s<sup>-1</sup>. The surface redox peaks are attributed to the oxidation and reduction of Ag and its oxides. The assignment of the peaks is the same as that for Ag(pc) and Ag(40 μm) catalysts, although some potential shifts might occur depending on the nature of Ag. Co<sub>3</sub>O<sub>4</sub> redox peaks (main peak is expected at 1.5V) are small, and thus underlay with the large Ag peaks. The charge of the redox peaks of Ag is higher when Ag is in contact with Co<sub>3</sub>O<sub>4</sub> than that of pure Ag. Integration of the first and second cathodic peaks of Ag gives a surface charge, which varies with the composition of the mixture, as shown in Fig. 11b. The mixed catalyst containing 10% cobalt spinel revealed the highest surface charge, indicating that thicker oxide layer is formed on this catalyst. This suggests that Ag/Ag-oxide redox reaction could be facilitated when Ag surface atoms are in contact with cobalt oxide in their mixture. Thus, Co<sub>3</sub>O<sub>4</sub> could catalyze the Ag reaction in their mixture. This effect is supported by the XRD analysis of Ag and Ag+Co<sub>3</sub>O<sub>4</sub> catalyst pristine electrodes and at 1.8V, as shown in our paper.[5] The results showed the higher ratio of Ag/Ag-oxides at 1.8V at the mixed catalyst compared to the pure Ag<sub>311</sub>. This has also been observed for CoPC@Ag electrode.[16] Remarkably, the Ag<sub>2</sub>O reduction peak at around 0.8V is shifted to less positive potential in the mixed catalyst than in pure Ag<sub>311</sub>, as can be seen in Fig. 11a and in main chapter. This suggests a stronger interaction of oxygenated species on Ag<sub>311</sub>+Co<sub>3</sub>O<sub>4</sub> than on Ag<sub>311</sub>. This feature has also been observed for Ag-Co/C catalyst.[17]

For the 10 wt% mixed catalyst, the surface charge of the second cathodic peak corresponds to  $80 \times 1000 \mu\text{C cm}^{-2} / 260 \times 2 \mu\text{C cm}^{-2} = 154$  monolayers (considering  $260 \mu\text{C cm}^{-2}$  for Ag monolayer). Since one layer of Co<sub>3</sub>O<sub>4</sub> is about 0.2 nm thick, thus we get  $154 \times 0.2 \text{ nm} = 31 \text{ nm}$  of the catalyst, which is close to the 50 nm Co<sub>3</sub>O<sub>4</sub>, indicating the partial coverage of the 1 μm Ag particles with Co<sub>3</sub>O<sub>4</sub>.



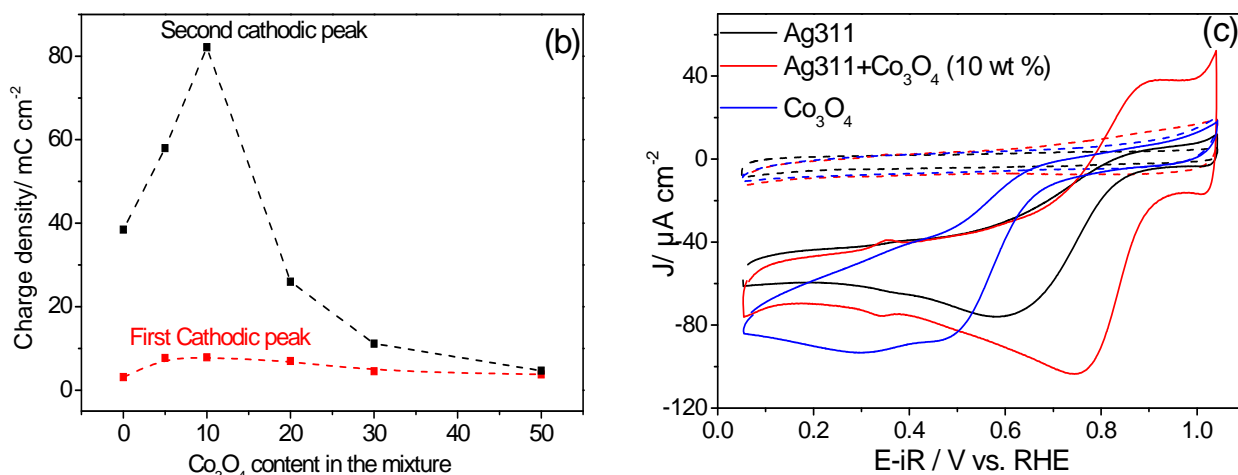


Fig. 11. (a) CVs on different electrodes ( $1 \text{ mg cm}^{-2}$ ) in Ar-saturated  $0.1 \text{ M LiOH}$  with  $50 \text{ mV s}^{-1}$ . (b) Charge density of the first and second cathodic peaks obtained by integration of the respective curve in (a) for different compositions. (c) ORR on three catalysts in stagnant  $0.1 \text{ M LiOH}$  solution with  $50 \text{ mV s}^{-1}$ , dashed lines are in Ar-solution.

Fig. 11a also shows the variation of OER current density at different compositions of the mixed catalyst. Therefore, optimization of the composition is necessary to achieve the best catalytic performance. 10-20 wt%  $\text{Co}_3\text{O}_4$ -containing catalyst exhibits the optimized OER activity in terms of current density, see Fig. 11a. The number of electrons transferred ( $n$ ) is 3.99 for this mixed catalyst, and less than 2% peroxide is detected at the ring, see Fig. 12. ORR polarization curves, which are obtained on Ag311,  $\text{Co}_3\text{O}_4$  and Ag311+ $\text{Co}_3\text{O}_4$  (10 wt%) in a stagnant solution and  $50 \text{ mV s}^{-1}$  are shown in Fig. 11c. The half-wave potential ( $E_{1/2}$ ) for ORR at the mixed catalyst is approximately 100 mV or 260 mV more positive than at Ag311 or  $\text{Co}_3\text{O}_4$ , respectively.

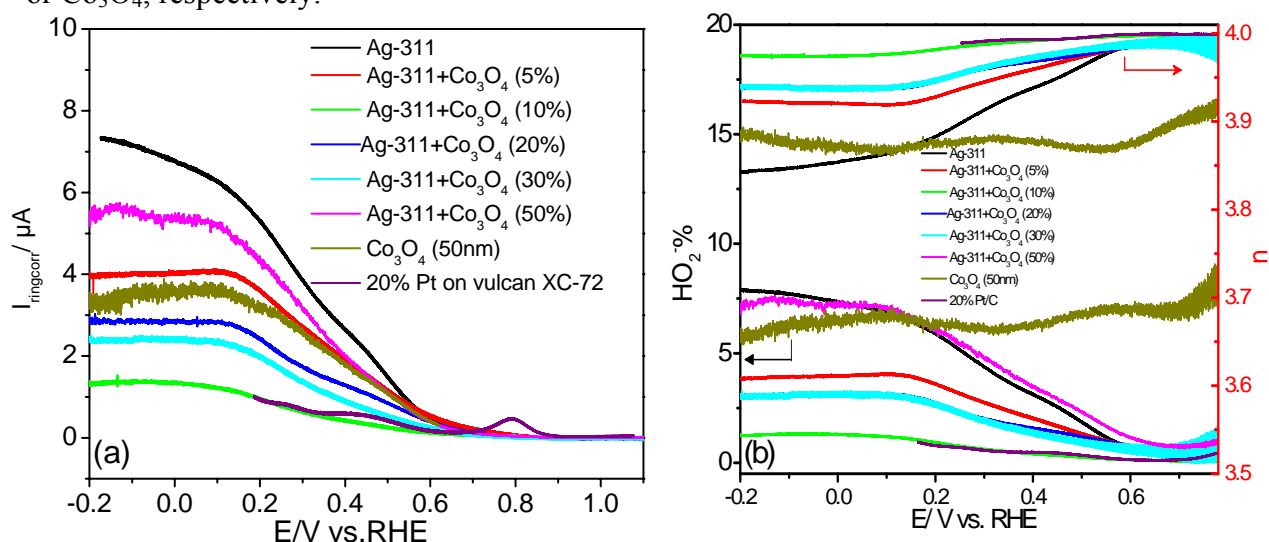


Fig. 12. (a) Corrected-ring currents at ORR/OER on Ag311+ $\text{Co}_3\text{O}_4$  (x %) on GC electrodes ( $1 \text{ mg cm}^{-2}$ ) in  $\text{O}_2$ -saturated  $0.1 \text{ M LiOH}$  solution at 960 rpm with  $5 \text{ mV s}^{-1}$ , anodic sweep. (b)  $\text{HO}_2^-$  % and  $n$  value in anodic scan of ORR.

Furthermore, the kinetics of ORR on these catalysts are investigated by Tafel plots ( $\lg J_k$  vs. E). Tafel slopes give an idea about the rate determining step in reactions. Two different methods are used to draw Tafel plots: first from the intercept of Koutecky-Levich (K-L) plots ( $1/J_{lim}$  vs.  $1/\omega^{1/2}$ ) at different potentials; and second by mass transport-correction of the measured current according to the following equation:  $J_k = (J_{lim} \times J) / (J_{lim} - J)$  where,  $J_{lim}$  is the diffusion-limiting current density, and  $J$  is the measured current density.

Tafel plots for Ag311+Co<sub>3</sub>O<sub>4</sub> (10 %) catalyst in 0.1M LiOH obtained with 10 mV s<sup>-1</sup> from the two methods are shown in Fig. 13a. The curves from the two methods are consistent. Tafel slope of ~ 130 mV dec<sup>-1</sup> is obtained between 0.82-0.75 V without iR-correction.

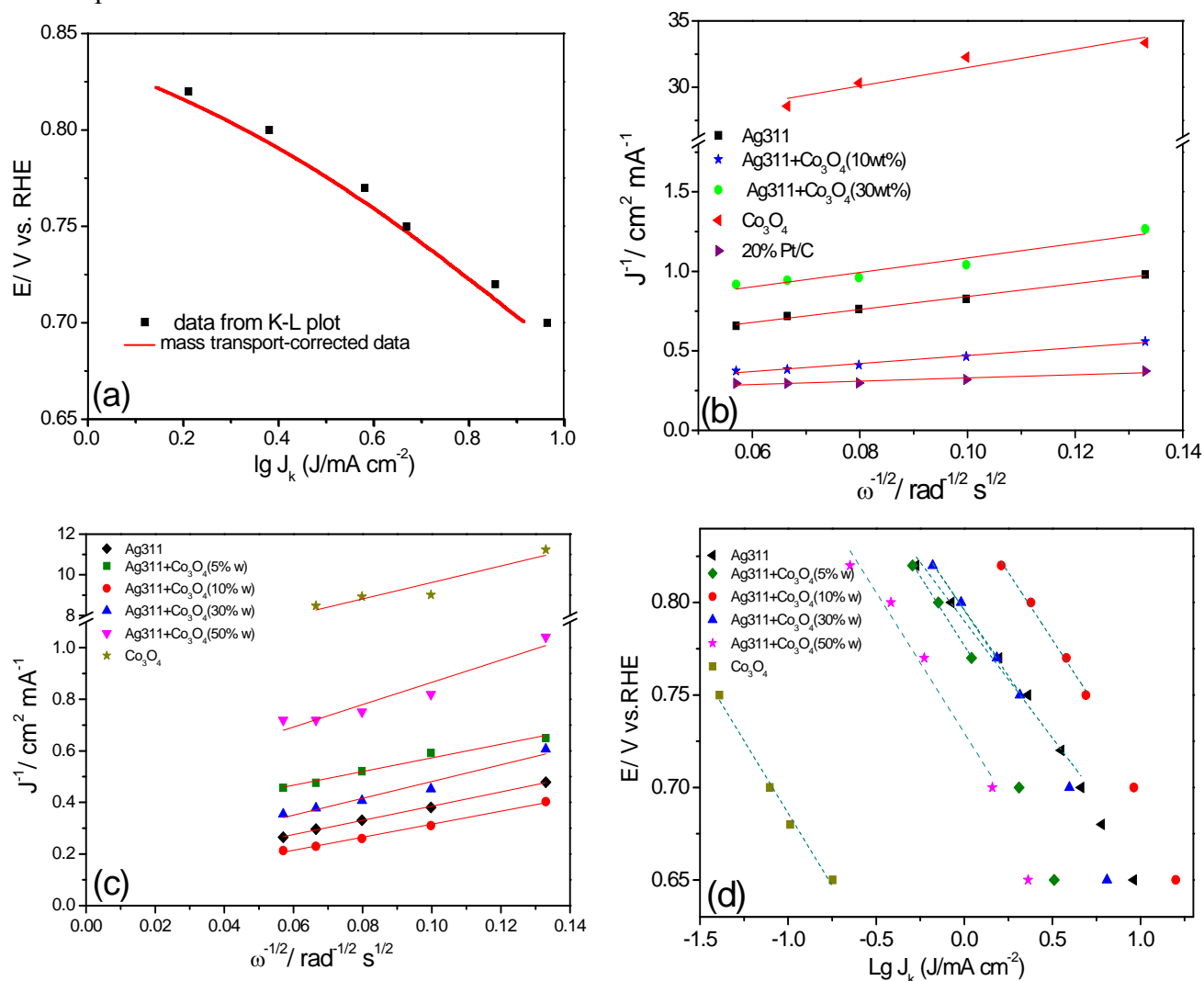


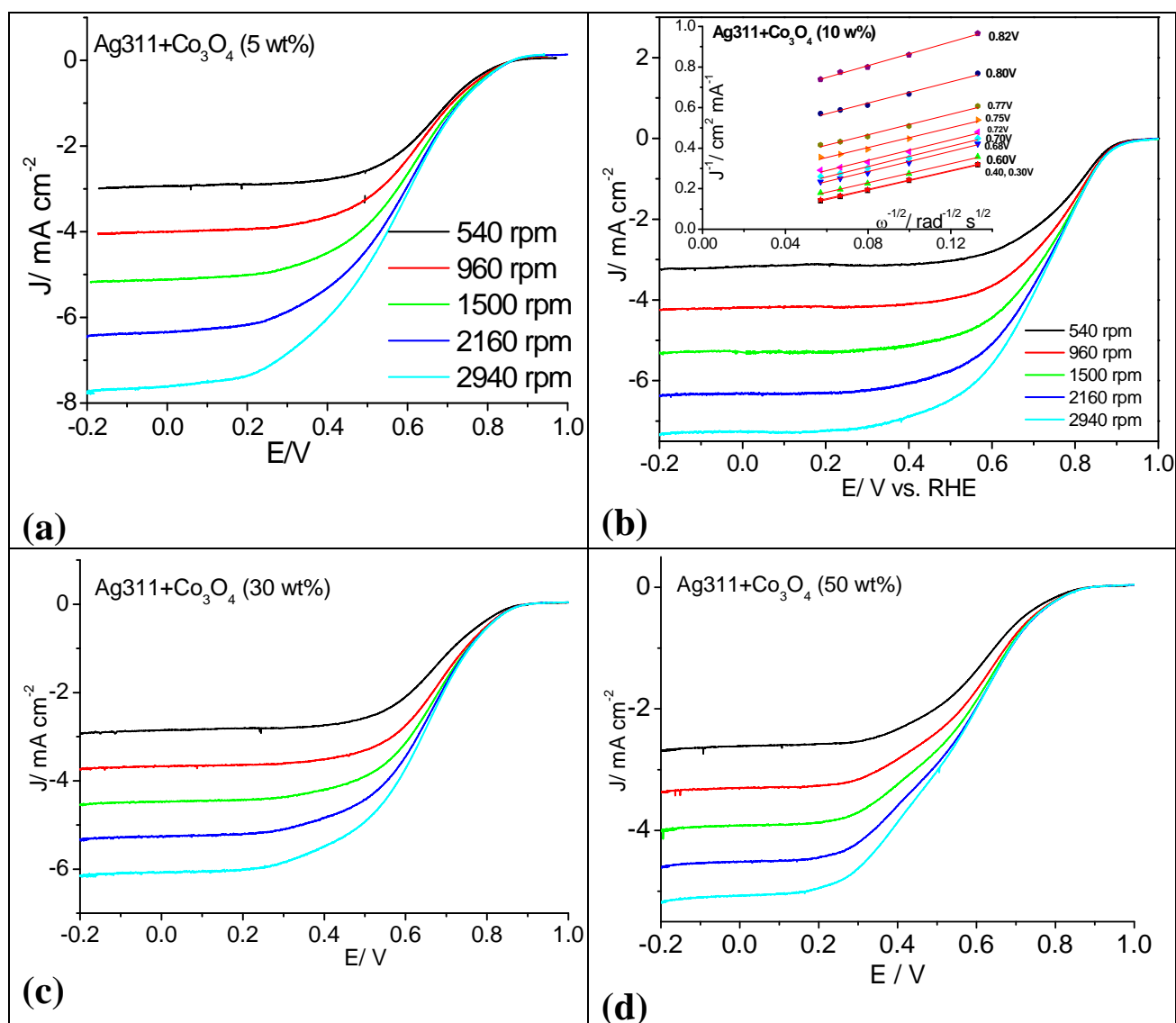
Fig. 13. (a) non-iR corrected Tafel plots at Ag311+ Co<sub>3</sub>O<sub>4</sub> (10 %) catalyst in 0.1M LiOH with 10 mV s<sup>-1</sup> obtained from the respective K-L plots (dots) or from mass-transport corrected currents (line). K-L plots for different catalysts scanned with 10 mV s<sup>-1</sup> at (b) 0.75 V<sub>RHE</sub> and (c) at 0.65V<sub>RHE</sub>. (d) Tafel plots obtained from K-L plots data at 10 mV s<sup>-1</sup>.

Fig. 14 shows the RRDE curves of different mixed catalysts obtained with 10 mV s<sup>-1</sup> at various rotation rates. In all cases, well developed plateaus for the diffusion limited currents are noticeable. Inset of Fig. 14b is an example of the K-L plots obtained for the Ag+Co<sub>3</sub>O<sub>4</sub> (10 %) catalyst at different potentials. K-L plots are linear and parallel, implying a first-order

reaction with respect to the dissolved oxygen concentration.[18] K-L plots have a y-axis intercept at higher potentials, which is related to the contribution of the kinetic current in the total current. On the other hand, at potentials below 0.4V, the K-L plots pass through the origin, indicating a pure diffusion limited process.

Levich plots ( $J_{lim}$  vs.  $\omega^{1/2}$ ) for the various catalysts are displayed in Fig. 14e, where the limiting currents are obtained from the respective data in Fig. 14. From the slope of Levich plot, the total number of electrons transferred during ORR is calculated, and is found to be close to  $4e^-/O_2$ , which is in agreement with that obtained from the ring currents.

K-L plots at different catalysts are compared: as examples, K-L plots at 0.75 V (Fig. 13b) and 0.65V (Fig. 13c) are shown. K-L slopes of the mixed catalysts are closer to that of Ag, but lower than that of  $Co_3O_4$ , suggesting similar kinetics of the mixed catalyst to Ag in ORR region, and the predominance of Ag role in the mixture for ORR. Tafel plots obtained from the corresponding K-L plots at different potentials for different catalysts are shown in Fig. 13d. Tafel slopes without iR-correction are  $\sim 140$  mV  $dec^{-1}$  for all catalysts of ORR, which are less than that at  $Co_3O_4$  ( $155$  mV  $dec^{-1}$ ), indicating slow kinetics at  $Co_3O_4$ .



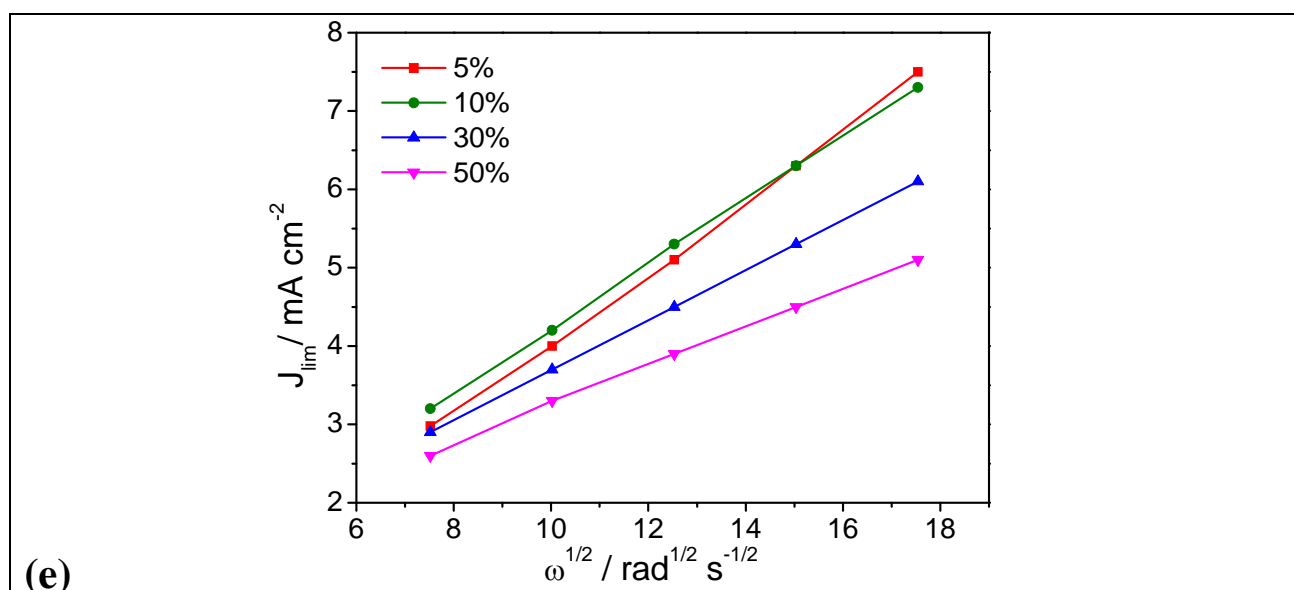


Fig. 14. RRDE measurements on Ag311+Co<sub>3</sub>O<sub>4</sub> (x %) on GC electrodes (a to d) in O<sub>2</sub>-saturated 0.1M LiOH solution at different rotation rates with 10 mV s<sup>-1</sup>. Loading for all: 1 mg cm<sup>-2</sup>. (e) Levich plot of ORR for different electrodes.

ORR/OER at 20% Co<sub>3</sub>O<sub>4</sub>-containing catalyst at different rotation rates is also obtained in a higher concentration (1M LiOH) solution, as shown in Fig. 15. An expansion of the anodic scan in ORR region is shown in Fig. 15b. The inset shows K-L plots at different potentials. Similar behavior to 0.1M LiOH is observed. However, lower diffusion limited current is observed.

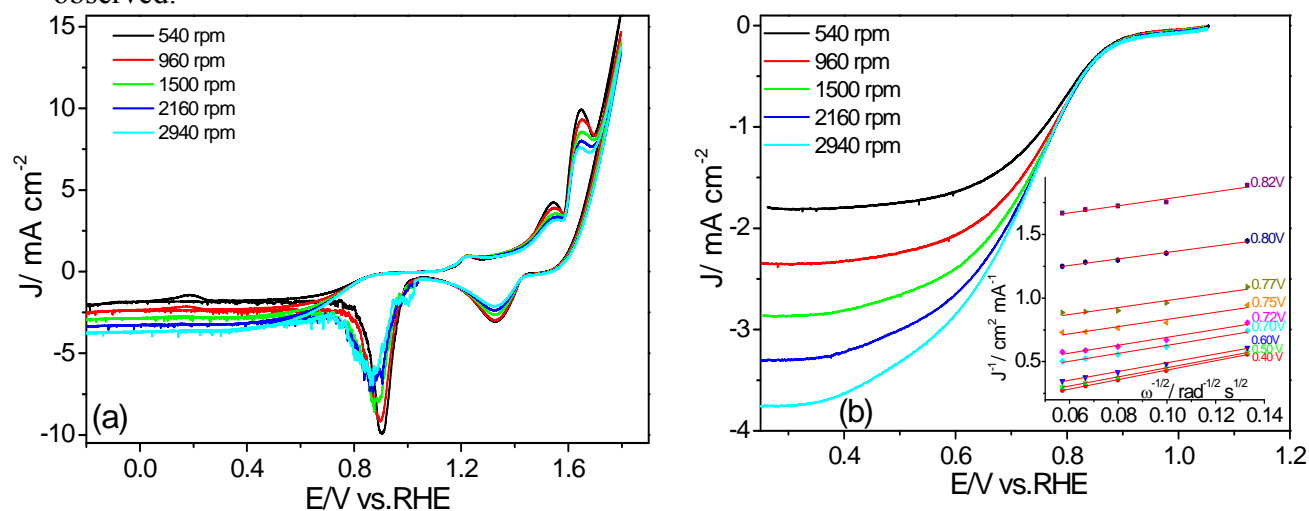


Fig. 15. (a) RRDE results on 20% mixed catalyst in 1M LiOH solution with loading 1 mg cm<sup>-2</sup> and 10 mV/s at different rotation speeds. (b) Anodic scan of ORR region, inset is K-L plots at different potentials on the same electrode.

#### A.6. Surface characterization of the Ag311+Co<sub>3</sub>O<sub>4</sub> mixed catalysts

Fig. 16a shows low-magnification SEM image of Ag311+Co<sub>3</sub>O<sub>4</sub> (10 w%) with a loading of 1 mg cm<sup>-2</sup> on GC without Nafion binder. The inset is a part of the surface with higher magnification, which shows the Co<sub>3</sub>O<sub>4</sub> nanoparticles with brighter contrast supported on the darker large Ag microparticles. On the other hand, addition of Nafion is important to fix the catalyst on the substrate, and has no significant effect on activity. Better distribution of the

catalyst is observed when Nafion is used, as shown in Fig. 16b, but the images are slightly blurred due to Nafion, and the contrast between Ag and  $\text{Co}_3\text{O}_4$  is not high. Higher magnification SEM with Nafion in another region of the electrode is also shown in Fig. 16c. The surface is also monitored after performing several ORR/OER cycles: the electrode was emersed at 1V from the solution, and SEM images were captured. Some morphological changes are observed, which might be due to roughening or rearrangement of the particles on the surface, see Fig. 16d.

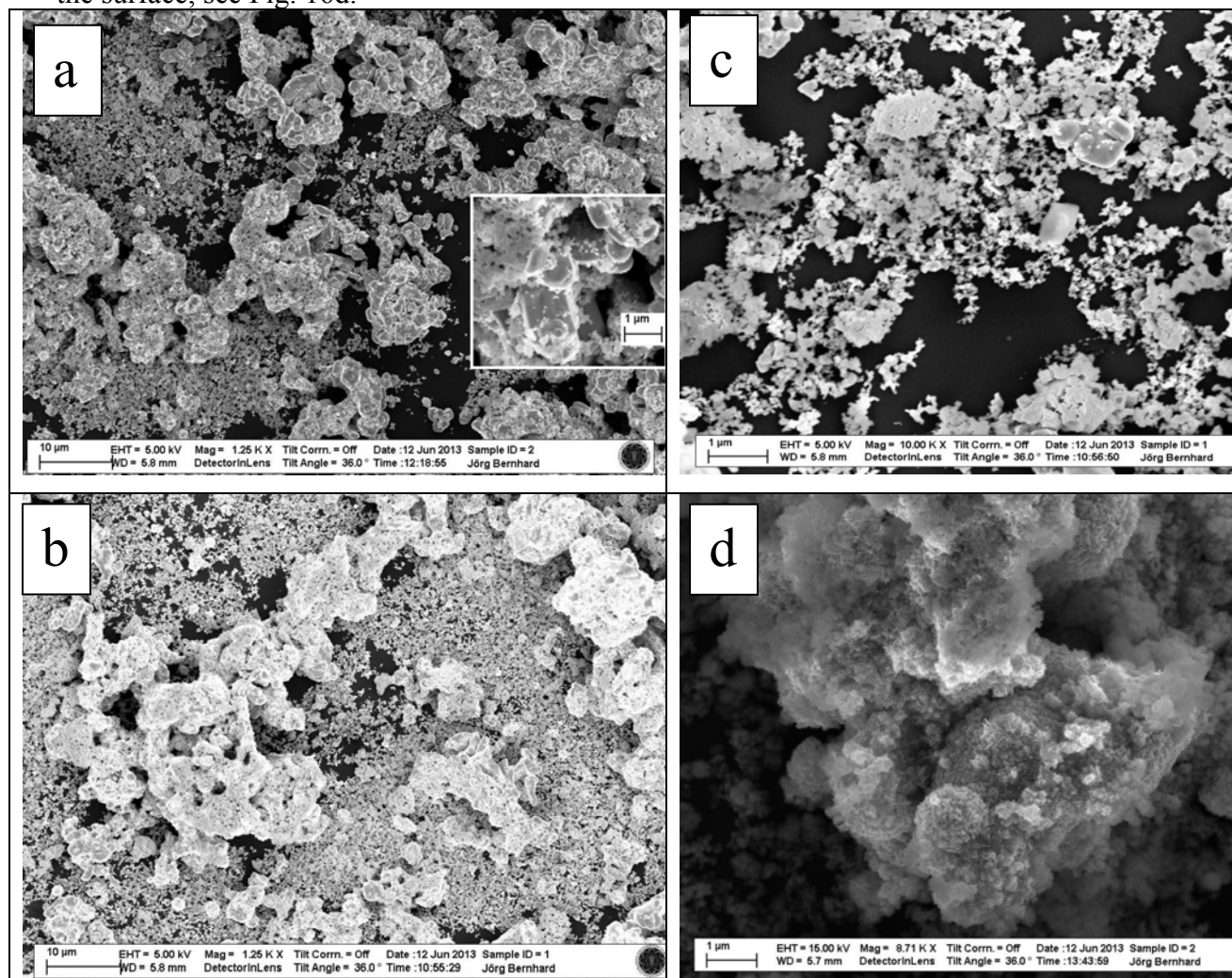


Fig. 16. SEM images of  $\text{Ag}_{311}+\text{Co}_3\text{O}_4(10\%)/\text{GC}$  catalyst with  $1\text{mg cm}^{-2}$  (a) without Nafion; inset is a higher magnification, and (b) with Nafion. Higher magnification of the same sample with Nafion before cycling (c) and after several cycles (d).

#### A.7. $\text{Ni}+\text{Co}_3\text{O}_4$ mixed catalyst

Fig. 17. shows RRDE measurements at  $\text{Ni}+\text{Co}_3\text{O}_4$  (10 wt%) at different rotation rates (540-2940 rpm). The onset potential of ORR is about 0.65V, which is comparable to that obtained on  $\text{NiCo}_2\text{O}_4$  catalyst.[19] OER onset is at about 1.55V. The ORR reduction currents increase monotonically with the rotation speed increase. The percentage of  $\text{HO}_2^-$  is in the range of 35 to 65% for all rotations, see inset of Fig. 17. The unexpected lower  $\text{HO}_2^-$  % at higher rotation rates could be due to passivation of the Pt ring or contaminants on it.

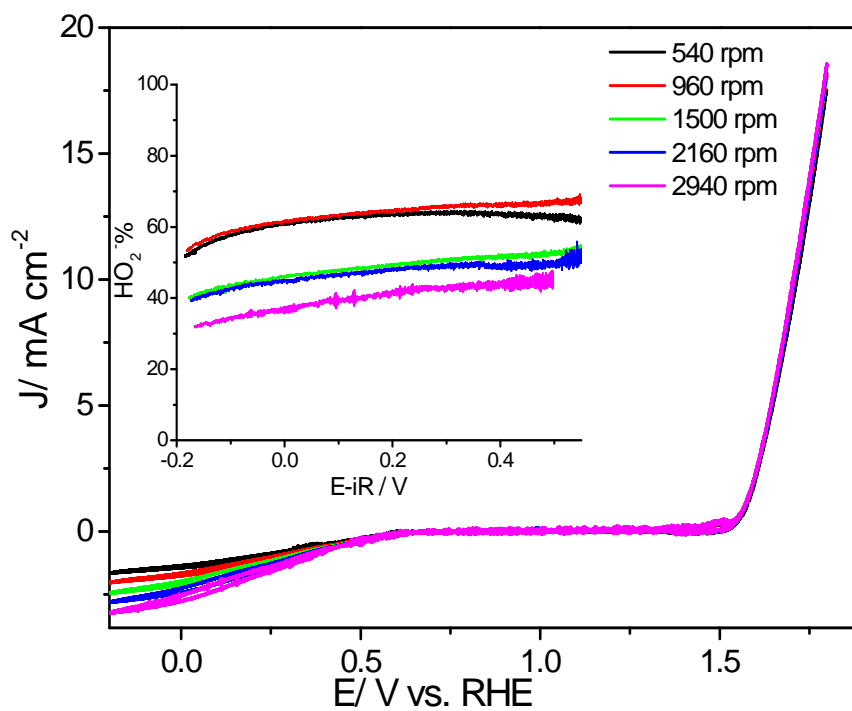


Fig. 17. RRDE measurements at Ni+Co<sub>3</sub>O<sub>4</sub> (10 w%) on GC at different rotation rates and with 5 mV s<sup>-1</sup> in O<sub>2</sub>-saturated 0.1M LiOH solution. Inset is the corresponding peroxide anion yield. Loading is 1 mg cm<sup>-2</sup>.

## A.8. References

- [1] L. Jiang, A. Hsu, D. Chu, R. Chen, *Journal of Electroanalytical Chemistry* 629 (2009) 87-93.
- [2] N.M. Markovic, H.A. Gasteiger, P.N. Ross, *Journal of Physical Chemistry* 99 (1995) 3411-3415.
- [3] Q. Tang, L. Jiang, J. Qi, Q. Jiang, S. Wang, G. Sun, *Applied Catalysis B: Environmental* 104 (2011) 337-345.
- [4] D. Šepa, M. Vojnović, A. Damjanovic, *Electrochimica Acta* 15 (1970) 1355-1366.
- [5] H.M.A. Amin, H. Baltruschat, D. Wittmaier, K.A. Friedrich, *Electrochimica Acta* 151 (2015) 332-339.
- [6] T. Nakagawa, N.S. Bjorge, R.W. Murray, *Journal of the American Chemical Society* 131 (2009) 15578-15579.
- [7] M. Wohlfahrt - Mehrens, J. Heitbaum, *J. Electroanal. Chem.* 237 (1987) 251 - 260.
- [8] Y. Lee, J. Suntivich, K.J. May, E.E. Perry, Y. Shao-Horn, *The Journal of Physical Chemistry Letters* 3 (2012) 399-404.
- [9] N.I. Andersen, A. Serov, P. Atanassov, *Applied Catalysis B: Environmental* 163 (2015) 623-627.
- [10] K.-N. Jung, S.M. Hwang, M.-S. Park, K.J. Kim, J.-G. Kim, S.X. Dou, J.H. Kim, J.-W. Lee, *Scientific Reports* 5 (2014) 7665.
- [11] D. Wittmaier, S. Aisenbrey, N. Wagner, K.A. Friedrich, *Electrochimica Acta* 149 (2014) 355-363.
- [12] B.S. Yeo, A.T. Bell, *Journal of the American Chemical Society* 133 (2011) 5587-5593.
- [13] Y. Wang, X. Lu, Y. Liu, Y. Deng, *Electrochemistry Communications* 31 (2013) 108-111.
- [14] J.A. Koza, Z. He, A.S. Miller, J.A. Switzer, *Chemistry of Materials* 24 (2012) 3567-3573.
- [15] J. Suntivich, E.E. Perry, H.A. Gasteiger, Y. Shao-Horn, *Electrocatalysis* 4 (2013) 49-55.
- [16] J. Guo, H. Li, H. He, D. Chu, R. Chen, *Journal of Physical Chemistry C* 115 (2011) 8494-8502.
- [17] F.H.B. Lima, J.F.R. de Castro, E.A. Ticianelli, *Journal of Power Sources* 161 (2006) 806-812.
- [18] K.J.J. Mayrhofer, D. Strmcnik, B.B. Blizanac, V. Stamenkovic, M. Arenz, N.M. Markovic, *Electrochimica Acta* 53 (2008) 3181-3188.
- [19] Z.-Q. Liu, Q.-Z. Xu, J.-Y. Wang, N. Li, S.-H. Guo, Y.-Z. Su, H.-J. Wang, J.-H. Zhang, S. Chen, *International Journal of Hydrogen Energy* 38 (2013) 6657-6662.



## Appendix B: Investigation of stability of propylene carbonate-based electrolyte at different electrodes: Effect of water

### B.1. Introduction

The electrochemical stability and performance of propylene carbonate (PC) solvent have been extensively studied in Li-ion batteries. Therefore, we started with it as a first candidate. Organic carbonates are shown to decompose in Ar-saturated solutions, releasing CO<sub>2</sub> during oxidation, and the decomposition potential depends on the electrode material and the water content.[1, 2] Qualitative investigations of the decomposition of organic electrolytes are carried out by DEMS at different electrodes. Semi-quantitative comparison of the amount of evolved gas is possible as long as the same conditions are employed. The aim of this work was also to adjust the DEMS set up and cells for organic systems, and to check the stability of the classical solvent PC. This part of the work was done at the very beginning of our Li-O<sub>2</sub> project in 2012. We investigated the electrochemical behavior upon oxidation and reduction of PC in LiClO<sub>4</sub> salt by online DEMS technique. The influence of water on the decomposition of the electrolyte was also investigated. These preliminary results gave important indications in terms of stability. Thus, this work is extended to other organic electrolytes, and is considered as a preliminary step for the study of ORR and OER in aprotic electrolytes.

### B.2. Experimental

The DEMS cell used here is the dual-thin layer cell, which is described elsewhere.[3-5] The working electrode is a 1 cm diameter disc with an exposed geometric area of 0.283 cm<sup>2</sup>, which is defined by Teflon spacers underneath the electrode. The electrolyte is 1M LiClO<sub>4</sub> in PC. The electrolyte passes through the cell from the inlet to the working electrode with a flow rate of 5 μl s<sup>-1</sup>, where electrochemical reactions take place, and the volatile products are swept away with the electrolyte into the second compartment, where a permeable membrane (Gore Tex®, Germany) is placed as the interface to the quadruple mass spectrometer (Balzer QMG 422, Pfeifer Vacuum). A saturated Ag/AgNO<sub>3</sub> electrode in PC is used as the reference electrode (SSE). It has a potential of 0.65V vs. SCE.[6] The reference electrode was placed at the inlet of the electrolyte. Two Pt counter electrodes were employed to reduce the ohmic drop: the main counter electrode at the electrolyte outlet, while another counter was placed at the inlet. The main counter electrode was connected via a resistance of 100 Ω, whereas the second via 100 kΩ in order to get better distribution of the current in the cell. All CVs and MSCVs were recorded with a home made potentiostat with 10 mV/s, and in Ar-saturated solution. The initial water content of water was reduced by purging the solution continuously with Ar for some time prior to and during the experiment. Due to the low vapor pressure of PC, the total pressure inside the ionization chamber is low (at least one order of magnitude lower than in the case of aqueous media). Thus, the ion reactions inside the ion source can be neglected.[1]

LiClO<sub>4</sub> (battery grade, Sigma-Aldrich) and Propylene carbonate (anhydrous 99.7%, Aldrich) were used as received. Milli-Q water was used (18.2 MΩ cm, Millipore, Germany). The electrodes used in this investigation are GC, Pt, Au and BDD. BDD electrode was purchased from Adamant La-Chaux-de-Fonds, Switzerland. DDD consists of a layer of 1 μm diamond doped with 6000 ppm boron on a 1 μm thick silicon wafer. The other electrodes are polycrystalline electrodes. The electrodes were first polished to a mirror finish with 0.05 μm

alumina slurry on a polishing sheet fixed on a rotating machine. The electrodes were then cleaned with acetone (Aldrich, 99.5%) and Milli-Q water, and then dried with KIMTECK wipes. Highly pure Ar (Air Liquide, 99.999%) was used for purging the electrolyte.

### B.3. Results and discussion

The electrolyte plays a crucial role in the rechargeability because the decomposition products of the electrolyte will likely have a negative effect on the recharge potential and turn-over efficiency of the Li-air battery. Different electrocatalytic activities of different electrode materials can significantly influence the course of electrolytic decomposition reactions.[7] Comparison of the behavior of PC at different electrode materials is shown in Fig. 1. The CV is featureless at narrow potential window and without observation of any volatile products in the MSCV. Within this potential region (-1.5 to +1.5 V vs. SSE), PC is stable towards electrochemical decomposition. However, expanding the potential gradually to larger limits in the cathodic and anodic directions leads to appearance of ionic currents of different masses, indicating decomposition as shown in MSCV of Fig. 2.

The fact that the anodic and cathodic currents are quite stable with cycling can be taken as a hint that a passivating film is formed upon reduction and is possibly reoxidized upon oxidation. PC decomposes at certain potentials in the anodic and cathodic limits depending on the electrode material. Obviously, the evolution of decomposition products in the negative-going scan coincides well with the cathodic peak in the CV. Thus, the faradaic currents are attributed to electrolyte decomposition and electrode passivation (since in Ar-sat. solution). Therefore, the faradaic charge could overestimate the coulombic efficiency when oxygen reduction and evolution is studied in this electrolyte. Therefore, this electrolyte is unsuitable for ORR/OER. Several decomposition products and byproducts are detected here using DEMS, and include CO<sub>2</sub> (m/z 44), propene (m/z 41), propanal (m/z 58), hydrogen (m/z 2), and 2-ethyl-4-methyl-dioxalane (m/z 87), as shown in Fig. 2, 3. In agreement with Novak et al., signals for masses 41, 58 and 87 were observed upon oxidative decomposition of PC.[8] CO<sub>2</sub> (m/z=44) was detected as the main decomposition product upon both oxidation and reduction of PC.[9, 10] This assesses the feasibility of our setup and procedure. No oxygen evolution for OER was noticed since the solution is oxygen-free, as shown in Fig. 3. Small ionic currents for mass 58 are observed at higher potential, Fig. 3.

The potential stability window of PC depends on the electrode material: the stability is found in the following order: BDD>GC>Au>Pt. This could be due to the higher activity of Au and Pt towards electrolyte degradation than GC and BDD. At potentials more negative to -1.5V, hydrogen evolution is observed at Pt due to presence of traces of water in solution. In addition, hydrogen evolution potential is shifted to more negative values from Pt to BDD as shown from the signal of (m/z 2). BDD shows the widest potential window, in which PC could be stable. A mass signal for propene appears at carbon-containing electrodes at higher potentials; whereas it is absent in case of active metals as Pt and Au electrodes. Similar behavior has been observed in literature for PC at active carbon, and was attributed to a reductive solvent decomposition product, which is possibly formed together with alkyl carbonates[9] according to scheme 1a. When PC is oxidized, the produced CO<sub>2</sub> and propylene oxide might further react and form other by-products with masses of 58 and 87. These mass signals are observed at potentials more positive to 1.5V (vs. SSE) only at BDD and GC

electrodes. These signals were also observed by mass spectrometry in 1M LiClO<sub>4</sub>/PC on graphite.[11]

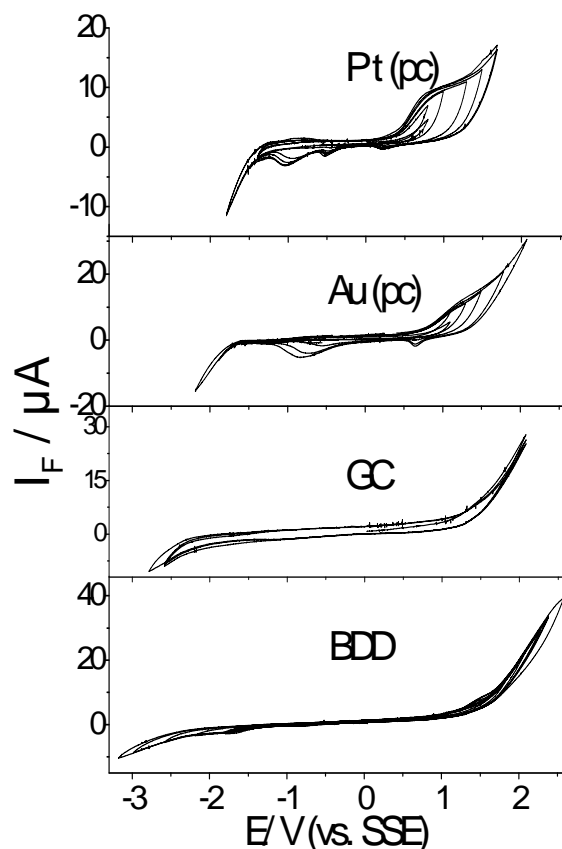


Fig. 1. CVs in Ar-saturated 1M LiClO<sub>4</sub>/PC at different electrodes with various potential windows, scan rate=10mV/s, flow rate: 5 $\mu\text{s}^{-1}$ .

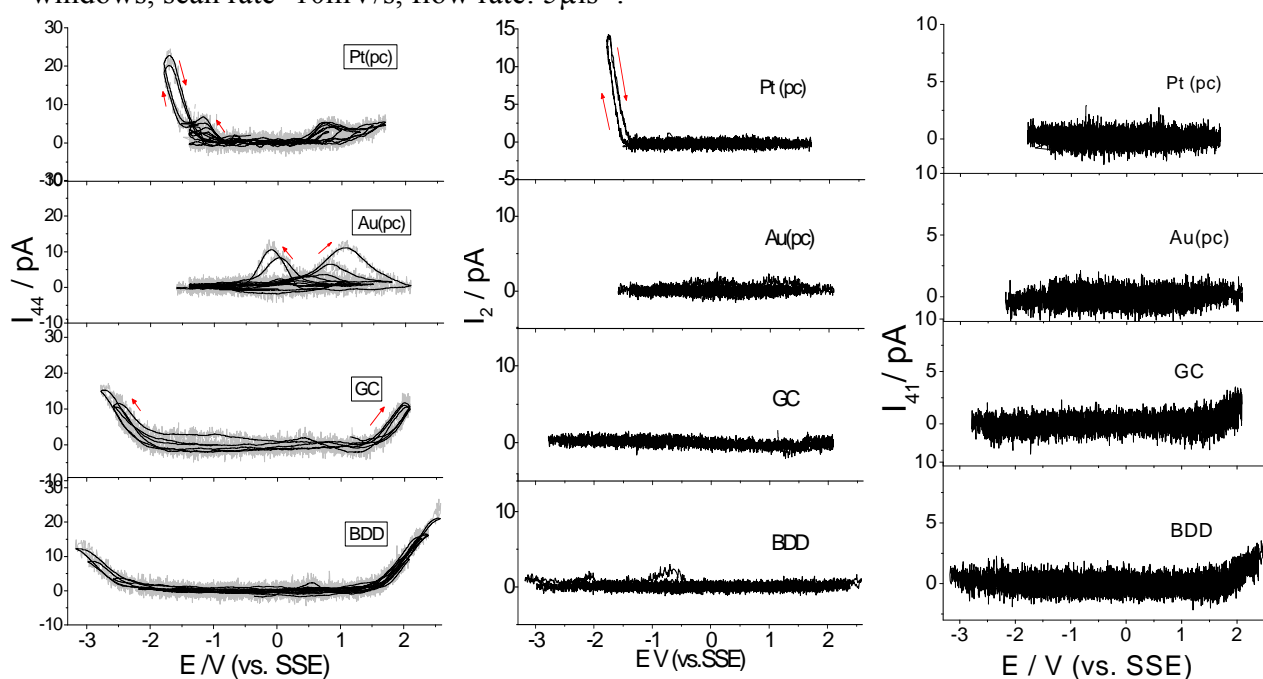


Fig. 2. MSCVs for masses  $m/z = 44$  (left), 2 (middle) and 41 (right) representing CO<sub>2</sub>, H<sub>2</sub> and propene, respectively, at different electrodes in 1M LiClO<sub>4</sub>/PC with scan rate of 10mV/s. Flow rate: 5 $\mu\text{s}^{-1}$ .

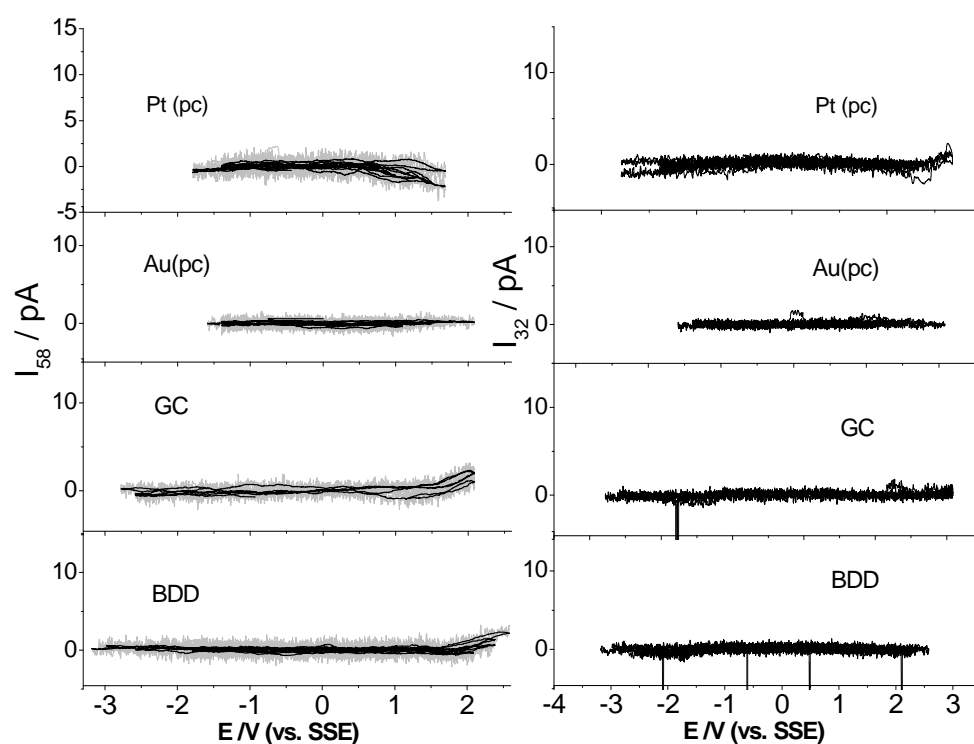
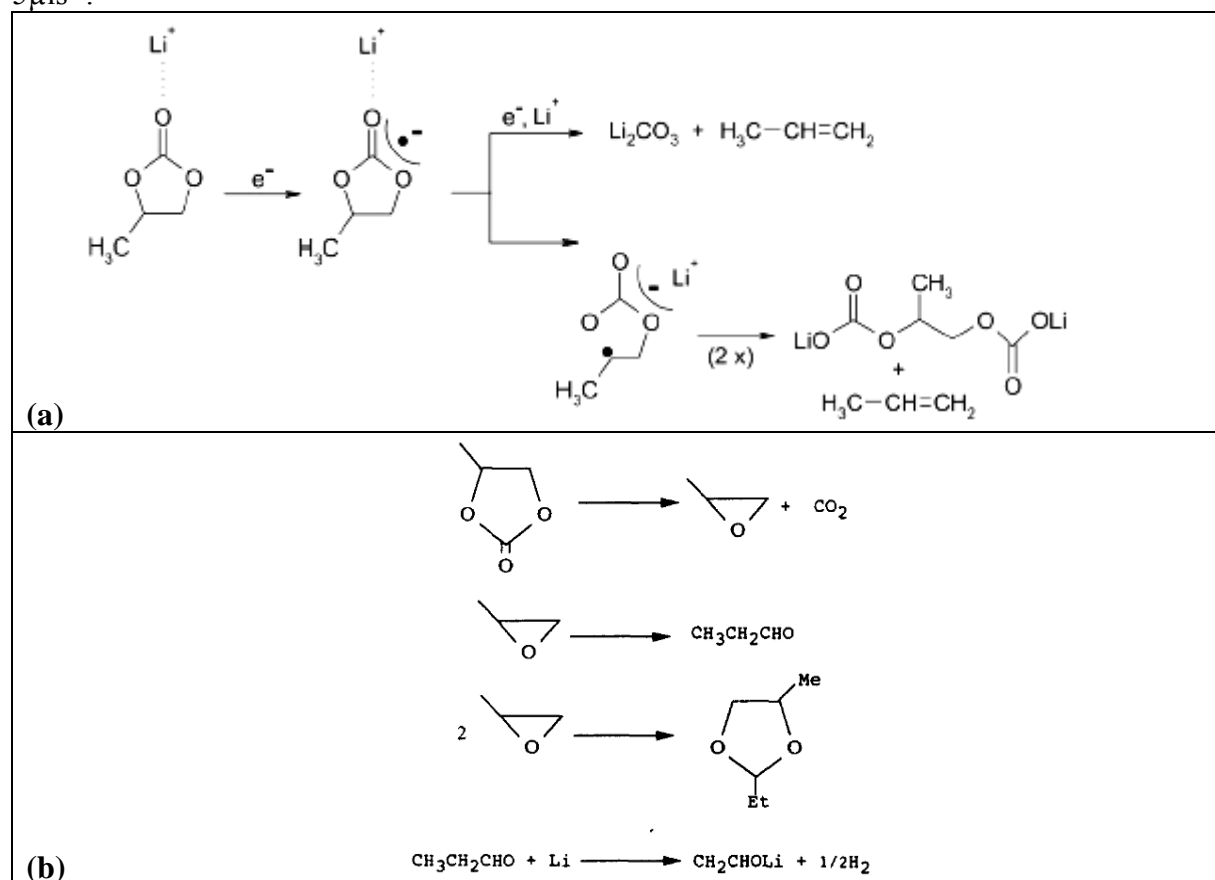
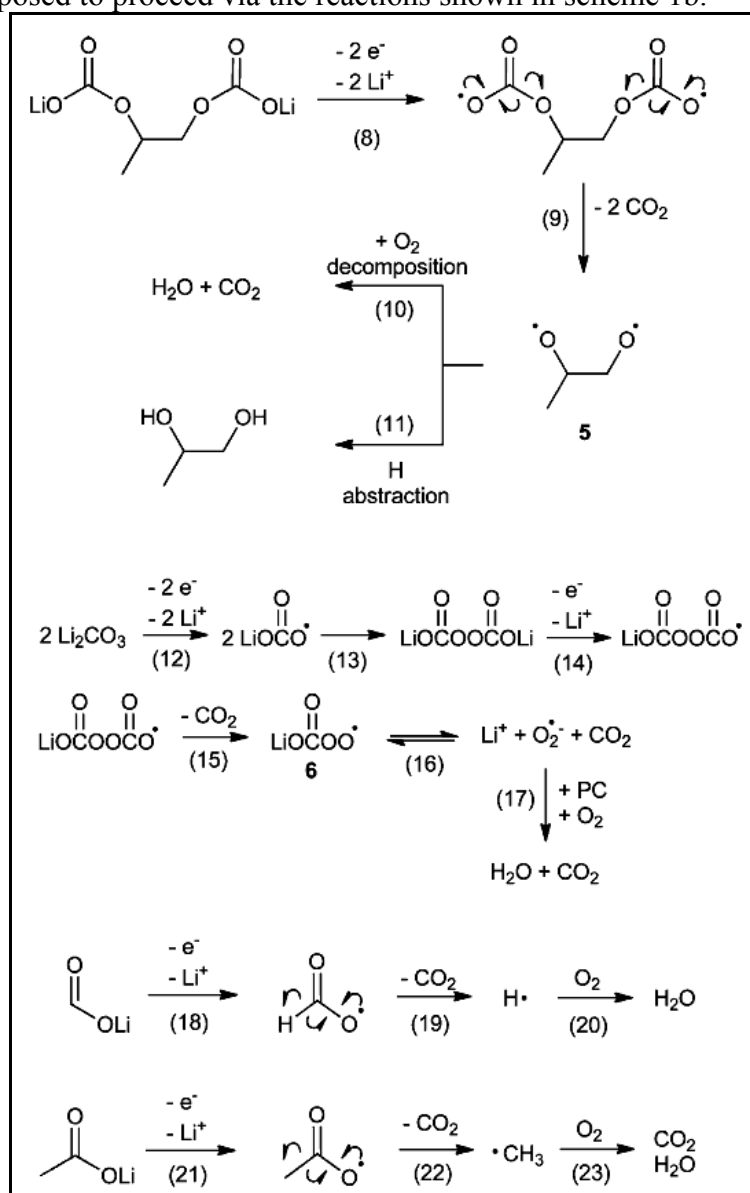


Fig. 3. MSCVs for masses  $m/z=58$  (left) and  $32$  (right) representing propanal and  $O_2$  respectively, at different electrodes in  $1M LiClO_4/PC$  with scan rate of  $10mV/s$ . Flow rate:  $5\mu s^{-1}$ .



Scheme 1. Proposed mechanisms upon reduction of PC. (a) is reprinted from [9], and (b) is reprinted from [11].

These results revealed that PC is instable solvent for Li-air battery applications. Quantitative and qualitative analyses demonstrate the possible decomposition products. Previous reports proposed that  $\text{CO}_2$  evolution is a result of side reactions with the electrolyte.[9, 12] Here, at all electrode materials, there is a major signal for mass 44. This is most probably due to  $\text{CO}_2$  evolution. Except GC, the only source of  $\text{CO}_2$  is the solvent PC. Thus,  $\text{CO}_2$  evolution is an indicative of electrolyte decomposition. PC is oxidized, releasing  $\text{CO}_2$ , which originates possibly from carbonate group or other alkyl carbonate species, see scheme 2. Oxidation of PC is assumed to proceed via the formation of an intermediate as shown in scheme 2. Oxidation of  $\text{C}_3\text{H}_6(\text{OCO}_2\text{Li})_2$ , which is formed in the cathodic scan, leads to several products, which react with protons (from  $\text{H}_2\text{O}$  traces) or with  $\text{O}_2$  (traces from atmosphere) forming  $\text{CO}_2$  and  $\text{H}_2\text{O}$ . While cathodically, PC is reduced to alkylcarbonate, which can be protonated to release  $\text{CO}_2$ . [1] The formation of a passive film is assumed to consist of  $\text{Li}_2\text{CO}_3$  and oligomeric alkyl carbonates according to scheme 1a.[9] This passive layer could help in the stability of PC against lithium. Evolution of  $\text{CO}_2$ , propanal and  $\text{H}_2$  during reduction of the electrolyte is proposed to proceed via the reactions shown in scheme 1b.



Scheme 2. Proposed mechanism for oxidation of PC.[10]

The effect of water on electrolyte decomposition is investigated since metal-air batteries are supposed to work under ambient conditions. The effect of water in PC was firstly studied by Vielstich and coworkers on Pt electrode using DEMS.[6] Here, influence of water on the decomposition of PC is studied at BDD electrode in 1M LiClO<sub>4</sub>/PC containing different amounts of added water (see Fig. 4). The current at the anodic peak between 1 and 2V increases with addition of water. Each MSCV of  $m/z=44$  shows a maximum between +1 to +2 V (vs. SSE), which is followed by a monotonic increase at higher potentials. This maximum correlates with the plateau in the CV, and the monotonic increase is due to bulk oxidation of PC or side reactions. This peak cannot be only assigned to PC decomposition since parallel reactions like water and ClO<sub>4</sub><sup>-</sup> decomposition cannot be excluded. Noticeably, higher water content leads to a stronger generation of CO<sub>2</sub>. This observation is in agreement with a previous report.[6] The cathodic peak at about -3.5V vs. SSE is assigned to the intercalation of the solvated Li<sup>+</sup> ions and formation of SEI[7] or the reaction of residual water with electrolyte since addition of water shifts this peak to more negative potentials and increases its current as shown in Fig. 4. The maximum of this peak is shifted to more negative potentials with increasing water content.

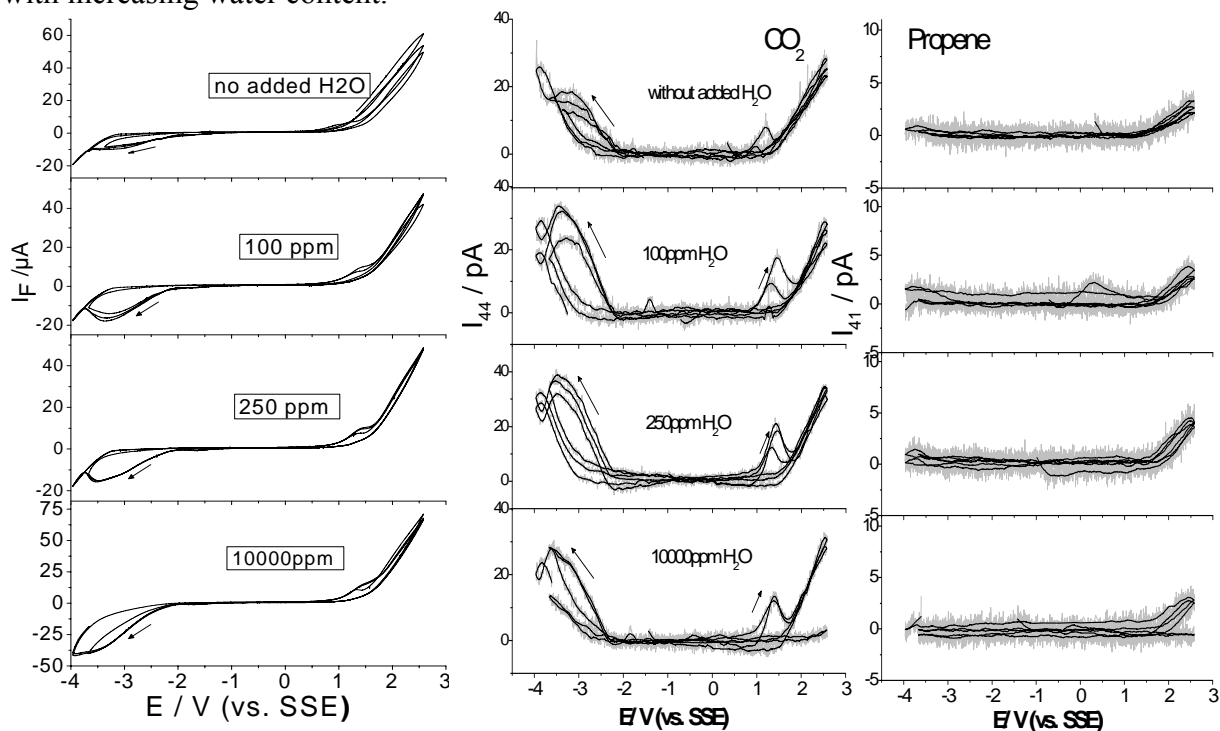


Fig. 4. CVs (left) and MSCVs of masses  $m/z=44$  (middle) and  $m/z=41$  (right) at BDD electrode in Ar-saturated 1M LiClO<sub>4</sub>/PC with scan rate of 10mV/s, flow rate: 5 $\mu$ l s<sup>-1</sup>.

Semi-quantitative determination of the initial water content in the solution is done by standard addition method, where the signal of H<sub>2</sub> is recorded in PC solutions containing known water contents, see Fig. 5. Plot of the amount of evolved H<sub>2</sub> versus the amount of added water showed a linear relation, Fig. 5 (right). Hydrogen evolution begins at potentials more negative to -2.5V vs. SSE. The straight line intercepts the x-axis at ca. 850 ppm, which corresponds to the initial amount of water in this solution, as shown in Fig. 5 (right). Most of the water originates from the LiClO<sub>4</sub> salt since it is used as received without further drying, and from

humidity in the solvent and electrolyte, which is gained during solution transfer to the cell. This solution was not prepared in the Glove box. The results discussed above give a clear insight into the stability of  $\text{LiClO}_4/\text{PC}$  on different electrode materials.

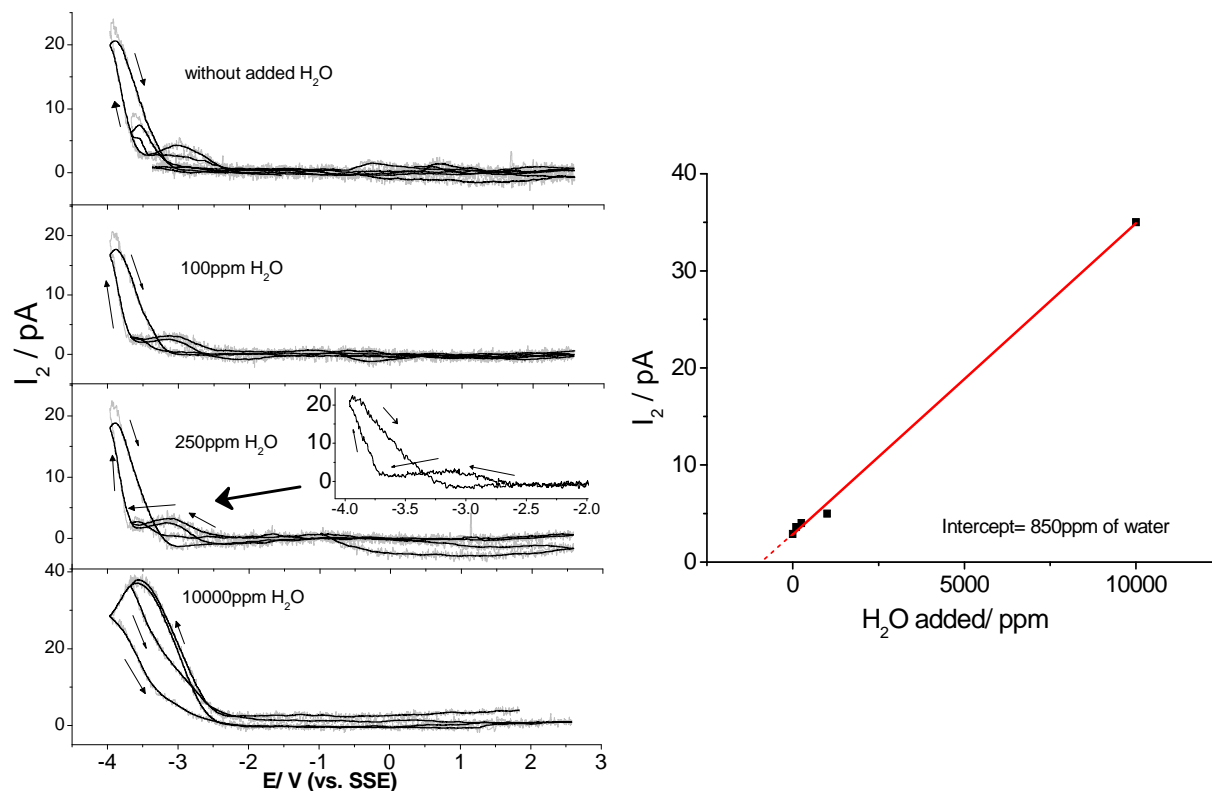


Fig. 5. MSCVs (left panel) of masses  $m/z = 2$  representing  $\text{H}_2$  at BDD electrode in 1M  $\text{LiClO}_4/\text{PC}$  containing different with scan rate of  $10\text{mV/s}$ , flow rate:  $5\mu\text{s}^{-1}$ . Right panel: plot  $\text{H}_2$  peak ionic current vs. the amount of added water.

#### B.4. References

- [1] G. Eggert, J. Heitbaum, *Electrochimica Acta* 31 (1986) 1443-1448.
- [2] E. Cattaneo, B. Rasch, W. Vielstich, *Journal of Applied Electrochemistry* 21 (1991) 885-894.
- [3] H. Baltruschat, *Journal of the American Society for Mass Spectrometry* 15 (2004) 1693-1706.
- [4] Z. Jusys, J. Kaiser, R.J. Behm, *Electrochimica Acta* 49 (2004) 1297-1305.
- [5] H. Baltruschat, in: A. Wieckowski (Ed.), *Interfacial Electrochemistry*, Marcel Dekker, Inc., New York, Basel, 1999, pp. 577 - 597.
- [6] B. Rasch, E. Cattaneo, P. Novak, W. Vielstich, *Electrochimica Acta* 36 (1991) 1397-1402.
- [7] R. Imhof, P. Novak, *Journal of the Electrochemical Society* 145 (1998) 1081-1087.
- [8] R. Imhof, P. Novak, *Journal of the Electrochemical Society* 146 (1999) 1702-1706.
- [9] M. Hahn, A. Wursig, R. Gallay, P. Novak, R. Kotz, *Electrochemistry Communications* 7 (2005) 925-930.
- [10] S.A. Freunberger, Y. Chen, Z. Peng, J.M. Griffin, L.J. Hardwick, F. Bardé, P. Novák, P.G. Bruce, *Journal of the American Chemical Society* 133 (2011) 8040-8047.
- [11] M. Arakawa, J.-i. Yamaki, *Journal of Power Sources* 54 (1995) 250-254.
- [12] B.D. McCloskey, D.S. Bethune, R.M. Shelby, T. Mori, R. Scheffler, A. Speidel, M. Sherwood, A.C. Luntz, *The Journal of Physical Chemistry Letters* 3 (2012) 3043-3047.



**Conferences:**

- 4<sup>th</sup> conference on Chemistry, **Chem. 04**, organized by the Chemistry Department, Faculty of Science, Cairo University, Apr. 2006 (Organizing committee).
- 7<sup>th</sup> **International Symposium** on "New Trends in Chemistry", Cairo, Egypt, Jan., 2008.
- 5<sup>th</sup> conference on Chemistry, **Chem. 05**, organized by the Chemistry Department, Faculty of Science, Cairo University, Mar., 2008 (Organizing committee).
- 4<sup>th</sup> **International conference on scientific research and its applications**, Cairo University, Dec., 2008.
- 8<sup>th</sup> **International Symposium on New Trends in Chemistry**, Cairo, Egypt, Jan., 2009.
- 2<sup>nd</sup> **Congress of African Societies of Chemistry**, Cairo, Egypt, Jan., 2009 (Organizing committee).
- 1<sup>st</sup> International Green Renewable Energy Conference **IGREC**, Dec, 2009, Cairo, Egypt
- 5<sup>th</sup> **International conference on scientific research and its applications**, Cairo University, Dec., 2009.
- 2<sup>nd</sup> **Winter school of electrochemistry**, Feb. 2012, Kleinwalsertal, Austria.
- **GDCh Electrochemistry 2012** conference, Sep. 2012, Munich, Germany.
- Poster: "Strom aus Luft und Li", **3. Kompetenztreffen Elektromobilität in NRW**, 27. Nov. 2014, Essen, Germany
- Oral: "Efficient Electrocatalytic Oxygen Reduction and Water Oxidation at Metal oxide+ Ag Mixed Electrode in Alkaline Media, **109. AGEF-Seminar**, Nov. 2015, Forschungszentrum Jülich, Germany
- Poster: " Bifunctional electrocatalytic effect for oxygen reduction and evolution in Li-O<sub>2</sub> batteries: RRDE and DEMS insights" , International Battery Association **IBA2016**, Mar. 2016, Nantes, France.
- Oral: Electrocatalytic activity of Co<sub>3</sub>O<sub>4</sub>-based catalyst in DMSO electrolyte and study of G4-DMSO mixed solvent for Li-O<sub>2</sub> batteries" **67<sup>th</sup> Annual Meeting of ISE**, Aug. 2016, The Hague, Netherlands.

**Publications:**

- "Nanotube Arrays as Photoanodes for Dye Sensitized Solar Cells Using Metal Phthalocyanine Dyes" *Nada F. Atta, Hatem M.A. Amin, Mohamed W. Khalil, Ahmed Galal, Int. J. Electrochem. Sci.*, 6 (2011) 3316–3332
- "Synthesis and Photoelectrochemical Behavior of a Hybrid Electrode Composed of Polyaniline Encapsulated in Highly Ordered TiO<sub>2</sub> Nanotubes Array" *Nada F. Atta, Ahmed Galal, Hatem M.A. Amin, Int. J. Electrochem. Sci.*, 7 (2012) 3610–3626
- "Monodispersed Gold Nanoparticles Decorated Carbon Nanotubes as an Enhanced Sensing Platform for Nanomolar Detection of Tramadol" *Nada F. Atta, Rasha A. Ahmed, Hatem M.A. Amin, Ahmed Galal, Electroanalysis*, 24 (2012) 2135-2146
- "Modified carbon-free silver electrodes for the use as cathodes in lithium-air batteries with an aqueous alkaline electrolyte", *Dennis Wittmaier, Norbert Wagner, K. Andreas Friedrich, Hatem M.A. Amin, Helmut Baltruschat, Journal of Power Sources*, 265 (2014) 299-308

- " **A Highly Efficient Bifunctional Catalyst for Alkaline Air-Electrodes Based on a Ag and Co<sub>3</sub>O<sub>4</sub> Hybrid: RRDE and Online DEMS Insights**" *Hatem M.A. Amin, Helmut Baltruschat, Dennis Wittmaier, K. Andreas Friedrich*, *Electrochimica Acta*, 151 (2015) 332–339
- " **A carbon-free Ag-Co<sub>3</sub>O<sub>4</sub> composite as a bifunctional catalyst for oxygen reduction and evolution: spectroscopic, microscopic and electrochemical characterization**" Hatem M.A. Amin, C. J. Bondue, S. Eswara. U. Kaiser. H. Baltruschat, submitted
- " **On the role of metal oxide in oxygen evolution reaction: isotope labeling together with DEMS approach**" H. M. Amin, H. Baltruschat, in preparation
- " **Oxygen reduction and evolution reaction in a mixed organic electrolyte: RRDE and DEMS study**" H. M. Amin, H. Baltruschat, in preparation

**Patent:**

- " **Bifunktionaler Katalysator als Kathodenmaterial für die Metall-Luft Batterie**" D. Wittmaier, N. Wagner, H. M. Amin, H. Baltruschat, DE 10 2014 102 301.8